Title
Slow Photoelectron Velocity-Map Imaging and Infrared Photodissociation Spectroscopy of Cryogenically-Cooled Ions

Author
Babin, Mark

Publication Date
2021

Peer reviewed|Thesis/dissertation

Slow Photoelectron Velocity-Map Imaging and Infrared Photodissociation Spectroscopy of Cryogenically-Cooled Ions

by

Mark Christopher Babin

A dissertation submitted in partial satisfaction of the

requirements for the degree of

Doctor of Philosophy

in

Chemistry

in the

Graduate Division

of the

University of California, Berkeley

Committee in charge:

Professor Daniel M. Neumark, Chair
Professor Richard J. Saykally
Professor Hartmut Häffner

Fall 2021

Slow Photoelectron Velocity-Map Imaging and Infrared Photodissociation Spectroscopy of Cryogenically-Cooled Ions

Abstract

Slow Photoelectron Velocity-Map Imaging and Infrared Photodissociation Spectroscopy of Cryogenically-Cooled Ions

by

Mark Christopher Babin

Doctor of Philosophy in Chemistry

University of California, Berkeley

Professor Daniel M. Neumark, Chair

Both slow photoelectron velocity-map imaging of cryogenically cooled anions (cryo-SEVI) and infrared photodissociation (IRPD) spectroscopy are employed to probe anions and cations, respectively. Such techniques are capable of providing insight into the vibrational, electronic, and geometric properties of these small molecules, which are facilitated by the high resolution afforded by each method. Further, recent developments have enhanced the abilities of cryo-SEVI to probe vibrationally excited anions (IR-cryo-SEVI), and plans are underway on further improving the cooling abilities of the machine (cryo-cryo-SEVI), allowing for an expanded range of viable molecular targets. In the meantime, there is a vast array of viable molecular species accessible to both cryo-SEVI and IRPD, with systems studied here falling into the categories of free radicals, interstellar species, and metal oxide clusters.

Anion photoelectron spectroscopy (PES) is a powerful technique for studying transient neutral species, owing to the ease with which stable anions are photodetached to access these states. Cryo-SEVI is a high-resolution variant of anion PES that exploits the resolving properties of velocity-map imaging by employing a tunable laser source to achieve sub millielectronvolt (meV) resolution for many species. This is further enhanced by the cryogenic cooling of anions in a radiofrequency ion trap prior to photodetachment, greatly improving spectral clarity and giving access to a larger array of systems.

The systems capable of being studied by cryo-SEVI, however, are limited by the ability to cool them sufficiently. To this end, development of a second ion trap has begun, allowing for the study of larger species, especially metal oxides, which are of considerable temperature entering the trap. Installing this second trap should then give access to larger clusters, as well as allow for the introduction of a reaction gas to study how such species react with small molecules, possibly elucidating catalytic reaction mechanisms.

Meanwhile, IRPD spectroscopy, a complementary method to cryo-SEVI, can readily char-

acterize the structures of large metal oxide clusters. Here, cations (I^+) are mass selected, collected in an ion trap, and messenger-tagged with He. These species are then irradiated with intense, tunable IR light and extracted into a time-of-flight mass spectrometer to determine the depletion of I^+He as a function of photon energy. IRPD spectra then yield vibrational frequencies with comparable resolution to cryo-SEVI, allowing for the determination of geometries and vibrational frequencies when compared with simulation.

Carbon and silicon carbide clusters are structurally complex species of great interest in interstellar, plasma, and combustion chemistry. Cryo-SEVI spectra of C_7 and C_9 allow for the extraction of previously unresolved vibrational frequencies, as well as evidence of vibronic coupling effects to numerous electronic excited states. Small silicon carbides are important astrochemically as a number of them have been observed in interstellar space, though the relative energetics of many of these species are in question, as there exist multiple low-lying stable isomers. SEVI spectra of 4-atom silicon carbides (Si_3C, Si_2C_2, and SiC_3) shed light on this energetic ordering, elucidate new vibrational frequencies in these species, and observe the first Si_2C_2 structure with a permanent dipole.

Among the free radicals studied are the nitrate radical (NO_3) and the hydroxy radical (OH). Cryo-SEVI spectra of NO_3 reveal the extent to which vibronic coupling shapes this molecule's vibrational structure, quelling a controversy surrounding the position of the ν_3 mode of this species. Study of the hydroxy radical was facilitated by recent development of IR-cryo-SEVI, wherein anions are vibrationally pre-excited prior to photodetachment, allowing for the probing of previously inaccessible regions of the neutral potential energy surface. This method, showcased by the photodetachment of vibrationally-excited OH^-, results in newly allowed features to arise in the spectra of this molecule as well as characterization of the anion's vibrational frequency without the use of a messenger-tag, as is in IRPD.

Transition metal oxides serve as a catalysts for many fundamental reactions in chemistry, with the active site often occurring at molecular-scale defects. Given the challenge of studying such active sites, it has become commonplace to use small gas-phase clusters as models for these defect sites, which have the benefit of being easy to produce and tractable for theoretical comparison. The cryo-SEVI spectra of ZrO_2 reacting with H_2O revealed the coexistence of two structural isomers of the product, arising from a "hot" ion distribution "frozen in" to the cold, trapped population. Comparison of the electron affinities of this and the titanium analogue of the system, as well as the un-reacted clusters, provides insight into the reactivity of these clusters. Further, the IRPD spectra of $(NiO_m)(Al_2O_3)_n(AlO)^+$ with m = 1-2 and n = 1-3, a model for Ni/Al_2O_3 - industrial catalyst for oxidative dehydrogenation with high selectivity, are presented. Comparison with theory shows that the structures formed lead to under-coordinated Nickel centers that may elucidate the catalytic mechanism of bulk Ni/Al_2O_3. Finally, cryo-SEVI spectra of NdO characterize the energetics of this species, including detachment transitions to high-lying excited states that may help explain previous observations from atmospheric release experiments.

To Mom and Dad,
for letting me dream.

Contents

Acknowledgments

These past six years have been monumental in more ways than I can enumerate - there is little I can say has not changed in this time. For me, personally, these years have been filled with learning, as much about myself as about science, countless adventures, and an incredible group of friends and mentors who have spurred them. I am immensely thankful to these folks, without whom, I would not be the scientist or person I am today. I will do my best to thank each of them below, though words fail to capture the depth of gratitude I have for each one of them.

First and foremost, I must thank my thesis advisor - Prof. Daniel Neumark. For the sage advice, for assembling such a remarkable group of researchers, for pushing me when I needed it, and for all the support when I failed. It's been an honor to work with you, and I will sincerely miss being in the group.

Thanks to the SEVI lineage, all that I have accomplished was done standing on the shoulders of giants. Thanks to Matthew Nee and Andreas Osterwalder for building SEVI, thanks to Jia Zhou for optimizing it, to Etienne Garand and Tara Yacovitch for showing us all what it can do. Thanks to Jongjin Kim and Christian Hock for building out the cryo trap and opening the floodgates. Thanks to Marissa Weichman and Jessalyn DeVine for pushing the limits of the machine and for being such incredible mentors - I'm as sorry for the endless stream of questions and chatter as I am appreciative of your patience and guidance. Many thanks to Jessalyn for the years of mentorship and for the gift of confidence, common sense, and wonderful memories. Thanks to Marty DeWitt, the next to take the reigns of SEVI - getting everything up and running again (i.e. rebuilding the whole machine), let alone building IR-cryo-SEVI, was no easy task, but we did it. You and Jascha are going to do amazing things - I'm so excited for you both!

Thanks to the Neumark group in full - I and the machine would have ceased functioning long ago if it were not for every single one of you. Thanks to Blake Erickson and Zachary Heim, for being constant sounding boards for my terrible ideas, for all the scheming, for party planning and so, so much more. You two are some of my best friends. To Erin Sullivan and Issac Ramphal, for being remarkably caring and kind people, for always being down to chat, and for sharing far more than I could ever need to know. To Lou Barreau, Romain Geneaux, and Hugo Marroux, for countless late nights, ski trips, and barbecues - we are so lucky to have had you as postdocs and even more so to have you as friends. You all have made me laugh to the point of tears more times than I can count. To Alice Kunin, for more advice and patience than I deserved. To James Gaynor, for friendship and sage career advice. To Steve Saric, Chin Lee, Marvin Pohl, Weili Li, Katherine Lunny, Megan Asplund, Masafumi Koga, Catherine Saladrigas, Andrew Ross, Nicolette Puskar, Eric Haugen, Walt Yang,and Leonardo Coello for the advice, guidance, perspective, and good times. Best of luck to the senior students - it's hard but worthwhile work.

Thanks to Michelle Haskins, our group admin and a living saint (sorry for the sacrilege). I've always said, without you, this group was nothing, and the past year without you has proven that very nearly true. Thank you for doing literally everything, for getting us paid,

for fixing my innumerable mistakes, for every reminder, and for teaching me so much about administration. Your retirement was well earned, and I wish you all the best in it.

Thanks to the machine shop folks, Doug Scudder, Clint Jessel, and the now retired Eric Granlund - without you, we'd be crushed under the rubble of our machine. Thanks to Mike Brateng and all the folks in the wood shop - we'd be completely out of space without you. Thanks to Carl Lamey and Roy Washington in the loading dock, for the deliveries, the loans, and all the help.

Thanks to Knut Asmis, Ya-ke Li, and Sreekanta Debnath and all the free electron laser folks for being such wonderful collaborators and hosts during my visit to the Fritz Haber Institute. Berlin is a marvelous city and my trip was a highlight of my Ph.D.

Thanks to the many theorists that I have been so fortunate to work with and for teaching me so much about the dark art of computations. Thanks to Ali Taka and Hrant Hratchian for all the hard work on the hydrolysis of metal oxides - that work wouldn't have seen the light of day without you. Thanks to Lan Cheng for his heroic efforts on NdO, I wouldn't wish calculating the excited states of lanthanides on my worst enemy, so thank you for taking it on. It's been a joy working with you, and I'm very glad that we've become friends. To Hua Guo, for all the help on the transition state work, past and future.

Thanks to the countless faculty who have spent their time in D22, from whom I have learned so much. Thanks to Mark Johnson, Bob Field, Roland Wester, and many others for poking and prodding the experiment and my mind.

Thanks to Sean Roberts and Mike Azzaro for giving me my first taste of what spectroscopy and experimental physical chemistry could look like and guiding a very lost undergraduate.

Thanks to Joel Adlen and the rest of the 4th floor staff for keeping the lights on, and this place running. Thanks to Prof. Matthew Francis for all of the advice, for trying to (and actually succeeding in) change things for the better, for listening to me and the rest of the students.

Thanks to my many compatriots in the CGLC for dragging the department into the modern era. Thanks to Dr. Chrissy Stachl and Dr. Marco Lobba for getting me involved and pioneering the way. Thanks to all of those who helped us push that along and to those that are now carrying the torch forward. Thanks to my comrades in the union for teaching me how to organize and for fighting the unfair labor practices that plague our workplace.

And of course, thanks to John Stanton, for everything. Were it not for you, I'd still be a confused pre-med. Thank you for teaching me, quite literally, about quantum chemistry and its many joys. Thanks for being the best instructor I ever learned from, the best ally in our mini-wars, the best unofficial advisor I could ask for. I look forward to many more dinners in "Columbus".

Thanks to all of the friends I have made along the way - you all kept me sane and grounded (or some approximation of that) during this time. While I could write another few hundred pages on all of the memories I've made with everyone, I fear that might cause this thesis to get rejected, so I will be a little more brief.

First, thanks to Blake Erickson - I feel so lucky that we became such good friends over these past five and half years. From classes together, qualing together, to graduating together, we've been in this together from the start and I could not be happier to have done it all with you. We've done so much that I honestly am having a hard time selecting what I want to mention in this paragraph, but it feels very on brand to talk about Galveston, which is where I think we went from good friends to best friends. The absurdity of that experience, from late night drinks and meeting cowboys, to the gun-knife and Tiki Wheat, to going to Gizmo will always make me laugh to the point of tears when retelling it. Beyond that, we've done so much, and I can honestly say you helped me get through this past nightmare year and a half. Thanks so much for the game nights, ski trips, Yosemite, floating, beer trips, shared beer, 4th of July, late night spades, and the hundreds of other things I don't have space to write about here. We're finally out of here!

Thanks to Zach Heim - I really lucked out asking you to live with me all those years ago. People don't give you enough credit for being such a kind person, because you're one of the most thoughtful people I've had the good fortune of meeting. Beyond that, you're maybe the most ridiculous person I've met (in the best possible way) - I'll miss our late nights of just going off on the strangest tangents. Thanks for the sage advice over the years, for putting up with my nonsense, and for all the great memories - from destroying ceiling tiles to destroying bathtubs, its always a riot when you're around.

Thanks to the Beer Bois for being an everlasting source of good times. A special thank you to the Sac Squad - Blake Erickson, Eugene Kim, Charles Winslow, and Zachary Heim - for always being on one, always being down for a trip, and for teaching me we can cuvée anything. Thanks to Team Rally - Valerie McGraw, Robinson Flaig, and Luke Bertels (when he's not kicked out) - for always being a source of resplendent joy, good times, great memories, and better yet stories. Thanks to the many friends I've made at Berkeley, Sheena Louisa, Naomi Biggins, Julian Hassinger, Michael Boreen, Matthias Loipersberger, Daniel Brauer, Diptarka Hait, Katherine Oosterbaan, Shoshana Jarvis, Raymond Blackwell, and the countless others, for all the fun we had together. Thanks to the many friends I've made elsewhere, including Dr. Charles Markus, Kelly Hunter, Dr. Brett Marsh, and Dr. Laura McCaslin, it's been amazing getting to know everyone and I'm excited to continue working adjacent to you all for a long time.

Thanks to the countless friends from home that have be sources of strength, wisdom, guidance, shelter, and everything else. Thanks to Joel and Shivi for putting me up (and putting up with me) during a pandemic, thanks to D, Taylor, Jacob, Olivia, Katherine, and the rest of my Seattle friends for being the best chosen family I could have asked for. Thanks to my scattered Longhorns, Logan, Brandon, and Huy for being an incredible resource, sounding board, and source of joy. Thanks to Liz for being my counsel on everything interpersonal and beyond.

Thanks to Hannah for making me a better person in every facet of my life and for putting up with my mania while writing this - I don't deserve you.

Finally, thanks to my parents, Brad and Kerry Babin, for the unconditional love and support - I wouldn't have been able to do any of this without you.

Part I

Background and Methods

Chapter 1

Introduction

1.1 Overview

Developing an understanding of the electronic structure of molecules is integral to chemistry - it offers explanations for chemical structures, reaction mechanisms, dynamics, and energetics. The work comprising this thesis harnesses the power of slow electron velocity-map imaging spectroscopy, a high-resolution variant of pulsed anion photoelectron spectroscopy, as well as infrared photodissociation spectroscopy, to tackle this question for a number of small molecules. These experiments, when coupled with computational chemistry, serve to provide remarkable insight into the electronic, vibrational, and even rotational structure of these molecules, how these levels interplay, and where conventional treatments fail to explain them.

This chapter aims to introduce the reader broadly to the technique of anion photoelectron spectroscopy before diving into the physics that govern this technique. A similar treatment of infrared photodissociation spectroscopy follows. As both experimental techniques rely heavily on computational methods, and a considerable amount of computational work was performed for this thesis, an introduction to computational methods commonly used for treating experimental spectra are reviewed. Finally, motivation for the particular classes of molecules that we study using these methods are presented.

1.2 Anion Photoelectron Spectroscopy

Anion photoelectron spectroscopy (PES) is a robust method used to study neutral species and is capable of probing a wide variety of systems. Nearly any neutral can be probed with anion PES, provided that the corresponding anion can be produced in vacuum and that the electron affinity of the neutral corresponds to an energy accessible via laser radiation. Given these loose restrictions, this technique provides spectroscopic access to a wide array of elusive and exotic species: radicals, clusters, and metastable or unbound species are all readily studied in exquisite detail.

Such studies are facilitated by the ease with which anions can be manipulated with electromagnetic fields, allowing for trapping, steering, and mass selection of these species. In a typical experiment, these properties are exploited such that a packet of molecular anions, M^-, is directed towards and irradiated by a laser beam. Provided that the laser photon energy ($h\nu$) exceeds the binding energy of the anion and electron, a photoelectron may be ejected:

$$M^- \xrightarrow{h\nu} M + e^- \tag{1.1}$$

Following photodetachment, the kinetic energy distribution of the nascent electrons is measured. This distribution often shows discrete features that correspond to detachment to specific neutral electronic, vibrational, and even rotational quantum states, depending on the experimental resolution and energetics of the states in question. These discrete transitions can then be mapped onto the neutral potential energy surface(s) *via* conservation of energy - as the energy imparted into the system by the photon must be conserved between surpassing the binding energy of the electron to a given neutral state (eBE) and the kinetic energy of the outgoing photoelectron following photodetachment (eKE):

$$eBE = h\nu - eKE \tag{1.2}$$

Such a process is schematically shown in Figure 1.1, where photodetachment from an anion (M^-) results in detachment to different vibrational levels of the neutral ground state (M) and excited state (M^*).

The eKE distribution collected thus directly yields the electron affinity (EA) of the neutral species as well as relative energetics of the electronic, vibrational, and rotational levels of the neutral. Depending on the experimental conditions, vibrational and electronic characterization of the anion can be done directly if the anions are not in their ground electronic and vibrational states when photodetached. Regardless, the relative intensity of features in a PES spectrum provide an indirect route to determining the difference in equilibrium geometries between the anionic and neutral structures, allowing for some characterization of the anions irrespective of their starting initial states.

1.2.1 History of the Method

Anion PES has its origins in the photoionization of neutral species,[1] wherein a neutral species is irradiated with light of sufficient photon energies for it to eject a photoelectron, resulting in a cation and free electron. Such a process typically requires high photon energies, spanning the UV, VUV, and XUV regimes (photon energies $\gtrsim 5$ eV), and requiring light sources that, until recently,[2,3] were not readily incorporated into table-top laboratory experiments.

Anion PES, conversely, often requires photon energies spanning the infrared, visible, and ultraviolet regimes, where there are considerably more light sources readily integrated into laboratory experiments. These sources also have the benefit of having high power outputs,

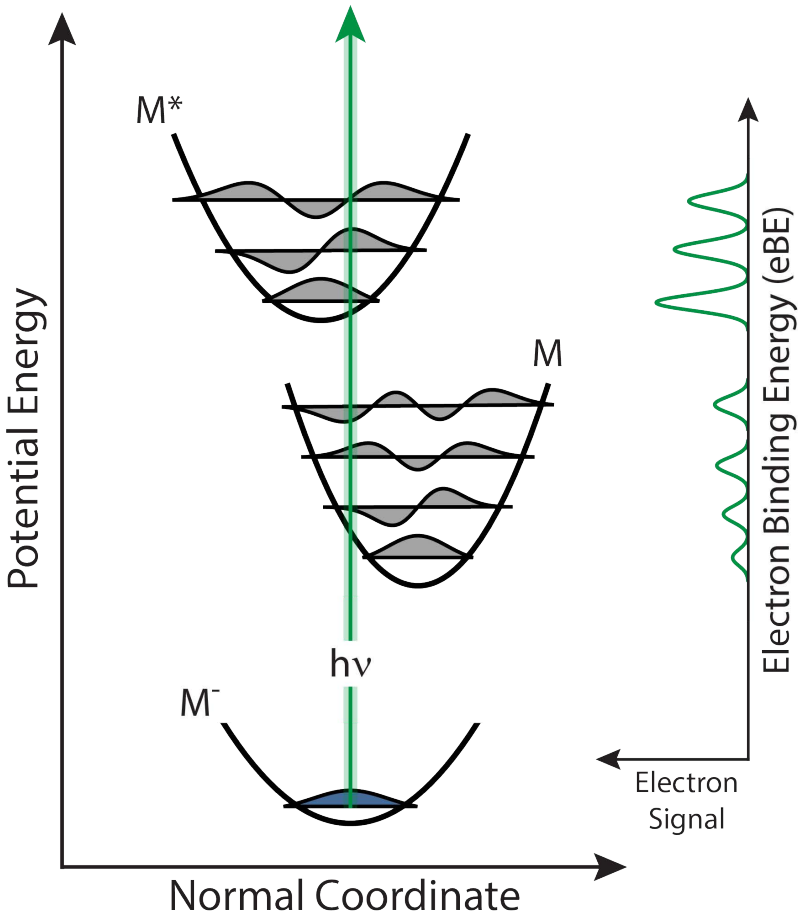

Figure 1.1: Energy diagram of a typical anion photoelectron spectroscopy experiment.

allowing for the studying of anions, whose sources often produce lower sample densities than are achievable for neutral species.

The first reported anion PES experiment was performed by Jan Hall and coworkers, who used the method to measure the electron affinity of the excited helium atom.[4] In their experiment, as with many other anion PES studies spanning the next two decades, a continuous ion source and continuous-wave (cw) laser were employed to generate the photoelectrons that were detected using a hemispherical energy analyzer. Such cw anion PES experiments

were harnessed to study myriad atomic and small molecular species and clusters to great success by the likes of Lineberger, Ellison, Bowen, and many others.[5]

Pulsed anion PES was first reported by Johnson and coworkers[6] in 1986 and was further developed by the Johnson group, Smalley group,[7] and our group[8–11] throughout the 1980's. These advances were spurred by the availability of more flexible pulsed laser sources and an interest in studying anionic molecular clusters that were more readily produced *via* pulsed sources. Such experiments detected eKE distributions using the time of flight (TOF) of the detached electrons, either using the field-free or magnetic bottle schemes.[12]

Despite its applicability to a remarkably broad range of systems,[13] the utility of anion PES has historically been limited by the energy resolution of eKE detection methods. Hemispherical analyzers yield a resolution around 50 cm^{-1},[14] while the best TOF eKE measurements range from 40-80 cm^{-1},[15] with magnetic-bottle TOF analyzers around 150 cm^{-1}.[16]

Later, the advent of ion imaging[17] and subsequently velocity-map imaging[18] (VMI) would revolutionize PES experiments - the high collection efficiency, ability to detect low-eKE electrons, and concurrent measurement of photoelectron angular distributions made this scheme quite attractive for PES. The Sanov group was the first to harness the power of photoelectron imaging in negative ion experiments,[19,20] whose resolution depends on the eKE of the detached photoelectrons, with a relatively constant ΔeKE/eKE of $\sim$3% for the original Eppink-Parker design.[18] This means that early VMI designs limited resolution to around 250 cm^{-1} for eKEs of 1 eV, which has been significantly improved in recent years, as discussed in Chapter 2.

These various detection schemes allowed for the resolution of electronic bands as well as partially resolved vibrational structure, with clearly-resolved vibrational structure present only in systems for which the Franck-Condon profile was amenable, precluding the extraction of vibrational frequencies in all but the luckiest of cases. Further, resolution poses a particular problem for species with low frequency vibrations that can show in the spectrum, as well as in cases where warm ion temperatures lead to hot bands and spectral congestion.

Zero Electron Kinetic Energy (ZEKE) spectroscopy, first developed by Müller-Dethlefs and coworkers[21,22] for studying neutral species, provided a possible route for solving the resolution problem. In this method of PES, the laser wavelength is scanned, and only electrons detached at threshold, with essentially zero kinetic energy, are detected. Our group was the first to adapt this technique to studying anions, yielding a resolution as high as 1 cm^{-1} for atomic systems, with molecular anions yielding typical peak widths of $\sim$10 cm^{-1} due to rotational broadening.[23,24]

While this provided an avenue for PES experiments with considerably improved resolution, it came at the expense of the versatility of conventional anion PES experiments. Neutral ZEKE experiments are performed by exciting an electron to a high-lying Rydberg state which are subsequently pulsed-field ionized shortly before detection.[25] Anionic systems do not support Rydberg states, meaning that such a method is only suited to study a small fraction of molecular systems. Further, the physics of anion ZEKE is quite different from its neutral counterpart - photodetachment transitions near threshold are governed by the Wigner threshold law, meaning that certain symmetries can suffer from poor threshold cross

section (see 1.2.3.2), eliminating them from contention as ZEKE systems.[26] Nevertheless, this technique is quite powerful when the system in question in amenable, as has been the case for molecular and cluster anions.[27–30]

Around this time, another variant of anion PES, photodetachment microscopy, was developed by the Blondel group.[31,32] In this method, atomic anions are photodetached very near to threshold in the presence of an electric field, which creates an interference pattern when the photoelectrons are imaged. From this, the eKE can be determined with remarkable precision, and has been instrumental in measuring atomic EAs with great accuracy, as well as the OH and SH diatomics.[33] Much like anion ZEKE, however, this method suffers from a limited set of available species - photodetachment microscopy, to date, appears incapable of studying more complex molecular systems and extended energy ranges.

Thus, at the start of the new millennium, anion PES still lacked a methodology capable of achieving high-resolution while retaining the flexibility of conventional anion PES. Slow photoelectron velocity-map imaging (SEVI) spectroscopy was developed to satisfy these criteria.[34]

1.2.2 SEVI and Cryo-SEVI

Slow photoelectron velocity-map imaging (SEVI) spectroscopy is a high-resolution variant of the pulsed anion photoelectron imaging experiments pioneered by the Sanov group. Here, ions are photodetached using a tunable light source at various fixed wavelengths and the kinetic energy distributions of the resulting photoelectrons are measured with a VMI lens. As previously mentioned, and will be further expounded upon in Section 2.5, the VMI method has a roughly constant resolving power Δv within a single image. As eKE is quadratic in velocity, the uncertainty in the eKE is thus $v\Delta v$, meaning that improved resolution is obtained for slower photoelectrons. This is magnified, quite literally, by the use of low extraction voltages on the VMI plates, which are selected to enhance the focus of the slowest electrons onto a position sensitive detector, leading to improved spatial resolution. This effect is then exploited by the tunable light source, allowing for the collection of a high-resolution photoelectron image of selected transitions over a narrow energy range. Repeating this process at a number of photon energies results in a multiple high-resolution windows over the complete spectrum, which are then concatenated to yield a full photodetachment spectrum.[35]

A typical SEVI experiment, illustrated below in Figure 1.2, is initiated by taking an overview scan at relatively high photon energy, mapping out the energies of transitions in the system (blue trace). Using the overview spectrum then as a roadmap, the detachment energy is then tuned to 5-50 cm^{-1} above the eBE of the feature of interest (red trace), elucidating the structure that lies in this region. These high-resolution windows are then scaled to match the relative intensives observed in the overview spectrum, which is less sensitive to the relative detachment cross-section than the high-resolution scans (see 1.2.3.2), to yield a complete photodetachment spectrum with remarkable resolution. As of this writing, the current VMI spectrometer is capable of achieving peaks as narrow as 1.2 cm^{-1} full-width at half-maximum

(fwhm) for atomic systems[36] and 1.3 cm^{-1} for diatomics,[37] a substantial improvement over the resolution of conventional methods ($\sim$100 cm^{-1}). Further, while poor cross sections can render certain systems difficult to measure with SEVI, requiring detachment at higher eKE, ultimately resulting in lower resolution, the fwhm of features in these scenarios are routinely $\sim$20 cm^{-1}. SEVI is thus able to bridge the gap between the resolution of ZEKE and the flexibility of conventional anion PES.

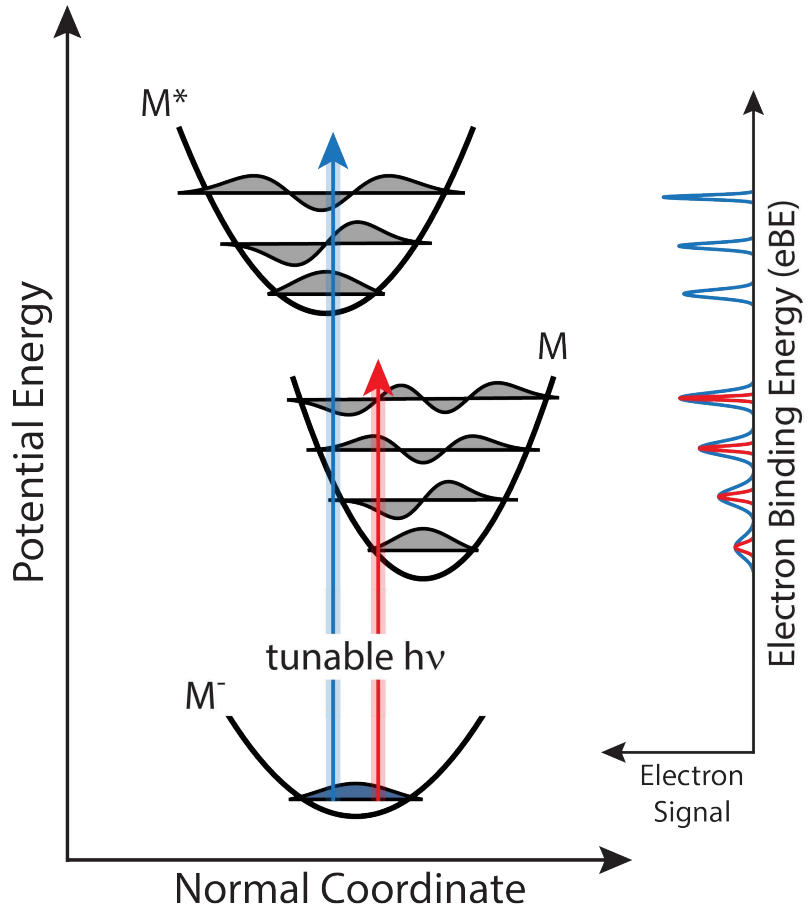

Figure 1.2: Energy diagram of a typical cryo-SEVI experiment.

Cryo-SEVI

For polyatomic anions, things are more complicated. While SEVI is able to obtain high-resolution photodetachment spectra of larger systems, ion temperature quickly becomes limiting in the clarity, interpretability, and resolution of their spectra. Population of excited vibrational and electronic states in anions leads to spectral congestion through the appearance of hot and sequence bands, greatly complicating the analysis of the spectra. Further, the rotational degrees of freedom in these system result in intrinsically broadened linewidths for an experiment which lacks rotational resolution, defined as having an experimental resolution smaller than the rotational constant, B, of the system in question. For typical polyatomic molecular systems, these range between 0.5-5 cm^{-1},[38] meaning that the intrinsic resolution of SEVI is insufficient to clearly resolve many rotational transitions, resulting in experimental peak widths that are limited by the underlying rotational contour of the transition ($\sim$15 cm^{-1} prior to cooling),[39] though in favorable systems partial or full rotational resolution is possible.[37,40–42]

The need for cold ions should be readily apparent - reducing ion temperatures should de-clutter SEVI spectra as well as further improve its resolution. Supersonic expansions of gases serve to cool neutral species readily, though producing cold, thermalized anions with this method is more challenging. While the expansion does cool the anion precursors - often neutrals - the passage of this gas through a filament ionizer or discharge source to generate ions leads to heating following the expansion, leaving too low of pressures for the newly birthed anions to undergo a sufficient number of collisions to cool. Further, ions produced *via* laser ablation are exceptionally challenging to cool in supersonic jet expansions, due to cluster heating during condensation[43] (see Chapter 11).

For this reason, considerable work has been put into developing ion trapping and cooling methods,[44,45] with buffer gas cooling of trapped ions the prevailing method. Here, ions are spatially confined using electromagnetic fields in a region of high gas pressure, promoting a large number of collisions between the cold inert buffer gas and the ions, allowing for thermalization of the two populations. Given that the ions are spatially localized while the buffer gas is not, the buffer gas is free to collide and thermalize with the walls of the ion trap, which can be cooled to cryogenic temperatures. This method is broadly applicable, serving to cool vast majority of molecular anions.[46] Further, the degree of cooling can be controlled through trap residence time and the buffer gas pressure. This control, however, does not alter the kinetics of cooling in our experience - buffer gas cooling tends to favor kinetic trapping,[47,48] wherein the "hot" isomer distribution is "frozen-in" to the trap, leading to populations of cold ions that are distinctly non-Boltzmann. These effects have played to our advantage, as shown in Chapters 8 and 11.

Dieter Gerlich and coworkers were the first to employ radio-frequency (RF) ion traps for cryogenic ion cooling,[44] and their pioneering work has been adapted and incorporated into numerous experiments in chemical physics.[45] Notable among these are other PES experiments that have employed cryogenic ion traps, Lai-Sheng Wang and coworkeres were the first to report PES of cryo-cooled anions, using a RF 3D quadrupole trap[49,50] and finding that cooling considerably improved their spectral clarity. Concurrently, Bernd von Issendorff's group also constructed a 12-pole linear multipole ion trap for studying water[51] and aluminum[52] clusters

coupled to a magnetic bottle spectrometer.

The spectrometer built for Bernd von Issendorff was constructed by Christian Hock and detailed in his thesis,[53] submitted shortly before he came to UC Berkeley to construct the trap in the current iteration of our experiment. This trap, an RF octupole ion trap, was designed and incorporated into the SEVI machine located in Berkeley by mid-2012. The modified machine was dubbed "cryo-SEVI", and will be discussed in detail throughout Chapter 2.

An octupole was selected for the trap as a balancing act. Higher-order multipoles have the benefit of having flatter potentials near the radial center of the trap, leading to sharper potentials further from the center. This leads to less RF heating, wherein the micro-motion of the anions in the oscillating RF field is perturbed by collisions with a buffer gas, pushing it further up the potential landscape and imparting heat into the ion, rather than cooling it. While this effect is certainly undesirable, the cost for avoiding such an occurrence in higher-order multipoles is that they have considerably worse spatial confinement of their ions, making extraction from these traps an experimental challenge. An octupole trap represents a compromise between RF heating and spatial confinement, allowing for ions to cool sufficiently for our purposes while also allowing for efficient extraction into the next stage of the experiment. More detail of the experimental considerations, as well as machine drawings, for the trap can be found in the thesis of Jongjin Kim.[39]

This trap is coupled to a closed-cycle helium refrigerator to cool the trap and buffer gas down to a measured temperature of 4.7 K. In practice, this trap is capable of cooling ions to measured electronic temperatures[54] as low as 10 K and rotational temperatures down to $\sim$ 17 K.[37,41,55] These values are quite good, considering higher-order traps optimized for cooling in the Wester group are only able to achieve slightly colder temperatures.[56] At these temperatures, anions are in their ground electronic and vibrational states, with only the first few rotational levels being populated. This manifests as considerably narrower features in our spectra, with spectral peak widths of $\sim$ 2 cm^{-1} achievable for molecular systems, compared to the $\sim$15 cm^{-1} fwhm features observed prior to the trap's installation.

The installation of the cryo-trap into SEVI also granted us access to a considerably larger set of systems, including large aromatic systems,[36,57,58] bare metal oxide clusters,[55,59–64] and reacted metal oxide clusters.[65,66] Further, the ability to tune ion temperature has proven to be a useful tool for cryo-SEVI studies to elucidate vibrational and electronic structure of neutral and anionic species, as is highlighted in Chapter 9.

1.2.3 Fundamentals

1.2.3.1 PES Selection Rules

Photoelectron spectroscopy is a somewhat unique spectroscopic method in that transitions observed here are not bound state to bound state (bound-bound), but bound-continuum, owing to the fact that the photodetached electron can take any value of kinetic energy and angular momentum necessary for a given transition. This leads to somewhat relaxed

selection rules compared to bound-bound methods, though derivation of selection rules for both methods begin with Fermi's Gold Rule:[67]

$$I \propto \left| \left\langle \Psi^f \right| \mu \left| \Psi^i \right\rangle \right|^2 \cdot \rho \cdot \delta(\Delta E - h\nu) \tag{1.3}$$

for the transition intensity (I) between an initial (i) and final (f) state after absorption of a linearly polarized photon, where $|\Psi^i\rangle$ is the wavefunction describing the initial state (here that of the anion), $\left|\Psi^f\right\rangle$ is the wavefunction of the final state (here that of the neutral and photoelectron), μ is the dipole moment, and ρ is the density of final states. The inclusion of the $\delta(\Delta E - h\nu)$ term enforces conservation of energy upon photon absorption - ΔE is the difference in energy between the initial and final states, and is follows the relation

$$\Delta E = \text{eKE} + \text{eBE} \tag{1.4}$$

for photoelectron spectroscopy.

For the transition between our initial and final states (i.e. $|\Psi^i\rangle \rightarrow \left|\Psi^f\right\rangle$) to be 'allowed', Equation 1.3 must be non-zero, imposing two restrictions: first, that ΔE must be equal to the photon energy, and that the dipole moment matrix element

$$M = \left\langle \Psi^f \right| \mu \left| \Psi^i \right\rangle \tag{1.5}$$

is non-zero.

The first restriction is governed by the energy conservation term, which for bound-bound transitions gives the resonant frequency for the transition. Here, eKE can take any value, so instead this term imposes a minimum value for ΔE - the lowest possible eBE of the system, the electron affinity. Therefore, for a photodetachment transition to occur, $h\nu$ must be *at least* that of the electron affinity of the system. This minimum energy requirement stems from the fact that the free electron eigenfunctions form a continuum, resulting in

$$0 \neq \delta(\Delta E - h\nu) \quad \text{for} \quad h\nu \geq EA$$

This is directly analogous to the photoelectric effect in bulk materials, wherein a photoelectron can only be detached if the photon energy exceeds the workfunction of the material.[68,69]

The second restriction is not quite so simple. Here, we will treat our wavefunctions within the Born-Oppenheimer (BO) approximation, such that the electronic and nuclear degrees of freedom of the system can be treated as separable (i.e. independent), owing to the dramatic difference in the timescales and energies of these two wavefunctions oscillate within. Under this approximation, we can write the complete molecular wavefunction as a product of the electronic (e), vibrational (v), rotational (r), and spin (s) components:

$$\Psi = \psi_e \cdot \psi_v \cdot \psi_r \cdot \psi_s \tag{1.6}$$

Note: for the time-being, we will ignore ψ_r, as rotational structure is rarely resolved in anion PES experiments, unless the rotational constant is sufficiently large, as in Chapter

6, for the photodetachment of OH^-. We will conclude this section with a discussion of the rotational selection rules for anion PES.

One further approximation is required to simplify derivation of our selection rules - the Condon approximation[70] (or the 'sudden' approximation), which assumes that the transition in question occurs without any change in nuclear coordinates. As a result, the electronic and nuclear contributions to the dipole moment μ can be separated

$$\mu = \mu_e + \mu_{nuc} \tag{1.7}$$

Applying Equations 1.7 and 1.6 to Equation 1.5 and imposing the $M \neq 0$ condition results in

$$0 \neq \left\langle \psi_e^f \right| \mu_e \left| \psi_e^i \right\rangle \left\langle \psi_v^f | \psi_v^i \right\rangle \left\langle \psi_s^f | \psi_s^i \right\rangle + \left\langle \psi_e^f | \psi_e^i \right\rangle \left\langle \psi_v^f \right| \mu_{nuc} \left| \psi_v^i \right\rangle \left\langle \psi_s^f | \psi_s^i \right\rangle \tag{1.8}$$

The second term here is zero, as the initial and final electronic states are orthogonal, as they are nondegenerate eigenstates of the same N-electron Hamiltonian (i.e. $\left\langle \psi_e^f | \psi_e^i \right\rangle = 0$). The resulting expression thus contains three non-zero factors from which the electronic, vibrational and spin selection rules are derived:[71]

$$I \propto \left| \left\langle \psi_e^f \right| \mu_e \left| \psi_e^i \right\rangle \right|^2 \left| \left\langle \psi_v^f | \psi_v^i \right\rangle \right|^2 \left| \left\langle \psi_s^f | \psi_s^i \right\rangle \right|^2 \tag{1.9}$$

In order for the transition intensity to be non-zero, each of these three terms must be non-zero, and we will consider each. The first term specifies the electronic symmetry conditions required for a given condition, the second is the Franck-Condon (FC) factor, which specifies the relative intensity of transitions between different vibrational states within an electronic band, and the final specifies the allowed change in electronic spin.

The simplest of these restrictions is the $|\left\langle \psi_s^f | \psi_s^i \right\rangle|^2 \neq 0$ term, which states that the electronic spin must be conserved between initial and final states, or that the transition cannot alter the spin of the complete system. In anion PES, a given transition results in the photodetachment of an electron, carrying away with it a spin of $1/2$, requiring that the remaining neutral molecule must have a change in spin of $\pm 1/2$. This, in turn, requires a change in spin multiplicity of ± 1 for the neutral from the anion. Therefore, single-photon detachment from a doublet anion can access both the singlet and triplet manifolds of the corresponding neutral.[72–74] This is considerably different from bound-bound electronic spectroscopy, wherein the initial and final states must have identical electronic spins, and leads to a considerable number of bright spin states.

The next restriction to consider is the electronic symmetry condition, $|\left\langle \psi_e^f \right| \mu_e \left| \psi_e^i \right\rangle|^2 \neq 0$. Here, we evaluate this using group theory - an often useful tool for molecular spectroscopy. The integral expressed in this term is non-zero if the product of the irreducible representations (Γ_i) of the three quantities involved include the totally symmetric representation, Γ_A:

$$\Gamma_A \in \Gamma_e^f \otimes \Gamma_\mu \otimes \Gamma_e^i \tag{1.10}$$

It is important to note that the irreducible representation of the dipole, Γ_μ transforms as (x, y, z) within the point group. This can be further simplified by applying the Koopman approximation, often referred to as the frozen-core approximation, which assumes that the wavefunction of the outgoing photoelectron, Γ_e^{elec}, is independent from and orthogonal to the remaining occupied molecular orbitals (MOs), $\Gamma_e^{(0)}$, of the neutral, i.e. $\Gamma_e^f = \Gamma_e^{(0)} \otimes \Gamma_e^{elec}$. Applying to this Equation 1.10, we get

$$\Gamma_A \in \Gamma_e^{(0)} \otimes \Gamma_e^{elec} \otimes \Gamma_\mu \otimes \Gamma_e^{(-)} \tag{1.11}$$

This formulation highlights the difference between the selection rules of bound-bound transitions and those that arise from photodetachment - the wavefunction of the outgoing photoelectron can take any symmetry and angular momentum, meaning there are no dipole-forbidden transitions in PES (as there are in optical electronic spectroscopy). In the simplest picture, detachment from an atomic orbital that is well described by a spherical harmonic wavefunction parameterized by ℓ (i.e. here a good quantum number for the system), results in a photoelectron departing an orbital of angular momentum ℓ in partial waves of angular momentum $\ell \pm 1$. This angular momentum of the outgoing photoelectron uniquely impacts both the photoelectron cross section and angular distribution, as is further discussed in Sections 1.2.3.2 and 1.2.3.3.

In the case of $NO_3^{0/-}$, where the vibrationally-averaged point group is D_{3h}, the ground electronic state of the anion and neutral are $^1A_1'$ and $^2A_2'$, respectively. Here, photodetachment from the anion to the neutral ground state ($\tilde{X}^2A_2' \leftarrow \tilde{X}^1A_1'$) must proceed with an irreducible representation of A_2', as $\Gamma_A = A_1' \in A_2' \otimes A_2'$. This can be thought of as detaching an electron from an atomic MO with A_2' symmetry. Within this point group, A_2' transforms as R_z, meaning this detachment occurs from an s-like MO and thus carries away $\ell = 1$. Conversely, detachment to the second excited state, $\tilde{B}^2E'$, results in a photoelectron of E'. As E' transforms as (x, y) in this point group, detachment is occurring from a p-like MO, so this detachment transition carries with it $\ell = 0, 2$.

While PES benefits from relaxed electronic selection rules that give rise to no dipole-forbidden transitions, in many cases photodetachment transitions abide by the Koopman approximation well - the assumption that the outgoing photoelectron was ejected suddenly, leaving behind a 'frozen-core' of electrons. This essentially leaves the MOs of the anion and neutral identical, save for the neutral having one fewer electron, and, importantly, implies that there is no electronic rearrangement during photodetachment. This 'restriction' can preclude anion PES from being able to probe certain electronic configurations, namely some excited states of species with nearly degenerate valence electrons, as is the case in NdO (see Chapter 9). This effect is not a strict selection rule, and can be violated in systems with strong multireference character, often metal oxides.[59,64,65]

The final consideration in Equation 1.9 is the $|\langle\psi_v^f|\psi_v^i\rangle|^2 \neq 0$ term - the FC factor, which governs the selection rules for vibrational transitions and their intensities within an electronic band. The symmetry considerations used above in the electronic selection rule again come to play here - this term is non-zero when

$$\Gamma_A \in \Gamma_v^f \otimes \Gamma_v^i \tag{1.12}$$

In many cryo-SEVI experiments, the anions are taken to be in their ground vibrational state, or $\Gamma_v^i = \Gamma_A$, leading to non-zero FC factors only for transitions that terminate in totally symmetric vibrational wavefunctions. In the case of NO_3 the totally-symmetric stretch, which has symmetry of A_1', satisfies this requirement for any quanta along this normal mode (i.e. a transition from the anionic ground vibrational state to the neutral ground state can terminate in neutral states of NO_3 with 1, 2, 3, ... quanta along this mode). For the remaining three normal modes in this species, only even quanta along these modes can be observed, as $\Gamma_1 \otimes \Gamma_1 \in \Gamma_A$ always holds true for a point group. This leads to the vibrational selection rules that govern PES: $\Delta v = 0, \pm 1, \pm 2, ...$ for totally symmetric vibrational modes and $\Delta v = 0, \pm 2, \pm 4, ...$ for non-totally symmetric modes.

These selection rules, however, are only sufficient to guarantee $|\left\langle \psi_v^f \middle| \psi_v^i \right\rangle|^2$ is not analytically zero - they do not guarantee that a transition is sufficiently intense as to be observed. The relative intensity of these transitions is governed by the magnitude of the FC factor, which is connected to the difference between the anion and neutral equilibrium geometries. Large displacements along one or more normal coordinates between the anion and neutral will result in significant FC intensity and an extended progression along this mode (i.e. observation of many transitions involving this mode), though this is with the caveat that the geometries are sufficiently similar to the FC factors to be non-zero.

This principle is illustrated in Figure 1.3, which shows FC simulations for photodetachment of a linear triatomic anion (ABA) to a (non-)linear neutral (ABA), where the neutral A-B bond length is increased by 10% and 25% of the anion equilibrium geometry, r_e, or the A-B-A bond angle is changed by 10°, 24°, and 46°. In the first series (top of Figure 1.3), displacement along the totally-symmetric stretching normal mode ($\omega_{ss} = 1355$ cm^{-1}) is increased, leading to an extended progression wherein transitions to neutral states with more quanta along this normal mode gain intensity concurrently with a decrease in intensity of the vibrational origin. The second series (bottom of Figure 1.3) shows a similar trend, though displacement and activity are along the bending mode of the molecule ($\omega_{bend} = 667$ cm^{-1}), which now connects the two molecular geometries. Together, this shows that as displacement along a normal mode increases, so does the FC-overlap for transitions to vibrationally excited states of the neutral. This trend, however, only holds so long as the two geometries are sufficiently similar - the top-right pane of Figure 1.3 is magnified by a factor of 250, indicating that for this species a displacement of $\Delta r = 0.25 r_e$ is sufficient to perturb the geometries past the point of good FC-overlap. Notably, the anti-symmetric stretching mode of this molecule is never active in these simulations, as $r_{(A_1-B)} = r_{(A_2-B)}$ in both the neutral and anion - were this species to break-symmetry (i.e. $r_{(A_1-B)} \neq r_{(A_2-B)}$, taking the molecular symmetry from $D_{\infty h}$ to $C_{\infty v}$), the anti-symmetric stretch would be gain intensity at the expense of the symmetric stretch. From these simulations, it should be clear that the FC profile observed *via* PES is remarkably sensitive to the molecular geometries observed, allowing for determination of *both* structures, despite cryo-SEVI often only observing transitions

involving neutral vibrations.

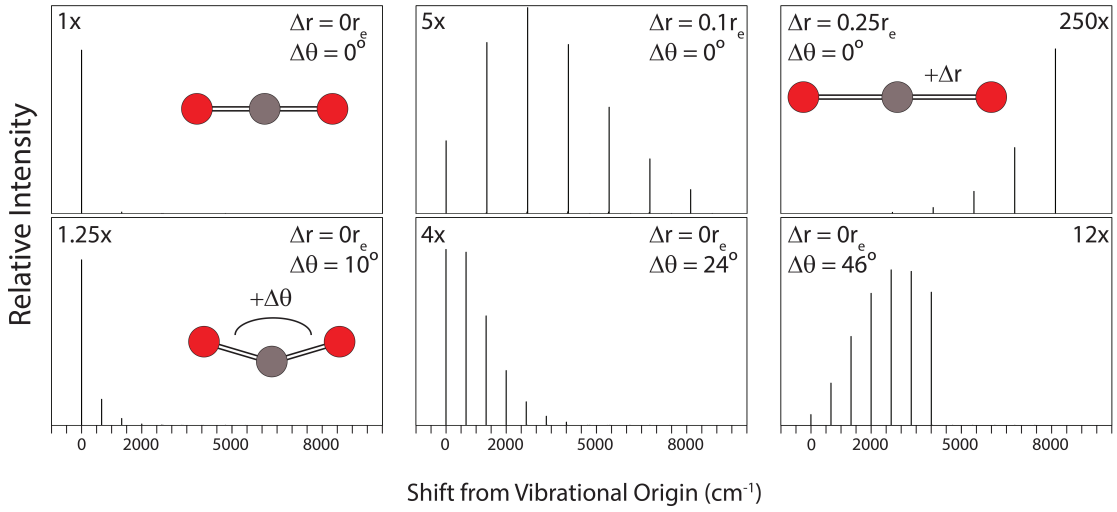

Figure 1.3: Franck-Condon simulations for detachment from a linear triatomic anion (of the form ABA, with A-B bond length r_e and A-B-A angle θ) to a neural of the same form, with A-B bond lengths $r + \Delta r$ and bond angle $\theta + \Delta\theta$. Top: changes in the relative intensities of transitions as a function of bond length, showing activity along the totally-symmetric mode. Bottom: change ins the relative intensities of transitions as a function of bond angle, showing activity along the bending-mode.

Finally, the slight intensity in the symmetric stretch in the top left panel of Figure 1.3 arises from a difference in the anion and neutral vibrational frequencies for this mode, $\omega_a = 513\ \mathrm{cm}^{-1}$ and $\omega_n = 667\ \mathrm{cm}^{-1}$, respectively. Such a difference in frequency can be related to the shape of the electronic potential surface that supports these vibrational wavefunctions (i.e. harmonic oscillators of differing force constants).

For more complex molecules the relationship between geometry displacement and FC profile largely remain true provided the normal modes between the anion and neutral are similar and are harmonic in nature. It is important to note that while transitions to neutral states with even quanta along non-totally-symmetric modes are FC allowed, they are not typically observed without a substantial difference in harmonic frequency between the anion in neutral, as displacement along such modes would imply that either the anion or neutral breaks symmetry.

In principle, all vibrational modes of a molecule can be observed in a PES spectrum, given favorable conditions. This, however, is rarely the case - often only a few modes are FC active, potentially leaving transitions to vibrations of interest inaccessible. Notably, vibrational motion involving free OH,[75] NH,[76] and CH bonds[77] are rarely observed as the anion and neutral bond lengths change very little upon photodetachment for pure single bonds. This leaves broad swaths of the neutral potential energy surface inaccessible to cryo-

SEVI, unless the FC or harmonic approximations are violated as is discussed in Section 1.2.3.4. These occurrences, while somewhat common in cryo-SEVI experiments, are not a general solution to the blind spots imparted to the experiment by FC considerations. Motivated by an interest in bypassing this limitations, we have recently modified the cryo-SEVI machine to allow for vibrational pre-excitation of our anions, as is discussed in detail in Chapter 3 and the results of which are shown in Chapter 6.

In rare cases, conditions are met such that cryo-SEVI is able to observe partial[40–42] or complete rotational profiles.[37] In such cases the selection rules for rotational transitions can be determined by treating near threshold photodetachment as the sequence:[75,78,79]

$$M^-(J") + h\nu \rightarrow M + e^-(J_C) \tag{1.13}$$

$$M + e^-(J_C) \rightarrow M(J') + e^- \tag{1.14}$$

where $J"$ is the angular momentum of the negative ion, J' that of the final-state neutral, and J_C as the total angular momentum of the neutral-electron complex. Given the absorption of a single photon, angular momentum conservation dictates $J_C = J", J" \pm 1$. The photodetached electron can then carry any partial wave component of angular momentum away, greatly complicating the next step. If, however, we assume that this detachment process is undergone very near threshold, very nearly pure s-wave ($\ell = 0$) detachment should be observed due to the Wigner threshold law (see Section 1.2.3.2). This approximation only holds if the underlying assumption - that the symmetries of the anion and neutral states allow for s-wave detachment - holds true. In practice, s-wave detachment is required for cryo-SEVI to achieve sufficient resolution to observe rotational transitions, so this assumption is fair. Under this approximation, the only angular momentum the outgoing electron carries away with it a spin of $1/2$, resulting in the final selection rules of $J' = J" \pm 1/2, \pm 3/2$. Further, the dipolar selection rules involved in the absorption of the photon dictate a change in polarity, though it is highly unlikely that this will impact cryo-SEVI spectra, given Λ-splittings are typically on the order of 0.1 cm^{-1},[80] far below the resolution limit of cryo-SEVI.

1.2.3.2 Photodetachment Cross Sections

The cross section for photodetachment of an anion near threshold is governed by the angular momentum and kinetic energy of the outgoing electron, meaning this is intimately tied to the symmetry of the molecular system in question.

Provided that a photoelectron is detached from an atomic orbital with well defined ℓ, it is well described by a superposition of spherical harmonic partial waves with $\Delta\ell = \pm 1$ (Section 1.2.3.1). The near-threshold photodetachment cross section, σ, for a given partial wave component with angular momentum ℓ has an eKE dependence governed by the Wigner threshold law:[81]

$$\sigma \propto (\text{eKE})^{\ell+1/2} \tag{1.15}$$

This particular relation does not hold for PES generally, but rather is specific to *anion* PES. The derivation of this law is commented on succinctly by Rau,[82] who outlines that Equation 1.15 is capable of being determined without knowing anything about "the reaction zone", where photodetachment occurs and uniquely dictates the physics of photodetachment itself. Instead, it is possible to derive this threshold law by considering the reverse process. At long-range, the photoelectron and neutral share a charge-induced dipole interaction, $V(r) \propto -1/r^4$ (assuming the neutral does not have a significant dipole moment). Bringing these two particles together, then, from $r = \infty$ to $r = r_0$, where r_0 is the edge of "the reaction zone" wherein the electron is attached, is sufficient to know the physics of photodetachment.

Now, beyond the electrostatics involved, a photoelectron with angular momentum ℓ experiences a centrifugal potential, $V(r) \propto \ell(\ell+1)/r^2$. Upon bringing these two particles together, in all cases except $\ell = 0$, the centrifugal potential introduces a barrier of considerable height compared to that of the electrostatic potential, as shown in Figure 1.4. Photoelectrons with insufficient kinetic energy to surmount the barrier, i.e. the "slow" photoelectrons sought after for SEVI, must then tunnel through the barrier. Treating this simple potential with Wentzel-Kramers-Brillouin (WKB) theory[67] to determine the tunneling rate returns Equation 1.15.

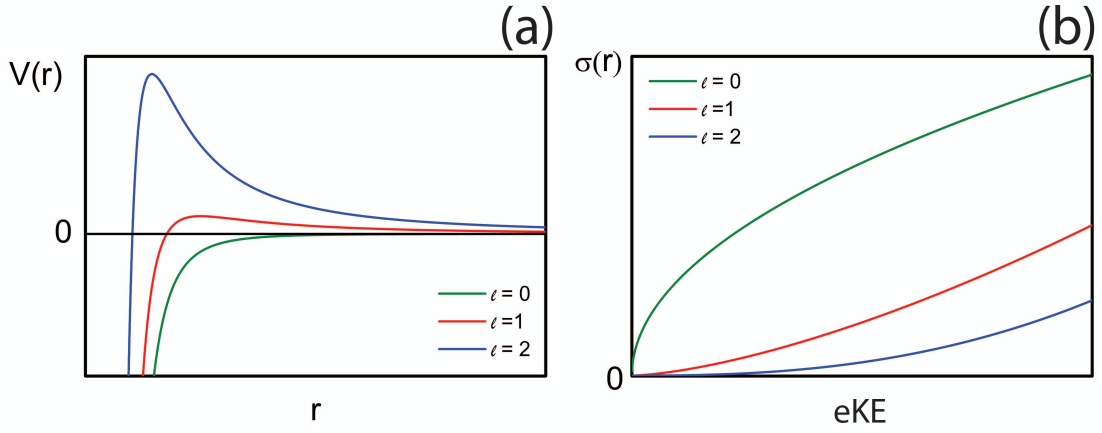

Figure 1.4: (a) Illustration of the potential, $V(r)$, experienced by the photoelectron during anion photodetachment, as a function of its angular momentum, ℓ. (b) Behavior of the photodetachment cross section, σ, for various values of ℓ as a function of eKE, governed by the Wigner Threshold law.

The physical implications of this law, as they pertain to SEVI, are monumental - Equation 1.15 implies that only photoelectrons detached with $\ell = 0$ retain meaningful detachment cross section close to threshold. This relationship outlines the rigidity of ZEKE experiments, which strictly imposed this condition for its operation, greatly limiting the number of species capable of being studied. In SEVI, typical eKEs are on the order of 10-1000 cm^{-1}, causing $\ell = 0$ partial to waves dominate. Higher values of ℓ, however, can be observed further

from threshold and thus at lower resolution. Therefore, the Wigner threshold law ultimately governs the achievable resolution for a given SEVI image, as limited signal near threshold from transitions with $\ell \neq 0$ often prevents detection of features with very low eKEs ($\lesssim 30$ cm^{-1}).

It is worth noting the limitations of this threshold law. First, it does not hold for photoionization of neutrals - in this case, the electron leaves behind a cationic core, resulting in a Coulomb potential of the form $V(r) \propto -1/r$. This, in turn, means there is no barrier, and there is therefore no significant ℓ or eKE dependence to the cross section of these processes.

For anions, the law does have a few limitations. First, Equation 1.15 is a *threshold* law, meaning that it does not hold for high eKE's, where the photoelectrons have kinetic energies well above the barrier height, thus rendering the tunneling assumption inaccurate. This is, in part, why SEVI spectra are scaled to the overview spectrum, as these spectra are less sensitive to threshold effects.

Beyond this, Equation 1.15 was derived for photodetachment from *atomic* anions. Molecules are more complicated, owing to their permanent dipole moments and molecular orbitals for which ℓ is not well-defined. Reed *et al.*[83] was the first to tackle this problem, finding once more that the symmetry of the detachment transition within the molecular point group can be used to determine the partial waves of the outgoing photoelectron, as was done in the example of NO_3 in the previous discussion of selection rules. This information can then readily be used to draw conclusions about the threshold behavior of a given transition to great effect, as highlighted in Chapter 5.

Additional models have been developed to treat small molecules, namely the s&p model developed by the Sanov group[84,85] (Section 1.2.3.3.2) and has been recently refined by our group[86] and the Gibson group[87] to include contributions from d orbitals.

Finally, in the event that the anion in question does have a notable dipole moment (> 1.5 Debye), the assumptions that lead to Equation 1.15 begin to fail. As noted by Roland Wester and coworkers,[88] modifications to the law must be made when performing high-resolution photoelectron spectroscopy on CN^- ($\mu \approx 1.45$ D), owing to the mixing of partial waves when the molecule is polar, leading to an exponential value of $\lambda + 1/2$ rather than $\ell + 1/2$, where λ is no longer an integer. In cases where the anion possess an even larger permanent dipole moment, such as in the case of C_3N^- ($\mu = 2.72$ D), strong deviations from Equation 1.15 occur,[89] and the threshold law developed by O'Malley[90] becomes relevant:

$$\sigma \propto (\mathrm{eKE})^{\ell+1/2}\left(1 + \frac{\mathrm{eKE} \cdot \ln(\mathrm{eKE})}{2}\right) \tag{1.16}$$

1.2.3.3 Photoelectron Angular Distributions

Following photodetachment, the distribution of photoelectrons varies as a function of angle with respect to the laser polarization axis. Much like the photodetachment cross section described above, this distribution is governed by the angular momentum of the outgoing photoelectron, and so is intimately tied to the symmetry of the transition in question. Photo-

electron imaging experiments like SEVI allow for the measurement of photoelectron angular distributions (PADs) simultaneously with the eKE distribution. For a one-photon photodetachment transition with linearly polarized light, PADs are described by the differential cross section for photodetachment at a given solid angle, $d\sigma/d\Omega$:[91]

$$\frac{d\sigma}{d\Omega} = \frac{\sigma_{\text{tot}}}{4\pi}\Big[1 + \beta P_2(\cos\theta)\Big] \tag{1.17}$$

where θ is the angle of the photoelectron velocity vector relative to the polarization axis of the laser, P_2 is the second-order Legendre polynomial with $P_2\cos(\theta) = \frac{1}{2}(3\cos^2\theta - 1)$, and β is the anisotropy parameter. As shown in Figure 1.5, the anisotropy parameter is bounded between $\beta = -1$ and $\beta = 2$, giving PADs peaked perpendicular and parallel to the laser polarization axis, respectively, with $\beta = 0$ yielding an isotropic PAD.

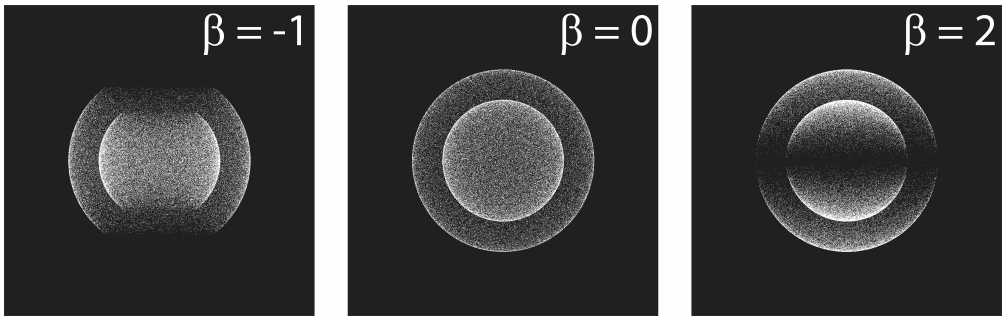

Figure 1.5: Simulated VMI images for transitions with parallel ($\beta > 0$), isotropic ($\beta = 0$), and perpendicular ($\beta < 0$) angular distributions for a vertically polarized laser pulse (i.e. vertical on the page). Each simulated image contains 10^5 electrons, representative of the typical number of events in a SEVI image.

The origin of a lab-frame distribution despite random orientation of the anions prior to photodetachment is curious. This effect stems from Equation 1.3, which dictates that for bound-bound transitions, absorption probability is maximized when the electric field vector of the light aligns with the transition dipole moment, connecting the lab and molecular frames. In deriving Equation 1.17, this assumption is made,[92] before averaging the angular dependence of the transition probability over all rotational orientations of the molecule, which can be conveniently formulated in terms of the Eulerian angles, ϕ, θ, ψ. Transforming between the two frames and integrating returns Equation 1.17.

The anisotropy parameter β can be predicted with numerous models, as will be discussed in the sections below.

1.2.3.3.1 Cooper-Zare Model As the anisotropy parameter depends on the angular momentum of the outgoing electron, ℓ, determined by the selection rules listed above for

detachment from atomic orbitals (or MOs that are similar in nature), it can be predicted as a function of ℓ. The Cooper-Zare formula predicts β using the following:[91]

$$\beta = \frac{\ell(\ell-1)\chi^2_{\ell,\ell-1} + (\ell+1)(\ell+2)\chi^2_{\ell,\ell+1} - 6\ell(\ell+1)\chi^2_{\ell,\ell-1}\chi^2_{\ell,\ell+1}\cos(\delta_{\ell+1}-\delta_{\ell-1})}{(2\ell+1)[\ell\chi^2_{\ell,\ell-1} + (\ell+1)\chi^2_{\ell,\ell+1}]} \tag{1.18}$$

where ℓ is the angular momentum of the atomic orbital from which detachment occurs. Here, $\chi_{\ell,\ell\pm1}$ and $\delta_{\ell\pm1}$ are the radial matrix elements and phase shifts, respectively, for the dipole-allowed outgoing photoelectron partial waves with angular momenta $\ell \pm 1$.

This model was then modified by Hanstorp,[93] who realized that Equation 1.18 depends only on the ratio of $\chi_{\ell,\ell+1}/\chi_{\ell,\ell-1}$, as these radial matrix elements change as a function of eKE following the Wigner threshold law for low eKEs ($\sigma_{\ell\pm1} \propto \chi^2_{\ell,\ell\pm1}$). This allows for the dipole matrix elements to be replaced with terms that explicitly involve the eKE and a scaling factor, A, for the relative intensity of the $\ell+1$ and $\ell-1$ detachment channels. Combining these with Equation 1.18 yields

$$\beta = \frac{\ell(\ell-1) + (\ell+1)(\ell+2)(A_\ell \cdot \mathrm{eKE})^2 - 6\ell(\ell+1)(A_\ell \cdot \mathrm{eKE})\cos(\delta_{\ell+1}-\delta_{\ell-1})}{(2\ell+1)[\ell + (\ell+1)(A_\ell \cdot \mathrm{eKE})^2]} \tag{1.19}$$

Following this formulation, detachment from an s-orbital can only then yield p-wave detachment ($\ell_{electron} = 1$), as discussed above. In the absence of partial wave interference, this yields a $\beta = 2$ anisotropy parameter independent of eKE. Detachment from atomic orbitals with higher ℓ values opens up more detachment channels, leading to a superposition of partial waves that can interfere and give a more complex β value that is strongly eKE dependent.

This discussion, however, requires that ℓ be a good quantum number for the orbital from which detachment occurs, which is often not the case for MOs. In such cases, there still exists a relationship between β(eKE) and ℓ. One approach to treating this is the s&p model developed by the Sanov group.[20,85]

1.2.3.3.2 S&P Model This model is relatively simple, yet surprisingly effective at predicting PADs - owing largely to the use of group theory to make such predictions. This model, however, is limited to treating species with single-centered sp-hybridized molecular orbitals, meaning that it works well for most, but not all small organic radicals.[86,94] This limitation stems from the models central thesis - which considers the detached orbital as a superposition of just s- and p- components, as these should dominate near threshold, per the Wigner threshold law. The fraction of p-character in an orbital is denoted by γ. Under these assumptions, Equation 1.19 can be simplified as:[95]

$$\beta = \frac{2Z \cdot \mathrm{eKE} + 2A \cdot \mathrm{eKE}^2 - 4\mathrm{eKE} \cdot \cos(\delta_2 - \delta_0)}{A^{-1} + 2A \cdot \mathrm{eKE}^2 + Z \cdot \mathrm{eKE}} \tag{1.20}$$

where B is a constant similar to A in the Hanstorp construction, representing the relative scaling of the $s \rightarrow p$ and $p \rightarrow s$ detachment channels. Here, $Z = \frac{1-\gamma}{\gamma}\frac{B}{A}$. The value of the fraction B/A depends on the assumptions used[84,96] (in the case of a $2s2p$ hybrid orbital, the fraction takes a value of $8/3$, for example). This thus makes the s&p model a straightforward method for interpreting experimental PADs in terms of the orbital angular momentum of the system.

This treatment has been expanded by the Sanov group to treat single-centered orbitals of arbitrary angular momentum.[97] The now generalized framework here was expanded by our group[86] and the Gibson group[87] to include contributions from d-orbitals, assuming that the molecular orbitals involved were hydrogenic in nature.

1.2.3.3.3 Computational Methods While the s&p and spd models work well for some systems, there are a number of systems for which these fail to treat the anisotropy parameter - often cases where the molecular symmetry is low, where group theory becomes less useful, or in cases where the molecular orbital point group symmetry differs from that of the molecule (often the case for metal oxide clusters). Thankfully, there are some means of computing the dependence of the β parameter on eKE for a system using *ab initio* electronic structure methods. This method, developed by the Krylov group[98] allows calculation of photodetachment Dyson orbitals using an implementation of coupled cluster theory. These can then be used to determine the detachment cross section as well as the PAD as function of eKE for a given system.[99] More details on this and other computational methods for treating PADs are presented in 1.4.8.2.

1.2.3.4 Non-Franck Condon Effects

As mentioned above, the Franck-Condon (FC) approximation holds well for the vast majority of transitions observed by SEVI. In some instances, however, it fails to represent some transitions - these are often some of the most intriguing aspects of these systems. Such transitions can reveal vibronic coupling - a mixing of vibrational and electronic levels in a molecule, arising from a coupling of nuclear-electronic motion, i.e. a breakdown of the Born-Oppenheimer approximation. Additionally, these effects can reveal anharmonic effects wherein the harmonic approximation is violated, or can arise from indirect detachment of photoelectrons.

Here, we highlight common cases responsible for the breakdown of the FC-approximation in SEVI spectra, how they manifest in our spectra, give molecular examples, and what these processes reveal about these molecules.

1.2.3.4.1 Herzberg-Teller Coupling By far, the most common of these effects to appear in SEVI spectra is Herzberg-Teller (HT) coupling, also known as psuedo-Jahn-Teller (pJT) coupling. Here, the electronic and vibrational degrees of freedom mix (a breakdown of the Condon approximation (i.e. Equation 1.7 is no longer valid), such that the electronic dipole moment μ_e depends on both the electronic and nuclear coordinates. An expression

for coupling between Born-Oppenheimer states can be derived by expanding μ_e in a power series of nuclear coordinates. Once again, group theory proves to be powerful here, and these considerations can be greatly simplified using this framework.

Two vibronic states $|a\rangle$ and $|b\rangle$, representing some states $|a\rangle = |\psi_v^a\rangle |\psi_e^a\rangle$ and $|b\rangle = |\psi_v^b\rangle |\psi_e^b\rangle$, respectively, can be represented by their vibrational and electronic symmetries given by $\Gamma_v^{a,b}$ and $\Gamma_e^{a,b}$, respectively. These states can couple provided

$$\Gamma_A \in \Gamma_v^a \otimes \Gamma_e^a \otimes \Gamma_v^b \otimes \Gamma_e^b \tag{1.21}$$

where Γ_A is again the totally symmetric representation within the relevant molecular point group. This coupling results in a mixing of vibronic levels between $|a\rangle$ and $|b\rangle$, resulting in an admixture of the zero-order vibronic levels (i.e. no longer pure states) expressed as $|\Psi_a\rangle = A_{aa}|a\rangle + A_{ab}|b\rangle$ and $|\Psi_b\rangle = A_{ba}|a\rangle + A_{bb}|b\rangle$. Importantly, if $|b\rangle$ is FC-forbidden (i.e. $\langle\Psi_{anion}|b\rangle = 0$), then it should not appear in PES spectra in the absence of this coupling scheme, but if $|a\rangle$ has non-zero FC overlap with the anion ground state (i.e. $\langle\Psi_{anion}|a\rangle \neq 0|$), then detachment *can* be observed. Here, the intensity borrowed from $|a\rangle$ will result in the transition having contributions to its electronic character from $|a\rangle$ (contributed from the $A_{ba}|a\rangle$ term in $|\Psi_b\rangle$) while appearing in the spectrum near the binding energy associated with $|b\rangle$.

While this may sound quite exotic and therefore uncommon, it is anything but - HT coupling has been observed in a considerable number of molecules by SEVI,[41,65,100–104] most commonly in the neutral, and manifests in the SEVI spectra of NO_3 (Chapter 5), carbon clusters (Chapter 7), and silicon carbides (Chapter 8). This coupling is readily detected by SEVI owing to the different electronic character of the transition, which in turn impacts the angular momentum of the outgoing photoelectron ℓ_e. As outlined in Sections 1.2.3.2 and 1.2.3.3, this change in ℓ then has distinct impacts on both the PES cross section as well as the PAD, both of which are measured by SEVI natively - the imaging component yields PADs for each scan, and the scanning nature of the experiment probes transitions at a number of photon energies.

For a detailed description of how these manifest in SEVI spectra, as well as important considerations when making HT coupling assignments, review Chapter 5 covering the case of NO_3 where vibronic coupling is remarkably important. In brief, transitions involving the ν_4 transition to the $\tilde{X}^2A_2'$ neutral ground state are formally FC-forbidden, as this mode is not totally-symmetric ($\Gamma_e = e'$ in the D_{3h} point group). These transitions, however, can become active in the SEVI spectrum through HT coupling to a FC-allowed vibrational level in the $\tilde{B}^2E'$ electronically excited state of the neutral. Such a process was observed in the original anion PES spectrum of NO_3 taken by our group in 1991,[105] but was called into question.[106] Revisiting this system with cryo-SEVI revealed that this transition's PAD differs considerably from the vibrational origin (which must be FC-allowed) as does its intensity as a function of eKE - clear signs of HT coupling.

1.2.3.4.2 Jahn-Teller & Renner-Teller Coupling Jahn-Teller (JT) and Renner-Teller (RT) couplings are less common in cryo-SEVI spectra. In these coupling schemes, vibrational levels within a single degenerate electronic state of non-linear (JT) or linear molecules (RT) occur. As with HT coupling, group theory dictates that JT and RT coupling can only occur between states with the same total vibronic symmetry. As this coupling all occurs in the same electronic state, $|a\rangle$ and $|b\rangle$ are represented by the same $|\psi_e\rangle$ and so the following relation must be satisfied

$$\Gamma_A \in \Gamma_e \otimes \Gamma_{\nu_1} \otimes \Gamma_e \otimes \Gamma_{\nu_2} \tag{1.22}$$

where the superscript of the electronic state has been dropped, and $\Gamma_{\nu_{1,2}}$ are the characters of the two vibrational states in consideration. Note that while the product of any two irreducible representations always includes the totally symmetric representation ($\Gamma_A \in \Gamma_i \otimes \Gamma_i$), the product of representations for linear species can also include other symmetries as well, allowing for Γ_{ν_1} and Γ_{ν_2} to differ in symmetry.

In SEVI spectra, these effects often manifest as shifting and splitting of vibrational structure within a degenerate state,[104,107] though in rare cases, RT coupling can lend intensity to FC forbidden transitions.[108]

1.2.3.4.3 Anharmonic Effects In some instances, the assumption that each molecular normal mode can be treated as an independent oscillator - one made commonly when treating SEVI spectra - breaks down, owing to the shape of the potential surface. Such breakdowns often come from either double-well potentials or anharmonic coupling, both of which are reasonably-common.

Double-well potentials can lead to a number of effects in PES, but most commonly results in the appearance of transitions to non-totally symmetric vibrational levels. In the case of planar molecules, this often results in activity of the umbrella mode,[42,61] owing to the double-well potential associated with breaking molecular symmetry. Such a process occurs when a vibrational mode distorts a molecule such that it breaks planar symmetry, leading to a double-well potential surface splitting the vibrational levels supported by such a surface, most famously occurring in the umbrella mode of ammonia.[109] If such a double-well surface is capable of supporting both the left and right wavefunctions on the anionic potential and both sides of the well are populated, this will give rise to a doublet of transitions following photodetachment.[42,110] While anharmonic effects were not at play, they were considered as a possible explanation for the low-frequency doublet structure arising in the structure of detachment from $ZrO(OH)_2^-$ in Chapter 11.

Beyond double-well potentials, anharmonic terms in the vibrational potential energy surface can also give rise to perturbations that allow mixing of different vibrational energy levels, giving rise to anomalous transitions.[36,86] Such couplings typically occur only when levels of the same symmetry reside very near one another in energy and within the same electronic state. Such a requirement follows from Equation 1.21 - given that the electronic

symmetry is the same for both species, and the square of any irreducible representation includes the totally symmetric representation (i.e. $\Gamma_A \in \Gamma_i \otimes \Gamma_i$), leading to

$$\Gamma_a \in \Gamma_{\nu_1} \otimes \Gamma_{\nu_2} \tag{1.23}$$

Similar logic then implies that the the two vibrational modes coupled must then also have the same symmetry (i.e. $\Gamma_{\nu_1} = \Gamma_{\nu_2}$).

Notably coupling of this type does not demonstrate any of the characteristic effects (distinct anisotropy or threshold behavior) that make HT coupling so easy to assign in SEVI spectra. Nevertheless, this process has been observed in the SEVI spectra of anthracenyl anions[36] as well as *p*-pyridinide anions.[86]

1.2.3.4.4 Vibrational Autodetachment The final non-FC process to consider arises from a breakdown of our most fundamental assumption about PES - if Equation 1.1 is no longer true, then photoelectrons are not arising from a direct detachment transition and the considerations that follow must be re-evaluated. Electrons originating from such a process therefore do not have PADs or cross sections that are governed by the physics outlined in Sections 1.2.3.2 and 1.2.3.3.

Such a process is referred to as autodetachment, wherein an electron is emitted by some other means than photodetachment. This can occur when the incident photon is resonant with a particular anion excitation that lies higher in energy than the neutral binding energy. In such a case, the anion can absorb the photon, promoting it to some metastable excited state (A^{*-}) that then spontaneously detaches an electron through a non-radiative process[111,112]

$$A^- \xrightarrow{h\nu} A^{*-} \rightarrow A + e^- \tag{1.24}$$

Such a process is non-Born-Oppenheimer in nature, as this requires the vibrational (or rotational) and electronic degrees of freedom to mix in order to couple the autodetaching state to the neutral plus free-electron continuum. The resulting signature of this process in a SEVI spectrum is the drastic change in intensity (or appearance of) one feature in the spectrum over the narrow range of wavelengths for which the photon energy is resonant with the transition that promotes the anion to its metastable state (A^{*-}).

Such a process can give rise to transitions for which direct detachment from the anion ground state is FC-forbidden, as the neutral vibrational states accessed by this process are governed the propensity rules outlined first by Simons.[112] Such forbidden transitions are observed in the SEVI spectra of a considerable number of molecules,[36,42,101,113] including the spectra of $Si_2C_2^-$ presented in Chapter 8, and in the case of the vinylidene anion (H_2CC^-), where the autodetachment process is outlined exquisitely.

1.3 Infrared Vibrational Action Spectroscopy

Aside from the cryo-SEVI experiments performed at UC Berkeley, complementary infrared vibrational action spectroscopy experiments were performed at the Fritz Haber Institute (FHI) in Berlin, Germany in collaboration with the Asmis group. These methods are an excellent probe of the vibrational and geometric structure of large cluster ions that often are too complex for cryo-SEVI in its current incarnation to explore.

These methods differ from conventional infrared absorption spectroscopy, in which infrared light passes through a sample and the remaining intensity of light is recorded as a function of wavelength. This process is governed by Beer's law, which states that at each wavelength, the absorbance A of a sample is given by:

$$A = \log(I_0/I) = \sigma \cdot n \cdot l \tag{1.25}$$

where I_0 is the initial intensity of light impinging upon the sample, I is the intensity of the transmitted light, σ is the absorption cross-section, n is the number density of the sample, and l is the pathlength of the light through the sample.

Signal-to-noise is a common issue in many spectroscopic techniques, and infrared absorption is no exception. There exists some threshold below which detection of absorbed light, either due to the cross section, path length, or number density being too low. In the case of gas-phase experiments utilizing molecular ion beams, the predominant way by which gas-phase clusters are formed, direct absorption measurements are challenging,[114,115] owing to the low number density, n.

To circumvent this limitation, action spectroscopic techniques, including PES and as those employed at the FHI, measure an event that occurs as a result of absorption of a photon. The techniques used at the FHI and detailed below making use of mass spectrometry techniques to measure a change in mass as a result of absorption of IR light. In the Asmis group, this is often done *via* IR photodissociation (IRPD) and IR multiple photon dissociation spectroscopy (IRMPD).

1.3.1 Infrared Photodissociation (IRPD)

IRPD experiments are conducted by mass-selecting ions ($I^{+/-}$) before subsequently trapping them in a cryogenically-cooled radiofrequency ion trap. Much like cryo-SEVI, this trap serves to cool the clusters to their ground vibrational state, but also serves to allow for "tagging" of the clusters. In this process, the clusters are complexed with a weakly bound species, a tag, M, that should only loosely perturb the geometry and vibrations of the species, as well as dissociate once $I^{+/-}$ is vibrationally excited by the IR radiation.[116] The low temperatures of the trap facilitate the complexation of the ionic clusters ($I^{+/-}$) with the molecular tag, though such a technique is possible, albeit more challenging, in the absence of a trap.[117]

Following this, the species is irradiated by IR light, resulting in a depletion of the tagged complex, $I^{+/-}\cdot M$, in the mass spectrum as the IR wavelength is scanned:

$$\mathrm{I}^{+/-} \cdot \mathrm{M} \xrightarrow{h\nu} \mathrm{I}^{+/-*} \cdot \mathrm{M} \rightarrow \mathrm{I}^{+/-} + \mathrm{M} \tag{1.26}$$

In order to carry out these experiments, an intense, tunable, and narrow source of IR radiation is needed. The IRPD experiments detailed in this thesis were performed at the infrared free electron laser (FEL) facility at the FHI.[118] The FEL can produce wavelengths between 400-3000 cm^{-1}, with a fwhm of 0.5% of the photon energy. A table-top IR source is also a viable option for higher IR frequencies.

1.3.2 IR Selection Rules

The features that appear in an IRPD spectrum are dictated by the selection rules that govern vibrational transitions. The starting point for these is once again Fermi's Golden Rule (Equation 1.3), which gives us the probability for absorption of a linearly polarized photon. Considering only vibrational transitions, which depend only on the nuclear dipole moment, μ_n, the intensity of a vibrational transition is represented as:

$$I \propto \left| \left\langle \psi_\nu^f \right| \mu \left| \psi_\nu^i \right\rangle \right|^2 \tag{1.27}$$

where $\left|\psi_\nu^{i,f}\right\rangle$ are initial and final vibrational wavefunctions. Important to note here is that the nuclear dipole moment, μ, is a function of the molecular bond lengths, and changes as the molecule vibrates. Vibrations along one of the n vibrational normal coordinates, q_j, then lead to changes in this function, which can be expressed in a Taylor expansion around its equilibrium value, $\mu(0)$

$$\mu = \mu(0) + \sum_j^n \left(\frac{d\mu}{dq_j}\right)_0 q_j + ... \tag{1.28}$$

Combining Equations 1.27 and 1.28 leads to

$$\begin{aligned} \left\langle \psi_\nu^f \right| \mu \left| \psi_\nu^i \right\rangle &= \left\langle \psi_\nu^f \right| \left[\mu(0) + \sum_j^n \left(\frac{d\mu}{dq_j}\right)_0 q_j + ... \right] \left| \psi_\nu^i \right\rangle \\ &= \mu(0) \left\langle \psi_\nu^f \middle| \psi_\nu^i \right\rangle + \sum_j^n \left(\frac{d\mu}{dq_j}\right)_0 \left\langle \psi_\nu^f \right| q_j \left| \psi_\nu^i \right\rangle + ... \end{aligned} \tag{1.29}$$

As normal modes (i.e. vibrational states) are orthogonal within the same electronic band, $\left\langle \psi_\nu^f \middle| \psi_\nu^i \right\rangle = \delta_{if}$, meaning that a transition to a new vibrational state such that $f \neq i$ causes the first term in the simplified Equation 1.29 above to be zero, leaving

$$\left\langle \psi_\nu^f \right| \mu \left| \psi_\nu^i \right\rangle = \sum_j^n \left(\frac{d\mu}{dq_j}\right)_0 \left\langle \psi_\nu^f \right| q_j \left| \psi_\nu^i \right\rangle \tag{1.30}$$

assuming 2nd order and above terms are negligible.

Take, for example, the term for the k^{th} vibrational normal mode:

$$\left(\frac{d\mu}{dq_k}\right)_0 \left\langle \psi_\nu^f \right| q_k \left| \psi_\nu^i \right\rangle \tag{1.31}$$

which can be re-written as

$$\left(\frac{d\mu}{dq_k}\right)_0 \left\langle \nu_k^f \right| q_k \left| \nu_k^i \right\rangle \prod_{j\neq k}^{n} \left\langle \nu_j^f \middle| \nu_j^i \right\rangle \tag{1.32}$$

owing to the orthogonality of each normal coordinate.

From this, we are able to extract the selection rules for IR spectroscopy - for a vibrational transition along normal coordinate q_k to be IR active, equation 1.32 must be non-zero, so each of the three terms must be non-zero.

The first term implies that if mode k is to be IR active, displacement along this normal coordinate must cause the dipole moment of the molecule to change. The second term, under the harmonic approximation, implies that only transitions with $\Delta\nu_k = \pm 1$ are active (as this integral is zero for all other transitions).[119] The third term will be non-zero only if all quantum numbers $\nu_{j\neq K}$ remain unchanged during the transition, as each distinct wavefunction is orthogonal.

The second and third conditions stated above rely on the harmonic approximation, and imply that overtone and combination band transitions are forbidden. Inclusion of higher-order terms (i.e. anharmonicity) can relax the second condition, allowing overtones with $\Delta\nu_k = \pm 2, \pm 3, ...$ Combination bands result from a coupling between normal modes that violates the independent oscillator assumption made above.

1.3.3 IRPD and Cryo-SEVI

While the vast majority of this thesis will tout the cryo-SEVI method, IRPD spectroscopy is, in many ways, complementary to our technique. Some components of the experiments themselves are similar - they both employ ions, and with that use similar sources, ion optics, cryogenic trapping, and rely on mass selection. Further, both techniques allow for the extraction of molecular vibrations, and with them molecular geometries. Such information is able to be gleaned from both spectra thanks to their comparable resolution, on the order of a few cm^{-1}, depending on the system (for SEVI) or FEL bandwidth (for IRPD at the FEL).

Where IRPD really flourishes is in the investigation of larger molecular clusters, for which SEVI spectra are untenable. This comes about thanks to the extended progressions in a number of vibrational modes observed in the PES spectrum. This leads to a particularly congested Franck-Condon envelope, that even with narrow linewidths and cold ions, can sometimes result in unresolved vibrational structure. IRPD, by contrast, does not have this issue as there is often only one feature for each IR active mode, leaving spectra of even

very large clusters - such as those presented in Chapter 10, which contain up to 20 atoms, 8 of which are metallic - relatively simple. Further, as all transitions are within the same electronic band here, there are fewer considerations about the non-FC behavior described above in Section 1.2.3.4. So while SEVI spectra may contain more information for a given cluster, this can become problematic for larger clusters where this complexity precludes interpretation - an issue that IRPD often does not suffer for larger clusters.

1.4 Theoretical Methods

The high resolution afforded by cryo-SEVI and IRPD allow for (and often require) the combining of theory and experiment to elucidate a full picture of the molecular physics displayed by the system in question. The following section outlines the fundamentals of the theoretical methods often employed in conjunction with these experiments, including Hatree-Fock (HF) theory (Section 1.4.2), on which density-function theory (DFT, Section 1.4.3) and wavefunction-based methods, such as Møller–Plesset (MP, Section 1.4.4.1) and coupled-cluster (CC, Section 1.4.4.2) theories are built. These methods, as well as multi-reference methods (Section 1.4.4.3), and excited state calculations (Section 1.4.6), have been utilized to understand cryo-SEVI and IRPD experiments, including the simulation of Franck-Condon profiles (Section 1.4.8.1) as well as Photoelectron Angular Distributions (Section 1.4.8.2). Together, these simulations provide insight into the molecular geometries, energy levels, couplings, and dynamics that govern the anions and neutrals studied by these methods.

Of course, these computations are no longer done by hand, as there is a suite of software packages capable of handling these computations. A summary of these programs, as well as common uses and user notes, are outlined in Section 1.4.8.3.

1.4.1 Electronic Structure Theory

The fundamental equation governing non-relativistic quantum chemistry is the time-independent Schrödinger equation[70]

$$\hat{H}(\mathbf{R}, r)\Psi(\mathbf{R}, r) = E(\mathbf{R})\Psi(\mathbf{R}, r) \tag{1.33}$$

where $\mathbf{R}$ are the nuclear coordinates of the system and r the electronic variables. In quantum chemistry, this equation is solved as a function of r with $\mathbf{R}$ fixed (i.e. $F(r)_{\mathbf{R}}$). To do so requires treatment of the Hamiltonian,

$$\hat{H} = -\frac{1}{2}\sum_{i=1}^{N}\hat{\nabla}_i^2 - \frac{1}{2}\sum_{i=1}^{M}\frac{1}{M_A}\hat{\nabla}_A^2 - \sum_{i=1}^{N}\sum_{i=1}^{M}\frac{Z_A}{r_{iA}} + \sum_{i=1}^{N}\sum_{j>i}^{M}\frac{1}{r_{ij}} + \sum_{A=1}^{M}\sum_{B>A}^{M}\frac{Z_A Z_B}{R_{AB}} \tag{1.34}$$

here shown in atomic units, where Z is the nuclear charge, M_A is the ratio of the mass of nucleus A to the mass of an electron, R_{AB} is the distance between nuclei A and B (i.e.

$R_{AB} = |\mathbf{R}_A - \mathbf{R}_B|$), r_{ij} is the distance between electrons i and j, and r_{iA} is the distance between electron i and nucleus A. M and N are the number of electrons, and

$$\hat{\nabla}^2 = \frac{\partial^2}{\partial x^2} + \frac{\partial^2}{\partial y^2} + \frac{\partial^2}{\partial z^2} \tag{1.35}$$

The solutions to this equation are E - the total energy, which is an eigenvalue of $\hat{H}$ with a corresponding eigenfunction (i.e. wavefunction) Ψ. Solving this equation is simplified greatly by employing the Born-Oppenheimer approximation[120] - separating the motion of the electrons from that of the nuclei. This assumption is central to quantum chemistry and holds for the vast majority of molecular systems. Such an assumption is fair as the nuclei are considerably heavier than the electrons, allowing for one to treat the electrons in a molecule to be moving in a field of fixed nuclei. Within this approximation, the second and last terms of Equation 1.34 can be neglected, allowing for a simplified Hamiltonian operator that describes the electrons

$$\hat{H}_e = -\frac{1}{2}\sum_{i=1}^{N}\hat{\nabla}_i^2 - \sum_{i=1}^{N}\sum_{i=1}^{M}\frac{Z_A}{r_{iA}} + \sum_{i=1}^{N}\sum_{j>i}^{M}\frac{1}{r_{ij}} \tag{1.36}$$

where the solution of the corresponding electronic Schrödinger equation takes the form

$$\hat{H}_e\Psi_e = E_e\Psi_e \tag{1.37}$$

which includes the solutions for the total electronic energy, E_e, and electronic wavefunction Ψ_e.

Solving the eigenvalue problem presented above yields a set of eigenvalues $E_0 \leq E_1 \leq E_2 \leq ...$ corresponding to a set of eigenfunctions $\Psi_0, \Psi_1, \Psi_2, ...$ that describes the distribution of electrons for a fixed nuclear position. Additionally, the total energy can be obtained by adding the nuclear-nuclear repulsion energy (the final term in Equation 1.34) to the electronic energy.

$$E_{tot} = E_e + E_n \tag{1.38}$$

Together, Equations 1.36 1.38 constitute the "electronic problem", which is treated by the different electronic structure methods outlined below. The existence of such a variety of methods originates from the presence of electron correlation, precluding the exact (analytic) solution of these equations for all but the most trivial of systems.

One common approximation employed to solve Equation 1.36 is the mean-field approximation, in which the wavefunction is approximated as an antisymmetrized product of one-electron wavefunctions, namely molecular orbitals determined by considering the electron as moving within an average field of all other electrons. Such a treatment allows for the use of the well-known Slater determinant wave function[121,122]

$$\Psi = \frac{1}{\sqrt{n!}} \begin{pmatrix} \chi_1(1) & \chi_2(1) & ... & \chi_n(1) \\ \chi_1(2) & \chi_2(2) & ... & \chi_n(2) \\ \vdots & \vdots & & \vdots \\ \chi_1(n) & \chi_2(1) & ... & \chi_n(n) \end{pmatrix} \tag{1.39}$$

where χ_i is the product of molecular orbital ψ_i and a spin function α or β. Determining the optimum set of MOs by variationally minimizing the energy in an approach termed "self-consistent field" or the SCF approximation.

1.4.2 Hartree-Fock Theory

The archetypal SCF method is the Hartree-Fock (HF) approximation, which itself constitutes the first step towards more accurate approximations, as outlined in Sections 1.4.4.1 and 1.4.4.2 below.

The simplest anti-symmetric wavefunction that can be used to describe the ground state of an N-electron system is a single Slater determinant

$$|\Psi_0\rangle = |\chi_1\chi_2 \cdots \chi_N\rangle \tag{1.40}$$

The best wavefunction of this form, per the variation principle, is the one that yields the lowest possible energy

$$E_0 = \langle\Psi_0| \hat{H}_e |\Psi_0\rangle \tag{1.41}$$

where $\hat{H}_e$ is the full electronic Hamiltonian. The parameter that can be varied to optimize this function is the choice of spin orbitals - by systematically varying the spin orbitals ($\chi_i(j)$) with the constraint that they remain orthonormal;

$$\langle\chi_i|\chi_j\rangle = \delta_{ij} \tag{1.42}$$

until the energy E_0 is minimum, one can determine the equation for the best (HF) spin orbitals. This equation takes the form

$$f(i)\chi(\mathbf{x}_i) = \epsilon\chi(\mathbf{x}_i) \tag{1.43}$$

where $f(i)$ is an effective one-electron operator, called the Fock operator, of the form

$$f(i) = \frac{1}{2}\nabla_i^2 - \sum_{A=1}^{M} \frac{Z_A}{r_{iA}} + \nu^{HF}(i) \tag{1.44}$$

where $\nu^{HF}(i)$ is the average potential experience by the ith electron due to the presence of the other electrons. The essence of the Hartree-Fock approximation is to replace the complicated many-electron problem by a one-electron problem in which electron-electron repulsion is treated in an average way.

Here, the HF potential depends on the spin orbitals of the other electrons (i.e. the operator depends on its eigenfunctions), and so the HF equation (Equation 1.43) is nonlinear. This requires the equation to be solved iterative, in a process referred to as the SCF method.

In such a process, an initial guess at the spin orbitals is made, allowing for the calculation of the average field (ν^{HF}) seen by each electron, allowing for the solution of Equation 1.43 to determine a new set of orbitals. These are then fed through the same process until self-consistency is reached (i.e. until the fields no longer change, leading to the input and output orbitals converging to the same function).

Such a process leads to a set of orthonormal HF spin orbitals with a corresponding set of orbital energies. The N spin orbitals with the lowest energies are called the occupied orbitals, while the remaining orbitals are referred to as virtual (or unoccupied) orbitals. The Slater determinant formed from the occupied orbitals is the HF ground state wavefunction and the best approximation to the ground state of the system of the single determinant form.

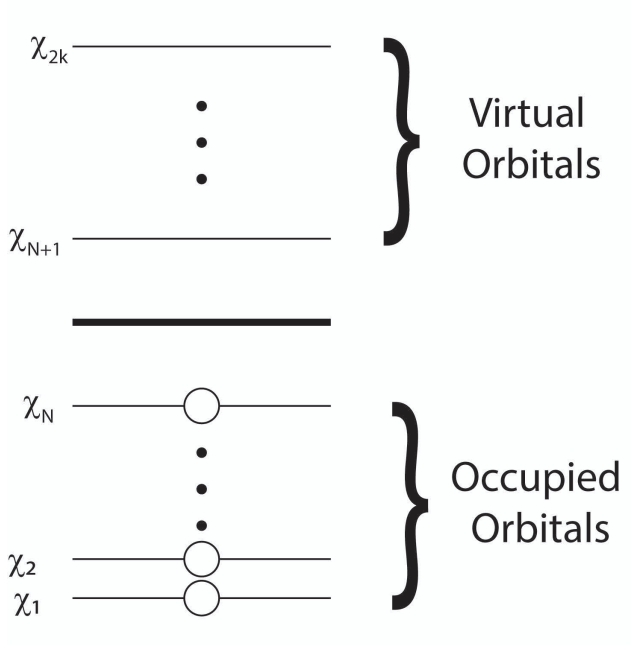

Figure 1.6: The Hartree-Fock ground state determinant, $|\chi_1, \chi_2, ...\chi_N\rangle$.

There are, however, an infinite number of possible solutions to Equation 1.43 - these are reduced in practice by the use of a finite set of spatial basis functions

$$\psi_i(\mathbf{r}) = \sum_{\mu} = c_{\mu i}\phi_{\mu}(\mathbf{r}) \tag{1.45}$$

which allows for expansion of the HF wavefunctions in this basis, allowing for the solution of the coefficients when iterating these wavefunctions through Equation 1.43. This reduces the HF equation to the Roothaan-Hall matrix equation[123,124]

$$FC = \epsilon SC \tag{1.46}$$

where F is the Fock matrix, C is a square matrix of the orbital coefficients, S is the atomic orbital overlap matrix with elements

$$S_{\mu\nu} = \int \phi_\mu(\mathbf{r})\phi_\nu(\mathbf{r})d\mathbf{r} \tag{1.47}$$

and ϵ is a diagonal matrix containing the orbital energies. Here, it should be clear that the use of a basis set with K spatial functions leads to a set of $2K$ spin orbitals (i.e. K with α spin and K with β spin), bounding the number of orbital solutions. Here, we have N occupied spin orbitals and a complementary set of $2K - N$ virtual orbitals. Of course, the larger and more complete the basis set of choice, the greater the degree of flexibility in the expansion and the lower expected energy, E_0, until a limit is reached - known as the Hartree-Fock limit. This limit is often above what is required for modern chemical applications, as the error associated with this limit is well above "chemical accuracy", or substantially larger than the energies involved in many current chemical questions (i.e. well above kcal/mol energies needed for structural determination).

This limit comes about from the HF approximation's explicit neglect of the instantaneous electron-electron correlations that are averaged out by the SCF procedure. Many other wavefunction-based methods (Section 1.4.4) have been developed to explicitly treat this correlation energy and achieve higher accuracy.

1.4.3 Density Functional Theory

Similar to Hartree-Fock theory described above, Density Functional Theory (DFT) is a SCF method, though the treatment here is different, and will be discussed below. Importantly, these calculations have proven to provide chemical accuracy for low computational costs,[125,126] allowing for their implementation to treat large systems. For this reason, DFT has emerged as perhaps the most dominant quantum chemistry methodology.[127]

Because of this relatively cheap computational cost, which translates to less computational time and thus less monetary cost, and relatively high accuracy, we often employ DFT computations to understand cryo-SEVI spectra. At times, these are preliminary calculations to determine if a molecule is amenable to being studied (i.e. has a good FC profile, see Section 1.4.8.1), while at other times, these calculations are used to explain the spectra in full (See Chapters 10 and 11).

Density Functional Theory is a theory, primarily, of electron ground state structures based on the electron density, $\rho(\mathbf{r})$, rather than the many-electron wavefunction, $\Psi(\mathbf{r}_1, ..., \mathbf{r}_N)$ employed in HF and its extensions (see Section 1.4.4). There are a number of distinct similarities and differences between these two theoretical frameworks. For example, the many-electron wavefunctions used in wavefunction-based methods are comprised of single-electron orbitals, which are analogous to the Kohn-Sham orbitals used by DFT. Additionally,

both the many-electron wave function and electron density are often constructed by using the SCF approach. Importantly, however, DFT methods are able to introduce electron correlation directly into the SCF method, while the methods outlined in Section 1.4.4 must introduce this after the SCF calculation. This allows for DFT calculations to be much cheaper than these methods, but introduces the central sin of DFT - while the DFT approach is exact in principle, in practice, it relies on modeling an unknown exchange-correlation energy functional. Determining more accurate functionals is an active field of research, and has lead to a considerable number of DFT functionals in the quantum chemist's toolkit.

1.4.3.1 DFT Theory

DFT was developed by Hohenberg, Kohn, and Sham,[128,129] and is based on earlier work from Dirac,[130] who showed that the exchange energy of a uniform electron gas can be computed exactly from the charge density. This methodology, now termed "orbital-free" DFT, benefits from the direct connection to density alone - allowing for a direct approach wherein the equations involved only rely upon this density. The shortcoming, however, is that treating the kinetic energy is untenable for many systems. Kohn and Sham realized that this could be circumvented by using an indirect approach in which the kinetic energy is computed exactly for a non-interacting reference system - the Kohn-Sham determinant. It was this development that made DFT into a practical tool for chemical calculations, and for which Kohn won the Nobel prize in 1998.

Within this framework, the ground state electronic energy, E, is[129]

$$E = E_T + E_V + E_J + E_X \tag{1.48}$$

where E_T is the kinetic energy, E_V is the electron-nuclear interaction energy, E_J is the Coulombic self-interaction of the electron density, $\rho(\mathbf{r})$, and E_X is the exchange-correlation energy. Importantly, E_V and E_J are known to take the form

$$E_V = -\sum_{A=1}^{M} Z_A \int \frac{\rho(\mathbf{r})}{|\mathbf{r} - \mathbf{R}_A|} d\mathbf{r} \tag{1.49}$$

and

$$E_J = \frac{1}{2} \int \int \frac{\rho(\mathbf{r}_1)\rho(\mathbf{r}_2)}{r_{12}} d\mathbf{r}_1 d\mathbf{r}_2 \tag{1.50}$$

where $\mathbf{r}$ is the electron coordinate, $\mathbf{R}_A$ are the nuclear coordinates of the Ath nucleus, and $\mathbf{r}_{12} = |\mathbf{r}_1 - \mathbf{r}_2|$ is the distance between two electrons. Importantly these equations can be solved exactly, though E_T and E_X cannot be solved exactly in terms of the electron density. These terms are represented in this framework as

$$E_T = \sum_{i=1}^{N} \langle \rho(\mathbf{r}) | \frac{1}{2} \hat{\nabla}^2 | \rho(\mathbf{r}) \rangle \tag{1.51}$$

and

$$E_X = \int f[\rho(\mathbf{r}), \hat{\nabla}\rho(\mathbf{r}), ...]\rho(\mathbf{r})d\mathbf{r} \tag{1.52}$$

Minimizing E with respect to the unknown Kohn-Sham orbital coefficients is similar to the SCF procedure performed for the HF calculations described above. Importantly, though, the inclusion of E_X here allows for the treatment of electron correlation in a manner that is ignored in HF theory. As shown above in Equation 1.52, the form that this takes is ambiguous, constituting the need for treatment with approximate density functionals to treat this.

1.4.3.2 Functionals

In DFT, "functionals" are the approximate forms that have been developed by many researchers that aim to treat the final component in Equation 1.48, and include exchange functionals, correlation functionals, and exchange-correlation functionals. Conventionally, these functionals are thought to reside on five rungs of a ladder ("Jacob's Ladder")[131] to classify them. The first rung of these depend only on (spin) density (ρ_σ), or the local spin-density approximation (LSDA). Such functionals are exact for the uniform electron gas, but perform substantially worse for molecules whose electron density is anything but uniform. To improve upon this, the density gradient, $\hat{\nabla}\rho_\sigma$, is added to account for the inhomogeneity of the density. These generalized gradient approximation (GGA) functionals comprise the second rung of the ladder, and perform significantly better than LDSA functionals for molecules.

To further improve upon these functionals, two additional ingredients can be added, the Laplacian of the density, $\nabla^2\rho_\sigma$, and the kinetic energy density

$$\tau_\sigma = \sum_i^{n_\sigma} |\nabla\psi_{i,\sigma}|^2 \tag{1.53}$$

Functionals that employ at least one of these ingredients reside on the third rung of the ladder and are called meta-GGAs. Such functionals further improve on the calculation of thermochemistry, kinetics, barrier heights, and some non-covalent interactions.

The fourth rung of Jacob's Ladder are termed hybrid density functionals - which include the most popular functional of the modern era, the B3LYP functional.[132,133] Within this rung are both "Global" hybrid (GH) functionals (including B3LYP) and "range-separated hybrids (RSH). GH functionals introduce a fraction of "exact" (HF) exchange to a function in the first three rungs, meaning this treatment can be applied to LSDA, GGA, or meta-GGA functions. For example, the B3LYP functional is

$$E_{xc}^{B3LYP} = c_x E_x^{HF} + (1 - c_x - a_x)E_x^{Slater} + a_x E_x^{B88} + (1 - a_c)E_c^{VWN1RPA} + a_c E_C^{LYP} \tag{1.54}$$

where Becke's 1988 functional (B88)[133–135] is augmented with the Lee, Yang, and Parr correlation function. The coefficients here can be determined either by empirically fitting to a data set of molecular properties (as was done for B3LYP), or can be motivated by theoretically treating some parameters.

A more recent approach for introducing exact exchange is through range separation. In such functions, the exact exchange contribution is split into both a short-range and long-range component, usually done by "turning on" the short- or long-range components at distances set by a fitting parameter ω, which is unique to each functional.

The final rung of the ladder is comprised of functionals that not only use occupied orbitals (*via* exact exchange), but also virtual orbitals (*via* MP2, see Section 1.4.4.1 below, or through the random phase approximation (RPA)). Such functionals are referred to as double hybrid (DH), and provide high accuracy, but at the cost of larger computational effort.

In recent years, there has been development of methods capable of describing non-covalent interactions - especially dispersion. Such treatment can be augmented into any of the functions in Jacob's Ladder, in practice, but this does not always yield favorable results - some semi-empirical functionals were parameterized using data sets without non-covalent interactions, leading to an overestimation of these effects already.

The question of what functional should be used to calculate certain properties of a particular chemical system is perhaps the most pertinent question for many chemists who dabble in theory. Unfortunately, this is highly system specific, as each functional is parameterized to address different needs, and each molecule has distinct properties that may or may not be adequately captured by a functional in question. Often it is useful to consider the theory literature, who frequently reviews the viability of certain functionals in particular cases.[127,136–140] In general, we have found Martin Head-Gordon's ωB97X-D functional,[141] which resides on the fourth rung, to perform well for a vast array of systems, including small radicals (primarily organic species) and metal oxides,[66] though more rigorous treatments are sometimes required.

1.4.4 Wavefunction-based Methods

As outlined above, HF theory can give a qualitatively correct picture of molecules, but frequently struggles to give quantitatively correct results. This deficiency arises from the fundamental assumption of the HF approximation, that electrons move independently within molecular orbitals subject to a mean field imposed by the neighboring electrons. Such an approximation overlooks the "correlation energy" of the electron-electron interaction, which is often critical for understanding molecular properties. As such, there exist a wide variety of procedures to estimate the magnitude of this error and correct for it. Such methods are often based on Hartree-Fock or Hartree-Fock-like wavefunctions, and are thus termed "wavefunction-based" methods. Importantly, the results of this method *can* be systematically improved, unlike the DFT methods described in the previous section. This, however, comes with a higher associated computational cost, which can become prohibitive for sufficiently high levels of theory and/or large molecules.

Such corrections fall into a few main categories. First, perturbative treatment of pair correlations between electrons, which can recover $\sim 80\%$ of the correlation energy in stable species, these are discussed below in Section 1.4.4.1. Second, self-consistent treatment of pair correlations, which can routine recover $\sim 95\%$ of the correlation energy, described in Section 1.4.4.2. Beyond this are active space methods, aimed to obtain a description of electron correlation in highly correlated systems - such as those with multireference character (often metal oxides), or diradicals. This class of theory is described in Section 1.4.4.3

1.4.4.1 Møller–Plesset Perturbation Theory

Møller–Plesset Perturbation Theory is a widely used method to approximate the correlation energy of molecules.[142] Second-order Møller–Plesset Perturbation Theory (MP2) is probably the simplest useful wave-function based electron correlation methodology, and is often based on the HF wavefunction, Ψ_0 which itself is an approximate solution to the exact Hamiltonian for the system. This wavefunction and its corresponding energy, E_0 however, are exact solution to he HF-Hamiltonian, H_0. If it is assumed the the HF wavefunction and energy are near the exact wavefunction, Ψ and energy, E, then the Hamiltonian then becomes

$$H = H_0 + \lambda V \tag{1.55}$$

where V is a perturbation, and λ is a dimensionless parameter. Then, by expanding the exact wavefunction and energy in terms of their HF counterparts, substituting into the Schrödinger equation, multiplying by Ψ_0, and integrating over all space returns the following expressions for the nth-order (MPn) energies:

$$E^{(0)} = \langle \Psi_0 | \, H_0 \, | \Psi \rangle_0 \tag{1.56}$$

$$E^{(1)} = \langle \Psi_0 | \, V \, | \Psi \rangle_0 \tag{1.57}$$

$$E^{(2)} = \langle \Psi_0 | \, V \, | \Psi \rangle^{(0)} \tag{1.58}$$

Here, the HF energy is then the sum of the zeroth- and first-ordered energies, and the electron correlation energy is then higher order terms, i.e.

$$E_{corr} = E_0^{(2)} + E_0^{(3)} + E_0^{(4)} + ... \tag{1.59}$$

where $E_0^{(n)}$ is the MPn energy.

The MP2 method is thus the simplest wavefunction-based treatment of electron correlation. Benchmarking of this methodology shows that it performs exceptionally for small closed-shell molecules,[143] where it outperforms more expensive methods for geometry optimizations and other molecular properties. This method has the advantage over DFT methods of properly incorporating long-range forces, namely dispersion. It does, however, struggle for open shell systems, for which the HF determinant is a poor starting point. This is a

particularly limiting shortcoming for use with cryo-SEVI, where detachment between and anion necessitate that one species is open-shell.

1.4.4.2 Coupled Cluster Theory

Another method for treating pair correlations is the coupled-cluster method, where the cluster operator contains all single and double substitutions,[144] CCSD. This method performs only slightly better than MP2 when calculating structures and frequencies for closed-shell species, but vastly outperforms MP2 when treating open-shell species, such as radicals.

The full derivation of the CCSD approach is beyond the scope of this chapter - for this, the reader is referred to one of many references available.[70] In brief, the CCSD wavefunction takes the form

$$|\Psi_{CCSD}\rangle = \exp\left(\hat{T}_1 + \hat{T}_2\right)|\Phi_0\rangle \tag{1.60}$$

where the single and double excitation operators, $\hat{T}_{1,2}$ can be definite by their actions on the reference determinant, here a single-determinant function (typically the HF determinant)

$$\hat{T}_1 = \sum_{i}^{occ}\sum_{a}^{virt} t_i^a \hat{a}^a \hat{a}_i \tag{1.61}$$

$$\hat{T}_2 = \frac{1}{4}\sum_{ij}^{occ}\sum_{ab}^{virt} t_{ij}^{ab} \hat{a}^a \hat{a}^b \hat{a}_i \hat{a}_j \tag{1.62}$$

where $\hat{a}^a = \hat{a}_a^\dagger$ and $\hat{a}_i$ are the creation and annihilation operators, respectively, while i and j stand for occupied states, and a and b for unoccupied states. Together, these operators act on the reference function, $|\Phi_0\rangle$ to convert it into a linear combination of the singly and double excited Slater determinants, if applied not in the exponential form show in Equation 1.60. Apply the exponential cluster operator to the wavefunction, allows for the generation of more than double excited determinants, due to the powers of $\hat{T}_1$ and $\hat{T}_2$ that appear in the expansion of this function, i.e. expanding the operator $\exp\left(\hat{T}\right)$ in a Taylor series yields

$$\exp\left(\hat{T}\right) = 1 + \hat{T} + \frac{1}{2!}\hat{T}^2 + ... = 1 + \hat{T}_1 + \hat{T}_2 + \frac{1}{2}\hat{T}_1^2 + \frac{1}{2}\hat{T}_1\hat{T}_2 + \frac{1}{2}\hat{T}_2\hat{T}_1 + \frac{1}{2}\hat{T}_2^2 + ... \tag{1.63}$$

The coefficients t_i^a and t_{ij}^{ab} are weights of each excitation, and must be solved to determine the approximate solution $|\Psi_{CCSD}\rangle$.

This expansion can, of course, be extended to include higher-orders, including triple excitations (CCSDT) and even quadruple excitations (CCSDTQ), though the computational cost increases exponentially for each method. For this reason, a perturbative triple excitation method has been developed, termed CCSD(T),[145] which is cheaper than CCSDT (and only modestly more expensive than CCSD). The inclusion of these higher-order terms is necessary,

however, for some systems such a diradical species or strongly correlated systems, referred to as multi-reference systems, as more than one determinant shows significant contributions to the resulting wave function.

Nevertheless, coupled-cluster theory represents the "gold standard" for computational chemistry, and is often employed or required to compute molecular geometries and vibrational frequencies to a sufficient level for agreement with cryo-SEVI spectra. This method, however, does fail on occasion - treatment of strongly-correlated systems, such as metal oxides, poses a challenge for this method.[146] To address this, new implementations have been developed using complex-valued wavefunctions, which correspond to multi-determinant real-valued HF wavefunctions,[63] as shown in Chapter 9.

1.4.4.3 Complete Active Space Methods

As mentioned above, conventional wavefunction methods perform exceptionally well for many chemical systems, where correlation is weak-to-intermediate in strength. In certain cases, however, these methods fail to adequately capture the full effect of electron correlation, preventing the accurate determination of molecular structures and properties.

To treat this, the complete active space (CAS) family of methods were developed.[147] Here, a subset of the system's orbitals and electrons are "active" in the calculation and the full configuration interaction problem is solved exactly in this subspace. All other occupied orbitals are treated with a mean-field approach, and the unoccupied orbitals are virtual. For CASSCF, the orbitals composing these sets are optimized to obtain the lowest energy. Related is CASPTn, which is a perturbative method within the CAS framework.

Such a treatment scales rapidly with the size of the active space, with the current limit residing around 18 electrons in 18 orbitals for the most intense calculations. Common use is substantially smaller.

1.4.5 Other Ground-State Methods

Beyond the methods outlined above are a substantial body of theoretical work and methodologies that are designed to address specific problems that the above methods fail to capture adequately. Most relevant among these are the Multi-configurational self-consistent field method (MCSCF) and multi-reference configuration interaction (MRCI) methods.[148] These methods are designed for use with systems that cannot be adequately described by a Hartree-Fock wavefunction - the underlying requirement of all the methods described above (save DFT, but this has similar failure points to HF). This occurs for molecular ground states that are nearly degenerate, most commonly when a number of low-lying states are present.

Additionally, the above section has explicitly treated the *electronic* problem - we have not discussed vibrational or rotational treatments, though these are often not an issue provided the electronic problem is solved. There are some cases, however, where there is a coupling of vibrational and electronic levels that significantly perturb these levels and render conventional methods inadequate. In such cases, model Hamiltonians for the system in

question[100,104] (see Chapter 5) or full potential energy surfaces must be constructed for the system and quantum dynamics simulations must be performed to adequately capture the physics at hand.[41,149]

In practice, this work is best left to professional theorists, who make wonderful collaborators - rarely do experimentalists perform such extensive computational work.

1.4.6 Excited State Methods

Thus far, the discussion of methods has been limited to those that address the *ground*-state. Molecular excited states represent a completely different, and often more challenging, problem. This difficulty stems from the much greater diversity in the character of excited state wavefunctions, making it difficult to develop broadly applicable methods.

Recent developments, however, have brought about a suite of single-reference methods for treating excited states that give qualitative, and occasionally quantitative agreement with experimental observations.[150] These methods, however, perform poorly for states with two-electron excitation, and many struggle with excited states for open-shell wavefunctions.

As with ground-state methods, there is a compromise to be made between cost and accuracy. Two of these methods are described below.

1.4.6.1 Time-Dependent Density Functional Theory

The Time-Dependent Density Functional Theory (TD-DFT) framework allows for the determination of excited states of molecules.[151,152] This is based on the Runge-Gross theorem, which shows that for a given initial wavefunction, there exists a unique map between the time-dependent external potential of a system and its time-dependent density, allowing for a system relying on $3N$ variables to be represented fully by its density, which depends only on 3. Notably, unlike ground-state DFT, there is no minimization principle here, meaning that there is no way to ensure the converged value is the minimum energy, leading to fairly large errors.

A common approach to solving this is done by applying an electric field that varies in time to the ground state density and calculating poles in the response, corresponding to Bohr frequencies, i.e. excitation energies. Computationally, this is done by solving the eigenvalue equation[150,153]

$$\begin{pmatrix} A & B \\ B^\dagger & A^\dagger \end{pmatrix} \begin{pmatrix} x \\ y \end{pmatrix} = \omega \begin{pmatrix} -1 & 0 \\ 0 & 1 \end{pmatrix} \begin{pmatrix} x \\ y \end{pmatrix} \tag{1.64}$$

where A is a matrix of the form

$$A_{ia,jb} = \langle \rho(\mathbf{r})_i^a | \, H \, | \rho(\mathbf{r})_j^b \rangle = (\epsilon_a - \epsilon_j)\delta_{ij}\delta ab - (ja||ib) \tag{1.65}$$

with again, the subscripts a, b, i, and j representing unoccupied and occupied orbitals as before. Elements B can be computed similarly. This equation is then solved iteratively for a

few values of ω. A complete review of the mathematics and theorems involved can be found in Ref [150].

This method has become popular recently due to its low computational cost relative to other excited state methods and relative accuracy, given it natively addresses electron correlation effects to some degree. This method, however, does fail for high-lying states (i.e. beyond the first few excitations) - generally defined as any beyond the first Rydberg state.[154] Within this limitation, many functionals are able to achieve accuracies of ~ 0.3 eV.[155]

This resolution is sufficient in many cases for cryo-SEVI, where TD-DFT calculations are most commonly performed to determine the relative energetics of excited states that may be involved in vibronic coupling. Here, accuracy of ~ 0.5 eV is permissible, as this is often used to bolster coupling arguments along with experimental data. This method, however, does not perform exceptionally well in the case of cryo-SEVI experiments on excited states of molecules, where term energies are measured by cryo-SEVI on the order of cm^{-1}, or 0.0001 eV. In such cases, more accurate (and expensive) methods are often required.

1.4.6.2 Equation of Motion Theory

Electronically excited states of molecules can be determined at a similar level of theory as coupled-cluster by employing the equation-of-motion (EOM) method.[156] Such a treatment is able to determine term energies with accuracies of 0.1 eV, with those arising from single excitations performing better. This accuracy, however, comes at a substantially increased computational cost than TD-DFT.

Here, the excite-state wavefunction. Ψ_{es} is expressed as

$$|\Psi_{es}\rangle = \mathcal{R}\,|\Psi_{gs}\rangle \tag{1.66}$$

where Ψ_{gs} is the ground-state wavefunction, and $\mathcal{R}$ is the excitation operator of the form

$$\mathcal{R} = \mathcal{R}_0 + \mathcal{R}_1 + \mathcal{R}_2 + ... \tag{1.67}$$

where

$$\mathcal{R}_n = \frac{1}{n!^2} \sum r_{ijk...}^{abc...} a^\dagger i b^\dagger j c^\dagger k... \tag{1.68}$$

Here the usual notation is used, i.e. i, j, k represent orbitals that are occupied, while a, b, c are unoccupied. Additionally, the ground-state wavefunction is given by the coupled-cluster approximation (Equation 1.60). Combining this with Equation 1.66 returns:

$$H\mathcal{R}\exp(T)\,|\Phi_0\rangle = E\mathcal{R}\exp(T)\,|\Phi_0\rangle \tag{1.69}$$

As both $\mathcal{R}$ and T are excitation operators, they commute, allowing for the above to be rewritten as

$$[\exp(-T)H\exp(T) - E]\mathcal{R}\,|\Phi_0\rangle = 0 \tag{1.70}$$

which is an eigenvalue problem involving an effective Hamiltonian, $\bar{H}$,

$$\bar{H} = \exp(-T)H\exp(T) \tag{1.71}$$

While the above equation exact, it must be truncated at some point for computational reasons (often at the CCSD level), allowing for scaling that is on the order of N^6, though this includes treatment of correlation effects.

The identity of $\mathcal{R}$ depends on the calculation performed, and can be used to conserve the number of electrons and total spin (for bound-bound excited states), or not conserve electrons (for treatment of doublet radicals and open-shell species), or allow for a spin-flip (for treatment of diradicals).

Together, these options are useful for treating cryo-SEVI data when looking at excited states of neutrals, whether they are involved in coupling or observed in our spectra, and anions, in the event that excited states play a role in the spectra. Further, this method allows for the calculation of Dyson orbitals (see Section 1.4.8.2), which allow for simulation of PADs and photodetachment cross sections.

1.4.7 Basis Sets

Many of the previous discussions involve mention of "basis sets", and their implementation deserves some attention. Such a construction is a set of functions combined to model molecular orbitals that make computations tractable.[157]

As with many aspects of theory, there are myriad options, each optimized and tested on and for specific use-cases. Such a variety may be daunting for the newcomer to use, and for this reason, there are a number of tools to assist with selecting the proper basis set, most useful among them the "Basis Set Exchange".[158] This database is publicly available and allows for the selection of the elements comprising the species to be studied, returning basis sets that are suitable for treatment of such elements. Further, there are a number of reviews in the theory literature outlining the strengths of certain basis sets combined with methods.[159] What follows is a discussion of why some of these basis sets are "good" in certain cases.

1.4.7.1 Basis Set Basics

Basis sets have been constructed from a number of different functions, including Gaussian, plane wave, delta, and Slater.[160] These each have their own utility, but the most commonly-used basis sets for small molecules utilize Gaussian functions. The number of basis functions used depends on the number of electrons in the valence shell and in the molecular core, as well as if the atom is light (i.e. H or He) or heavy (else). While larger basis sets tend to perform better, contracted basis sets are much more computationally efficient and calculations employing these finish substantially faster. As with all other aspects of calculation, there is a balancing act between cost (time) and accuracy.

Many basis sets employed in chemistry are "split-valence" basis sets, wherein there are multiple basis functions corresponding to each valence atomic orbital. The size of these are denoted by double-, triple-, quadruple-zeta, and beyond for historical reasons, where a larger quantity employs more functionals. As the different orbitals employed have different spatial extents, these combinations allow for representation of the electron density over in a more appropriate manner for molecular systems.

Among these split-valence basis sets are the common Pople basis sets,[161] which have names of the form $j-x1(k+,l+)G(m,n)$ where j = 3,4,6, k is the number of sets of diffuse functions on heavy atoms, l is the number of diffuse functions on light atoms, and m,n refer to the polarization function sets on heavy and light atoms, respectively. For example, the 3-21+G** basis set contains polarization functions on heavy atoms and hydrogen, as well as diffuse functions on heavy atoms. These basis sets are very efficient for DFT calculations, but tend to perform worse for post-HF methods (i.e. MP2, CCSD).

In these cases, the Dunning basis sets[162] are ideal - as they have been optimized for converging these calculations. This basis uses the notation aug-cc-pVXZ, where $X = D,T,Q,5$ is the variable to denote double-, triple, quadruple-zeta, etc. The "aug-" denotation on the front is optional, but introduces an augmentation to add diffuse functionals that treat core electron correlation and diffuse molecular orbitals, as can arise in anions and some excited states. Note, however, that the Dunning set is only optimized for for the first three rows of the periodic table.[163]

There are also a few other specialized basis sets worth noting, namely the def2[164] and ANO[165] basis sets. The def2 basis set series has been employed for use with d-block metals,[65] which both the Pople and Dunning basis sets are unable to treat. This basis set was specifically optimized for treating elements Rb to Rn, and so is a good set to use for inorganic species. Similarly, the ANO set has been optimized for the first six periods and is an all-electron basis set that includes scalar-relativistic effects, which treats well heavier elements. Further, this method was optimized for multireference methods (CASSCF/CASPT2), and so is ideal for these applications.[165]

Importantly, notation used commonly in the chemical literature for theory uses the format method/basis set. So a calculation performed at the CCSD level, using the augmented correlation-consistent double-zeta Dunning basis, as was done for the Si_2C_2 molecule in Chapter 8, would be denoted CCSD/aug-cc-pVDZ.

1.4.7.2 Effective Core Potentials

Treatment of the lower half of the periodic table in quantum chemical calculations becomes increasingly difficult, owing to the larger number of electrons in heavy atoms as well as the increased importance in treated relativistic effects. Both of these issues stem from a large number of *core* electrons.

As core electrons do not play a major role, at least directly, in governing chemical behavior, they can be modeled using simpler potentials, greatly reducing the computational cost of treating them. Such pseudopotentials are termed Effective Core Potentials (ECPs), and

take on a few forms. "Large-core" ECPs include all non-valence shells, while "small-core" ECPs include the valence and the outermost non-valence shell. Small-core ECPs come at an increased computational cost, but return significantly improved results. Further, ECPs are constructed either on non-relativistic or quasi-relativistic all-electron calculations.

There exist a number of these ECPs, developed at Los Alamos,[166] Stuttgart,[167–169] and elsewhere.[170–172] These potentials have been optimized for treatment of very different atoms, leading to specific use cases for each. In practice, we rarely employ the ECPs on cryo-SEVI, given the relatively small size of molecules studied by the method.

1.4.7.3 Practical Notes

Selecting a basis set is very important for the accuracy and cost of a calculation. The use of any of the above listed basis sets is likely sufficient for initial calculations, provided the set is capable of treating the elements in the molecule being studied. Beyond this, though, there are a few considerations.

First, it is imperative that the same basis set be used for calculations that are to be directly compared, i.e. when computing properties of an anion and neutral of the same species or when comparing ground and excited state calculations for the same molecule. Changing basis sets between these computations will introduce systematic errors that cannot be separated.

Second, a review of the literature on the molecule in question or the theory literature broadly should be performed - often prior computations have been performed on molecules studied by cryo-SEVI. These should be used as a good starting point for choice of basis set and level of theory.

Third, when performing excited state calculations, a basis set appropriate for a ground state DFT or HF calculation will generally be appropriate to describe valence excited states. Many excitations, however, involve contributions from diffuse Rydberg orbitals, which often require the use of diffuse functions. For this reason, choosing a basis set that includes these is imperative for accurate excited state calculations.

1.4.8 Theory and SEVI: In Practice

Typical computations performed for cryo-SEVI experiments range from DFT to CCSDT, depending on the performance of each method. The selection of the method is often system dependent, but DFT is often first performed, given its relatively low cost, before post-HF methods are employed.

The most commonly performed calculation for cryo-SEVI is a geometry optimization and frequency calculation. In such a calculation, a guess geometry is given by the user, and the program used will make small changes, optimizing the energy at each step, and determine the minimum energy structure (i.e. the "optimized" geometry). This process is effectively solving the electronic problem at each step for a fixed nuclear configuration, and iterating over a number of nuclear configurations.

Once the geometry has been determined, the vibrational frequencies for such a geometry can be determined. This is done by determining the force constants for each normal mode, owing to the differential of the potentials - this is done either analytically or numerically. Either method, however, returns the vibrational frequencies as well as the normal modes associated with these energies.

Such calculations are performed on both the anion as well as the neutral and are imperative for the simulation of cryo-SEVI spectra (see Section 1.4.8.1), which requires the geometry, normal modes, and frequencies for both initial and final states.

Often, the neutral geometry will have been determined by theory or experiment, but the anion will be unexplored. On occasion, multiple low-lying structures of the neutral and/or anion are stable, and require calculation of all possible structures, in a number of spin-states, to determine the lowest energy structure as well as which structure(s) are appearing in the cryo-SEVI spectrum (see Chapters 8 and 11). In such instances, it is sometimes necessary to search for possible geometries. There exist algorithms designed to search for these structures,[173] which have not yet been implemented for our experiments, owing to the small size of the systems studied here.

Beyond searching for molecular geometries, calculation of Dyson orbitals are commonly performed to predict detachment cross-section and PADs (see Section 1.4.8.2). Other common calculations for cryo-SEVI include anharmonic vibrational calculations, excited state calculations, and isomerization barrier searchers. In all cases, where calculations are to be performed using an optimized geometry, such as excited state calculations, it is imperative that the level of theory remain constant between the geometry optimization and other calculation. Variations in the level of theory will lead to different optimized geometries, so changes here lead to calculations on non-optimized structures which are ultimately meaningless, physically. For example, excited state ordering may change significantly depending on the difference in level of theory (i.e. geometry optimized at B3LYP/aug-cc-pVDZ and excited state calculations at the EOM-CCSD/aug-cc-pVTZ level will have *significant* variance from TD-DFT B3LYP/aug-cc-pVDZ).

Additionally, future work using IR-cryo-SEVI (Chapter 3) will likely require an increase in high-level (i.e. CCSD or higher) calculations with anharmonic corrections for anions. Such calculations are notably expensive, so use of software optimized for these calculations, namely CFOUR,[174] is *strongly* recommended.

Finally, while the scope of computation available to the experimentalist is constantly expanding, many computations go beyond what can (or should) be performed by the lay-chemist. In this case, it is advisable to collaborate with theorists, who specialize in many of the field cryo-SEVI often encounters, including vibronic coupling, quantum dynamics simulation, rigorous geometry searching, and high-level theory (model Hamiltonians, CCSDTQ, multireference methods).

1.4.8.1 Franck-Condon Simulations

While the geometry optimizations and frequency calculations discussed above can be used to get an idea of the positions of features that appear in cryo-SEVI spectra, a full simulation of the photoelectron spectra is required to make an assignment. Namely, calculation of the Franck-Condon overlap between the various vibrational wavefunctions of the anion and neutral is performed to model our data. These simulations are often performed using the ezSpectrum software package,[175] which requires the molecular geometry, normal mode displacements, and vibrational frequencies to perform such a calculation.

This is done for each vibrationally excited neutral level, $\phi_{\mathbf{n}}^{N}$, each of which are determined by $\mathbf{n} = (n_1, n_2, ..., n_M)$, where M is the number of vibrational modes in the species. As such, ezSpectrum computes the following $2M$-dimensional integral

$$\int\int \phi_0^A(\mathbf{q}_A)^* \phi_{\mathbf{n}}^N(\mathbf{q}_N) d\mathbf{q}_A d\mathbf{q}_N \tag{1.72}$$

where the normal coordinates of the anion and neutral are expressed as $\mathbf{q}_{N,A}$.

The above integral is valid only when the anion and neutral normal coordinates are largely parallel. In the event that they are not (a common occurrence), a transformation between anion and neutral coordinates must be performed. Normal modes of the initial and target states (i.e. anion and neutral, respectively) are related by the Dushinsky transformation[176]

$$\mathbf{Q'} = \mathbf{JQ} + \mathbf{K'} \tag{1.73}$$

where $\mathbf{Q}$ and $\mathbf{Q''}$ are the normal coordinates of the neutral and anionic states, $\mathbf{J}$ is the Duschinsky rotation matrix, and $\mathbf{K'}$ is the difference in anion and neutral geometries, in terms of the anion normal coordinates.

As discussed in Section 1.2.3.1, the FC profile of a molecule is exquisitely sensitive to the geometry of both the initial and final states. For this reason, discrepancies between simulated FC profiles and cryo-SEVI data do not necessarily imply that non-FC behavior is occurring. This is true in the case of Si_2C_2, presented in Chapter 8, for which distortion along the ν_3 normal coordinate was required to find satisfactory agreement between theory and experiment. Such distortion represented a small change in bond lengths and angles of a few percent, but decreased the simulated intensity along this mode by an order of magnitude.

1.4.8.2 Photoelectron Angular Distribution Simulations

It is often useful to simulate the Photoelectron Angular Distributions observed from cryo-SEVI spectra. As discussed in Section 1.2.3.3, these distributions relay crucial information about the electronic character of a photodetachment transition. Modeling these PADs, then, allows for the determination of the states involved in such transitions and confirmation of assignments involving vibronic coupling.

Derivation of the mathematics involving PADs involve the central assumption that the photodetached electron comes from an anionic molecular orbital. This can be modeled by

a Dyson orbital,[98,177] which is a one electron orbital defined as the overlap between the N-electron molecular wave function and the N-1 electron wave function of the corresponding neutral

$$\phi^d(r_1) = \sqrt{N} \int \Psi_I^N(r_1, ..., r_N)\Psi_F^{N-1}(r_2, ..., r_N)dr_2...dr_N \tag{1.74}$$

where $\Psi_{I,F}$ are the initial and final states, whose superscripts denote the number of electrons in each wavefunction. The position of each electron is denoted by r_i for $1 - N$, where N is total number of electrons in the neutral.

Calculation of these Dyson orbitals can be done using the EOM methods described above in Section 1.4.6.2, and the output of these calculations can be fed into the ezDyson software package to calculate the PAD and detachment cross section as a function of eKE.

Such calculations for the PAD are performed by determining the matrix elements $\langle \phi^d | \hat{r} | \psi_k \rangle$ where $|\psi_k\rangle$ is the wavefunction used to treat the outgoing photoelectron, here a plane-wave with momentum k. This plane-wave is treated as a super-position of spherical waves, and importantly (see Chapter 7), placed on the center of mass of the molecule in question. This can have profound effects on the calculated differential and total cross sections, as well as the anisotropy parameter that can be calculated by this method. From this plane-wave expansion, the coefficients of the partial waves, C_{klm} can be determined, allowing for the explanation of near-threshold effects of cross section and determination of the contributions of different angular momenta to the outgoing electron.

While this method has served us well, it does have some limitations. First, it is computationally expensive, though this concern is mitigated somewhat by our recently-granted access to the Molecular Graphics and Computation Facility (MGCF), which has substantially increase the computational power we wield. The second, and more persistent issue is that the EOM method typically require a closed-shell reference. The code implemented in Q-Chem (see Section 1.4.8.3) allows for treatment of either the anion or neutral through electron detachment or attachment, respectively, both of which yield accurate results. In the rare case, however, that both species are open-shell, these methods are not viable, and require an alternative treatment.

Fortunately, Liu and coworkers[178] have developed a means of calculating PADs using standard DFT methods by employing the frozen-core approximation. Such a treatment uses a similar analysis as the ezDyson package, though is computationally much cheaper, in that it does not require EOM-CC calculations. While this code requires that the frozen-core approximation holds for the system under investigation, this restriction is not terribly limiting in our experience, given that most Dyson orbitals strongly resemble molecular orbitals of the anion.

1.4.8.3 Computational Software Packages

There exist a number of commercial software packages capable of handling the vast array of computational needs presented by cryo-SEVI. Above, we discussed both the ezSpectrum

and ezDyson packages, both developed by Anna Kylov's group at USC, for determining FC profiles and PADs, respectively. These require input files from the user that can be complicated, though some scripts are provided to aid in the writing of such input files.

These scripts work well with outputs from one of the major electronic structure packages, Q-Chem. This software is capable of handling any of the methods detailed in this section, though older versions have had trouble implementing CCSD(T). This package, unlike the ezX packages, is not hosted locally, but instead on the Molecular Graphics and Computational Facility's (MGCF's) server. This is necessary to expedite calculations, which can now be performed at speeds orders of magnitude improved when compared to the computations performed on the old Neumark group cluster, Aether.

Q-Chem is a very powerful software package,[179] and is our primary means of performing Dyson orbital and EOM-CC calculations, as many other software packages have not yet implemented these. Many of the calculations in this thesis were performed using Q-Chem. The downside of this package, however, is that all inputs must be created by hand with little support from a user interface or otherwise.

The Gaussian software package[180] is another viable option for electron structure theory calculations. While there are often less options presented here than Q-Chem, the graphical interface, GaussView, is remarkably helpful in constructing guess geometries. Some calculations on this package run slower than on other packages, but this is rarely limiting, as can be seen by the number of calculations performed in this thesis using Gaussian. Additionally, the outputs of Gaussian are not readily converted into the input files for ezSpectrum, nor are the provided scripts able to handle this task. For this reason, home-built scripts have been written to handle this, though they will need to be modified as Gaussian is updated. The current script, which handles Gaussian 16 outputs, is given in the Appendix.

The CFOUR software package[174] is also available on the MGCF - this program has been built and optimized for post-HF methods (MP2, coupled-cluster), and runs these calculations remarkably fast for the level of theory. It is therefore *strongly* recommended that these calculations are run on this software, especially the forthcoming anion anharmonic calculations required for IR-cryo-SEVI.

Finally, the ORCA software package[181] contains code to handle many DFT, MP2, coupled-cluster, and multireference calculations. This has been optimized for metal oxides and larger molecules, so multireference calculations (CASSCF, CASPT2, NEVPT, MRCI, etc) on metal oxides should be run using this package, if attempted.

1.5 Systems of Interest

Over the years, we have used the SEVI technique (complemented often by IRPD) to study a wide variety of molecular systems. These species can broadly be categorized as free radicals or molecular clusters - both are quite amenable for study by these techniques and have provided insight into these species broadly.

Many of the small molecules studied by SEVI over the years have been motivated by an interest in better understanding combustion chemistry, heterogeneous catalysis, atmospheric chemistry, and the contents of interstellar space. These are, of course, only part of the consideration - as spectroscopists, we're deeply interested in uncovering the underlying physics of these small molecules, and it is entirely fair to say that some species have been studied due to a fascination with these phenomena. Neumark group members and alumni know of Dan's fascination of the F + H_2 reaction, which falls into the category of transition state spectroscopy pioneered by the Lineberger group and pushed further by our group.

The following sections outline the broad categories of species often studied by SEVI, many of which pertain to the following chapters of this thesis.

1.5.1 Free Radicals

Free radicals are an important class of molecules containing an unpaired electron, which can impact their chemical behavior remarkably.[182–184] This is highlighted by the crucial role these species play in combustion chemistry,[185,186] atmospheric chemistry,[187,188] organic synthesis,[189] and biology.[190] Despite their ubiquity, these species are rather challenging to study with many spectroscopic methods. As open-shell species, radicals can be challenging to produce without by-products and with large number densities, owing to their generally high reactivities and short lifetimes. Fortunately, radicals typically have positive electron affinities, so production of stable, closed-shell anions is readily achieved using conventional gas-phase ion sources. Thus, anion PES is uniquely suited to probe the vibronic structure of these elusive neutral species *via* photodetachment of their corresponding anions.

SEVI, especially following the addition of the ion trap, is particularly well-suited to study these species - many larger radicals, particularly polycyclic aromatic hydrocarbons (PAHs) have a number of low-frequency modes and often small rotational constants that can lead to considerable spectral congestion. Cold anions reduce much of this complexity, leading to the elucidation of the complex vibronic structure of these species.

One such example is presented in Chapter 5, which discusses the cryo-SEVI spectroscopy of the nitrate radical, NO_3. This radical plays an immense role in the atmosphere, where it serves as the primary oxidizer in the nighttime troposphere, reacting to form HNO_3, N_2O_5, and organic nitrates that are subsequently incorporated into aerosols. Together, this mediates the formation of acid rain and NO_x cycles in the atmosphere, and is responsible for the largest source of uncertainty of the concentration of NO_x, O_3, and OH in atmospheric models.[191,192] To understand this reactivity, it is imperative to understand the vibronic structure of this molecule, which should mediate reactions, though this is no easy task, as the nitrate radical has five electronic states residing within 2 eV, and thus has considerable mixing between its electronic and vibrational levels. We obtained vibrationally-resolved spectra from cold NO_3^- anions, showing unambiguously that the role of vibronic coupling in this species is larger than had been previously thought and settling a long-standing controversy around the vibrational level structure of this molecule.

Chapter 6 presents cryo-SEVI spectra of the hydroxy radical, OH, following vibrational pre-excitation using a tunable IR source. This experiment is the first performed using the modified machine, using the newly termed "IR-cryo-SEVI" technique, wherein cold molecular ions are selectively excited using an infrared transition to an excited vibrational level shortly before being photodetached. Such a method, as shown in this chapter, should be generalizable to any anion with IR-active modes, allowing for probing of new regions of the neutral potential energy surface due to a change in the selection rules for detachment from vibrationally excited anions as compared to detachment from the ground state. Our preliminary results on OH reveal a rotationally-resolved spectrum, thanks to the colossal rotational constant of this radical (B $\approx$ 19 cm^{-1}), that shows a 30% depletion in signal arising from the ground state of the anion, $n, \nu, J = 0$, upon irradiation with IR light resonant with the R(0) transition in OH$^-$ (3591.53 cm^{-1}). This depletion is accompanied by the appearance of five new features, corresponding to all allowed photodetachment transitions from the newly populated rovibrational state of the anion. Further, by scanning the IR laser, this method can also serve as a novel action technique to obtain vibrational spectra of anions without the need for a perturbative molecular tag, as is used in IRPD. Here, this is demonstrated by measuring the vibrational frequency of the R(0) transition in OH$^-$ as 3591(1.2) cm^{-1}.

1.5.2 Interstellar Species

In interstellar space, there is a extremely low density of matter, and what exists is at remarkably cold temperatures ($\sim$ 2 K)[193] and constantly irradiated by UV radiation. Despite, and perhaps because of, these extreme conditions, a rich complexity of clusters and radicals abound in space. Quite a few of these species have been identified,[194] thanks in large part to the work of countless researchers doing both laboratory and telescopy studies, though likely the vast majority of these intersteller species remain unknown. The identification of these species is often done by assigning diffuse interstellar bands (DIBs) - ubiquitous absorption features in interstellar space arising from the species that constitute the cosmos - to transitions measured in the laboratory of specific molecules. Assignment of DIBs remains one of the predominant questions in astrochemistry, with accurate spectroscopic characterization of these species in the laboratory, by various techniques, including SEVI, remaining a crucial component in answering this question.

In Chapter 7, the cryo-SEVI spectra of the linear cumulene carbon clusters, C_7 and C_9 are discussed. Carbon clusters (C_n) are an extensively researched family of clusters with relevance to interstellar, plasma, and combustion chemistry.[195–198] Spectroscopic signatures of small ($n < 10$) carbon clusters have been identified in a variety of astrochemical measurements, establishing their presence in comets,[199] the circumstellar shells of carbon-rich stars,[200,201] and the interstellar medium.[202] Given the apparent ubiquity of these species throughout the known universe, there is considerable interest in accurate measurements of their vibrational frequencies and energetics, as these quantities aid in the assignments of astronomical data and in the formulation of chemical mechanisms by which these species are generated and depleted. Small C_n carbon clusters are predominantly linear, while cyclic

structures become important beginning around $n = 10$, and at larger n still, spheroidal fullerene cages dominate.[195] For even relatively small carbon clusters, such as C_7 and C_9, the vibrational and electronic structure is quite complicated. In this work, we were able to extract a number of previously unmeasured vibrational frequencies in both species, and measure the spin-orbit splitting in the C_7^- anion. Non-FC behavior in both species were observed, owing to HT coupling in both neutral species, though this coupling does not seem to perturb the geometry of these species. Finally, a comparison of the detachment cross section of linear C_5, C_7, and C_9, reveals that addition of more carbon atoms to the linear chains results in photodetachment from delocalized molecular orbitals with increasing nodal structure, resulting in threshold photodetachment cross sections that differ considerably from simple symmetry considerations.

Chapter 8 discusses the cryo-SEVI spectroscopy of 4-atom silicon carbide, Si_mC_n clusters - another class of bare Group 14 clusters of astronomical importance. Small silicon carbides have been detected in the circumstellar envelop of carbon-rich stars, such as IRC+10216,[203–208] suggesting more silicon carbides may exist in space. In this work, we characterized three species, SiC_3, Si_2C_2, and Si_3C, extracting a number of vibrational frequencies for the neutrals, owing to HT coupling in every cluster. Further, signatures of vibrational autodetachment were present in the dominant isomer Si_2C_2, though both other low-lying isomers were present in the SEVI spectra. Further, observation of the trapezoidal form of this species suggests that this species may be detectable in the interstellar medium due to its permanent dipole moment. Collectively, these spectra, when coupled with previous PES spectra and our *ab initio* calculations, reveal the energetic ordering of the isomers of these species.

1.5.3 Clusters

Understanding heterogeneous catalysis is one of the principle goals of modern physical chemistry. In such processes, catalysts are often based on transition metal oxides serve to catalyze many fundamental reactions, with the active sites often residing at molecular-level defects such as step, edges, vacancies, site impurities, or where the local stoichiometry and binding motifs differ from the bulk surface.[209–211] Investigating these sites with surface-science techniques, however, can be challenging given the difficulty to definitively probe surface defects as they comprise a relatively small fraction of the surface. Further, reproducing atomic-scale defects on a bulk surface can be remarkably challenging.

It has become commonplace, then, to use gas-phase ionic clusters as a proxy for studying these defect sites.[212–217] These model systems benefit from the ease at which gas-phase clusters can be produced, mass-selected, and controlled to select for charge, stoichiometry, or other desirable characteristics, before being studied with spectroscopic methods that can illuminate how these factors impact chemical behavior.[218–222] The results of these studies can then be reliably computed using high-level theory, owing to the small size of the systems involved, allowing for the elucidation of reaction mechanisms.

This, however, is dependent on the spectra having discernible vibrational structure - an issue that often plagued early anion PES studies on metal oxide clusters, which rarely yielded vibrationally-resolved spectra, owing to the high-temperatures associated with the clusters produced. The introduction of a cryogenic ion trap into SEVI has greatly reduced these complications, however, and has improved our ability to probe these clusters, allowing for the extraction of a wealth of information about the vibronic and geometric structure of these clusters and their isomers that were previously unresolvable.

This is highlighted in Chapter 9, which details the cryo-SEVI study of NdO. The involvement of a lanthanide in this system leads to remarkably multireference character, owing to the involvement of f-orbitals in this system. Nevertheless, spectra of the ground and excited state of this species reveal both electronic and vibrational transitions that are clearly resolved. The ground state manifold can be assigned using previous laser-induced fluorescence measurements, while the higher-lying structure remains out of reach of current computational methodologies. Appearance of anionic hotbands, due to incomplete cooling of these anions, demonstrates the challenge of cooling these metal oxide species, even with the cryo trap.

Chapter 10 focuses on the IRPD study of Nickel-doped aluminum oxide cations $(NiO_m)(Al_2O_3)_n(AlO)^+$ with m = 1-2 and n = 1-3. Alumina-supported nickel-based catalysts, Ni/Al_2O_3, constitute an important class of catalytic materials with a wide range of industrial applications, such as natural gas reforming for syngas production[223,224] and oxidative dehydrogenation of alkanes.[225,226] Recent reports have found this catalyst to be highly selective when compared to pure NiO crystallites, though the source of this selectivity is under debate - originating either from Ni in its common +2 oxidation state or in the +3 state, promoting the isolation of electrophilic oxygen (O^-). Using IRPD, we resolved a number of vibrational transitions that, when compared to simulated spectra, reveal the structures of these clusters correspond to the insertion of an Ni-O moiety into an Al-O bond of the corresponding $(Al_2O_3)_{1-3}(AlO)^+$ clusters, resulting in doubly or triply coordinated Ni^{2+}. Larger clusters, however, appear to support a biradical species comprising a terminal oxygen radical anion (Al-$O^{\cdot -}$) and a Ni^{3+} species, which may result in the highly selective mechanism of these materials.

As shown in Figure 1.7 below, many small gas-phase clusters are capable of reacting with small molecules such as CH_4,[227–231] leading to the formation of intermediates, transition states, and products. Introduction of these reactant gases to the clustering channel of our ablation source (see Section 2.2.2) allows for the generation of anion+reactant complexes that can proceed along the anionic analogue to this surface, allowing access to different regions of this reactive surface.

Modification of our ion source to allow for the introduction of a reactant gas, as outlined in Chapter 3 of Jessalyn DeVine's thesis,[232] has allowed us to probe the reaction surface of Group IV clusters interacting with water, as is detailed in Chapter 11, which details the reaction of $ZrO_2^{0/-}$ with water. The spectra of this reacted cluster are considerably more complex than that of $TiO_2^{0/-}$, resulting from the observation of two isomers of the

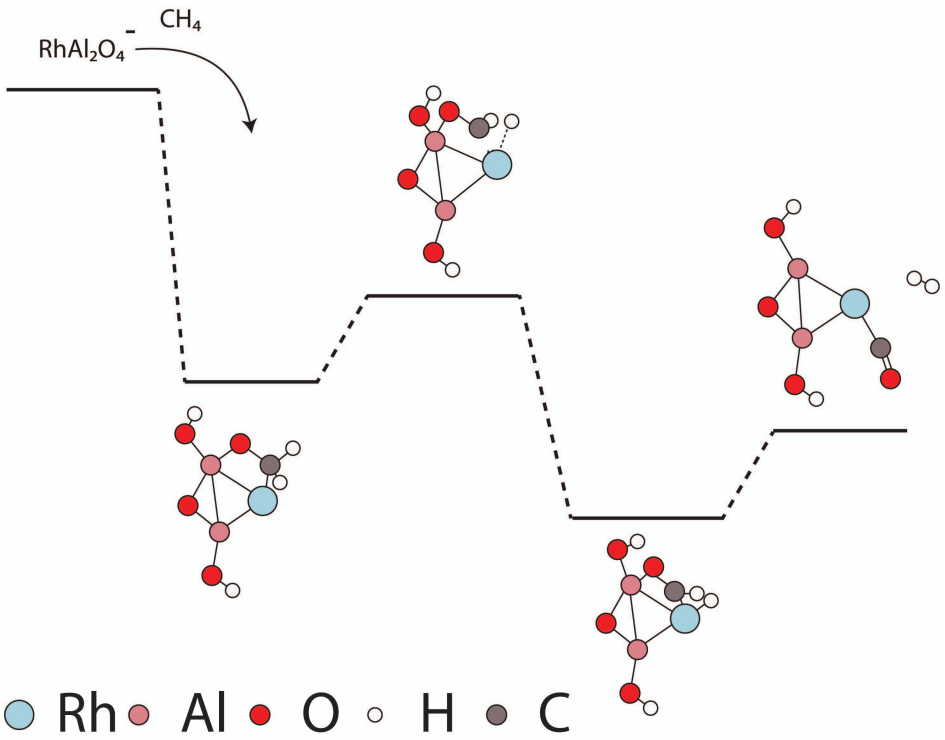

Figure 1.7: Simplified reaction pathway for methane conversion to H_2 by $RhAl_2O_4^-$ in the gas-phase. Computed structures from Li and coworkers.[227]

Zr-containing cluster. The appearance of two isomers here, but not in the Ti-containing system originates from the higher bond enthalpy of Zr-O as compared to Ti-O, resulting in a hotter cluster population entering the trap that is subsequently "frozen-in" by the kinetic trapping of the ion trap.[47,48] Finally, the relative EA's of both Group IV species when bare and reacted with water provides some insight into the relative reactivity of these clusters.

Both of these reactions, however, go to completion well before being probed, i.e. the products are formed readily by the hot clusters, which have sufficient thermal energy to surpass any barriers in the reactive surface. In order to probe the intermediates of these clusters, some degree of temperature control is required when reacting these clusters. For this reason, as well as studying larger clusters, which tend to give unresolvable structure owing to the increased number of FC-active modes and increased initial temperature, a second cryo-trap is to be installed into the instrument. Such a "pre-cooling" trap is detailed in Chapter 4 and in the forthcoming thesis of Marty DeWitt.

1.5.4 Transition State Spectroscopy

Chemists have long dreamed of being able to trace chemical reaction paths by determining the structures of intermediates. Paramount among these is the observation of transition states (TS), proclaimed as one of the "Holy Grails" of chemistry.[233] These transient species reside in the the transition-state region of the potential energy surface, where chemical bond formation and cleavage occur. Understanding this region of the potential surface can provide insights into the fundamental interactions that govern chemical reactivity. Therefore, there is significant interest in characterizing reaction TS's, their dynamics, and how these are impacted by the states of the parent reactants.

To this end, numerous experimental methods have been devised, though direct probing of TS's has proven challenging. Anion PES remains one of the few ways to spectroscopically access neutral transitions states on unimolecular surfaces,[234] and remains the only means of doing so for bimolecular surfaces.[235] Here, photodetachment from a bound anion of similar geometry to the desired neutral transition state results in a PES spectrum that is particularly sensitive to the shape of the neutral potential surface. It is then possible to observe Franck-Condon structure in modes orthogonal to the reaction coordinate as well as sharp features corresponding to transitions to discrete quantum states that are quasibound along the reaction coordinate. These resonances along the reaction coordinate are remarkable probes of the surface near the transition state, allowing for an unparalleled examination of these surfaces and serve as an excellent testing ground for theory.

The Lineberger group was the first to report anion PES transition state spectroscopy, probing unimolecular isomerization in the 1980s.[236,237] It was the Neumark group that pushed transition state spectroscopy into studying bimolecular reactions in the late 1980s and early 1990s with studies of hydrogen abstraction reactions and heavy-light-heavy systems.[238] Since, the technique has flourished in our group, having been used to study increasingly complex systems, as large as the F+CH_3OH reaction.

While this thesis does not contain a chapter outlining transition state spectroscopy, the promise of extending transition state spectroscopy has motivated the development of IR-cryo-SEVI (outlined in Chapter 3), which aims to probe the isomerization dynamics of vinylidene (H_2CC) to acetylene (HCCH) previously studied by our group[40,41,113] and others[14,236,237] by "turning on" the FC-activity of the isomerization coordinate. Such an experiment should allow for probing of new regions of the transition state potential surface, providing a glimpse of the 1,2-hydrogen shift in action. The report of this new study, as well as of transition state spectroscopy of the F+NH_3 reaction are forthcoming.

Chapter 2

Experimental Methods

2.1 Overview

The SEVI apparatus and method have been described in detail previously in the literature,[5,35,54,239] as well as in the Ph.D. theses of a number of previous graduate students.[39,232,240–244] A diagram of the machine in its current state is shown below in Figure 2.1, where major components are labelled.

The individual components that comprise the machine are detailed in the following sections. First, the ion source is detailed - anions are produced either using a filament ionizer (Section 2.2.1) or *via* laser ablation (Section 2.2.2). These ions are then guided through radiofrequency ion guides into the cryogenic ion trap (Section 2.3). It is within this ion trap that the ions are thermalized to the ground vibrational and electronic states before being extracted into a time-of-flight mass spectrometer (Section 2.4). Anions of the desired mass are then photodetached and the kinetic energy distributions of the resulting photoelectrons are imaged with a velocity-map imaging (VMI) spectrometer (Section 2.5). The voltages applied to this VMI lens are optimized to detect and magnify slow photoelectrons on the imaging detector, yielding high resolution. Individual electron events are processed and binned (Section 2.6) to acquire 2D images from which the 3D distribution of electron velocity vectors can be reconstructed (Section 2.7). Correlation of the radius of electron in an image and its kinetic energy is performed using a calibration, constructed from the photodetachment of atomic anions, for which the energetics of these transitions are know to exceptional precision (Section 2.8). Detachment itself is performed using a tunable-wavelength laser system capable of producing light from the mid-IR to the near-UV (Section 2.10).

The SEVI machine comprises five differentially pumped regions, labeled 1-5 in Figure 2.1. Regions 1-3 are connected *via* O-ring seals, while 4 and 5 are connected using ConFlat (CF) hardware. Notably, the chamber containing the cryo-trap (region 3) was machined by Y. T. Lee in the early 1960's while a graduate student with Bruce Mahan at UC Berkeley. Each region is pumped by a dedicated magnetically levitated turbomolecular pump (TMP) that itself is backed by a mechanical pump. The pumps used for each region are listed in

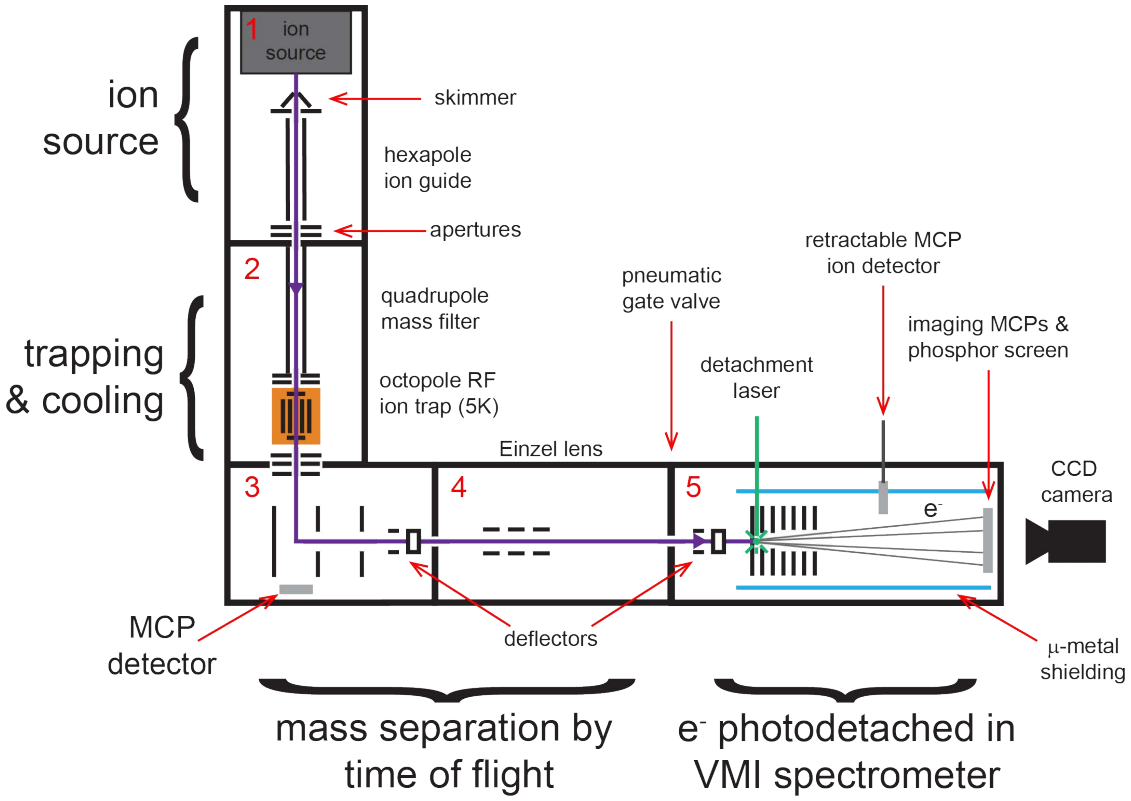

Figure 2.1: Diagram of the cryo-SEVI apparatus

Table 2.1, and typical chamber pressures, along with foreline pressures, are listed in Table 2.2. It should be noted that the pressure in the detector region has improved by two orders of magnitude over the past few years. This is the result of a few factors, namely baking the chamber, leak testing (many of the bolts holding this chamber together were loose), and replacing the battery in the TMP controller for the pump that evacuates the detector region. The controller is dated, and the circuit that powers the pump itself runs through the battery - any degradation in the battery therefore results in a decrease in current applied to the pump. Changing this battery out was found to improve pressures by an order of magnitude.

Many components within the machine are pulsed - to allow for use of a time-of-flight mass spectrometer. To enable this, a series of pulse generators are employed to pulse each component and ensure the relative timings share an internal clock. These units are three Quantum Composers pulse generators (model 9520, see the Appendix for full part number), labelled Q1, Q2, and Q3, that output transistor-transistor logic (TTL) pulses. The timing on each of the eight controllable channels on these boxes, labelled as $A_{1,2,3}$-$H_{1,2,3}$ where the letter indicates the channel and the subscript indicates which of the three boxes it resides, as well as their dependencies are outlined in Table 2.3. The first of these boxes (Q1) is internally triggered at 20 Hz and controls the timings for generating and trapping ions. Q1 is also used

Region	Turbo Pump	Pumping Speed for N_2 (L/s)	Backing pump
1	Seiko Seiki STP-A2203C	2200	Welch DuoSeal 1397
2	Boc Edwards STP-H2001K	2200	Edwards E2M40
3	Shimadzu TMP-803M	800	Edwards E2M18
4	Shimadzu TMP-303M	320	Edwards E2M18
5	Seiko Seiki STP-400	420	Varian SD-300

Table 2.1: Pumps used for cryo-SEVI.

Region	Chamber Pressure (Torr)		Foreline Pressure (Torr)	
	off	running	off	running
1	5×10^{-8}	2×10^{-5}	5×10^{-3}	2×10^{-2}
2	5×10^{-8}	2×10^{-6}	5×10^{-3}	8×10^{-3}
3	5×10^{-8}	2×10^{-7}	5×10^{-3}	5×10^{-3}
4	5×10^{-8}	2×10^{-8}	5×10^{-3}	5×10^{-3}
5	5×10^{-10}	1×10^{-9}	1×10^{-2}	1×10^{-2}

Table 2.2: Standard pressures in the cryo-SEVI vacuum chambers while running and when the machine is off.

to trigger the second pulse generator (Q2), whose outputs controls the timings of the mass selection, detachment, and imaging components of the experiment. Much like before, Q2 triggers the third box (Q3), which is mostly reserved for triggering new components in the dual-trap setup (see Chapter 4).

These pulse boxes also trigger the oscilloscope that we use to measure our ion signal on various detectors throughout the instrument. Of the four channels on the oscilloscope, the first is dedicated to the trapped ion detector in Region 2, the second for the retractable ion detector in Region 5, the third for the fast photodiode used to measure the laser pulse, and the fourth is the trigger, input by channel A on Q2. Importantly, the resistance of these oscilloscope channels can be changed, and should be 50 Ω for channels 1-3, and 1 MΩ for channel 4.

2.2 Anion Source

SEVI employs two methods of ion production: a circular filament ionizer to produce molecular anions and a laser ablation cluster source. Both sources employ a low-repetition rate

Channel	Source	Delay	Width	Trigger
A1	T0	5 ms	10 μs	Even-Lavie Valve Driver
B1	A	100 μs	1 μs	Ionizer Anode Pulser
C1	A	-2.8 ms	10 μs	Trap Gas Valve Driver
D1	A	37 ms	1 ms	Trap Exit Electrode
E1	F	-300 μs	10 μs	Ablation Nd:YAG Flashlamps
F1	A	180 μs	10 μs	Ablation Nd:YAG Q-switch
G1	A	100 μs	10 μs	Ablation Reactant Valve Driver
H1	D	-1 ms	10 μs	Trigger for Q2 & Q3
A2	H2	20-90 μs	4 μs	WMC 1 + Scope
B2	A2	230-930 ns	3 μs	WMC 2
C2	A2	var.	10 μs	Detachment Nd:YAG Q-switch
D2	C2	-110 to -180 μs	10 μs	Detachment Nd:YAG Flashlamps
E2	A2	var.	1 μs	MCP Gate
F2	A2	var.	3 μs	Mass Gate Deflectors
G2	H2	-300 μs	100 μs	CCD Camera
H2	H1	1 ms	10 μs	Re-define T_0 for Q2
A3	H1	-232 μs	10 μs	IR Nd:YAG Flashlamps (10 Hz)
B3	A3	260 μs	10 μs	IR Nd:YAG Q-switch (10 Hz)
C3				Empty
D3				Empty
E3				Empty
F3				Empty
G3				Empty
H3	H1	1 ms	10 μs	Re-define T_0 for Q2

Table 2.3: Typical timings and dependencies used for triggering various components of the cryo-SEVI apparatus as of May 2021. Channels ending in 1-3 correspond to outputs of the three Quantum Composers pulse generators. Owing to development of IR-cryo-SEVI, some channels may be changed soon.

Even-Lavie (EL) valve[245] that opens for 40-80 μs and is backed with 150-200 psi helium carrier gas containing trace molecular precursors and reactants as needed. The valve is triggered at 20 Hz, though it was running at 10 Hz since its installation, owing to a rate limiting dipswitch on the EL controller. This switch sets the maximum repetition rate delay between adjacent pulses, resulting in a 20 Hz trigger signal only triggering the valve at 10 Hz. Development of IR-cryo-SEVI (Chapter 3) led to this discovery, where detachment signal was only observed at 10 Hz, commensurate with ion signal on both ion detectors (when not averaging) showing ions produced at 10 Hz. Operational notes on this valve are presented

in the Appendix.

2.2.1 Filament Ionizer

We employ a filament ionizer to produce a variety of organic molecular anions. Our ionizer was commercially produced by the same Israeli company that built our EL valve (LAMID Ltd.). Important to note, however, is that their ionizers are no longer in production, requiring that we service them ourselves. Notes on how this should be done are provided in the Appendix.

The ionizer itself consists of a loop of thoriated tungsten filament (1" diameter) mounted 1/4" after the valve nozzle, with the nozzle centered within the loop. A current of 3-4 A DC is applied to the filament while in operation, resulting in thermionic emission of electrons. The filament concentrically surrounds a cylinder of grounded mesh, and is itself concentrically surrounded by a metal anode. Both the anode and the filament are pulsed to -300 V for ~ 150 μs, directing the electrons inwards, bombarding the gas pulse from the EL valve.

The electrons from the ionizer, primary electrons, collide with the carrier gas, producing secondary electrons that then react with the entrained molecular precursors. In this mechanism, chemistry is usually initiated by dissociate electron attachment to a neutral molecular precursor,[246] which is not a particularly clean source of anions, in that various side-products are often formed. This is forgivable, as our desired species will later be mass-selected, allowing for separation of products, though it is sometimes necessary to use functionalized precursors to selectively produce certain isomers. This is most commonly done by attaching a good leaving group, such as $Si(CH_3)_3$, to a particular site in the neutral precursor where electron attachment is desired. Such a method has allowed for the production of *ortho-*, *para-*, and *meta-* PAH species and other radical species.[36,57,86,94]

Such precursors can be entrained in the helium carrier gas in a number of ways. For gaseous precursors, we employ a manifold to fill our source cylinder with a mixture of ~0.1-1% precursor in helium. When working with volatile liquids, the vapor pressure is often sufficient to pull some off the liquid sample into the source cylinder, which is then filled with helium. Nonvolatile liquids and solid precursors can be loaded into a cartridge chamber within the EL valve, such that the carrier gas flows over the precursor prior to reaching the vacuum chamber. Additionally, a heater or home-built cooling jacket can also be attached to the EL valve to control the valve temperature, enabling heating to encourage vaporization or cooling to prevent degradation of sensitive molecular samples in the cartridge.

Upon exiting the valve and exposure to secondary electrons, a number of molecular anions of interest can be generated. In some cases, this can be done directly - as in the case of producing NO_3^-, where 2% dinitrogen tetroxide (N_2O_4) was used:

$$N_2O_4 + e^- \rightarrow NO_3^- + NO \tag{2.1}$$

Often, however, the source chemistry is not quite as direct, requiring the addition of trace NF_3 or N_2O to produce F^- or O^-, respectively

$$NF_3 + e^- \rightarrow F^- + NF_2 \tag{2.2}$$

$$N_2O + e^- \rightarrow O^- + NO \tag{2.3}$$

These atomic anions are used for calibration (see Section 2.8 below), as well as hydrogen-abstractors, allowing for the production of deprotonated species of interest, such as the vinylidene anion

$$H_2C{=}CH_2 + O^- \rightarrow H_2C{=}C^- + H_2O \tag{2.4}$$

or in the study of CH_3CO, for which we employ the previous discussed trimethylsilyl-substitution in tandem with F^- to produce CH_3CO^-

$$CH_3COSi(CH_3)_3 + F^- \rightarrow CH_3CO^- + FSi(CH_3)_3 \tag{2.5}$$

which is facilitated by the strength of the fluorine-silicon bond,[247] allowing for site-specific deprotonation.

Additionally, it is possible to produce weakly bound clusters with the ionizer, such as the NH_3F^- anion, allowing for transition state spectroscopy to be performed on the F + NH_3 reaction surface (publication forthcoming)

$$F^- + NH_3 \rightarrow NH_3F^- \tag{2.6}$$

Finally, some clusters and small molecules (such as OH^- or FH_2^-) can be synthesized directly in the ion trap *via* reactions with H_2. These reactions, however, have been found to produce anions that are rotationally much warmer than if produced in the ionizer. Further, it should be noted that the filament ionizer used produces relatively hot ions compared to the grid discharge used prior to the installation of the cryogenic ion trap.[242]

2.2.2 Laser Ablation

Laser ablation is a versatile method for the production of clusters from materials with low vapor pressure, allowing for the probing of a new class of species - metal oxides (M_xO_y). As mentioned in Section 1.2.1, the development of laser ablation cluster sources by the Smalley group[248,249] in the 1980's lead to the development of pulsed anion PES, as a result of the requirements of the method, as outline below.

The current ablation setup in the SEVI machine was designed and implemented in 2013 by Jongjin Kim. A detailed description of this configuration, along with design considerations, are presented in his thesis,[39] and an overview of daily use and maintenance are provided in the Appendix. In brief, the ablation setup is mounted to the EL valve such that the gas expansion out of the nozzle enters directly enters the gas channel. Slightly prior to the valve opening ($\sim 120\,\mu$s), a pulse of 532 nm light is focused onto a solid disk sample target through an orthogonal entrance channel. The disk is translated and rotated to ensure each pulse hits a fresh spot on the sample. This reduces heating and ensures that the surface is evenly

ablated in a spiral pattern, facilitating good transfer from the target into the gas channel. Translation and rotation are enabled by two DC motors mounted inside vacuum and fitted with water cooling jackets to prevent overheating. Cooling water is pumped through these jackets by a commercial water chiller (Coherent T255P), which maintains water temperatures of ~ 25 C.

The laser used for this is a Q-switched neodymium-doped yttrium-aluminum-garnet (Nd:YAG) laser operating at 20 Hz, originally a Continuum NY60B-2 unit built in December 1990. The power required to achieve sufficient ion signal to photodetach is in the range of 2-10 mJ/pulse (40-200 mW), depending on the system. In early 2021, it was found that this laser was incapable of producing more than 2 mJ/pulse, resulting its retirement. Since then, a new laser ablation laser, a Litron Nano S 120-20, has been installed, which is capable of producing up to 85 mJ/pulse (1.7 W) with a considerably higher energy density, owing to a smaller spot size at the laser aperture. Laser ablation has not yet been attempted with this new system, but the high power output promises to greatly increase the ion flux with laser ablation.

The pulse from such a laser serves to vaporize the surface, creating a plasma of atomic cations and electrons. This plasma is then quenched by a pulse of buffer gas that initiates collisional cooling and condensation of the atoms into clusters. These clusters are then carried by the buffer gas through a confined clustering channel to facilitate further cluster growth and collisional cooling prior to expansion into vacuum. The dominant species of ablation sources are cationic clusters and neutrals, though a sufficient amount of anions are produced for our needs *via* electron attachment to neutral clusters.

While the added versatility of laser ablation is remarkable, the clusters it produces are hot. There are a number of reasons for this - first, the initial plasma that is formed contains electronically excited species that can impart this energy into the subsequently formed clusters. Second, cluster condensation is a significant source of heat, as the enthalpy of each newly formed bond in a cluster is imparted into the cluster. This is especially prominent in strongly bound species, such as metal oxides, leading to the formation of many isomers.[60,66,101,103] Third, growth events can occur at any point in the clustering channel, meaning that the cluster population experiences various degrees of collisional cooling and is thus poorly thermalized. For these reasons, laser ablation was not an optimal source configuration for SEVI until the installation of the cryogenic ion trap.

It is worthy of note that we employ a disk target configuration, as opposed to the more commonly used rod target. This is, in part, because commercial sputtering targets are sold as disks that fit our specifications (1" diameter, 1/4" thick) - though the tolerances on such targets are often larger than those of our target holder, leading to targets that can become lodged in their mount. Nevertheless, the ability to purchase targets for a variety of metals, metal oxides, and semiconductor materials has proven to be remarkably useful. Further, disk targets are less likely to jam while rotating than rod targets and have the added benefit that they are markedly simpler to align than rod targets. Following extended use, targets will have a smaller radius (rods) or thickness (disks), which leads to complications in alignment for rods, while consumption of the flat side of disks presents no issues, provided the target

is pushed in place with a spring.

In this thesis, the laser ablation source was used in tandem with cryo-SEVI to study the C_7^- and C_9^- carbon clusters, 4-atom silicon carbides ($Si_xC_y^-$), and NdO^-. The formation of the carbon and silicon carbide species was performed by ablation a disk of silicon carbide, generating both sets of clusters. Meanwhile, NdO was formed from ablating a solid disk of Nd. Notably, we have found it unnecessary to add oxygen to the buffer gas mixture to generate metal oxides from targets here, owing to the trace oxygen in the gas lines and residual oxides on the target surface.

The study of the hydrolysis of ZrO_2^- was facilitated by the addition of a second pulsed valve and channel to our ablation source. This laser ablation reactor was designed and implemented by Jessalyn DeVine and follows early designs from the Smalley group,[250] as well as more recent configurations assembled in the Jarrold group[251] and the Asmis group.[252] The reactor allows for the introduction of a reactant gas in a narrow channel following the clustering channel, thereby encouraging reactions between the newly-formed clusters and the reactant gas of interest. In the study of ZrO_2^- with H_2O, helium was bubbled through water, ensuring a trace amount was carried into the reaction channel, leading to the formation of the $ZrO_3H_2^-$ anion. Full details of the source are provided in Jessalyn's thesis,[232] and those for the production of $ZrO_3H_2^-$ can be found in Chapter 11.

2.3 RF Ion Guides and Trap

The original design of SEVI had the ion source coupled directly into the time-of-flight mass spectrometer. This was changed during the major re-design of 2011-2012, where cryo-SEVI was built, and a new source chamber, radiofrequency (RF) ion guides, as well as a cryogenic ion trap (all of regions 1 and 2 in Figure 2.1) were introduced. Details of the design on these components are detailed in the literature[54] and JongJin Kim's thesis.[39]

The following sections aim to describe the fundamentals for the operation of these RF ion optics (Section 2.3.1), their implementation in cryo-SEVI (Section 2.3.2), and how they are used for cooling (Section 2.3.3).

2.3.1 Principles of Operation

RF multipoles have become an invaluable tool for manipulating gas-phase ions - quadrupoles have become commonplace in mass spectrometry, and higher order multipoles have become ubiquitous as ion guides or traps. In particular, these traps have the benefit of large effective trapping depths (on the order of 1 eV), substantially higher than the traps available for neutral species ($10^{-4} - 10^{-7}$ eV),[253] allowing for the trapping of ions with significant kinetic energy. Gerlich and others have extensively studied the use of multipoles for ion guiding and trapping, and present a detailed review of the field.[44,45]

Briefly, RF ion traps and guides typically employ a linear geometry of cylindrical symmetry. The electric potential, as a function of time, can be represented for an ideal two-dimensional multipole configuration of order n with infinite extension along the z axis by

$$V(r,\theta,t) = V_0 \cos(n\theta)\Big(\frac{r}{R_0}\Big)^n \sin(\omega t) \tag{2.7}$$

where V_0 is the RF amplitude, R_0 is the inscribed radius of the RF electrodes (see Figure 2.2), and ω is the angular frequency. In practice, such a field is generated by $2n$ cylindrical electrodes of radius ρ arranged to form a cylinder of inscribed radius R_0. The optimal electrode radius to approximate the curvature of the ideal multipole potential of Equation 2.7 is satisfied if the diameter of the rods fulfill the relation

$$\rho = \frac{R_0}{(n-1)} \tag{2.8}$$

Our ion trap, for instance, is an octupole ($n = 4$) and uses rods 3/32" in radius, necessitating that the inscribed radius is 9/32".

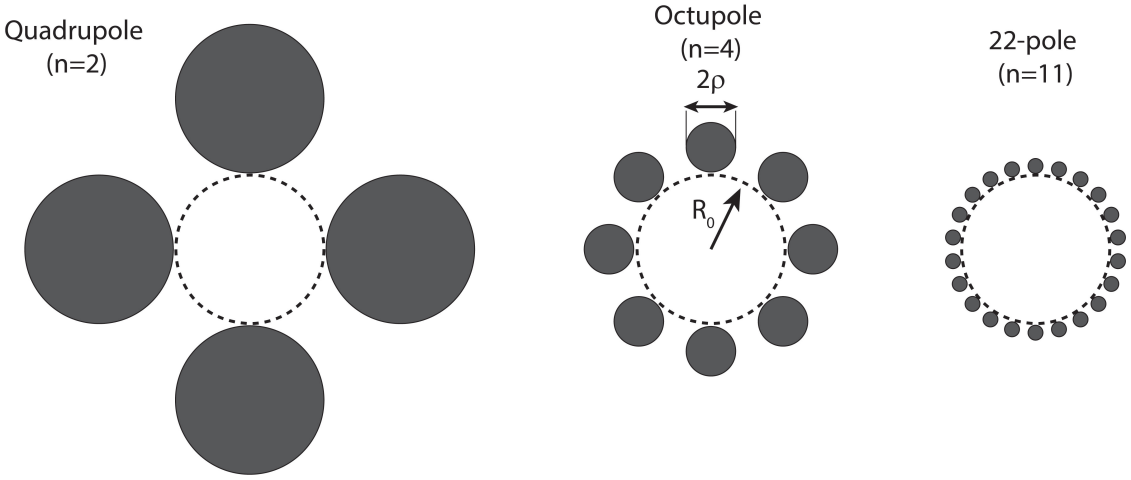

Figure 2.2: Electrode configuration for an ideal RF multipole of order $n = 2$, 4, 11 using a fixed value of R_0.

The dynamics of ions in the multipole trap's time-dependent field can only be solved analytically for $n = 2$, leading to well-defined conditions for stable trajectories wherein the particle does not collide with an electrode and remains axially confined for quadrupoles. For $n > 2$, solutions to these equations are not analytically solvable, requiring the treatment of the field with the effective potential approximation. The ideal two-dimensional multipole field of Equation 2.7 can be treated by averaging the time rapid oscillatory motion ("micromotion") of the particle while maintaining the slower drift motion, leading to a time-independent pseudopotential

$$V_{eff}(r) = \frac{q^2 n^2 V_0^2}{4m\omega^2 R_0^2}\left(\frac{r}{R_0}\right)^{2n-2} \tag{2.9}$$

For large n, this potential has a nearly field-free region central region with a rapidly increasing potential as a function of r, as shown in Figure 2.3a. For this reason, the 22-pole trap has become commonplace is gas-phase experiments,[254] as it generates a potential that results in very little RF micromotion in the center. Such micromotion leads to RF heating, wherein the ions enter regions with a high field gradient as the sign oscillates, quickly becoming repulsive and imparting energy into the trapped species.

Importantly, the effective potential picture fails when the amplitude of micromotion exceeds a critical value, leading to energy exchange between the slow drift motion and the rapid micromotion, causing the ion to be ejected from the trap. While this value cannot be determined analytically, numerical simulations have found that stable trajectories are typically found for $\eta < 0.3$, where[255]

$$\eta = 2n(n-1)\frac{|q|V_0}{m\omega^2 R_0^2}\left(\frac{r}{R_0}\right)^{n-2} \tag{2.10}$$

In practice, the only tunable parameter here is the RF amplitude (V_0), as few RF power supplies can adjust the RF frequency. Experimental work by the Wester group[256] has measured the effective trap depth of their 22-pole trap, showing that it follows Equation 2.9 until a critical voltage. At this voltage, the effective trapping depth hits an inflection point and begins to decrease monotonically with voltage, indicating that above this voltage η is too large to provide stable trapping for large r. A plot indicating such an inflection in the potential is included in Figure 2.3b

Recently, we have observed a related phenomena in our instrument, wherein OH^- anions leaving the trap were rotationally hot (T $\sim$ 100 K) compared to previous measurements (T $\sim$ 22 K). It was found that increasing the RF voltage applied to our octupole trap to $>$ 200 V resolved this issue, indicating that we were operating in conditions for which η was below the optimal value (i.e. $V_0 << V_c$ in Figure 2.3b). As $\eta \propto V_0/m$ this effect will be more pronounced for low mass species, such as OH^-, and will likely apply most strongly to rotational temperature (though may result in vibrational or electronic heating).

2.3.2 Ion Optics in Cryo-SEVI

Following the formation of our anions in the source chamber, the ions pass through a number of ion optics before reaching the ion trap, these are outlined schematically in Figure 2.4 below, and typical operating voltages are provided in Table 2.4.

The ions first encounter a skimmer and an aperture (ap1) to collimate the output from the EL valve and maximize coupling from the source into the RF guides. As such, the voltages applied to the skimmer and ap1 are particularly important for ion transmission - small changes to these voltages can greatly impact the number of ions that reach the detector

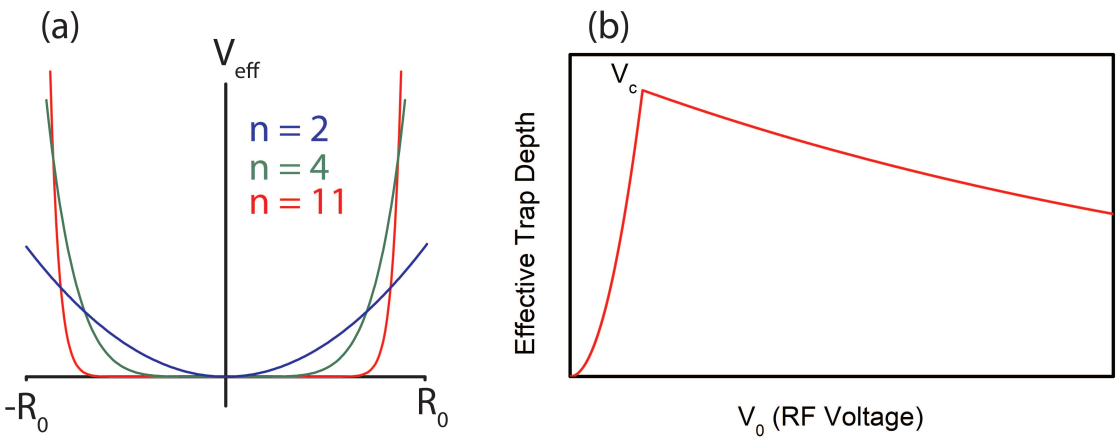

Figure 2.3: (a) Effective trapping potentials, given by Equation 2.7, for multipoles of order n = 2, 4, 11. (b) Schematic of effective trap depth measured by the Wester group in Reference [45], wherein the trap depth follows the ideal curve until a critical voltage, V_c is reached, after which, the effective potential approximation fails.

(region 5). Following ap1, the ions are then passed into a hexapole RF ion guide to guide the ions into the next region of the machine and further collimate the ion packet. In addition to the RF voltage applied to the hexapole, the six rods that comprise this optic are held at a slight bias relative to ground. We have found that while ion transmission is relatively insensitive to the RF voltage applied to the hexapole, the DC bias voltage is quite important, and must be tuned significantly depending on the source chemistry.

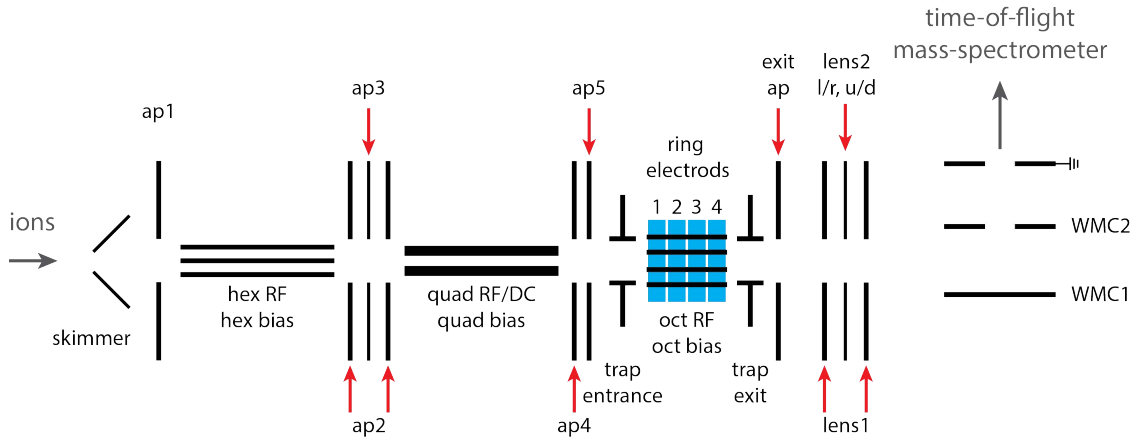

Figure 2.4: Schematic of the various ion optics in the cryo-SEVI machine.

Optic	Voltage
EL valve	0V
skimmer	-20V to -100V
ap1	-5V to -50V
hex RF	100-300 Vpp, f=3MHz
hex bias	-5V to -20V
ap2	20 to 80V
ap3	-20 to 80V
quad RF/DC	mass dependent, f=0.63MHz or 1.25MHz
quad bias	-10V to 10V
ap4	20 to 40 V
ap5	60 to 100V
trap entrance	-5V to -10V
oct RF	300-600 Vpp, f=3MHz
oct bias	0V to 1V
ring electrodes 1, 2, 3, 4	-100V, -10V, 10V, 100V
trap exit	-16V pulsed to 16V for extraction
exit ap	-3V to -20V
lens1	15V to 190V
lens2	2V to 30V
lens2 l/r	-5V to 5V
lens2 u/d	-5V to 5V
WM1	1.85 kV
WM2	1.72 kV
WMC DC bias	4 V

Table 2.4: Typical voltages applied to the ion optics in the cryo-SEVI machine.

Following the hexapole, the ions pass through a set of three apertures (ap2, ap3) in an Einzel lens configuration, which serve both as the differential pumping aperture separating regions 1 and 2 (ap3) as well as to couple the hexapole output into an RF quadrupole. The quadrupole is powered by one of two RF oscillator heads, allowing for mass selection over different mass ranges: one head operates at 1.25 MHz for mass selection up to 300 m/z, while the second operates at 0.63 MHz for mass selection up to 1000 m/z. The quadrupole can be operated as another ion guide, akin to the hexapole, or as a quadrupole mas filter (QMF) with the addition of a DC quadrupole field in addition to the RF field. An additional bias can be applied to the entire quadrupole, as another parameter to tune the mass distribution of the ions.

While it is useful to mass-select prior to the ion trap, so as to improve the number density

of the desired species in the ion trap, this is often challenging when using the filament ionizer, as the desired ions are sometimes not produced until further along the ion flight path or even in the trap. This option, however, is particularly helpful when generating ions *via* laser ablation, as there is often a significant number of by-products formed that can lead to over-filling the trap.

Upon exiting the quadrupole, the ions pass through two more apertures (ap4, ap5) and approach the ion trap and associated ion optics. A cutaway view of this part of the instrument is shown below in Figure 2.5. Cryo-SEVI employs an octupole trap in a linear geometry that is populated with a cold buffer gas mixture. Our ions are trapped here for 37 ms and undergo collisions with the cold gas, allowing them to cool to their ground vibronic state. Ions are trapped radially by alternating RF voltages applied to the octupole rods and axially by the trap entrance, exit, and ring electrodes held at low DC voltages.

The ion trap itself is a linear RF octupole trap, selected as a balance between the radial trapping potentials of a quadrupole and the common 22-pole trap. Equation 2.7 and Figure 2.3 illustrate that while the center of the $n = 4$ potential is not as flat as the $n = 11$ potential, it is much better than the $n = 2$ potential - leading to much less RF heating of the anions that experience buffer gas collisions in the wings for the radial potential.[257] Further, the radial confinement is dramatically better in the $n = 4$ case than in $n = 11$, allowing for efficient extraction of ions out of the trap and into the time-of-flight spectrometer that follows. This latter consideration - extracting ions *out* of the trap - is rather uncommon for RF trapping experiments, leading to the popularity of the 22-pole trap, which is ideal for loading high number densities of particles and cooling them efficiently.

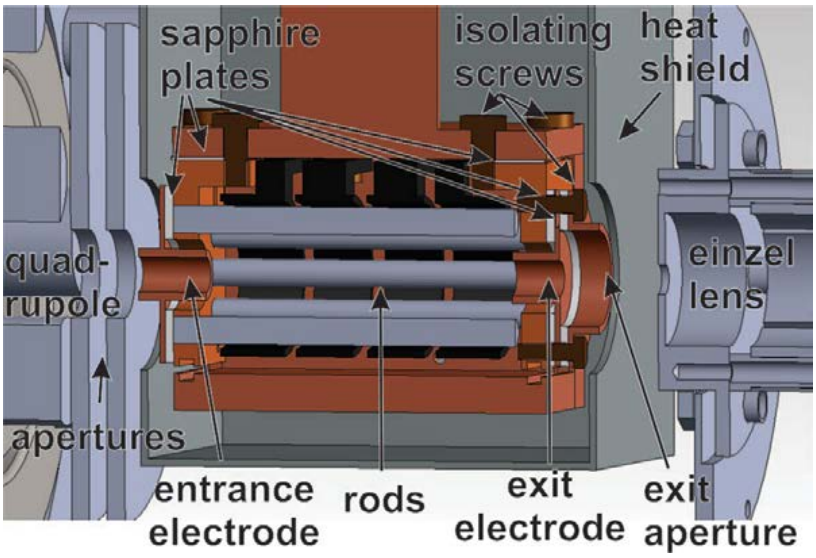

Figure 2.5: Cross section of the octupole ion trap, reproduced from Reference [39]

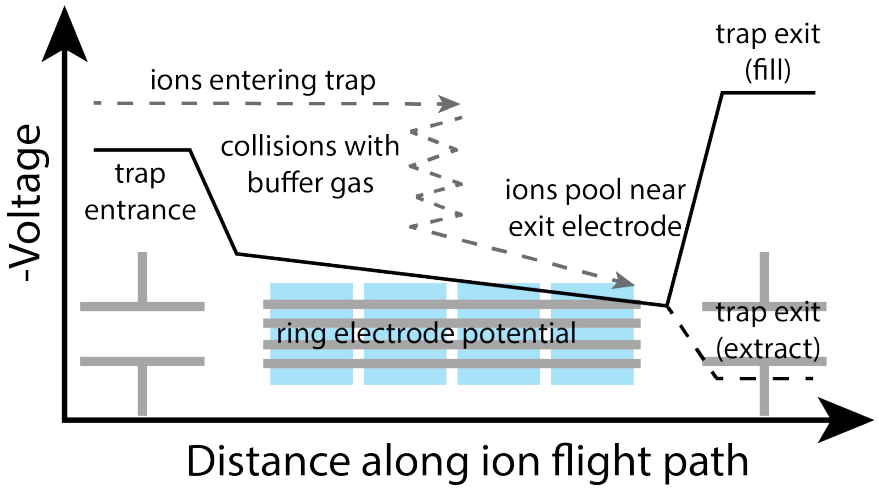

Figure 2.6: Schematic of the axial trapping potentials in the ion trap.

The voltages applied axially in the trap are also designed to enhance transmission and extraction efficiency, as shown in Figure 2.6. The voltage on the entrance electrode is tuned to a small repulsive (negative) voltage to allow for fast-moving ions from the source to enter the trap and prevent them from leaving after colliding with cold buffer gas. Similarly, the exit electrode is set to a small negative voltage during trapping, though this is pulsed to a positive voltage for ion extraction. Between these two electrodes are four ring electrodes that surround the octupole rods, creating a sloped potential that encourages ions to pool

near the exit electrode in preparation for extraction. The electrodes are electrically isolated using sapphire plates, as these are excellent electrical insulators and thermal conductors at cryogenic temperatures. While the ring electrodes and the octupole rods are physically separated to maintain electrical isolation, the set screws holding these components in place have drifted over the years, placing these components in contact. In early 2021, the trap was dismantled and repaired to resolve this issue - details of troubleshooting and repairing these complications are presented in the Appendix.

Following the trap is a microchannel plate (MCP) ion detector, mounted collinearly with the ion trap axis. Such a detector has proven integral to optimizing source, guiding, and trapping conditions to maximize ion formation and transmission independent from complications introduced by further components downstream. In April 2021, a diode in the circuit for the MCP failed, requiring the replacement and rewiring of the MCP. Figure 2.7 displays the circuit diagram for this MCP, where the Zener diode that failed is now replaced by a 560 kΩ resistor. As such, we now power this MCP with 3 kV, instead of 3.5 kV, and routinely see 5-10 V of ion signal on this detector, instead of 0.5-1 V.

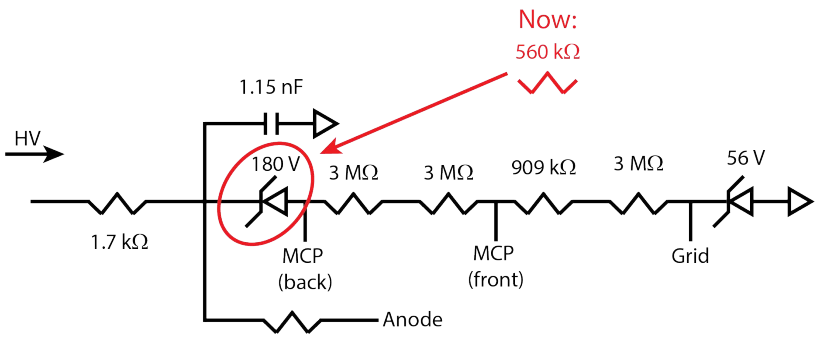

Figure 2.7: Circuit diagram for powering and reading off the MCP stack making up the trap detector. The 180 V Zener diode circled in red was replaced in April 2021 with a 560 kΩ resistor, resulting in the detector becoming about an order of magnitude more sensitive.

The purpose of our ion trap is to confine ions such that they can be collisionally cooled with a cryogenic buffer gas inside the trap, thermalizing the anions to low internal and translational temperatures. This is done by holding the trap itself at cryogenic temperatures, allowing for the buffer gas - itself not trapped - to thermalize through collisions with the trap surfaces. For this reason, the octupole rods are encased by a copper box (Brown in Figure 2.5), which is in contact with the 4 K second stage of a closed-cycle helium refrigerator (Sumitomo; cold head RDK-408D2, F-70L chiller). This box is then itself encased in by heat shielding (another copper box) that is in contact with the 40 K of the same cooling unit, preventing radiative heating of the trap from the room-temperature chamber. The temperature of both the trap and shield are measured using two silicon diodes (Lakeshore DT-670C-ET) mounted on either end of the inner trap enclosure. A cartridge heater is mounted on the exterior of the trap enclosure (but inside the shielding) to allow for the

temperature of the trap to vary and is controlled by a Stanford Research Systems CTC100 cryogenic temperature controller. Special care must be taken when operating the trap with H_2, as well as servicing the helium refrigerator - required every few months as there is a small leak in the lines connecting it to the cold head. Details of these precautions and procedures are outlined in the Appendix.

Prior to the ions reaching the trap ($\sim$ 100 μs), the trap is filled with buffer gas from a pulsed valve (Parker General Valve, Series 9), which is open for 300-600 μs. This valve is backed by $\sim$ 3 psi of He or an 80:20 He:H_2 buffer gas mixture via a vacuum regulator. Inside the chamber, the buffer gas formerly was pre-cooled to 40 K through thermal contact between the stainless steel tubing that backs the valve and the shielding for the trap, but this was found to be unnecessary and is no longer done. While operating, the vacuum chamber surrounding the trap (region 2) is at a pressure of 3-6$\times 10^{-6}$ Torr, corresponding to a pressure within the trap enclosure of $\sim 1 \times 10^{-3}$ Torr when conductance out of the two apertures computed (see Equation 4.2 and the following discussion). As our ions reside in this trap for 37 ms, the majority of our 20 Hz experimental cycle, they are expected to undergo between 10^3-10^4 collisions while in the trap.[54]

2.3.3 Buffer Gas Cooling

We typically consider the ions in our trap to be fully thermalized by the time they depart the trap. For this reason, temperature of the ions can be used to describe the translational (T), vibrational (V), rotational (R), and electronic (E) degrees of freedom for these systems. Collisions with cold buffer gas are assumed to be elastic collisions, meaning that collisions impart energy into the cold buffer gas while removing it from the anions. The T$\rightarrow$T energy transfer pathway occurs rapidly, owing to the continuum of translational energy states that are available in this temperature regime. Such a process is expected to thermalize the anion translational temperature close to that of 5 K within $\sim$ 100 collisions, or 0.1-10 μs.[46] Similarly, the R$\rightarrow$T channel is also fairly effective, as the energy spacing between rotational levels is small for most systems studied by SEVI, meaning that energy transfer is still rapid, and rotational cooling occurs quickly. The V$\rightarrow$T channel, however, is much slower, again owing to the relative spacing of the levels - here dramatically larger. As such, vibrational cooling is thus typically the most challenging to achieve, with previous work showing that vibrational levels more efficiently couple to rotational and vibrational levels (i.e. V$\rightarrow$R,V).[258] For this reason, we often use a buffer gas mixture of 80:20 He:H_2, where the addition of H_2 introduces both vibrational and rotational levels for anion vibrations to couple. Further, it is possible to run the trap at 10 Hz and double the trap residence time. While preliminary studies have shown this does not greatly impact the measured anion temperatures, these were performed while the EL valve was operating at 10 Hz.

Ion temperatures are also particularly sensitive to the pressure of buffer gas within the trap, with higher pressures generally leading to better cooling.[55,62,63] This can be controlled by altering the duration the pulsed valve is open in each cycle, an advantage provided over the use of a continuous leak valve. Further, use of a pulsed valve is advantageous as the

buffer gas pressure is highest as the anions enter (i.e. are at their warmest temperatures) and decreases over the experimental cycle as gas conducts out of the entrance and exit apertures. Thus, the ions undergo few collisions during extraction, thereby minimizing heating.

Ion temperatures are estimated by analysis of detachment spectra from a number of anions. Temperatures are determined by the relative intensities of features corresponding to electronic, vibrational, or rotational excitation in the anions - provided there is sufficient resolution to observe such levels. For example, the relative intensities of different spin-orbit peaks in the cryo-SEVI spectrum of C_5^- and C_7^- can be fit to a Boltzmann distribution, allow for the extraction of the spin-orbit temperature for these systems as 10(2) K and 14(2) K, respectively.[54,102,108] Similarly, our recent work on OH^- (see Chapter 6), which has a large rotational constant, allowed for the determination of the rotational temperature of this species as 22 K. A similar treatment can be applied to vibrationally excited anion states (i.e. hot bands) if they are populated, though this is rarely the case.

We thus estimate that our ion temperature are on the order of 20 K - a factor of 4 higher than the trap temperature. This is unsurprising, as even 22-pole traps have trouble cooling small molecules to $T_R \lesssim 20$ K,[56] owing in part to RF heating of ions in the trap, heating during their extraction, and the effects of *ortho-* and *para-* hydrogen in the trap. All of these effects are made worse by over-filling of the trap, where space-charge effects can push the ions higher up the trap's potential surface (increasing RF heating), and there is a higher density of ions, leading to more heating collisions as they exit.

2.4 Mass selection

Upon exiting the ion trap, the ions are extracted into an orthogonal Wiley-McLaren (WMC) time-of-flight (TOF) mass spectrometer.[259] Steering into this spectrometer is done by a a combination deflector / einzel lens assembly built by Jongjin Kim and Christian Hock and is detailed in Jongjin's thesis.[39] The voltages applied to this optic are particularly important for ensuring good ion transmission to the detector, as will be outlined below.

The WMC-TOF was installed when the experiment was upgraded from ZEKE to SEVI in the early 2000's by Matthew Nee and Andreas Osterwalder[240] (see Figure 2.8), and is set up to both separate in space and time ions of different masses as well as to spatially and temporally focus the ion packet of a desired mass into the laser interaction region of the VMI spectrometer. Such a design uses a WMC-TOF, wherein the ions are injected along a starting plate that is pulsed to a repulsive voltage (V_1), pushing ions along the time of flight axis. Upon reaching the second acceleration region, the second plate is pulsed to a voltage (V_2), further accelerating them before they reach a field-free region, allowing for the separation of ions of differing mass based on their time of flight.

For simplicity, consider a single-stage TOF mass spectrometer. A voltage difference between the two plates (i.e one that is pulsed, the other is grounded), ΔV, generates a field that imparts a particle of charge q with a kinetic energy of $E = \Delta V q$. Relating this to the kinematic kinetic energy, the velocity of an ion is then described by

$$v_{ion} = \sqrt{\frac{2q\Delta V}{m}} \tag{2.11}$$

Thus, after ions travel through a field-free flight tube of distance d, ions of mass m arrive at the detector at a time $t = d/v \propto \sqrt{m}$.

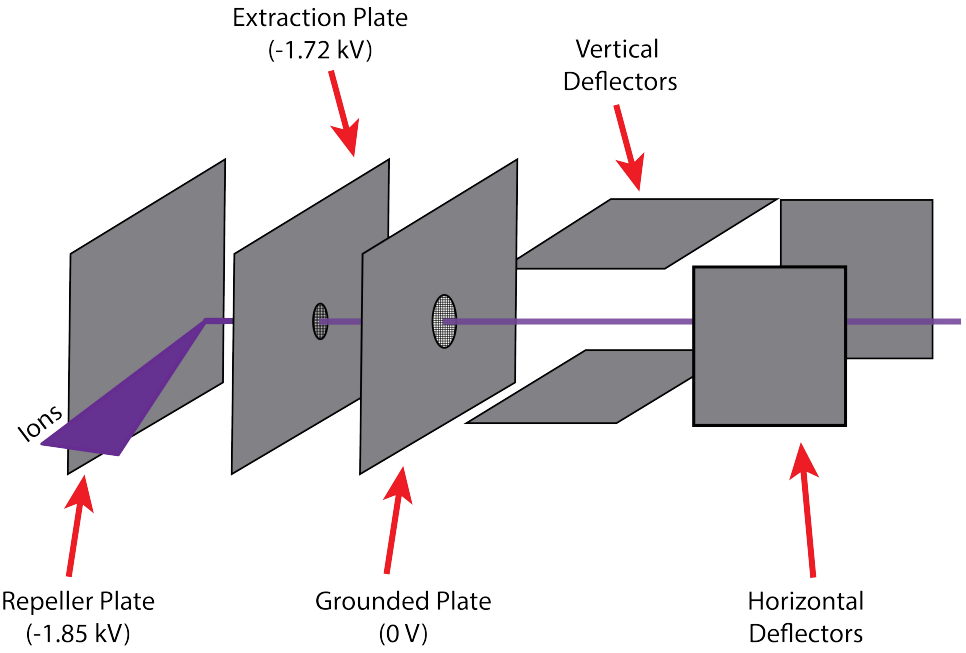

Figure 2.8: Schematic of the Wiley-McLaren mass spectrometer plates and first set of deflectors along the ion flight path after extraction from the ion trap.

The addition of a second accelerating region to the WMC-TOF complicates the equations of motion that describe the velocity of our anions, but to first-order, Equation 2.11 should hold. The benefit of adding a second acceleration region is the introduction of focusing conditions that can be optimized such that ions are spatially or energetically focused.[260] In cryo-SEVI, spatial focusing is desired, as to maximize the number of ions detached in the interaction region by a single laser shot. Such spatial focusing conditions come about from basic electrostatics - if the ion packet entering between two charged plates (in the simple one-acceleration-region design) has some initial spread along the TOF axis, then those closer to the plate will reside in the field longer, imparting more kinetic energy to them. At a certain point along the TOF axis, then, these faster ions will overtake the slower ions that got a head start - at this point in space the ions are spatially focused. The second acceleration region introduced by the WMC-TOF provides additional tunable parameters that determine the

location of the spatial focus (i.e. the voltage and relative timing of this second acceleration plate).

The quality of this spatial focus relies heavily on the initial spatial distribution of the ion packet as it enters the WMC-TOF from the ion trap, though this can be corrected somewhat by the WMC-TOF focus. Spread along this TOF axis (i.e. left/right out of the trap) introduces a TOF spread in the ion packet. For this reason, great care must be taken to ensure a clean ion packet coming from the trap. This is ensured by the home-built deflector/einzel lens optic mentioned above. In essence, this component is an einzel lens whose center electrode contains four discrete elements, allowing for up/down and left/right steering of the ion packet while maintaining spatial focusing. Such a design is rather compact and was required by spatial considerations, as the distance between the trap exit and entrance to the TOF should be minimized to maximize ion transmission.

Given the importance of the spatial location and focus of the ion packet coming from the trap, it should be no surprise that the lens/deflector has proven essential for optimization of ion transmission from the trap into the WMC-TOF and into the detector region. Both ion transmission and the ion packet shape (i.e. single or multiple Gaussian) are strongly impacted by the voltages applied to this optic, as well as those applied to the exit aperture (which controls the kinetic energy of the ions exiting the trap). Further, it has been established that ions confined in linear RF multipole traps form donut-like spatial distributions around the trap axis,[39,257] leading to an ion TOF distribution composed of multiple Gaussian functions and reducing the number of ions that may be detached. It is thus imperative to regain a pseudo-spherical ion packet prior to mass separation by focusing the ion packet out of the trap with the einzel lens.

Finally, the WMC-TOF design does impart some uncertainty to the ion velocity spread, unlike the previously used Bakker-type collinear TOF mass spectrometer.[261,262] The impact of this is minimized by the orthogonal orientation of the TOF axis to the trap extraction and the detector, as the velocity spread from the trap translates to a left/right spread in velocity that can be corrected by ion optics along the flight path, and the velocity spread introduced by the WMC-TOF itself is much smaller than the final velocity of the photoelectrons accelerated by the VMI, meaning that to first-order, this spread can be neglected.[240]

The first two WMC-TOF plates are held at a low DC voltage ($\sim$ 4 V) while the ions are extracted from the trap, before being pulsed to 1.85 and 1.72 kV, respectively, to accelerate the ions. The apertures on both of these plates are covered with mesh grids to improve the homogeneity of the acceleration field, while the third plate is grounded so as to establish a field-free region following it. The relative timing at which the first two plates are pulse has been found to be particularly important to achieve good ion transmission, with a slight delay (230-930 ns) being favorable and dependent on the mass of the system. Lower masses tend to favor a lower delay time.

Upon exiting the plates of the WMC-TOF, the ions fly through a $\sim$ 2 m field-free flight tube before reaching the laser interaction region. Along this flight path are two sets of up/down and left/right ion deflectors, each consisting of a pair of plate electrodes parallel to the ion trajectory. The voltages between the two plates impart force to the ions as they

pass through the plates, directing them up/down or left/right. The first set of plates are positioned very shortly after the WMC plates, while the second are stationed just before the entrance to the VMI lens. Collectively, these deflectors are used to steer the ion packet through three 3 mm apertures into the interaction region. Poor steering of the ion packet can lead to the ejection of electrons from the anions as they glance off an aperture and scatter electrons into the interaction region. Importantly, the second set of deflectors ("Golden Gate" and "Tilden", left/right and up/down, respectively) can also be used as a mass gate, ensuring only the anions of the desired mass enter the interaction region - often necessary when the source chemistry produces ions with TOF's that are similar to those of the detached electrons for the species of interest. This is done by holding the left/right deflectors nearest the interaction region at -50 V and pulsing them to the correct voltage for ion transmission at a set delay time to pass the ions of interest.

Following each set of deflectors is an einzel lens to improve the spatial focus perpendicular to the TOF axis for each ion packet. The second einzel lens was found to be superfluous in the mid-2010's and is rarely used, while the first is operated at a voltage of 2.42 kV.

The TOF of ions are recorded on a retractable detector mounted after the VMI lens. This detector comprises two chevron stacked 1" MCP and a current collection anode, the circuit for which is outlined in the thesis of Matthew Nee.[240] Typical time of flights range from $\sim$ 10-50 μs, depending on the mass of the anion and the delay between the pulsing of the two WMC plates. Calibration of these TOF's are performed by collecting the mass spectra of carbon clusters, C_n (n = 2-16) as well as tagged and reacted species C_nH_2 and C_nH, which are formed *via* laser ablation and tagging/reactions in the trap.

A pneumatic gate valve resides along the TOF axis, allowing for the isolation of this chamber from the rest of the machine and preventing the venting of this chamber while components in the source or trapping region are serviced.

2.5 VMI Spectrometer

The WMC-TOF sends the ions into the interaction region of a velocity-map imaging (VMI) spectrometer, which is used to measure the velocity distribution of the nascent photoelectrons following photodetachment. Our VMI spectrometer is a key component in SEVI, as it allows for the collection of spectra with energy resolution as high as 1 cm^{-1}.

As pointed out in Section 1.2.1, high-resolution photoelectron spectroscopy borrows from the field of ion imaging. Most important among these works is the pioneering work of Chandler and Houston, who resonantly ionized molecular fragments after photodissociation using a homogeneous electric field between two electrodes to project the spatial distribution of these fragments onto a 2D detector.[17] The resulting images contained information about both the kinetic energy release (radial dimension) as well as the anisotropy of the process (angular dimension). Such images proved to be monumentally useful for ion imaging,[263] and the technique was further improved by Eppink and Parker nearly a decade later,[18] who accidentally discovered that the electric field without mesh grids at the plate apertures

magnifies the ion image, greatly improving the achievable resolution. The Eppink-Parker VMI lens comprises two acceleration regions (three plates - the repeller, extractor, and grounding plate) with apertures not covered with a mesh grid. Such a design allows for lensing of the electric field around the apertures, focusing charged particles with different initial positions but identical velocity vectors to the same point on the detector, as shown in Figure 2.9 below.

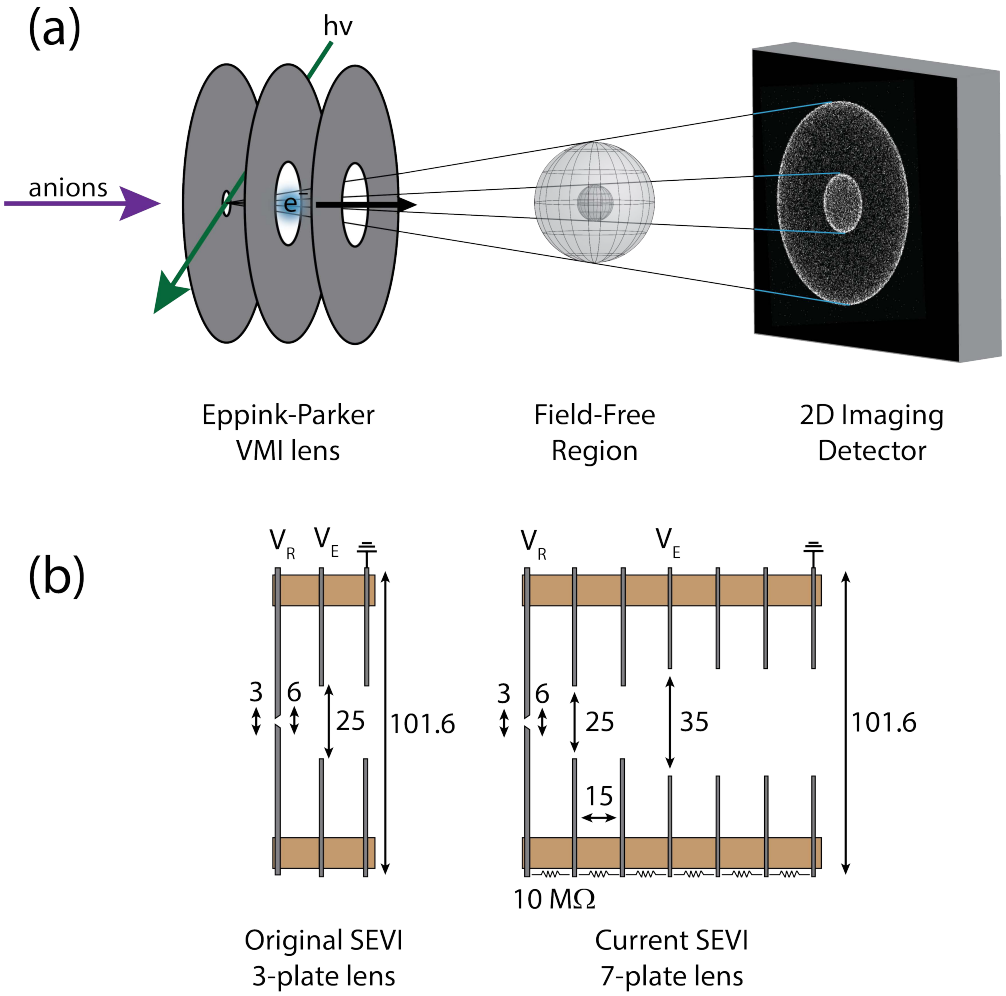

Figure 2.9: (a) Illustration of an Eppink-Parker VMI spectrometer imaging photoelectrons from the detachment of F^-. (b) Configurations of the 3- and 7-plate VMI lenses formerly and currently in the SEVI machine. Electrodes are displayed in gray, while Vespel spacers in brown. In both, ions enter from the left and the laser intersects between the first two plates. All lengths listed are in millimeters.

In the SEVI apparatus, the WMC-TOF sends ions into the VMI collinearly, causing

any spread in ion velocity to be orthogonal to the detector plane, preventing the blurring of images from this velocity spread.[264] Prior to entering the VMI, these ions pass through three 3mm apertures, the third of which is the first electrode in the VMI setup, the repeller plate. The two prior apertures exist for historical reasons - formerly the tube the ions enter containing these two apertures was pulsed to reference the ions to the repeller voltage. As this is no longer done, such a tube is now held at the DC voltage of the repeller plate and serves as a convenient means to mount the VMI lens.

A standard 3-plate Eppink-Parker VMI was used in cryo-SEVI until late 2014, when it was modified by Marissa Weichman. The new design, detailed in her thesis,[244] took motivation from contemporary reports in the literature of improved resolution from modified VMI lenses.[218,265–269] Many of these reports introduced a third acceleration region to allow for another tunable parameter, yielding improved resolution, though at the cost of increased complication while operating. Instead, our design maintains the two-acceleration region, now employing seven plates instead of the conventional three. These additional four plates serve to smooth the field gradient in each acceleration region and guard against the penetration of stray fields that can distort VMI images.[244] In practice, these additional plates are at voltages linearly interpolated between the repeller, extractor, and ground electrodes by 10 MΩ resistors wired in series. All plates are constructed from non-magnetizeable stainless steel 316 and are coated with colloidal graphite (Aerodag). The plates are spaced by 15 mm using four sets of Vespel spacers and mounted with non-magnetizeable brass.

In both the basic Eppink-Parker VMI design and our modified VMI, the voltage on the repeller (V_R) is tuned to change the size of the image on the detector, while the extractor voltage (V_E) is tuned with respect to V_R in order to focus the image. These images contain roughly constant absolute velocity space resolution, Δv. This means that the absolute energy resolution ΔeKE can be be expressed by

$$\Delta\text{eKE} = mv\Delta v \tag{2.12}$$

which shows a linear dependence on velocity. It is then clear that the highest absolute energy resolution is achieved for photodetachment transitions with very low eKE.

In practice, the highest resolution images we have obtained so far correspond to features with eKE $\sim$ 5 cm^{-1}, yielding linewidths of $\sim$ 1 cm^{-1}, with V_R = -170 V.[36,37] For detachment transitions with higher eKEs, we use $V_R \approx -300$ V, representing a compromise between image magnification on the detector and low sensitivity to stray fields. This setting works well for eKEs $\approx$ 100-1500 cm^{-1}, where the measured fwhm ranges from $\sim$5 to $\sim$20 cm^{-1} over this range, depending on the system. For transitions with higher eKEs, namely collection of low-resolution overview spectra, we use a $V_R \approx$ -600 V, resulting in a lesser degree of magnification and allowing for a wider range of eKEs to be imaged simultaneously. In all cases V_E is tuned to optimize the focus of the lens, with $V_E \approx 70\%$ V_R.

These values represent a nearly factor of 2 improvement in the energy resolution of our cryo-SEVI spectra for photodetachment transitions with eKEs of 100-500 cm^{-1}, when compared to the old design. This is particularly useful when photodetaching from species

with poor detachment cross section near threshold, where many weaker transitions are able to be imaged.

In a SEVI experiment, ions are irradiated by an orthogonal photodetachment laser pulse between the first two VMI plates. The detached photoelectrons are then accelerated into the $\sim$ 50 cm long VMI flight tube, which is shielded from external magnetic fields by two layers of μ-metal shielding. Fitting of the electron time of flight using data from 2015-2021, as shown in Figure 2.10, has shown that this value is linearly dependent on its precursor anion's time of flight through the WMC-TOF. This fit holds for all $V_{R,E}$ voltages detailed above, and through different WMC-TOF calibrations. Such a function then allows for the prediction of electron time of flights, accurate to $\pm 0.1\,\mu$s, for previously uncharacterized systems, and was particularly helpful when studying the nitrate radical (NO_3, see Chapter 5), where background noise was comparable to the ion signal.

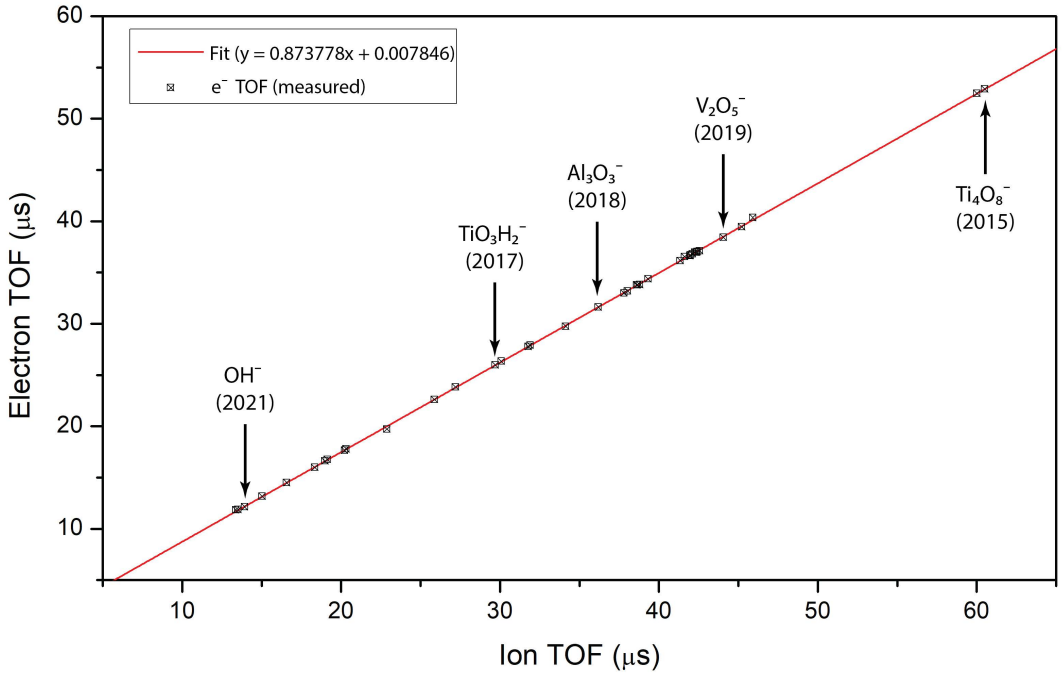

Figure 2.10: Fitting of e^- TOF data from 2015-2021 to a linear function in precursor ion TOF. The fit is able to predict electron TOF for a system of known ion TOF (and thus known mass) within 0.1 μs for most systems.

During this flight-time, the electron cloud expands until it intersects an imaging detector

75 mm in diameter, consisting of of two chevron-stacked imaging-quality MCPs coupled to a phosphor screen. Electrons striking the MCPs create an electron cascade, that itself produces a bright spot on the phosphor screen, the back of which is photographed with a charge-coupled device (CCD) camera (IDS UI-2230SE-M) mounted outside of the vacuum chamber and uses an exposure time of 100 μs

The front of the first MCP is grounded, while the back of the second MCP is pulsed from +1 kV to +2 kV over the window in which electrons arrive to reduce background noise from dark counts during the remainder of the experimental cycle time. The phosphor screen is held at +6 kV, and was purchased along with the MCPs as a commercial imaging assembly from Burle (now Photonis, part number 39082). The MCP pore diameter is 25 μm, with a 32 μm center-to-center pore spacing, 8° pore bias angle relative to the plate surface, and a 40:1 pore length:diameter aspect ratio.

2.6 Data Acquisition

Images from the CCD camera are analyzed after each experimental cycle for individual electron events, the centroids[268,270] of which are calculated and binned into either a 1024 × 1024 or 2200 × 2200 grid. Prior to the VMI modification, 1024 × 1024 images were the default, as they match the camera's native resolution. The improved resolution of the new lens, however, leads to this bin size limiting spectral resolution at times.

The processing of these images is performed by the NuACQ software developed by the Suits group,[271] though we have recently modified the code and a new data acquisition software suite is in development. The spectra collected in this thesis have exclusively used the NuACQ software, which is detailed below. Details of the modifications to the NuACQ software and new program for data acquisition will be outlined in the forthcoming thesis of Marty DeWitt.

Photoelectron events are processed to determine the centroid of a spot, determined using the center of mass (COM). Such a method was developed for astronomy[272] and super-resolution microscopy,[273] where the intensity distribution observed is roughly Gaussian. In such situations - distant stars, small fluorophores, or photoelectrons - a centroid can be calculated for a spot of n illuminated pixels as

$$\eta_{\mathrm{COM}} = \frac{\sum_{i}^{n} \eta_i I_i}{\sum_{i}^{n} I_i} \tag{2.13}$$

where $\eta = x, y$ and I_i is the intensity of the i^{th} pixel. This intensity-weighted COM calculation is remarkably cheap computationally and should be free of artifacts.[268] The low computational cost of this method allows for the calculation of up to hundreds of centroids per frame in real time at our experimental repetition rate of 20 Hz. Upon being calculated, the coordinates of the centroid, x_{COM} and y_{COM}, are added to a 2D histogram of the position of these events. A typical SEVI experiment collects between 10^5-10^6 electron events

per image, over $\sim 10^5$ experimental cycles, depending on both the noise and signal levels, respectively.

The implementation of centroiding has proven immensely helpful, ultimately improving the resolution of our spectrometer and correcting for spatial inhomogeneities in the imaging MCPs and the CCD camera. Such corrections come about from the treatment of each electron spot as a single event, irrespective of size or brightness, so nonuniformity in the detector spatial response is mitigated. This is particularly important as the imaging MCPs we employ are quite old at this point, and the electron spots produced are significantly dimmer in the center than the edges, owing to the different amount of activity each region sees while the experiment is running. As such, in a raw image, the center of our images - where the slowest electrons are mapped - would then be significantly under represented. Centroiding completely eliminates this issue.

The improved resolution comes about in a similar manner - each electron spot is 100's of microns in diameter on the phosphor screen, corresponding to ~ 10 pixels in diameter on the CCD camera array. Centroiding reduces each of these blurred spots down to a single pixel, with the COM calculations interpolating to sub-pixel resolution, greatly improving the achievable resolution of the spectrometer.

Finally, the use of centroiding allows for the correction of issues with the CCD array. Common issues with these types of detectors are hot pixels, which are always lit, and fixed pattern noise (FPN), where particular pixels give brighter intensities under uniform illumination. Without centroiding, these issues can lead to artifacts in the spectra that can be confused for real structure,[39] making them difficult to address in post-processing.[243] Hot pixels are discounted in our method, as we discard spots smaller than a few pixels in area. FPN is also largely averaged out by the COM calculations, as these treat the response of several adjacent pixels.

While centroiding has many benefits for imaging, it does come with a few costs. First, the method struggles to treat overlapping spots, which are rejected by NuACQ. This is particularly limiting for slow photoelectrons, as these have these smallest radius on the detector, and thus, the highest likelihood of overlapping. Such concerns limit us to collecting spectra with < 50 events per shot.

Motivated by this limitation, a new algorithm for determining the center of spots was developed by Marty DeWitt and implemented in the NuACQ code. Using this method, images are processed by taking the derivative of the intensity profile and interpolating where it changes sign to find the local maximum. Such a method, while reducing the achievable resolution by an order of magnitude, allows for the determination of the centroid of overlapping electron spots with high confidence. The loss in resolution is minor, as we still achieve sub-pixel resolution and are thus limited by the VMI focus, rather than the imaging detector or processing. Images taken while studying the vibrational pre-excitation of OH^- (Chapter 6) have shown that this method does not impact our functional resolution while improving data acquisition rates for low-eKE photoelectrons by a factor of 3.

2.7 Image Reconstruction

The two-dimensional velocity-map images produced using the VMI apparatus are a projection of the three-dimensional electron velocity distribution. To retrieve the desired spectrum in electron kinetic energy necessitates the reconstruction of the original velocity distribution from the measured projections.

Such a reconstruction is possible through the cylindrical symmetry of the 3D photoelectron distribution, where electrons detached with the same velocity lie along spheres of the same sphere, referred to as a Newton sphere. Such a symmetry comes about from the photoelectron angular distribution, which breaks the spherical symmetry of the Newton spheres in all cases but isotropic angular distributions (i.e. $\beta = 0$). The cylindrical symmetry axis is then defined by the laser polarization axis, which is illustrated along with its effect on SEVI images in Figure 2.11. The cylindrical symmetry of these spheres allows for their parameterization in two dimensions, the laser polarization axis (z for SEVI) and $r = \sqrt{x^2 + y^2}$. Thus, a slice through the Newton sphere in the x-z plane contains sufficient information for reconstruction of the desired eKE distribution.

Importantly, rotating the laser polarization axis effectively projects the Newton sphere in different planes. For isotropic spheres, this effect makes no impact, but for detachment transitions with anisotropic angular distributions (i.e. $\beta \neq 0$), the symmetry is reduced to cylindrical coordinates, resulting in two projections that show sharp structure and a third that is blurred.

These blurred images occur when the laser is horizontally polarized, as detachment is no longer occurring in the plane of the detector and the cylindrical symmetry of the experiment with respect to the detector plane is now broken. This comes about as the electric field for horizontally polarized light oscillates in the plane orthogonal to the detector (i.e. pointing towards the detector, or along the ion flight path). For this reason, SEVI experiments always employ vertically polarized light in our experiments, i.e sampling the x-z plane (leftmost component of Figure 2.11).

The distribution we desire is then the velocity map, $F(z, r)$ and the projection of this onto a 2D detector, as is measured by SEVI, is referred to as $D(z, x)$. In order to relate these, a reconstruction of the full 3D velocity distribution of the electrons, $P(x, y, z)$, from the data must be performed. For a given distribution, the corresponding ideal image, $A(x, z)$, is the projection onto the (x, z) plane

$$A(x, z) = \int_{-\infty}^{\infty} P(x, y, z) dy \tag{2.14}$$

The cylindrical symmetry of the experiment allows for a direct one-to-one mapping between $A(x, z)$ and the velocity-map, $F(z, r)$ by the Abel transform[274,275]

$$A(z, x) = 2 \int_{x}^{\infty} F(z, r) \frac{r}{\sqrt{r^2 - x^2}} dr \tag{2.15}$$

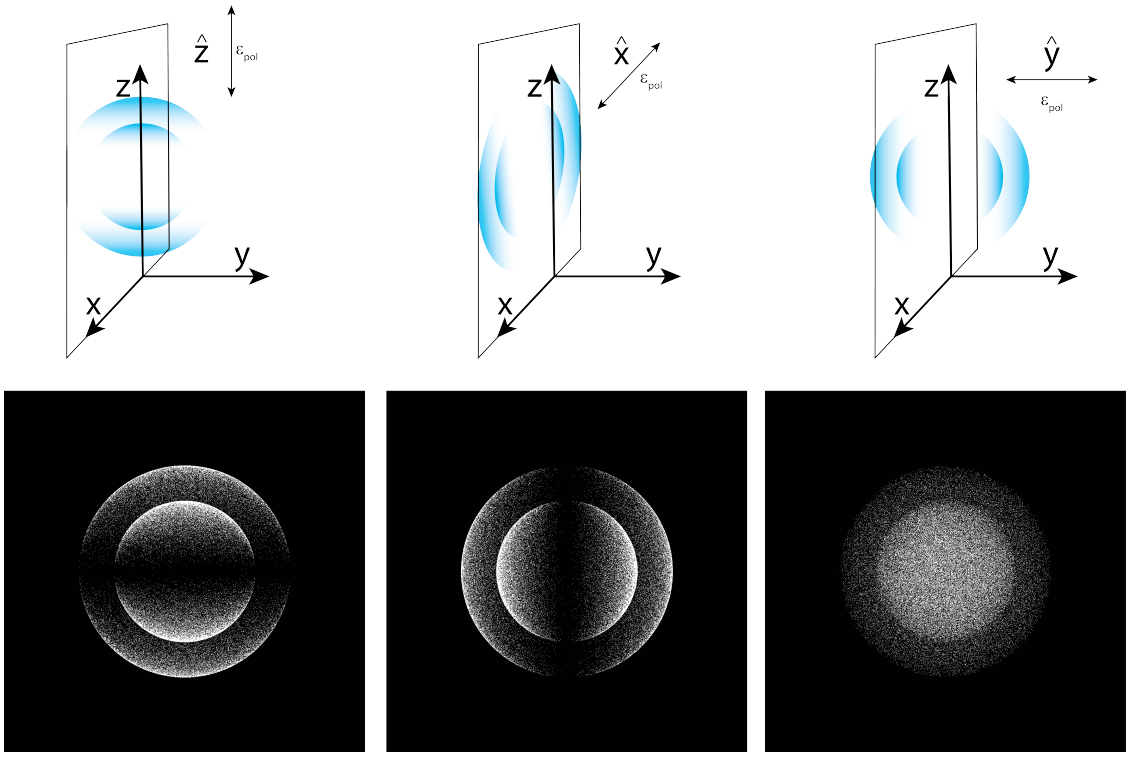

Figure 2.11: Illustrations of initial 3D Newton spheres generated by laser polarization along each of the three principal axes (top). The 2D plane in which the Newton spheres are imaged (x-z) is depicted along with the laser polarization axis. (Bottom) Simulated SEVI images (slices along each dimension, D) corresponding to projection of the Newton sphere onto the 2D imaging detector.

Obtaining a reconstruction of $F(z,r)$ from a measured $D(z,x)$ image can be achieved through the inverse-Abel transform

$$F(z,r) = -\frac{1}{\pi}\int_r^\infty \frac{\partial D(z,x)}{\partial x}\frac{dx}{\sqrt{x^2-r^2}} \tag{2.16}$$

Abel inversion, however, is made challenging by the sparely populated images often collected by VMI experiments, leading to a large amplification of experimental noise. For this reason, a number of methods have been developed to circumvent this issue, including the Hansen and Law recursive implementation,[274] BASEX[276] and pBASEX,[277] and the maximum entropy methods developed by Bernhard Dick.[275,278]

Early SEVI experiments employed the Hansen-Law numerical inverse-Abel transforms and occasionally the BASEX family of reconstruction methods until 2014, when the Maximum Entropy Velocity Legendre Reconstruction (MEVELER) method was developed. Comparison of these methods is detailed in many prior SEVI theses,[39,232,244] showing that the

MEVELER method out performs the other two methods significantly for SEVI.

2.7.1 Maximum Entropy Methods

Maximum entropy methods avoid numerical inversion of the data $D(z, x)$, instead aiming to determine the velocity-map $F(z, r)$ corresponding to an image $A(z, x)$ *via* Equation 2.15 by maximizing the quantity

$$\mathrm{Pr(F|D)} = \frac{\mathrm{Pr(D|F)Pr(F)}}{\mathrm{Pr(D)}} \tag{2.17}$$

corresponding to maximising the probability that the map F describes the velocity-map that gave rise to the image A. Importantly, Pr(D) is a constant for each image, leading to the maximizing of Pr(F|D) to require the maximization of the conditional probability Pr(D|F) and the *a priori* probability of the map, Pr(F).

This allows for optimization of the conditional probability, using a likelihood estimator L such that

$$\mathrm{Pr(D|F)} \propto e^{-L} \tag{2.18}$$

This parameter allows for a quantification of the agreement between the data (D) and the image (A) arising from the same velocity-map (F). For a counting experiment like SEVI, where Poisson statistics govern the likelihood of detection events, the likelihood estimator is given by

$$L_p = \sum_J \left(A_J - D_J \ln A_j + \ln \left(D_J! \right) \right) \tag{2.19}$$

where the summation over J is performed over each pixel in the data set. This value is minimized below some critical value, L_0 as the first step in minimizing Equation 2.17.

The remaining step is to maximize the *a priori* probability of a given map, i.e. Pr(F). Importantly, multiple maps F can result in $L_p < L_0$, requiring determination of the most probable map, as defined by

$$\mathrm{Pr(F)} = e^{\alpha S} \tag{2.20}$$

where S is the entropy function of the map, defined relative to some default map B (here, a crude inverse-Abel transform of the data D)

$$S = \sum_J F_J \ln \left(\frac{F_J}{eB_J} \right) \tag{2.21}$$

Thus, the optimum velocity-map F that satisfies the $L_p < L_0$ criteria is the one that maximizes the entropy S, equivalent to minimizing the information contained in the map. As such, the optimum F then does not contain any information not present in the data, D.

The the resulting map F obtained in this method is then transformed using Equation 2.15 to obtain the image $A(x, z)$.

The above treatment can be further improved by using the symmetry of the experiment, by expressing the electron distribution $P(x, y, z)$ in cylindrical coordinates $P(\nu, \theta)$, where ν and θ are the velocity and angle of the electron along a given Newton sphere. These distributions can then be expressed in terms of the Legendre polynomials, $\mathcal{P}_\ell$

$$P(\nu, \omega) = \frac{1}{\nu^2} \sum_\ell Q_\ell(\nu) \mathcal{P}_\ell(\cos\theta) \tag{2.22}$$

where $Q_\ell(\nu)$ can be expressed as

$$Q_\ell(\nu) = \nu^2(2\ell + 1) \int_0^\pi P(\nu, \theta) \mathcal{P}_\ell(\cos\theta) \sin\theta d\theta \tag{2.23}$$

owing to the orthogonality of the Legendre polynomials.

If we then assume that the 3D electron distribution is well described by a linear combination of a small number of Legendre polynomials, we can then apply Equations 2.22 and 2.23 to construct a matrix $\mathbf{Q}$ with elements $Q_{k\ell} = Q_\ell(\nu_k)$ that is then used in the minimization of L and maximization of S. For cryo-SEVI experiments, only the $\ell = 0, 2$ represent physically meaningful functions, as $\mathcal{P}_0(\cos\theta) = 1$ and returns the photoelectron spectrum, while $\mathcal{P}_2(\cos\theta)$ describes the angular distribution of the photoelectrons, per Equation 1.17.

Thus, the anisotropy parameter of each transition in a cryo-SEVI spectrum are calculated by integrating $Q_0(\nu)$ and $Q_2(\nu)$ over the peak width,

$$\beta = \frac{\int Q_2(\nu) d\nu}{\int Q_0(\nu) d\nu} \tag{2.24}$$

Importantly, implementation of the Legendre polynomial basis results in the output no longer being the direct velocity-map F, but instead the $Q_\ell(\nu)$ functions, where the $Q_0(\nu)$ function returns the direct photoelectron spectrum. Such a treatment reduces the amount of experimental noise that is transferred to the MEVELER reconstruction, resulting in lower noise baselines without the introduction of inversion artifacts or an oscillatory baseline as occurs with the BASEX family of methods.

For this reason, all SEVI spectra presented in this thesis are reconstructed using the MEVELER algorithm.

2.8 Energy Calibration

The radii of the Newton spheres in SEVI images are roughly proportional to the velocity (i.e. $\nu \propto R$), meaning that the eKE scales as R^2. In practice, the proportionality constants that define this relationship change as the laser path is altered into the VMI interaction region (i.e. between the first two plates), requiring that we re-optimize the VMI focusing conditions and re-calibrate the energy scale for our VMI images after the laser beam path is altered.

Notably, following the modifications to the VMI lens outlined in Section 2.5, we found that the spectrometer's energy calibration required an addition of an R^4 term to sufficiently treat the measured energy distributions. As such the radii of features in our reconstructed images are related to the electron kinetic energy by

$$\mathrm{eKE} = a_2 R^2 + a_4 R^4 \tag{2.25}$$

where $a_{2,4}$ are constants determined for a particular set of VMI voltages by collecting SEVI spectra of well-known atomic anion photodetachment transitions. Atomic systems are convenient for this purpose as the relative energies of the states involved are known to high precision, and atomic lines are not broadened by rotational or vibrational structure. The atomic anions used to calibrate the our VMI spectrometer depend on the photon energies output by the laser configuration (see Section 2.10) and are detailed in Table 2.5.

	Ni^-	O^-	S^-	F^-	Cl^-
Precursor	Ni (solid)	N_2O (gas)	H_3CSSCH_3 (liquid)	NF_3 (gas)	CH_2Cl_2 (vapor)
Laser Setup	Raman Shifter	532-pumping, IR-DFG, & OPO/OPA	355-pumping	doubling BBO1	doubling BBO2
EA (cm^{-1})	8727.97[j]	11784.676(7)[a]	16752.974(5)[a]	27432.446(19)[b]	29138.59(22)[c]
Anion levels (cm^{-1})	$^2D_{5/2}$: 0	$^2P_{3/2}$: 0 $^2P_{1/2}$: 177.13(5)[d]	$^2P_{3/2}$: 0 $^2P_{1/2}$: 483.5352(34)[e]	^1S: 0	^1S: 0
Neutral levels (cm^{-1})	$^3D_2$: 0 $^3F_4$: 605.18[j] $^3D_3$: 809.94[j]	$^3P_2$: 0 $^3P_1$: 158.265 $^3P_1$: 226.977[f]	$^3P_2$: 0 $^3P_1$: 396.055 $^3P_1$: 573.640[g]	$^2P_{3/2}$: 0 $^2P_{1/2}$: 404.10[h]	$^2P_{3/2}$: 0 $^2P_{1/2}$: 882.3515[i]
H_2 trap	No	No	No	Yes	Yes

Table 2.5: Calibration species, their precursors, and the atomic levels and photodetachment transitions used to calibrate the SEVI spectrometer. Also noted: laser configuration for which each species is used as a calibrant and ability to produce species with H_2 in the trap. [a] = Ref [279], [b] = Ref [280], [c] = Ref [281], [d] = Ref [282], [e] = Ref [283], [f] = Ref [284], [g] = Ref [285], [h] = Ref [286], [i] = Ref [287], [j] = Ref [288]

Prior to calibrating, the VMI focus is optimized by tuning the extractor plate voltage (V_E) relative to that of the repeller *via* a potentiometer. Images are then acquired as the potentiometer settings are stepped until a minimum in the width of photodetachment features (in pixels) is found, corresponding to the sharpest image. This must be completed for each repeller voltage setting to be used, as different relative voltages can impact the focus of images. From here, a calibration can be established - it is important that these steps are followed in the listed order above, as different extractor voltages will change the diameter of the rings in the VMI image.

A calibration curve is then built from many SEVI images of the same atomic transitions at several photon energies. The radii of these features are then extracted and plotted against

the electron kinetic energy of the transitions, determined as eKE = hν - eBE, where the eBE's of the transitions are know to high precision (see Table 2.5 below). We then apply a least-squares fit of Equation 2.25 to the data to relate the measured values of R to eKE and obtain values for $a_{2,4}$.

The energy calibration in the IR deserves warrants an additional note. When using the Raman Shifter, IR-DFG, or the IR OPO/OPA system (see Section 2.10 and 3.5.6), there are few well-characterized atomic anions with electron affinities that can be photodetached by the photon energies generated by these light sources (<0.9 eV) that are readily made in our source. Instead, we have found it convenient to align the output of the dye laser or the OPO, respectively, to be collinear with the IR output, using this light to acquire SEVI images of O^- to calibrate the spectrometer.

2.9 Circularization of VMI Images

At times, our images are distorted by imperfect shielding in the field-free region of the VMI spectrometer, resulting in the appearance of slight deformations in the angular dimension. While these deformations have the greatest impact on features with large radii, and thus high eKEs, it is sometimes desirable to correct for these issues in our images. Treatment of these angular deformations can be achieved through a circularization algorithm developed by Gascooke and coworkers,[289] whose provided software well addresses this issue.

Briefly, an accumulated image is converted from Cartesian to polar coordinates, highlighting angular deformations as oscillations within each ring of an image. From here, an inverse Abel transform centered around $r = 0$ is performed to give a number of constant-angle features corresponding to a ring in the original image. Each feature, i, is isolated and fit to the relation

$$I(r,\theta) = I_i(\theta)\exp\Big[-\frac{(r-r_\theta)^2}{2\sigma_i^2}\Big] \tag{2.26}$$

where $I_i(\theta)$ is related to the PAD of the transition and

$$r_\theta = r_i + \sum_{n=1}^{N}\left(A_n^{(i)}\sin n\theta + B_n^{(i)}\cos n\theta\right) \tag{2.27}$$

Fitting parameters β_i (folded into $I_i(\theta)$ in Equation 2.26), σ_i, r_i, $A_n^{(i)}$, and $B_n^{(i)}$ are typically determined to sufficient accuracy with $N = 3, 4$.

Upon determining the radial dependence of the trigonometric coefficients, $A_n(r) = a_n(r)$, by fitting each value of $A, B_N^{(i)}$ to a linear function in r, the circularization algorithm can be applied. In this method, each (x, y) in the image is converted to its polar coordinate (r, θ), then the intensity value at this coordinate is shifted to a corrected coordinate $(r + \Delta 4, \theta)$ with

$$\Delta r(r,\theta) = \sum_{n=1}^{N} \left(a_n r \sin n\theta + b_n r \cos n\theta\right) \tag{2.28}$$

The circularized image is then processed using the same methods and calibrations as the raw images.

2.10 Photodetachment Laser

In order to collect the highest resolution SEVI images, a tunable, narrow-bandwidth photodetachment laser, capable of producing light from the near-IR to the near-UV continuously. must be employed. Such a requirement is satisfied by the Nd:YAG pumped dye laser we use along with subsequent nonlinear frequency mixing processes. Together, this allows for the production of tunable light ranging from 0.3-5.6 eV, as is shown in Figure 2.12.

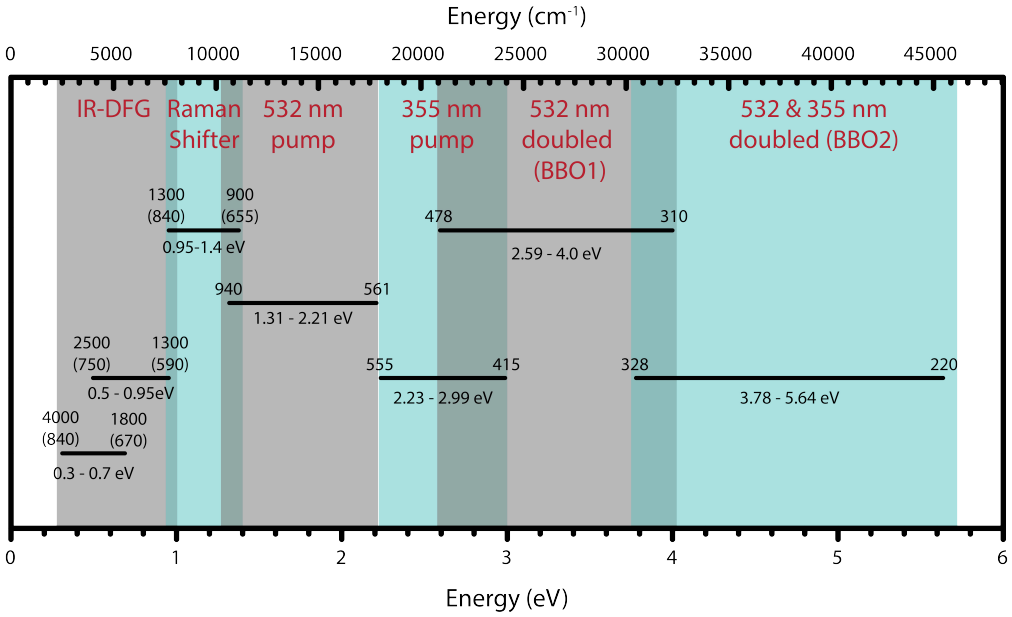

Figure 2.12: Operating regions accessible with different laser configurations. Numbers above each range indicate the output wavelength in nanometers, while numbers in parentheses are the corresponding dye wavelengths required to produce the desired output frequency, in nanometers.

2.10.1 Nd:YAG

Our photodetachment light source is based on a QuantaRay Pro 290-30 from SpectraPhysics, which has been modified to run at 20 Hz and replaced an older Continuum Powerlite 9020 laser in early 2017. The laser comprises four flashlamp housings, two making up the oscillator cavity and two making up the amplification stage. As shown in Figure 2.13, the oscillator cavity is bounded by two 1064 high reflecting (HR) mirrors, the output of which is directed to the amplifier *via* two steering mirrors. Upon exiting the amplifier, the light then passes through a quarter wave plate ($\lambda/4$) before entering the harmonic generation unit, containing multiple β-barium borate (BBO) crystals for nonlinear optical processes, before being separated by mirrors for the designated wavelength. Notably, unlike previous pump lasers used by SEVI, this laser does not contain an internal shutter, so a beam dump must be placed in front of the exit aperture when the laser is warming up.

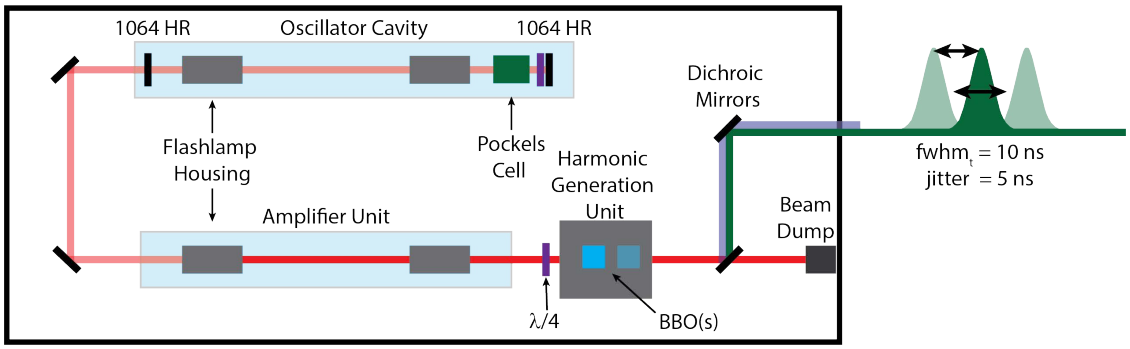

Figure 2.13: Schematic of QuantaRay Pro 290-30 laser used in cryo-SEVI.

The QuantaRay Pro 290-30 produces pulses $\sim$ 10 ns in duration with a measured jitter of $\sim$ 5 ns. While our model is equipped with an injection seeding unit, the piezoelectric stage on the back mirror of the oscillator cavity is broken and has since been removed, preventing use of this unit. We control the laser power output *via* tuning the Q-switch trigger timing, while the timing of the laser firing with respect to the rest of the cryo-SEVI apparatus is controlled through the flashlamp trigger timing. The second (532 nm) or third (355 nm) Nd:YAG harmonics are used to pump the dye laser, with maximum power outputs of $\sim$ 18 W of 532 nm and $\sim$ 9 W of 355 nm light, though rarely do we pump the dye laser with $>$ 4 W.

Since its installation, the QuantaRay Pro 290-30 has had a number of issues, ranging from the shattering of a YAG rod within the final amplification stage, poor beam stability and collimation, significant drift in output power, and electrical issues. These issues have been addressed and many of the details of these fixes are outlined in the Appendix. Importantly to note, however, are the electrical issues that plagued the amplifier of this laser in 2021. The laser is nearly 15 years old, and the circuitry that provides the simmer voltage to the flashlamps has degraded some, decreasing the voltage applied below the minimum value

required to flash the lamps ($\sim$ 160 V). This has been addressed by replacing the flashlamps with a specialized flashlamps (SpectraPhysics, part number 90100357) which have a lower simmer voltage requirement. Importantly, the vendor has a back stock of the original (problematic) flashlamps, so it is important to specify the problem / part number when ordering replacements.

2.10.2 Dye Laser

The output of this laser is then used to pump a Radiant Dyes Narrowscan dye laser installed in 2012. The dye laser can produce fundamental dye light from 420-955 nm (1.30-2.95 eV) using various commercial dyes. The fundamental light can then be frequency doubled to access the near-UV spectral region (see Section 2.10.3), mixed with the 1064 Nd:YAG fundamental to access the IR (see Section 2.10.4), or passed through a Raman shifter to access the near-IR (see Section 2.10.5). Commonly used dyes and their operating ranges, as well as their concentrations when dissolved in methanol for the oscillator, are listed in Table 2.6. The dye solutions used in the amplifier of the dye laser are diluted by a factor of 3-4 as compared to their oscillator concentrations. Further mixtures of dyes with adjacent gain curves can be mixed together to access regions between the individual wavelength regions accessible.

It is important to stay well within these dye curves, as amplified stimulated emission (ASE) can become a significant contribution when the laser output is low. In such a regime, the presence of ASE introduces unnecessary spectral congestion to SEVI images, and should be avoided when possible. This issue is thankfully mitigated when the fundamental dye light is used in nonlinear processes, as these processes are strongly dependent on the crystal angle in which the process happens (see Section 3.2.5), allowing for the conversion of just the dye light and not ASE.

Dye efficiencies range between 10-20% of the Nd:YAG pump power, depending on the dye and wavelength. This is slightly reduced by the use of a Bethune amplifier cell geometry,[290] which slightly sacrifices efficiency to produce a homogeneous spatial beam profile and is especially important for the nonlinear processes detailed in the following sections. Photodetachment of anions requires between 20-100 mW of light, depending on the ion signal and photodetachment cross section. For many cases, pumping the dye laser with 1-4 W of Nd:YAG light is sufficient to achieve appreciable photodetachment signal, though the use of the Raman shifter and IR difference frequency generation (IR-DFG) are particularly limited in power. In such situations, the pump power can be increased, as the damage threshold for the dye laser is reported as 1 Joule/pulse at 532 nm, or 20 W at 20 Hz.

The fundamental dye light is produced with a vertical polarization, while frequency doubling and IR-DFG schemes produce horizontally and vertically polarized light, respectively. This light is then directed through the vacuum chamber through CaF_2 windows mounted at Brewster's angle and a series of light baffles and apertures on either side of the interaction region. The light is directed into the machine using two or three prisms, depending on if the light is horizontally or vertically polarized, respectively, resulting in vertically polarized

532 nm pumped dyes					
Dye	Conc. (g/L)	Fundamental (nm)	Doubled (nm)	DFG (μm)	Raman Shifted (nm)
LDS 925 (Styryl 13)	1.00	928-955	464-478		
LDS 925/867 mix		875-930	438-465		
LDS 867	0.15	856-872	428-436		
LDS 867/821 mix		841-870	420-435		
LDS 821 (Styryl 9)	0.14	803-826	401-413	3.27-3.69	1.26-1.21
LDS 798 (Styryl 11)	0.15	785-808	392-404	2.99-3.36	1.17-1.22
LDS 765	0.15	749-776	374-388	2.53-2.87	1.09-1.15
LDS 751 (Styryl 8)	0.15	735-759	367-380	2.37-2.65	1.06-1.11
LDS 722 (Pyridine 2)	0.26	705-740	352-370	2.09-2.43	0.99-1.07
LDS 698 (Pyridine 1)	0.30	675-710	337-355	1.85-2.13	0.94-1.01
LDS 698/DCM mix		655-680	327-340	1.70-1.88	0.90-9.48
DCM	0.35	620-655	310-328	1.49-1.70	
R 640 (Rhodamine 101)	0.14	611-618	305-309	1.44-1.47	
R 640/610 mix		605-612	302-306	1.40-1.44	
R 610 (Rhodamine B)	0.20	587-602	293-301	1.31-1.39	
R 610/590 mix		570-590	285-295		
R 590 (Rhodamine 6G)	0.14	561-575	280-288		
355 nm pumped dyes					
Dye	Conc. (g/L)	Fundamental (nm)	Doubled (nm)	DFG (μm)	Raman Shifted (nm)
C 540a (Coumarin 153)	2.50	536-555	268-278		
C 503 (Coumarin 307)	0.40	490-523	245-262		
C 480 (Coumarin 102)	0.40	480-490	240-245		
C 460 (Coumarin 47)	0.25	448-476	224-238		
C 440 (Coumarin 120)	0.20	432-449	220-225		
S 420 (Stilbene 3)	0.20	420-425			

Table 2.6: Laser dyes used in the Radiant NarrowScan dye laser, their concentrations when diluted in methanol for the oscillator dye cell, and typical operating wavelengths. These ranges can be limited by the dye laser alignment and the oscillator grating settings employed.

light at the interaction region. The light is focused into the interaction region using a CaF_2 lens with a 1 m focal length. Alignment of the beam is optimized by centering the light on three irises external to the machine that have been aligned with a telescope to be centered on the internal components.

The output frequency of the dye laser is measured using a Coherent WaveMaster (part

number 33-2650), which employs a grating to determine the wavelength to 0.001 nm. Notably, the damage threshold for this unit is 100 mW and care should be taken to reduce the dye laser output below this threshold while measuring. Additionally, we employ an Ocean Optics USB4000 UV-Vis spectrometer to characterize the gain curve and ASE of a given dye. The center wavelength measured with this unit differs by > 1 nm from the WaveMaster, so measurements of the dye output should not be trusted with this unit.

The output of the dye laser can then be modified to expand the spectral regions accessible for SEVI experiments. Importantly, the optics involved are now modular, meaning that all of the optics required for each set-up is now housed in its own box along with duplicate optics in the event of damage. Care should be taken to maintain these kits and purchase replacements as spares are pulled to reduce waiting on part lead times.

2.10.3 Frequency Doubling

The output of the dye laser can be frequency doubled for all 532 nm pumped dyes and 355 nm pumped dyes. Doubling is accomplished in one of two BBO crystals from Radiant Dyes, cut at different angles to facilitate doubling in different frequency regimes. These crystals, BBO1 and BBO2, are used to frequency double wavelengths >300 nm and between 220-320 nm, respectively.

Both crystals are in mounts that allow them to be placed in the rotation stage built into the dye laser housing, allowing for the crystal angle to to tuned on an axis normal to the laser table. Following either crystal is a BBO compensating crystal mounted in its own rotation mount such that it rotates in the opposite direction, leaving the beam path unchanged as both crystals are angle-tuned. Both stages are motorized and controlled by an external touch-pad computer, which allows for selecting of motor steps between 0 and 300,000. Higher motor step values correspond to higher photon energies being doubled.

Following the output of the dye laser, a harmonic separator unit comprised (Inrad Optics 752-104) is mounted on the table to separate the dye fundamental from the doubled light. This unit, consisting of four prisms that can be translated along one axis, removes the majority of the fundamental dye light by inspection on a note card. To ensure that there is no residual fundamental, the composition of the beam following the separator can be checked with the UV-Vis spectrometer. This is particularly important in cases where the fundamental has sufficient photon energy to detach the species of interest, as was the case for NdO when doubled light was used to access the excited states of this species (see Chapter 9).

Notably, the BBO2 crystal can produce light as high in energy as 220 nm (5.6 eV), though the UV becomes increasingly difficult to work with as the photon energy increases. Photons with energies above $\sim$ 4 eV surpass the workfunction of steel and aluminum, resulting in scattered UV photons generating spurious electrons that are collected with near unit efficiency. The noise issue was particularly challenging when collecting spectra of NO_3 (see Chapter 5), where the detachment cross section is particularly low and the photon energies employed were 3.9-4.2 eV.

Previously, it was found that using lenses to telescope the beam to a smaller spot size or using a pinhole to clean up the beam profile was helpful in these scenarios. In 2019, it was found that these methods did not provide much support, owing to the increase divergence of the beam upon diffracting off of a pinhole or through telescoping. In an effort to reduce this noise, new light baffles made of anodized aluminum were designed and installed with 5 mm skimmer apertures. While installation of this new baffling did not readily improve the noise in the machine, venting the detector and subsequently pumping it down revealed a direct correlation between the detector pressure and the laser noise. A decrease in pressure from 9×10^{-7} to $1\times^{-8}$ Torr was found to reduce the noise from 20 (e^-/shot)/mW to 0.2 (e^-/shot)/mW while using 295 nm (4.20 eV) light.

As such, baking the chamber to expel sticky species, particularly water, was found to greatly improve the background noise, has improved the vacuum in the detector region from 1×10^{-8} Torr to $\sim 5 \times 10^{-10}$ Torr since. This, coupled with the experiment now running at 20 Hz, meaning laser noise is not being averaged into the experiment, allows for measurement of spectra well above the former limit of $\sim$ 4.5 eV.

2.10.4 Infrared Difference Frequency Generation

The output of the dye laser can also be combined with the Nd:YAG fundamental (1064 nm) to produce photons with energies below 0.95 eV in a process known as Infrared Difference Frequency Generation (IR-DFG). Such a process greatly expanded the range of photon energies capable of being produced and was first used by Marissa Weichman in 2016 to generate photon energies between 0.3-0.95 eV (4.2-1.3 μm).[244] Since this time, we have changed the Nd:YAG laser that pumps the dye laser to the QuantaRay Pro 290-30 we currently use, and a new setup was optimized by Jessalyn DeVine.[232]

In brief, following the second harmonic generation unit within the Nd:YAG, the vertically polarized 532 nm light is reflected off of two HR mirrors and into the dye laser, while the elliptically polarized 1064 nm fundamental is sent directly out of the laser. The 1064 nm arm is then reflected off of a 1064 nm HR mirror (CVI Y1-1025-45) onto a thin film polarizer (TFP, CVI Optics TFP-1064-PW), which is rated for high power and operates at 56°. This optic reflects the vertically polarized component of the beam onto yet another 1064 nm HR mirror, directing this light into the dye laser, while the remaining horizontally polarized light is transmitted through the TFP and into a beam dump. Inside the dye laser, the 1064 passes through one final HR mirror to align it with the dye light within two $LiNbO_3$ crystals mounted on the motorized stages in the dye laser, comprising the nonlinear medium in which IR-DFG happens and a compensating crystal. Importantly, the 1064 nm and dye light must be aligned both within the crystal and $\sim$ 2 m further down the laser table to ensure good overlap.

The $LiNbO_3$ crystals used for IR-DFG are $16 \times \times 11 \times 30$ mm in size and cut at 56° and 48° (Sirah Lasertechnik, DFM-2400-T and DFM-3800-T, respectively) for production of 1.3-2.5 μm and 1.8-4 μm light, respectively. Production of such light requires dye light in the 590-750 nm and 670-840 nm ranges, respectively. The crystals are mounted such

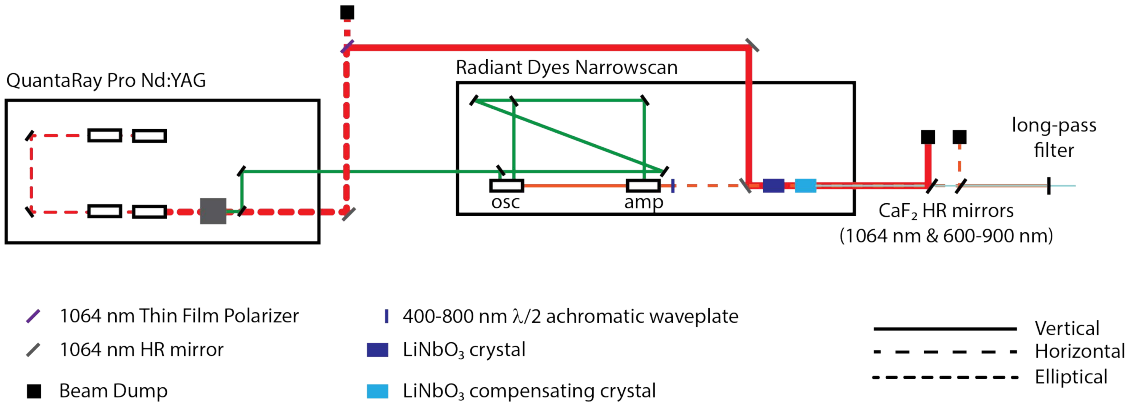

Figure 2.14: Infrared difference frequency generation setup used with the QuntaRay Pro Nd:YAG.

that the optical axis (in the 16×30 mm plane) lays parallel to the table. As with SHG, a compensating crystal crystal is placed after the IR-DFG medium, here another $LiNbO_3$ crystal3 mm long and mounted similarly.

Importantly, these crystals are designed for type-I nonlinear mixing where the polarization of $\omega_{1,2}$ is orthogonal to ω_3 where $\omega_{1,2} < \omega_3$. Here, $\omega_{1,2}$ are the DFG signal and Nd:YAG fundamental, respectively, while ω_3 is the input dye light. For this reason, the dye light polarization is rotated prior to entering the crystal by a 400-800 nm achromatic half-wave plate ($\lambda/2$, Thorlabs AQWP05M-600), ensuring it enters with horizontal polarization and the output IR light is vertically polarized. The dye light then passes through the back of the 1064 HR mirror and into these crystals.

The spatial overlap of these two beams is critical for efficient production of DFG light. The dye laser spot is ~ 4 mm in diameter exiting the Bethune cell, while the 1064 nm spot is substantially larger (~ 10 mm). As the amount of IR light produced is limited by the dye laser power, there is surplus 1064 nm light, precluding the need for telescoping this beam down to match the spot size of the dye light. Temporal overlap is also critical, but given that the difference in beam path is small ($\Delta l < 1$ m) relative to the pulse duration (~ 10 ns fwhm), a delay stage is not required to optimize this.

The output beam then passed through two CaF_2 HR mirrors coated for 1064 nm and 600-900 nm, respectively, to separate the 1064 nm and dye light from the desired IR output (Eksma Optics, custom orders). To filter out any residual high-frequency light, the beam then passes through a long-pass filter with cut-on wavelength 900 (Thorlabs FEL900) or 1100 nm (Thorlabs FEL1100), depending on the DFG energies to be used. Following this, the light then enters the CaF_2 prism assembly to steer it through a 1 m CaF_2 lens and into the machine. The output of this process and alignment are performed using a sensitive, fast-responding pyroelectric detector (Thorlabs ES111C).

As mentioned in Section 2.8, the fundamental dye light is used to calibrate the IR-DFG

setup. This follows under the assumption that the dye light is perfectly collinear with the DFG light, owing to the strict alignment requirements of both the dye and 1064 nm light above. The fundamental dye light is then used to detach O^-, with with the 600-900 CaF_2 mirror replaced with a CaF_2 window of identical width and the long-pass filter removed, to leave the beam path unchanged while transmitting the visible dye light.

2.10.5 Raman Shifter

The final modification to the dye light that can be applied is the use of a Raman shifter cell, bridging the gap between output frequencies at the low-end of the dye laser range and the high-end of the IR-DFG setup. The Raman shifter setup was first implemented in 2017 by Jessalyn DeVine and has been used to study the hydrolysis of Group IV metal oxides[65,66] (see Chapter 11) as well as NdO (see Chapter 9).

In brief, the dye light is passed through a cell containing H_2, inducing Raman scattering with this molecule. The most intense line in the Raman spectrum of H_2 is the $Q(1)$ feature in the 1-0 vibrational band, corresponding to a Raman shift of 4155.201 cm^{-1}.[291] It is then possible to collect this shifted light, at a frequency $\omega_s = \omega_d - 4155.201$ cm^{-1}, where ω_d is the input dye light frequency. To produce shifted light over the energy range of 1.0-1.4 eV, dye wavelengths of 840-655 nm must then be employed, corresponding to the output of the dye laser when pumped with 532 nm light from the Nd:YAG.

In such a setup, the output of the dye laser is focused through a BK7 plano-convex lens with a +500 mm focal length (Thorlabs LA1908-AB) into a tube 64 cm in length and containing $\sim$ 400 psi of H_2. Upon exiting the tube, the light is re-collimnated by another +500 lens before passing through a 600-900 nm dichroic mirror (Thorlabs DMLP900) to remove the dye-light fundamental. To remove any residual dye-fundamental light, the beam then passes through a long-pass filter with cut-on wavelength 900 (Thorlabs FEL900) or 1100 nm (Thorlabs FEL1100), depending on the wavelength to be generated. The resulting beam then has the same diameter as the incident beam, but with a frequency red-shifted by 4155.201 cm^{-1}.

Importantly, Raman scattering is not a perfectly coherent process (the depolarization ratio of H_2 is measured as 0.01048(4)),[292] resulting in the output polarization of the shifted light being slightly elliptical. To correct for this the Raman-shifted light is passed through a linear polarizer (Thorlabs LPNIRE100-B) following the long-pass filter, to ensure only the vertical component of the beam is transmitted into the chamber. Following these optics, the light is then transmitted through the standard prism and lens assembly into the vacuum chamber.

Importantly, the efficiency of the Raman shifter cell is impacted by the pressure of gas within the cell, with higher pressures leading to higher efficiency. There is a balance to strike, however, as the increase in pressure can lead to collisional broadening. Grossmann and co-workers[293] report a 15% efficiency for production of 940 nm light in a similar cell to ours using 200 psi, though we have found that to produce appreciable intensity at longer wavelengths requires a cell pressure of 380 psi. With this set-up, we have measured efficiencies

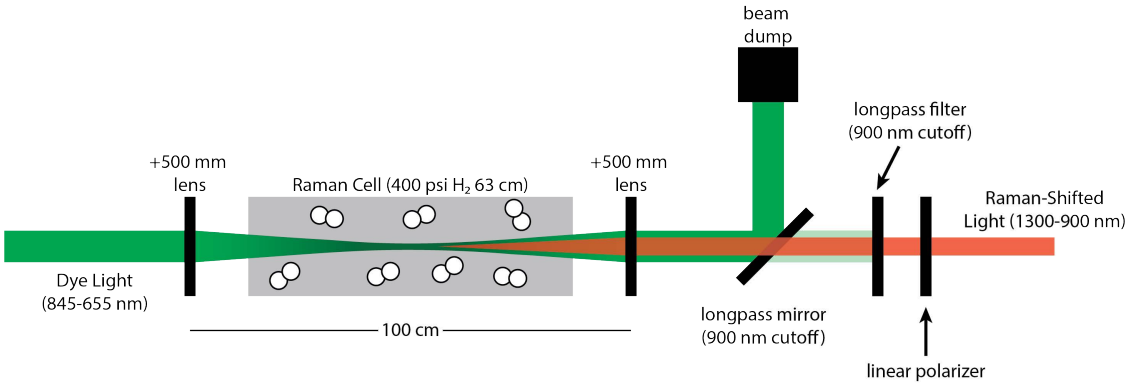

Figure 2.15: Schematic of the Raman shifter setup. Note that the incident dye light and the Raman-shifted light have the same beam diameter in the lab.

as high as 18% for $\sim$ 1025 nm light, which drops to a maximum of $\sim$ 8% efficiency when producing $\sim$ 1225 nm light. In all cases, increasing the pulse power of the dye laser entering the Raman cell dramatically increases the efficiency, often by nearly an order of magnitude (see figure 2.11 in the thesis of Jessalyn DeVine for a detailed plot of dye efficiencies).[232] Importantly, the spectra collected using the Raman shifter do not appear broadened relative to those taken with the raw dye laser output, indicating that collisional-broadening of the Raman-shifted light is minimal.

Chapter 3

IR-cryo-SEVI

3.1 Introduction

The previous two chapters have been dedicated to outlining cryo-SEVI and its many strengths - the ability to probe the vibronic structure of elusive species in high resolution is remarkable. This, however, is requisite upon a few experimental considerations aligning for our needs - good detachment cross section, *s*-wave detachment, and as outlined in Section 1.2.3.1, sufficient Franck-Condon overlap to observe vibrational structure. These conditions are often met for the variety of systems studied by cryo-SEVI, though even when they do, they only provide a glimpse into the full neutral potential energy surface, owing to the weak activity or inactivity of many non-totally symmetric modes or bends, particularly free OH,[75] CH,[77] and NH[76] stretches. While this is not limiting in terms of probing vibronic structure of many molecules, in some cases these blind spots prevent the observation of some truly fascinating phenomena.

Consider, for instance, the unimolecular isomerization reaction of vinylidene (H_2CC) to acetylene (HCCH), which occurs through a 1,2-hydrogen shift,[294] and has been studied extensively by our group and others.[14,40,41,113,236,237,295,296] Previous cryo-SEVI investigation into this species found signatures of isomerization through the ν_5 anti-symmetric stretching and ν_6 in-plane rocking modes, which were able to couple to highly vibrationally excited states of acetylene *via* tunneling. Such an observation was facilitated by the appearance of the FC-forbidden 6_0^1 and 5_0^1 photodetachment transitions, activated through HT coupling to an excited electronic state of the neutral, resulting in very weak features. Studying other photodetachment transitions involving these modes would be of considerable interest to understanding the coupling between these two states, ultimately providing insight into the fundamentals of isomerization. Unfortunately, transitions to odd quanta along these modes from the anion ground state are FC-forbidden by symmetry, preventing such a study using cryo-SEVI where anions are vibrationally cold.

In order to circumvent this limitation in vinylidene, and in anions generally, would require a change in the selection rules of the technique. While this is not possible, changing the

initial state from which photodetachment occurs can provide access to new regions of the neutral potential surface, as excited vibrational states will have different FC-overlap integrals (Equation 1.9). Increasing ion temperatures may allow for some vibrational modes to be populated, but high-frequency modes would require substantial vibrational temperatures, and as is discussed in Section 1.2.2, such a temperature would lead to considerable spectral congestion and rotational broadening. An alternative to this problem is selectively pre-exciting the anions prior to photodetachment *via* an IR photon.

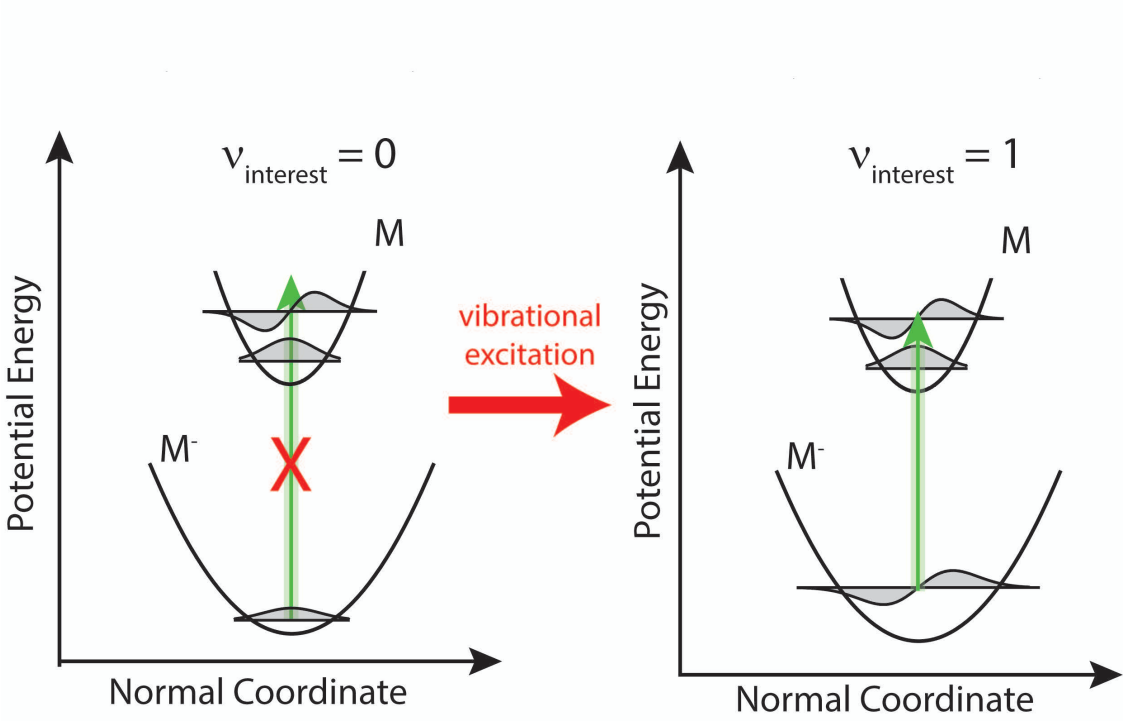

Figure 3.1: Schematic diagram of vibrational pre-excitation for anion PES.

In such a scheme, shown in Figure 3.1, anions cooled to their vibrational ground states in the cryo-trap will be irradiated with IR photons of an energy selected to be resonant with a vibrational transition of interest. Photodetachment from these vibrationally excited anions provides FC-overlap with the sequence band, ν_1^1, allowing for the probing of previously inaccessible regions of the neutral potential surface. Such a scheme should be generally applicable to any anionic species provided the vibrational mode in question is IR-active (as governed by Equation 1.32) and sufficient population transfer from the ground state to the vibrationally excited state can be achieved.

The remainder of this chapter details the incorporation of such a tunable IR source into cryo-SEVI, termed IR-cryo-SEVI, including the underlying physics of how such light is produced (Section 3.2), design considerations that went into the components integrated (Section 3.3), the final setup of the machine with these components (Section 3.4), how this

system operates (Section 3.5), future considerations for this new instrument (Section 3.6), and a table of all components involved in this new build (Section 3.7).

3.2 Principles of Operation: Non-linear Optics

The light source required for IR-cryo-SEVI produces light through the use of Difference-Frequency Generation (DFG), which itself falls into the category of non-linear optics. In such a process, two photons of different frequencies - termed the pump (ω_1) and the signal (ω_2), where $\omega_1 > \omega_2$, are mixed to create a third photon at the difference of their frequency ($\omega_3 = \omega_1 - \omega_2$), termed the idler. Here, we outline the physics that allows for such a process in brief (a full consideration of these phenomena are presented in Boyd).[297]

3.2.1 Background

The name "non-linear optics" originates from the non-linear response of a material system to an applied optical field as a function of the strength of the optical field. This was first discovered by Franken *et al.* in 1961,[298] who observed second-harmonic generation (SHG) shortly after the demonstration of the first working laser by Maiman in 1960.[299] This timeline is no coincidence - the advent of lasers represented the first light sources capable of producing high enough intensities for non-linear phenomena to occur.

For such a process to occur, we must consider the dipole moment per unit volume, or polarization $\tilde{P}(t)$, of a material system, which depends on the strength of an applied optical field, $\tilde{E}(t)$. In the case of linear optics, the induced polarization can be described by

$$\tilde{P}(t) = \epsilon_0 \chi^{(1)} \tilde{E}(t) \tag{3.1}$$

where $\chi^{(1)}$ is the linear susceptibility and ϵ_0 is the vacuum permittivity. Expanding the polarization in a power series in the field strength then returns an expression which is non-linear in $\tilde{E}(t)$, allowing for the description of non-linear phenomena by

$$\tilde{P}(t) = \epsilon_0 \big[\chi^{(1)} \tilde{E}(t) + \chi^{(2)} \tilde{E}^2(t) + \chi^{(3)} \tilde{E}^3(t) + ... \big] \tag{3.2}$$

which can be expressed more simply as

$$\tilde{P}(t) \equiv \tilde{P}^{(1)}(t) + \tilde{P}^{(2)}(t) + \tilde{P}^{(3)}(t) + ... \tag{3.3}$$

where $\chi^{(2)}$ and $\chi^{(3)}$ are the second- and third-order non-linear optical susceptibilities. Further, $\tilde{P}^{(2)}(t)$ and $\tilde{P}^{(3)}(t)$, are the second- and third-order non-linear polarization of the material, though for the processes relevant here (SHG and DFG), we will only need the second-order term.

3.2.2 Second-Harmonic Generation

Let us consider the process of SHG, which occurs in our detachment Nd:YAG to produce 532 nm light - here, the electric field of the laser can be represented as

$$\tilde{E}(t) = Ee^{-i\omega t} + \text{complex conjugate} \tag{3.4}$$

If this beam is then incident upon a crystal with $\chi^{(2)} \neq 0$, a non-linear polarization is created in the medium, as expressed by Equation 3.3. Substituting in Equation 3.4 returns:

$$\tilde{P}^{(2)}(t) = 2\epsilon_0\chi^{(2)}EE^* + (\epsilon_0\chi^{(2)}E^2e^{-2i\omega t} + \text{complex conjugate}) \tag{3.5}$$

From Equation 3.5, we see that the expression for the second-order polarization has two terms: the first, which does not depend on ω, and the second, which depends on 2ω. Importantly, it is the second term then can lead to the generation of radiation at the second harmonic frequency.

An important symmetry consideration of the polarization above is that all even-order coefficients must disappear for media with inversion symmetry. This arises as inverting the vector along which the field propagates, i.e. $\vec{P} \rightarrow -\vec{P}$ and $\vec{E} \rightarrow -\vec{E}$, introduces a minus sign here, while inverting the direction in the medium, i.e. $\vec{r} \rightarrow -\vec{r}$ leaves an inversion-symmetric medium unaffected. Therefore, SHG (and all second order processes) can then only occur in media without inversion symmetry. While many media do not satisfy this condition, a special subclass of materials, termed "non-linear crystals", which are discussed in more detail in Section 3.2.5, do.

SHG can also be thought of as two photons of frequency ω interacting in the medium. This interaction converts the two photons into a photon of frequency 2ω. Such a process is shown in the schematic below.

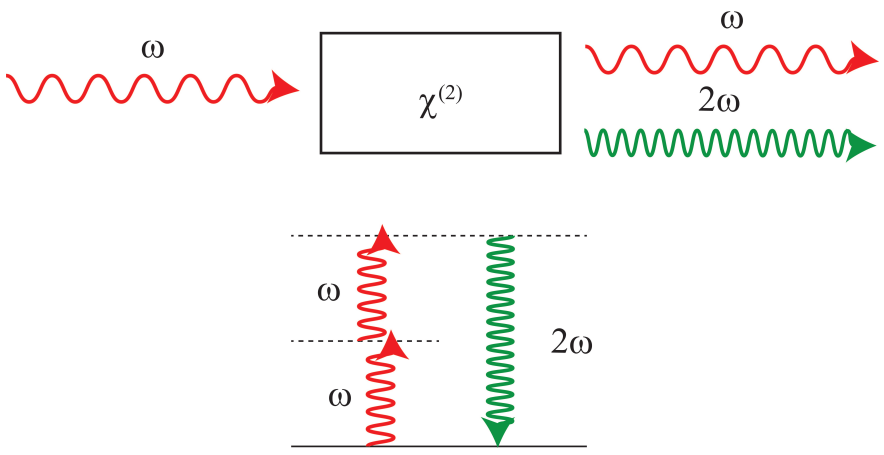

Figure 3.2: Schematic of second-harmonic generation occurring in a non-linear crystal (top), and energy-level diagram of the process (bottom).

3.2.3 Difference-Frequency Generation

Similar to SHG are the processes of Sum- and Difference-Frequency Generation (SFG and DFG, respectively), which can be thought of as a more general expression of SHG. Here, the incident light has two distinct frequencies, often originating from the spatial and temporal overlap of two laser pulses. This field can be expressed as

$$\tilde{E}(t) = E_1 e^{-i\omega_1 t} + E_2 e^{-i\omega_2 t} + \text{complex conjugate} \tag{3.6}$$

As above, SFG and DFG require a non-linear medium for which $\tilde{P}^{(2)} \neq 0$ and can be expressed by Equation 3.3. Once more substituting in the expression for our field here returns

$$\begin{aligned}\tilde{P}^{(2)} = \epsilon_0 \chi^{(2)} \big[& E_1^2 e^{-2i\omega_1 t} + E_2^2 e^{-2i\omega_2 t} + 2E_1 E_2 e^{-i(\omega_1+\omega_2)t} \\ & + 2E_1 E_2^* e^{-i(\omega_1-\omega_2)t} \big] + 2\epsilon_0 \chi^{(2)} \big[E_1 E_1^* + E_2 E_2^* \big]\end{aligned} \tag{3.7}$$

Expressing this using the notation

$$\tilde{P}^{(2)}(t) = \sum_n P(\omega_n) e^{-i\omega_n t} \tag{3.8}$$

where the summation includes all positive and negative frequencies ω_n. The complex amplitudes of the various frequency components of the non-linear polarization are then given by:

$$\begin{aligned} P(2\omega_1) &= \epsilon_0 \chi^{(2)} E_1^2 \quad \textbf{(SHG)} \\ P(2\omega_2) &= \epsilon_0 \chi^{(2)} E_2^2 \quad \textbf{(SHG)} \\ P(\omega_1 + \omega_2) &= 2\epsilon_0 \chi^{(2)} E_1 E_2 \quad \textbf{(SFG)} \\ P(\omega_1 - \omega_2) &= 2\epsilon_0 \chi^{(2)} E_1 E_2^* \quad \textbf{(DFG)} \\ P(0) &= 2\epsilon_0 \chi^{(2)} (E_1 E_1^* + E_2 E_2^*) \quad \textbf{(OR)} \end{aligned} \tag{3.9}$$

Each term in Equation 3.7 is thus represented by one of the above expressions, and are labeled with the physical process described, where (OR) is the optical rectification, which will be ignored here. Equation 3.9 above details succinctly the relationship between SHG and SFG/DFG and implies that all four nonzero frequency components may be simultaneously output from a non-linear medium. This however, is rarely observed in practice, as the output of a particular component of the above expression can only be efficiently produced if certain phase-matching conditions (Section 3.2.5) are satisfied. These conditions restrict the practical generation of these non-linear signals to typically only one (i.e. SHG, SFG, or DFG), by properly selecting the polarization of the input radiation and the orientation of the non-linear crystal.

Let us now focus on DFG briefly. This process is described by a non-linear polarization

$$P(\omega_1 - \omega_2) = 2\epsilon_0 \chi^{(2)} E_1 E_2^* \tag{3.10}$$

which is displayed below in Figure 3.3, and where the frequency of the generated wave is the difference of the two fields applied. Here, it is important to note that conservation of energy requires a photon at the higher input frequency, ω_1 must be destroyed to generate two photons, one at ω_3 and another at ω_2, expressed as

$$\omega_3 = \omega_1 - \omega_2 \tag{3.11}$$

This then means that the lower input frequency (ω_2) is amplified during DFG, in a process termed optical parametric amplification (OPA). This can be thought of as the crystal absorbing a photon of frequency ω_1, exciting it to a virtual level. This level then decays by a two-photon emission that is stimulated by the presence of the ω_2 field, as is shown in the bottom of Figure 3.3.

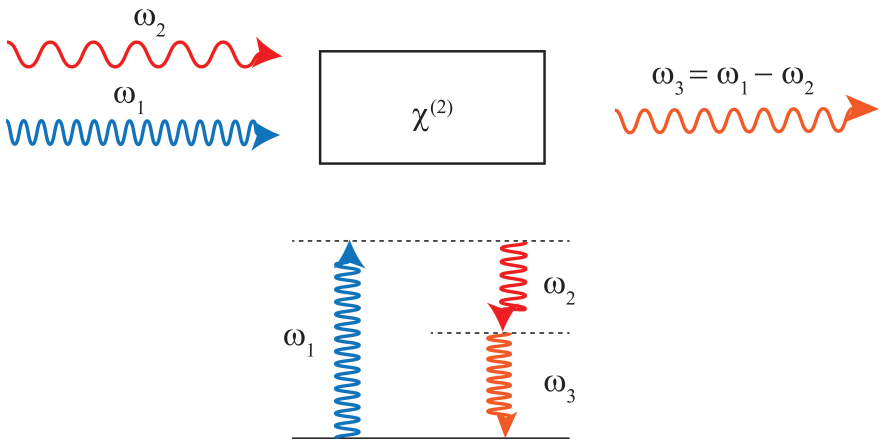

Figure 3.3: Schematic of difference-frequency generation occurring in a non-linear crystal (top), and energy-level diagram of the process (bottom).

3.2.4 Optical Parametric Oscillation

Related to optical parametric amplification is Optical Parametric Oscillation (OPO), wherein the non-linear medium that facilitates DFG is placed in an optical resonator. Such a setup only requires one input frequency (the "pump" at ω_p), and allows for the build-up of the ω_2 or ω_3 fields, due to the cavity. Here, $\omega_2 + \omega_3 = \omega_p$. OPOs are commonly used at infrared frequencies as other sources of tunable IR radiation are sparse. Any pair of frequencies ω_2 and ω_3 that sum to ω_1 satisfy energy conservation, and so are allowed. The selection of particular output frequencies is then possible through adjusting the phase-matching condition.

3.2.5 Phase Matching

To understand the requirements of phase matching, we will treat the incident beams as plane waves. Such an assumption is good when the laser beam is wide enough to neglect the effect of focusing. The spatial component of the incident light is proportional to $\exp(i\vec{k_\omega}\vec{r})$, where $\vec{k_\omega}$ is the wave vector of the incident light at a particular frequency, ω.

In the simplest case, we will assume that the incoming and outgoing waves are collinear along z, so that $\vec{k_\omega} = k_{z,\omega}$. Further, we will assume the the crystal has a thickness L and extends from $z = 0$ to $z = L$. The non-linear process can occur at any position along the the crystal length, where at each position the dipole emitter generated can be expressed by the non-linear polarisation generated by the incoming wave (i.e. $|exp(ik_{z,\omega}z)|^2 = \exp(i2k_{z,\omega}z)$ for SHG). In the case of SHG, the plane waves emitted in the forward direction have double the frequency and are of the form $\exp(-ik_{z,2\omega}z)$. The efficiency of this process can be determined by summing all contributions from different positions, leading to the conversion efficiency per unit length:

$$\eta = \frac{1}{L^2}\Big|\int_0^L e^{(i2k_\omega z)}e^{(-ik_{2\omega}z)}dz\Big|^2 = \frac{1}{L^2}\Big|\int_0^L e^{(i\Delta kz)}dz\Big|^2 = \Big(\frac{\sin(\Delta kL/2)}{\Delta kL/2}\Big)^2 \tag{3.12}$$

where $\Delta k = 2k_\omega - k_{2\omega}$ for SHG. From the above expression, it should be obvious that this can be generalized for other non-linear processes, where Δk generally is represented as

$$\Delta k = k_1 + k_2 - k_3 \tag{3.13}$$

and describes the wavevector mismatch of the process. Note that the sinc function has a maximum for $\Delta k = 0$ where $\eta = 1$. Achieving a wavevector mismatch, Δk, of zero is often difficult as the refractive index of materials changes with monotonically with frequency (i.e. $n(\omega)$), precluding perfect phase matching with collinear beams.

This limitation, however, can be circumvented in birefringent materials, for which the refractive index not only depends on the wavelength, but also on the polarization direction of the light relative to the crystal axes. Thus, achieving $\Delta k = 0$ *can* be performed by tuning the angle of these crystals with respect to the incident light. There are two types of angle tuned phase matching, Type I and Type II. In Type I, the signal and idler have the same polarization, while in Type II, they have different polarizations.

It is standard to describe the type of phase matching used with three letters denoting whether the corresponding wave is ordinary (o, light parallel to the optical axis) or extraordinary (e, light perpendicular to the optical axis) with respect to the birefringent media. Here, the optical axis is the direction within the crystal in which a ray of transmitted light suffers no birefringence. The first letter corresponds to the pump, the second, the signal, and the third, the idler.

Importantly, the refractive index for e-waves is not only a function of wavelength, but also of crystal angle. It is this dependence, in particular, that is exploited when tuning the

angle of the incident beam with respect to the crystal, to select a different signal/idler pair. This is the fundamental aspect that allows for the construction of a *tunable* IR light source as is needed for IR-cryo-SEVI.

3.3 Design Considerations

As stated at the start of this chapter, there are two considerations for the development of IR-cryo-SEVI:

1. A transition involving the IR mode in question is IR active (and has an appreciable absorption cross-section)

2. A transition involving the IR mode in question occurs at an energy for which photons can be generated with appreciable intensity

The first of these considerations is rather straightforward to assess - symmetry considerations can be used to quickly determine the IR-activity of a mode, and even cheap computational methods can give a reasonable estimate of the IR absorption intensity. Although this consideration is easily evaluated, it can also be strictly limiting - transitions that are IR-inactive or have very weak IR intensities are not viable targets for IR-cryo-SEVI. Fortunately, there are many IR-active modes available for probing, provided they can be excited.

3.3.1 Tunable Infrared Light

The second consideration is the main focus of this section - the approach of vibrational pre-excitation is aimed to be a general solution, requiring a source capable of producing IR radiation over a wide range of photon energies, as to to be able to pump various vibrational modes of various species. The need for a tunable IR source is compounded by the underlying requirement that the anion frequency of interest be known to relatively high precision, or at least that of the IR source's bandwidth (fwhm ~ 3 cm^{-1}). Unfortunately, this is rarely the case - anion vibrational frequencies are not commonly studied. This can be ameliorated, to some degree, with the use of high-level theory to obtain a reasonable estimate of the anion vibrational frequency, and thus the required photon energy to pump the transition. As these values, even for remarkably expensive methods, often differ from the experimental value by a few wavenumbers, a tunable IR source is then required to search for transitions of interest.

While there exist a number of commercial IR sources that produce good flux over the near-IR, few extend into (or near) the mid-IR and far-IR, where a number of molecular vibrations of interest lie, including the ν_6 vibration of H_2CC^- (~ 875 cm^{-1}, or $\lambda = 11.5\,\mu$m). Further, given that some molecular vibrations have low IR cross sections, good flux throughout this region is imperative. Finally, there exists a Goldilocks criteria on the bandwidth - we need a sufficiently narrow linewidth to selectively excite the particular vibration of interest (and not

other nearby vibrations), without being so narrow that scanning to find the actual transition becomes a hindrance.

For this reason, the LaserVision OPO/OPA system, manufactured by Dean Guyer (an early Leone graduate student), was purchased. The system is used in many labs that need tabletop IR sources for IRPD or similar action spectroscopies,[300–302] and is capable of producing tunable IR light from 1.35 - 5 μm natively, which can be extended out to 16 μm with the addition of an external crystal, and has a bandwidth of ~ 3.5 cm^{-1} when pumped with an unseeded laser (1.7 cm^{-1} with a seeded laser). Details of this system, as well as its use, are described in Section 3.4.

3.3.2 Signal Limitations

The other concern in developing such a method is that the signal will be too low to detect. There are a number of experimental considerations that could reduce signal - loss of IR power due to absorption by water or carbon dioxide in the lab air, poor temporal or spatial overlap, incorrect IR frequency, improper focal position, and many others.

The first of these is the lab humidity - a common concern in labs that use IR light sources. We monitor our room humidity with a temperature and humidity sensor, finding that the lab ranges between 30-50% relative humidity (4600-7700 ppm H_2O by weight). This can be reduced with a dry-air (or nitrogen) source and a sealed enclosure around the laser system - Parker sells a number of dry N_2 generators that come recommended by the Fleming group, who has used them with very little hassle. Alternatively, the house dry air can be used - this comes to our lab at $\sim$ 35 psi and has a relative humidity of $\sim$ 8%, though there is considerable particulate in our gas line as of this writing. While there is a noticeable drop in the IR intensity between the output of our light source and the entrance to the chamber on a note card, this is not currently a limiting factor, and so the ambient conditions are what the IR light sees.

The remaining considerations have proven to be the bulk of the challenge in getting this system operational. The procedure we developed for maximizing overlap in space and time is outlined below in Section 3.5.2, while determining the correct IR frequency is outlined in Section 3.5.3. Assuming that all of these parameters have been optimized, the question remains - how much signal can we expect to observe?

This answer depends on a number of factors. First, the IR cross section of the interaction in question and the photon flux in this spectral region, which, when combined, relate the fraction of ions excited by each laser shot. Second, the velocity of the ion packet and the delay between the IR light and dye light, which relate to the number of remaining vibrationally-excited anions that are irradiated by the photodetachment laser. Finally, the detachment cross section of the species in question and the flux of the detachment laser, combining to give the fraction of ions detached by each laser shot.

If we are interested in determining the *maximum* allowable signal from excited anions, we can make a few assumptions. First, we assume that the photodetachment probability for ground-state and vibrationally-excited anions are the same, and are thus sampled equally by

the detachment laser pulse. Second, we will assume that our ion population is saturated with IR photons such that the maximum number of anions are excited, achieving a 50% excitation of the population. This upper-bound is set as a population inversion is not possible in these systems (i.e. the relaxation rate must be greater than or equal to the excitation rate). Finally, we will assume the IR laser pulse is broader in space and time than the detachment laser pulse.

Under these assumptions, the question can be reframed - what fraction of ions that are vibrationally excited are then photodetached? If the ion packet and both lasers are perfectly overlapped in space and time, then this fraction is 100% of the anions excited are then exposed to the detachment laser, giving a 50% depletion signal at maximum. If however, the beams are not overlapped in space or time, this is no longer the case.

Take, for example, the case in which the beams are spatially overlapped, but temporally delayed. Given the jitter of both lasers (±1 ns for the IR source, and ± 5 ns for the dye laser), this is a likely scenario. In such a situation, the IR pulse excites some population of the ion packet, which itself is in motion. After some time delay, the detachment laser pulse strikes the same spot as the IR laser, but in this delay time, some fraction of the excited population has translated out of the focal spot of the detachment laser, decreasing the fraction of ions that are both vibrationally excited and photodetached. Such a scenario is shown diagrammatically below in Figure 3.4.

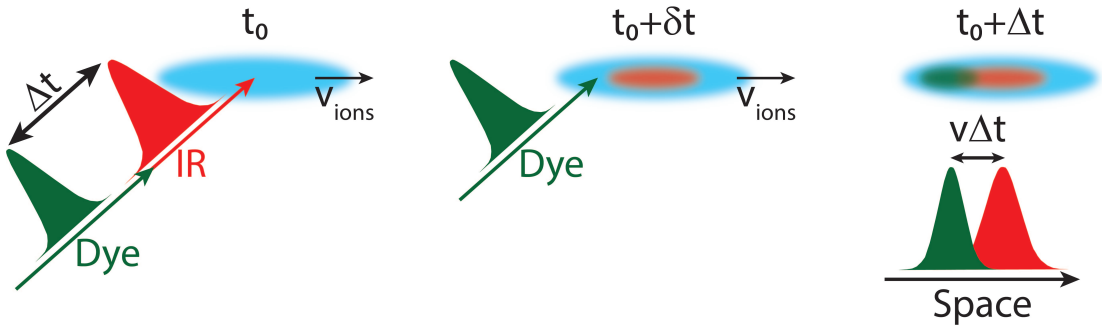

Figure 3.4: Cartoon outlining the relationship between temporal delay between spatially overlapped pulses and the resulting spatial mismatch of excited anions, due to the motion of the ion packet.

In the simplest treatment of this - assuming that none of the excited anions relax during this time delay - we can model the fraction of ions that see both laser pulses by the overlap of three Gasussian functions in space. This is a fair assumption, as the OPA and dye laser outputs are reported to be Gaussian in space, and the ion packet shape can vary, but is typically optimized for a Gaussian distribution on the MCP detector in the VMI region prior to photodetachment.

The fwhm of each distribution can then readily be measured; the radius of the two laser beams, r_0 can be measured directly prior to focusing, while the ion packets can be calculated

taking the fwhm in time and multiplying by the velocity of the ions, given by Equation 2.11.

The fwhm of the Gaussian beam profiles at the point of interaction can be determined by the focused beam spot size, R_f, which can be determined using:[303]

$$R_f = \frac{2\lambda f(\lambda)}{\pi r_0} \tag{3.14}$$

where λ is the wavelength of the light in question, and $f(\lambda)$ is the focal length of the optic, which depends on the refractive index of the material, itself a function of wavelength.

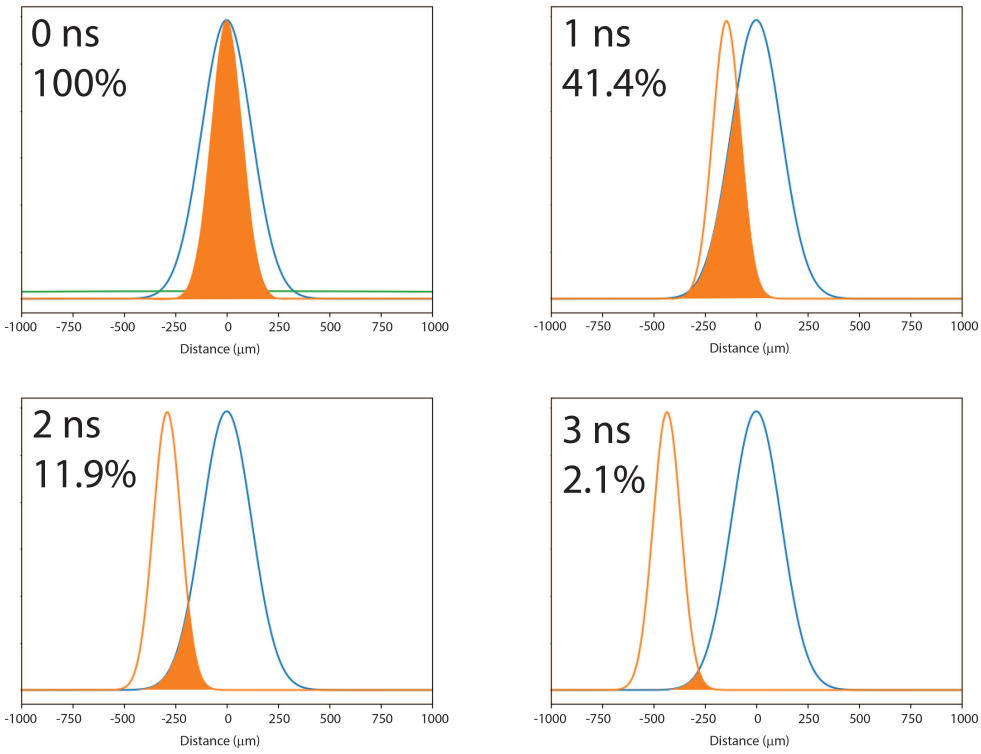

Figure 3.5: Simulations of differing overlap of IR (blue) and dye (orange) pulses at different time delays, accounting for speed of the ion packet and spatial profiles of the beams. Associated overlap percentages are reported, highlighting that slight temporal (or spatial) mismatches result in significant losses of signal. Here, variations of the ion packet over these time variations are ignored, owing to the relatively short timescales relevant, as exemplified in the top left panel, where a Gaussian distribution describing the ion packet's spatial distribution is plotted in green.

Take for example, the case of pre-excitation and detachment of OH^- (Chapter 6). Here, the ions are travelling at a velocity of 145 μm/ns (ΔV = 1.85kV, m = 17), and the fwhm

of the ion packet in time was $\sim$ 40 ns, leading to a spatial fwhm of 5.797 mm. Further, the measured spot size for both the dye laser and IR light (r_0) were 0.5 cm, with focal lengths of 1.0 m for the dye laser (λ = 660 nm) and 0.477 m for the IR light (λ = 2777 nm). These values in Equation 3.14 yield R_f values of 170 and 337 μm for the dye and IR light, respectively.

We can then model the three spatial distributions with maxima at μ_{ions}, μ_{IR}, and μ_{dye} and $\sigma_{ions,IR,dye} = \text{fwhm}_{\text{ions,IR,dye}}(2\sqrt{2\ln 2})^{-1}$. Given that the curvature of the ion packet should vary little in shot time delays, the distribution describing the ion packet can be assumed to be a constant, allowing for us to treat just the overlap of the two laser distributions. This is shown in Figure 3.5 below for a number of different time delays where the blue curve is the ion packet exposed to the IR light and orange is the detachment laser pulse. In each panel the delay between pulses is varied, with 0 as perfect overlap. This bounds the observable fraction of ions detached, in this ideal case, between and 2% and 100% of those that absorbed an IR photon (translating to 1-50% depletion signal).

In reality, the fraction of ions that absorb an IR photon will vary in each system and for each vibrational transition, though we observed a $\sim$30% depletion in ground-state signal from OH^- when pumping the R(0) rovibrational transition ($\sim$12 mJ/pulse, or $\sim 1.7 \times 10^{17}$ photons/pulse), which does not have a notably strong IR intensity (calculated as 81 KM/mole, at the CCSD/aug-cc-pVTZ level), indicating that such estimates give the right order of magnitude for observable signal when the set-up is optimized.

3.4 Instrumental Overview

Taking into account the considerations outlined above, we were successfully able to integrate such an IR system into cryo-SEVI and take spectra of vibrationally excited anions. This light source is a combination of an OPO and OPA used to generate photons between 1.35-16 μm with sufficient flux for our needs. The pulses have fwhm of ~ 3 cm^{-1} spectrally and ~ 6 ns temporally. Here, we outline the system itself as well as the incorporation of the system into the existing machine.

3.4.1 LaserVision OPO/OPA

The LaserVision system is shown below in Figure 3.6 and comprises four main sections; the pump laser (Section 3.4.1.1), the OPO arm (Section 3.4.1.2), the OPA arm (Section 3.4.1.3), and the far-IR generation arm (Section 3.4.1.4).

The system, which operates at 10 Hz - owing to the frequency of the pump laser - is capable of putting out near-IR (nIR), mid-IR (mIR), intermediate-IR (iIR) and far-IR (fIR) signal over various ranges of wavelengths and powers, as outlined below:

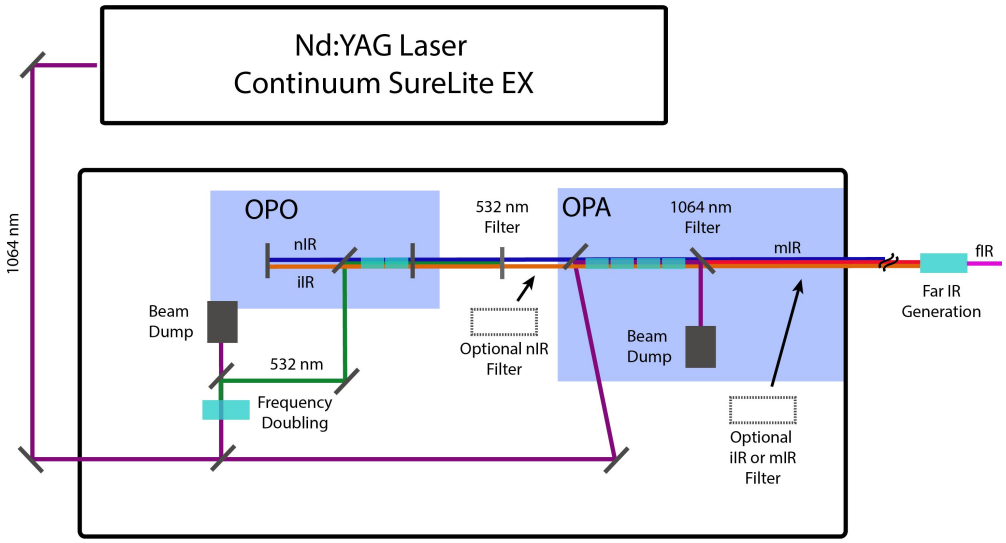

Figure 3.6: Schematic of the LaserVision OPO/OPA used in cryo-SEVI. The system is pumped by the fundamental of a Nd:YAG (1064 nm, purple), which encounters a beamsplitter to pump both the OPO and OPA. The light that drives the OPO arm is then frequency doubled (532 nm, green), and sent to the OPO, which produces nIR (blue) and iIR (orange) light. The output of the OPO then is filtered to remove the 532 nm light, and optionally the nIR. The remaining light then enters the OPA and mixes with the 1064 nm light to form mIR (red) light. The output of this is then optionally filtered or optionally converted to fIR (pink) using an external crystal 2m from the OPO/OPA system.

Name	Wavelength Range	Power	Polarization
Near IR	710-880 nm		horizontal
Intermediate-IR	1.35-2.218 μm	$\sim$12 mJ	horizontal
Mid-IR	2.218-5 μm	7 - 0.3 mJ	vertical
Far IR	4.7-16 μm	2 - 0.1 mJ	vertical

These outputs correspond to signal and idler out of the OPO and OPA, as shown below in Figure 3.7.

It should be noted that there is a crossing point where power for the iIR drops off before significant power in the mIR begins, leaving a dead-zone between $\sim$ 4650-4750 cm^{-1} (2.1-2.15 μm), which may be an issue in the future or when using this system for cryo-SEVI (see Section 3.5.6).

The crystals in each of the three arms are on motorized stages, controlled using custom software written for the unit, allowing for the selection of particular IR wavelength to be produced (though we have found this be be slightly inaccurate - see Section 3.5.3 for more). The software does this while maintaining optimal power, $E_{max}(\lambda)$ by using a fitting curve for

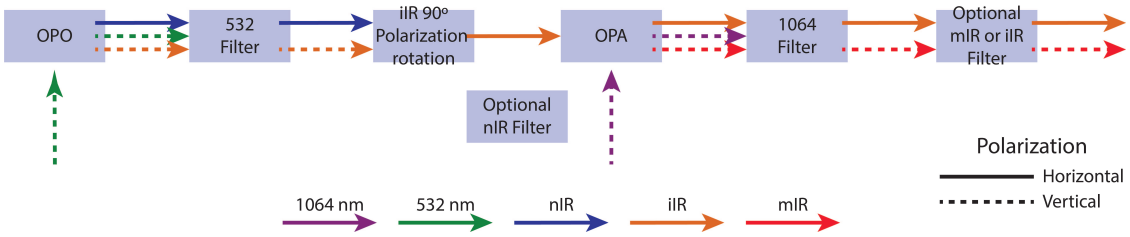

Figure 3.7: Abridged diagram of beams entering and exiting the LaserVision system. Note, this diagram differs from the LaserVision manual in that the mIR and iIR are swapped here, correcting an issue in the manual.

each motor to determine its relative position to the nIR signal wavelength and optimizing the crystal angle for power. These curves do occasionally need to be re-calibrated over time to maintain optimal power in the system - doing so is thoroughly outlined in the digital manual and can be done through the motor control software.

One operational note: while the software is intuitive for the most part, it occasionally enters "Demo Mode" when the connection between the Ethernet ports and motor controllers are disrupted, requiring the system and computer be restarted to return to operation.

3.4.1.1 Pump Laser

The OPO/OPA system is designed for use with an Nd:YAG laser operating at 1064 nm and 10 Hz as a pump source, specifically, the Surelite EX (manufactured by Continuum, now Amplitude). This is due to the strict beam quality requirements imposed by the LaserVision system to generate the IR outputs, for which 10 Hz Nd:YAG lasers perform superior to other Nd:YAG repetition rates.

The SureLite EX is a relatively simple laser compared to the Nd:YAG laser that pumps the dye laser - it has only one oscillator flash lamp / YAG crystal housing and no amplifier nor harmonic generation unit and produces pulses 4-6 ns in duration. The laser, while it does not have an injection seeder, does have the capability to be upgraded with one without being sent back to the factory, reducing the linewidth of the laser from 1 to 0.005 cm^{-1}, and narrowing the output of the LaserVision from a reported 3.7 to 1.7 cm^{-1}. The laser power is controlled by tuning the Q-switch trigger timing, with a maximum power output of 9.5 W at a Q-switch timing of 260 μs, while the timing of the laser with respect to the rest of the experiment is controlled *via* the flashlamp trigger timing.

Given the importance of the beam quality of this laser for use with pumping the LaserVision, it is important to note some issues with the laser's beam profile. These have stemmed either from poor alignment of the rear mirror, leading to a particularly bad beam profile at the output, or from poor alignment of the cylindrical lens at the output of the oscillator cavity, leading to a strong divergence in the beam over a distance of 4 m. Both have since been fixed, as outlined in the Appendix.

Once the beam profile is suitable, the 1064 nm output of this laser can then be directed into the LaserVision OPO/OPA with two external mirrors, allowing for fine control over the beam direction. The beam entering the system first meets the entrance aperture and telescope, which adjusts the beam profile before hitting a beam splitter, dividing the horizontally polarized pump into two beam lines: one for the OPO, and one for the OPA.

3.4.1.2 OPO

The 1064 nm light in the OPO arm, upon leaving the beamsplitter, is then frequency doubled in a KTP crystal to form the 532 nm input for the OPO. The power of this is modulated by a half-wave plate mounted in a rotation stage that is placed before the KTP crystal, allowing for the extent of conversion from 1064 to 532 nm to be controlled. After doubling, the light is then steered into the OPO with two 532 nm high reflecting mirrors (HR mirror).

The OPO is configured as a linear cavity with two KTP crystals between a rear mirror and output coupler. Here, the 532 nm light enters the oscillator and is transformed *via* parametric conversion to a nIR signal and iIR idler. The two crystals are oriented with their optical axes pointed in opposite directions to compensate for beam steering as the crystal rotates.

From here, the output of the OPO, which is roughly an ellipse with a vertical long axis is sent to a Dove prism, where it is rotated 90°. This both assists with phase-matching concerns in the OPA as well as improved output beam profile. The polarization of then rotated by a MgF_2 waveplate so that the OPA crystals can be angle-tuned in the horizontal plane rather than vertical plane. From here an Si filter can optionally be placed in the beam path to filter out the signal (nIR) from the OPO.

3.4.1.3 OPA

The other arm of the 1064 nm pump light makes up the OPA arm. This first passes through a 1064 nm attenuator, formed once more by a half waveplate in a rotation mount, here effective because the polarization of the 1064 nm light needs to be rotated by 90° to satisfy phase matching conditions for the OPA. From here, it is directed to the OPA by two 1064 HR mirrors.

The OPA stage consists of two pairs of KTA crystals, again matched as to prevent different pointing as the crystals are rotated. Here, the iIR idler from the OPO serves as the signal wavelength and the 1064 nm as the pump, amplifying the iIR signal and creating the mIR signal through difference frequency generation. The output pulses are of opposite polarization: iIR is horizontally polarized while the mIR is polarized vertically.

The remainder of the beampath serves to clean up the beam. First, the residual OPA pump (1064 nm) is removed by a separator mirror (a 1064 HR mirror with high throughput for 1.45-5 μm), which directs the pump into a beam dump while passing the iIR signal and mIR idler. From here, an optional stack of silicon plates, set at Brewster's angle can be placed in the beam, allowing for a transmitted beam that is strongly polarized vertically or

horizontally. The face of this filter makes either a "C" or "U" as it is rotated, passing vertical (mIR) or horizontal light (iIR), respectively.

3.4.1.4 Far-IR

In order to generate light beyond ~ 5 μm, the fIR extension unit must be employed. This consists of an $AgGaSe_2$ crystal mounted to an external motor mount at a minimum distance of 2 meters. This distance is specified to ensure that the collimation of the iIR and mIR is good, as these two beams serve as the signal and idler for another difference frequency generation process to output in the fIR. As such, the divergence of the fIR is strongly dependent on these two beams.

The crystals used here are particularly easy to burn and hard to obtain. For this reason, Dean Guyer has been searching for an alternative, and recently reported success with a ZGP crystal (C- was used, but YS- should have improved transmission). Using such a crystal should allow for the production of ~ 3.5 mJ/pulse at 5 μm and nearly 1 mJ/pulse at 12.6 μm (793 cm^{-1}). To date, these crystals have not been purchased, but offer a promising alternative to the $AgGaSe_2$ crystals we currently own.

3.4.2 Beam alignment

With the light source determined, the remaining considerations regard placement of the system within the lab and beam steering. Placing both laser systems on the same table and sending the beams collinearly was not possible, given the space required for the LaserVision OPO/OPA, meaning that a new laser table was required, as well as shielding. Getting the beams collinear, or nearly so, from this setup would require an annular mirror, which our colleagues at Lawrence Berkeley National Laboratory (LBNL) who use this for 4-wave mixing strongly recommended against, given the complications it introduces in terms of alignment.

An alternative option was to send the IR beam vertically down into the chamber - this require the construction of new Brewster tubes, required to pass the far-IR light produced by this system, as the current windows are CaF_2, which has good transmission from 200 nm to 8 μm, and mounted at the Brewster angle for this particular material. While this is a benefit, it would require moving the turbo under the detector region of the chamber as well as steering the IR beam near eye height, a hazard not worth the simplicity.

For this reason, we decided on orienting the system such that the IR beam and the dye-light are collinear but counter propagating. The setup, shown in Figure 3.8, has the LaserVision and pump laser compactly placed on the laser table (3' wide by 6' long), with the 1064 nm light of the pump laser steering off of two HR mirrors and into the LaserVision system. The output light is then sent off of one or two gold mirrors, depending on the polarization of the light, onto a periscope comprised of two gold mirrors, before being sent through a CaF_2 lens and reflecting off of one final gold mirror and into the chamber.

This setup has a number of advantages without too many drawbacks. First, this layout allows for a simple alignment procedure to be developed - by using the same 3 iris used for

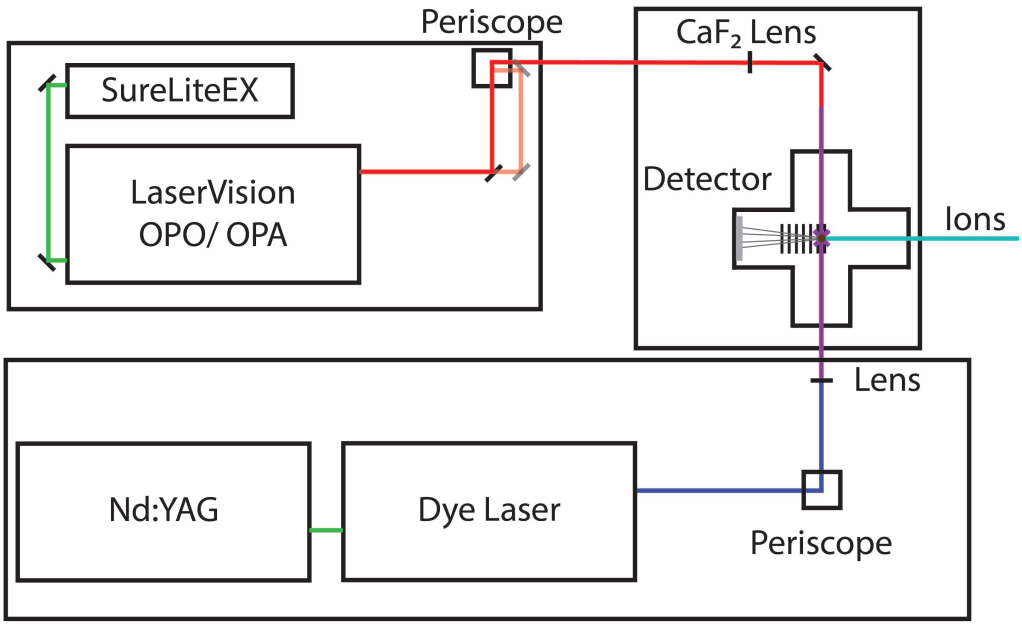

Figure 3.8: Schematic of the table layout for IR-cryo-SEVI, displaying beam paths for both horizontal (dark) and vertical (light) outputs from the OPA.

dye-light alignment, the steering of the IR laser can be assumed to be roughly overlapped with the dye light. The mirror nearest the periscope, the mirror on the top periscope mount, and the mirror nearest the chamber are used to align onto the three iris. Fine tuning can then be done while running the experiment to maximize signal.

Second, the inclusion of a lens for the IR light on the other side of the chamber has the benefit of not interfering with the dye-light focal length. Further, given the focal lengths of the two CaF_2 lenses (1 m for dye, 0.4 m for IR) and distance between the exit apertures of the dye laser and OPO/OPA system from the focal point of the lens ($\sim$ 5 m and $\sim$ 4 m, respectively), both beams are sufficiently divergent at this point as to not cause damage to the other system. In fact, measuring the dye-light power at the exit port of the LaserVision system shows an order of magnitude decrease in power, which is completely blocked by the filter at the exit of the LaserVision system.

Finally, this layout allows for the placement of the far-IR generating crystal to be mounted at least 2 m from the LaserVision output, and very near the IR-lens. This distance is required to ensure good beam profiles on the OPA outputs and avoid crystal burning. Further, given that the divergence of the far-IR is greater than any other output, the generation of this beam so close to the chamber ($<$0.5 m) should maximize the transmission into the chamber.

The drawbacks of this setup are limited. In this geometry, the IR light passes slightly above the power supplies for the detector MCPs and phosphor screen, which is a hazard

mitigated by the use of beam tubes between the table and the laser enclosure next to the detector region. Further, steering of the beam is facilitated by one unprotected gold mirror very near the chamber (after the IR lens), which is often burned by the highly-focused dye light exiting the chamber. This could be resolved by the inclusion of a filter for the dye light that passes the IR, though the options here are limited - very few commercial solutions exist to block visible light while passing the IR, especially over the broad ranges that we operate at. The final complication introduced by this setup will manifest when the far-IR is used - in such an instance, at least the window on the LaserVision port of the chamber must be changed allow passage of this light. These considerations are discussed further in Section 3.6.

3.5 Operation

Actually using the LaserVision system is remarkably straightforward, owing to both a well-engineered system and a very detailed manual with a plethora of practical information. Running the system starts with a warm-up period for the pump laser, which must run 30 minutes before the internal shutter will open. Following this, the beam steering is double checked briefly on the irises inside the LaserVision at lower power (both attenuators turned down). On the rare occasion that the beam has drifted, re-aligning the system, thoroughly detailed in the manual, takes no more than an hour - substantially faster than the dye laser. Once the alignment is sufficient, the system is ready to run at full power, with the full range of outputs available through the motor control software.

The ease of use of this system, and low maintenance requirements thus far facilitated integration into cryo-SEVI and allowed for us to optimize a number of aspects of the experiment. Among these are a change in data collection methodology (Section 3.5.1), determining spatial and temporal overlap between the IR beam and the dye light (Section 3.5.2), correctly determining the IR wavelength (Section 3.5.3), and finally, appropriately placing the IR focusing lens to maximize signal (Section 3.5.4.1). Upon overcoming these experimental hurdles, we were able to perform IR-cryo-SEVI (Section 3.5.4) as well as use it as a novel action spectroscopic technique. Further, we have found that the output of this system is sufficient to perform cryo-SEVI in the IR, in place of performing IR-DFG with the dye laser to achieve these wavelengths (Section 3.5.6).

3.5.1 Data Collection

Given that the LaserVision system operates at 10 Hz while the rest of the instrument operates at 20 Hz, some modifications were required to ensure that signal from pre-excited anions was not averaged out. To do so, we opted for collecting shot-on, shot-off data, as is common in pump-probe experiments.

This required modifications to our data acquisition software. As outlined in Section 2.6, this program, NuACQ, processes each photograph taken by the CCD camera in our detector,

detects individual electron events, and calculates the centroids of these events, binning them into either a 1024×1024 or 2200×2200 grid. NuACQ was modified to alternate the bin in which each image is stored, effectively creating two images each collected at 10 Hz. One should then correspond exclusively to transitions from ions that we vibrationally pre-excited, while the other should completely devoid of them. The the full detail of this modification, as well as the development of a new centroiding algorithm and new data acquisition software will be outlined in the forthcoming thesis of Marty DeWitt.

3.5.1.1 10 Hz Operation

Upon modifying this code, we found that only one image was being populated. Further testing, i.e. binning into four images, binning only shots when the IR laser is on or off, and using high photon energies from the detachment laser to generate noise off the chamber walls, indicated that the origin of this was not the software - noise was detected at 20 Hz, but we were detecting ions at 10 Hz.

Further troubleshooting indicated that the ions were arriving at the retractable MCP detector in the VMI region at 10 Hz, and leaving the trap at 10 Hz. The ultimate source of this issue was tracked down to the EL valve driver. While triggered at 20 Hz, the driver has a manual override on the side of the box, limiting the repetition rate at which it drives the valve to the value listed - here 10 Hz. As the switch is recessed into the box and near the back, it is unlikely this had been touched since installation, indicating cryo-SEVI likely had been running at 10 Hz for over a decade.

3.5.1.2 Results

With the machine running at 20 Hz, we were able to collect on/off SEVI spectra. Taking such spectra is ideal, in that fluctuations in laser power and ion signal are common and should be random, meaning that each image should see impacts from these similarly. This allows for a direct comparison between the observed intensities in each spectrum and suggests the reconstruction errors should be comparable in both spectra.

In running, we have found that this is not quite true - we have found that there is consistently more intensity in one image than another, by $\sim 3-5\%$ throughout the day, even when the IR light source is turned off. This is shown in Figure 3.9, where O^- is photodetached far from threshold, as part of the hole-burning experiments described in the following section. Here, 20 Hz detachment signal from the dye laser without presence of IR is binned into two images that are plotted as the red and black traces, showing a $\sim 4\%$ variation in signal levels between the traces.

The source of such a discrepancy is unclear, though it appears for a number of different molecular and atomic systems when both warm and cold, and at various trapping and source conditions. While this does make finding weak signal more challenging, it is not yet limiting to performing IR-cryo-SEVI. The next sections outline circumventing the issue of low signal.

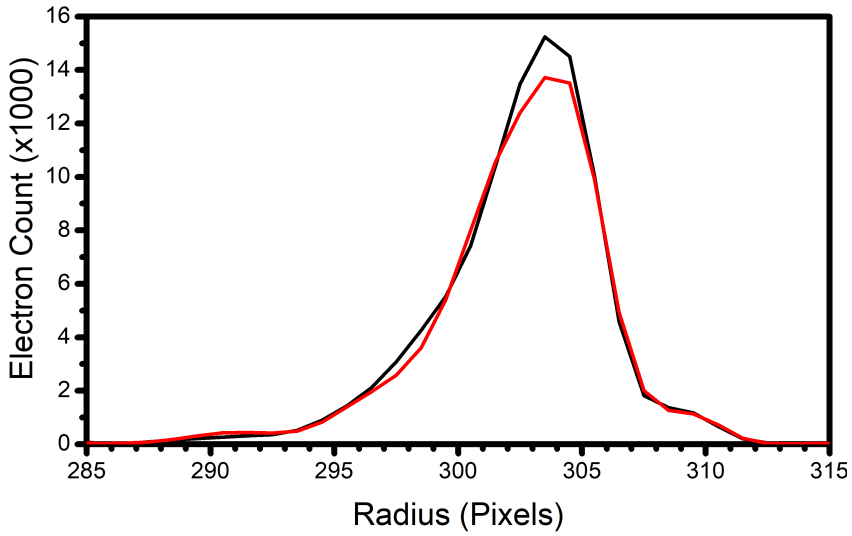

Figure 3.9: Signal variance observed in cryo-SEVI at 10 Hz, for detachment of O^- using the dye laser at 20 Hz, without IR pre-excitation.

3.5.2 Spatial and Temporal Overlap

As indicated in Section 3.3.2, achieving spatial and temporal overlap is crucial for the success of IR-cryo-SEVI - perfectly overlapped beams in space, with a 3 ns delay, result in an order of magnitude drop in observed signal compared to perfect temporal overlap. Misalignment of the beams focal spots by only a millimeter will result in a similar drop in signal, putting strict requirements on the alignment.

In order to satisfy these requirements, alignment of both beams was first performed by centering them on three irises aligned with the light baffles in the VMI chamber. To overlap the beams in time, a fast photodiode was set up on the IR-side of the chamber to measure the arrival time of each beam. As each pulse has a $\sim$ 5 ns fhwm, this temporal overlap is coarse. The relative timing between each laser is determined by the TTL pulse that triggers the LaserVision pump laser is set to a fixed delay off of the TTL pulse that triggers the dye laser pump, ensuring that as the dye laser timing is scanned in search of detachment signal, the LaserVision signal follows.

To test that the LaserVision output was in the correct space and time, the output of the OPO (800 nm) was used to detach O^-, allowing for a finer tuning of the beam to intersect the ion packet. The signal observed from the detachment of O^- was strong, meaning that overlap between the two signals could then be determined through PES hole burning of O^-.

In such a process, both the dye laser (625 nm) and the LaserVision system (800 nm)

are operated simultaneously, both at wavelengths capable of photodetaching O^-. Much like vibrational pre-excitation, if a photon from the OPO is absorbed, this should lead to the appearance of a new feature, here at much lower eKEs, corresponding to a bleach in the dye laser detachment signal. Given the difference in photon energies employed, these features should appear sufficiently separated on the detector as to be easily observed. Such an experiment has the benefit of not requiring the IR photon to be resonant with the transition in question, removing one point of uncertainty.

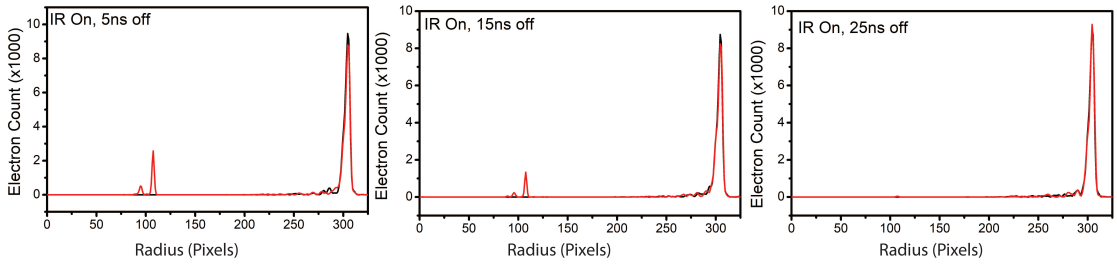

Figure 3.10: O^- hole burning SEVI plots using both the dye laser (625 nm, black trace) and the output of the OPO (800 nm, red trace) at various delay times between these two light sources. Signal from the dye light appears at $\sim$ 300 pixels, while that from the OPO appears at $\sim$ 100.

As shown in Figure 3.10, such a method proved remarkably useful, in that it provided a sensitive probe for optimizing both spatial and temporal overlap. Optimizing the spatial overlap resulted in a depletion of 7.5%, while optimizing the temporal overlap resulted in a substantial increase in signal from the OPO coupled to a depletion in dye-light signal. We found, ultimately, the a delay between the two pulses of about 3 ns on the photodiode was ideal. Such a measured delay corresponds to temporally overlapped beams, as the photodiode sees the LaserVision output before entering the chamber, while it measures the dye light upon exiting. The difference in path length for these two beams is then $\sim$ 1 meter, corresponding to a 3 ns difference in time.

Notably, this methodology works well for optimizing the nIR (and, consequently, the iIR which should be collinear with this output), but *can* fail to align the mIR if the pointing out of the OPA is not aligned with that of the OPO, which can lead to the mIR missing the chamber entirely when the nIR is properly aligned. Filtering for just the mIR with the Si filter and checking the mIR alignment should determine if this is an issue, which can be fixed by tweaking the final 1064 HR mirror prior to the OPA, as is outlined in the LaserVision manual. Fine-tuning the alignment of the mIR should be done with an IR power meter behind each iris.

3.5.3 Calibration

With the spatial and temporal overlap of the system optimized, the remaining component to optimize before performing IR-cryo-SEVI is the photon energies output by the OPO/OPA. As the first step in the experiment is a bound-bound transition, this photon energy must be resonant with such a transition, within the laser bandwidth - here ~ 3 cm^{-1}.

This, however, is complicated by the fact that measuring IR light with high precision is much more challenging than measuring light in the visible. Few commercial wavelength meters are available that can measure from 1-16 μm. The easier solution, as is employed in the Asmis and Wester groups, is to measure the nIR output of the OPO, which is bounded between 710-880 nm and so measurable by the wavelength meters commonly used (in our lab, a Coherent WaveMaster). As this wavelength serves as the seed for the OPA, the output of the OPA can then readily be determined using Equation 3.11, provided the Nd:YAG fundamental is known to sufficient precision.

A simple HTML and JavaScript program was created to calculate the mIR and iIR output given a measured nIR frequency, or to input a desired molecular vibrational frequency (in cm^{-1}) and be given the required nIR output to be measured. This code for this simple program is provided in the Appendix. HTML was chosen for this program to provide for a simple user interface as well as the manual for the LaserVision system is written in HTML, so a browser is often already open.

With these components in place, the last remaining challenge was actually measuring the nIR output of the OPO. This is done by measuring the small amount of nIR that leaks out of the rear mirror of the OPO, which is spatially separated from the 532 nm pump thanks to a 532 HR mirror immediately in front of the rear mirror. This, however, is not easy. The wavemeter probe that was originally used was coupled to a fiber that leads to a grating in the meter. This probe has a low damage threshold (100 mW for internal components, lower for external), which is often surpassed when measuring the dye laser output, leading to significant damage to the probe and an elevated limit of detection for lower power signals.

A new probe was ordered to resolve this issue, and the UV-Vis (OceanOptics USB4000) was used in the meantime. Upon receiving the new probe and testing, it was found that the UV-Vis calibration is off, reading wavelengths that differ by 1-2 nm from the wavemeter. While this is not problematic for use with the dye laser, this is insufficient for our needs. As such, the wavemeter is the only means of measuring the nIR of the OPO.

This leads to the final complication - tuning the output of the OPO such that there is sufficient power to be detected without surpassing the damage threshold of the detector is challenging. At present, this is the limiting factor in using the LaserVision system, with time to measure the output wavelength commonly exceeding that of using the system to take a cryo-SEVI image. A solution to this was suggested by Roland Wester, based on the method his group has developed, but has not yet been implemented. This is discussed in detail in Section 3.6.1.

Finally, the motor controls allow for the selection of the nIR-fIR wavelength, we have found it most helpful to use just the nIR and monitor the output, given this is the value we

are measuring. At the time of this writing, we have found that the reported value by the software is consistently $\sim$ 1.2 nm above the measured value. Additionally, this value can change, especially if a value is overshot and then returned to (i.e. 0.1 nm too red, then use the controls to blue-shift by 0.1 nm), due to motor backlash.

3.5.4 IR-cryo-SEVI

With the wavelength determined as well as the spatial and temporal overlap optimized, IR-cryo-SEVI can be performed on a test system. The requirements for performing such an experiment are knowledge of (or at least a reasonable estimate of) the vibrational frequency in question in the anion and neutral, needed to both excite the species and predict the location of the now-allowed transition. Further, it is beneficial to have an estimate of the rotational constant, B, of the species in question - if this value is comparable to the laser bandwidth, a particular rovibrational level may need to be selected.

Take, for example, the hydroxy radical (OH), chosen as the vibrational frequency, as well as rotational constant, are well studied in both the neutral and anion. Here, the rotational constant is relevant as $B_{anion} \approx B_{neutral} \approx 20$ cm^{-1}, meaning that the spacing between the rotational levels, at low J, is substantially larger than the laser bandwidth. For this reason, selected rovibrational transitions in the anion can be excited.

This task is facilitated by the previous measurement of the rovibrational spectrum of OH^- by Saykally and coworkers in 1986.[304] This spectrum, however, was collected at a rotational temperature near 1000 K, substantially higher than our measured rotational temperature of $\sim$ 25 K. As such, the relative intensities of each transition differ considerably and must be simulated at our rotational temperature. These simulations, shown below in Figure 3.11, indicate that there is meaningful intensity in only three transitions, originating from $J = 0, 1$ levels of the anion, as the majority ($\sim$ 75%) of the anions are at the $J = 0$ level at this temperature.

For this reason, we selected the R(0) transition, $(1, 1) \leftarrow (0, 0)$; (ν, J), in OH^-, which resides at 3591.53 cm^{-1}.[304] From this excited level, the rotational selection rules outlined in Section 1.2.3.1 (see Equation 1.13) allow for detachment to 5 new states, listed below in Table 3.1 when the spin-orbit splitting of the neutral is factored in.[75]

The positions of these features are readily calculated using the known constants of both molecules, allowing for the detachment laser frequency to be selected very near threshold (3.5 cm^{-1} above each feature), facilitated by the good detachment cross section near threshold for this system.

In a general system, where the anion and neutral frequencies may not be known, or known to this precision, a similar treatment can be performed using calculated values for the known (or suspected) geometries. Further, an exploration of which sequence bands have the strongest Franck-Condon overlap is worth considering, as well as where they may reside in the IR-cryo-SEVI spectrum. In the case of OH^-, the 1_1^0 transition is much better spectrally isolated than the 1_1^1 transition, as this it resides $\sim$3600 cm^{-1} below any features in the cold spectrum of OH^-. This feature was not selected for study as the calculated relative intensity

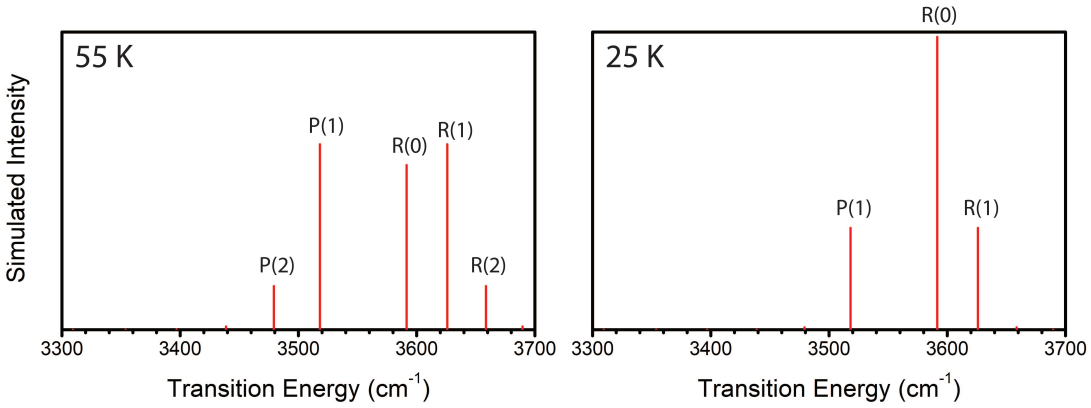

Figure 3.11: Simulations of the rovibrational transitions of OH^- at 55 K (left) and 25 K (right). Both simulations are plotted on the same vertical scale.

Vibrational Transition (v"-v')	Rotational Transition (J"-J')	Ω (OH)	Expected eBE (cm^{-1})
1-1	3/2-1	3/2	14717.93
1-1	5/2-1	3/2	14798.66
1-1	1/2-1	1/2	14844.82
1-1	3/2-1	1/2	14903.5
1-1	5/2-1	1/2	15000.67

Table 3.1: Allowed near-threshold photodetachment transitions for OH^- in the (1,1) (ν, J) state. Vibrational and Rotational transitions are denoted as final-initial state pairs.

is 10^{-4} that of the 0_0^0 transition, while the 1_1^1 is comparable in intensity (i.e. $\sim 10^0$) to the vibrational origin.

With a transition selected, it is also worthwhile to simulate the expected rovibrational spectrum of the molecule in question at a reasonable temperature ($\sim$ 25 K), to select a particular transition in some instances, and generally to determine the number of transitions that may be pumped simultaneously by the IR light.

3.5.4.1 Lens Focal Length

Early efforts at performing IR-cryo-SEVI saw little depletion and commensurate sequence band appearance, if any. The root of this issue was determined to be the position of the CaF_2 lens used to focus the IR light into the detachment region. Moving the lens by $\sim$ 1 cm

was found to increase the weak signal shown in Figure 3.12a into the markedly strong signal in 3.12b, resulting from a near 30% depletion is signal originating from the ground state of OH^-

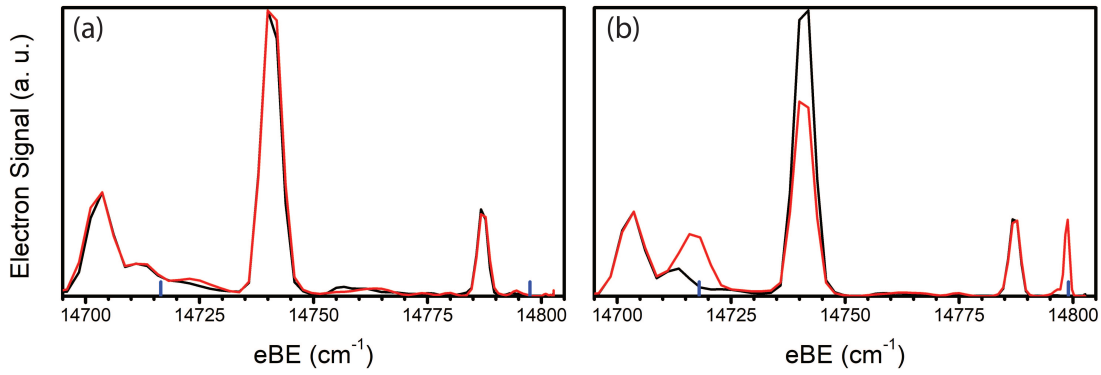

Figure 3.12: Early IR-cryo-SEVI spectra of OH^-. The left trace displays signal before the lens position was optimized, while the right displays signal after. In both plots, red traces are "IR-On" images, black traces are "IR-off" images, and blue sticks are the expected sequence bands originating from vibrationally excited OH^-.

The reason for this shift originates from the change in focal length of the optic as a function of refractive index, which itself depends on the wavelength of light. The focus of a plano-convex lens, as is used here, can be calculated using

$$\frac{1}{f(\lambda)} = \frac{n(\lambda) - 1}{R} \tag{3.15}$$

where R is the curvature radius of the convex surface on the lens and $n(\lambda)$ is the refractive index. The refractive index of CaF_2 ranges from 1.427 at 1.35 μm to 1.3268 at 9 μm.[305–308] For a CaF_2 optic with a nominal focal length of 400 mm, this leads to a change in focus of nearly 30%, i.e ranging from 400mm to 523mm - a change of 12.3 cm. As such, the lens focuses to different positions as the wavelength of the OPA output changes, leading to significantly decreased flux at this region.

Further, it is imperative that the IR spot remain larger than the dye laser spot, as highlighted in Section 3.3.2, and changing focus of the optic leads to variable spot sizes that could further reduce signal.

For this reason, the lens is mounted on a linear translation stage, allowing for its position to be shifted without disrupting the IR beam alignment. While significant changes in the IR frequency will necessitate moving of this optic and the translation stage, working with frequencies in a narrower range should be viable using this model. For example, the focal

length of the lens at $\sim$ 3600 cm^{-1} (OH^- R(0) transition) and $\sim$ 2600 cm^{-1} (the H_2CC ν_5 vibrational transition), differs only by $\sim$2 cm.

Importantly, the lens position should be checked after moving to ensure that the height and left-right position do not alter the beam path. This can be done readily by removing the optic, aligning the beam path, and replacing the optic, moving it as necessary to return the same beam steering.

3.5.5 Action IR Spectroscopy

IR cryo-SEVI can also be used as an infrared spectroscopic technique, capable in principle of determining the vibrational spectra of cryogenically cooled anions. As outlined above, upon becoming resonant with the anion vibrational transition, the IR photon should be absorbed, leading to a depletion in signal from the ground vibrational state of the anion and introducing new features into the PES spectrum. The intensity of this depletion and growth of new features should relate to the quantity of IR light absorbed. Monitoring the changes in intensity of these features as the IR wavelength is scanned can then be used as a means of probing the anion vibrational frequency directly and without the need for a messenger tag, as in the case of IRPD. Such a method is then able to measure true anion frequencies without perturbations from these loosely associated species. Importantly, this is only possible with cryo-SEVI, not conventional anion PES, as such an observation necessitates vibrational state resolution.

In practice, this can be done by leaving the dye laser color fixed, as to avoid changes in detachment cross section, while scanning the OPO/OPA output over the vibrational transition in the anion. The frequency of the vibration in question can then be determined by integrating the intensity of the feature corresponding to the photodetachment transition turned on by vibrational pre-excitation, normalizing this to another feature in the spectrum (to account for fluctuations in ion signal, laser power, and number of experimental cycles), and plotting the normalized intensities as a function of the IR frequency. Fitting this data to a Gaussian distribution then returns a mean, the vibrational frequency, and a standard deviation, the uncertainty in the measurement.

As shown in Figure 6.3 and described in greater detail in Chapter 6, such a measurement allows for the determination of anion vibrational frequencies with an uncertainty comparable to that of other IR-action methods, $\sim$1 cm^{-1}. This corresponds to a fwhm of $\sim$3 cm^{-1} for the fit, matching nicely with the reported linewidth of the LaserVision system's output.

Of course, OH^- is a special case in that the rotational constant is considerably larger than the fwhm of the laser, leading to the pumping of just one rovibrational transition. The majority of the molecules IR-cryo-SEVI will likely study have B values that are comparable to or smaller than the laser bandwidth, meaning that many transitions may be pumped at once, leading to rotational broadening of the measured IR-action spectrum, similar to cryo-SEVI.

Given the reported values for OH^-, when searching for vibrational frequencies in anions without known values, it is possible (and likely beneficial) to step the laser $\sim$1 cm^{-1} at a

time. This step size should ensure sufficient signal to observe a vibrational transition when the photon energy is resonant, while also maximizing the step size, and thus minimizing search time.

In practice, this search remains the most substantial challenge of implementing IR-cryo-SEVI. Looking for unknown vibrational frequencies can be complicated by many of the other factors described in the previous sections, so it becomes challenging to ensure that the lack of signal is due to an incorrect photon energy. This is not ideal as a full photoelectron image must be captured and worked up to determine if the IR photons are resonant with a transition in the anion, resulting in relatively long data acquisition times while searching. As such, this procedure is currently being optimized for reproducibility.

In certain systems for which the ν_1^0 sequence band has appreciable intensity, and ν is IR-active, it may be viable to rapidly search for these transitions by positioning the dye laser below the 0_0^0 transition and monitoring the camera for the appearance of photoelectrons arising from vibrationally excited anions. Such a method has the benefit of allowing for a rapid scan for the IR wavelength until signal is observed, greatly reducing data acquisition times.

3.5.6 IR Photodetachment

The final mode of operation for the LaserVision system is to instead use it as a source of tunable light for photodetachment, rather than pre-excitation. There are a number of interesting systems that have EA's below 0.95 eV, which are inaccessible by the detachment laser configuration without IR-DFG, as is outlined in Section 2.10. While IR-DFG setup allows us to access photon energies down to ~ 0.4 eV, it is often rather tedious to set up and gives low flux at many wavelengths. Further, the non-linearity of the process requires good dye signal, limiting which regions of the dye gain curves are viable for use, further limiting the range of photon energies accessible.

Conversely, using the OPO/OPA is exceptionally straightforward and produces good flux in most of the IR, allowing for its use as the detachment light source for certain systems. This is demonstrated by the ease in which data on CH_3CO was collected, and will be highlighted in the forthcoming paper on this system wherein we used this light source to probe this small radical with great success.

To do so, however, introduces a few new complications. First is calibrating the VMI with an atomic system, as is done with the dye laser. We have found that O^- can readily be detached by the OPO output, which should be collinear to the OPA output (though this should be checked, as the mIR can walkoff from the iIR and nIR) and therefore allows for a straightforward calibration method that mimics what is done for the dye laser.

In calibrating the OPO output, we were reminded that maintaining a vertical polarization is of the utmost importance. This is particularly relevant here as the mIR and iIR polarizations are orthogonal, requiring a re-alignment of the periscope when switching between the two systems. Failure to do so results in images that are broadened significantly, as shown in Figure 3.13 below for the detachment of CH_3CO^-. As outlined in Section 2.7,

this originates from the projection of the Newton spheres of electrons occurring no longer in a plane orthogonal to the detector.

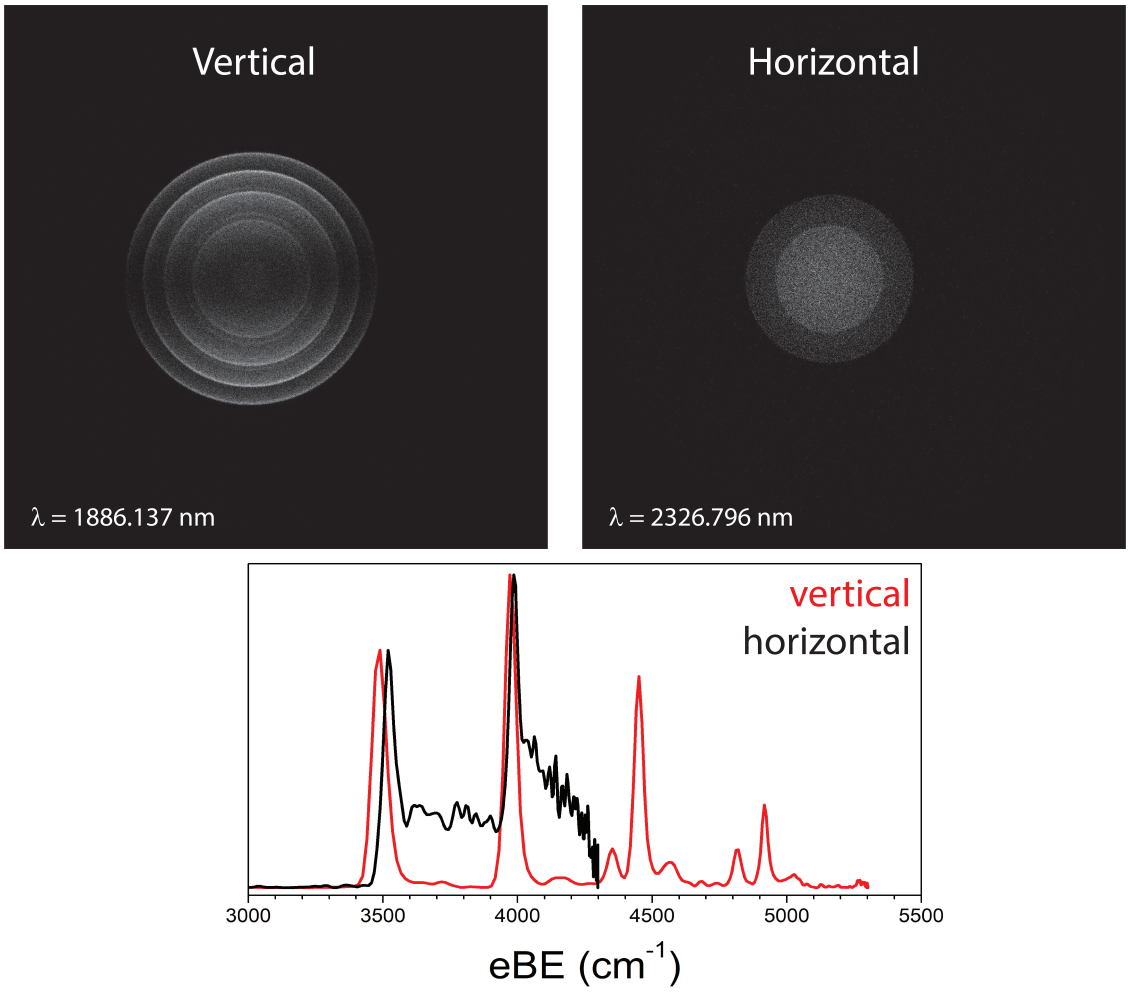

Figure 3.13: SEVI images for the detachment of CH_3CO^- using both vertically and horizontally polarized light atop SEVI spectra of each worked-up image. The slight shift in the peak centers between each image is due to the blurring of images.

Beyond this, it is also important to ensure that the OPA output that is not being used (i.e. iIR or mIR), as well as the OPO output (nIR) is completely filtered out before entering the chamber. Failure to do so may result in multiple detachment transitions being observed simultaneously if the contaminant light has sufficient energy to photodetach the species in question. The stack of Si filters at the end of the LaserVision output leaves some residual light, and requires the use of a longpass, shortpass, or notch filter. These are rather limiting,

unfortunately, as their damage thresholds are low, greatly restricting the output power. The use of a dichroic mirror may help, as these tend to have higher damage thresholds, though one would likely need to be custom made, as few are commercially available for the wavelengths currently employed.

In detaching CH_3CO, it was found that the iIR still leaks through while trying to use the mIR only, requiring the use of these filters, while the mIR output (while the iIR is near threshold) was at sufficiently low photon energies as to not detach CH_3CO. This allowed for external filters to be avoided while using the iIR, greatly speeding up data acquisition time compared to the mIR, where the LaserVision power was attenuated significantly to avoid damaging an external filter. While this was found to reduce data acquisition rates, it did not prevent data collection.

3.6 Future Considerations

IR-cryo-SEVI remains a fledgling methodology - while we have proven it to be viable, there are a few quality of life improvements to be made to facilitate its continued success. Further, a few components have yet to be explored, and there are a considerable number of systems that would be of interest to study with this method.

3.6.1 On-line OPO Measurements

Paramount among the quality of life improvements is determining a facile way to measure the output wavelength of the OPO. Such an improvement would greatly improve the ability to use this system for IR-cryo-SEVI, IR-action, and cryo-SEVI using this source as the detachment laser.

The Wester group was kind enough to share details of how they monitor their wavelength as it scans in real time. They do this by taking part of the near-IR beam that leaks out of the resonator and reflected by the pump input mirror. This beam is then reflected towards a fiber coupler at the opposite corner of the laser box. A 5 cm tube suppresses stray light on the fiber input. In addition there is a longpass filter (Thorlabs FEL0550) to suppress 532 nm light on the fiber input.

Such an setup should be relatively simple to implement, and many of the components to do so have been ordered. The current wavemeter, however, does not directly log its outputs. Additionally, the WaveMaser operates using a grating, rather than an interferometer, leading to inconsistent measurements requiring longer than the duration of an experiment to acquire. For this reason, a WS5 wave meter from HighFinesse, capable of measuring wavelengths more accurately and easily, per recommendations from the Asmsis and Wester groups, is being acquired. Integration of this wavelength meter into the experiment, which can read out measurements in real time, should allow for automation of IR-cryo-SEVI, greatly reducing data acquisition times.

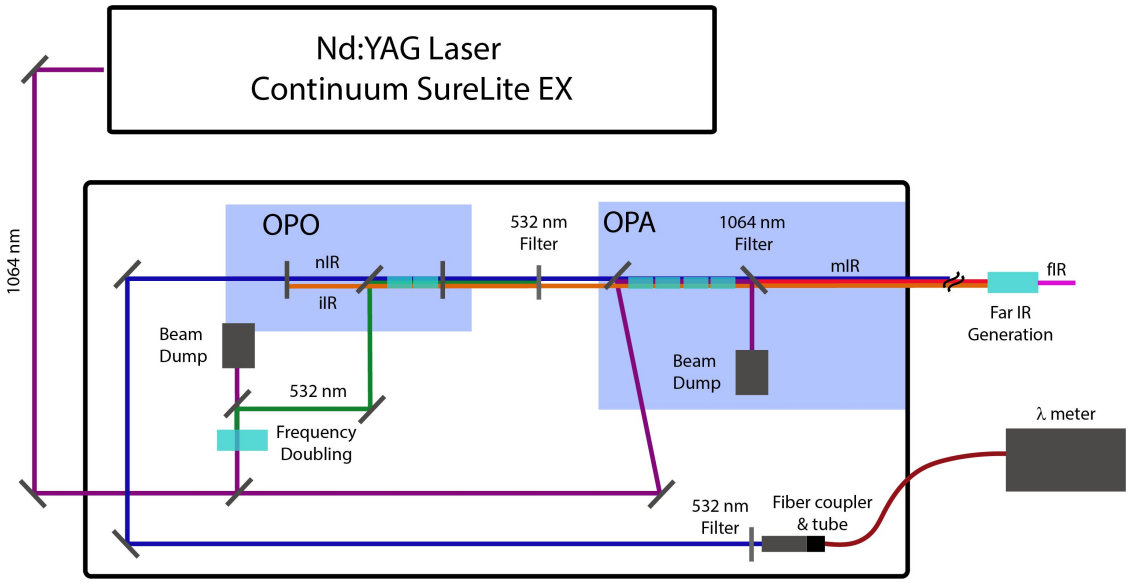

Figure 3.14: Diagram of LaserVision system with on-line monitoring setup from the Wester group; the OPO output that leaks out the back is redirected and filtered to be measured continuously.

3.6.2 Using the fIR

Another consideration for future use is the far-IR, as this has yet to be employed. While the motorized stage for the crystal was aligned when the system was installed, the beam pointing has been moved considerably, likely requiring this to be re-optimized.

Further, depending on the wavelength employed, the window(s) into the machine will need to be changed to allow for passage of this light. The current windows are CaF_2, which transmits light from 0.2-8 μm. This is ideal for many uses in IR-cryo-SEVI, but if the fIR pushes beyond this limit, another material will need to be employed, namely ZnSe, which transmits light out to 16 μm. For this reason, two ZnSe windows were purchased for use with the fIR.

As the refractive index of this material is considerably different from CaF_2, the Brewster Angle θ_B, defined as

$$\theta_B = \arctan \frac{n_2}{n_1} \tag{3.16}$$

where $n_{1,2}$ are the refractive indices of the medium of the incoming beam and the other medium, respectively. Here, these are that of air ($n_1 \approx 1$) and that of the window ($n_2 \approx 1.4$ for CaF_2 and $n_2 \approx 2.4$ for ZnSe). Given the difference in refractive indices of CaF_2 and ZnSe, the Brewster angles are $\sim 55^o$ and $\sim 67^o$, respectively requiring that these windows be mounted on different Brewster tubes to maximize transmission. New tubes for the ZnSe

windows have been machined at this angle and are mounted onto CF25 (2.125") to allow them to be interchanged with the CaF_2 Brewster tubes readily.

The final complication is that materials with good transmission in the fIR rarely have good transmission of the visible, meaning that there may be complications with the dye light if both windows are changed to be ZnSe. In such a case, the window might block a large amount of dye light, complicating the observation of signal, and possibly resulting in burning of the window or heating that could lead to cracking.

One possible solution is to use a CaF_2 window on the dye-light port and a ZnSe window on the fIR side, allowing for maximum transmission into the chamber, though concerns of burning or damaging these windows still persist.

3.6.3 Systems of Interest

There are a number of systems for which IR-cryo-SEVI could provide insight into and span the basis of systems we often study with cryo-SEVI, including metal oxide clusters, small radicals, and transition states. Below are a few selected systems that would be of interest to study using this method, though there are considerably more viable systems.

3.6.3.1 Vinylidene

This chapter began with motivation for the development of IR-cryo-SEVI, for which H_2CC was an example system. This species was the primary motivator for the development of this technique, as it should be viable to pump the ν_1, ν_5, and ν_6 vibrations in the anion, allowing for probing of the isomerization dynamics of this small molecule. Previous work from the Johnson group has probed the anion vibrational frequencies, showing that the ν_1 and ν_5 frequencies reside around 2600 cm^{-1} and have good IR absorption cross sections.[296] Notably, the ν_1 mode is totally symmetric and does not couple to the HCCH manifold of states (i.e. is not a normal coordinate coupled to isomerization), while the ν_5 anti-symmetric stretch does couple to these states. A comparison of the IR-cryo-SEVI spectra of H_2CC^- with each of these modes vibrationally excited should allow for signals of isomerization to be determined directly. Similarly, the ν_6 in-plane bending mode is an isomerization normal coordinate, again allowing for the probing of the isomerization dynamics and their vibrational mode dependencies. This mode, however, has an IR cross section that is much lower ($\sim 0.2\times$ that of the $\nu_{1,5}$ modes) and has not been measured, but calculated to reside near 850 cm^{-1}, requiring the use of the fIR.[40,295]

3.6.3.2 Reactions of the Hydroxyl radical

In a similar vein to the vinylidene experiments, probing of bimolecular transition states involving OH are of particular interest given the ubiquity of water as well as atmospheric considerations. In both the OH^- + OH and OH^- + H_2 reactions, there exist a double-well potential in the anionic reaction surface, each of which have relatively low barriers.[309–311] In

such cases, exciting the vibrational modes in the reaction intermediates formed should allow for the surmounting of this transition state barrier in the anionic surface, allowing for the formation of different species and probing of different regions of the neutral reactive surfaces. This is shown below in Figure 3.15.

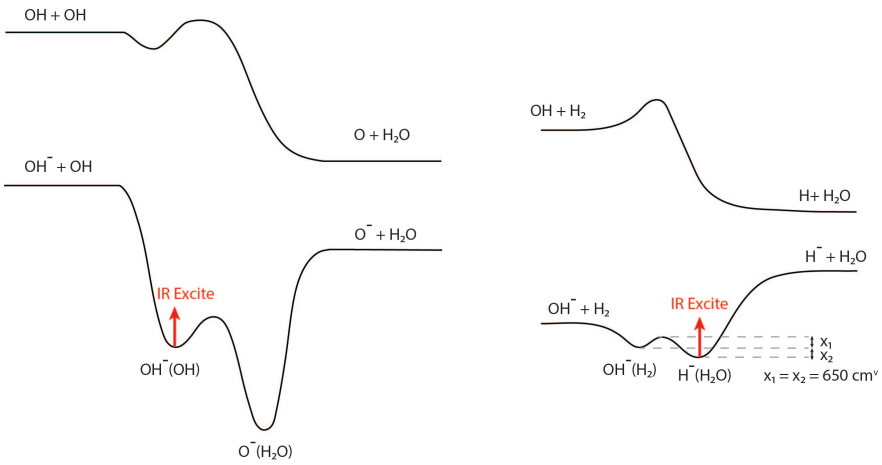

Figure 3.15: Reaction pathways for OH^- with OH (left) and H_2 (right). Both anion surfaces have double-wells that may be surmounted by vibrationally pre-excited anions, allowing for probing of different regions of the neutral reaction surface.

Further, recent theoretical work suggests that the O-O stretching motion plays a crucial role in the the transition-state dynamics, indicating that vibrational pre-excitation could elucidate this mechanism.

3.6.3.3 The Nitrate Radical

In our studies of the nitrate radical (NO_3, see Chapter 5), a central question was the role of vibronic coupling between the $\tilde{B}$ electronic state of NO_3 and the ν_3 vibrational mode, which resides within 10 cm^{-1} of the ν_1 mode. Given the poor near-threshold behavior of FC-allowed features, observing the splitting between these two features was not possible. One solution to this, however, is the excitation of the ν_3 mode in the anion, as this should have a good IR cross section and considerably higher vibrational frequency, allowing for the observation of the 3_1^1 transition below the vibrational origin. This would allow for the determination of the neutral vibrational frequency (as the position of this feature must correspond to the difference in frequency between the anion and neutral molecules, with the anion frequency being measured by IR-cryo-SEVI).

3.6.3.4 Metal Oxide Clusters

A number of small metal oxides have previously been studied by cryo-SEVI.[55,61,64,103] Among these, there are good candidates for IR-cryo-SEVI owing to their good IR cross sections at frequencies easily accessed by our IR light source. These include $Al_2O_2^-$, $Al_3O_3^-$, Fe_3O^-, and $Zr_2O_4^-$. In these systems, determining the vibrational frequencies of the anions, as well as the effect of pre-excitation on the photodetachment spectra, could prove useful for future studies and understanding the catalytic abilities of these species and for distinguishing between isomers.

Further, given the high density of states in these species, it is possible that intramolecular vibrational energy relaxation (IVR) may occur. In such circumstance, vibrational modes other than those initially populated by vibrational pre-excitation may be populated on a timescale competitive with photodetachment, resulting in the appearance of a number of new features commensurate with the depletion of FC-allowed features originating from vibrationally cold anions. Mapping out the coupling between these modes, as well as the timescales for this process, is of fundamental interest.

3.7 Table of Components

Below is a list of all components purchased while developing IR-cryo-SEVI, including vendor and part number. Note that not all optics purchased are in use, but nearly every other component is on the table.

Note that the two aluminum breadboards listed under the "Optics" section are mounted onto the Unistrut stand holding up the detector chamber, and are used to mount optics near the port, including a gold mirror, the CaF_2 lens that focuses the IR, as well as the motorized crystal mount for generation of fIR light.

Item	**Vendor**	**Part Number**
Laser Components		
SureLite EX Nd:YAG	Amplitude	RVF # 161150
FL611-06 FLASHLAMP	Amplitude	203-001900
Optical Table, 0.9 x 1.8 m, M6 Threads	Newport	M-RPR-36-8
OPO/OPA system with far-IR extension	LaserVision	Custom
Optics		
1" mIR Enhanced Gold Mirror	Thorlabs	PF10-03-M02
1" CaF_2 lens	Thorlabs	La5370
VIS/IR Detector Card, 400 - 640 nm, 800 - 1700 nm	Thorlabs	VRC2
1" IR Bandpass Filter, 1.75 µm, FWHM = 500 nm	Thorlabs	FB1750-500
1" IR Bandpass Filter, 2.50 µm, FWHM = 500 nm	Thorlabs	FB2500-500
1" IR Bandpass Filter, 2.00 µm, FWHM = 500 nm	Thorlabs	FB2000-500
Aluminum Breadboard 8" x 8" x 1/2", 1/4"-20 Taps	Thorlabs	mb8
Aluminum Breadboard 4" x 6" x 1/2", 1/4"-20 Taps	Thorlabs	MB4
Magnetic Laser Safety Screen, 300 mm x 75 mm	Thorlabs	TPSM2/M
Lens Mount for 18 mm Optics, 8-32 Tap	Thorlabs	LMR18
2.40μm, 25mm, Infrared Longpass Filter	Edmund Optics	68-653
Periscope		
Rotating Beam Steering Assembly, Imperial	Thorlabs	Rs99B
Tip/Tilt Rotation Beam Steering Assembly, Metric	Thorlabs	RS99T
1.25" Studded Pedestal Base Adapter, 1/4"-20 Thread	Thorlabs	BE1
1" Pillar Post, 1/4"-20 Taps, L = 12"	Thorlabs	RS12
1" Pillar Post, 1/4"-20 Taps, L = 3", 8-32 Adapter Included	Thorlabs	RS3
Laser Enclosure		
Blackcore Foam Board	Blick Art	13202-2006
Table-Guard Connector	Kentek	PT-TGC1
Table-Guard Panels 36"x12"	Kentek	PT-TG36
Table-Guard Panels 6"x12"	Kentek	PT-TG6
Table-Guard Panels 12"x12"	Kentek	PT-TG12
Lens Tube Cover, 24" Long	Thorlabs	SC2L24
2 in. PVC Coupling	Home Depot	232750
Brewster Tubes		
304ss Tube, 0.12" Wall, 3/4" OD	McMaster-Carr	89495K195
DN25CF Mini ConFlat Flange, Non-Rotatable, 304ss	MDC Vacuum	110006
50mm x 5mm, 8-12μm Coated, ZnSe Window	Edmund Optics	39-438
Temperature and Humidity Probe		
Temperature and Humidity Data Recorder	McMaster-Carr	3272K57
Software/USB Cord for Temperature and Humidity Probe	McMaster-Carr	3053K91
Active USB 2.0 Extension Cable	Digikey	TL1877-ND

Chapter 4

Dual-trap SEVI

4.1 Introduction

As mentioned in Section 1.5.3, the studies of molecular clusters, produced *via* laser ablation have elucidated the limits of cryo-SEVI. The clusters enter our trap with considerable internal energy, owing to the heating of these clusters during condensation, wherein the bond enthalpy is deposited into the cluster upon forming a new bond.[43] This process limits cryo-SEVI in two major ways: first, larger clusters enter the trap with much more internal energy than smaller clusters. Second, if we are interested in probing cluster reaction pathways, the only option currently is to introduce reactant gases at the end of the cluster source, where the clusters are remarkably hot, causing reactions to proceed to completion and leaving us blind to any stable intermediates that might be formed.

The first scenario presents a problem as it limits the size of clusters viable for study using cryo-SEVI. The large internal energy, coupled with the increase in low-frequency modes as cluster grow, leads to spectra with few, if any, vibrationally-resolved transitions. Removing this excess energy is complicated by the population of low-frequency modes here - buffer gas cooling works exceptionally well in terms of translational and rotational cooling, but in the absence of a vibrational mode of comparable frequency, can struggle with vibrational cooling. The relative timescales for cooling, shown in seconds, are presented in Figure 4.1

Importantly, vibration-to-vibration cooling occurs on a similar timescale as translation-to-rotation cooling where rotationally hot anions transfer their energy into the translational degrees of freedom of the cold buffer gas. Unfortunately, translation-to-vibration cooling is four orders of magnitude slower, given the larger spacing of the energy levels associated with molecular vibration.[312]

For this reason, we add H_2 to our cryo-trap, to introduce a species with both rotational and vibrational modes that might couple to the hot species of interest. This has worked exceptionally well for small clusters and free radicals, who often have vibrational frequencies not dissimilar to that of the H_2 (4342 cm^{-1}). Coupling of such a high-frequency mode to the very low-frequency modes often populated in larger clusters, however, is inefficient, and

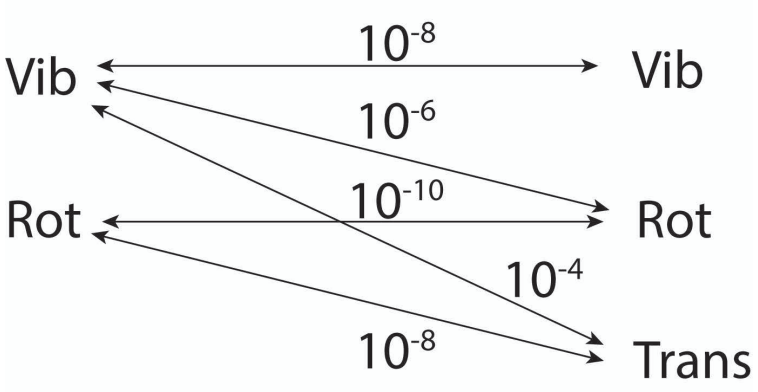

Figure 4.1: Schematic of the energy transfer process that occurs in thermal molecular collisions, where the typical relaxation times, in seconds, characterizing the particular mode of energy transfer for a gas at atmospheric pressure.

leads to vibrationally-hot clusters leaving our ion trap.

Further, the cryogenic temperatures of our ion trap, ~ 4 K, prevent the addition of other species that might remove energy more efficiently, as these temperatures are well below the freezing point of heavier noble gases and molecules - even the H_2 we add to the trap currently freezes onto the walls of the trap during operation. Running the trap at hotter temperatures and populating it with heavier gases, as is shown below in Figure 4.2, results in comparable cooling of these large clusters, suggesting that some vibrational cooling occurs at such temperatures.

While this limitation applies to larger clusters, the other limitation applies to reactions of small clusters. There is a growing body of work showing that a variety of small clusters are reactive to common gases and may provide insight into the reaction mechanism of catalysis.[213] Many of these studies are performed using mass spectrometry, allowing for determination of complexation and/or reactions occurring, but without the ability to probe the structures involved. This gap in knowledge is something cryo-SEVI is uniquely suited to study, if these clusters can be prepared.

Modifications to our ablation source, outlined in Chapter 3 of Jessalyn DeVine's thesis,[232] allow for the introduction of a reactant gas shortly after cluster formation and prior to expansion into vacuum. While this advancement enabled the to study the reactions of Group IV metal oxides with water[65,66] (see Chapter 11), the observed species were the products of the reaction, owing, in part, to the high initial energies of the reactants. The theoretical reaction pathway for these clusters are presented below in Figure 4.3, which show that these reactions are exothermic with only a buried barrier.

If we are generally interested in probing the reaction surface, especially those that are endothermic, it is imperative to be able to generate anions at various points along this surface, requiring that they do not immediately proceed to completion prior to photodetachment due

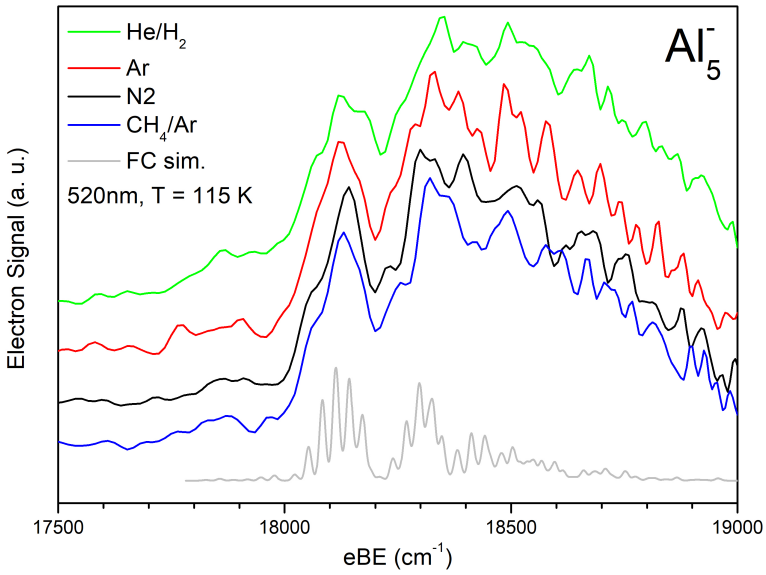

Figure 4.2: SEVI spectra of Al_5^-, taken at a trap temperature of 115 K with various buffer gas mixtures used, as well as a Franck-Condon simulation at 115 K.

to the surplus of thermal energy they possess.

In order to resolve both of these issues, we took inspiration from the Garand group, who recently developed a dual-trap IRPD instrument in their group.[314] Such an instrument uses similar RF multipole traps to those employed by SEVI, with the first cooled with a liquid nitrogen (LN2) cryostat instead of a closed-cycle helium refrigerator, as we use. Their second trap is very similar to ours, as it operates at ∼4 K. The introduction of the first trap serves to cool their ions, allowing for solvent molecules to condense onto the ions they produce *via* electrospray, before bringing them to a second cryo-trap, allowing for D_2 tagging and further cooling.

Following this idea, we have decided to implement a second cryo-trap into the instrument, in what we are tentatively calling cryo-cryo-SEVI. Our intent with such a design to is to use the first trap to "pre-cool" our ions before entering the existing trap. The higher trap temperatures in the pre-cooling trap should allow for the introduction of heavier trap gasses with higher freezing-points, such as Ar or CH_4, that should better remove energy from larger clusters. Further, the variable temperature of this trap should allow for the addition of a reactant gas to cooled clusters at various internal energies, allowing for more precise control over the region of the reactive surface the anions reside in.

One important note is that the spectra of larger clusters may be complicated by the formation of more than one isomer. Given the substantial internal energies of these larger

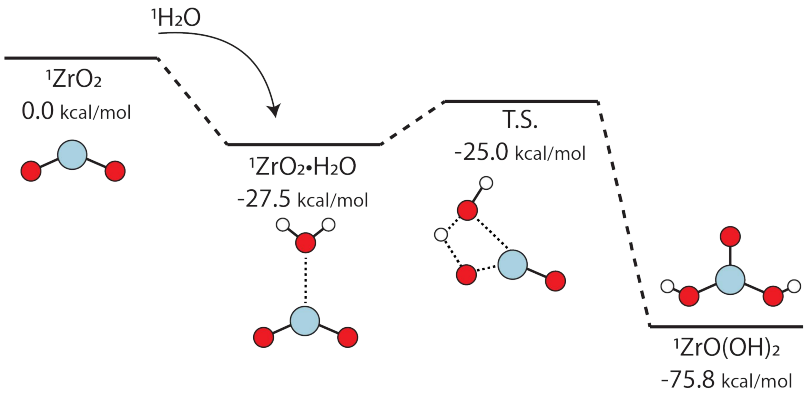

Figure 4.3: Theoretical reaction pathway of ZrO_2 with H_2O, on the singlet surface, as calculated by Dixon and coworkers.[313] The reaction pathway shows a buried transition state separating a reaction intermediate and final product state.

clusters, a number of different isomers are likely energetically accessible, which would then be frozen into the cold population *via* the kinetic trapping within the ion trap. The observation of multiple isomers in our spectra for a number of species produced *via* laser ablation, including Ti_2O_4 and Zr_2O_4,[60] silicon carbides (Chapter 8), $ZrO(OH)_2$ (Chapter 11), and even in other sources, such as the $NiAl_xO_y$ species in Chapter 10, suggests this is possible. Resolving this issue may require the addition of an ion-mobility spectrometer (IMS) or similar device to cryo-SEVI in the future.

4.2 Design Considerations

Adding a second trap, in principle, is much simpler than adding the first. Given the success of the first trap, both in its operation and simplicity of use, we have decided to duplicate the design as much as possible. This means that many of the machine drawings for the initial trap should be re-usable without significant modifications, save for changing the coupling piece atop the trap to fit the LN2 cryostat, rather than the cold-head on the He compressor. The modular design of the trap, wherein the box is constructed of six copper pieces screwed together, rather than milled out of a solid piece of copper, should allow for further modifications to be made as needed, such as the addition of a second general valve for introduction of reactant gases after some delay time, allowing for the ions to cool for a specified amount of time prior to reacting.

That being said, the incorporation of such a second trap into the instrument does require a few considerations. These are detailed in the following subsections.

4.2.1 Chamber Layout

The first consideration when adding components into the machine is the chamber design and layout. Ideally, only the ideal layout would be considered, but in the actual lab, space restraints are a concern. Fire code requires a 3 foot-wide walkway throughout the lab, in our case between all cambers and supports and the wall. For this reason, early designs of the build included a quadrupole bender, snaking the machine into an "S" shape (see Figure 4.4 below).

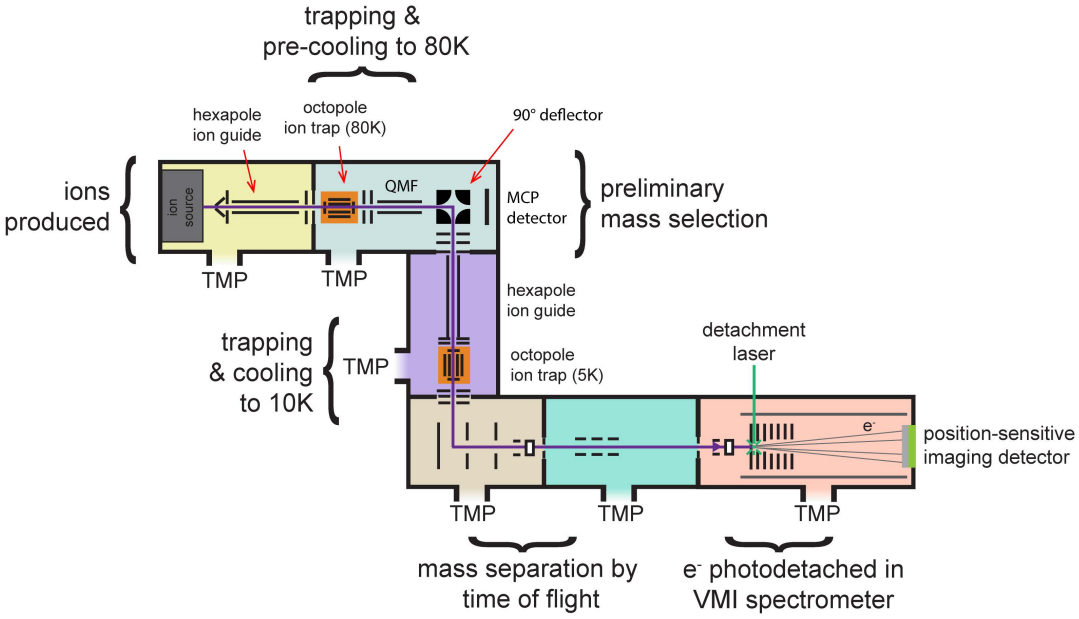

Figure 4.4: Original design of dual-trap SEVI

Such a design has the benefit of extending the chambers easily to add an IMS into the machine. It did, however, violate fire code in that the chamber would be too close to the door, requiring alterations to the lab and former SEVI office (D22 and D23, respectively). For this reason, the wall between the lab and former office was knocked down, to create a way into D22 by using the door of D23, thereby circumventing the issues with fire code. Such a move also requires moving of the small electrical rack that houses the multipole boxes. Both the wall and rack moving processes were stalled by the SARS-CoV-2 pandemic of 2020.

In the meantime, the design was re-evaluated, and the additional complications of adding a bender, as well as the associated cost and complication in daily-use, ultimately lead to a design without the bender, instead extending the "L" of SEVI counter-propagating to the ion path, as shown in Figure 4.5 below.

This new design benefits from the simplicity of keeping the ion path relatively unchanged from the original cryo-SEVI design, greatly simplifying the required electronics, and presum-

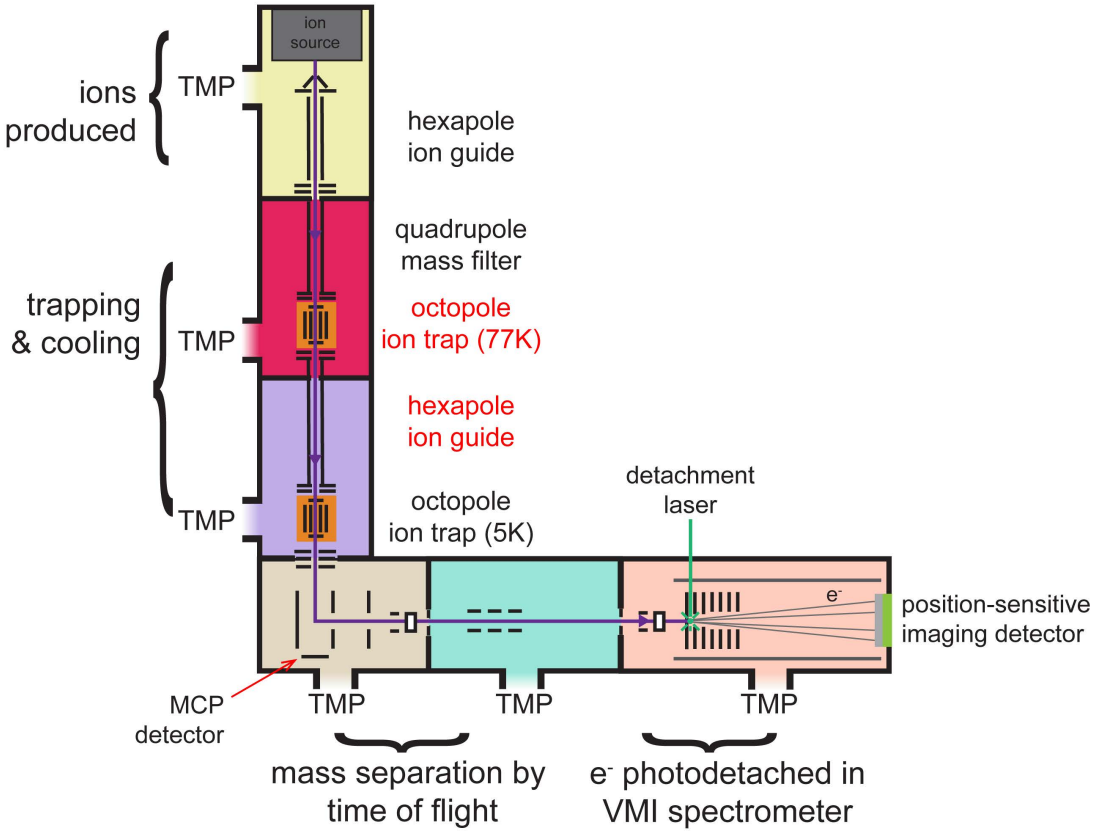

Figure 4.5: Current design of dual-trap SEVI, with new ion optics highlighted in red text.

ably the daily operation of the machine. In this design, the ions essentially pass through the same optics - a skimmer, apertures, hexapole, apertures, quadrupole, apertures, octupole trap - though the trap they enter is now the pre-cooling trap. This is achieved by leaving these optics, which are all mounted on the same flange, untouched, only translating them to provide space for the new LN2-cooled trap. Following the pre-cooling trap, an ion guide will be installed to guide ions from one trap to another (see Section 4.2.4 below).

Further, the source chamber is mounted to its stand *via* well-aligned ball-bearings, allowing for it be moved along the ion propagation direction without altering the alignment of the ion optics, as determined upon servicing the cryo-trap (see the Appendix). Extending the chamber to the edge of this mounting retains sufficient space as to not violate fire code while providing sufficient space (∼2 feet) for the addition of a CF200 (10 inch ConFlat, 15" in length) 6-way cross as well as short adapter chambers to the source and He-trapping chambers, which are both O-ring seals.

The choice of a 6-way cross was made as 1. this would provide sufficient space in vacuum for the pre-cooling trap and associated electronics, 2. the commercial availability of such a

chamber, 3. the ease of mounting a new turbo-molecular pump to this chamber. The six ports will be connected to the source and He-trapping chambers (front & back, along the ion path), the LN2 cryostat and turbo pump (top & bottom), and electronic feedthroughs and viewing window (left & right). Such a layout was chosen as the LN2 cryostat must be refilled with LN2, requiring that it sits vertically upright on the chamber. Similarly, the turbo must be mounted vertically, necessitating its mounting on the bottom of the chamber. Feedthroughs were elected to be placed on the side-flange to avoid spilling LN2 onto them when filling the cryostat, thereby damaging the components or welds, leading to vacuum leaks. Finally, a viewport is advantageous in the event of servicing the trap.

As of this writing, the alterations to the wall and lab layout are still pending, though the wall will be removed to give additional lab space, much needed after the addition of the IR laser table.

4.2.2 Pumping

While the construction of the trap remains largely unchanged (see Section 4.3), its use will be considerably different, given the higher temperatures, different gases used and second gas source. Together, these components result in considerably higher gas loads on the pump, and need some consideration.

First, the conductance out of the trap must be considered. This however, is predicated on the gas-load delivered into the trap. This can be calculated by using the conductance out of the trap-gas valve using the following:[315]

$$C = \frac{D^4 P}{L\eta} \tag{4.1}$$

where D is the diameter of the tubing, P is the pressure backing the valve, L is the length of the tube, and η is the viscosity of the gas. Given that the design remains unchanged, and only the identity of the gas varies here, η is the only parameter changing. At 273 C, $\eta_{He} = 1.87$ mPa·s, while $\eta_{Ar} = .021$ mPa·s, though at colder temperatures they approach one another - at 100 K, $\eta_{He} = 9.6$ μPa·s, while $\eta_{Ar} = 7.1$ μPa·s.[316] Therefore, at the operational temperatures of both traps, it is safe to assume that similar valve timings should deliver similar gas loads into the trap. The conductance out of the trap is then determined by[315]

$$C = A\sqrt{\frac{kT}{2\pi m_0}} \tag{4.2}$$

where T is the trap temperature, k is Boltzmann's constant, A is the area of the orifice (here a circle 0.4 cm in diameter, and doubled to account for the entrance and exit apertures), and m_0 is the mass of the gas. From this equation, it is clear that changing only the trap temperature and gas identity should only alter T and m_0. Methane is 4 times as heavy as helium, and argon 10 times as heavy, meaning that they should conduct out of the trap at $\sim 50\%$ and $\sim 30\%$ the rate of He, at the same temperature. Elevating the temperature to

that of LN2 (77 K), however counteracts this - with the conductance for Ar and CH_4 at this temperature comparable and twice that of He at 5 K. Heating the pre-cooling trap to 300 K doubles these conductance rates yet again, resulting in total gas-loads up to 4 times that of what the turbo in the He-trap experiences.

All things equal, this would result in a 4-fold increase in the pressure of the pre-cooling trap chamber compared to the He-trapping chamber, resulting in operational pressure $\sim 1 \times 10^{-5}$ Torr. Such a value would be fine - the source chamber operates at pressures between 2-10 times this value, depending on the situation. This, however, assumes that pumping He and Ar are comparable. They are not.

The steady state mass throughput of many turbo pumps is limited by thermal considerations. With Ar being a thermally insulating gas, this severely limits the amount that can be pumped without overheating the pump. This is made worse for magnetically levitated turbos, such as the ones we commonly use, as there is no contact between the rotor and pump body when operating, so high argon loads can overheat the rotor beyond $\sim$ 120 C, at which point most rotor alloys become slightly elastic, allowing them to surpass the tolerance and crashing the pump.

Fortunately for us, this problem is common in the semiconductor industry, and therefore commercial solutions are available. Many turbo pump manufacturers, including Shimadzu, Pfeiffer, Leybold, and others, have turbos specifically engineered to handle high Ar gas loads. The throughput of these pumps (7.5-20 Torr·L/s) greatly surpasses the gas-loads we anticipate out of the trap ($\sim$ 10 L/s of Ar at 10^{-3} Torr) by a factor of 10^3, despite their slightly lower listed pumping speeds ($\sim$1400 L/s).

4.2.3 Ion Trap Design Modifications

While the design of the original cryo-trap works exceptionally well, there are some small modifications to be made for the pre-cooling trap. First among these is the removal of the shield on the trap, which is installed to reduce thermal heating of the trap. This is necessary for the He-trap as the He refridgerator has two stages - one at 43 K, with a cooling power of 50 W, and a second at 4.2 K with a cooling power of 1 W. Given that the radiative heating in the chamber is $>$ 1 W at 4.2 K, a cold shield is needed to reduce this value below that of the cold-head. The pre-cooling trap does not suffer from this issue - by the Stefan-Boltzmann law, the power radiated per area, P/A is given by:

$$\frac{P}{A} = \sigma T^4 \tag{4.3}$$

where T is the temperature and σ is the Stefan-Boltzman constant. Assuming a perfect black body, $\sigma = 5.67 \times 10^{-}8$ W m^{-2}K^{-4}. Generalizing to the case of emission and absorption between an object and its surroundings at different temperatures, with the power radiated from an object given by

$$P = A\sigma(T^4 - T_s^4) \tag{4.4}$$

where T_s is the temperature of the surroundings. When $T < T_s$, as is the case here, this results in absorption of thermal radiation. Assuming the surface area of the trap, A, is ~ 0.02 m^2, results in absorption of ~ 10 W of thermal energy when held at 77 K and the surroundings are at 300 K. The cooling power of the LN2 cryostat for this design is well over 50 W at 77 K, meaning that shielding is unnecessary.

Removing such shielding, while not completely necessary, does improve quality of life. On the current He-trap, heating the trap itself is rather quick, taking ~ 30 minutes, thanks to the cartridge heater attached to it. The shield, however, does not have a direct heat source, resulting in it warming through the radiative heating process described above, taking on the order of 4 hours to surpass 0 C, and allowing the chamber to be vented without concerns of ice forming on or in the trap. Given that the LN2 cryostat is a single-stage chiller, as compared to the two-stage He cold head, heating times should be much quicker for the LN2 trap.

The other modification to the trap is the addition of a second gas source, allowing for the addition of a reactant gas at variable times, effectively allowing for the selective addition of this gas at different ion temperatures. Such a modification should readily be made to the trap following initial testing, given that the side of the trap can readily be removed and machined, or an alternate siding can be machined.

Here, as is the case in the He-trap, buffer (and reactant gas) will be introduced by a Parker pulsed valve, which is mounted onto the trap chamber walls. The valve itself is designed with gas-tight seals made with elastomer o-rings, meaning that it must remain above ~ 270 K before the o-rings freeze and the valve leaks. To avoid such an issue, the valve is to be mounted to the trap wall using a thermally insulated spacer, comprised of Vespel (the He-trap uses a piece 1, 1/3" OD, 1/4" ID, 1" long). Addition of a second valve should only require boring out another small aperture for gas introduction, as well as some tapped holes for screws to bolt-down the (threaded) plastic spacer.

The remainder of the original trap design is to remain unchanged, and is outlined in Section 4.3.1 below.

4.2.4 Ion Steering and Detection

While the first segment of the ion trajectory is left essentially unchanged, steering out of the pre-cooling trap into the He-trap requires the installation of an ion guide and focusing optics to maximize transmission. Here, we again took inspiration from the Garand group, deciding to place an RF hexapole ion guide between the two traps - this is not dissimilar from the current machine design, which mates a quadrupole to the ion trap. The RF voltage applied here will be supplied by a commercial voltage supply and high-Q head, from Ardara (see Section 4.3.2 below). The RF voltage supplied depends, in part, on the capacitance of the hexapole rods - which at present is assumed to be the same as the current hexapole, though this likely will need to be modified, given the different lengths of the two optics.

As in the current cryo-SEVI setup, apertures will be placed on both ends of the ion guide, to help focus the ions into the guide - given that the potential of the hexapole results in a

tighter spatial focus than the octupole traps, this should improve loading into the guide, as well as mitigate stray RF fields. Further, minimizing the field-free (or low-field) distance the ions experience between the optics helps improve transmission as well. For this reason, the end of the newly-installed ion guide will be placed ~ 0.1" from the entrance of the He-trap, mirroring the distance between ap5 and the trap entrance aperture in cryo-SEVI.

The location of the hexapole entrance, relative to the pre-cooling trap, is slightly more complicated. In the current cryo-SEVI design, there is an MCP (the "trap detector") along the ion path following the He-trap, used to determine if ions are being trapped and troubleshooting. This has been immensely helpful, and so the dual-trap design also involves the introduction of a pre-cooling trap detector for similar reasons. Unlike the case of cryo-SEVI, however, this MCP cannot remain stationary, as the ions continue along orthogonal to the surface of this detector into the He-trap. For this reason, a retractable MCP, much like the one used in the VMI-region of the instrument is to be installed.

The location of this MCP along the ion flight path is, thankfully, not dictated by the ions themselves. On the trap detector for the He-trap, signal from free ions striking the MCP appears ~ 100 μs after the valve is opened. As the distance between this MCP and the EL valve is $\sim$ 1.5 m, this means that shortening the path by a factor of 2-5 should not significantly impact our ability to observe this signal on the trap detector. Further, the ions coming out of the trap are delayed by 37 ms, meaning that there is a very clear difference between the two ion populations. This is shown in Figure 4.6 below, which details the relative timings.

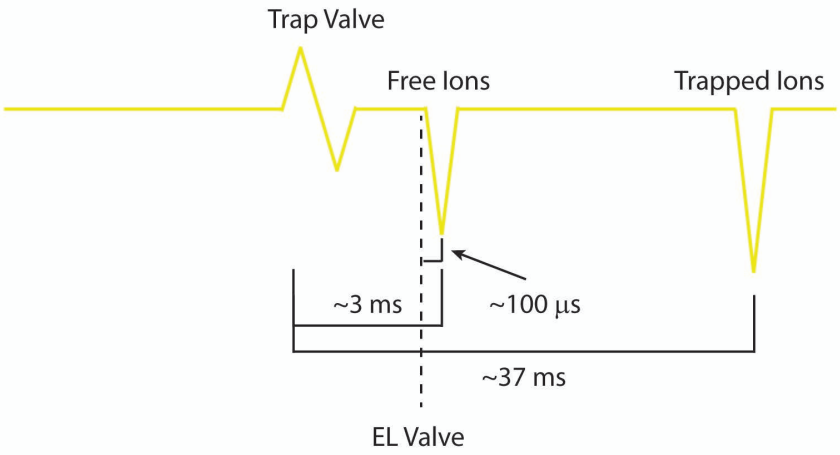

Figure 4.6: Diagram of cryo-SEVI trap ion detector MCP readout. Arrival of free ions and trapped ions relative to the trap value ($\sim$ 3 and $\sim$ 37 ms, respectively) and relative to the EL valve ($\sim 100\,\mu$s and $\sim$ 34 ms) are depicted.

Installing such a detector, however, does require both physical space for the MCP as well as some distance to ensure that these do not arc while powered, given that we usually power

our MCPs with voltage on the order of kV. Such a distance is governed by Paschen's Law,[317] which empirically determines the breakdown voltage, V_B required for an arc:

$$V_B = \frac{Bpd}{\ln(Apd) - \ln\left[\ln\left(1 + \frac{1}{\gamma_{se}}\right)\right]} \tag{4.5}$$

where p is the pressure (in pascals), d is the gap distance in meters, γ_{se} is the secondary-electron-emission coefficient, A is the saturation ionization in the gas at a particular E/p, and B is related to the excitation and ionization energies.

The physical mechanism that this law describes comes about from the acceleration of an electron in a field - with lower mean free paths (that depend on pressure), the electron will be accelerated to higher velocities before colliding, possibly resulting in ionization of a gas molecule, whose newly-liberated electron will then undergo a similar process, leading to a chain reaction that creates an arc as a cascade of electrons are released. At higher gas pressures, when pd is high, more collisions happen, randomizing the electrons direction and reducing this effect. Conversely, at low pd, the collision probability is low, also reducing this effect. This leads to a minima in the Paschen curve for a particular gas.

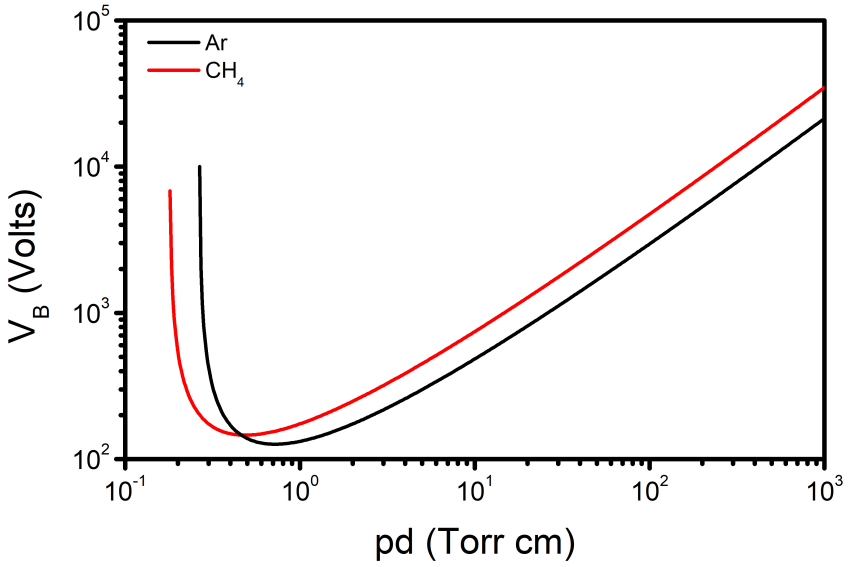

Figure 4.7: Paschen curves for Ar (black) and CH_4 (red).

This plot was constructed for Argon where $A = 11.5$ (cm·Torr)$^{-1}$ and $B = 176$ V (cm·Torr)$^{-1}$, measured over the range of E/p (Vcm^{-1}Torr^{-1}) of 100-600,[318] and γ_{se} of .058, determined at atmosphere. While this range is considerably lower than our needs (i.e. ~ 1

cm, 10^{-3} Torr, and ~ 2 kV), it was measured at much higher pressures (and voltages) than our needs require, indicating that we should be on the "upswing" of this curve, and so this is an appropriate approximation. This in indicted in the plot, as it breaks down at critical pd of $\sim$0.25 Torr·cm (where the denominator in Equation 4.5 becomes zero), indicating that these constants are not constant on the extrema. Near this value ($pd = .27$ Torr·cm), the breakdown voltage is 2 kV. These constants have been measured for CH_4 as well ($A = 17$, $B = 300$),[319] showing a larger V_b ($\sim$ 220 V),[320] and a sharper increase as pd decreases, indicating its use in the trap should not impact this as well.

At shorter distances, or lower pressures, this formulation is predicted to hold. While there appears to be little information on Paschen curves or constants at low pressure, there is work from the lithography community of short gaps (10's of microns), indicating that even at a 10 μm gap, the arcing voltage in Argon is roughly 240 V.[321] Together, this suggests that a 1 cm gap between the back MCP and the hexapole should be sufficient (here $pd = 10^{-3}$Torr·cm). This assumes the construction is a pair of chevron-stacked MCPs where the front of the first MCP is held at ground while the back is held at a floating voltage.[322] The minimum distance, however, should also consider the tolerance of the retractable MCP arm to translate the MCPs into and out of the ion path, which may introduce some mechanical instability in the location of the MCP. This may require the chamber be modified to allow for the linear translation stage for the MCP to be placed in a particular location relative to the trap.

4.3 Current Status

All this being said, the status of the machine as of this writing is as follows: nearly all components have been purchased for the build, with the machining of the chamber and trap to begin soon. The components purchased include some of the materials for the trap machining, including the rods for the octupole and hexapole, as well as indium foils.

These components are enumerated in Section 4.3.1, along with context for their purchase, as well as tabulated in Section 4.3.2 along with their vendor and part number.

4.3.1 Current Design

Components for building the trap itself were purchased, though they are limited to indium foil, Vespel, sapphire windows, and the octupole rods. Here, like in the design of the He-trap, indium foil is used in place of vacuum grease to ensure thermal contact between all mating pieces of the trap (walls of the box, cryostat, etc). This was chosen to reduce of grease contamination. As mentioned above in Section 4.2.3, the general valve used to introduce gases to the trap seizes at low temperatures and needs an insulating spacer to avoid this. For this purpose, a 3" long by 1.5" wide piece of Vespel was purchased, which should be sufficient for two spacers. Similarly, Sapphire windows, 31.75 mm in diameter, 1 mm thick, uncoated, were purchased from Edmund to serve as electrical insulators between the ring electrodes and RF end blocks and the rest of the trap. The Octupole rods are 3/16" diameter

stainless-steel (316) rods precision ground, purchased from McMaster-Carr, selected to satisfy the Dieter conditions of an octupole trap of diameter 9/32".[44,45] Similarly, the rods for the hexapole are 5/32" stainless-steel (316), purchased from the same vendor, selected again to satisfy the multipole conditions. For a good explanation of these criteria, see Chapter 3 of Jongjin Kim's thesis,[39] which outlines many of these components as well. The RF voltages applied to these rods will be supplied from a Dual RF power supply controller in conjunction with High-Q Heads custom built for our needs by Ardara Technologies.

Gas is introduced to the trap *via* a pulsed general valve, requiring both the valve and the driver - both of which are purchased from Parker. The valve itself is backed by gas at a pressure of $\sim$ 5 psi, requiring a vacuum regulator in the line - a stainless steel high-purity, absolutely pressure line regulator purchased from Matheson. This is then connected to the pre-cooling trap gas-cylinder *via* a standard gas regulator - CGA 580 for Ar, CGA 350. This gas will escape the trap into the chamber, a 6-way CF200 cross from Nor-Cal Vacuum, before being evacuated by a turbomolecular pump, a Pfeiffer ATH 1603M pump, with a pumping speed of 1360 L/s for N_2 and optimized for high Ar throughput. Such a pump will be backed by either an Edwards E2M28 (Ideal Vacuum) or Welch 1397 (Duniway) mechanical pump - both purchased refurbished for our needs.

The trap will be cooled by a liquid nitrogen cryostat, Model VPF-100 from Lakeshore Cryotronics (originally Janis). This model is custom mounted onto an LF flange, and is capable of outputting temperatures ranging from 77-500 K thanks to the 0.4 L LN2 reservoir. The coldhead of the cryostat can be attached to the trap *via* 4 tapped holes (M3) on a 1" diameter bolt. The temperature of the trap itself will be modulated by a temperature controller built for this cryostat, allowing for temperatures to be controlled with a $\pm$50 mK stability.

Trapped and free ions will be detached *via* a pair of chevron-stacked MCPs mounted onto a linear translation stage. Both components already exist in the lab as spares. The power supply for the MCPs was purchased from Spellman, allowing for power up to 6 kV to be supplied. Timings for everything that must be pulsed will come from one of the three pulse generators we own from Quantum Composers, Model 9528, which has 8 independent channels.

4.3.2 Table of Components Purchased

Below is a list of all components purchased for the trap, including vendor and part number:

Item	Vendor	Part Number
Octupole Rods	McMaster-Carr	1263K54
Hexapole Rods	McMaster-Carr	1263K48
Indium Foil	McMaster-Carr	8898N12
Vespel	McMaster-Carr	87405K48
Sapphire Windows	Edmund Optics	43-637
General Valve	Parker	009-1643-900
General Valve Driver - Iota One	Parker	060-0010-900
Vacuum Regulator	Matheson	SEQ3494
6-way Cross	Nor-Cal Vacuum	6C-800
Turbo	Pfeiffer	CKF00052
Edwards M28	Ideal Vaccum	P101034
Dual RF Power Supply Controller	Ardara	E-53-201
RF High-Q Head	Ardara	E-54-101
LN2 Cryostat	Lake Shore Cryotronics	A0/VPF-100
Trap Temp Controller	Lake Shore Cryotronics	335
HV Power Supply	Spellman	SL6PN30/115Vac
9528 Pulse Generator	Quantum Composers	9528-AT20-AT20-AT20 -AT20-IA15-S-S-US

Other small components (KF, and CF fittings, gaskets, bevels, BNCs, etc) were also purchased in preparation for this build and are detailed in the Appendix.

4.4 Looking Forward

While the initial engineering concerns have been considered above, this build is not yet done (or started in earnest), so there is a considerable amount left to be done to bring it into reality. First is the machining of the trap itself, as well as any modifications to the chamber that are needed for an ion gauge or MCP. Following this is the assembling of the many components, leak testing, voltage checks, testing the cooling, ensuring ions are trapped, and finally examining a test system. Many of this will be detailed in the forthcoming thesis of Marty DeWitt, as much of the remainder of this build will take place under his watchful eye along with Dr. Jascha Lau.

Part II

Free Radicals & Interstellar Species

Chapter 5

Vibronic Coupling in the Nitrate Radical

The content and figures of this chapter are reprinted or adapted with permission from M. C. Babin, J. A DeVine, M. DeWitt, J. F. Stanton, D. M. Neumark, "High Resolution Photoelectron Spectroscopy of Cryogenically-Cooled NO_3^-" *J. Phys. Chem. Lett.* **11**, 395 (2020).

Abstract

High-resolution anion photoelectron spectra of cryogenically cooled NO_3^- anions obtained using slow photoelectron velocity-map imaging are presented and provide new insight into the vibronic structure of the corresponding neutral radical. A combination of improved spectral resolution, measurement of energy-dependent intensity effects, temperature control, and comparison to theory allows for full assignment of the vibronic features observed in this spectrum. We obtain a refined electron affinity of 3.9289(14) eV for NO_3. Further, the appearance of Franck-Condon forbidden transitions from vibrationally cold anions to neutral states with excitation along the NO_3 ν_4 mode confirms that these features arise from vibronic coupling with the $\tilde{B}^2E'$ excited state of NO_3 and are not hot bands as has been suggested. Together, the suite of experimental and simulated results provides clear evidence that the ν_3 fundamental of NO_3 resides near 1050 cm^{-1}, addressing a long-standing controversy surrounding this vibrational assignment.

5.1 Main Text

The nitrate radical (NO_3) was one of the first free radicals to be observed spectroscopically[323] and is one of the most important radicals in atmospheric chemistry. This species serves as the primary oxidizer in the nighttime troposphere, when photolysis by sunlight ceases and its concentration builds up.[324] Under these conditions, NO_3 reacts to form HNO_3, N_2O_5, and organic nitrates that are subsequently incorporated into aerosols, providing the largest source of uncertainty of the concentration of NO_x, O_3 and OH in atmospheric models.[191,192] This interesting chemistry has motivated numerous experiments utilizing FTIR,[325–334] dispersed

fluorescence (DF),[335–337] diode laser spectroscopy,[338,339] matrix isolation spectroscopy,[340,341] cavity ringdown spectroscopy,[342,343] and anion photoelectron spectroscopy,[105] as well as several theoretical studies,[344–351] to characterize the electronic and vibrational structure of NO_3. Despite this extensive body of work, the nitrate radical still presents a significant challenge to both theory and experiment.[106,331,334,350] In this Letter, we address questions recently posed in the literature about the vibronic structure of the $\tilde{X}^2A_2'$ ground state of NO_3 using high resolution photoelectron spectroscopy of cryogenically cooled NO_3^- and accompanying theory.

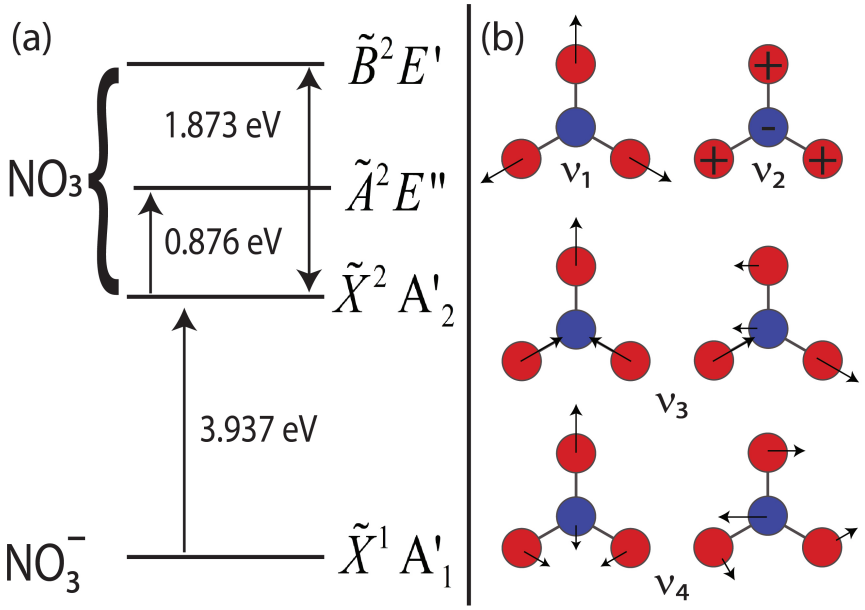

Figure 5.1: Electronic levels (a) and vibrational modes (b) in NO_3^- and NO_3. The "±" signs signify out of plane motion.

The spectroscopy of NO_3 is complicated by the existence of two excited electronic states ($\tilde{A}^2E$" and $\tilde{B}^2E'$) that lie roughly 1 and 2 eV, respectively, above the ground $\tilde{X}^2A_2'$ state, as shown in Figure 5.1a. These three states exhibit a wealth of vibronic mixing that results from both Jahn-Teller (JT) and pseudo-Jahn-Teller (pJT) couplings.[105,342,348] The potential energy surface for the ground state is known to be quite flat by virtue of a strong $\tilde{X}^2A_2'$ $\tilde{B}^2E'$ pseudo-Jahn-Teller interaction, with both theory and experiment predicting symmetric (D_{3h}) and asymmetric (C_{2v}) structures at various times.[344,345,347,352–354] While the D_{3h} stationary point has not been unambiguously demonstrated to be a minimum or a (second-order) saddle point between equivalent C_{2v} structures, it is clear that the vibrationally averaged ground state structure has D_{3h} symmetry.[348]

Strong vibronic mixing between the ground $\tilde{X}^2A_2'$ state with the $\tilde{B}^2E'$ excited state was first suggested by Weaver *et al*,[105] whose photoelectron spectrum of NO_3^- is presented in Figure 5.2a. Peak **a**, located 360 cm^{-1} above the 0_0^0 vibrational origin, was assigned to

the Franck-Condon (FC) forbidden 4_0^1 transition involving the ν_4 degenerate bend of the neutral, which becomes allowed through pJT coupling. More recent theoretical work has shown that a relatively simple vibronic model accounts qualitatively for this behavior as well as a number of other spectroscopic properties of NO_3, such as the $\tilde{X} - \tilde{B}$ absorption spectrum and the DF spectrum in which the ground state is accessed from the lowest vibronic level of the $\tilde{B}^2E'$ state.[348] This vibronic model also questioned the prior assignment of the strongest infrared absorption of NO_3 ($\sim$1492 cm^{-1}) to the ν_3 degenerate stretch,[338] ascribing it instead to a combination level; the true ν_3 position was calculated to be nearly 500 cm^{-1} lower. Subsequent and more quantitative work[350] predicted that ν_3 and the totally symmetric stretch (ν_1) fundamentals reside close together (within 10 cm^{-1}), and that the former is the main contributor of intensity to the peak found $\sim$1050 cm^{-1} above the origin, **b**, in the NO_3^- photoelectron spectrum (Figure 5.2a). This implies that peak **b** may comprise both the FC-allowed 1_0^1 and FC-forbidden 3_0^1 transitions contradicting the original assignment to the 1_0^1 transition by Weaver *et al.* The reassignment of the ν_3 frequency has led to numerous studies of the vibronic levels and spectra of NO_3.[326,329,330,332–334,340,341,343,355,356] Particularly noteworthy is a recent paper by Hirota[106] that questions the very existence of strong $\tilde{X}^2A_2'$ $\tilde{B}^2E'$ vibronic coupling, referencing work by Yamada and Ross[357] that claims peak **a** in Figure 5.2a was mis-assigned by Weaver *et al.* and instead corresponds to the FC-allowed 4_1^3 hot band.

The present study aims to address both of these critiques of the Weaver spectral assignments by using slow photoelectron velocity-map imaging of cryogenically-cooled anions (cryo-SEVI)[54] to revisit the photodetachment spectrum of NO_3^-. Compared to the experiments of Weaver *et al.*, cryo-SEVI offers considerably higher resolution, removal of hot bands via cryogenic cooling of anions, and facile evaluation of the electron kinetic energy (eKE) dependence of peak intensities and photoelectron angular distributions (PADs). The latter two attributes shed light on the nature of the electronic states accessed by photodetachment, demonstrating that the ν_4 and ν_3 fundamentals in the $\tilde{X}^2A_2'$ state of NO_3 gain intensity through vibronic coupling to the $\tilde{B}^2E'$ state. We confirm the initial assignment set forth by Weaver for **a** as the ν_4 fundamental, and find that **b** is indeed dominated by the proximate 3_0^1 band. Excellent agreement between our experimental spectra and high-level calculations affirms these assignments.

The cryo-SEVI spectrum of the $\tilde{X}^2A_2' \leftarrow \tilde{X}^1A_1'$ photodetachment transition of NO_3^- is presented in Figure 5.2b, where a low-resolution overview spectrum is displayed atop high-resolution composite spectra taken at several photon energies. In addition, the cryo-SEVI results are compared to a simulated photoelectron stick spectrum, constructed using a 3-state Köppel-Domcke-Cederbaum (KDC) vibronic Hamiltonian for NO_3.[358] Electron binding energies (eBEs) relative to the neutral electron affinity (EA) are given in Table 5.1 for all labelled transitions, alongside the KDC-predicted values and peak assignments. Details of the cryo-SEVI and theoretical methods are provided in Sections S1 and S2, respectively, of the Supporting Information (SI). A complete listing of the eigenvalues of the KDC Hamiltonian and the experimentally determined parameters with a comparison to literature values are presented in Tables 5.2 and 5.3, respectively, of Section 5.2.

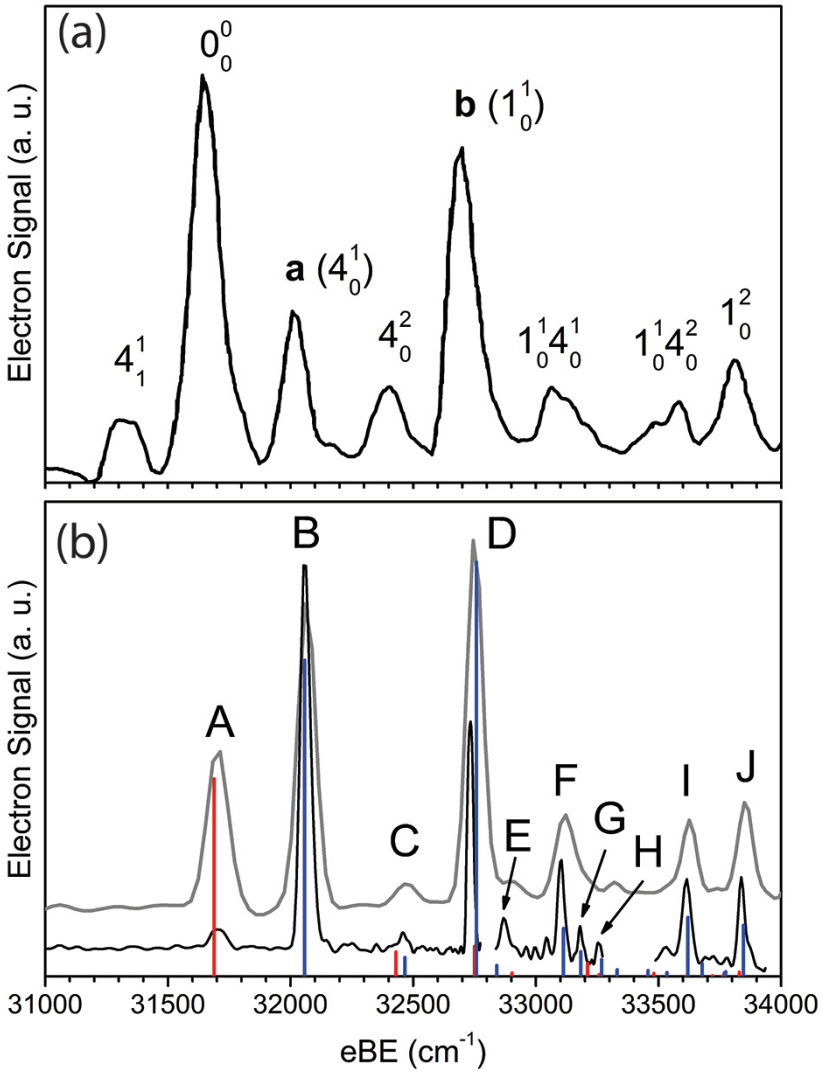

Figure 5.2: Photoelectron spectra of the of the $\tilde{X}^2A_2' \leftarrow \tilde{X}^1A_1'$ transition of NO_3^- as reported in Ref [344] (a) and this work using cryo-SEVI (b). In (b), a low-resolution spectrum (grey, hν = 35137 cm^{-1}) sits above both high-resolution scans (black, variable photon energy) and a simulated photoelectron stick spectrum. Red sticks represent FC-allowed transitions and blue sticks represent transitions that gain intensity through pJT-coupling.

There are several notable differences between the Weaver and cryo-SEVI spectra. First, the improvement in resolution provides a more precise EA for neutral NO_3. This is best obtained by fixing the shift from the origin for the narrowest feature in our spectrum, peak G, to the corresponding value from IR measurements, 1492 cm^{-1}, and subtracting the vibrational frequency from this peak position in eBE. This procedure yields an EA of 3.9289(14)

Peak	eBE (cm^{-1})	eBE-EA (cm^{-1})	Assignment	KDC
A	31707(25)	-	0_0^1	-
B	32045(8)	356	4_0^1	369
C	32459(14)	770	4_0^2	777
D	32733(12)	1044	3_0^1	1069
E	32871(14)	1182	4_0^3	1152
F	33102(14)	1413	$1_0^1 4_0^1$	1424
G	33181(11)	1492	$3_0^1 4_0^1$	1494
H	33256(12)	1567	4_0^4	1579
I	33609(12)	1920	$3_0^1 4_0^1$	1931
J	33837(11)	2148	3_0^2	2157

Table 5.1: Positions, shifts relative to the EA extracted from peak G (31689(11) cm^{-1}), assignments, and corresponding KDC eigenvalues for detachment transitions in the cryo-SEVI spectrum of NO_3^- presented in Figure 5.2b. Uncertainties in peak positions correspond to one standard deviation obtained from a Gaussian fit to the corresponding feature in the high-resolution scan.

eV, an order of magnitude more precise than the value of 3.937(14) eV determined by Weaver *et al.* Another notable difference is the absence of the 4_1^1 feature in the cryo-SEVI spectrum. The absence of this hot band suggests negligible population of vibrationally excited anions, as is typical for cryo-SEVI experiments, where ions usually have internal temperatures on the order of 10 K.[54,239] Given the disappearance of the 4_1^1 hot band, but not the disputed 4_0^1 feature (B), in the cryo-SEVI spectrum, we can confidently reject the reassignment of the latter as the 4_1^3 hot band.[106] Peak B (**b** in Figure 5.2a) is indeed the originally-assigned FC-forbidden 4_0^1 transition, which gains its activity through vibronic coupling to the $\tilde{B}^2E'$ excited state, in agreement with our simulated photoelectron spectrum.

Based on the assignment of peak B, we assign C and E to the 4_0^2 and 4_0^3 transitions. The position of the 4_0^3 transition (Table 5.1) is consistent with previous infrared measurements in neon matrices[340] and in the gas phase.[333] In these works, the value of 1173 cm^{-1} for the e' sublevel of $3\nu_4$ has been confirmed by both isotopic and rotational analyses, respectively, leaving no dispute about this assignment to the $\ell = \pm 1$ vibrational angular momentum sublevels of the NO_3 $\nu_4 = 3$ state.

FC-forbidden features such as B acquire non-zero intensity through pJT-coupling to an excited electronic state with appropriate symmetry.[71] Within the (crude) Born-Oppenheimer approximation, the $\nu_4 = 1$ level of the $\tilde{X}^2A_2'$ state and $\nu_4 = 0$ level of the $\tilde{B}^2E'$ state can be written as $|a_0\rangle = |\nu_4 = 1\rangle \left|\tilde{A}_2\right\rangle$ and $|b_0\rangle = |\nu_4 = 0\rangle \left|\tilde{E}'\right\rangle$, respectively; the transition from the anion ground state $|0\rangle = |\nu = 0\rangle \left|\tilde{A}_1'\right\rangle$ to $|a_0\rangle$ is FC-forbidden because the ν_4 mode is

not totally symmetric, whereas photodetachment to $|b_0\rangle$ is FC-allowed. However, states $|a_0\rangle$ and $|b_0\rangle$ each have overall E' vibronic symmetry and can thus mix by pJT-coupling, leading to two new states $|a\rangle = c_{1a}|a_0\rangle + c_{1b}|b_0\rangle$ and $|b\rangle = c_{2a}|a_0\rangle + c_{2b}|b_0\rangle$, each of which is an admixture of the two zero-order vibronic levels. By this vibronic coupling mechanism, the 4_0^1 transition acquires intensity and can be observed. A similar mechanism applies to the 4_0^3 transition (E).

The role of vibronic coupling can also be seen in the dependence of peak intensities and photoelectron angular distributions on the eKE.[14,58,359] The spectra in Figure 5.2 show that the relative intensity of the vibrational origin (A) is much higher in the Weaver spectrum than in any of the cryo-SEVI spectra, a consequence of the lower photon energies used in the current work. This intensity dependence is explored in greater detail in Figure 5.3a, in which three cryo-SEVI spectra taken at different photon energies and normalized to the intensity of peak B are shown. The integrated intensities of peaks A, B, and D (normalized to peak B) are plotted as a function of eKE for all experimental spectra in Figure 5.3b. These data show that at lower eKE, the intensity of peak A drops off much more than that of B and D (**a** and **b** in the Weaver spectrum). Hence, the near threshold detachment cross section of the FC-allowed peak A is very different from B, which is allowed only through pJT coupling. The similar intensity dependence of B and D suggests that vibronic coupling is also responsible for a substantial portion of the intensity of D, as discussed in more detail below.

The photoelectron angular distributions (PADs) were also determined at multiple photon energies. The functional form of a PAD is given by[91]

$$\frac{d\sigma}{d\Omega} = \frac{\sigma_{tot}}{4\pi}\left[1 + \beta P_2(\cos\theta)\right] \tag{5.1}$$

where σ_{tot} is the total detachment cross section, $P_2(x)$ is the second-order Legendre polynomial, θ is the angle of the outgoing photoelectron with respect to the laser polarization axis, and β is the anisotropy parameter, which ranges from -1 (perpendicular detachment) to +2 (parallel detachment). Figure 5.4 shows β for peaks A, B, and D as a function of photon energy. Clearly, not only the intensity but also the PAD of A exhibits a markedly different energy dependence that those of B and D.

The pJT-coupling mechanism is reflected in the striking differences in the eKE-dependent intensities and PADs of A and B. We first consider Figure 5.3, which shows that as the eKE is lowered, the intensity of the FC-allowed peak (A) is suppressed relative to the vibronically-allowed peak (B). This effect arises because photodetachment cross sections at low eKE are governed by the Wigner threshold law,[81]

$$\sigma \propto (\text{eKE})^{\ell+1/2} \tag{5.2}$$

where σ is the detachment cross section and ℓ is the angular momentum of the detached electron. Thus, at low eKEs, the lowest-ℓ detachment channels dominate. For detachment to the $\tilde{X}^2A_2'$ state of NO_3, selection rules for molecular photodetachment prohibit detachment

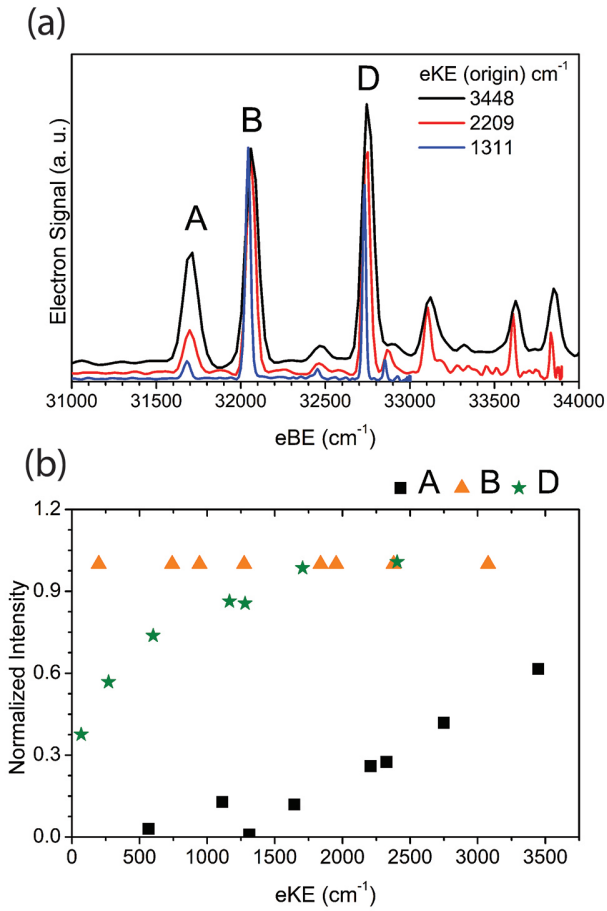

Figure 5.3: (a) Cryo-SEVI spectra of NO_3^- at several photon energies illustrating the differing signal attenuation for features A, B, and D as eKE decreases. The intensity of each scan has been normalized to B. Photon energies used are 35137 (black), 33898 (red), and 32801 cm^{-1} (blue). (b) Integrated intensities of features A, B, and D, normalized to B in each scan, for all cryo-SEVI scans, three of which are shown in (a).

of $\ell = 0$ electrons, and p-wave detachment dominates.[83,360] Hence, the cross section for a FC-allowed transition to the $\tilde{X}^2A_2'$ state, such as the 0_0^0 transition, drops precipitously as the eKE is lowered.

In contrast, the 4_0^1 transition terminates in a neutral level with some contribution from the $\tilde{B}^2E'$ electronic state, detachment to which can proceed via $\ell = 0$ (s-wave) detachment. The less severe near-threshold attenuation of s-wave detachment then yields the observed enhancement in relative intensity of the 4_0^1 vs. the 0_0^0 transition as eKE is lowered. This situation, in which FC-allowed transitions are suppressed at low eKE relative to pJT-active features, was seen in the cryo-SEVI spectrum of the indenyl anion,[58] though the effect is much more pronounced here because the total cross section for detachment to the $\tilde{X}^2A_2'$

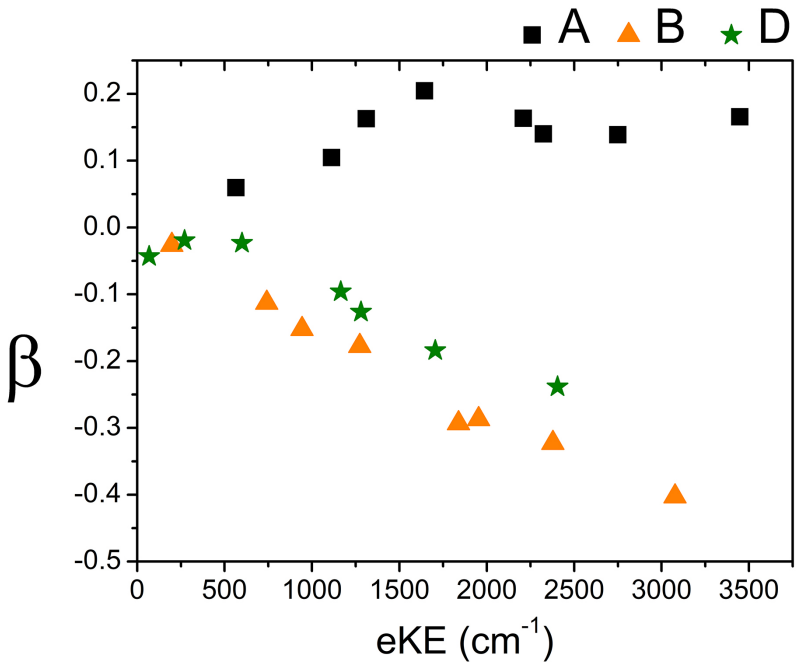

Figure 5.4: Measured anisotropy parameter, β, of the features A, B, and D extracted from spectra obtained at multiple photon energies

state is relatively low, as discussed previously.[105] Hence, a small amount of vibronic mixing with the $\tilde{B}^2E'$ state markedly affects the intensity of a pJT-active transition.

These effects also govern the eKE-dependent PADs in Figure 5.4. Differing PADs in a single photodetachment band are a clear signature of vibronic coupling effects.[14,65] As the PAD reflects the angular momentum of the detached electron,[361] the partial wave components that play a role in Eq. 5.2 are intimately connected to the PADs of different detachment transitions, and differences in threshold behavior tend to occur together with different PADs.[65,102] This is true in NO_3, where the PAD for A is consistent with p-wave detachment, while B displays the expected trend for a transition comprising of s- and d-wave detachment. The disparity in the PADs of A and B, coupled with their threshold behavior, unequivocally shows that B gains its intensity through pJT-coupling.

We now consider peak D. Its relative intensity remains high even at eKEs below 100 cm 1, and its anisotropy parameter β becomes increasingly negative as the photon energy increases, showing similar behavior to peak B. These two trends suggest that D gains much of its intensity through the same pJT-coupling mechanism as B, and is not solely the FC-allowed 1_0^1 transition assigned previously. Only two states of e' symmetry, the appropriate symmetry to pJT-couple to the $\tilde{B}^2E'$ state, plausibly reside near this feature, namely $3\nu_4$ and the ν_3 fundamental. As E has been assigned to the transition 4_0^3 both here and via IR spectroscopy, D is then dominated by the 3_0^1 transition.[348]

The identification of the pJT-coupled 3_0^1 transition in our spectrum provides the first published experimental evidence confirming the theoretical prediction that ν_3 lies well below 1492 cm^{-1}, and the predicted frequency (1069 cm^{-1})[350] is in reasonable agreement with our experimental value of 1044(16) cm^{-1}. The transition cannot be observed directly as it attenuates too rapidly near threshold, where cryo-SEVI could otherwise achieve sufficient resolution[58] to observe the splitting between the ν_1 and ν_3 fundamentals.

Our findings address recently posed questions regarding the photoelectron spectrum of NO_3^-, refute the reassignment of B as the 4_1^3 hot band, and provide the first experimental confirmation that the ν_3 fundamental resides several hundred cm^{-1} below the 1492 cm^{-1} band to which it has been assigned and within 10 cm^{-1} of the ν_1 fundamental. Together, these results inform an understanding of vital importance regarding vibronic coupling in the $\tilde{X}^2A_2'$ ground state of NO_3 that should lessen the controversy surrounding both the vibrational level structure of this radical and the extent that vibronic coupling manifests in the ground electronic state.

5.2 Supporting Information

5.2.1 Experimental Methods

The cryo-SEVI method has been described in detail previously.[34,35,54] In this work, nitrate anions are generated by passing 1% NO_2 in N_2 through a pulsed Even-Lavie solenoid valve fitted with a circular filament ionizer.[245] Dissociative electron attachment to N_2O_4, which is in equilibrium with NO_2 in the gas mix, results in the formation of NO_3^-. Following formation, ions pass through a skimmer, a radiofrequency (RF) hexapole ion guide, and a RF quadrupole mass filter before being directed into a linear RF octupole ion trap held at 5 K and filled with a buffer gas mixture of 20:80 H_2:He. Collisions with the cold buffer gas result in effective vibrational, rotational, and electronic cooling of the ions, leading to internal temperatures of nearly 10 K.[54,239]

After ∼40 ms, the ions are extracted into an orthogonal Wiley-McLaren time-of-flight mass spectrometer[259] and focused into the interaction region of a seven-plate velocity-map imaging (VMI) electrostatic lens assembly.[18,36] In the VMI spectrometer, ions are photodetached by the frequency-doubled output of a dye laser pumped by the second harmonic of a Nd:YAG laser operating at 20 Hz.

The resulting photoelectrons are projected onto a 2D detector comprising two chevron-stacked microchannel plates coupled to a phosphor screen, which is photographed by a CCD camera after each laser shot.[17] Each image is analyzed for individual electron events for which the centroids are calculated and binned in a 1024 × 1024 grid.[271] The three-dimensional electron velocity distribution is reconstructed from the accumulated images using the Maximum Entropy Velocity Legendre Reconstruction (MEVELER) algorithm.[275] The radial position of features in the reconstructed image is related to electron kinetic

energy (eKE) by acquiring VMI images for detachment from atomic Cl^- at several photon energies.[280]

The VMI spectrometer has an approximately constant resolving power, ΔeKE/eKE,[18] yielding the best eKE resolution for slow electrons. As such, a SEVI spectrum is acquired by first taking an overview spectrum at a relatively high photon energy before tuning the detachment laser to energies slightly above features of interest. This procedure results in a collection of high-resolution spectra over narrow energy windows that are concatenated and scaled to match intensities in the overview spectrum, which is less sensitive to variation of the photodetachment cross section with photon energy. Spectra are plotted aa function of electron binding energy (eBE), given by eBE = hν - eKE.

5.2.2 Computational methods

Apart from the qualifications listed below, the simulated photoelectron spectrum was calculated with the same method and vibronic Hamiltonian used, and fully documented, in Simmons et al.[350]

In this work, 2,000 Lanczos recursions were used together with a direct product basis of 14,062,500 basis functions (12 for v1, 25 for the two components of ν_3 and 25 for the two components of ν_4) to obtain the vibronic energy levels of the $\tilde{X}$ and $\tilde{B}$ states of the neutral, the former of which are relevant to the study at hand. This size of basis and number of steps in the iterative diagonalization suffices to converge all roots of the $\tilde{X}$ state up to about 2,200 cm^{-1}, which is an improvement upon the results of Simmons,[350] where levels were only well-converged up to about 1,950 cm^{-1}.

The stick spectra were obtained by assuming a (constant) photodetachment cross section ratio of 100, which is four times that used in Simmons to obtain a satisfactory ratio of the origin and 4_0^1 peak heights in the spectrum of Weaver et al.[105] In that spectrum, the kinetic energy of ejected electrons was roughly 0.6-0.7 eV in the region of greatest interest (0-1,100 cm^{-1}). The higher ratio used here, while empirical in nature, is qualitatively consistent with the smaller characteristic eKE (*ca.* 0.3-0.4 eV) used in the survey spectrum.

Energies of levels with e' and a_2' vibronic symmetry found by these calculations are listed in Table 5.2 below, along with cross-sections obtained from the intrinsic vibrational overlaps, as combined with the empirical cross-section ratio.

Level	Relative Intensity	Vibronic Symmetry
0	1	a_2'
368.9	1.599	e'
740.7	0.12411	a_2'
776.8	0.09596	e'
1061.1	0.1525	a_2'
1068.6	2.09476	e'
1151.6	0.05556	e'
1213.9	0.01745	a_2'
1423.9	0.24332	e'
1494.2	0.1256	e'
1522.1	0.06493	a_2'
1568.8	0.00959	a_2'
1578.9	0.08577	e'
1642.4	0.03443	e'
1768.6	0.02989	e'
1792.5	0.01579	a_2'
1845.4	0.01989	e'
1923.3	0.00165	a_2'
1931.3	0.29874	e'
1989.2	0.06533	e'
2031.2	0.00322	a_2'
2072.2	0.00256	a_2'
2079.7	0.17064	e'
2085	0.16998	e'
2140.1	0.0222	a_2'
2157.2	0.16103	e'

Table 5.2: Eigenvalues of the KDC Hamiltonian corresponding to e' and a_2' vibronic levels (in cm^{-1}) of NO_3 within 2200 cm^{-1} of the vibrational origin.

Parameter	cryo-SEVI	Literature Value	KDC
EA (eV)	3.9289(14)	3.937(14)[a]	-
4_0^1	356(13)	365[b]	369 (e')
4_0^2	770(26)	772[c]	777 (e')
3_0^1	1044(16)		1069 (e')
4_0^3	1182(18)	1173[d]	1152 (e')
$1_0^1 4_0^1$	1413(18)	1414[d]	1424 (e')
$3_0^1 4_0^1$	1492(11)	1492[e]	1494 (e')
4_0^4	1567(16)		1579 (e')
$3_0^1 4_0^2$	1920(17)	1927[c]	1931 (e')
3_0^2	2148(15)	2155[f]	2157 (e')

Table 5.3: Experimental parameters for NO_3 extracted from the cryo-SEVI spectrum of the corresponding anion and comparison to the theoretical values obtained in the current work as well as available literature values.
[a] = Ref [105], [b] = Ref [330], [c] = Ref [332], [d] = Ref [333], [e] = Ref [329], [f] = Ref [334]

Chapter 6

Vibrational Pre-Excitation of the Hydroxy Radical

The content and figures of this chapter are reprinted or adapted with permission from M. DeWitt, M. C. Babin, D. M. Neumark, "High Resolution Photoelectron Spectroscopy of Vibrationally Excited OH^-" *J. Phys Chem. A* **125**, 7260 (2021).

6.1 Abstract

The effect of vibrational pre-excitation of anions on their photoelectron spectra is explored, combining slow photoelectron velocity-map imaging of cryogenically cooled anions (cryo-SEVI) with tunable IR radiation to pre-excite the anions. This new IR cryo-SEVI method is applied to OH^- as a test system, where the R(0) transition of the hydroxyl anion (3591.53 cm^{-1}) is pumped. Vibrational excitation induces a 30% depletion in photodetachment signal from the $\nu = 0$, J = 0 ground state of the anion and the appearance of all five allowed, rotationally-resolved photodetachment transitions from the OH^- ($\nu = 1$, J = 1) level, each with peak widths between 1-2 cm^{-1}. By scanning the IR laser, IR cryo-SEVI can also serve as a novel action technique to obtain the vibrational spectrum of OH^-, giving an experimental value for the R(0) transition of 3591(1.2) cm^{-1}.

6.2 Introduction

Anion photoelectron spectroscopy (PES) is a powerful and versatile method for determining electron affinities, the vibrational and electronic energy levels of neutral species created by photodetachment, and the geometric changes that occur upon photodetachment.[5,246,362–365] It has been applied with considerable success to free radicals, clusters, and reaction transition states.[5,366–368] In favorable circumstances, anion PES yields resolved vibrational structure. The extent of this vibrational structure is generally governed by Franck-Condon considerations; only totally symmetric vibrational modes in which there is a normal coordinate

displacement upon photodetachment are active in the PE spectrum. Hence, for example, one does not typically observe vibrational motion involving free OH,[75] NH,[76] and CH[77] bonds since the anion and neutral bond lengths change very little upon photodetachment. Likewise, transitions involving non-totally symmetric modes are weak; odd $\Delta\nu$ transitions in such modes are symmetry-forbidden in the absence of vibronic coupling,[14,105] and even $\Delta\nu$ transitions require a large frequency change to gain appreciable intensity in a photoelectron spectrum.[71] However, if the anion is vibrationally excited, new vibrational levels of the neutral become accessible by photodetachment. The effects of vibrational hot bands on the photoelectron spectrum of the vinylidene anion (H_2CC^-) were considered by Johnson,[296] while Continetti and Guo showed that vibrational pre-excitation of the $F^-(H_2O)$ anion enables one to access otherwise inaccessible regions of the $F+H_2O$ potential energy surface.[369] In this paper, we explore the effect of infrared laser excitation of an anion, OH^-, upon its photoelectron spectrum.

The hydroxyl radical and corresponding anion have a rich spectroscopic history. The microwave spectrum of the radical was measured by Townes in 1955,[370] and since then the high resolution spectroscopy of this species has been mapped out in great detail.[371–373] OH has a $^2\Pi$ ground state with a spin-orbit splitting of 126.2923 cm^{-1} between the $\Omega = 3/2$ and $1/2$ fine structure levels and a rotational constant, B_e, of 18.91083(106) cm^{-1}.[374]

The hydroxide anion has likewise been investigated by a series of state-of-the-art spectroscopic techniques. Rotationally resolved photodetachment transitions were observed in a series of high resolution laser photodetachment threshold measurement experiments by Lineberger[79,375–377] and, more recently, by Wester.[378,379] The rotationally resolved infrared spectrum of OH^- was measured by Saykally using velocity-modulation spectroscopy[304] and by Schlemmer via laser-induced reactivity (LIR) in a cold ion trap.[380] Blondel used photodetachment microscopy to obtain well-resolved rotational transitions between OH^- and the fine structure levels of OH and determined a refined rotational constant of 18.7352(3) cm^{-1} for the anion.[75]

Here, we combine slow electron velocity-map imaging of cryogenically cooled OH^- (cryo-SEVI)[54] with infrared pre-excitation to investigate the effect of vibrational excitation upon its photoelectron spectrum. Cryo-SEVI is a high-resolution variant of photoelectron spectroscopy in which cryogenically cooled anions are photodetached with a tunable laser, and the resulting photoelectrons are analyzed using a velocity-map imaging system designed specifically to measure the kinetic energies of slower electrons with greater precision.[5,54] The combination of cryogenic cooling and slow-electron imaging yields photoelectron spectra with energy resolution as high as 1-2 cm^{-1}, and in the case of OH^-, we obtain well-resolved rotational features. Upon infrared pre-excitation, the IR cryo-SEVI spectrum reveals new rotationally resolved features resulting from photodetachment transitions between the $\nu = 1$ levels of OH^- and OH.

6.3 Experimental Methods

The cryo-SEVI method has been previously described in detail.[5,35,54] In this work, O^- anions are generated by expanding a dilute gas mixture of N_2O in helium backing gas through a pulsed Even-Lavie valve,[245] equipped with a circular filament ionizer. Electrons from the ionizer induce dissociative attachment of N_2O to produce O^-. The ions are directed through a radiofrequency (RF) hexapole ion guide, a RF quadrupole mass filter, and into a cryogenically cooled linear RF octupole ion trap held at 5 K. The ions are stored in the trap for ∼40 ms, where they are collisionally cooled with an 80:20 He:H_2 buffer gas mixture to their ground electronic state. Inside the trap, O^- anions react with H_2 molecules to form OH^- anions, which are rotationally and vibrationally cooled by further collisions with the buffer gas.

The ions are extracted from the trap into an orthogonal Wiley-McLaren time-of-flight mass spectrometer and guided into the laser interaction region of a seven-plate velocity-map imaging (VMI) spectrometer.[18,36] Vertically polarized light from a dye laser pumped by the second harmonic of a Nd:YAG laser operating at 20 Hz is focused to a spot size of ∼0.01 mm^2 and used to photodetach OH^- anions. The dye laser system can produce radiation between 220 nm and 1.8 μm with a spectral bandwidth of < 0.1 cm^{-1} and pulse energies up to 15 mJ. The resulting photoelectrons are projected onto a 2D detector that comprises two chevron-stacked microchannel plates coupled to a phosphor screen.[17] A CCD camera photographs the phosphor screen after each laser shot, and the centroids of the photoelectron events in each image are calculated and binned in a 1024 × 1024 grid in real time.[271]

Several modifications to the cryo-SEVI technique are required to facilitate the selective vibrational excitement of cryogenically-cooled anions using infrared radiation prior to photodetachment (IR cryo-SEVI). On alternating experimental cycles, anions are vibrationally excited prior to photodetachment using the horizontally polarized mid-infrared (mIR) output of a tabletop OPO/OPA laser system (LaserVision), pumped by a Nd:YAG laser (Continuum SureLite EX) operating at 10 Hz. The infrared (IR) laser system can produce radiation between 1.3 μm and 16 μm with a spectral bandwidth of ∼3.5 cm^{-1} and pulse energies up to 4 mJ.[381] The mIR beam is rotated to ensure vertical polarization in the interaction region and focused to a spot size of ∼0.07 mm2. It is aligned to be collinear and counterpropagating to the visible beam from the dye laser. The IR laser system is triggered such that the mIR light excites the ion packet less than 1 ns before photodetachment.

Photoelectron centroids are accumulated over several thousand experimental cycles into two VMI images, depending on whether the IR laser system was triggered in that cycle, allowing for photodetachment images with and without IR pre-excitation to be acquired simultaneously. The radial and angular photoelectron distributions are reconstructed from each accumulated image using the Maximum Entropy Velocity Legendre Reconstruction (MEVELER) method.[275] The electron kinetic energy (eKE) distributions are related to the radial distributions by acquiring images of the well-characterized detachment transitions of O^- at several different photon energies.[279]

Due to the roughly constant resolving power (ΔeKE/eKE) of the VMI spectrometer,

slow photoelectrons give the highest resolution features.[18,36] For this reason, cryo-SEVI and IR cryo-SEVI spectra are acquired by first taking an overview spectrum at a relatively high photon energy before tuning the detachment laser to energies slightly above features of interest. Narrow windows surrounding the high-resolution features are concatenated together and scaled to match the relative intensities of the overview spectrum, resulting in a single high-resolution photoelectron spectrum. Cryo-SEVI and IR cryo-SEVI spectra are plotted against electron binding energy (eBE), given by eBE = hν-eKE. A difference spectrum is also calculated by subtracting the eKE distributions with and without IR pre-excitation.

6.4 Results and Discussion

The cryo-SEVI and IR cryo-SEVI spectra of OH^- are presented in Figure 6.1. Figure 6.1a shows the spectrum with no IR excitation, Figure 6.1b shows the vibrationally excited IR cryo-SEVI spectrum with the IR laser tuned to the R(0) rovibrational transition of OH^- at 3591 cm^{-1},[304] and Figure 6.1c shows the difference spectrum. In all three scans, the black traces are high resolution scans taken at several photon energies slightly above threshold for each feature. The blue trace in Figure 6.1a is a low-resolution overview scan taken at a relatively high photon energy. The red traces in Figure 6.1b are from high-resolution scans taken with the IR laser on and represent either new or depleted features resulting from IR excitation.

As discussed previously,[75,376,378] the near-threshold photodetachment of OH^- is dominated by s-wave detachment with electron orbital angular momentum $\ell = 0$. Combining this with the unit angular momentum provided by the photon results in a photodetachment rotational selection rule of J' - J" = ΔJ = $\pm 1/2$, $\pm 3/2$, where J' and J" are the total angular momentum quantum numbers of the neutral and negative ion, respectively. Due to the change in spin between anion and neutral, it is more convenient to use the quantum number N = J - S (total angular momentum without spin) when considering transitions between rotational levels. For OH^-, N" = J", while in the $^2\Pi_{3/2}$ ($^2\Pi_{1/2}$) state of OH, N' = J' - 1/2 (N' = J' + 1/2). Detachment transitions are labeled O, P, Q, R, and S indicating ΔN of -2, -1, 0, +1, and +2, respectively. The rotational selection rule $\Delta J = \pm 1/2, \pm 3/2$ dictates that transitions in the S branch of the $^2\Pi_{3/2}$ manifold and transitions in the O branch of the $^2\Pi_{1/2}$ manifold are formally forbidden; similar selection rules were seen in the anion zero electron kinetic energy (ZEKE) spectrum of SH^-.[23] Following Goldfarb et al,[75] transitions to $\Omega' = 3/2$ and 1/2 levels of OH are labeled in Figure 6.2 with indices of 3 and 1, respectively. The R3(0) transition, for example, corresponds to detachment from the N" = 0 state of the anion to the N' = 1 (J' = 3/2) state of the $\Omega' = 3/2$ series in the neutral.

The cryo-SEVI and IR cryo-SEVI spectra (Figs. 1a and 1b) exhibit a number of well-resolved transitions to both of the spin-orbit states of the neutral radical, with typical peak widths of 2-5 cm^{-1} FWHM. Peak assignments are given in Table 6.1, with rotational transitions as indicated in Figure 6.2 and vibrational transitions labeled as $\nu' - \nu$", where ν' and ν" are the vibrational quantum numbers in the neutral and anion, respectively. The previously

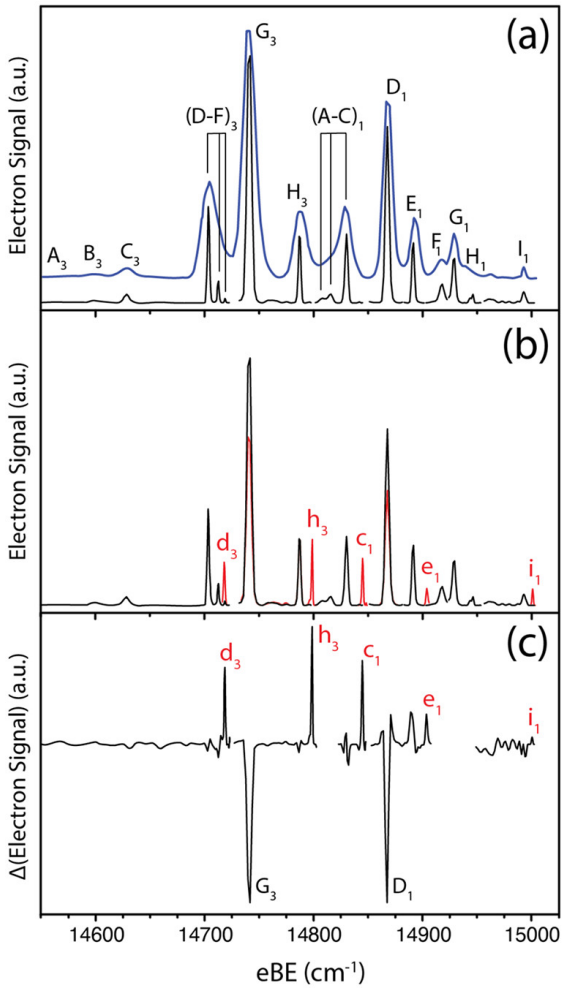

Figure 6.1: Cryo-SEVI spectrum (a), IR cryo-SEVI (b), and difference spectrum (c) of the $\tilde{X}^2\Pi \leftarrow \tilde{X}^1\Sigma^+$ detachment of OH^-. The blue trace is an overview spectrum taken with a photon energy of 15004.07 cm^{-1}, while the black traces are high-resolution scans taken near threshold, and the red traces are high-resolution scans that show new or depleted features after IR pre-excitation. Subscripts of 3 and 1 indicate transitions to OH levels with $\Omega' = 3/2$ and $\Omega' = 1/2$. respectively.

reported transition energies in Table 6.1 were determined by computing the expected shift in energy of the R3(0) and R1(0) transitions, reported by Goldfarb *et al.*,[75] based on the energy spacings between known rotational levels in OH^- and OH, given by Rosenbaum *et al.*[304] and Mélen et al,[373] respectively.

The largest feature in Figure 6.1a, labeled G3, is the R3(0) transition between the lowest vibration-rotation levels of OH^- and OH, thereby yielding an electron affinity of the OH radical of 14741(2) cm^{-1}, in good agreement with that reported by Goldfarb *et al.*[75] Beyond

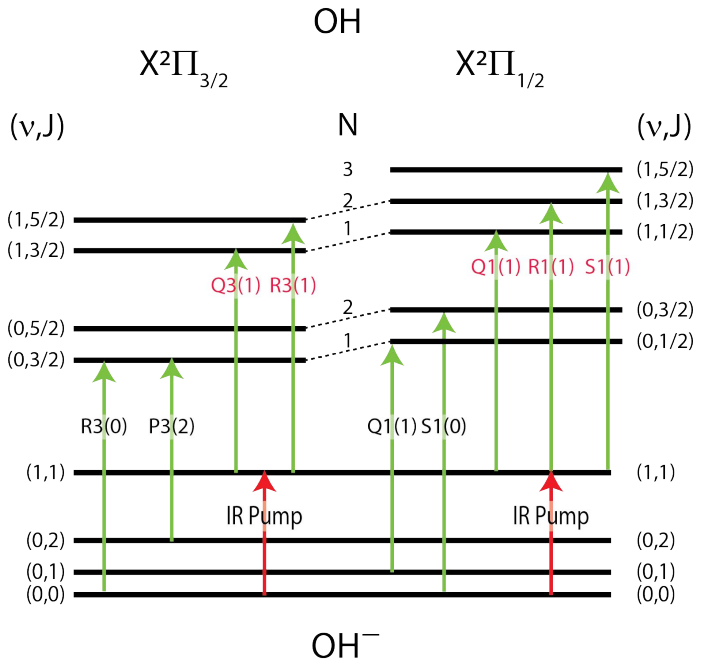

Figure 6.2: Relevant rovibrational energy levels of OH^- and OH. Arrows depict some experimentally observed transitions originating from the ν" = 0,1 levels of OH^-.

this, the spectrum reveals two overlapping sets of peaks, $(A\text{-}H)_3$ and $(A\text{-}I)_1$, that correspond to detachment to different rotational levels of the $^2\Pi_{3/2}$ and $^2\Pi_{1/2}$ states of neutral OH, respectively. Many of the features observed in the cryo-SEVI spectrum have been previously reported by Schulz *et al.*[376] and Goldfarb et al,[75] allowing for their direct assignment. Features $(A\text{-}C)_3$ correspond to the P3 branch, features $(D\text{-}F)_3$ correspond to the Q3 branch, $(G\text{-}H)_3$ correspond to the R3 branch, $(A\text{-}C)_1$ correspond to the Q1 branch, and $(D\text{-}F)_1$ and H_1 correspond to the R1 branch. We clearly observe the weak S1(0) and S1(1) features G_1 and I_1, in previous work,[75] only the S1(0) transition was reported, and that was barely visible.

While there are a few features in the cryo-SEVI spectrum originating from anion rotational levels with J > 2, the most intense features arise from transitions from the J = 0 and 1 levels, indicating the ions are rotationally cold. The rotational temperature of the anions can be estimated by fitting the ratio of the intensities of the R3(0) and R3(1) features to a Boltzmann rotational distribution, given by

$$\frac{I_1}{I_0} = 3e^{-2hcB_0/k_bT} \tag{6.1}$$

where I_0 and I_1 are the intensities of the R3(0) and R3(1) peak, respectively, h is Planck's

Label	eBE	Vibrational Transition	Rotational Transition	Reported Energy*
A_3	14568(4)	0-0	P3(4)	14568.98
B_3	14600(4)	0-0	P3(3)	14600.18
C_3	14628(3)	0-0	P3(2)	14628.64
D_3	14704(1)	0-0	Q3(1)	14703.54
E_3	14713(1)	0-0	Q3(2)	14712.36
d_3	14718(1)	1-1	Q3(1)	14717.93
F_3	14718(2)	0-0	Q3(3)	14718.37
G_3	14741(2)	0-0	R3(0)	14740.98
H_3	14787(1)	0-0	R3(1)	14787.26
h_3	14799(1)	1-1	R3(1)	14798.66
A_1	14809(3)	0-0	Q1(3)	14805.51
B_1	14816(2)	0-0	Q1(2)	14816.39
C_1	14830(1)	0-0	Q1(1)	14829.99
c_1	14845(1)	1-1	Q1(1)	14844.82
D_1	14868(2)	0-0	R1(0)	14867.43
E_1	14891(1)	0-0	R1(1)	14891.29
e_1	14904(2)	1-1	R1(1)	14903.5
F_1	14918(2)	0-0	R1(2)	14917.69
G_1	14929(4)	0-0	S1(0)	14928.74
H_1	14945(2)	0-0	R1(3)	14945.97
I_1	14993(2)	0-0	S1(1)	14992.58
i_1	15001(2)	1-1	S1(1)	15000.67

Table 6.1: Peak positions, assignments, and calculated energies for detachment transitions for the cryo-SEVI and IR cryo-SEVI spectra of the $\tilde{X}^2\Pi \leftarrow \tilde{X}^1\Sigma^+$ photodetachment of OH^- in Figure 6.1. Transitions from vibrationally-excited anions are shown in red. All values are reported in cm^{-1} and uncertainties in peak positions correspond to one standard deviation obtained from a Gaussian fit to the high-resolution scan of the experimental peak.
*Reported transition energies were calculated based on the experimental values of R3(0) and R1(0), reported by Goldfarb,[75] and the expected shifts in energy based on rotational energy level spacings reported by Rosenbaum and Mélen.[304,373]

constant, c is the speed of light, B_0 is the rotational constant of OH^- (18.7354(16) cm^{-1}),[75] k_b is Boltzmann's constant, and T is the rotational temperature of the anion. When comparing the intensities of these two peaks at a photodetachment energy of 666.48 nm, a rotational temperature of roughly 25K is estimated, which is only slightly higher in temperature than the cryogenic trap and similar to rotational temperatures of OH^- measured by Otto *et al.* while held in a 22-pole RF ion trap held at 8 K.[378]

In the IR cryo-SEVI spectrum (Figure 6.1b), the R(0) rovibrational transition of OH^- anions was pumped using 2.78 μm (3591 cm^{-1}) light on alternating experimental cycles prior to photodetachment, forming anions in the (ν", J") = (1,1) rovibrational level. In these spectra, there is a clear reduction in the relative intensities of peaks G3 and D1, indicating a $\sim$30% depletion of the (0,0) population of the detached anions. Conversely, five new features appear (d_3, h_3, c_1, e_1 and i_1) and correspond well with the calculated values for detachment from the (1,1) rovibrational level of OH^- to the (ν', J') = (1,3/2) and (1,5/2) levels in the $^2\Pi_{3/2}$ state and to the (1,1/2), (1,3/2), and (1,5/2) levels in the $^2\Pi_{1/2}$ state. These, in fact, are all of the expected transitions from a J" = 1 rotational level in the anion based on the $\Delta J = \pm 1/2, \pm 3/2$ selection rule. Each appears within 15 cm^{-1} of a nearby ground-state transition due to the slight difference in vibrational frequency between the anion and neutral, demonstrating the necessity for a high-resolution technique, such as cryo-SEVI, to resolve these features. Note that although the 0-1 hot band photodetachment transition would be well separated from the ground state SEVI transitions, the Franck-Condon factor for this transition is roughly four orders of magnitude smaller than that for the 0-0 transition, hence observation of 0-1 rovibrational transitions via cryo-SEVI would be exceptionally challenging.

Figure 6.1c shows the IR cryo-SEVI difference spectrum, calculated by subtracting the photoelectron distribution of the cryo-SEVI spectrum from that of the IR cryo-SEVI spectrum and normalizing to the G_3 depletion feature. Transitions arising from vibrationally excited anions in the IR cryo-SEVI spectrum appear as positive features in the difference spectrum, while transitions from states depleted by vibrational excitation appear as negative features. As the cryo-SEVI and IR cryo-SEVI spectra are acquired simultaneously, experimental variations in ion signal or detachment laser power should affect both spectra identically, greatly simplifying the comparison of these data and the generation of difference spectra. However, slight variations are still present, which can lead to peaks from the non-excited spectrum appearing in the difference spectrum, such as peak E_1 appearing as a positive peak, as well as causing noise in the difference spectrum that could be mistaken for very weak signal – this is most prevalent in the high eBE range of Figure 6.1c, where the weak feature i_1 is comparable in intensity to noise.

IR cryo-SEVI can also be used as an infrared spectroscopic technique, capable in principle of determining the vibrational spectra of cryogenically cooled anions. Typically, anion vibrational frequencies are mapped out with action spectroscopic techniques in which anions are complexed with weakly bound "tags" such as Ar or D_2 that are shed when the anion is vibrationally excited.[116,230] These tags can result in small perturbations of the anion vibrational frequencies. IR cryo-SEVI circumvents this effect by instead scanning the output of the OPO/OPA while monitoring the electron signal – a maximum in the sequence band intensity in the cryo-SEVI spectrum should be achieved when the IR frequency matches the transition energy. This is shown in Figure 6.3a, which displays representative IR cryo-SEVI spectra in this IR scanning mode where feature h_3 grows in as the photon energy is scanned through the R(0) transition in OH^-. The uncertainty in the anion vibrational frequency determined by this method can be related to the intensity of the feature as a function of IR wavelength – plotting the integrated area of h_3 as a function of energy and fitting it to a

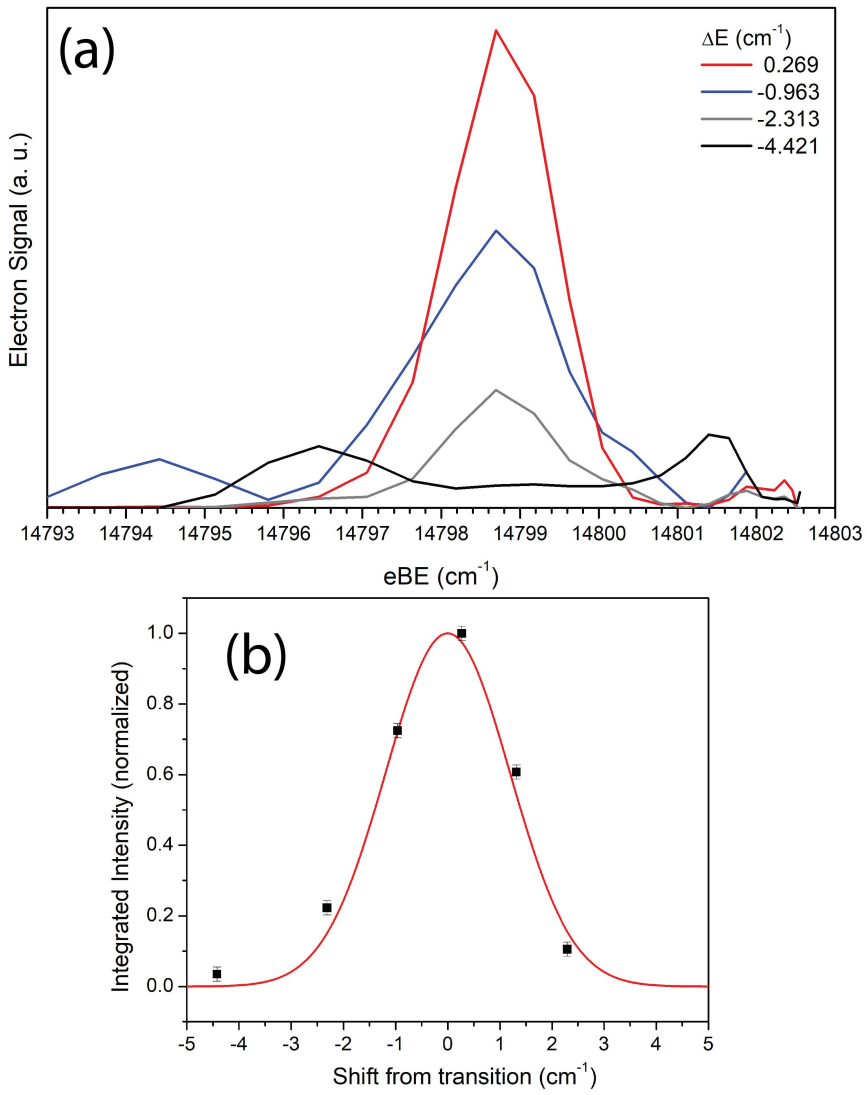

Figure 6.3: (a) Representative IR cryo-SEVI spectra of feature h_3 taken with a fixed detachment frequency ($h\nu$ = 14802.5 cm^{-1}) while the IR wavelength is scanned across the R(0) transition of OH^-. (b) Plot of integrated intensity of h_3 as a function of IR wavelength (black squares) and fit to Gaussian (red trace). The integrated intensity is normalized to the most intense transition measured.

Gaussian distribution, as is plotted in Figure 6.3b, returns a FWHM of 2.80 cm^{-1}, comparable to the reported bandwidth of the LaserVision output. One-sigma errors in the reported vibrational frequency are then 1.2 cm^{-1}. In the case of OH^-, we find the R(0) rovibrational transition energy to be 3591(1.2) cm^{-1}, encompassing the value of 3591.5254 cm^{-1} measured by Rosenbaum *et al.*[304] The six IR cryo-SEVI spectra used to generate the IR spectrum

in Figure 6.3b were each accumulated for around 20,000 experimental cycles, equating to roughly 1.5 hours of data collection in total. Compared to infrared photodissociation of tagged anions, the necessity of obtaining a reasonably high quality photoelectron spectrum at each IR wavelength limits the utility of IR cryo-SEVI as a means of obtaining an infrared spectrum over a large frequency range, but improved collection and data analysis methods may narrow this gap in the near future.

The large rotational constant of the hydroxide anion made it possible to monitor the effect of IR excitation on specific rotational transitions in the cryo-SEVI spectrum, which would typically not be feasible for polyatomic systems. However, in our experience, the rotational profiles of cryo-cooled anions are around 5 cm^{-1} wide,[5] which matches well with the 3 cm^{-1} bandwidth of the IR laser system. It should thus be possible to vibrationally excite most of the anion population and observe new vibrational features in the photoelectron spectrum from transitions to neutral vibrational levels that are inaccessible from the anion ground state. One can, for example, excite IR active, non-totally symmetric modes in the anion, as this will enable one to access normally inactive, non-totally symmetric modes of the neutral species. Such an experiment would be of particular interest for the vinylidene anion H_2CC^-, where it has been shown that excitation of non-totally symmetric modes of neutral H_2CC drives isomerization to HCCH.[41] This experiment will be facilitated by previously measured and calculated vibrational frequencies for the vinylidene anion.[295,296] Overall, the range of applicability of IR cryo-SEVI remains to be determined, but any anion with a relatively isolated vibrational origin transition in its cryo-SEVI spectrum is a viable candidate.

6.5 Conclusion

We introduce a new technique, slow photoelectron velocity-map imaging of cryogenically cooled anions with selective vibrational excitation (IR cryo-SEVI), which combines infrared vibrational excitation with the high photoelectron energy resolution of cryo-SEVI. The efficacy of this technique is demonstrated on a diatomic, OH^-, through the appearance of new features in the photoelectron spectrum after vibrational excitation, corresponding to all observable photodetachment transitions from the $\nu = 1$, J = 1 level of the anion. These results highlight the capabilities of IR cryo-SEVI to probe unexplored regions of neutral potential energy surfaces via selective addition of sequence bands along normal coordinates that would normally be inactive owing to Franck-Condon considerations, as well as a new action technique capable of collecting vibrational spectra of anions with $\sim$1 cm^{-1} resolution.

Chapter 7

Vibronic Structure of C_7 and C_9

The content and figures of this chapter are reprinted or adapted with permission from M. C. Babin, J. A. DeVine, M. L. Weichman, D. M. Neumark, "Slow photoelectron velocity-map imaging of cold C_7^- and C_9^-" *J. Chem. Phys.* **149**, 174306 (2018).

7.1 Abstract

High-resolution anion photoelectron spectra of cryogenically cooled C_7^- and C_9^- clusters obtained using slow photoelectron velocity-map imaging are presented, providing insight into the vibronic structure of neutral C_7 and C_9. These spectra yield accurate measurements of vibrational frequencies for the neutral clusters as well as electron affinities of 3.3517(4) and 3.6766(14) eV for C_7 and C_9, respectively. In the C_7^- spectrum, transitions involving the previously unreported ν_1 and ν_2 symmetric stretching modes, as well as the ν_9, ν_{10}, and ν_{11} asymmetric bending modes, are assigned. Spin-orbit splitting is observed for several transitions in this spectrum, giving an energy difference of 28(6) cm^{-1} between the $^2\Pi_{1/2g}$ and $^2\Pi_{3/2g}$ spin-orbit levels of the C_7^- anion. In the spectrum of C_9^-, transitions involving the previously unreported symmetric stretch ν_1 and the asymmetric bend ν_{11} are observed. In both spectra, several features are assigned to Franck-Condon forbidden transitions involving the doubly-degenerate ν_{10} and ν_{11} modes of C_7 and the ν_{13} and ν_{14} modes of C_9. The appearance of these transitions is attributed to Herzberg-Teller coupling between electronic states of the neutral clusters. Additional FC-forbidden transitions to states previously observed in gas-phase infrared experiments are observed and attributed to vibronic coupling between electronic states of the anion, resulting in non-totally-symmetric character in the anion's full vibrational ground state. Finally, consideration of the energy dependence of detachment cross sections and Dyson orbital analyses reveal that addition of more carbon atoms to the linear chain results in photodetachment from delocalized molecular orbitals with increasing nodal structure, leading to threshold photodetachment cross sections that differ considerably from simple symmetry considerations.

7.2 Introduction

Carbon clusters (C_n) are an extensively-researched family of clusters with relevance to interstellar, plasma, and combustion chemistry.[195–198,382] Spectroscopic signatures of small ($n < 10$) carbon clusters have been identified in a variety of astrochemical measurements, establishing their presence in comets,[199] the circumstellar shells of carbon-rich stars,[200,201] and the interstellar medium.[202] Given the apparent ubiquity of these species throughout the known universe, there is considerable interest in accurate measurements of their vibrational frequencies and energetics, as these quantities aid in the assignments of astronomical data and in the formulation of chemical mechanisms by which these species are generated and depleted. Here, we report high-resolution anion photoelectron spectra of cryogenically cooled C_7^- and C_9^- linear carbon chains, providing a number of previously unreported vibrational frequencies and insight into the vibronic structure of these important species.

The vast body of experimental and theoretical work concerning carbon clusters has demonstrated clear structural trends in the anionic and neutral C_n species. Small carbon clusters ($n < 10$) containing an odd number of atoms have linear geometries while even-numbered clusters have additional energetically low-lying ring structures.[383–385] Larger species ($n \geq 10$) preferentially form rings and fullerenes.[386,387] Following this trend, both neutral and anionic C_7 and C_9 are found to be linear cumulenes through experimental and theoretical studies. The neutral clusters have been characterized with ion mobility spectrometry,[388] matrix isolation spectroscopy,[389–396] infrared laser absorption spectroscopy,[394–404] resonant multiphoton ionization spectroscopy,[405] and electronic structure calculations.[385,406–408] This body of work shows that both neutral species have closed-shell $^1\Sigma_g^+$ ground electronic states.[384,406,409] While not as well-characterized as their neutral counterparts, the C_7^- and C_9^- anions have been found to have open-shell $^2\Pi_g$ and $^2\Pi_u$ ground states, respectively, from investigations using rare gas matrices,[391,410–412] resonance enhanced multiphoton electron detachment,[413–415] and electronic structure calculations.[416–418]

Anion photoelectron spectroscopy (PES) is a powerful technique for interrogating the vibronic structure of size-selected neutral clusters via photodetachment of the corresponding anion.[366,367] The first PES study on C_7^- and C_9^- was carried out by Yang and coworkers,[419] though these spectra did not have sufficient resolution to extract any vibrational properties of the neutral clusters. Higher resolution PE spectra by Arnold *et al.*[420] yielded vibrationally-resolved spectra and electron affinities (EAs) of 3.358(14) and 3.684(10) eV for C_7 and C_9. Several neutral vibrational frequencies were extracted from these experiments, but these spectra showed considerable additional unresolved vibrational structure underlying the more intense transitions.

Slow electron velocity-map imaging of cryogenically-cooled anions (cryo-SEVI) is a high-resolution variant of traditional anion PES wherein cryogenically-cooled anions are detached by a tunable laser. The resultant electrons are then detected using a velocity-map imaging (VMI) spectrometer optimized for the detection of slow electrons, giving photoelectron spectra with sub-meV resolution.[5] Previously, we have applied this technique to the C_5^- carbon chain.[54,108] Here, we report cryo-SEVI spectra of $C_7^-$and C_9^-, revealing considerably more

vibrational structure than was seen by Arnold *et al*,[420] much of which can be assigned by comparison to Franck-Condon (FC) simulations and enabling the measurement of previously unreported vibrational frequencies for C_7 and C_9. The spectra also show spin-orbit structure, giving a splitting of 28(6) cm^{-1} for the C_7^- anion, and provide refined EAs of 3.3517(4) and 3.6766(14) eV for C_7 and C_9. A number of FC-forbidden features are observed for both clusters and are attributed to vibronic coupling effects in either the neutral or anionic species, depending on the symmetry of the neutral excited vibrational state. Finally, an inspection of the photon energy dependence of the cryo-SEVI spectra, complemented by a Dyson orbital analysis, suggests that increasing the length of small linear carbon chains results in the detachment of photoelectrons with higher angular momentum than expected based purely on symmetry considerations.

7.3 Experimental methods

The cryo-SEVI method has been described in detail previously.[34,35,54] In this work, carbon cluster anions are generated with a laser ablation source using a frequency-doubled Nd:YAG laser focused onto a rotating and translating graphite disk. The resulting plasma is entrained within a pulse of He carrier gas from an Even-Lavie solenoid valve[245] before passing through a skimmer. The ions then pass through a radiofrequency (RF) hexapole ion guide and a RF quadrupole mass filter before being directed into a linear RF octupole ion trap held at 5 K and filled with a buffer gas mixture of 20:80 H_2:He. Collisions with the cold buffer gas result in effective vibrational, rotational, and electronic cooling of the ions, leading to internal temperatures of around 10 K.[54,239]

After approximately 40 ms, the ions are extracted into an orthogonal Wiley-McLaren time-of-flight mass spectrometer[259] and focused into the interaction region of a VMI electrostatic lens assembly.[18] The cryo-SEVI spectra of C_7^- and several of the C_9^- scans were taken using a standard three-plate Eppink-Parker VMI lens assembly, while the remainder of the C_9^- data was taken using an updated design utilizing a seven-plate VMI lens.[36] In the VMI spectrometer, ions are photodetached by the frequency-doubled output of a dye laser pumped by the second harmonic of a Nd:YAG laser operating at 20 Hz.

The resulting photoelectrons are projected onto a 2D detector comprising two chevron-stacked microchannel plates coupled to a phosphor screen, which is photographed by a CCD camera after each laser shot.[17] Each image is analyzed for individual electron events for which the centroids are calculated and binned in a 1024 $\times$ 1024 grid.[271] The three-dimensional electron velocity distribution is reconstructed from the accumulated images using the Maximum Entropy Velocity Legendre Reconstruction (MEVELER) algorithm.[275] The radial position of features in the reconstructed image is related to electron kinetic energy (eKE) by acquiring VMI images for detachment from atomic F^- at several photon energies.[280]

In addition to the eKE distributions, VMI provides the photoelectron angular distribution (PAD) associated with each detachment transition, given by[91]

$$\frac{d\sigma}{d\Omega} = \frac{\sigma_{tot}}{4\pi}\left[1 + \beta P_2(\cos\theta)\right] \tag{7.1}$$

where σ_{tot} is the total detachment cross section, $P_2(x)$ is the second-order Legendre polynomial, θ is the angle of the outgoing photoelectron with respect to the laser polarization axis, and β is the anisotropy parameter. The anisotropy parameter, which ranges from -1 (perpendicular detachment) to +2 (parallel detachment), reflects the angular momentum of the detached electron and is thus tied to the electronic character of each photodetachment transition.[361]

The VMI spectrometer has an approximately constant resolving power, ΔeKE/eKE,[18] yielding the best eKE resolution for slow electrons. As such, a SEVI spectrum is acquired by first taking an overview spectrum at a relatively high photon energy before tuning the detachment laser to energies slightly above features of interest. This procedure results in a collection of high-resolution spectra over narrow energy windows that are concatenated and scaled to match intensities in the overview spectrum, which is less sensitive to variation of the photodetachment cross section with photon energy. Spectra are plotted as a function of electron binding energy (eBE), given by eBE = hν - eKE.

7.4 Computational methods

Electronic structure calculations for $C_7^{0/-}$ were carried out at the RCCSD(T)/aug-cc-pVTZ level of theory[421–423] in order to determine the geometries, normal modes, and harmonic frequencies of the anionic and neutral clusters. Due to the computational expense of performing calculations on $C_7^{0/-}$ at the RCCSD(T) level, the MP2/cc-pVDZ level of theory was chosen to calculate the geometries, normal modes, and harmonic frequencies of $C_9^{0/-}$ given its successes in previous studies of carbon clusters[393,424] and similar performance compared to the CCSD(T) level of theory for small clusters.[425] Calculations for $C_7^{0/-}$ were carried out using the Molpro 2010.1 software package,[426] while those for $C_9^{0/-}$ were performed using Gaussian 09.[427] Clusters were restricted to linear geometries, as recommended by previous theoretical and experimental studies.[384,409,420] Calculated electron affinities are zero-point corrected and calculated geometries are presented in Tables 7.5 and 7.6 of the supplementary material (Section 7.8).

The equilibrium geometries and normal modes were used to calculate the Franck-Condon profile for the $\tilde{X}^1\Sigma_g^+ \leftarrow \tilde{X}^2\Pi_g$ and $\tilde{X}^1\Sigma_g^+ \leftarrow \tilde{X}^2\Pi_u$ detachment transitions of C_7^- and C_9^-, respectively, with the ezSpectrum v3.0 software package.[175] All modes were treated in the harmonic approximation and FC overlap integrals were calculated using full Duschinsky mixing of all normal modes.[176] To better match experiment, FC simulations presented in Figure 7.1 use scaled vibrational frequencies as described in Section 7.8.4 of the SM and presented in Tables 7.7 and 7.8. Those using calculated frequencies are presented in Figure 7.5 and 7.6 of the SM, alongside the experimental spectra.

Dyson orbitals for the $\tilde{X}^1\Sigma_g^+ \leftarrow \tilde{X}^2\Pi_g$ and $\tilde{X}^1\Sigma_g^+ \leftarrow \tilde{X}^2\Pi_u$ detachment transitions of C_7^- and C_9^-, respectively, were calculated using Q-Chem 4.4 at the EOM-EA-CCSD/6-311++G** level.75-77 These orbitals are one-electron wavefunctions that reflect the change in electronic structure of the anion upon detachment.[428,429] They were used as an input for the ezDyson v4.0 software package[99] to calculate the total detachment cross section and the partial wave component decomposition of the outgoing electron as a function of eKE (see Table 7.9 in the SM) by determining the overlap of the Dyson orbital with a plane-wave expansion in a spherical wave basis at the centroid of the Dyson orbital.[98] The resultant anisotropy parameters as well as those extracted from experiment are shown in Figure 7.7 and 7.8 of the SM and the cross sections are discussed in Section 7.6.3.

Excited state energies for $C_7^{0/-}$ and $C_9^{0/-}$ clusters were calculated utilizing the time-dependent density functional theory (TDDFT) framework at the B3LYP/cc-pVDZ level within Q-Chem 4.4.[430] Calculations were performed using the optimized ground state geometries. To assess the likelihood of vibronic coupling playing a role in the experimental spectra, the derivative coupling vectors[431] (see Section 7.8.3 of SM) between the neutral ground states and excited $^1\Pi_u$ and $^1\Sigma_u^+$ states were calculated for both neutral clusters at the same level of theory. These vectors are illustrated in Figure 7.9 and 7.10 of the SM and discussed in Section 7.6.2.

7.5 Results

The cryo-SEVI spectra of the $\tilde{X}^1\Sigma_g^+ \leftarrow \tilde{X}^2\Pi_g$ and $\tilde{X}^1\Sigma_g^+ \leftarrow \tilde{X}^2\Pi_u$ transitions of C_7^- and C_9^- are presented in Figure 7.1a and Figure 7.1b, respectively. In both figures, lower resolution overview spectra taken relatively far from threshold (blue) are shown atop higher resolution SEVI scans (black) taken at several photon energies. Simulated FC profiles, scaled to match the intensity of peak A1, are shown as red sticks.

The spectra of both species are dominated by a single peak (A1) attributed to the vibrational origin, above which considerable vibrational structure is resolved spanning ~ 3000 cm^{-1} in eBE. In the spectrum of C_7^-, a less intense peak (A1') lies 28 cm^{-1} below A1. As our experiment yields vibrationally cold anions,[239] it is unlikely that this structure below the vibrational origin corresponds to a vibrational hot band. We thus assign A1 and A1' to detachment from the lower ($^2\Pi_{1/2g}$) and upper ($^2\Pi_{3/2g}$) spin-orbit state of the anion, respectively, to the vibrational ground state of the $^1\Sigma_g^+$ neutral. The minimum peak width achievable for features A1 in the spectrum of C_7^- and C_9^-, respectively, is 6 and 22 cm^{-1}.

Beyond the vibrational origin, both high-resolution spectra reveal two sets of peaks (A2-A10/B1-B13 in the C_7^- spectrum and A2-A10/B1-B6 in the C_9^- spectrum) that correspond to transitions to vibrationally excited states of neutral C_7 and C_9. Positions in eBE and assignments (see Section 7.6) of these features are summarized in Tables 7.1 and 7.2 for the spectra of C_7^- and C_9^-, while calculated and experimental parameters obtained for C_7 and C_9, along with literature values, are summarized in Tables 7.3 and 7.4, respectively. Features are assigned as belonging to the "A" or "B" series of peaks based on several attributes. As

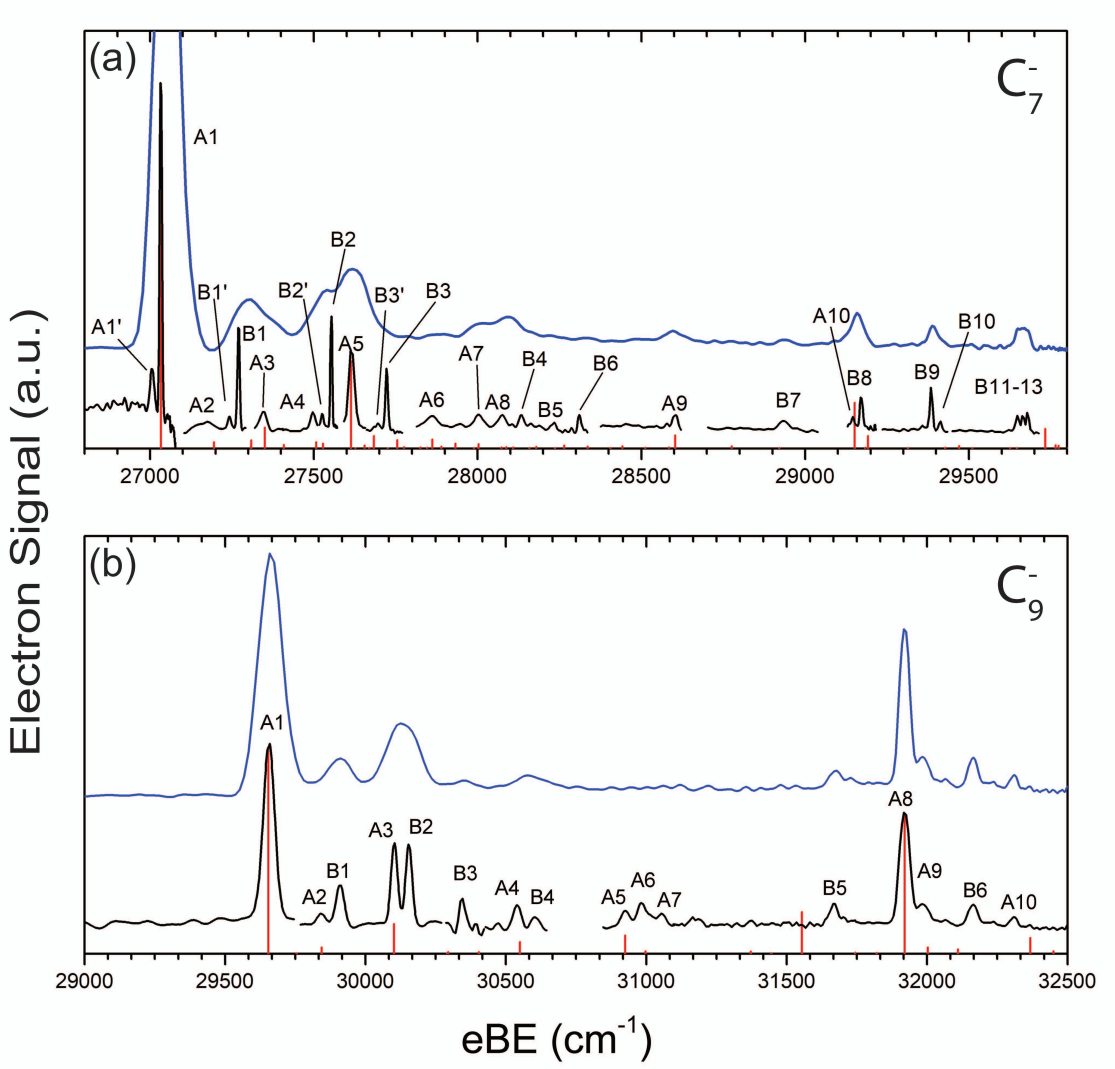

Figure 7.1: (a) Representative IR cryo-SEVI spectra of feature h_3 taken with a fixed detachment frequency ($h\nu$ = 14802.5 cm^{-1}) while the IR wavelength is scanned across the R(0) transition of OH^-. (b) Plot of integrated intensity of h_3 as a function of IR wavelength (black squares) and fit to Gaussian (red trace). The integrated intensity is normalized to the most intense transition measured.

discussed below, the "A" and "B" peaks exhibit differing degrees of attenuation at low eKE as well as differing photoelectron angular distributions (in the case of C_7^-). Additionally, only the "A" peaks appear in Franck-Condon simulations of the spectra.

Peak	eBE (cm^{-1})	Shift (cm^{-1})	Assignment
A1'	27005(5)	-28	0_0^0
A1	27033(3)	0	0_0^0
A2	27195(31)	162	11_0^2
B1'	27242(5)	209	10_0^1
B1	27270(3)	237	10_0^1
A3	27346(11)	313	$10_0^1 11_0^1$
A4	27499(10)	467	10_0^2
B2'	27526(4)	493	$10_0^2 11_0^1$
B2	27553(2)	521	$10_0^2 11_0^1$
A5	27614(14)	581	3_0^1
B3'	27696(4)	663	10_0^3
B3	27722(4)	690	10_0^2
A6	27860(15)	827	9_0^2
A7	28004(15)	971	7_0^2
A8	28076(11)	1044	$3_0^1 10_0^2$
B4	28131(2)	1098	$3_0^1 10_0^2 11_0^1$
B5	28231(7)	1198	$7_0^2 10_0^1$
B6	28311(5)	1278	$3_0^1 10_0^3$
A9	28602(10)	1570	2_0^1
B7	28931(11)	1899	5_0^1
A10	29152(14)	2119	1_0^1
B8	29171(3)	2138	4_0^1
B9	29385(4)	2352	$1_0^1 10_0^1$
B10	29412(4)	2380	$2_0^1 10_0^3 11_0^1$
B11	29647(6)	2614	$2_0^1 10_0^4 11_0^1$
B12	29664(4)	2631	$2_0^1 3_0^1 10_0^2$
B13	29679(4)	2647	$1_0^1 10_0^2 11_0^1$

Table 7.1: Peak positions, shifts from peak A1, and assignments for the SEVI spectra of the $\tilde{X}^1\Sigma_g^+ \leftarrow \tilde{X}^2\Pi_g$ photodetachment of C_7^- given in Figure 7.1a. All transitions originate from the $\tilde{X}^2\Pi_{1/2u}$ state of the anion except those marked with a prime; these transitions originate from the $\tilde{X}^2\Pi_{3/2u}$ anion state. Uncertainties in peak positions correspond to one standard deviation obtained from a Gaussian fit to the high-resolution scan of the experimental peak.

Peak	eBE (cm-1)	Shift (cm-1)	Assignment
A1	29654(11)	0	0_0^0
A2	29844(17)	190	11_0^2
B1	29906(7)	252	14_0^1
A3	30102(12)	448	4_0^1
B2	30152(4)	498	13_0^1
B3	30344(11)	690	$4_0^1 14_0^1$
A4	30560(14)	906	4_0^2
B4	30604(4)	950	$4_0^1 13_0^1$
A5	30924(16)	1270	3_0^1
A6	30984(19)	1330	4_0^3
A7	31049(23)	1395	$4_0^2 14_0^2$
B5	31669(16)	2015	6_0^1
A8	31920(18)	2266	1_0^1
A9	31987(22)	2333	$4_0^3 13_0^2$
B6	32173(9)	2519	$1_0^1 14_0^1$
A10	32307(14)	2653	$1_0^1 4_0^1$

Table 7.2: Peak Positions, shifts from peak A1, and assignments for the SEVI spectra of the $\tilde{X}^1\Sigma_g^+ \leftarrow \tilde{X}^2\Pi_u$ photodetachment of C_9^- given in Figure 7.1b. Uncertainties in peak positions correspond to one standard deviation obtained from a Gaussian fit to the high-resolution scan of the experimental peak.

For both clusters, the distinction between these two groups of features is best depicted in Figure 7.2 where the intensity of A1 relative to B1 is shown at several photon energies. Far from threshold (blue curve), A1 is more intense than B1, but as the photon energy decreases, corresponding to detachment of lower-eKE electrons, the cross section of feature A1 is more rapidly attenuated leading to a lower relative intensity. Such differences in the threshold behavior can be related to the relative scaling of the detachment cross sections for low-eKE detachment, which is given by the Wigner threshold law,[81]

$$\sigma \propto (\text{eKE})^{\ell+1/2} \tag{7.2}$$

where σ is the detachment cross section and ℓ is the angular momentum of the detached electron. According to Eq. 7.2, photodetachment is suppressed more strongly at low eKE for detachment of higher ℓ electrons, owing to the centrifugal barrier experienced by the departing electron. Hence, the "A" peaks appear to correspond to detachment at higher values of ℓ than the "B" peaks. As a consequence, spectra for the "B" peaks can be obtained closer to threshold where cryo-SEVI resolution is better, leading to narrower features. Note that peaks A1 and B1 can be seen at considerably lower eKE values for C_7^- than for C_9^-. Since the resolution of cryo-SEVI is highest at low eKE, this difference leads to the larger

minimum peak width of A1 in the C_9^- spectrum, a point considered in more detail in Section 7.6.3.

Parameter	RCCSD(T)	Cryo-SEVI	Literature
EA (eV)	3.2677	3.3517(4)	3.358(14)[a]
ν_1	2159	2119(14)	
ν_2	1554	1570(10)	
ν_3	570	581(14)	548(90)[a]
ν_4	2198	2138(11)	2138.315[b]
ν_5	1922	1899(5)	1898.376[c]
ν_6	1080		1100.1[d]
ν_7	476	485(10)	496(110)[a]
ν_8	138		
ν_9	449	414(15)	
ν_{10}	240	237(5)	
ν_{11}	60	81(22)	

Table 7.3: Experimental parameters for C_7 extracted from the cryo-SEVI spectrum of the corresponding anion and comparison to the theoretical values obtained in the current work (RCCSD(T)/aug-cc-pVTZ) as well as available literature values. Note that the frequency for ν_{10} is determined from the location of feature B1, as this provides a more precise value than that of A4.
[a] = Ref [420], [b] = Ref [397], [c] = Ref [400], [d] = Ref [396]

Parameter	MP2	Cryo-SEVI	Literature
EA (eV)	4.3029	3.6766(14)	3.684(10)[a]
ν_1	2260	2266(21)	
ν_2	1901		1871[b]
ν_3	1246	1270(19)	1258(50)[a]
ν_4	450	448(17)	484(48)[a]
ν_5	2415		2079.67[c]
ν_6	2104	2015(19)	2014.278[d]
ν_7	1608		1601[e]
ν_8	865		
ν_9	579		
ν_{10}	320		
ν_{11}	131	95(15)	
ν_{12}	635		
ν_{13}	477	498(17)	
ν_{14}	230	252(12)	
ν_{15}	51		

Table 7.4: Experimental parameters for C_9 extracted from the cryo-SEVI spectrum of the corresponding anion and comparison to the theoretical values obtained in the current work (MP2/cc-pVDZ) as well as available literature values.
[a] = Ref [420], [b] = Ref [432], [c] = Ref [402], [d] = Ref [401], [e] = Ref [395]

The partial wave components that play a role in Eq. 7.2 are intimately connected to the PADs of different detachment transitions, and differences in threshold behavior often occur concurrently with different PADs.[65] Figure 7.7 shows that at low eKEs, the PADs of all features in the C_7^- spectrum are nearly isotropic ($\beta \approx 0$). As the photon energy increases, a discrepancy between the measured values of β for features A1 and B1 begins to form, with feature B1 maintaining $\beta \approx 0$ and peak A1 showing a more negative anisotropy. This pattern is not apparent in the C_9^- spectrum; Figure 7.8 shows that features A1 and B1 display similar PADs, with roughly isotropic ($\beta \approx 0$) distributions at eKEs ranging from 0.01-0.37 eV.

In order to better understand the differing threshold behavior and PADs of these two classes of features, we used the ezDyson software package to calculate total cross sections for the $\tilde{X}^1\Sigma_g^+ \leftarrow \tilde{X}^2\Pi_g$ and $\tilde{X}^1\Sigma_g^+ \leftarrow \tilde{X}^2\Pi_u$ transitions of C_5^-, C_7^- and C_9^-, shown in Figure 7.4. These calculations also provided the expected value of β for these transitions (Figure 7.7 and 7.8 in the SM) and the partial wave component for the detached electron (Table 7.9 in the SM) as functions of eKE. While all cross sections increase monotonically with eKE, the curvature of the cross section is more complex for C_9^- than for the other two clusters. The predicted value of β for detachment from C_7^- as a function of eKE is slightly positive at low eKE (0.01 eV) and decreases dramatically as the eKE increases (0.75 eV), while that

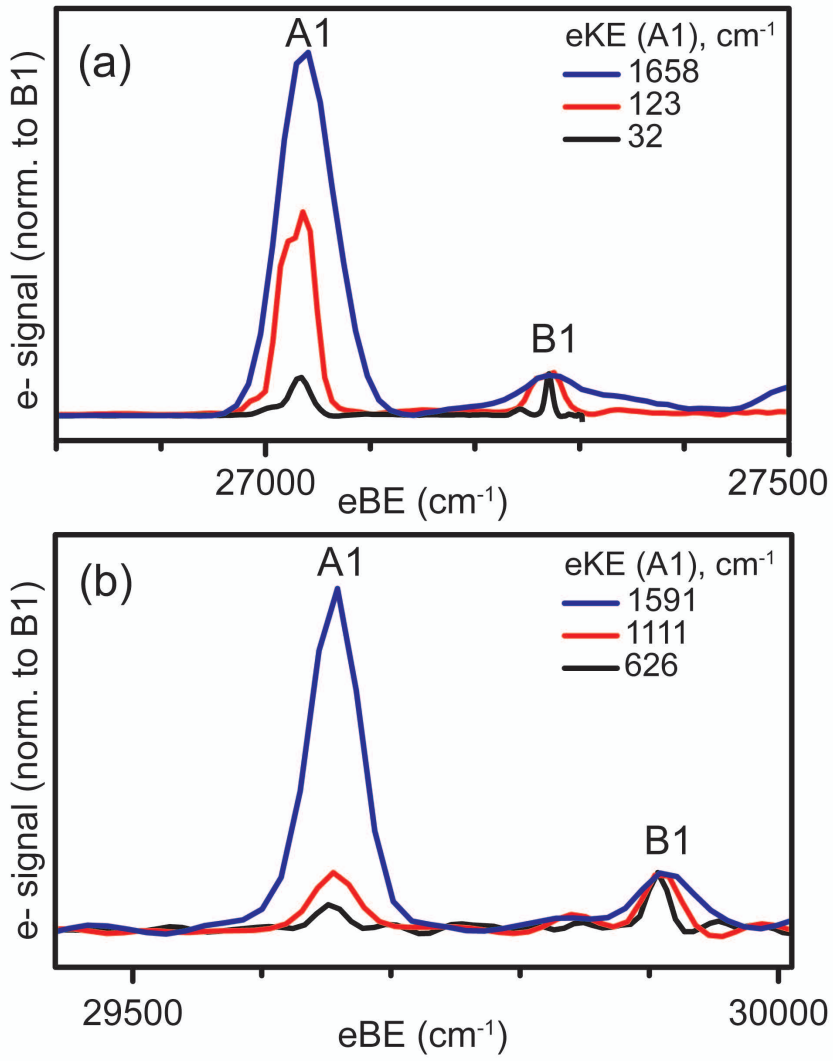

Figure 7.2: (a) Representative IR cryo-SEVI spectra of feature h_3 taken with a fixed detachment frequency ($h\nu$ = 14802.5 cm^{-1}) while the IR wavelength is scanned across the R(0) transition of OH^-. (b) Plot of integrated intensity of h_3 as a function of IR wavelength (black squares) and fit to Gaussian (red trace). The integrated intensity is normalized to the most intense transition measured.

of the C_9^- spectrum is nearly isotropic ($\beta \approx 0$) at low-eKEs and becomes roughly parabolic over a similar energy range.

These quantities are intimately related to the Dyson orbitals, which represent the molecular orbital from which the photoelectron is detached.[98,429] Our calculated Dyson orbitals for detachment from C_7^- and C_9^-, presented in Figure 7.3, are not localized around a single atom as in the case of photodetachment from closed shell anions to form free radicals,[36,433,434] but

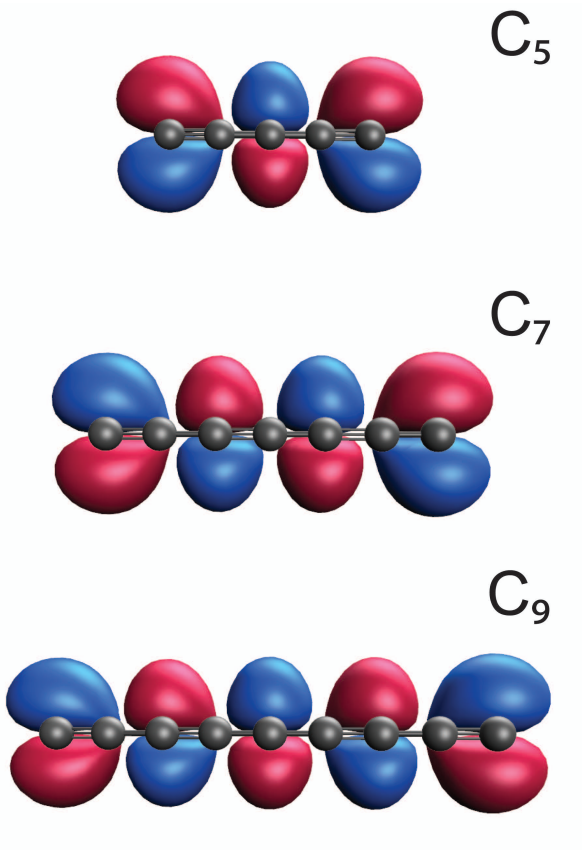

Figure 7.3: (a) Representative IR cryo-SEVI spectra of feature h_3 taken with a fixed detachment frequency ($h\nu$ = 14802.5 cm^{-1}) while the IR wavelength is scanned across the R(0) transition of OH^-. (b) Plot of integrated intensity of h_3 as a function of IR wavelength (black squares) and fit to Gaussian (red trace). The integrated intensity is normalized to the most intense transition measured.

encompass the entire carbon chain. Additionally, these calculations reveal that the Dyson orbitals display an increasing number of nodes as the chain is lengthened from 5 to 9 atoms. The implications of these findings will be discussed in more detail in Section 7.6.3.

7.6 Discussion

7.6.1 Franck-Condon allowed features

The vibrational assignments of peaks in the C_7^- and C_9^- cryo-SEVI spectra are provided in Tables 7.1 and 7.2, respectively. These assignments were informed by the results of our FC simulations as well as the previously reported photoelectron spectrum by Arnold *et al.*[420]

Features A1-A10 in the spectra of C_7^- and C_9^- are largely reproduced in the simulated spectra, and are thus assigned to Franck-Condon allowed transitions within the $\tilde{X}^1\Sigma_g^+ \leftarrow \tilde{X}^2\Pi_g$ and $\tilde{X}^1\Sigma_g^+ \leftarrow \tilde{X}^2\Pi_u$ photodetachment bands of C_7^- and C_9^-, respectively. FC allowed transitions include all $\Delta\nu$ transitions in totally symmetric vibrational modes (σ_g^+ for these species) and even $\Delta\nu$ transitions in non-totally symmetric modes, with the latter typically being weak for $\Delta\nu \neq 0$. A number of features (B1-B13 in C_7^- and B1-B6 in C_9^-) are not present in the FC simulation and are assigned to FC-forbidden transitions terminating in states with odd quanta of excitation along a π_u or σ_u^+ vibrational mode; these assignments will be justified in the next section. Tables 7.7 and 7.8 list the symmetries for all vibrational modes of both species, as well as experimental and theoretical frequencies.

Several features – A1, A5, and A7 in C_7^-, and A1, A3, and A5 in C_9^- – were resolved in the lower-resolution spectrum of Arnold *et al*;[420] these were assigned as the 0_0^0, 3_0^1, and 7_0^2 transitions in C_7, and the 0_0^0, 4_0^1, and 3_0^1 transitions in C_9. Our improved resolution gives refined values for the EA (3.5117 ± 0.0004 eV) as well as the symmetric stretching and π_g bending frequencies ($\nu_3 = 581 \pm 14$ cm^{-1} and $\nu_7 = 485 \pm 10$ cm^{-1}) of neutral C_7, neglecting anharmonicity in the ν_7 mode. Similarly, we are able to extract improved values for the EA (3.6766 ± 0.0014 eV) as well as the symmetric stretching frequencies ($\nu_3 = 1270 \pm 19$ cm^{-1} and $\nu_4 = 448 \pm 17$ cm^{-1}) of neutral C_9.

In the spectrum of C_7^-, comparison of the cryo-SEVI spectrum to our simulated FC profile allows the assignment of newly-resolved stretch fundamentals 2_0^1 (A9) and 1_0^1 (A10) as well as the doubly excited π_g bends 11_0^2 (A2), 10_0^2 (A4), and 9_0^2 (A6). These give frequencies of 2119(14), 1570(10), 414(15), 234(7), and 81(22) cm^{-1} for the previously unreported ν_1, ν_2, ν_9, ν_{10}, and ν_{11} modes, respectively. A similar analysis in the spectrum of C_9^- allows for the assignment of the stretch fundamental 1_0^1 (A9) and the doubly excited asymmetric bend 11_0^2 (A2), giving frequencies of 2266(21) and 95(15) cm^{-1}, respectively, for these two previously unreported modes.

As a result of the spin-orbit splitting in the $^2\Pi_g$ state of the C_7^- anion, several peaks are split into doublets (A1/A1', B1/B1', B2/B2', B3/B3'). Peaks A1', B1', B2', and B3' each sit 28 cm^{-1} below sharp features with similar labels (A1, B1, B2, and B3, respectively), corresponding to the splitting between the $^2\Pi_{1/2g}$ and $^2\Pi_{3/2g}$ spin-orbit levels of the C_7^- ground state, in good agreement with values calculated at the RCCSD(T) level of theory.[415] Due to the lower intensity of the peaks originating from the $^2\Pi_{3/2g}$ spin orbit state, compounded with the low intensity relative to A1 for features B4-B13 and A2-A10, only the transitions corresponding to detachment from the lower anion spin-orbit level are observed for these vibrational transitions. Based on the intensity ratio A1'/A1 and the extracted spin-orbit splitting, we obtain a spin-orbit temperature of 14 K for C_7^-, consistent with temperatures previously reported for ions cooled in our ion trap.[40,42,54]

7.6.2 Franck-Condon forbidden features

We now consider the vibrational assignments of the "B" series of peaks in both spectra, which are not present in our FC simulations. The spacing in both the B1-A4-B3 progression and between a number of A and B features in the spectrum of C_7^- (A7 $\rightarrow$ B5, A8 $\rightarrow$ B6, A10 $\rightarrow$ B9) is ~ 235 cm^{-1}, which matches well with our experimentally determined value for ν_{10} of 234(7) cm^{-1}. Additionally, the separation between a number of A and B features (B1 $\rightarrow$ A3, A4 $\rightarrow$ B2, A8 $\rightarrow$ B4) is on the order of ~ 60 cm^{-1}, which is congruent with our calculated and experimental values for the ν_{11} mode of 60 and 81(22) cm^{-1}. Similarly, in the spectrum of C_9^-, features B1 and B2 sit 252 and 498 cm^{-1} above the vibrational origin, matching well with our unscaled MP2/cc-pVDZ frequencies of the ν_{14} and ν_{13} bending modes at 230 and 477 cm^{-1}, respectively. We again see other features with anomalous threshold behavior sitting either 250 cm^{-1} (A3 $\rightarrow$ B3, A8 $\rightarrow$ B6) or 500 cm^{-1} (A3 $\rightarrow$ B4) above features with poor threshold behavior, suggesting involvement of the ν_{14} and ν_{13} bending modes in these features as well. We thus tentatively assign peaks B1-B6, B9-B13 in the C_7^- spectrum (B1-B4, B6 in the C_9^- spectrum) to transitions involving odd quanta along the non-totally symmetric ν_{10} and ν_{11} (ν_{14} and ν_{13}) vibrational modes, which are of π_u symmetry.

Such transitions are Franck-Condon forbidden, but can arise from Herzberg-Teller (HT) coupling to an excited electronic state with the appropriate symmetry.[71] Consider vibronic states a and b with electronic and vibrational symmetries Γ_{elec} and Γ_{vib}, respectively. These two states can be HT-coupled provided

$$\Gamma_{TS} \in \Gamma^a_{elec} \otimes \Gamma^a_{vib} \otimes \Gamma^b_{elec} \otimes \Gamma^b_{vib} \tag{7.3}$$

where Γ_{TS} is the totally symmetric representation within the molecular point group. If detachment to state b is FC-allowed, i.e. $\langle b|\Psi_{anion}\rangle \neq 0$, detachment to state a will reflect the electronic character of state b. This will then be reflected in the PADs and threshold behavior of these detachment transitions.

Following Eq. 7.3, these levels with $\Gamma^a_{vib} = \pi_u$ and $\Gamma^a_{elec} = \Sigma^+_g$ can only be observed if they mix with a state b that is FC-allowed for detachment from the anion, i.e. $\Gamma^a_{vib} = \sigma^+_g$. Thus, the observed features must arise from HT-coupling to an excited electronic state of Π_u symmetry. In C_7, such a state has been found experimentally in neon matrices[391] to lie 2.28 eV above the ground electronic state; this has been confirmed by Kolbuszewski who calculated a vertical term energy of 2.64 eV at the MRD-CI(+Q) level.[406] While the analogous excited state for C_9 has not been seen experimentally, our TDDFT calculations indicate a $^1\Pi_u$ state exists 2.80 eV above the ground state of the neutral.

In the case of C_7^-, the presence of vibronic coupling is affirmed by the discrepancy observed in the deferring PADs of features A1 and B1 at high eKE,[14,65] as shown in Figure 7.7. Peaks A1-A10 display a decrease in the anisotropy parameter β with increasing eKE, consistent with our calculated PAD for the $\tilde{X}^1\Sigma^+_g \leftarrow \tilde{X}^2\Pi_g$ transition (see Figure 7.7 in the SM). Conversely, features B1-B13 show isotropic PADs for all eKEs, which is characteristic of $\ell = 0$ detachment channels and consistent with these features originating from a state with different electronic character than that giving rise to A1-A10.

The assignment of these features as involving neutral states with excitation along ν_{10} and ν_{11} (ν_{13} and ν_{14} in C_9) is further supported by the derivative coupling vector[431,435] calculated between the $^1\Sigma_g^+$ ground and the $^1\Pi_u$ excited state of C_7 and C_9, which appear as a superposition of the ν_{10} and ν_{11} (ν_{13} and ν_{14} in C_9) vibrational modes (see Figure 7.9 and 7.10 in the SM). This indicates that the coupling between these electronic states occurs along the ν_{10} and ν_{11} (ν_{13} and ν_{14} in C_9) normal coordinates, resulting in relatively strong mixing of vibronic states involving excitation along these modes.

Note that three features, B7 and B8 in C_7^- and B5 in C_9^-, are assigned to transitions involving odd quanta along the σ_u^+ symmetric ν_5 and ν_4 modes of C_7 and the ν_6 mode of C_9, respectively. These assignments are made based on the agreement between the peak centers (1899, 2138, and 2015 cm^{-1}) and the experimentally observed gas-phase frequencies of 2138.315, 1898.376, and 2014.278 cm^{-1} for the ν_5 and ν_4 modes of C_7 and the ν_6 mode of C_9, respectively.[397–401,404] Transitions involving odd quanta along this FC forbidden mode could be explained by invoking HT-coupling in the neutral, which would require an excited neutral state of Σ_u^+ symmetry according to Eq. 7.3 The lowest state of this symmetry has been observed in neon matrices to reside 5.535 and 4.20 eV above the ground state of C_7 and C_9, respectively.[391] Our calculations at the TD-B3LYP/cc-pVDZ level, however, indicate that the matrix coupling element between the ground electronic and $^1\Sigma_u^+$ excited state of both C_7 and C_9 are identically zero, suggesting these features do not originate from HT-coupling to an excited neutral state.

These nominally FC-forbidden transitions may, however, result from vibronic coupling in the anion. If the vibronic ground state of the anion ($\Gamma_{vib}^a = \sigma_g^+$, $\Gamma_{elec}^a = \Pi_g$ for C_7^- and $\Gamma_{elec}^a = \Pi_u$ for C_9^-) couples to another vibronic level b which has σ_u^+ vibrational symmetry, the b-character in the anion ground state would result in nonzero Franck-Condon overlap with the σ_u^+-symmetric neutral vibrational levels for detachment from the vibrationally cold anions. This would require coupling to an excited state with Π_u (Π_g) symmetry for the C_7^- (C_9^-) anion. Forney and coworkers have observed these states as the lowest-lying excited states for both species, residing 1.978 and 1.622 eV above the ground state[436] of the C_7^- and C_9^- anions, respectively. This proposition is supported by our TD-B3LYP/cc-pVDZ calculations, as the magnitude of the matrix coupling element between the ground and excited state for both anions is comparable to the coupling element between the neutral ground and $^1\Pi_u$ excited state invoked above (see Table 7.10 of the SM).

7.6.3 Angular momentum trends in detachment from linear carbon chains

Based on symmetry arguments alone,[83] s-wave ($\ell = 0$) photodetachment near threshold is expected to dominate for detachment from a π_u orbital, the SOMO in C_5^- and C_9^-, whereas in C_7^-, p-wave detachment is the lowest-order partial wave that can occur. From the Wigner threshold law, Eq. 7.2, one would expect the photodetachment cross section of C_5^- and C_9^- to be larger than for C_7^- near threshold due to the centrifugal barrier inhibiting detachment

for larger ℓ. While this expectation is fulfilled for C_5^-, the results in Figure 7.2 indicate that the intensity of the vibrational origin actually drops off more quickly for C_9^- than for C_7^- as the eKE is lowered. This effect limits the attainable resolution for FC-allowed peaks in C_9^-, as the signals are weak at low eKE where the experimental resolution is highest. To explore the origin of this effect, consideration of the Dyson orbitals for the three anions and the partial wave contributions to the photodetachment cross section is necessary.

To assess the cross sections associated with the detachment transitions described by the calculated Dyson orbitals, we have utilized the ezDyson software package. Given the symmetry of the Dyson orbitals and the linear C_n (n = odd) cluster family, the partial-wave expansion performed by ezDyson is localized on the central atom of each molecule and at low eKEs is dominated by contributions from that atom's local environment. The structure of our Dyson orbitals around this central atom thus impacts these calculations both in the shape of the orbital locally around this central atom and the amplitude of this wavefunction.

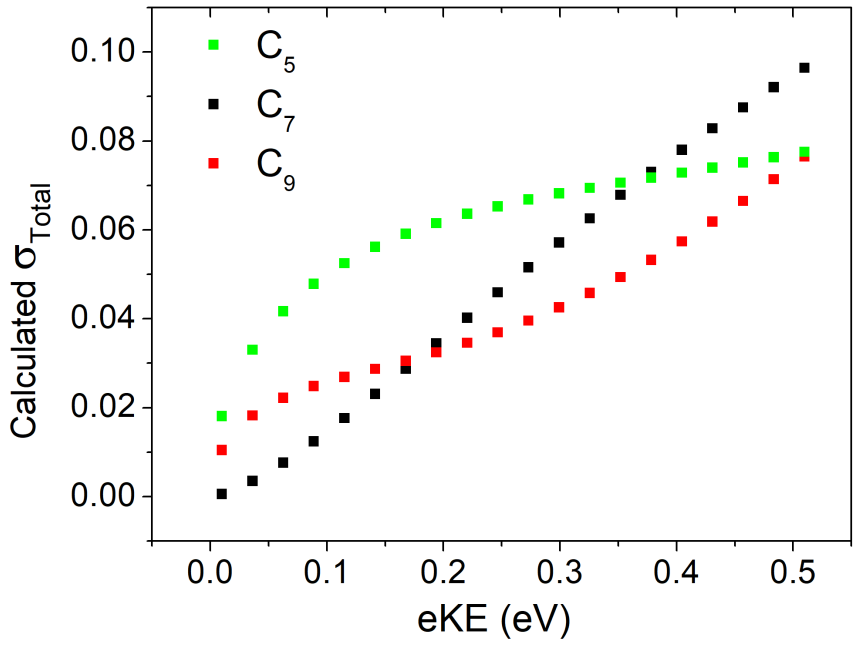

Figure 7.4: (a) Representative IR cryo-SEVI spectra of feature h_3 taken with a fixed detachment frequency ($h\nu$ = 14802.5 cm^{-1}) while the IR wavelength is scanned across the R(0) transition of OH^-. (b) Plot of integrated intensity of h_3 as a function of IR wavelength (black squares) and fit to Gaussian (red trace). The integrated intensity is normalized to the most intense transition measured.

From Figure 7.3, the Dyson orbitals around the central atom of C_5^- and C_9^- appear similar to an atomic p orbital, while for C_7^- the local orbital looks like an atomic d orbital, leading to s-wave detachment from the former and p-wave detachment from the latter at low eKEs.

At higher energies, where effects of the centrifugal barrier are less dominant, the increasing nodal structure of these orbitals for longer carbon chains favors spatial overlap with outgoing partial-waves of higher ℓ. As can be seen in Table 7.9 of the SM, photoelectrons with eKE = 0.10 eV are predominantly detached via s-wave for both C_5^- and C_9^-, while C_7^- is detached via p-wave. Upon reaching eKE = 0.51 eV, s- and p-wave detachment is still dominant for C_5^- and C_7^-, respectively, while d-wave detachment has become dominant from C_9^-. These findings are commensurate with our PAD measurements for detachment from C_5^- and C_7^-.[108] Further, as the three Dyson orbitals presented have similar amplitude, the increased nodal structure results in lower amplitude at the expansion center. This results in a lower calculated detachment cross sections near threshold, as seen in Figure 7.4, and is in agreement with the observation that the signal near threshold worsens as the chain length is increased.

Collectively, this analysis reveals that while conventional symmetry arguments correctly assess the detachment behavior of this family of clusters very near to threshold (eKE $\sim$ 0.10 eV), they fail to correctly predict behavior at moderate eKEs. Conversely, a Dyson orbital analysis qualitatively predicts the behavior of this class of linear clusters for all observed eKEs and can be understood by treating the local character of the Dyson orbital on the central atom as a quasi-atomic orbital from which the photoelectron is detached. As such, the nodal trend of our calculated Dyson orbitals in which the number of nodes observed increases with the chain length explains the trends we observe in the signal attenuation of this family of clusters near threshold as well as their PADs.

7.7 Conclusions

High-resolution cryo-SEVI spectra of C_7^- and C_9^- clusters are reported. We identify the previously unreported ν_1 and ν_2 symmetric stretches as well as the ν_9, ν_{10}, and ν_{11} asymmetric bending modes in the neutral C_7 cluster, report a spin-orbit splitting in the C_7^-, and confirm the assignment of the ν_3 and ν_7 modes previously reported by Arnold *et al.*[420] In the C_9 cluster, we identify both the ν_1 symmetric stretch and asymmetric ν_{11} bend and confirm the previously assigned ν_3 and ν_4 modes. Coupled cluster and MP2 calculations for C_7 and C_9, respectively, are used to produce FC-simulated spectra that are able to reproduce one set of our observed features. Those features not explained by FC-simulations are ascribed to the ν_{10} and ν_{11} modes of C_7 and the ν_{13} and ν_{14} modes of C_9, both of which appear through Herzberg-Teller coupling between electronic levels of the neutral cluster. Even though s-wave detachment is symmetry-allowed for both C_5^- and C_9^-, our experimental results and accompanying calculations indicate that higher partial waves contribute to the photodetachment signal near threshold as the carbon chain length increases.

7.8 Supplementary Information

7.8.1 Calculation of the derivative coupling vector in C_7 and C_9

In the case of two electronic states, A and B, the vibronic Hamiltonian takes the form

$$H = \begin{pmatrix} H_{AA}(R) & H_{AB}(R) \\ H_{BA}(R) & H_{BB}(R) \end{pmatrix} \tag{7.4}$$

where the electronic degrees of freedom have been integrated out of this expression and R represents the nuclear coordinates. For a state to diagonalize Equation 7.4 (and thus be a Born-Oppenheimer state at a particular geometry R), two conditions must be satisfied to obtain degeneracy in the Born-Oppenheimer representation: $H_{AA} = H_{BB}$ and $H_{AB} = 0$. Thus, degeneracies between two Born-Oppenheimer potential energy surfaces exists in a subspace of N-2 dimensionality, where N is the number of degrees of freedom. The two degrees of freedom that are now coupled make up a conical intersection and are defined by a pair of vectors g_{AB} and h_{AB}. Of these two vectors, h_{AB} is known as the nonadiabatic coupling vector and is defined as[431]

$$h_{AB} = \langle \Psi_A | \left(\partial \hat{H} / \partial R \right) | \Psi_B \rangle \tag{7.5}$$

This vector is closely related to the derivative coupling vector d_{AB}

$$d_{AB} = \langle \Psi_A | \left(\partial / \partial R \right) | \Psi_B \rangle = \frac{h_{AB}}{E_A - E_B} \tag{7.6}$$

which demonstrates well that the coupling between states becomes large as the energetic difference between the two states are nearly degenerate. It is this vector, d_{AB}, that we have calculated using the Time Dependent Density Functional Theory (TDDFT) framework to bolster our claims of vibronic coupling.

All TDDFT calculations are performed using the equilibrium geometry calculated for the ground state and were performed in Q-Chem 4.4.[437] These geometries can be found in Table 7.5 and Table 7.6 below. In order to calculate the derivative coupling vector, we first calculated the energies of the 10 lowest lying electronic states for each species at the B3LYP/cc-pVDZ level and determined the symmetry of each resultant electronic state. We then calculated the derivative coupling between the ground electronic state and one of $^1\Pi_u$ symmetry for coupling between neutral states which are displayed in Figures 7.7 and 7.8. The calculated derivative coupling vector calculated between the $^1\Sigma_g^+$ ground and the $^1\Pi_u$ excited state of C_7 (C_9) appears as a superposition of the ν_{10} and ν_{11} (ν_{13} and ν_{14}) vibrational modes. This indicates that the coupling between these electronic states occurs along the ν_{10} and ν_{11} (ν_{13} and ν_{14}) normal coordinates, which results in relatively strong mixing of vibronic states involving excitation along these modes. A similar procedure was followed for determining the derivative coupling vector between the ground electronic and excited $^2\Pi_u$ or $^2\Pi_g$ electronic states of C_7^- and C_9^-, respectively. The magnitude of all calculated vectors is presented in Table 7.10.

7.8.2 Franck-Condon Simulations

Franck-Condon (FC) simulations carried out for detachment from C_7^- and C_9^- using the geometries, normal modes, and frequencies calculated at the RCCSD(T)/aug-cc-pVTZ and MP2/cc-pVDZ levels of theory, respectively, are presented in Figures 7.5 and 7.6. All FC profiles have been manually shifted such that the vibrational origin occurs at the experimental value. To correct for expected systematic errors in the calculated force constants, the neutral (and anion in the case of C_7^-) frequencies are scaled to match experimentally derived values, resulting in the FC spectra presented in Figure 7.1a and 1b of the main text. All vibrational frequencies used are presented in Tables 7.8 and 7.9.

7.8.3 Figures

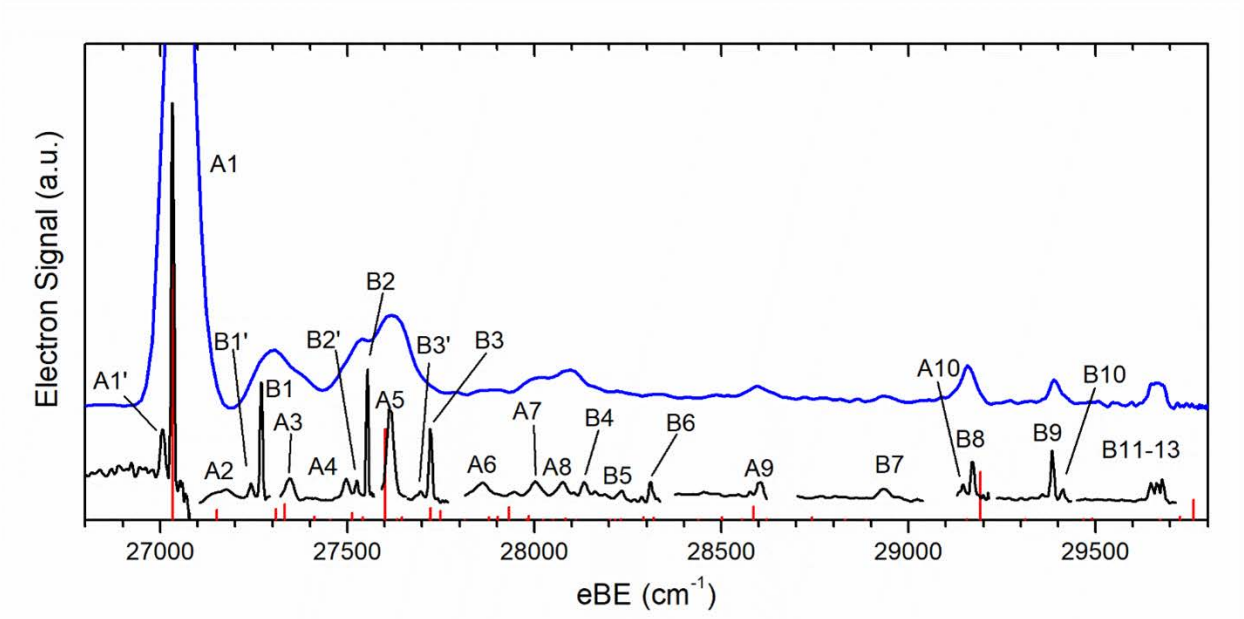

Figure 7.5: Cryo-SEVI spectrum of the $\tilde{X}^1\Sigma_g^+ \leftarrow \tilde{X}^2\Pi_g$ photodetachment of C_7^-, taken with the ion trap held at 5 K. A low-resolution overview spectrum taken with a photon energy of $h\nu = 29805$ cm^{-1} is shown in blue. The black trace is a high-resolution composite spectrum taken at many photon energies. A FC simulation stick spectrum, calculated utilizing our RCCSD(T)/aug-cc-pVTZ geometries and frequencies, is shown in red.

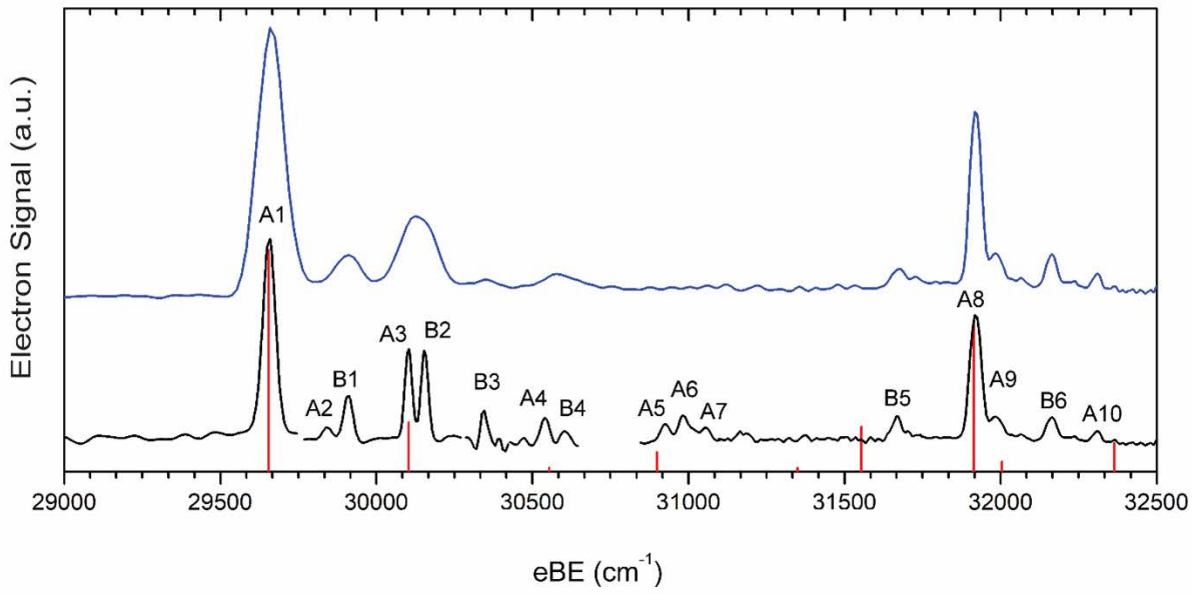

Figure 7.6: Cryo-SEVI spectrum of the $\tilde{X}^1\Sigma_g^+ \leftarrow \tilde{X}^2\Pi_u$ photodetachment of C_9^-, taken with the ion trap held at 5 K. A low-resolution overview spectrum taken with a photon energy of $h\nu = 32623$ cm^{-1} is shown in blue. The black trace is a high-resolution composite spectrum taken at many photon energies. A FC simulation stick spectrum, calculated utilizing our MP2/cc-pVDZ geometries and frequencies, is shown in red.

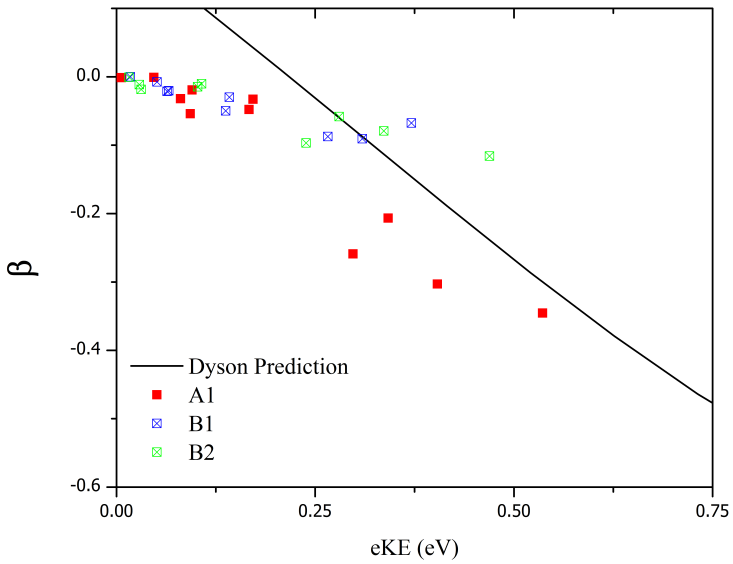

Figure 7.7: Measured anisotropy parameter, β , for peaks A1, B1, and B2 of the $\tilde{X}^1\Sigma_g^+ \leftarrow \tilde{X}^2\Pi_g$ photodetachment of C_7^- plotted as a function of eKE (colored squares) along with the predicted β value for FC allowed features (black line) from Dyson orbital calculations at the EOM-EA-CCSD/6-311++G** level. While there is some discrepancy at higher eKEs, it is not as significant as we have seen in previous systems,[65] likely as this trend is obfuscated by the overlap of features B1 (B2) with nearby A3 (A4-A5) that dominate the spectrum far from threshold.

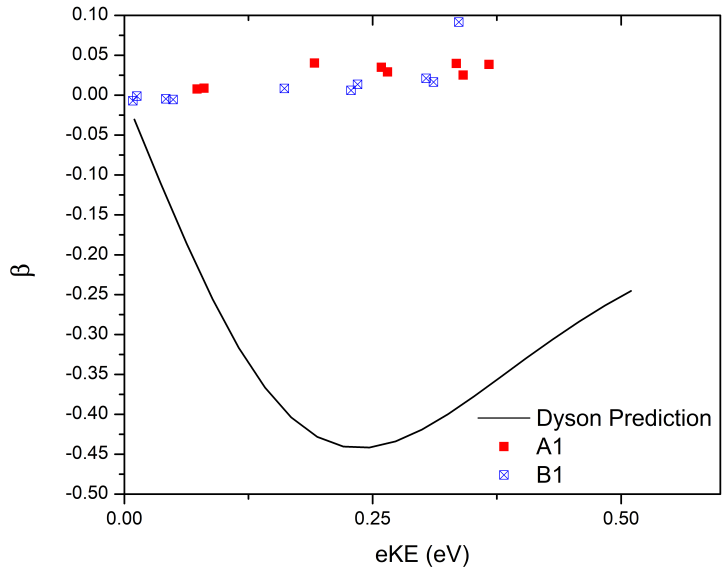

Figure 7.8: Measured anisotropy parameter, β , for peaks A1 and B1 of the $\tilde{X}^1\Sigma_g^+ \leftarrow \tilde{X}^2\Pi_u$ photodetachment of C_9^- plotted as a function of eKE (colored squares) along with the predicted β value for FC allowed features (black line), from Dyson orbital calculations at the EOM-EA-CCSD/6-311++G** level.

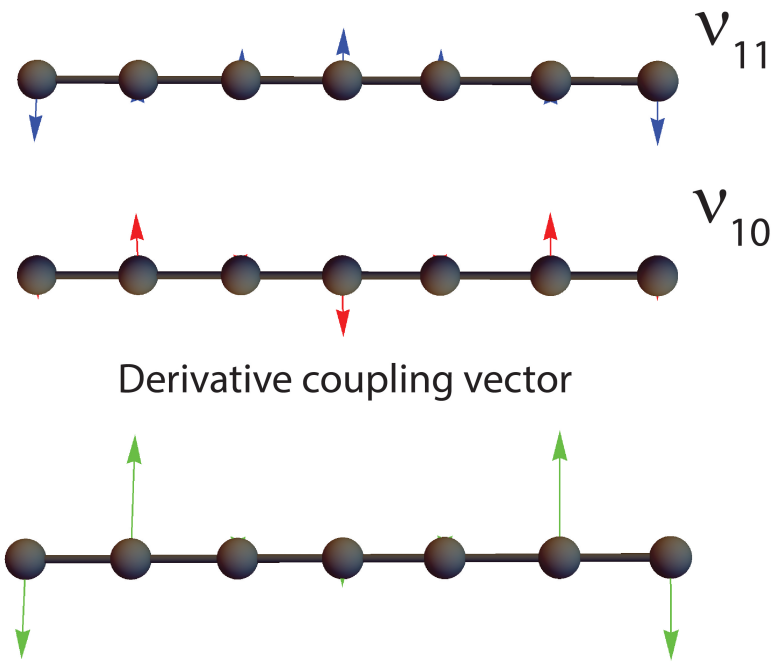

Figure 7.9: Illustrations of the modes active in Herzberg-Teller coupling and the calculated derivative coupling vector for C_7. Vibrational modes displayed are scaled by a factor of 5 and were calculated at the RCCSD(T)/aug-cc-pVTZ level of theory, and the derivative coupling vector is calculated using TDDFT at the B3LYP/cc-pVDZ level of theory without electron-translation factors.[435]

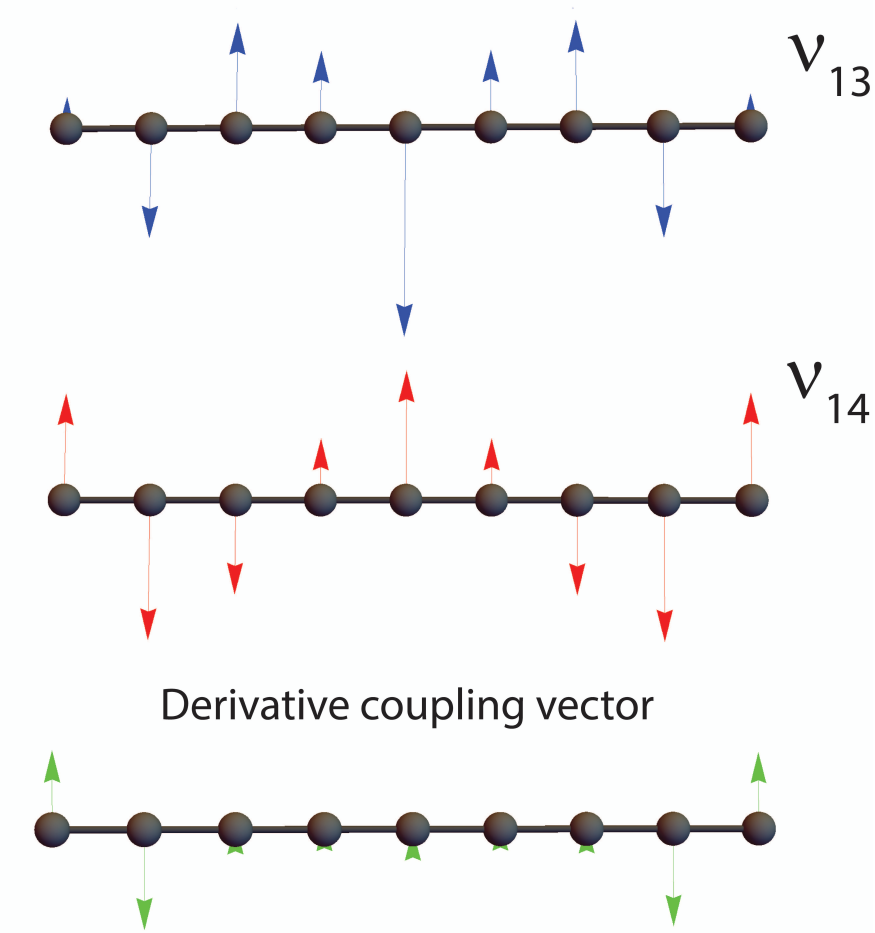

Figure 7.10: Illustrations of the modes active in Herzberg-Teller coupling and the calculated derivative coupling vector for C_9. Vibrational modes displayed are scaled by a factor of 5 and were calculated at the MP2/cc-pVDZ level of theory, and the derivative coupling vector is calculated using TDDFT at the B3LYP/cc-pVDZ level of theory without electron-translation factors.[435]

7.8.4 Tables

Parameter	C_7^- calculated	C_7 calculated
R_{c-c}, inner	1.283	1.279
R_{c-c}, middle	1.315	1.293
R_{c-c}, outer	1.287	1.297

Table 7.5: Calculated geometries for C_7 and C_7^- at the RCCSD(T)/aug-cc-pVTZ level of theory. Bond lengths are in
Angströms (Å)

Parameter	C_9^- calculated	C9 calculated
R_{c-c}, C5-C4	1.301	1.298
R_{c-c}, C4-C3	1.265	1.293
R_{c-c}, C3-C2	1.341	1.31
R_{c-c}, C2-C1	1.268	1.316

Table 7.6: Calculated geometries for C_9 and C_9^- at the MP2/cc-pVDZ level of theory. Bond lengths are in Ångströms (Å). In this naming scheme, the outermost carbon is labeled C1 and each subsequent carbon has an increasing index until the central carbon (C5) is reached.

mode	Calculated	Scaled
ν_1	2159	2119
ν_2	1554	1570
ν_3	570	581
ν_4	2198	2198
ν_5	1922	1922
ν_6	1080	1080
ν_7	476	485
ν_8	138	138
ν_9	449	414
ν_{10}	240	237
ν_{11}	60	81

Table 7.7: Vibrational frequencies in cm^{-1} for C_7 obtained at the RCCSD(T)/aug-cc-pVTZ level. The scaled frequencies, used in the Franck-Condon simulations presented in Figure 7.1A of the main text are also presented.

mode	Calculated	Scaled
ν_1	2260	2266
ν_2	1901	1901
ν_3	1246	1270
ν_4	450	448
ν_5	2415	2415
ν_6	2104	2104
ν_7	1608	1608
ν_8	865	865
ν_9	579	579
ν_{10}	320	320
ν_{11}	131	95
ν_{12}	635	635
ν_{13}	477	498
ν_{14}	230	252
ν_{15}	51	51

Table 7.8: Vibrational frequencies in cm^{-1} for C_9 obtained at the MP2/-cc-pVDZ level. The scaled frequencies, used in the Franck-Condon simulations presented in Figure 7.1B of the main text are also presented.

	eKE = 0.10 eV			eKE = 0.51 eV			eKE = 1.05 eV		
ℓ	C_5	C_7	C_9	C_5	C_7	C_9	C_5	C_7	C_9
0	0.9999	0	0.9993	0.7012	0	0.0958	0.1926	0	0.0027
1	0	1	0	0	0.9247	0	0	0.6384	0
2	0.0001	0	0.0007	0.2978	0	0.8765	0.7955	0	0.8316
3	0	0	0	0	0.0751	0	0	0.3573	0
4	0	0	0	0.001	0	0.0277	0.0119	0	0.1657
5	0	0	0	0	0.0002	0	0	0.0043	0

Table 7.9: Fractional partial wave decomposition for detachment from C_7 and C_9 (with C5 provided as a reference) at various photoelectron kinetic energies (eKE). Highlighted text represents the major partial wave contributions.

Molecule	Coupled Excited State	Coupling Element
C_7	$^1\Pi_u$	1.300153
C_7	$^1\Sigma_u^+$	0
C_7^-	$^2\Pi_u$	1.31986
C_9	$^1\Pi_u$	3.017684
C_9	$^1\Sigma_u^+$	0
C_9^-	$^2\Pi_g$	1.216312

Table 7.10: Matrix coupling elements calculated at the TD-B3LYP/cc-pVDZ level of theory.

Chapter 8

Vibronic Structure of Si_3C, Si_2C_2, and SiC_3

The content and figures of this chapter are reprinted or adapted with permission from M. C. Babin, M. DeWitt, M. L. Weichman, J. A. DeVine, D. M. Neumark, "High-resolution anion photoelectron spectroscopy of cryogenically cooled 4-atom silicon carbides" *Molecular Physics* **119**, e1817596 (2020).

8.1 Abstract

High-resolution anion photoelectron spectra of cryogenically cooled Si_3C^-, $Si_2C_2^-$, and SiC_3^- obtained using slow photoelectron velocity-map imaging (cryo-SEVI) are presented, providing insight into the geometries, energetics, and vibronic structure of the anionic and the neutral clusters. These spectra yield accurate vibrational frequencies for the neutral clusters. They also yield refined adiabatic detachment energies (ADEs) for the ground states of Si_3C^- and $Si_2C_2^-$ of 1.5374(6) eV and 1.9019(4) eV, respectively, while the ADE of a low-lying isomer of SiC_3^- is found to be 1.9050(7) eV. The cryo-SEVI spectra show that the ground state of $Si_2C_2^-$ is a distorted trapezoid, and represent the first confirmation of the distorted trapezoid structure of Si_2C_2, the only low-lying isomer of this cluster with a permanent dipole moment. Additional transitions are observed from two low-lying anion isomers: a linear structure and a rhombus. The spectrum of SiC_3^-, in combination with electronic structure calculations, suggests that the true ground state of SiC_3 is a ring structure with a transannular C-C bond, addressing a longstanding controversy surrounding this cluster. All three spectra exhibit Franck-Condon forbidden transitions; these are attributed to Herzberg-Teller coupling in Si_3C and SiC_3 and autodetachment from an excited electronic state of $Si_2C_2^-$.

8.2 Introduction

Small silicon carbides (Si_mC_n) are of considerable fundamental and applied interest as potential building blocks for the synthesis of novel nanoscale materials,[438] for their role in the low-pressure vapor deposition of solid silicon carbide,[439] and based on their detection in the circumstellar envelope of carbon-rich stars such as IRC+10216.[203–208] Since these clusters are intermediate between the pure carbon (C_n) and silicon (Si_n) clusters, whose structural trends are well documented,[383–387,425,440–442] they provide an excellent system to explore the nature of the organosilicon bond, potentially aiding in the engineering of nanostructured silicon carbides and assignment of astronomical data. These considerations have motivated myriad experimental and theoretical studies utilizing matrix isolation infrared spectroscopy,[443,444] Fourier transform microwave spectroscopy,[206,207,445–447] resonant two-color two-photon ionization (R2C2PI),[448–450] infrared-ultraviolet two-color ionization (IR-UV2CI),[451] anion photoelectron spectroscopy (PES),[452,453] and electronic structure calculations,[448,454–471] all aimed at characterizing the electronic and vibrational structure of small silicon carbides. Despite this extensive body of work, the Si_nC_m $(n+m=4)$ clusters still pose a significant challenge to both theory and experiment. In this work, we address longstanding questions surrounding the structures of Si_3C, Si_2C_2, and SiC_3 using high resolution photoelectron spectroscopy of cryogenically cooled anions and high-level *ab initio* calculations.

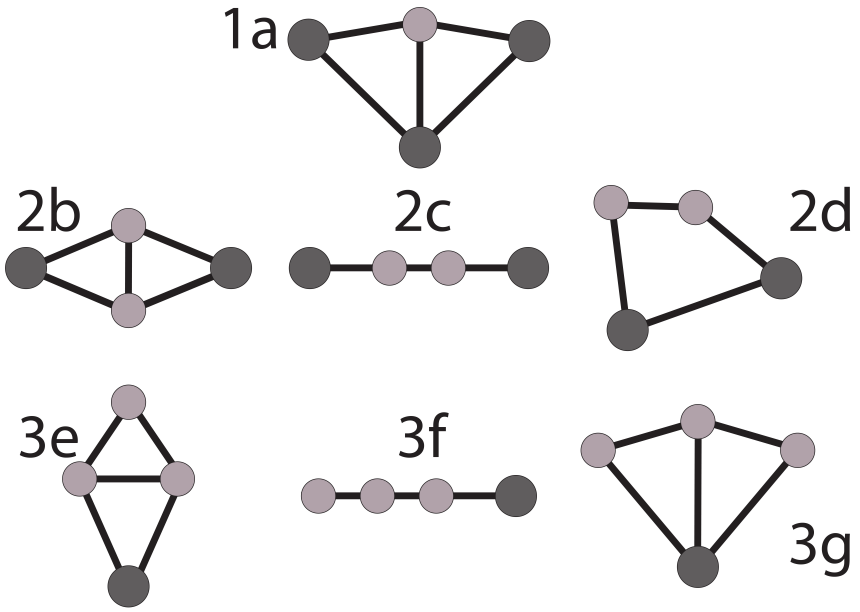

Figure 8.1: Structures of low-lying isomers of SiC_3 (1a), Si_2C_2 (2b-d),and SiC_3 (3e-g).

Proposed structures for the ground states of the 4-atom silicon carbide clusters ($Si_3C^{0/-}$, $Si_2C_2^{0/-}$, and $SiC_3^{0/-}$) are shown in Figure 8.1. Si_3C is perhaps the best characterized of the

three clusters. First detected in 1992 by Graham and co-workers[443] using FTIR of vaporized silicon carbides trapped in Ar matrices, five of six vibrational modes were reported and its structure was unambiguously determined as a 4-membered ring with a transannular Si-C bond (structure 1a). Since then, this structure of Si_3C has been confirmed by a number of gas-phase experiments[448–452] and calculated to be the ground state of this species,[448,460,461,466] while anion photoelectron spectroscopy of Si_3C^- has confirmed the ground state of the anion as structure 1a.[452]

It has been more challenging to characterize the ground states of the two other four-atom clusters. The ground state of neutral Si_2C_2 has been calculated to be a rhombic structure (2b),[455–458,461,463,464,470] lying less than 40 kJ/mol below both a linear isomer and a distorted trapezoid (2c,d, respectively), while the energetic ordering of structures 2c and 2d is method-dependent. This uncertainty was complicated when Graham and co-workers[444] observed vibrational bending modes tentatively assigned to all three isomers via Ar matrix FTIR spectroscopy. Since then, a recent R2C2PI study from Steglich and Maier[450] observed only contributions from the linear isomer (2c) in their jet-cooled expansion, though their probe energies are below the calculated IE of structure 2b, and the authors make no mention of 2d. Anion photoelectron spectroscopy by the Kaya group[452] showed both sharp and broad features, attributed to photodetachment from two anion isomers, but definitive assignments were hampered by the absence of resolved vibrational structure. Theoretical efforts to explain this spectrum have found either structure 2c or 2d to be the ground state for the $Si_2C_2^-$ anion.[461,463,470]

SiC_3 is perhaps the most contentious of the three. The ground state was first calculated to be a four-membered ring with a transannular C-C bond (3e), with a low-lying linear triplet state and a second rhomboidal Si-C transannular bonding structure (3f and 3g, respectively) within 20 kJ/mol.[459,462] Structure 3e was discovered shortly thereafter not only in the laboratory,[206,446] but also in the interstellar medium.[207] Subsequently, McCarthy *et al.* detected both structure 3g and 3f in a supersonic molecular beam via FT-microwave spectroscopy.[445,447] Following this, numerous experimental and theoretical studies were performed to ascertain the true ground state of SiC_3, with theorists determining the three structures lie withing a few kJ/mol of one another, though the ordering is method-dependent.[454,461,464,465,467–471] Anion photoelectron spectra revealed both sharp structure at high binding energies, assigned to the linear structure 3f by the Kaya group and confirmed by the Lineberger group, and two broad, weak features at lower binding energies attributed to the presence of one or more ring structures.[452,453] These studies were able to confirm the lowest-energy structure of SiC_3^- as the 3f linear species, in agreement with theory that suggests this structure is at least 40 kJ/mol more stable than either of the two ring isomers (3e,g).[461,462,470]

The present study uses slow photoelectron velocity-map imaging of cryogenically cooled anions (cryo-SEVI)[54] to obtain photoelectron spectra with highly resolved vibrational structure of Si_3C^-, $Si_2C_2^-$, and SiC_3^-. With the aid of Franck-Condon (FC) simulations, all bands are unambiguously assigned to specific structural isomers of the three clusters. Investigation into Si_3C^- allows for determination of the frequency for the previously unreported ν_4 vibra-

tional mode, with features having odd quanta along this mode appearing via Herzberg-Teller coupling. Our spectrum of $Si_2C_2^-$ reveals detachment from three anionic isomers, and establishes the distorted trapezoid 2d as the ground state of $Si_2C_2^-$. Significant FC-activity from photodetachment of structure 2d allows for characterization of the vibrational frequencies of the corresponding neutral species, including FC-forbidden transitions along the ν_6 normal mode that gains intensity through vibrational autodetachment. The cryo-SEVI spectrum of SiC_3^- provides the first information on the vibrational structure 3e of SiC_3, revealing non-FC activity along the ν_4 normal coordinate. Collectively, these spectra provide improved ADEs for structures 1a, 2b,c,d, and 3e, allowing for the determination of upper bounds for the energetic splitting of the neutral silicon carbide clusters. Coupling these experimental ADEs with *ab initio* calculations and experimental considerations suggests that the true ground sate of SiC_3 is a ring containing a transannular C-C bond (3e).

8.3 Experimental Methods

The cryo-SEVI method has been described in detail previously.[5,34,35,54] In this work, silicon carbide cluster anions are generated with a laser ablation source using a frequency-doubled Nd:YAG laser focused onto a rotation and translating silicon carbide disk. The resulting plasma is entrained within a pulse of He carrier gas from an Even-Lavie solenoid valve[245] before passing through a skimmer. The ions then pass through a radiofrequency (RF) hexapole ion guide and a RF quadrupole mass filter and are directed into a linear RF octupole ion trap held at 5 K and filled with a buffer gas mixture of 20:80 H_2:He. Collisions with the cold buffer gas result in effective vibrational, rotational, and electronic cooling of the ions, leading to internal temperatures near 10 K.[41,54,239]

After ∼40 ms, the ions are extracted from the trap into an orthogonal Wiley-McLaren time-of-flight mass spectrometer[259] and focused into the interaction region of a seven-plate velocity-map imaging (VMI) electrostatic lens assembly.[18,36] In the VMI spectrometer, ions are photodetached by the output of a dye laser pumped by the second harmonic of a Nd:YAG laser operating at 20 Hz.

The resulting photoelectrons are projected onto a 2D detector comprising two chevron-stacked microchannel plates coupled to a phosphor screen, which is photographed by a CCD camera after each laser shot.[17] Each image is analyzed for individual electron events for which the centroids are calculated and binned in a 1024 × 1024 grid.[271] The three-dimensional electron velocity distribution is reconstructed from the accumulated images using the Maximum Entropy Velocity Legendre Reconstruction (MEVELER) algorithm.[275] The radial position of features in the reconstructed image is related to electron kinetic energy (eKE) by acquiring VMI images for detachment from atomic O^- at several photon energies.[279]

The VMI spectrometer has an approximately constant resolving power, ΔeKE/eKE,[18] yielding the best eKE resolution for slow electrons. As such, a SEVI spectrum is acquired by first taking an overview spectrum at a relatively high photon energy before tuning the

detachment laser to energies slightly above features of interest. This procedure results in a series of high-resolution spectra over narrow energy windows that are concatenated and scaled to match intensities in the overview spectrum, which is less sensitive to variation of the photodetachment cross section with photon energy. Spectra are plotted as a function of electron binding energy (eBE), given by eBE = hν - eKE.

In addition to the eKE distributions, VMI allows for the determination of photoelectron angular distributions (PADs) associated with each detachment transition, given by[91]

$$\frac{d\sigma}{d\Omega} = \frac{\sigma_{tot}}{4\pi}\left[1 + \beta P_2(\cos\theta)\right] \tag{8.1}$$

where σ_{tot} is the total detachment cross section, $P_2(x)$ is the second-order Legendre polynomial, θ is the angle of the outgoing photoelectron with respect to the laser polarization axis, and β is the anisotropy parameter. The anisotropy parameter, which ranges from -1 (perpendicular detachment) to +2 (parallel detachment), reflects the angular momentum of the detached electron and is thus tied to the electronic character of each photodetachment transition.[361]

8.4 Computational methods

Electronic structure calculations for all isomers of $Si_3C^{0/-}$ and $Si_2C_2^{0/-}$ were carried out at the CCSD/aug-cc-pVDZ level of theory, while those for $SiC_3^{0/-}$ were carried out at the CCSD/aug-cc-pVTZ level.[416,421,422] Based on the calculated energetics of these species in previous work,[448,454–456,459,461,464,465,468,470,471] the calculations were restricted to the singlet manifold for all ring structures (1a,b,d,e,g), while both the singlet and triplet structures for the linear isomers (2c, 3f) were considered. All calculations were performed using Gaussian 16 (revision A.03).[180] Calculated adiabatic detachment energies (ADEs) are zero-point corrected. Calculated geometries are presented in Tables 8.7-8.24 while the energetics of the anion and neutral isomers are listed in Tables 8.25 and 8.26.

The equilibrium geometries and normal modes were used to calculate the Franck-Condon (FC) profiles for the relevant photodetachment transitions in Si_3C^-, $Si_2C_2^-$, and SiC_3^- with the ezSpectrum v3.0 software package.[175] All modes were treated in the harmonic approximation and FC integrals were calculated using full Duschinsky mixing of all normal modes.[176] To better match experiment, FC simulations use experimentally determined frequencies when available. The calculated and experimental values used in these simulations are presented in Tables 8.27-8.29 of the SI, while cryo-SEVI spectra with FC simulations using the calculated frequencies are presented in Figures 8.6-8.12 of the SI. In the case of $Si_2C_2^-$ and SiC_3^-, discrepancies between the simulated FC profiles and experiment were observed when the calculated structure were used. These were addressed by making small additional displacements to either the anion or neutral normal coordinates. Adjustments were made to the Si_2C_2 structure on the basis of better agreement between the calculated and experimental ADE for the distorted neutral species; this point is discussed in more detail in the SI.

For SiC_3^-, adjustments were made to the anion as microwave spectra have provided accurate experimental bond-lengths for the neutral species. Full details of these adjustments are presented in Sections S1 and S2 of the SI.

Excited state energies for the Si_3C, $Si_2C_2^{0/-}$, and SiC_3 clusters were calculated using the equation of motion coupled cluster (EOM-CCSD) framework[472–477] with the same basis set as used for geometry optimizations within Gaussian 16. Calculations were performed using the optimized ground state geometries unless otherwise stated. Term energies and state symmetries of the first four excited states are presented in Table S24 of the SI.

8.5 Results

The cryo-SEVI spectra of Si_3C^-, $Si_2C_2^-$, and SiC_3^-, are presented in Figures 8.2, 8.3, and 8.4 respectively. In these panels, a low-resolution overview spectrum (blue) is displayed atop high-resolution composite spectra (black) taken at several photon energies as well as simulated Franck-Condon profiles (red sticks) using adjusted geometries as described above.[416,421,422] Peak assignments, electron binding energies (eBEs), and shifts from peak A are given in Tables 8.1-8.3 for Si_3C, Si_2C_2, and SiC_3, respectively. A complete listing of experimental parameters with a comparison to literature values is included in Table 4. Computationally determined geometries, theoretical relative energetics of differing isomers, and spectra with FC simulations using calculated frequencies are presented in Figures 8.6-8.12 and Tables 8.7-8.30 of the SI.

The cryo-SEVI spectra of Si_3C, Si_2C_2, and SiC_3 represent significant improvements over previous anion photoelectron spectroscopy studies.[452,453] The improved resolution afforded by the cryo-SEVI method reveals a strong vibrational origin (peak A) followed by a progression of transitions to vibrationally excited states of the neutral clusters. Vibrational assignments are facilitated by comparison between FC simulations and the experimental spectra.

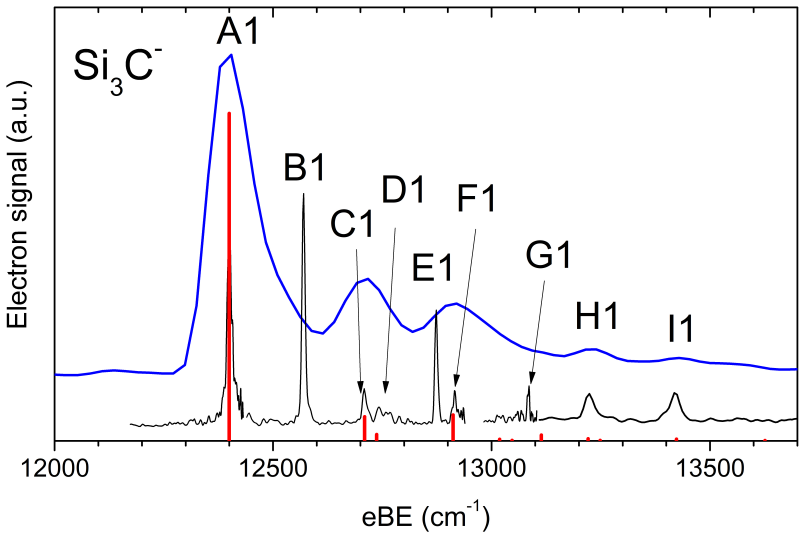

Figure 8.2: Cryo-SEVI spectra of Si_3C^-. A low-resolution spectrum (blue) sits above both high resolution scans (black, variable photon energies) and a simulated photoelectron stick spectrum for structure 1a (red).

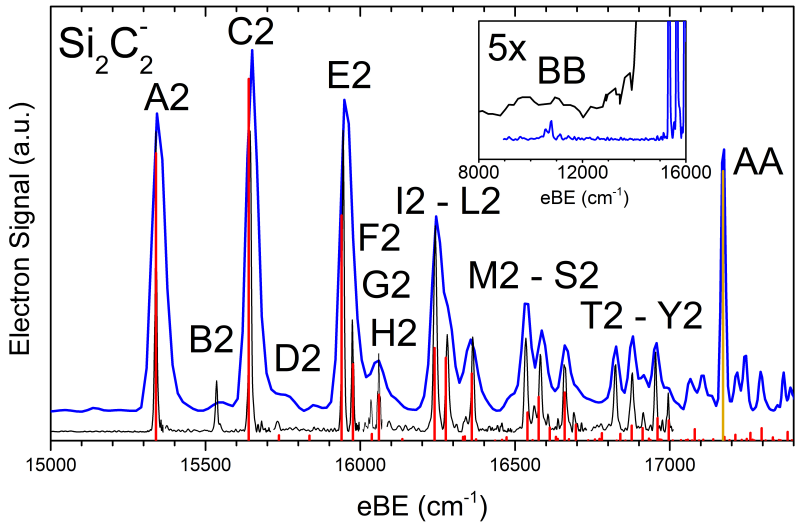

Figure 8.3: . Cryo-SEVI spectra of $Si_2C_2^-$. A low-resolution spectrum (blue) sits above both high resolution scans (black, variable photon energies) and a simulated photoelectron stick spectrum for structures 2d (red) and 2c (gold). Insert: magnification of low eBE region displaying weak cryo-SEVI signal (blue) below PES spectrum of Kaya *et al.* (black).[452]

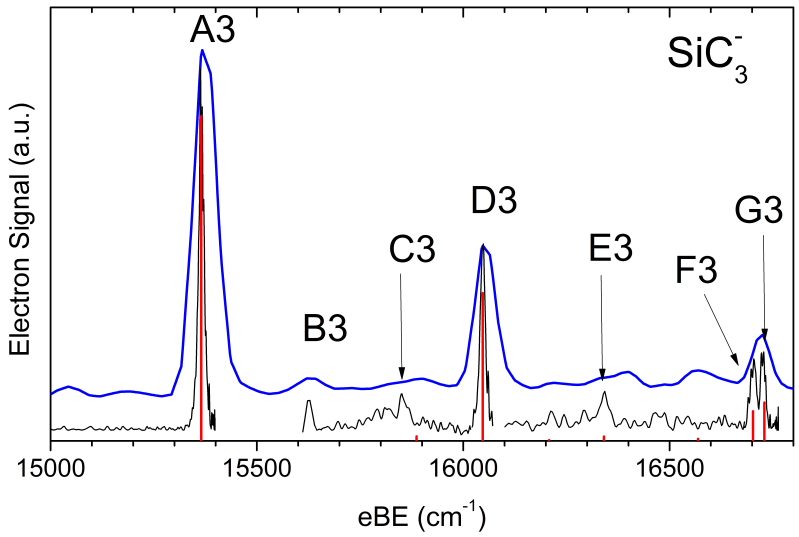

Figure 8.4: Cryo-SEVI spectra of SiC_3^- . A low-resolution spectrum (blue) sits above both high resolution scans (black, variable photon energies) and a simulated photoelectron stick spectrum (red).

8.6 Discussion

8.6.1 Spectral Assignments

8.6.1.1 Si_3C

The cryo-SEVI spectrum of Si_3C^- is presented in Figure 8.2 along with FC simulations for structure 1a, selected as this structure is known to be the ground state of $Si_3C^{0/-}$.[443,448–450,460,461] In this spectrum, features C1, D1, F1, G1, H1, and I1 are reproduced in the FC simulations, allowing for their assignment as the 3_0^1, 4_0^2, 2_0^1, 6_0^2, $2_0^1 3_0^1$, and 2_0^2 transitions. From these peak locations the frequencies of the ν_2, ν_3, and ν_6 normal modes of Si_3C may be inferred, as reported in Table 4; these values are in good agreement with those determined by Graham *et al.*[443] Though features B1 and E1 are notably absent from our FC simulations, their shifts from peak A1 match well with the FC-forbidden 4_0^1 and $3_0^1 4_0^1$ transitions, the appearance of which is discussed below. As feature B1 reports on the 4_0^1 transition, its position allows for the determination of the out-of-plane ν_4 normal mode in this species for the first time. Our experimental value of $\nu_4 = 171(6)$ cm^{-1} is in good agreement with our calculated value of 168 cm^{-1} as well as those reported in previous theoretical work.[448,460]

As both features B1 and E1 report on transitions involving odd quanta along the non-totally symmetric ν_4 mode, they are formally FC-forbidden, and their appearance is ascribed to Herzberg-Teller (HT) coupling to an excited neutral state. The signatures of HT coupling in anion photoelectron spectroscopy are well established, and come about due to borrowed electronic character from an excited state.[14,65,100,104,359,364,478–481] Transitions that are allowed only through HT coupling often have different photoelectron angular distributions than FC-allowed peaks. Moreover, in cryo-SEVI spectra, HT coupling leads to different relative intensities compared to FC allowed transitions as the photodetachment energy is varied, an effect that can be particularly pronounced when the electron kinetic energies are low. Comparison of the overview and high-resolution composite transitions in Figure 8.2 show that peaks B1 and E1 are enhanced at low eKE relative to FC-allowed transitions (see also Fig. S8), an effect also seen in the cryo-SEVI spectrum of NO_3^-.[100]

Peak	eBE (cm^{-1})	Shift (cm^{-1})	Assignment
A1	12400(9)	0	0_0^0
B1	12570(7)	170	4_0^1
C1	12710(10)	309	3_0^1
D1	12743(13)	343	4_0^2
E1	12873(7)	473	$3_0^1 4_0^1$
F1	12914(15)	514	3_0^1
G1	13084(6)	684	6_0^2
H1	13224(21)	824	$2_0^1 3_0^1$
I1	13420(25)	1019	2_0^2

Table 8.1: Peak positions, shifts from peak A1, and assignments for the detachment transitions in the cryo-SEVI spectrum of Si_3C presented in Figure 8.2. Uncertainties in peak positions correspond to one standard deviation obtained from a Gaussian fit to the corresponding feature in the high-resolution scan.

8.6.1.2 Si_2C_2

The cryo-SEVI spectrum of Si_2C_2 reveals substantially more vibrational structure than Si_3C. We find poor agreement between FC simulations for structures 2b and 2c of Si_2C_2 (Figures 8.6, 8.7 in the SI). FC simulations for structure 2d using the calculated geometries fare considerably better but overestimate the activity along the ν_2 and ν_3 normal coordinates. This is corrected for by adjusting the optimized geometry along the neutral ν_3 and ν_2 normal coordinates, bringing the observed structure closer to a C_{2v} trapezoid (see Section S1 and Figures 8.8, 8.9 of the SI). The resulting FC simulations involving the adjusted-Si_2C_2 structure, presented in Figure 8.3, are in excellent agreement with the experimental results. These simulations facilitate the assignment of nearly every transition observed in the cryo-SEVI spectrum, including the 2_0^1, 3_0^1, 5_0^1, 4_0^2, and 6_0^2 transitions (features H2, F2, C2, K2, and D2, respectively), as shown in Table 2. These assignments allow for the determination of the vibrational frequencies of the ν_2, ν_4, ν_5, and ν_6 modes of Si_2C_2 for the first time, while our experimentally determined value of 636(4) cm^{-1} for ν_3 in good agreement with the tentative assignment provided by Graham.[444]

Peak	eBE (cm^{-1})	Shift (cm^{-1})	Assignment
A2	15340(6)	0	0_0^0
B2	15536(7)	196	6_0^1
C2	15645(7)	305	5_0^1
D2	15733(9)	393	6_0^2
E2	15945(7)	605	5_0^2
F2	15975(7)	636	3_0^1
G2	16035(4)	695	$5_0^1 6_0^2$
H2	16060(8)	720	2_0^1
I2	16242(10)	903	5_0^3
J2	16281(9)	941	$3_0^1 5_0^1$
K2	16343(15)	1003	4_0^2
L2	16363(8)	1024	$2_0^1 5_0^1$
M2	16535(10)	1195	5_0^4
N2	16563(7)	1223	$2_0^1 4_0^2$
O2	16582(8)	1242	$3_0^1 5_0^2$
P2	16606(6)	1267	3_0^2
Q2	16639(4)	1299	$5_0^3 6_0^2$
R2	16661(9)	1321	$2_0^1 5_0^2$
S2	16691(6)	1351	$2_0^1 3_0^1$
T2	16824(9)	1484	5_0^5
U2	16878(10)	1538	$3_0^1 5_0^3$
V2	16914(7)	1574	$3_0^2 5_0^1$
W2	16954(7)	1614	$2_0^1 5_0^3$
X2	16976(4)	1636	$3_0^1 5_0^1 6_0^2$
Y2	16995(5)	1655	$2_0^1 3_0^1 5_0^1$
AA	17171(13)	1832	0_0^0 (2c, see text)

Table 8.2: Peak positions, shifts from peak A2, and assignments for the detachment transitions in the cryo-SEVI spectrum of Si_2C_2 presented in Figure 8.3. Uncertainties in peak positions correspond to one standard deviation obtained from a Gaussian fit to the corresponding feature in the high-resolution scan. Assignments are for isomer 2d unless stated otherwise.

Peak B2 is not reproduced by our FC simulations, but the position of this features matches well with the expected location of the FC-forbidden 6_0^1 transition. Unlike peaks B1 and E1 in the spectrum of Si_3C^-, feature B2 in $Si_2C_2^-$ only appears in one of 12 scans taken over a range of photon energies (Fig. S9), a clear indication of autodetachment from an excited anionic state.[42,113,482–484] Vibrational autodetachment is a non-Born-Oppenheimer process wherein vibrational and rotational degrees of freedom couple the autodetaching an-

ionic excited state to the (neural + free electron) continuum, permitting the observation of otherwise inaccessible neutral states.[112,485] In the present study, peak B2 is only observed when detached with a photon energy of 1.94930 eV (15,722 cm^{-1}), residing very near our calculated term energy of 1.9560 eV at the EOM-CCSD/aug-cc-pVDZ level for the $\tilde{C}$ state of structure 2d of $Si_2C_2^-$ and only 11 cm^{-1} below the calculated position of the FC-allowed 6_0^2 transition. As vibrational autodetachment preferentially occurs by loss of one vibrational quantum ($\Delta\nu = -1$) in a coupling mode whose normal coordinate changes the character of the anion orbital from which the electron is autodetached,[112] these results strongly suggest that the observed 6_0^1 transition in Si_2C_2 is facilitated by vibrational autodetachment from the $2\nu_6$ level of the $\tilde{C}$ state in $Si_2C_2^-$.

Our cryo-SEVI spectra also show evidence for contributions from multiple isomers; as shown in Figure 8.3, we see signal at ∼10,500 cm^{-1} (peak BB) and 17,172 cm^{-1} (peak AA) that has previously been attributed to other structures of Si_2C_2 by Kaya *et al.*[452] Feature BB is exceptionally weak and was collected at high eKE, producing a spectrum with low resolution that is assigned as structure 2b on the basis of previous assignments. At high eBE we observe an isolated sharp feature, peak AA, that clearly lies beyond the FC simulation for structure 2d. This peak is assigned to linear Si_2C_2 (structure 2c); it is reproduced by FC simulations for detachment from the linear anion that exhibit a strong vibrational origin without any other features of discernible intensity. Such a result agrees with previous findings on linear carbon and silicon carbide clusters that find photoelectron spectra dominated by a sharp vibrational origin and lacking an extended vibrational progression.[102,108,420,452,453,486]

8.6.1.3 SiC_3

The cryo-SEVI spectra of SiC_3 represents an investigation into the lowest-eBE region of previously reported PES spectra, ascribed to detachment from a low-lying ring structure of SiC_3^- in those studies.[452,453,462] The current work displays the first vibrationally-resolved spectrum in this region, allowing for the assignment of structure 3e as the origin of this band based on agreement between simulated FC profiles for this structure (as reported in Figure 8.4) and poor agreement for structure 3g. As detachment from linear SiC_3^- has been observed by Lineberger with a band origin at eBE higher than those explored in this work,[14] structure 3f was excluded from consideration.

Peak	eBE (cm^{-1})	Shift (cm^{-1})	Assignment
A3	15365(12)	0	0_0^0
B3	15626(15)	261	4_0^1
C3	15850(9)	485	4_0^2
D3	16047(11)	682	3_0^1
E3	16341(21)	976	2_0^1
F3	16702(15)	1337	1_0^1
G3	16726(12)	1361	3_0^2

Table 8.3: Peak positions, shifts from peak A3, and assignments for the detachment transitions in the cryo-SEVI spectrum of SiC_3 presented in Figure 8.4. Uncertainties in peak positions correspond to one standard deviation obtained from a Gaussian fit to the corresponding feature in the high-resolution scan.

FC profiles based on the optimized 3e geometry underreport activity in ν_3 and require additional displacement along the corresponding normal coordinate to adequately reproduce features C3, D3, E3, F3 and G3 in the experimental spectrum (see Section S2 and Figures 8.11, 8.12). The FC-simulations using this adjusted anion geometry are presented in Figure 8.4 and allow for the assignment of these peaks to the 4_0^2, 3_0^1, 2_0^1, 1_0^1, and 3_0^2 transitions, respectively. From these assignments, we are able to extract experimental frequencies for the ν_1, ν_2, ν_3, and ν_4 normal modes for the first time, as shown in Table 4 below. Feature B3 is once again not reproduced by our FC simulations. As the position of this feature aligns with the FC-forbidden 4_0^1 transition, a detachment cross section that diminishes more rapidly than the FC-allowed features as its photodetachment threshold is approached (see Figure 8.15 in SI), and a photoelectron angular distribution that differs from peak A3 (Figure 8.16 in SI), we assign this feature to the transition that gains intensity through HT-coupling.

	$\mathbf{Si_3C}$			$\mathbf{Si_2C_2}$			$\mathbf{SiC_3}$		
Parameter	Calc	SEVI	Lit	Calc	SEVI	Lit	Calc	SEVI	Lit
ADE (eV)	1.349	1.5374(6)	1.54(8)[a]	1.72	1.9019(4)	1.93(8)[a]	1.807	1.9050(7)	1.93(10)[a]
ν_1 (a_1),(a')	635		658.2[b]	1571			1429	1337(10)	
ν_2 (a_1),(a')	501	514(9)	511.8[b]	698	720(5)		982	976(12)	
ν_3 (a_1),(a')	299	309(7)	309.5[b]	616	636(4)	632[c]	675	682(8)	
ν_4 (b_1),(a')	169	170(6)		482	501(11)		261	261(10)	
ν_5 (b_2),(a')	1081		1101.4[b]	296	305(5)		1069		
ν_6 (b_2),(a")	343	342(8)	357.6[b]	193	196(5)		401		

Table 8.4: Experimental parameters for structures 1a, 2d, and 3e of SiC_3, Si_2C_2, and SiC_3, respectively, extracted from the cryo-SEVI spectrum of the corresponding anion, comparison to theoretical values obtained in the current work (CCSD/aug-cc-pVXZ, X = T for SiC_3, X = D for Si_3C, Si_2C_2), and available literature values. Reported ADEs are for the corresponding anions. Vibrational mode symmetries for Si_3C and SiC_3 are listed first, then those for Si_2C_2. All values are in cm^{-1} unless otherwise stated.
[a] = Ref [452], [b] = Ref [443], [c] = Ref [444]

8.6.2 Isomers and Energetics

Adiabatic detachment energies (ADE) are experimentally determined for each anion isomer by the position of the vibrational origin of the corresponding band in the cryo-SEVI spectrum. For Si_3C^- and SiC_3^-, the lowest energy transitions (peak A) yield ADEs of 1.5374(6) eV and 1.9050(7) eV for structures 1a and 3e, respectively. In the case of $Si_2C_2^-$, structures 2b, 2c, and 2d have been observed with ADEs of 1.30 eV, 2.1291(8) eV, and 1.9019(4) eV, respectively. These values represent an improvement by two orders of magnitude from those previously reported for structures 1a, 2c, and 2d,[452] and represent the first reported value for structures 2b and 3e.

An ADE is equal to the electron affinity of a particular Si_mC_n cluster only when the vibrational origin transition is between the anion and neutral ground state structures. Moreover, the photoelectron spectra of $Si_2C_2^-$ and SiC_3^- presented here and elsewhere exhibit multiple bands, but these do not involve photodetachment from common isomers. For this reason, these spectra alone do not provide enough information to constrain the relative energy ordering of isomers in either the neutral or anionic manifolds. Nonetheless, by comparing experiment and theory, one can obtain information on the anion and neutral energy orderings and place limits on the energy splittings between the various neutral and anion isomers. These considerations lead to the energetics in Figure 8.5 and are discussed in more detail below.

8.6.2.1 Si_3C

Our cryo-SEVI spectrum reports solely on structure 1a of Si_3C and no evidence of the presence of another isomer, in agreement with previous anion PES studies.[452] As our ions are cooled in a clustering channel in the laser ablation source and further in a cryogenic ion trap, the ions produced by the cryo-SEVI apparatus are likely the most stable anion isomers. This suggests that 1a is the global minimum on the Si_3C^- surface, in agreement with theory.[466,470] Further, as it has been established that structure 1a is the global minimum structure of Si_3C,[448] the measured ADE value of Si_3C^- is the adiabatic electron affinity of Si_3C, as show in Figure 8.5.

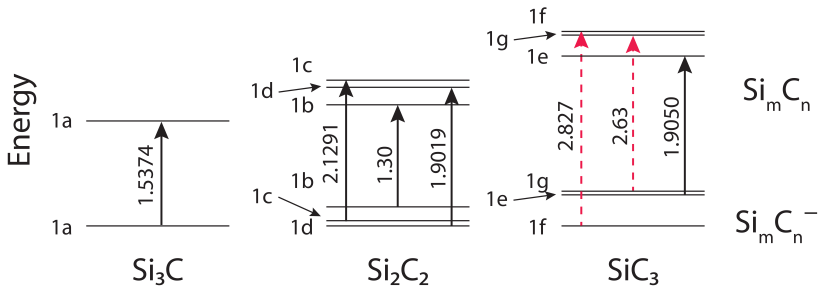

Figure 8.5: Energy level diagram of the various isomers and charge states of Si_3C, Si_2C_2, and SiC_3. Depicted level splittings for the anion and neutral manifolds are from our CCSD calculations, while the reported ADE values are in eV and experimentally determined in this work (black, solid) or that of Davico[453] (red, dashed)

8.6.2.2 Si_2C_2

It is well established that structure 2b is the global minimum for neutral Si_2C_2 whereas either 2c or 2d has been attributed to the global minimum on the anionic surface.[455,458,461,464,470] Our cryo-SEVI spectra, in combination with FC simulations, provide clear evidence that structure 2d is the anionic ground state and represent the first experimental confirmation of structure 2d for neutral Si_2C_2, the only low-lying isomer of Si_2C_2 with a dipole moment – suggesting this species may be observable in the ISM via its rotational spectrum. Bands from other isomers of Si_2C_2 in our cryo-SEVI spectra arise from higher-lying anionic states.

In accordance with these findings, our calculations suggest that structure 2d is the most stable form of $Si_2C_2^-$, with 2c and 2b residing 0.06 eV and 0.38 eV higher, while in the neutral species, 2d resides ∼0.2 eV above 2b and 0.13 eV below 2c (see Table 19 in SI). These calculations also predict ADEs of 1.15, 1.73, and 1.80 eV for structures 2b, 2d, and 2c of $Si_2C_2^-$, respectively, further supporting the assignments of the features observed at ∼1.30 eV, 1.9019(4), and 2.1291(8) eV as detachment from structures 2b, 2d, and 2c, respectively. The assignment of 2b is bolstered by the low relative intensity of the feature - the intensities

of these two bands report on the relative populations of the two isomers, suggesting a small population of $Si_2C_2^-$ in structure 2b, as would be expected for a high-lying anion isomer in our experiment. Similarly, the integrated intensity of all features reporting on structure 2c are dramatically lower than the intensity of those reporting on structure 2d, suggesting a lower population of structure 2c than 2d.

If structures 2b, 2c, and 2d of $Si_2C_2^-$ are assumed to be degenerate, then from the measured ADE values, the neutral structure 2b resides 0.87 and 0.59 eV below structures 2c and 2d, respectively. This value, however, is an upper bound to the neutral splitting, as the 2b anion is undisputedly higher in energy than the 2c and 2d anions, with our calculations suggesting it lies 0.38 eV above the 2d ground state. A similar analysis yields an upper bound for structure 2c residing 0.299 eV above 2d, which is likely close to the actual value as the appearance of both structures 2c and 2d with similar intensity here and in the previous work by Kaya[452] suggests that the isomers have similar energetics, in agreement with our calculated energy splitting of 0.059 eV between these two anions.

8.6.2.3 SiC_3

Finally, we return to the longstanding question surrounding the ground state of SiC_3, for which theoretical reports have shown strong method-dependence on the determined ground state structure.[454,461,464,465,467,468,470,471] Previous PES studies by Kaya[452] and Lineberger[453] have confirmed the ADE of the linear structure 3f as 2.827 eV and observed two other bands with ADEs of 1.93(10) and 2.629 eV, both attributed to ring structures. Our current investigation has revisited the lowest eBE feature and shows it to originate from structure 3e, while the 2.629 eV feature from Lineberger *et al.* is found to match well with our FC-simulations for structure 3g (Figure 8.17 in SI).

Much like in the case of Si_2C_2, the photodetachment transitions measured previously and here do not map onto a common neutral state. The measured ADE of structure 3e of SiC_3^- is 0.725 and 0.922 eV lower than structures 3g and 3f, respectively, and a similar treatment to that described for Si_2C_2 gives these values as upper bounds for the energetic splitting between the neutral isomers. This is likely close to the true splitting of structures 3e and 3g, though the latter of these upper bounds is a significant overestimation, as structures 3e and 3g of SiC_3^- has been calculated to reside $\sim$0.5 eV above the linear structure 3f both here and previously.[461,462,470] These calculations are supported by previous PES studies that observe an increase in intensity of the features corresponding to the ring isomers as experimental conditions are varied to favor hotter ion production.

For structure 3e to not be the ground state of SiC_3 would require its anion to reside nearly twice as high as predicted – close to a full eV above structure 3f. As it has been established that the cryo-SEVI apparatus tends to favor production of low-lying isomers,[60] the appearance of such an energetically unfavorable anion would be rather surprising. Further, we find poor signal to noise despite good ion signal, indicating a low population of structure 3e consistent with the calculated splitting of 0.5 eV. It seems unlikely, then, that the calculated energetics are in error by the factor of two required to impact the neutral

ordering. Collectively, the results presented here demonstrate that structure 3e is not the ground state of SiC_3^- but favor it as the global minimum of SiC_3.

8.7 Conclusion

High resolution cryo-SEVI spectra of Si_3C^-, $Si_2C_2^-$, and SiC_3^- are presented along with high-level *ab initio* calculations. Spectral assignments are readily obtained by comparison to simulated Franck-Condon profiles, revealing forbidden transitions in each cluster, ascribed to vibronic coupling in Si_3C and SiC_3 or vibrational autodetachment in Si_2C_2. Detachment from $Si_2C_2^-$ reveals the presence of three isomers of this anion present after cryogenic cooling, allowing for the determination of structure 2d as the ground state of $Si_2C_2^-$. Reinvestigation of the low eBE region of SiC_3^- shows structure 3e is responsible for this band, providing the first vibrational characterization of this isomer of SiC_3. Experimental ADEs are extracted from these spectra for structures 1a, 2b,c,d, and 3e of Si_3C^-, $Si_2C_2^-$, and SiC_3^-, representing an improvement of two orders of magnitude over previously reported values. Upper bounds on the energetic splitting of the Si_2C_2 and SiC_3 neutral clusters are established and suggest that the long-contested ground state of SiC_3 is a ring structure with a transannular C-C bond.

8.8 Supplementary Material

8.8.1 Si_2C_2 Distortions

In the case of Si_2C_2, significant discrepancies between the simulated FC profiles and experiment were observed with respect to the ν_2 and ν_3 normal modes (see Figure 8.8 below). These were addressed by making small displacements along various normal modes to the neutral geometry, as we have done before.[433] For a displacement of magnitude δ along normal mode ν_a, the transformed CCSD/aug-cc-pVDZ geometry is given by

$$\vec{r}^{(i)} = \vec{r}_{eq}^{(i)} + \delta\vec{q}_a^{(i)} \tag{8.2}$$

Where $\vec{r}_{eq}^{(i)}$ and $\vec{r}^{(i)}$ are the equilibrium and shifted positions of the i^{th} atom, respectively, and $\vec{q}^{(i)}$ is the displacement vector for the i^{th} atom associated with mode ν_a. Figure 8.9 demonstrates that a displacement of magnitude δ = -0.2 along the ν_3 and δ = -0.05 along the ν_2 provide exceptional agreement with the experimental spectrum. The ν_2 and ν_3 modes correspond to stretches of the C-C and a Si-C bond, respectively, shifting this structure toward a C_{2v} trapezoidal structure. Changes to the geometry of this structure are provided in Figure 8.18 below, and amount to fractional changes in all quantities except the Si-C bond length and angle, whose quantities change by ∼9%. Normal mode displacement vectors used for these adjustments of the neutral geometry are provided below in Tables 8.30 and 8.31

below. A similar treatment can be performed on anionic Si_2C_2 to give similar FC profiles for photodetachment.

This distorted geometry was used as a guess geometry for subsequent calculations at the CCSD(T)/aug-cc-pVDZ level, but was found less stable than the reported Si_2C_20/- 1d structure by ∼0.33 eV and ∼0.42 eV for Si¬2C2 and $Si_2C_2^-$, respectively, as shown in Table 19 below. Given both the relative stability of the neutral distortion over the anionic distortion, better agreement between the calculated ADE for the distorted neutral (2.05 eV) than the anionic distortion (1.31 eV), and better agreement between calculated excited states of $Si_2C_2^-$ and the photon energies of spectra showing autodetachment, we assume distortion to the neutral structure, rather than the anion.

8.8.2 SiC_3^- Distortions

Similar to the case of Si_2C_2, distortion along the neutral ν_3 normal coordinate was required to reproduce the observed intensities of features in this spectrum. It was found that a mere $\delta = 0.05$ distortion along the neutral ν_3 coordinate to the structure of SiC_3^- was sufficient to reproduce the intensity of features D, F, and G in this spectrum, corresponding to an average change in bond length and angle of 1% as show in Figure 8.21 below. This distorted geometry was used as starting point for subsequent calculations at the CCSD/aug-cc-pVDZ level, but was found to be less stable than the global minimum by 0.047 eV. Distortion to the anion was chosen over the neutral as microwave spectra have provided accurate experimental bond-lengths for the neutral species, while the anion is less well characterized.

8.8.3 Spectra with FC-simulations using calculated values

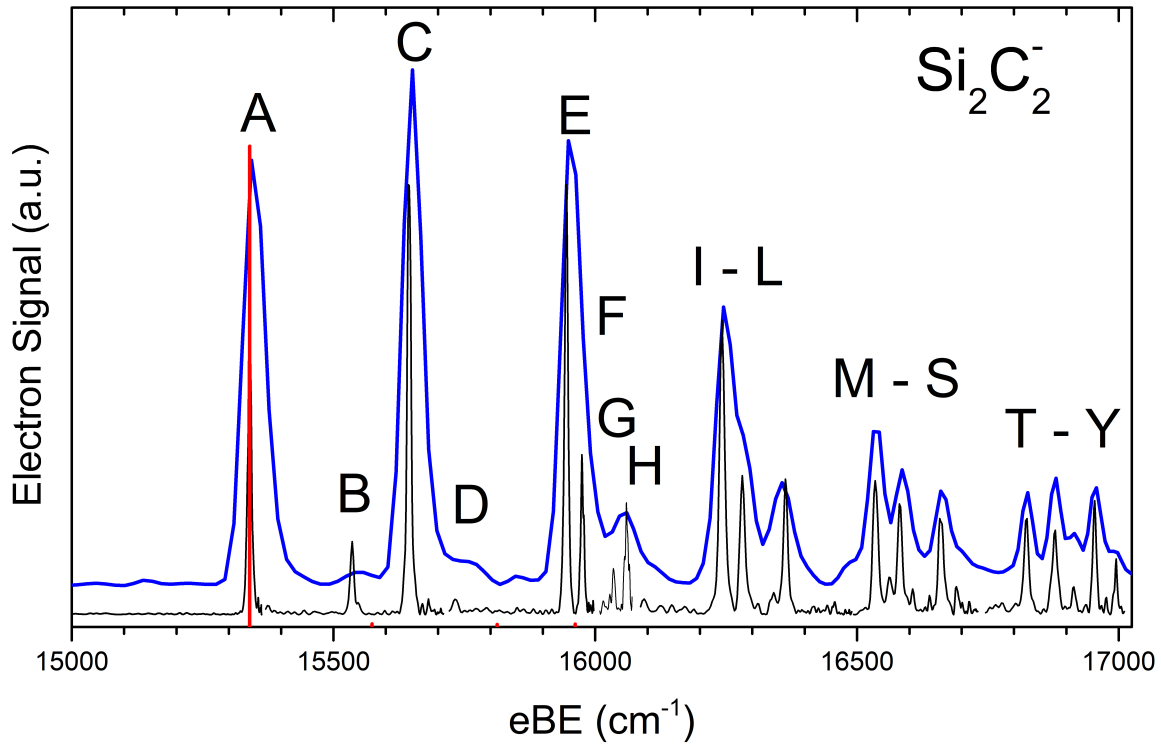

Figure 8.6: cryo-SEVI spectra of the $\tilde{X}^1A' \leftarrow \tilde{X}^2A$" transition of $Si_2C_2^-$ with Franck-Condon simulations for the linear isomer (1c, main text). Poor agreement between the simulated spectrum and experimental data exclude this isomer from consideration as a contribution to this spectrum.

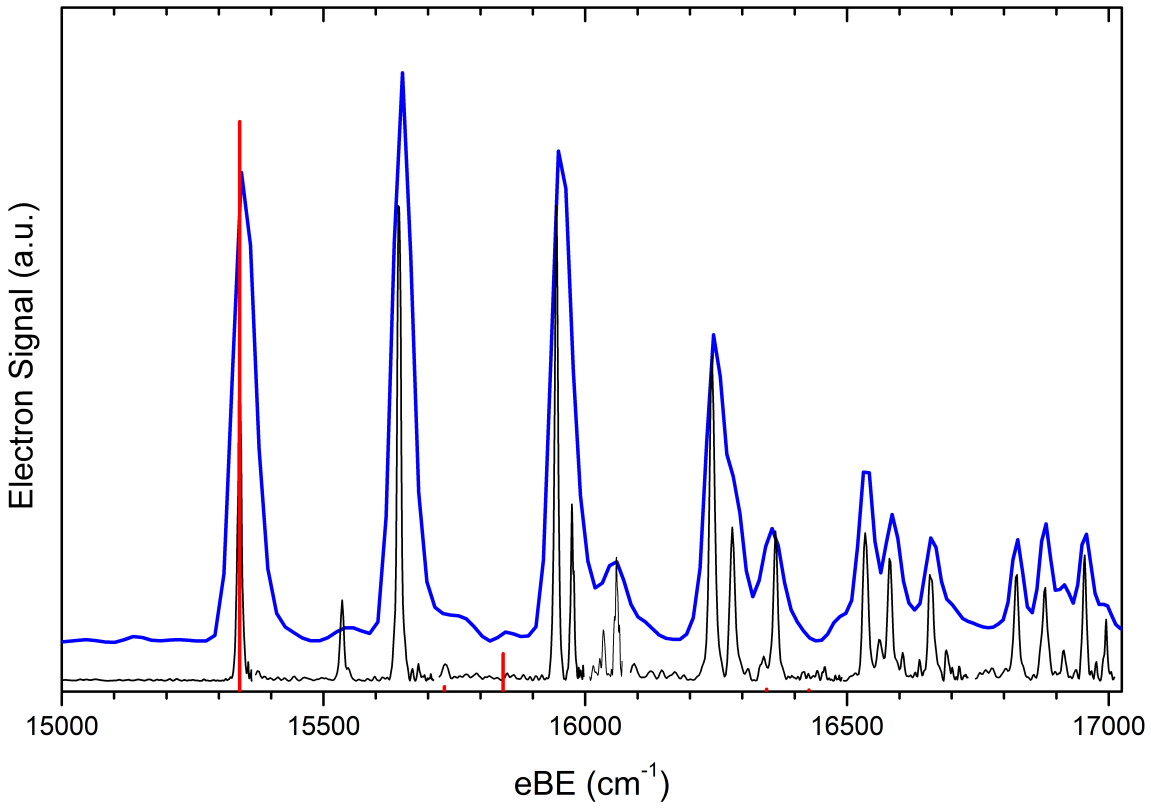

Figure 8.7: cryo-SEVI spectra of the $\tilde{X}^1A' \leftarrow \tilde{X}^2A$" transition of $Si_2C_2^-$ with Franck-Condon simulations for the rhombic isomer (1b, main text). Poor agreement between the simulated spectrum and experimental data exclude this isomer from consideration as a contribution to this spectrum.

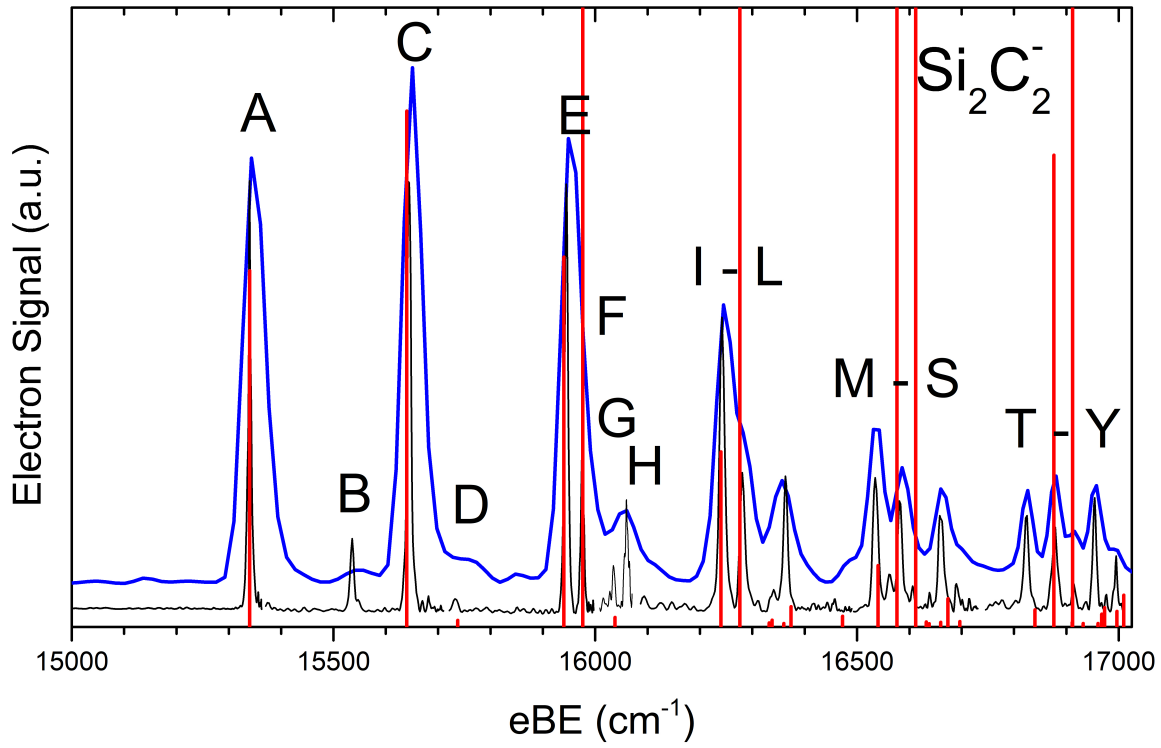

Figure 8.8: cryo-SEVI spectra of the $\tilde{X}^1A' \leftarrow \tilde{X}^2A$" transition of $Si_2C_2^-$ with Franck-Condon simulations for the distorted trapezoid isomer (1d, main text) using calculated values, rather than scaled values (see Table S22 below). Reproduction of the general structure of the experimental spectrum is present, though activity along the ν_3 mode is substantially higher than measured.

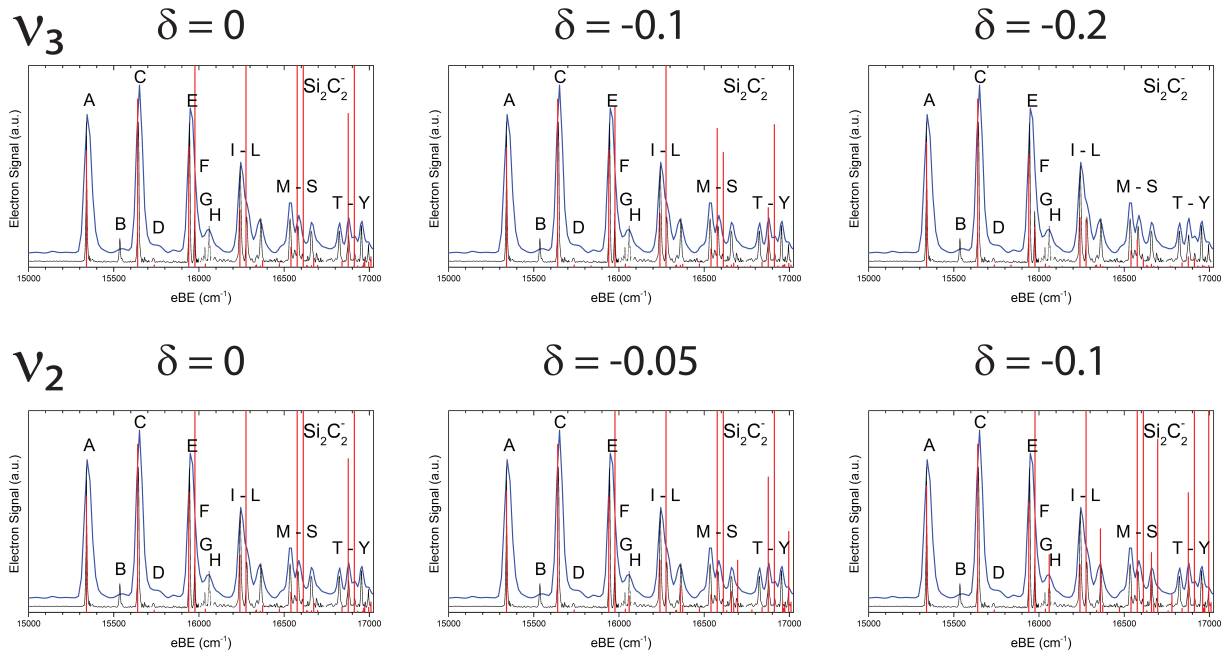

Figure 8.9: cryo-SEVI spectra of the $\tilde{X}^1A' \leftarrow \tilde{X}^2A$" transition of $Si_2C_2^-$ with Franck-Condon simulations for the distorted trapezoid isomer (1d, main text) with distortions along the ν_3 or ν_2 normal coordinates. Distortions along the ν_3 normal coordinate reduce the overestimation of the activity along this mode (features F, J, O, P, U, and V), while distortions along the ν_2 normal coordinate increase the intensity of transitions along this mode (features H, N, S, and W). Reproduction of the experimental spectrum is found by distorting by δ = -0.2 along the ν_3 and δ = -0.05 along the ν_2 normal coordinates.

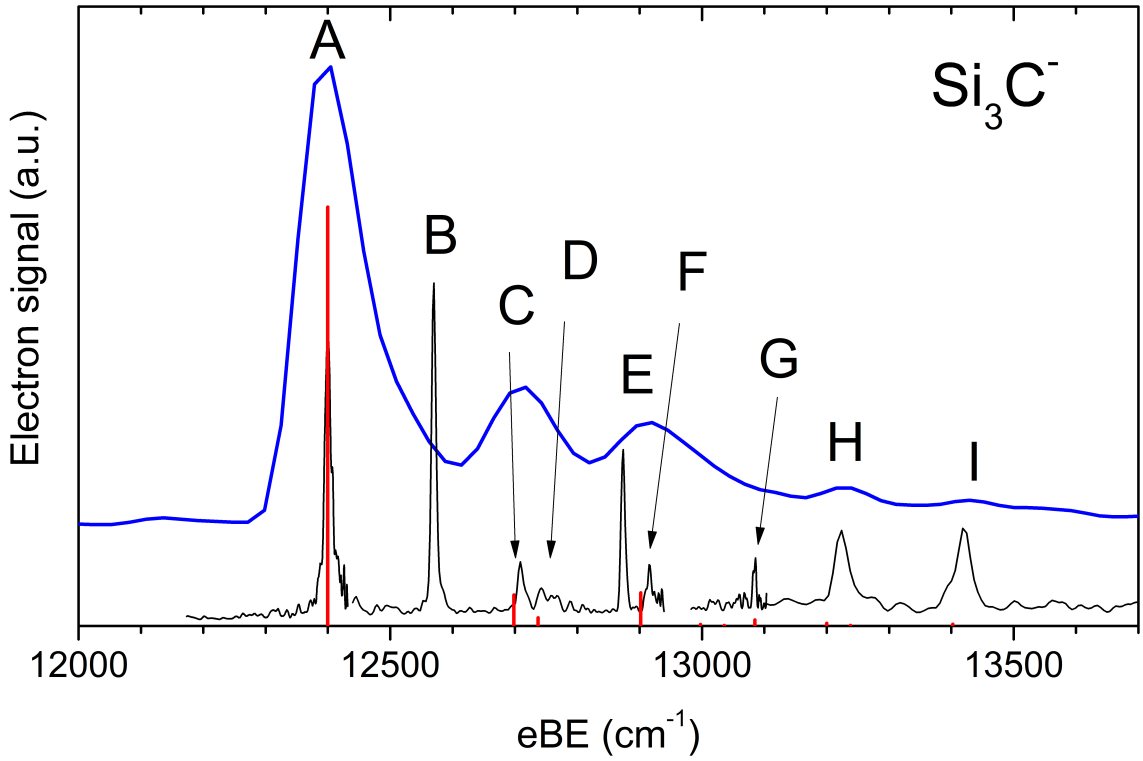

Figure 8.10: cryo-SEVI spectrum of the $\tilde{X}^1A_1 \leftarrow \tilde{X}^2A_2$ transition of Si_3C^- with Franck-Condon simulations using the calculated frequencies for Si_3C (1a, main text), rather than experimentally determined values (see Table S21 below).

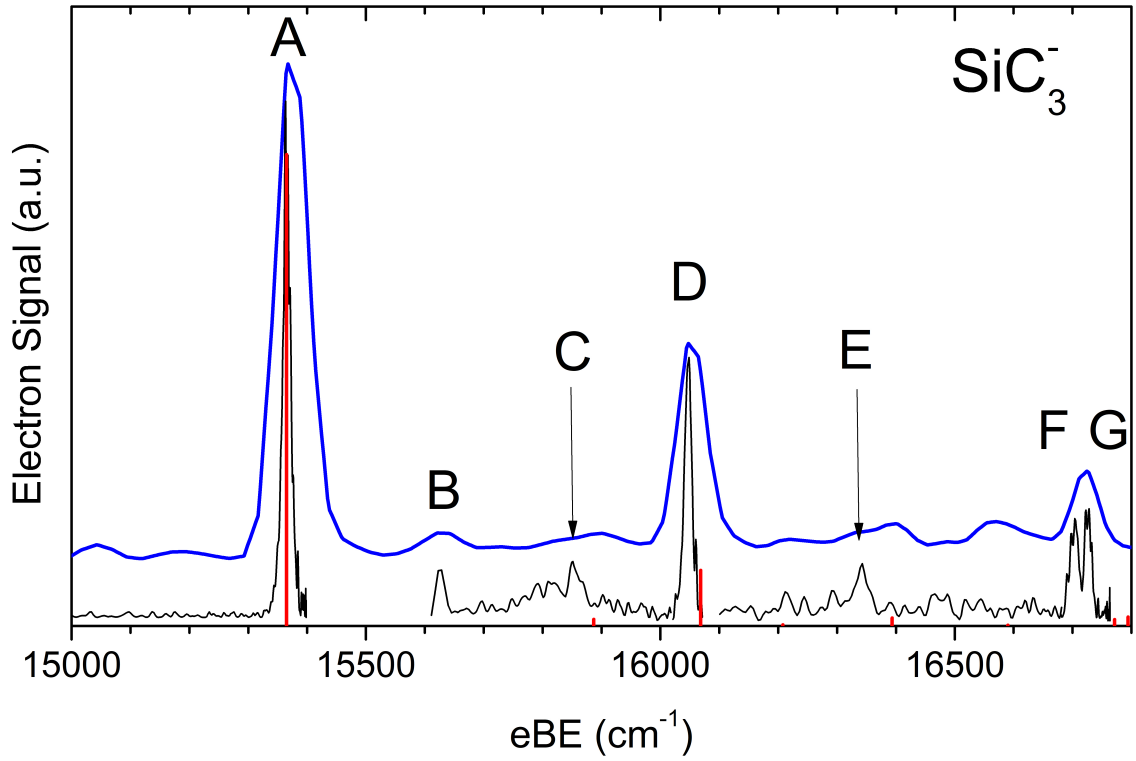

Figure 8.11: cryo-SEVI spectra of the $\tilde{X}^1A_1 \leftarrow \tilde{X}^2B_1$ transition of SiC_3^- with Franck-Condon simulations using the calculated frequencies for the transannular C-C bonding ring isomer (1e, main text), rather than experimentally determined values (see Table S23 below).

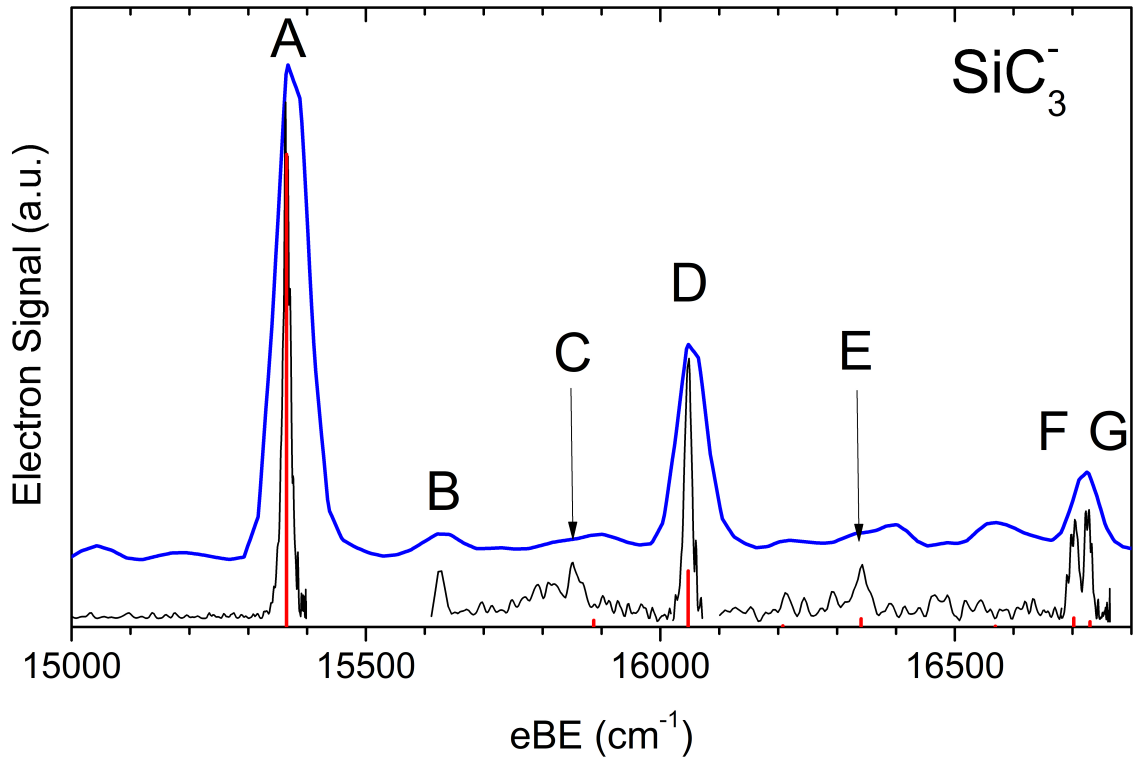

Figure 8.12: cryo-SEVI spectra of the $\tilde{X}^1A_1 \leftarrow \tilde{X}^2B_1$ transition of SiC_3^- with Franck-Condon simulations using the calculated geometry and experimental frequencies for the transannular C-C bonding ring isomer (1e, main text), rather than experimentally determined values (see Table S23 below).

8.8.4 Evidence of Herzberg-Teller coupling in Si_3C

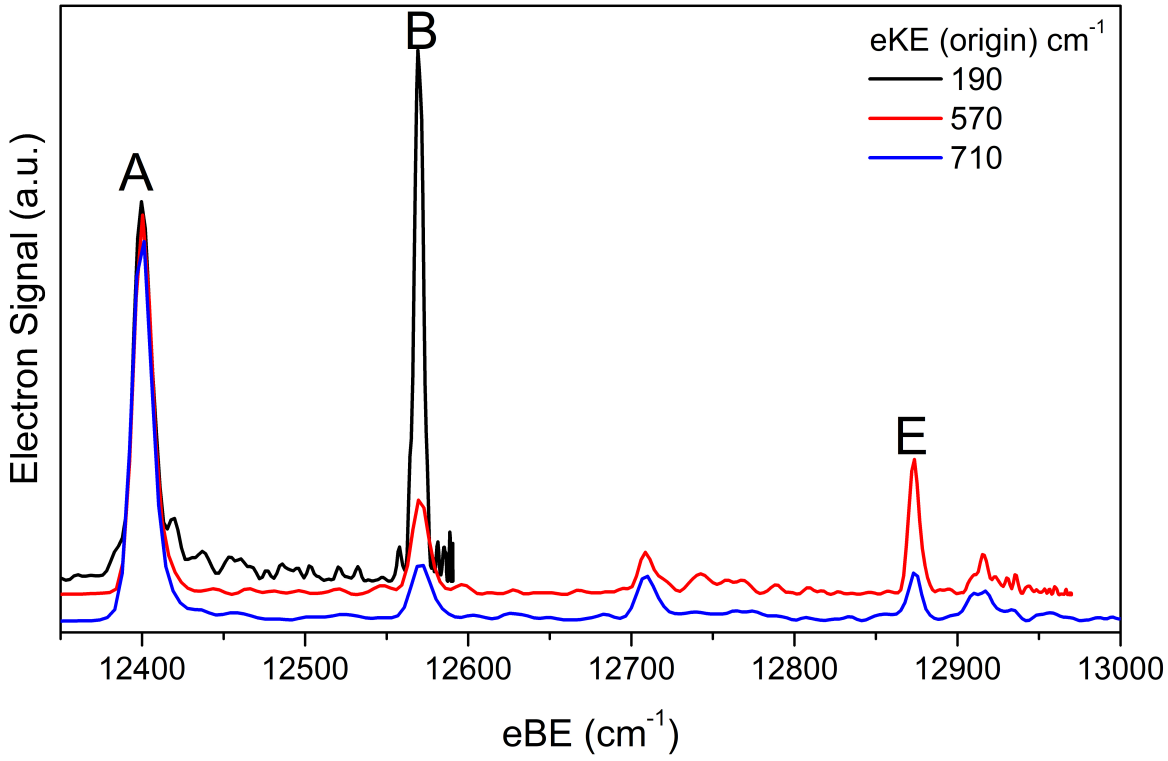

Figure 8.13: cryo-SEVI spectra of Si_3C^- at several photon energies displaying the differing signal attenuation for Features A, B, and E. The intensity of each scan has been normalized to peak A.

8.8.5 Evidence of Si_2C_2 vibrational autodetachment

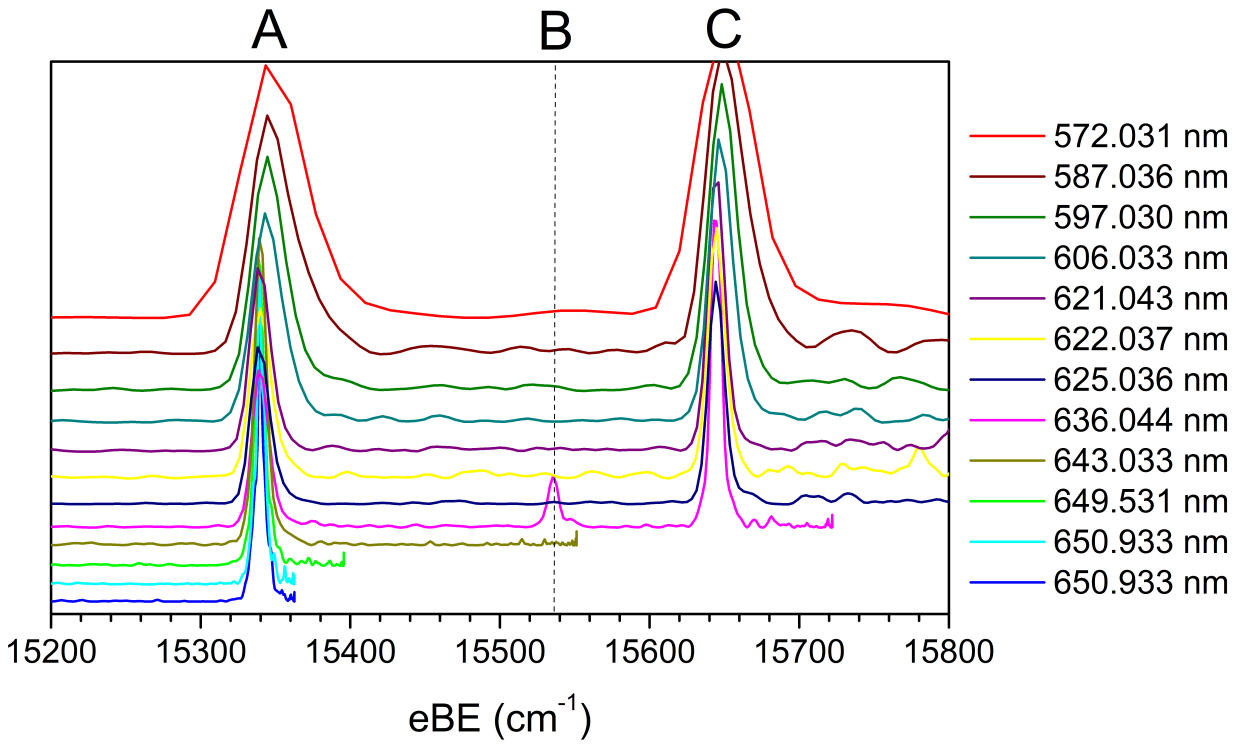

Figure 8.14: All cryo-SEVI spectra of $\tilde{X}^1A' \leftarrow \tilde{X}^2A$" transition of $Si_2C_2^-$ collected in this study, illustrating the appearance of the 6_0^1 transition (peak B, main text) at only one photon energy (636.044 nm, 1.94930 eV). This value is in good agreement with the EOM-CCSD value for the $\tilde{C}$ state of $Si_2C_2^-$ (see Table S18 below). The ordering of wavelengths used in the legend corresponds to the ordering presented in this waterfall plot.

8.8.6 Evidence of Herzberg-Teller coupling in SiC_3

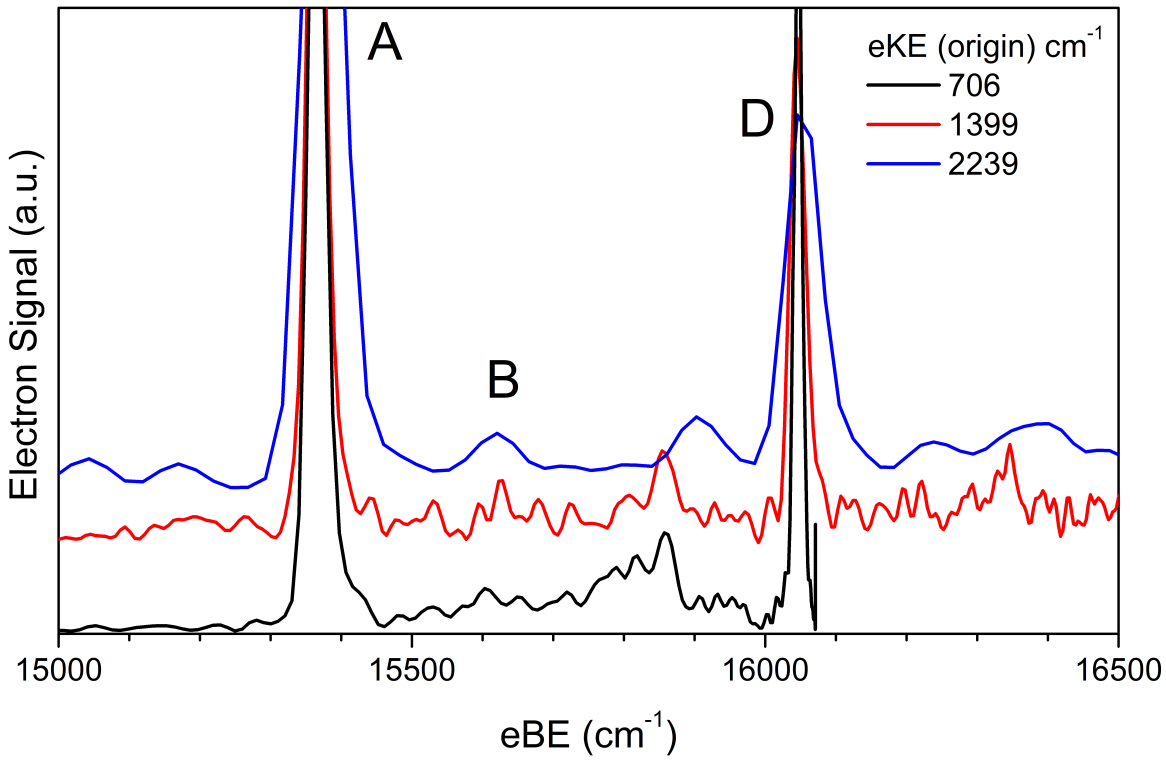

Figure 8.15: cryo-SEVI spectra of SiC_3^- at several photon energies displaying the differing signal attenuation for Features A, B, and E. The intensity of each scan has been normalized to peak A.

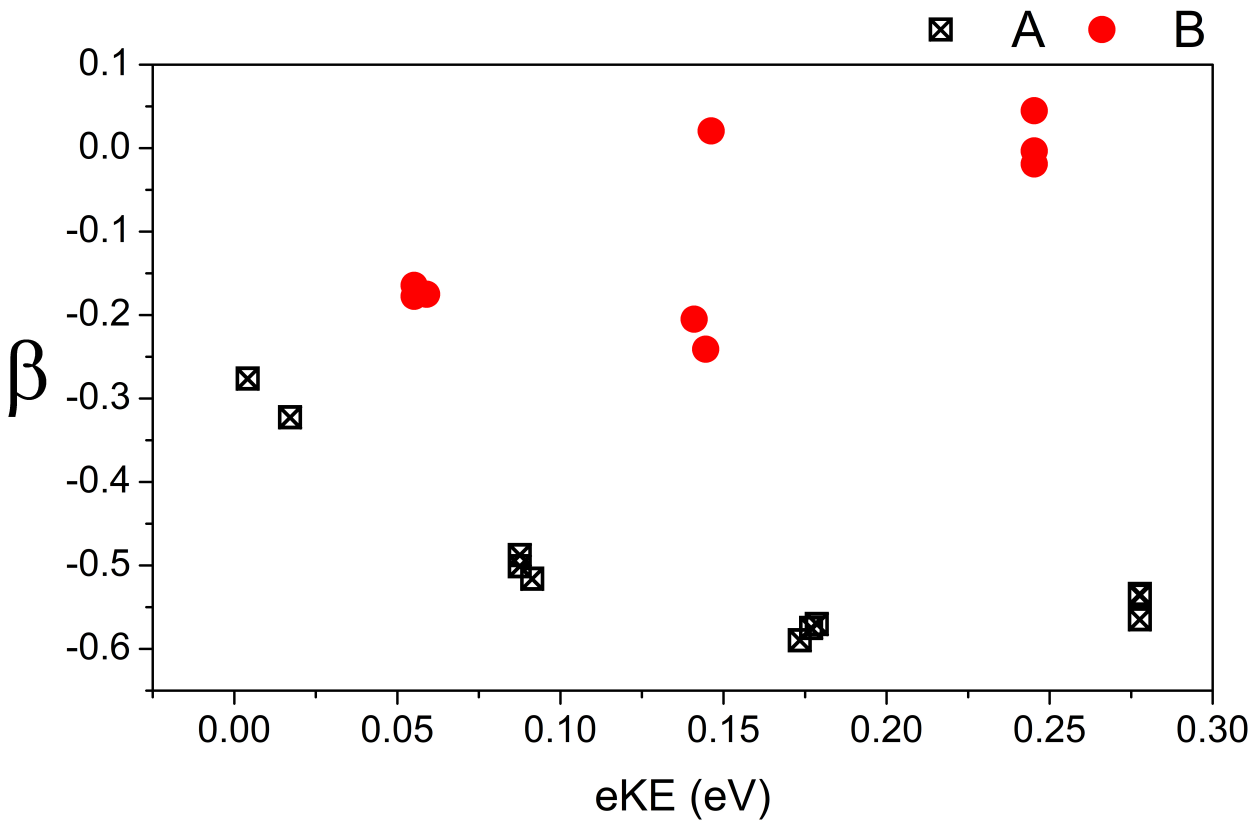

Figure 8.16: Measured anisotropy parameter, β, of features A and B in SiC_3 extracted from spectra obtained at multiple photon energies.

8.8.7 Evidence of SiC_3 structure previously observed

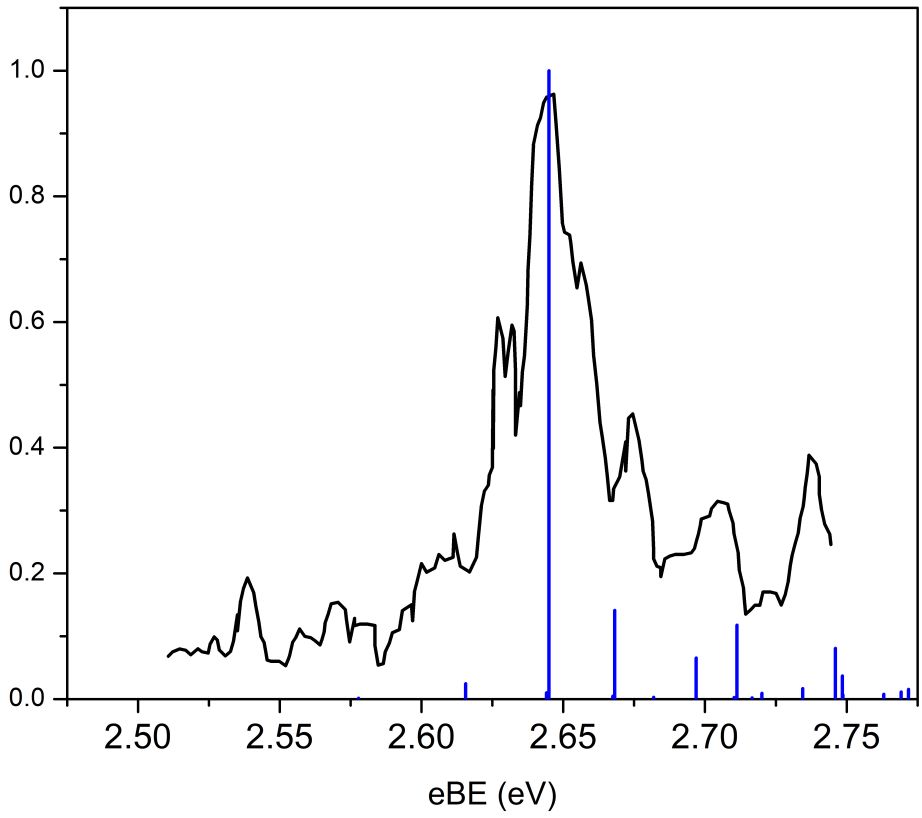

Figure 8.17: Blow-up of low eBE region from Lineberger *et al.*[453] Franck-Condon simulations for the Si-C transannular ring structure (1g main text) without scaling and including hot bands at 180 K, the reported ion temperature, are presented. Good agreement between our simulation and this data suggests observation of structure 1g with a reported adiabatic detachment energy of 2.63 eV.

8.8.8 Si_2C_2 distortion

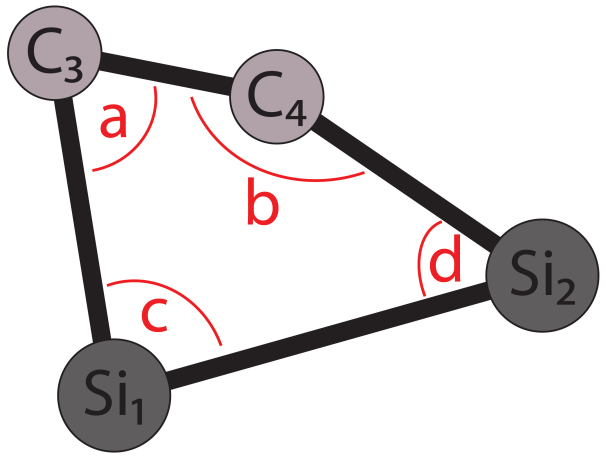

	Calculated	Distorted	Change	% Change
C_3-C_4	1.33292	1.28647	-0.04645	-3.485
C_4-Si_2	1.81603	1.99196	0.17593	9.688
Si_2-Si_1	2.54057	2.55527	0.0147	0.579
C_3-Si_1	2.02941	2.05461	0.0252	1.242
a	68.62104	74.31127	5.69023	8.292
b	156.4585	146.7521	-9.70637	-6.204
c	84.09963	85.40236	1.30273	1.549
d	50.82087	53.53429	2.71342	5.339

Table 8.5: Si_2C_2 geometry for the optimized structure (Calculated) and the structure used in Franck-Condon simulations (Distorted). Bond lengths are reported in Ångströms (Å) and bond angles (a-d) are reported in degrees.

8.8.9 SiC_3^- distortion

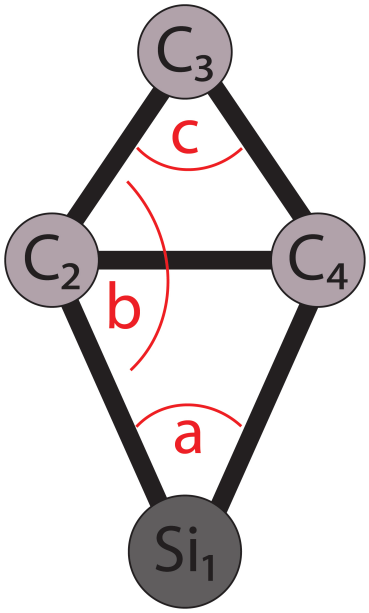

Figure 8.18

	Calculated	Distorted	Change	% Change
Si_1-$C_{2,4}$	1.89382	1.93488	0.04106	2.168
C_2-C_4	1.46841	1.43362	-0.03479	-2.369
$C_{2,4}$-C_3	1.42171	1.40867	-0.01304	-0.917
a	45.62113	43.48899	-2.13214	-4.673
b	126.0968	127.6679	1.57116	1.246
c	62.18531	61.17513	-1.01018	-1.624

Table 8.6: SiC_3^- geometry for the optimized structure (Calculated) and the structure used in Franck-Condon simulations (Distorted). Bond lengths are reported in Ångströms (Å) and bond angles (a-d) are reported in degrees.

8.8.10 Computationally determined geometries (used in main text)

Atom	X	Y	Z
C	0	0	-0.72989
Si	0	0	1.25055
Si	0	1.76598	-0.47477
Si	0	-1.76598	-0.47477

Table 8.7: Calculated geometry for Si_3C at the CCSD/aug-cc-pVDZ level of theory. All values in Ångströms (Å)

Atom	X	Y	Z
C	0	0	0.73647
Si	0	0	-1.218
Si	0	-1.79141	0.44921
Si	0	1.79141	0.44921

Table 8.8: Calculated geometry for Si_3C^- at the CCSD/aug-cc-pVDZ level of theory. All values in Ångströms (Å)

Atom	X	Y	Z
Si	-0.95911	2.74086	0
Si	1.48347	2.04206	0
C	-1.31378	0.74268	0
C	-0.00676	1.00418	0

Table 8.9: Calculated geometry for Si_2C_2 (structure 1d) at the CCSD/aug-cc-pVDZ level of theory. All values in Ångströms (Å)

Atom	X	Y	Z
Si	-0.92161	2.79736	0
Si	1.51447	2.02606	0
C	-1.38278	0.79518	0
C	-0.09776	0.85618	0

Table 8.10: Geometry for Si_2C_2 (structure 1d, distorted) used in the Franck-Condon simulations presented in Figure 8.2B of the main text. All values in Ångströms (Å)

Atom	X	Y	Z
Si	-0.87391	2.73971	0
Si	1.45929	2.11888	0
C	-1.34073	0.70961	0
C	-0.04082	0.96157	0

Table 8.11: Calculated geometry for $Si_2C_2^-$ (structure 1d) at the CCSD/aug-cc-pVDZ level of theory. All values in Ångströms (Å)

Atom	X	Y	Z
Si	0	0	1.1691
C	0	0.73895	-0.51453
C	0	-0.73895	-0.51453
C	0	0	-1.74272

Table 8.12: Calculated geometry for SiC_3 (structure 1e) at the CCSD/aug-cc-pVTZ level of theory. All values in Ångströms (Å)

Atom	X	Y	Z
Si	0	0	1.21297
C	0	0.73421	-0.53273
C	0	-0.73421	-0.53273
C	0	0	-1.75019

Table 8.13: Calculated geometry for SiC_3^- (structure 1e) at the CCSD/aug-cc-pVTZ level of theory. All values in Ångströms (Å)

Atom	X	Y	Z
Si	0	0	1.24097
C	0	0.71681	-0.55623
C	0	-0.71681	-0.55623
C	0	0	-1.76889

Table 8.14: Geometry for SiC_3^- (structure 1e, distorted) used in the Franck-Condon simulations presented in Figure 8.2B of the main text. All values in Ångströms (Å)

8.8.11 Computationally determined geometries (not used in main text)

Atom	X	Y	Z
Si	0	0	-2.40725
Si	0	0	2.40725
C	0	0	-0.64818
C	0	0	0.64818

Table 8.15: Calculated geometry for Si_2C_2 (structure 1c, triplet) at the CCSD/aug-cc-pVDZ level of theory. All values in Ångströms (Å)

Atom	X	Y	Z
Si	0	0	-2.41588
Si	0	0	2.41588
C	0	0	-0.64861
C	0	0	0.64861

Table 8.16: Calculated geometry for Si_2C_2 (structure 1c, singlet) at the CCSD/aug-cc-pVDZ level of theory. All values in Ångströms (Å)

Atom	X	Y	Z
Si	0	0	-2.39976
Si	0	0	2.39976
C	0	0	-0.66394
C	0	0	0.66394

Table 8.17: Calculated geometry for $Si_2C_2^-$ (structure 1c) at the CCSD/aug-cc-pVDZ level of theory. All values in Ångströms (Å)

Atom	X	Y	Z
Si	0	0	-1.70998
Si	0	0	1.70998
C	0	0.73214	0
C	0	-0.73214	0

Table 8.18: Calculated geometry for Si_2C_2 (structure 1b) at the CCSD/aug-cc-pVDZ level of theory. All values in Ångströms (Å)

Atom	X	Y	Z
Si	0	-0.02528	-1.73325
Si	0	0.02528	1.73325
C	0	0.7304	-0.01073
C	0	-0.7304	0.01073

Table 8.19: Calculated geometry for $Si_2C_2^-$ (structure 1b) at the CCSD/aug-cc-pVDZ level of theory. All values in Ångströms (Å)

Atom	X	Y	Z
Si	0	0	-2.391
C	0	0	-0.65311
C	0	0	0.64018
C	0	0	1.94893

Table 8.20: Calculated geometry for SiC_3 (structure 1f, singlet) at the CCSD/aug-cc-pVTZ level of theory. All values in Ångströms (Å)

Atom	X	Y	Z
Si	0	0	-2.3806
C	0	0	-0.65359
C	0	0	0.63564
C	0	0	1.94355

Table 8.21: Calculated geometry for SiC_3 (structure 1f, triplet) at the CCSD/aug-cc-pVTZ level of theory. All values in Ångströms (Å)

Atom	X	Y	Z
Si	0	0	-2.37429
C	0	0	-0.67579
C	0	0	0.65766
C	0	0	1.93742

Table 8.22: Calculated geometry for SiC_3^- (structure 1f, singlet) at the CCSD/aug-cc-pVTZ level of theory. All values in Ångströms (Å)

Atom	X	Y	Z
Si	0	0	0.94902
C	0	1.29946	-0.62169
C	0	-1.29946	-0.62169
C	0	0	-0.94917

Table 8.23: Calculated geometry for SiC_3 (structure 1g) at the CCSD/aug-cc-pVTZ level of theory. All values in Ångströms (Å)

Atom	X	Y	Z
Si	0	0	0.89918
C	0	1.31418	-0.5997
C	0	-1.31418	-0.5997
C	0	0	-0.9433

Table 8.24: Calculated geometry for SiC_3^- (structure 1g) at the CCSD/aug-cc-pVTZ level of theory. All values in Ångströms (Å)

8.8.12 Relative Energetics

	1c (triplet)	1b	1d	Distorted 1d
Anion Relative Energy	0.058667778	0.375299629	0	-
Neutral Relative Energy	0.330591299	0	0.200656864	0.330155916
Calculated ADE	1.797884409	1.150661	1.726618	2.056774
Experimental ADE	2.2[b]	1.3[a]	-	1.9019(4)[a]

Table 8.25: Relative energetics for isomers 1b-d of Si_2C_2 and $Si_2C_2^-$, calculated at the CCSD/aug-cc-pVDZ level. Values are reported in eV and are zero point energy corrected. The energetic value of the distorted 1d structure was calculated as a single point CCSD/aug-cc-pVDZ level and is zero point corrected using the correction value for 1d (0.239106572 eV). [a] = this work [b] = Ref [452]

	1f	1e	1e (dist)	1g
Anion Relative Energy	0.000000	0.521370	0.568990	0.554378
Neutral Relative Energy	0.276522	0.000000	-	0.254617
Calculated ADE	2.627914	1.806510	1.854130	2.034923
Measured ADE	2.827(7)[a]	1.9050(7)[b]	1.9050(7)[b]	2.63[a]

Table 8.26: Relative energetics of isomers 1e-g for SiC_3 and SiC_3^-, calculated at the CCSD/aug-cc-pVTZ level. Values are reported in eV and are zero point energy corrected. The energetic value of the distorted 1e structure was calculated as a single point CCSD/aug-cc-pVTZ level and is zero point corrected using the correction value for 1d (0.292821875 eV). [a] = Ref [453] [b] = this work

8.8.13 Computational Tables

Mode	Calculated	Scaled
$\nu_1(a_1)$	635	658
$\nu_2(a_1)$	501	512
$\nu_3(a_1)$	299	310
$\nu_4(b_1)$	169	169
$\nu_5(b_2)$	1081	1101
$\nu_6(b_2)$	343	357

Table 8.27: Vibrational frequencies (in cm^{-1}) for Si_3C obtained at the CCSD/aug-cc-pVDZ level. The scaled frequencies, representing the previously measured experimental values,[443] are used in the Franck-Condon simulations presented in Figure 8.2A of the main text are also presented.

Mode	Calculated	Scaled
ν_1 (a')	1571	1571
ν_2 (a')	698	720
ν_3 (a')	616	636
ν_4 (a')	482	495
ν_5 (a')	296	300
ν_6 (a")	193	199

Table 8.28: Vibrational frequencies (in cm^{-1}) for Si_2C_2 obtained at the CCSD/aug-cc-pVDZ level. The scaled frequencies, representing the experimentally determined values in this study, are used in the Franck-Condon simulations presented in Figure 8.2B of the main text are also presented.

Mode	Calculated	Scaled
$\nu_1(a_1)$	1429	1337
$\nu_2(a_1)$	982	976
$\nu_3(a_1)$	675	682
$\nu_4(b_1)$	261	261
$\nu_5(b_2)$	1069	1069
$\nu_6(b_2)$	401	421

Table 8.29: Vibrational frequencies (in cm^{-1}) for SiC_3 obtained at the CCSD/aug-cc-pVTZ level. The scaled frequencies, representing the experimentally determined values in this study, are used in the Franck-Condon simulations presented in Figure 8.2C of the main text are also presented.

State	Si_3C	Si_2C_2	Distorted Si_2C_2	$Si_2C_2^-$	SiC_3
$\tilde{A}$	2.0201 ($^1B_1$)	1.4834 (^1A")	1.1527 (^1A")	1.4387 (^2A")	1.9145 ($^1B_1$)
$\tilde{B}$	2.8307 ($^1A_2$)	2.5811 (^1A")	2.3366 (^1A")	1.4783 (^2A')	3.5693 ($^1A_2$)
$\tilde{C}$	2.9568 ($^1A_2$)	4.4238 (^1A')	3.9929 (^1A')	1.9560 (^2A")	3.5832 ($^1B_1$)
$\tilde{D}$	3.2157 ($^1B_1$)	5.2286 (^1A')	4.8351 (^1A')	3.1603 (^2A')	4.1274 ($^1A_2$)

Table 8.30: Calculated excited state energetics for all species of interest in the main text. All values and symmetries were determined at the EOM-CCSD/aug-cc-pVXZ level of theory, where X = D in all cases except SiC_3, where X = T. All values presented are in eV with states responsible for features in the cryo-SEVI spectra highlighted

Atom	X	Y	Z
Si	-0.11	-0.21	0
Si	0.34	-0.2	0
C	-0.38	0.19	0
C	-0.18	0.76	0

Table 8.31: Displacements of atoms in Si_2C_2 along the ν_2 normal coordinate. A shift of $\delta = 0.05$, as used in the Franck-Condon simulations presented in the paper, corresponds to the product of each displacement by 0.05.

Atom	X	Y	Z
Si	-0.16	-0.23	0
Si	-0.24	0.13	0
C	0.44	-0.31	0
C	0.5	0.55	0

Table 8.32: Displacements of atoms in Si_2C_2 along the ν_3 normal coordinate. A shift of $\delta = 0.2$, as used in the Franck-Condon simulations presented in the paper, corresponds to the product of each displacement by 0.2.

Part III

Metal Oxide Clusters

Chapter 9

Vibronic Structure of NdO

The content and figures of this chapter are reprinted or adapted with permission from M. C. Babin, M. DeWitt, J. A. DeVine, D. C. McDonald, S. G. Ard, N. S. Shuman, A. A. Viggiano, L. Cheng, D. M. Neumark, "Electronic structure of NdO via slow photoelectron velocity-map imaging spectroscopy of NdO^-" *J. Chem. Phys.* **155**, 114301 (2021).

9.1 Abstract

Electronically excited NdO is a possible product of the chemistry associated with the release of Nd into the ionosphere, and emission from these states may contribute to the observations following such experiments. To better characterize the energetics and spectroscopy of NdO, we report a combined experimental and theoretical study using slow photoelectron velocity-map imaging spectroscopy of cryogenically cooled NdO^- anions (cryo-SEVI) supplemented by wavefunction-based quantum-chemical calculations. Using cryo-SEVI, we measure the electron affinity of NdO to be 1.0091(7) eV and resolve numerous transitions to low-lying electronic and vibrational states of NdO that are assigned with the aid of the electronic structure calculations. Additionally, temperature-dependent data suggests contributions from the (2)4.5 state of NdO^- residing 2350 cm^{-1} above the ground anion state. Photodetachment to higher-lying excited states of NdO is also reported, which may help clarify observations from prior release experiments.

9.2 Introduction

The electron density of the ionosphere, a region of low density plasma in the upper reaches of earth's atmosphere, significantly impacts radio wave propagation, with the potential to reflect, refract, disperse, or absorb radiation dependent upon frequency.[487] The ionosphere is far from static, with predictable seasonal and diurnal variation[488] as well as unpredictable short term turbulence in the electron densities that can lead to a variety of communications issues. These effects have motivated significant research into the causes and dynamics of

ionospheric phenomena, such as equatorial plasma bubbles,[489] which are transient regions of reduced plasma density formed near the equator, and sporadic E-layers,[490] transient regions of enhanced electron density formed at lower altitudes than those typically associated with high electron concentrations. There have also been efforts to determine whether artificially produced plasma can prevent or mitigate the impacts of ionospheric variations. To this end, many ionospheric chemical release experiments have been performed, with the released species typically being materials such as barium or cesium that are easily vaporized, have low ionization energies, and have resonant excitations lying within the solar spectrum.[491] This approach is limited to daytime use, as electron production is dependent upon photo-ionization.

In recent years, attention has turned towards a different mechanism for plasma production: chemi-ionization. A range of metals, primarily lanthanides, form metal oxide cations with bond energies that exceed the ionization energy of the neutral oxide such that

$$M + O \leftarrow MO^+ + e^- \tag{9.1}$$

is energetically allowed and can proceed spontaneously.[492] It follows that the reverse reaction, dissociative recombination of the metal oxide cation, is endothermic and therefore sufficiently slow such that a long lived plasma is possible. The Metal Oxide Space Cloud (MOSC) experiment employed this chemistry by releasing samarium at altitudes where atomic oxygen was the predominant neutral species,[493–497] with Sm chosen as it is the easiest metal to vaporize for which chemi-ionization with atomic oxygen was thought to be exothermic. While previous flight experiments have employed chemical releases, and even chemi-ionization,[498] the diagnostics available in those earlier cases were more limited.

To determine the chemical species formed, the MOSC experiment applied a broad array of diagnostics, including optical spectra from 400 – 900 nm as well as time- and spatially-resolved plasma density measurements via ALTAIR radar. The observed plasma densities produced were well under predicted values. A subsequent re-evaluation of the thermochemistry of Sm plus O chemi-ionization found it to be much less exothermic than previously reported, as this process is nearly thermoneutral[499] and may in fact be slightly endothermic.[500] The lower-than-expected plasma density was thus likely due to a larger-than-predicted occurrence of dissociative recombination of the samarium oxide cation with an electron or a reduced efficiency of associative ionization in the first place. The kinetics of chemi-ionization reactions for a variety of lanthanide species were then studied in a flow tube, and samarium was found to stand out with a chemi-ionization rate constant at least an order of magnitude slower than the other lanthanides.[501,502]

Given the observed slow endothermic chemi-ionization of samarium and the deleterious impact of dissociative recombination on the density of produced plasma, alternative release species must be considered. Unfortunately, the efficiency and exothermicity of Equation 9.1 are anti-correlated with vapor pressures across the lanthanide series. Balancing these contrasting trends, neodymium retains a moderate vapor pressure while chemi-ionizing at the

collisional limit.[501] Furthermore, neodymium chemi-ionization is unambiguously exothermic (1.76 ± 0.10 eV) thereby eliminating any impact of dissociative recombination.[503,504]

In the late 1980's, the COPE II experiment released both samarium and neodymium, with optical diagnostics limited to standard photography.[498] The experiment took place in daylight such that visible clouds were formed from both releases, pink from samarium and green from neodymium. The pink cloud was observed to follow the magnetic field lines, while the green cloud moved with the neutral winds, leading researchers to conclude that samarium resulted in plasma production while neodymium did not. Considering later laboratory evidence that neodymium chemi-ionizes much more efficiently than samarium, this conclusion appears questionable, and a number of other possible explanations should be explored.

For example, the neodymium may not have been efficiently vaporized; however, it is then difficult to explain the source of the seemingly sharp, green emission. Alternatively, photoionization (instead of chemi-ionization) may have been the dominant process, although this should also have resulted in plasma from both species since the ionization energies are similar. Another possibility is that the observed emission in the visible spectrum was from neutral, not ionic, species. The observation that the samarium emissions moved along the magnetic field lines could have been a result of a steady state between chemi-ionization and dissociative recombination. In this picture, ionic species are dispersed by the magnetic field followed by recombination to yield neutral species along the field lines. The key to resolving this discrepancy lies in the spectroscopy, kinetics, and energetics of the lanthanide oxides and their cations, so that more definitive assignments may be made.

Spectroscopy of the atomic lanthanides is well characterized,[505] but the spectroscopy of the oxides is very much a work in progress.[506,507] SmO, NdO, and their cations have many low-lying electronic states due to their partially filled f-shells and are challenging to explore. Electronic states of NdO^+ with term energies of up to ∼5,000 cm 1 have been determined using pulsed-field ionization zero electron kinetic energy (PFI-ZEKE) spectroscopy.[504] A large number of electronic states of SmO were reported from slow photoelectron velocity-map imaging spectroscopy of cold SmO^- (cryo-SEVI).[62] Previous photoelectron spectra of NdO^- found the electron affinity (EA) of NdO to be 1.01(1) eV,[508] and emission and absorption lines of NdO have been reported in the region between 9500 – 20000 cm^{-1} at modest resolution.[509,510] A large number of bands at higher resolution were measured lying between 7500 and 12600 cm^{-1},[511] and laser induced fluorescence (LIF) identified low lying states in agreement with ligand field theory.[512,513] Complete active space self-consistent-field (CASSCF) and multireference configuration interaction (MRCI) calculations detail 54 states below 8000 cm^{-1},[514] amongst a number of theoretical efforts.[515–517]

Here, we utilize slow photoelectron velocity-map imaging spectroscopy of cryogenically cooled NdO^- anions (cryo-SEVI) in tandem with high-level quantum chemical calculations to investigate the electronic and vibrational structure of neutral NdO. The inherent high resolution of SEVI coupled with the spectral clarity afforded by detachment from cold ions reveals detailed spectroscopic information about neutral and anionic NdO ($NdO^{0/-}$). We obtain an accurate electron affinity for NdO along with term energies and fundamental vi-

brational frequencies for several low-lying electronic states of $NdO^{0/-}$. In addition to a wealth of information regarding the neutral's electronic states, manipulation of ion temperature shows evidence of detachment from an excited state of NdO^-. Several high-lying excited states of NdO are identified that may explain the green emission observed in Nd releases, though further theoretical work is required to make definitive state assignments.

9.3 Experimental Methods

The cryo-SEVI method and instrument have been previously described in detail.[34,35,54] In this work, NdO^- anions are generated by focusing the frequency-doubled output of a Nd:YAG laser operating at 20 Hz onto a rotating and translating neodymium target. The resulting plasma is entrained within a burst of helium carrier gas from an Even-Lavie pulsed valve,[245] which passes through a narrow clustering channel before expanding into vacuum.

Ions packets then pass through an electrostatic skimmer into a radiofrequency (RF) hexapole ion guide and a RF quadrupole mass filter, which is tuned to ensure that a narrow mass range of ions, encompassing NdO^-, are transmitted into the subsequent cryogenically cooled linear RF octupole ion trap. While trapped, ions undergo collisions with a buffer gas mixture of 80:20 He:H_2 held at 5 K. After ∼40 ms in the trap, ions are assumed to be cooled to their ground vibrational and electronic states. This cooling scheme has been shown to result in molecular temperatures as low as 10 K following extraction from the trap.[54]

The ions are extracted from the trap into an orthogonal Wiley-McLaren time-of-flight mass spectrometer[259] and steered to the laser interaction region inside a velocity-map imaging (VMI) spectrometer. $^{142}Nd^{16}O^-$ ions are photodetached by vertically polarized light from one of two laser configurations based on a tunable dye laser pumped by the second harmonic of a Nd:YAG laser operating at 20 Hz. Photon energies above 3 eV (24200 cm^{-1}, 415 nm) are generated by frequency-doubling the light from the dye laser. For photon energies below 1.3 eV (10500 cm^{-1}, 950 nm), the dye laser output is focused into a 63 cm long Raman cell containing 400 psi of H_2 and is red-shifted by 4155 cm^{-1} by the Q1(1) line in the H_2 Raman spectrum.[65,518] The Stokes shifted light is separated from residual dye light and anti-Stokes shifted light by a 900 nm long-pass dichroic mirror and passed through a linear polarizer to ensure the resulting beam is vertically polarized.

Photoelectrons generated in the interaction region are focused with the velocity map imaging (VMI) electrostatic lens[18,36] onto a position-sensitive detector comprising two chevron-stacked microchannel plates coupled to a phosphor screen.[17] A CCD camera captures photoelectron events on the screen, and their centroids are computed in real time.[271] Electron centroids are accumulated over several thousand experimental cycles to create a single VMI image for each photodetachment wavelength. The angular and radial photoelectron distributions are reconstructed from an accumulated image using the maximum entropy velocity Legendre reconstruction method.[275] The relationship between electron radial position and kinetic energy (eKE) is calibrated by acquiring VMI images of the well-characterized detachment transitions of atomic O^- and Cl^- at several photon energies.[279,281]

The VMI spectrometer has an approximately constant resolving power, ΔeKE/eKE, yielding the best eKE resolution for slow photoelectrons.[18,36] Thus, a SEVI spectrum is acquired by first taking an overview spectrum at a relatively high photon energy before tuning the detachment laser to energies just above the features of interest. This procedure results in a collection of high-resolution spectra, each of which spans a narrow energy window. These spectra are concatenated and scaled to match intensities in the overview spectrum, which is less sensitive to variations of the photodetachment cross section with photon energy. Spectra are plotted as a function of electron binding energy (eBE), given by eBE = hν – eKE.

In addition to eKE distributions, cryo-SEVI images contain information about the anisotropy of photodetachment transitions. Such photoelectron angular distributions (PADs) are described by[91]

$$\frac{d\sigma}{d\Omega} = \frac{\sigma_{tot}}{4\pi}\left[1 + \beta P_2(\cos\theta)\right] \tag{9.2}$$

where σ_{tot} is the total detachment cross section, $P_2(x)$ is the second-order Legendre polynomial, θ is the angle of the outgoing photoelectron with respect to the laser polarization axis, and β is the anisotropy parameter. The anisotropy parameter, which ranges from -1 (perpendicular detachment) to +2 (parallel detachment), reflects the angular momentum of the detached electron and is thus tied to the electronic character of each photodetachment transition.[361]

9.4 Computational Methods

Calculations of the low-lying electronic energy level structures for NdO^- and NdO were carried out to facilitate the assignment of the experimental spectra. The lowest-lying electronic states of NdO^- and NdO originate from the $Nd^+(6s^24f^3)O^{2-}$ and $Nd^{2+}(6s14f^3)O^{2-}$ manifolds of electron configurations, respectively. Spin-orbit coupling among the $4f$ electrons dominates the low-lying electronic energy level structures in these two species, similar to the corresponding cation NdO^+ that has the $Nd^{3+}(4f^3)O^{2-}$ configuration for its lowest electronic states.[504]

The present calculations use the state-averaged complete active space self-consistent-field (CASSCF) and N-electron valence second-order perturbation theory (NEVPT2) as implemented in the ORCA program package.[181,519–521] The differences between the NEVPT2 and CASSCF results serve to provide a reasonable estimate of dynamic correlation effects, as is discussed in Section 9.5. These computations were performed with the Nd $6s$ and $4f$ orbitals in the active spaces, i.e., an active space consisting of five electrons in eight orbitals for NdO^- and four electrons in eight orbitals for NdO. These calculations include 13 quartet states and 13 doublet states for NdO^- and 13 quintet states and 13 triplet states for NdO. Scalar-relativistic effects were taken into account using scalar-relativistic pseudopotentials (PP)[522] and the accompanying QZVP-PP basis sets.[523] Spin-orbit coupling effects

were considered using quasidegenerate perturbation theory within the active spaces. These calculations were carried out at the equilibrium bond length of NdO, 1.8 Å.

The local potential energy surfaces around the equilibrium structures for NdO^- and NdO were then computed, yielding equilibrium bond lengths, the NdO adiabatic electron affinity, and vibrational frequencies. Accurate calculations of the electron affinity of NdO as well as the structural properties require high-level treatment of dynamic correlation effects. The CASSCF, NEVPT2, and multireference configuration interaction with Davidson's size-consistency correction (MRCI+Q)[521] calculations for the vertical detachment energy (VDE) produce a substantial range of VDE values of 1562 cm^{-1}, 7138 cm^{-1}, and 4192 cm^{-1}, respectively. The highest-order method among these multireference approaches, MRCI+Q, lacks size-extensivity and might have difficulty in providing an accurate electron affinity. Instead, we have used scalar-relativistic coupled-cluster singles and doubles augmented with a noniterative triples [CCSD(T)][145] method for the calculations for the ground state properties of NdO^- and NdO. The ground states of NdO^- and NdO both have three unpaired $4f$ electrons occupying the ℓ_z = 1, 2, and 3 sub-levels. Therefore, we have optimized the high-spin quartet configuration $[4f(\ell_z{=}3,m_s{=}1/2)]^1[4f(\ell_z{=}2,m_s{=}1/2)]^1[4f(\ell_z{=}1,m_s{=}1/2)]^1$ for NdO^- and the high-spin quintet configuration $[6s(m_s{=}1/2)]^1[4f(\ell_z{=}3,m_s{=}1/2)]^1[4f(\ell_z{=}2,m_s{=}1/2)]^1$ $[4f(\ell_z{=}1,m_s{=}1/2)]^1$ for NdO in the Hartree-Fock calculations.

Note that these two configurations each correspond to a single complex-valued determinant; they consist of more than one single determinant when using real-valued wavefunctions. We thus use a complex-valued Hartree-Fock and CCSD(T) module[524] in the CFOUR program package[174] together with the scalar-relativistic one-electron Hamiltonian integrals of the spin-free exact two-component theory in its one-electron variant (the SFX2C-1e scheme).[525,526] Correlation-consistent triple-zeta basis sets[162,527] contracted for the SFX2C-1e scheme (cc-pVTZ-X2C) were used in these CCSD(T) calculations. The SFX2C-1e-CCSD(T) adiabatic electron affinity was augmented with a spin-orbit correction obtained from SO-CASSCF/NEVPT2 calculations.

9.5 Results

9.5.1 Experimental Results

Cryo-SEVI spectra obtained for detachment from NdO^- are presented in Figs. 1 and 2, showing two regions of structure: a low-eBE region between roughly 5500-10500 cm^{-1} (Fig. 9.1), and a high-eBE region between 15500-28000 cm^{-1} (Fig. 9.2). Both regions display extensive structure that is well resolved, though the high-eBE region is considerably more congested.

Peak positions and assignments of labeled features in Fig. 9.1 are reported in Table 9.1 along with a comparison to our CASSCF computations and term energies determined by rotational analysis of experimental LIF results by Linton and co-workers.[512] The weak transitions labeled in lowercase in Fig. 9.1A (a-g) are found to have temperature-dependent

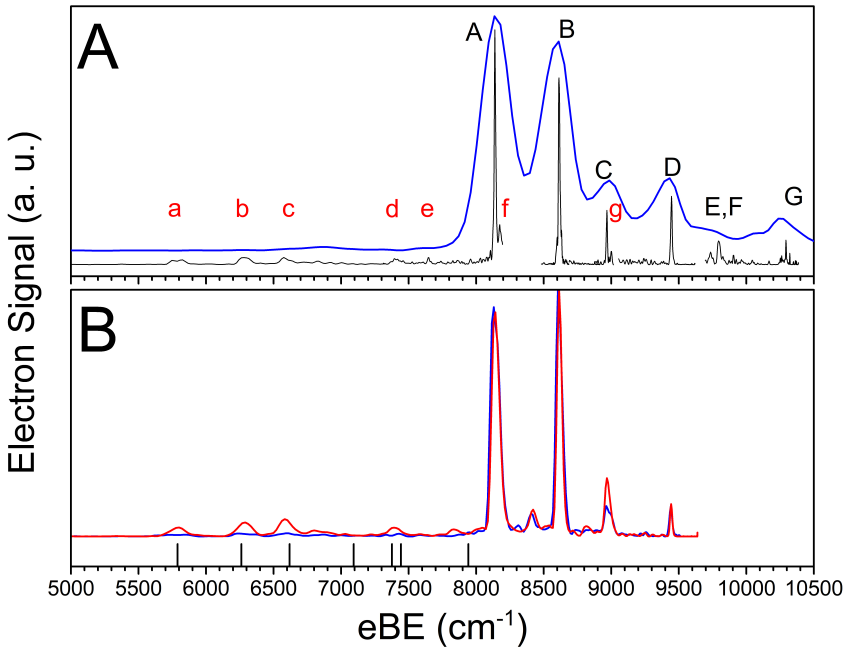

Figure 9.1: Low-eBE region of the cryo-SEVI spectrum of NdO^-. In A, the overview spectrum (blue, hv = 15625 cm^{-1}) is vertically offset from the high-resolution scans (black, variable photon energies). Peaks labeled in red lower-case exhibit temperature-dependent intensities and are therefore considered hot bands. In B, buffer gas pressure in the trapping chamber is varied from low (red) to high (blue). Lower pressures lead to less efficient cooling in the trap and corresponding enhancement of hot bands. Below are black sticks corresponding to allowed detachment transitions from the (2)4.5 excited state of NdO^- to known neutral levels of NdO as measured by Linton,[512] shifted in eBE by 2350 cm^{-1} to simulate features a-e.

intensities, as observed by acquiring spectra under different trapping conditions (Fig. 9.1B). Spectra were collected at two different buffer gas pressures, differing by a factor of 5, with lower pressures leading to less efficient cooling and warmer ions. As the intensities are higher for detachment from warmer ions, these peaks are assigned to vibrational or electronic hot bands and are discussed further in Section 9.6. The positions of features labeled in Fig. 9.2 are reported in Table 9.2 alongside available literature values.[513,517] In these tables, electronic states are labelled using Hund's case c notation with the $(N)\Omega$ convention common in the literature on NdO;[506,512,513,528] $(N)\Omega$ represents the Nth state with each value of Ω, the summed projections of the electronic orbital and spin angular momenta onto the internuclear axis. Assignments listed in Table 9.1 for the peaks with upper case letters originate from the anion ground state (see below) and refer to the neutral states. They include the vibrational transition, denoted as (ν'-ν"), where ν' is the vibrational quanta in the final neutral state

and ν" is the vibrational quanta in the anion.

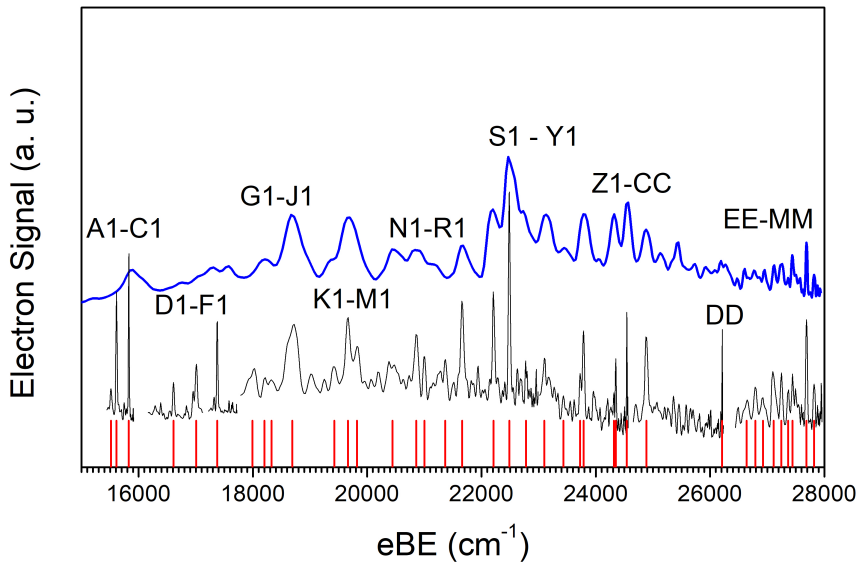

Figure 9.2: High-eBE region of the cryo-SEVI spectrum of NdO^-. The overview spectrum (blue, hv = 27977 cm^{-1}) is vertically offset from the high-resolution scans (black, variable photon energies), peak centers for each transition listed in Table 9.2 are displayed (red sticks) for clarity.

Peak	eBE	Shift	Assignment	CASSCF	Fluorescence
a	5658(28)	-2481	-	-	-
b	6295(27)	-1844	-	-	-
c	6594(35)	-1545	-	-	-
d	7416(35)	-723	-	-	-
e	7834(15)	-305	-	-	-
A	8139(6)	0	(1)4 (0-0)	0	-
f	8175(11)	36	(1)4 (1-1)	-	-
B	8614(8)	475	(1)5 (0-0)	529	473.691
C	8967(8)	828	(1)4 (1-0)	831	829.512
g	9000(8)	862	(1)4 (2-1)	-	-
D	9445(9)	1307	(1)5 (1-0)	1356	1303.909
E	9735(11)	1596	(2)4 (0-0)	1401	1587.241
F	9797(11)	1658	(1)4 (2-0)	-	1654.453
G	10293(6)	2155	(2)5 (0-0)	2084	2152.575

Table 9.1: Peak positions, shifts from peak A, assignments, and calculated transition energies (CASSCF) for transitions in the low-eBE cryo-SEVI spectra of NdO^- given in Fig 1A are reported in units of cm^{-1}. Cryo-SEVI values are compared to values previously reported for a rotational analysis of the NdO LIF spectrum.[512] Transitions labeled in lowercase have increasing intensity with increasing temperature (see Fig. 9.1B) and are therefore assigned as hot bands. Uncertainties in peak positions correspond to one standard deviation obtained from a Gaussian fit to the high-resolution scan of the experimental peak.

All features in the low-eBE region (Fig. 9.1) have PADs that are strongly parallel to the laser polarization ($1 < \beta < 1.8$), in agreement with the conventional PES measurements of Chi and co-workers.[508] Those in Fig. 9.2 vary – features A1-F1 have PADs aligned weakly parallel to the laser polarization ($-0.1 < \beta < 0.4$), while features lying higher in energy (eBE > 18000 cm^{-1}) tend to have PADs slightly perpendicular to the laser polarization ($-0.5 < \beta < 0$).

Peak	eBE	Shift	Configuration	Fluorescence
A1	15515	7376		
B1	15611	7472		
C1	15827	7688		
D1	16608	8469		
E1	17008	8869		
F1	17375	9236		
G1	17990	9851		
H1	18203	10064		
I1	18325	10186		
J1	18688	10549	$4f^4$	10506.03
K1	19423	11284		
L1	19663	11524	$4f^4$	11539.89
M1	19820	11681	$4f^4$	11699.06
N1	20441	12302		
O1	20855	12716		
P1	20997	12858	$4f^4$	12839.7
Q1	21364	13225		
R1	21660	13521		
S1	22207	14068	$4f^3 6p$	14081.33
T1	22484	14345		
SU1	22780	14641		
V1	23099	14960	$4f^4$	14969.57
W1	23434	15295		
X1	23726	15587		
Y1	23784	15645	$4f^3 6p$	15625.07
Z1	24314	16175	$4f^3 6p$	16168.38
AA	24348	16209		
BB	24542	16403		16397.25
CC	24884	16746	$4f^3 6p$	16737.93
DD	26211	18072		
EE	26639	18500		
FF	26792	18653		
GG	26924	18785		
HH	27112	18973		
II	27248	19109		
JJ	27367	19228		
KK	27442	19303		
LL	27688	19549		
MM	27820	19681		

Table 9.2: Peak positions for transitions in the high-eBE cryo-SEVI spectra of NdO^- given in Fig 3. Cryo-SEVI values are compared to relevant term energies determined for states observed in the LIF measurements of Effantin and co-workers.[513] Electron configurations determined by Kaledin via ligand field theory are reported.[517] All values are reported in cm^{-1}.

9.5.2 Computational Results

As shown in Table 9.3, the computed spectroscopic parameters at the SFX2C-1e-CCSD(T)/cc-pVTZ-X2C level for NdO and NdO^+ agree well with previously reported values. The computed adiabatic ionization energy of 44134 cm^{-1} for NdO also compares favorably with the recently measured value of 44427 cm^{-1} by Heaven and collaborators[504] – a value 0.5 eV higher than that previously reported.[529] The excellent agreement thus supports the new measured value and validates the accuracy of the present calculations. Similarly, the computed adiabatic electron affinity of NdO, 8093 cm^{-1}, is remarkably close to our measured value of 8139 cm^{-1}, suggesting that this methodology accurately captures the physics of these systems well.

Tables 9.4 and 9.5 outline the computed electronic energy level structure for $NdO^{0/-}$ at the CASSCF and NEVPT2 levels of theory. Interestingly, the low-lying electronic states of the neutral NdO are mainly composed of quintet scalar-relativistic wave functions with substantial contributions from the manifold of triplet states, while the contributions to the low-lying electronic states of the anion NdO^- are nearly exclusively from the quartet manifold. These computations are in fair agreement with previous MRCI calculations for NdO,[514] and the electronic level structure for NdO^- exhibits a similar pattern to that of NdO^+, which has the same open-shell portion of the electron configuration, $Nd^{2+}(4f^3)$. Further, as the level structure originates from spin-orbit coupling of the $4f$ electrons, the CASSCF calculations within the active space containing the $4f$ electrons captures most of these contributions, with the differences between the NEVPT2 and CASSCF results serving to provide a reasonable estimate of dynamic correlation effects. It should be noted, however, that given the enormous $4f$, $5d$, and $6p$ spin-orbit interaction matrix elements in the Nd atomic ion and the small relative size of the $4f$ orbital compared to the NdO bond length, this level structure can also be mapped from the atomic ion energy levels of Nd^{2+} using the atomic-ion-in-molecule picture.[530]

	NdO^-		NdO		NdO^+	
	Theory	Experiment	Theory	Experiment	Theory	Experiment
R_e (Å)	1.837	-	1.8	1.801	1.754	1.74
ω_e (cm^{-1})	780	792(6)	835	834.1	901	892.4
$\omega_e\chi_e$ (cm^{-1})	2.2	-	2.1	2.3	2.1	1.3
EA_a (cm^{-1})	-	-	8093	8139	-	-
IE_a (cm^{-1})	-	-	44134	44427	-	-

Table 9.3: Spectroscopic parameters for NdO^+, NdO, and NdO^-. The "theory" values have been obtained from SFX2C-1e-CCSD(T)/cc-pVTZ-X2C calculations as described in the text. The values of adiabatic ionization energy (IE) and adiabatic electron affinity (EA) have included SO-CASSCF/NEVPT2 spin-orbit coupling corrections of -28 cm^{-1} for IE and 315 cm^{-1} for EA. The experimental values for NdO^+ are taken from the work of Heaven and coworkers,[504] the experimental bond length of NdO is the R_0 value from Effantin and coworkers,[513] and the ω_e and $\omega_e\chi_e$ values are derived using the vibrational energy spacings determined by Linton and coworkers.[512]

Comparison of the computed term energies for these states of NdO with those previously measured by Linton and coworkers[512] finds that our CASSCF results agree more closely with the experimental values than NEVPT2 (see Table 9.4). Curiously, aside from the (1)5 state, a comparison of the CASSCF term energies to the previously reported values show our calculated energies lie below the measured value by an average of 175 cm^{-1}. The inclusion of dynamic correlation in NEVPT2 further reduces the computed values of the term energies, leading to larger deviation from the measured values. A similar underestimation of term energies was also observed in the SO-MRCI calculations previously reported by Heaven and collaborators.[504] Two approximations in the treatment of spin-orbit coupling involved in both the present calculations and those featured in the work of the Heaven group, i.e., the approximation in the construction of the spin-orbit integrals and the neglect of higher-order SO effects, are expected to be responsible for this discrepancy. A further study using more rigorous SO integrals and/or non-perturbative treatment of spin-orbit coupling will be of interest.

State	CASSCF	NEVPT2	Measured	Composition
(1)4	0	0	-	90%^{5}I + 8%^{5}H
(1)5	529	411	473.691	45%^{5}I + 42%^{3}I +9%^{5}H +3%^{3}H
(1)3	934	921	1156.005	60%^{5}H + 28%$^5\Gamma$ +9%$^5\Phi$
(1)2	1123	1123	1351.1	37%$^5\Phi$ + 34%$^5\Gamma$ +21%$^5\Delta$ + 7%$^5\Pi$
(1)1	1191	1188	-	33%$^5\Delta$ + 30%$^5\Pi$ + 22%$^5\Phi$ + 14% $^5\Sigma$
(1)0^+	1225	1232	-	49%$^5\Pi$ + 31%$^3\Sigma$ + 21%$^5\Delta$
(2)4	1401	1304	1587.241	27%^{3}H +27%^{5}H +25%$^5\Gamma$+9%$^5\Phi$+7%$^3\Gamma$
(2)3	1600	1503	1793.2	23%$^5\Phi$+21%$^3\Gamma$+18%$^5\Delta$+15%^{5}H +11%$^3\Phi$+5%$^5\Gamma$+5%$^5\Pi$
(2)2	1698	1602	1914.2	23%$^5\Gamma$ + 19%$^5\Pi$ + 18%$^3\Phi$ + 15%$^3\Delta$ + 12%$^5\Delta$ + 9%$^5\Sigma$
(2)1	1742	1648	-	19%$^5\Sigma$ + 22%$^5\Phi$ + 19%$^5\Pi$ + 14%$^3\Delta$ + 6%$^3\Sigma$ + 16%$^3\Pi$
(1)0^-	1753	1670	-	41%$^5\Delta$ + 24%$^5\Pi$ + 16%$^3\Sigma$ + 19%$^3\Pi$
(1)6	2014	1946	2123.875	61%^{5}I +12%^{5}H +24%^{3}I
(2)5	2084	1960	2152.575	42%^{5}I +3%^{5}H +47%^{3}I +7%^{3}H
(3)5	2742	2683	-	32%$^5\Gamma$+4%^{5}I +7%$^5\Phi$+33%^{5}H +3%$^3\Gamma$+4%^{3}I+13%^{3}H

Table 9.4: Computed levels of NdO from both CASSCF and NEVPT2, both using QZVP-PP basis sets with perturbative inclusion of spin-orbit coupling, along with state assignments, a comparison to experimental fluorescence measurements from Linton and co-workers,[512] and compositions in terms of the spin-free wave functions. Relative energetics are given in cm^{-1} with respect of the ground state of neutral NdO. "(m)n" refers to the m-th electronic state with Ω = n.

A recent ligand field study suggests that higher-lying electronic states of NdO originate from $Nd^{2+}(4f^4)O^{2-}$, $Nd^{2+}(6p^14f^3)O^{2-}$, $Nd^{2+}(5d^14f^3)O^{2-}$, and $Nd^{2+}(6s^24f^2)O^{2-}$ configurations,[517] though one may expect the $Nd^{2+}(6s^24f^2)O^{2-}$ configurations to dominate the photodetachment signal via the removal of a single f electron from the $Nd^{+}(6s^24f^3)O^{2-}$ configurations of NdO^-. We thus attempted a CASSCF calculation and a subsequent MRCI+Q calculation for the $Nd^{2+}(6s^24f^2)O^{2-}$ configurations with an active space containing two electrons in seven Nd $4f$ orbitals, forcing the $6s$ orbitals to be doubly occupied. Our results from this calculation, however, displayed substantial mixing of the Nd $6s$ orbital with the Nd 5d and $4f$ orbitals, suggesting that more complete calculations of these states require the use of an active space comprising the Nd $6s$, $6p$, $4f$, and $5d$ orbitals.

State	CASSCF	NEVPT2	Composition
(1)4.5	0	0	88%^{4}I + 9%^{4}H
(1)3.5	1000	1000	28%$^4\Gamma$ + 61%^{4}H +8%$^4\Phi$
(1)2.5	1135	1121	^{4}1%$^4\Gamma$ + 16%$^4\Delta$ +37%$^4\Phi$
(1)1.5	1206	1178	39%$^4\Delta$ + 31%$^4\Phi$ +19%$^4\Pi$
(1)0.5	1284	1257	20%$^4\Delta$+29%$^4\Sigma$+47%$^4\Pi$
(1)5.5	1898	1920	86%^{4}I + 12%^{4}H
(2)4.5	2724	2750	9%^{4}I +34%$^4\Gamma$+50%^{4}H +7%$^4\Phi$
(2)3.5	2929	2939	^{4}0%$^4\Phi$+29%^{4}H +15%$^4\Delta$+15%$^4\Gamma$
(2)2.5	3040	3056	^{4}0%$^4\Gamma$ + 35%$^4\Delta$ + 22%$^4\Pi$
(2)1.5	3097	3094	^{4}2%$^4\Phi$ + 30%$^4\Sigma$ + 27%$^4\Pi$
(2)0.5	3118	3120	^{4}2%$^4\Pi$+41%$^4\Delta$+16%$^4\Sigma$
(1)6.5	3907	3942	91%^{4}I + 9%^{4}H
(2)5.5	4729	4771	58%^{4}H +29%$^4\Gamma$+12%^{4}I
(3)4.5	4954	4983	^{4}3%$^4\Phi$+34%^{4}H +21%$^4\Gamma$
(3)3.5	5064	5098	^{4}6%$^4\Delta$+41%$^4\Gamma$+8%^{4}H +5%$^4\Phi$
(3)2.5	5131	5149	^{4}6%$^4\Pi$ + 38%$^4\Delta$ + 15%$^4\Gamma$
(3)1.5	5173	5188	^{4}4%$^4\Sigma$+32%$^4\Delta$+22%$^4\Phi$
(3)0.5	5194	5211	60%$^4\Pi$+30%$^4\Delta$+10%$^4\Sigma$

Table 9.5: Relative energies (cm^{-1}) of the lowest spin-orbit states for NdO^- obtained from CASSCF and NEVPT2 calculations using QZVP-PP basis sets with the perturbative inclusion of spin-orbit coupling, together with compositions in terms of the spin-free wave functions. "(m)n" refers to the m-th electronic state with Ω = n.

As such, our calculated term energy of 22370 cm^{-1} for the lowest lying state of NdO with the $Nd^{2+}(6s^24f^2)O^{2-}$ configuration, $[6s(m_s{=}1/2)]^2[4f(\ell_z{=}3,m_s{=}1/2)]^1[4f(\ell_z{=}2,m_s{=}1/2)]^1$, appears to be an overestimation, further indicating the need to use a larger active space. The inclusion of Nd 6*s*, 6*p*, 4*f*, and 5*d* orbitals in the active space is beyond our computational resources, so we focus our present discussions of computational results on the lowest-lying states described above.

9.6 Discussion

9.6.1 Low-eBE Structure of NdO

Features observed in the low-eBE cryo-SEVI spectra of NdO^- (Fig. 9.1) are analyzed through comparison with our theoretical results as well as the experimental fluorescence measurements of Linton and co-workers.[512] Features labeled A-G in Fig. 9.1 are well resolved, representing a significant improvement over the previously reported anion photoelec-

tron spectrum.[508] Previous experiments employing photoelectron spectroscopy of lanthanide monoxides[506,531–534] have shown that photodetachment from a metal-centered $6s$ orbital, as is the case for the NdO^- anion, imposes a $\Delta\Omega = \pm 1/2$ selection rule. Conversely, the selection rules for LIF impose a strict $\Delta\Omega = 0, \pm 1$ for transitions from the upper to lower state of NdO, while the preceding excitation to the upper state follow selection rules for dipole allowed transitions.[517] Nevertheless, the features observed here show exceptional agreement with the term energies of NdO determined from the LIF spectra of Linton and coworkers,[512] who identified the corresponding neutral states as belonging to the $\Omega = 4$, 5 manifolds; we thus consider the final neutral states reached in transitions A-G to belong to the same $\Omega = 4$, 5 states. Our results then strongly suggest detachment from an NdO^- ground electronic state with $\Omega = 4.5$, thus allowing photodetachment transitions to states with $\Omega = 4$, 5. Such transitions are depicted as blue solid lines in Fig. 9.3 atop an energy level diagram of various electronic and vibrational states of $NdO^{0/-}$ labeled with experimental and calculated energies. This assignment is supported by our CASSCF calculations, which find the (1)4.5 state of NdO^- as the ground state, with the nearest state, (1)3.5, residing 1000 cm^{-1} higher.

Peak A is the lowest-eBE feature whose intensity is not temperature dependent. This, combined with the excellent agreement between the positions of features A-G with the term energies from fluorescence measurements, as well as the spacing of low-lying CASSCF states of NdO, confirms that peak A represents photodetachment to the ground state of neutral NdO. We thus report an electron affinity for NdO of 1.0091(7) eV determined by the eBE of peak A, representing a significant improvement over the previously reported value of 1.01(1) eV[508] and comparing favorably to our calculated value of 1.0034 eV at the SFX2C-1e-CCSD(T)/cc-pVTZ-X2C level.

Beyond peak A, several features in the cryo-SEVI spectra show evidence of vibrational progressions for different NdO electronic states discussed above. Peaks A-C-F and B-D belong to vibrational progressions in the (1)4 and (1)5 states, respectively, while features E and G correspond to transitions to the next lowest-lying states of NdO in these Ω manifolds, (2)4 and (2)5, respectively. The spacings within the vibrational progressions A-C-F and B-D yields vibrational frequencies of 828(7) and 831(9) cm^{-1} for the 1(4) and 1(5) states of NdO, respectively. These values are in good agreement with those previously measured in the gas-phase, with Linton and co-workers finding values of 829.512 and 830.218 cm^{-1} for these states, respectively.[512]

These electronic assignments are supported by the PADs measured for the transitions in Fig. 9.1. The low-lying states of neutral NdO are predicted to differ in electron occupation from those of NdO^- by occupation of the $6s$ orbital, indicating that this is the orbital detached in the lower-eBE spectral region. This orbital is highly localized on the Nd atom; detachment from an atomic s orbital yields a photoelectron angular distribution parallel to the laser polarization,[91] in good agreement with what we observe experimentally for the low-eBE cryo-SEVI spectrum.

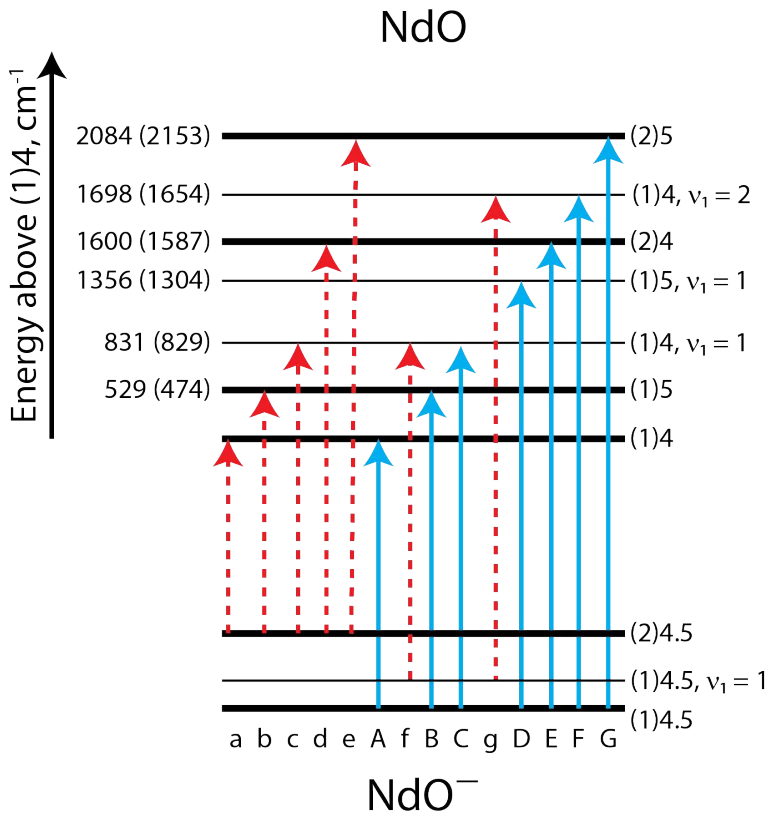

Figure 9.3: Energy level diagram of observed transitions from the (1)4.5 ground state (blue, solid lines) and proposed detachment from (2)4.5 excite state (red, dashed lines) of NdO^- to various states of NdO in the low-eBE region (Fig. 9.1). Energies of states are reported both for our CASSCF calculations and those previously reported by Linton and coworkers,[512] in parentheses.

9.6.2 Hot bands and structure of NdO^-

A number of weak features (a-g) labeled in red in Fig. 9.1A cannot be explained by previously observed transitions or our calculated transition energies from the (1)4.5 ground state of NdO^-. These features are found to have temperature-dependent intensities (Fig. 9.1B), suggesting they arise from excited states of the anion. To date, the only spectroscopic investigation of NdO^- was performed by Wilson and Andrews, who measured the NdO^- vibrational fundamental as 789.9 cm^{-1} in Ne matrices.[535] As the measured value for the NdO vibrational fundamental is red-shifted by 9 cm^{-1} in Ne matrices compared to the gas-phase,[512,535] it is reasonable to expect the gas-phase value of the NdO^- fundamental to reside at ~800 cm^{-1}, approximately 30 cm^{-1} below that of the neutral.

Based on the expected NdO^- vibrational frequency, we assign features f and g, which reside 36 and 34 cm^{-1} above peaks A and C, respectively, to the (1)4(1-1) and (1)4(2-1) sequence bands for detachment from the (1)4.5 ground state of NdO^-. Such an assignment allows for determination of the harmonic vibrational frequency of NdO^- in the ground (1)4.5 state as 792(6) cm^{-1}. While excited anion vibrations are not often observed in cryo-SEVI experiments, the good agreement with previous measurements of the anion vibrational frequency bolsters this claim. Further, the presence of these features in cold anions where features a-e are absent suggests these two families of peaks originate from different anionic states.

The remaining hot bands (a-e) cannot be explained by vibrational excitation of NdO^- and prove difficult to conclusively assign due to lack of prior spectroscopic investigations of the electronic states of this anion. We do, however, present one possible assignment of the observed hot bands by drawing on our calculated NdO^- state energies as well as the positions of neutral NdO states identified here and in fluorescence work. In Fig. 9.1B, black sticks show the eBEs expected for detachment to the NdO state levels calculated from the measurements of Linton and co-workers,[512] where the anion state is considered to be the (2)4.5 excited state of NdO^- with a term energy of 2350 cm^{-1}. Detachment from this state follows the same selection rules as for the (1)4.5 state, resulting in a set of simulated features that can account for features a-e as depicted in Fig. 9.1B and 3. It should be noted, however, that these simulations also show an expected hot band near 7100 where there is none – this missing transition corresponds to detachment to the $\nu = 1$ level in the (1)5 excited states of NdO. The intensity of this feature should be much weaker than the corresponding vibrational origin transition for this electronic state, explaining its absence in our spectrum.

The proposed term energy of 2350 cm^{-1} for the (2)4.5 excited state of NdO^- is supported by our CASSCF simulations, which predict such a level to reside 2724 cm 1 above the ground state. Further, the presence of anions trapped in low-lying excited states has been observed previously in cryo-SEVI studies,[64,65,101,103] though it is notable that the (2)4.5 state of NdO^- lies considerably above the anion ground state, and above 5 other excited states that are not present in the cryo-SEVI spectrum in Fig. 9.1B (see Table 9.5). As the buffer gas pressure in these warmer scans is only 20% that of colder scans, it is possible that thermal equilibrium is not achieved in the ion trap at the lower pressure, resulting in ion populations more closely mirroring those from the source.

9.6.3 High-eBE Structure of NdO

The high-eBE structure observed in the cryo-SEVI spectra of NdO^- in Fig. 9.2 is considerably harder to analyze than the low-eBE structure. The features observed in these spectra correspond to transitions with binding energies ∼7000-20000 cm^{-1} above feature A, where there is a significantly higher density of states. The irregularity of peak spacing in this region prevents clear assignment of vibrational progressions.

Prior experimental work is consistent with our measurements – fluorescence work by Linton *et al.*[512] and Effantin[513] as well as emission spectra from hot ^{142}NdO by Shenyavskaya

et al.[511] have collectively found states at term energies in the 10500-16500 cm^{-1} range that reside near features observed in the cryo-SEVI spectrum. These state assignments report the value of Ω based on relative intensities of P, Q, and R branches in each transition. These values are reported in the rightmost column of Table 9.2.

While some features in the cryo-SEVI spectra agree with prior experimental work in this energy regime, it is harder to treat this spectral region theoretically. To date, there are no theoretical studies on excited states of NdO with term energies above 8000 cm^{-1}. Given the computational cost of using an active space with Nd $6s$, $6p$, $4f$, and $5d$ orbitals, our calculations were restricted to an active space consisting of two electrons in seven Nd $4f$ orbitals, forcing a $4f^2 6s^2$ configuration. MRCI+Q calculations using such an active space suggest the term energies for the lowest lying state in this manifold should reside near 22000 cm^{-1}, though the failure of this method to reproduce the electron affinity of NdO raises questions about the accuracy of this value.

Nevertheless, some insight into these states can be gleaned from the cryo-SEVI spectra. Detachment from the $4f$ orbital of NdO^- is expected to have a significantly lower cross-section than from the $6s$ orbital,[536] in agreement with the reduced signal intensity observed for transitions in this energy region as compared to the low-eBE cryo-SEVI spectra. Further, the photoelectron angular distributions of features A1-F1 are roughly isotropic, while those of G1-MM are largely perpendicular to the laser polarization, suggesting these manifolds of transitions terminate in states with significantly different orbital occupations. Such an assertion is congruent with recent ligand field theory work that suggest states with term energies greater than 10000 cm^{-1} have $4f^4$ or $4f^3 6p$ configurations (Table 9.2).[517]

Previous PES studies of lanthanide oxides by the Jarrold group have observed "shake-up transitions" that violate the typical one-electron photodetachment rule, where one electron is detached from the anion while another is promoted, potentially allowing access to states with $4f^4$ or $4f^3 6p$ configurations.[506,532] This is one possible explanation for some of the features observed in this region of the cryo-SEVI spectrum, particularly peaks CC, J1, L1, and P1, which align with measured transitions involving states with $\Omega \neq 4, 5$ and are thus expected to be forbidden. Such shake-up transitions are expected to be weak, as are the allowed one-electron transitions removing an electron from the $4f$ orbital of NdO, making the distinction between allowed and shake-up transitions challenging.

9.7 Conclusions

Motivated by Nd release experiments, we have investigated both low- and high-lying excited states of NdO with term energies up to 2000 cm^{-1} and between 10000-20000 cm^{-1} above the ground state, respectively. Observed states agree well with the available literature data, and the lower energy region is fully assigned to transitions to various vibrational and electronic states of neutral NdO. Further, we report an electron affinity for NdO of 1.0091(7) eV in good agreement with the calculated value at the SFX2C-1e- SFX2C-1e-CCSD(T)/cc-pVTZ-X2C level. CASSCF and NEVPT2 calculations for excited states of $NdO^{0/-}$ agree well

with experimental values and support a proposed assignment for a low-lying state of NdO^-. Transitions in the higher energy states of NdO prove challenging to assign, owing to mixing of configurations having different occupations of the s and f orbitals in NdO.

Though the current work does provide some insight, further investigation into NdO is needed to ascertain the impact of multiple chemistries during these release experiments, ranging from theoretical exploration of high-lying states of NdO to the oxidation of Nd by molecular O2. Further, while a number of transitions observed in the high-eBE region of the cryo-SEVI spectra have term energies between 18000 and 20000 cm^{-1} (555-500 nm) that may explain the green emission observed during Nd release, increased computational precision for this system is required to determine the states involved and if such transitions are optically allowed.

Chapter 10

Structural Characterization of $NiAl_xO_y$

The content and figures of this chapter are reprinted or adapted with permission from Y. Li, M. C. Babin, S. Debnath, T. Iwasa, S. Kumar, T. Taketsugu, K. R. Asmis, A. Lyalin, D. M. Neumark, "Structural Characterization of Nickel-Doped Aluminum Oxide Cations by Cryogenic Ion Trap Vibrational Spectroscopy" *J. Phys. Chem. A* **125**, 9527 (2021).

10.1 Abstract

Nickel-doped aluminum oxide cations $(NiO_m)(Al_2O_3)_n(AlO)^+$ with m = 1-2 and n = 1-3 are investigated by infrared photodissociation (IRPD) spectroscopy in combination with density functional theory and the single component artificial force induced reaction method. IRPD spectra of the corresponding He-tagged cations are reported in the 400-1200 cm^{-1} spectral range and assigned based on a comparison to calculated harmonic IR spectra of low energy isomers. Simulated spectra of the lowest energy structures generally match the experimental spectra, but multiple isomers may contribute to the spectra of the $m = 2$ series. The identified structures of the oxides ($m = 1$) correspond to inserting a Ni-O moiety into an Al-O bond of the corresponding $(Al_2O_3)_{1-3}(AlO)^+$ cluster, yielding either a doubly or triply-coordinated Ni^{2+} center. The $m = 2$ clusters prefer similar structures in which the additional O-atom is either incorporated into a peroxide unit, leaving the oxidation state of the Ni^{2+} atom unchanged, or forms a biradical comprising a terminal oxygen radical anion $Al\text{-}O^{\cdot -}$ and a Ni^{3+} species. These clusters represent model systems for under coordinated Ni-sites in alumina-supported Ni catalysts and should prove helpful in disentangling the mechanism of selective oxidative dehydrogenation of alkanes by Ni-doped catalysts.

10.2 Introduction

Alumina-supported nickel-based catalysts, Ni/Al_2O_3, constitute an important class of catalytic materials with a wide range of industrial applications, such as natural gas reforming for syngas production[223,224] and oxidative dehydrogenation (ODH) of alkanes.[225,226] When

used in ODH catalysis, it has been assumed that the active species in these materials are NiO crystallites dispersed on alumina and nickel aluminate species ($NiAl_2O_4$), both with Ni in its common +2 oxidation state. These morphologies are believed to be responsible for the high selectivity of this class of catalyst as compared to unsupported pure NiO crystallites. However, more recently, the formation of Ni^{3+} species, which promote the isolation of electrophilic oxygen (O^-), has been invoked to explain the high selectivity for ethylene formation from ethane.[226] The complexity and inhomogeneity of the condensed phase reaction environment often precludes a complete molecular-level understanding of the active species and underlying reaction mechanisms. Therefore, it proves helpful to study small metal oxide clusters in the gas phase. Such clusters provide atom-specific insights into the interactions governing structures-reactivity correlations at the molecular level and ultimately can serve as isolated model systems for active sites in real catalysts.[213,216,230,537,538]

Here, we study the geometric and electronic structure of $Ni_xAl_yO_z^+$ clusters in order to identify such model systems for Ni/Al_2O_3 ODH catalysts. As charged clusters are required for mass selection, we have chosen mixed metal oxide cations with the composition $(NiO_m)(Al_2O_3)_n(AlO)^+$ with m = 1-2 and n = 1-3. For $m = 1$, the addition of the NiO moiety ensures formally fully oxidized clusters with all metal atoms in their most common oxidation state (Al^{3+} and Ni^{2+}). Addition of one more O atom in the $m = 2$ series allows for the study of oxygen-rich species, which may contain less common Ni^{3+} centres in combination with O^- species such as those invoked to explain enhanced ODH selectivity.

There exists a substantial body of work exploring the gas phase spectroscopy of aluminium oxide clusters.[103,539–552] Aluminium oxide anions have been investigated by UV photoelectron,[103,539–541,543,544,546] IR matrix-isolation[547] and IR resonance-enhanced multiphoton ionization spectroscopies.[545] Detailed structural information has also been obtained by infrared photodissociation (IRPD) spectroscopy of messenger-tagged anionic and cationic clusters.[548–552] These studies show that the $(Al_2O_3)_{1-4}(AlO)^+$ and $(Al_2O_3)_{1-6}AlO_2^-$ series indeed form electronically closed-shell structures composed exclusively of Al^{3+} and O^{2-}.[549,552] The preferred geometric structures are rather irregular and typically require a genetic algorithm for identification.[548] The corresponding IR spectra are complex and start to converge to that of amorphous alumina for systems containing more than ∼25 atoms.[552] Less is known concerning the spectroscopy of metal-doped aluminium clusters, which can represent challenging benchmarks even for advanced electronic structure methods.[553–555] Ni-doped aluminium oxide clusters have not been studied previously by theory or experiment.

In the following, we characterize the Ni-containing aluminum oxide cations $(NiO_m)(Al_2O_3)_n(AlO)^+$ with m = 1-2 and n = 1-3 using cryogenic ion trap vibrational spectroscopy.[556,557] IRPD spectra of the He-tagged cations are compared to predicted spectra from density function theory (DFT). Cluster structures are optimized using the automated reaction path search technique by the artificial force induced reaction method (AFIR),[558–560] allowing for a systematic search for molecular or cluster structures and chemical reaction pathways. We show that unambiguous structural assignments are possible based on a comparison to the spectra of low energy isomers. We then discuss the geometric and electronic nature of the Ni-site and identify clusters that may be particularly useful as model systems

in future reactivity studies.

10.3 Experimental Methods

The infrared photodissociation (IRPD) experiments were performed using a cryogenic ion trap tandem mass spectrometer[561,562] interfaced with widely tunable, intense IR radiation from the Fritz-Haber-Institute Free-Electron Laser (FHI FEL).[118] In brief, $Ni_xAl_yO_z^+$ cluster cations were prepared by laser ablation of a mixed Ni/Al rod (Ni:Al = 1:1 molar ratio) in the presence of 1% O_2 seeded in 6 atm He carrier gas. The subsequent beam of cations passes through a 4 mm diameter skimmer and is collimated in a radio frequency (RF) decapole ion guide. The desired cations are mass-selected using a quadrupole mass filter, deflected 90° by an electrostatic quadrupole deflector, and focused into a cryogenic RF ring-electrode ion trap. The trap is continuously filled with He buffer gas at an ion-trap temperature of 10 K. In the trap, the cations are accumulated, thermalized, and messenger-tagged through collisions with the buffer gas, forming $(NiO_m)(Al_2O_3)_n(AlO)^+ \cdot He_x$ (x = 1-3) complexes.

For IRPD experiments, all ions are extracted from the trap at 5 Hz and focused both temporally and spatially into the center of the extraction region of an orthogonally mounted reflection time-of-flight (TOF) tandem photofragmentation mass-spectrometer. Here, the ions are irradiated with a counter-propagating IR laser pulse produced by the FHI FEL (400-1200 cm^{-1}, bandwidth: ∼0.5% FWHM, pulse energy: 0.2-5 mJ). All parent and photofragment ions are then accelerated toward an MCP detector and monitored simultaneously. IRPD scans are recorded by averaging about 100 TOF mass spectra per wavelength step (3 cm^{-1}) and scanning the wavelength. Typically, at least three scans are averaged to obtain the final IRPD spectrum. The photodissociation cross section σ_{IRPD} is determined as described previously.[563,564]

10.4 Computational Methods

Initial screening of geometry structures of $(NiO_m)(Al_2O_3)_n(AlO)^+$ with m = 1-2 and n = 1-3 clusters was performed using the single-component artificial force induced reaction (SC-AFIR) method,[558–560] implemented in the GRRM17 package.[564,565] This method has been successfully used in our previous work for a systematic investigation of the optimized geometries, structural fluxionality and pathways of chemical reactions catalyzed by atomic clusters.[566–568] The collision energy parameter γ of the AFIR method was set to 100 kJ/mol. In the structural searches, DFT computations were performed with TURBOMOLE[569,570] using the def-SV(P) basis sets[571] with the BP86 functional[134,572] under the resolution of identity approximation.[573]

The obtained geometries are further refined using the Becke three-parameter exchange and Lee–Yang–Parr correlation functional (B3LYP)[132,135] and the def2-TZVP basis set[164,523] as implemented in the Gaussian 16 program package.[180] Harmonic vibrational frequencies and

IR intensities are determined at the B3LYP/def2-TZVP optimized geometries. All energies reported are zero-point energy (ZPE) corrected with the unscaled frequencies. Simulated spectra are derived from the B3LYP/def2-TZVP scaled harmonic frequencies and intensities and convoluted with a 15 cm^{-1} fwhm Gaussian line shape function to account for rotational band contours as well as the spectral width of the laser pulse. Best agreement is found for a scaling factor of 1.011.

To obtain a quantitative measure for the agreement of experimental and theoretical spectra, the cosine similarity score is used.[574] The score S expresses the similarity between two spectra, where the intensity of the experimental and predicted absorptions is represented by vectors A and B in Equation 10.1. The score can vary from zero to unity, with a value closer to 1 indicating greater similarity.

$$S = \cos(\theta) = \frac{A \cdot B}{||A||||B||} = \frac{\sum_{i=1}^{n} A_i B_i}{\sqrt{\sum_{i=1}^{n} A_i^2}\sqrt{\sum_{i=1}^{n} B_i^2}} \tag{10.1}$$

All systems studied here contain a Ni atom with a partially filled d shell and hence states of different multiplicity need to be considered with the high spin configurations typically yielding the most reliable single determinant wavefunction. For Ni^{2+} (d^8 configuration), this corresponds to the triplet state manifold and we therefore focus our discussion on these triplet states and their structures, energies and harmonic IR spectra. The corresponding open-shell singlet wavefunctions typically yield very similar, quasi iso-energetic structures with similar IR spectra (see Figure 10.8). For the systems containing a terminal oxygen radical anion the situation is more complex. Formally, these systems contain (up to) four unpaired electrons, three electrons delocalized over a Ni(-O-)$_3$ moiety, either in a high-spin (quartet) or low-spin (doublet) configuration, weakly coupled to the electron centered on the terminal oxygen atom. This yields states of either quintet, triplet or singlet multiplicity. However, the Ni(-O-)$_3$ high-spin solutions are found at higher energy than the low-spin ones. Therefore, the results for the triplet states containing the Ni low-spin configuration are shown. Note that also here the structures and spectra for the different multiplicities are very similar (see Figs. S3-5). Finally, it should be noted that D1 diagnostics (matrix 2-norm of coupled cluster amplitudes for single excitations) performed with the use of TURBOMOLE package demonstrates that the wavefunction of these structures possess essentially multi-configuration character due to the presence of degenerate and quasi-degenerate states.[575] Therefore, an improved description of the corresponding wavefunctions requires the use of the multireference *ab initio* theory such as CASPT2[576] and MRCI,[577] which goes far beyond the scope of the present study.

10.5 Results and Discussion

A representative mass spectrum of the metal oxide cations produced by laser ablation of an Al/Ni rod is shown in Figure 10.1. The pure aluminum oxide cations $(Al_2O_3)_n(AlO)^+$ with n = 1-3 are among the most abundantly formed ions. Their exceptional stability has been

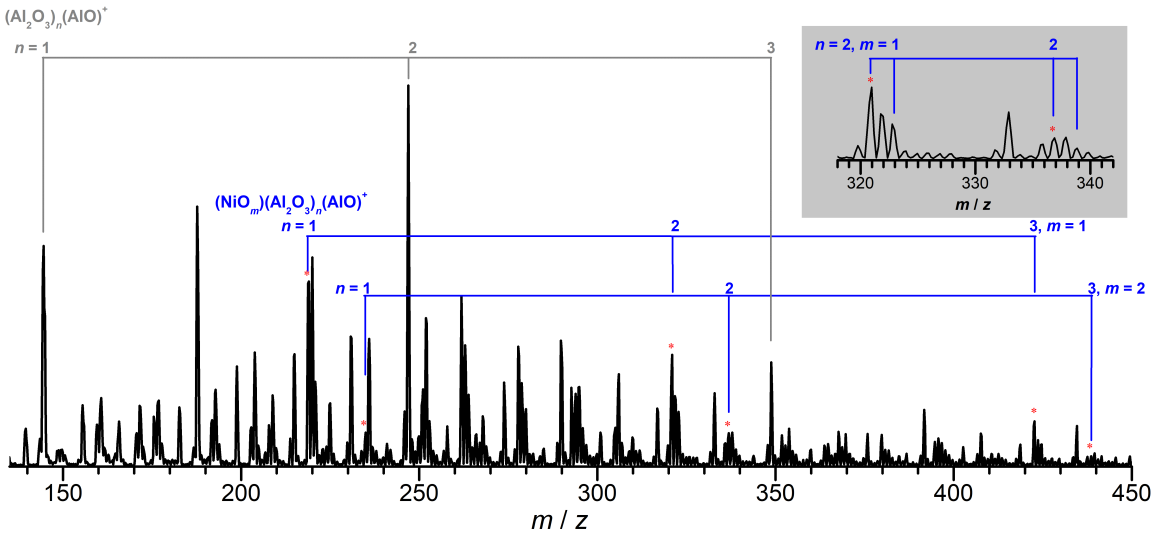

Figure 10.1: Quadrupole mass spectrum of the cations produced by laser ablation of an Al/Ni rod in the presence of 1% O2 seeded in He. The dominant mass progressions are labeled.

noted previously[549] and is a reflection of their closed electron shell combined with all atoms nominally being in their favored oxidation state, i.e. Al^{3+} and O^{2-}. Addition of $Ni^{2+}O^{2-}$ to this series yields the mixed metal oxides $(NiO)(Al_2O_3)_n(AlO)^+$ with n = 1-3, which are among the most prominent Ni-containing clusters in the mass spectrum, in line with the assumption that the most stable clusters contain the elements in their preferred oxidation state. Analysis of the relative mass peak intensities of the cations containing a single Ni atom reveals intensity patterns that reflect the natural isotope distribution of Ni, suggesting that the contribution of clusters with different stoichiometry but identical mass-to-charge ratio is small. (see inset in Figure 10.1).

IRPD spectra of the $(NiO_m)(Al_2O_3)_n(AlO)^+$ with m = 1-2 and n = 1-3 are shown in Figure 10.2. No absorption is observed above 1100 cm^{-1}. The most intense IR signals are

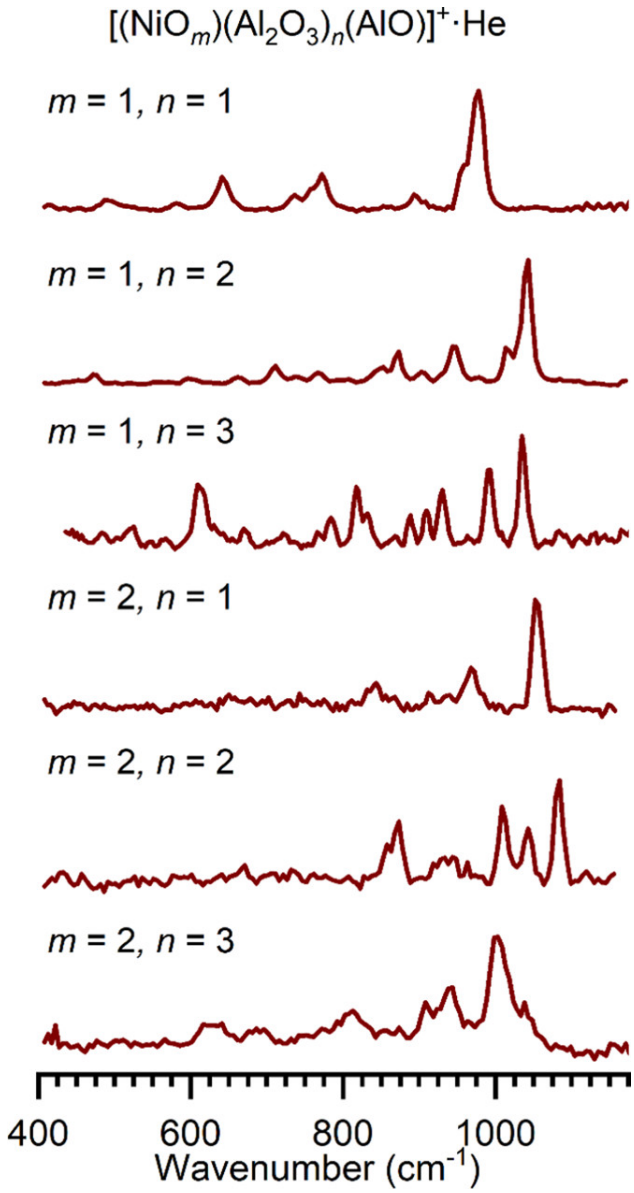

Figure 10.2: IRPD spectra of He-tagged $(NiO_m)(Al_2O_3)_n(AlO)^+$ cations (m = 1-2, n = 1-3) in the spectral region from 400 to 1175 cm^{-1} measured at an ion trap temperature of 10 K. The vertical scale for each figure is independent.

found at the highest wavenumbers, i.e. in the 900-1100 cm^{-1} spectral range, with the spectra of the $m = 2$ series (oxygen-rich) either exhibiting strong IR absorptions substantially blue-shifted (n = 1, 2) or at similar positions ($n = 3$) to those of the corresponding features in the spectra of the $m = 1$ series (oxides). The spectrum of the largest cluster ($n = 3$) in both series exhibits the largest number of bands and substantial IR activity is observed down to

600 cm^{-1}, suggesting the formation of irregular "amorphous-like" structures, as was reported previously for larger aluminum oxide anions.[552]

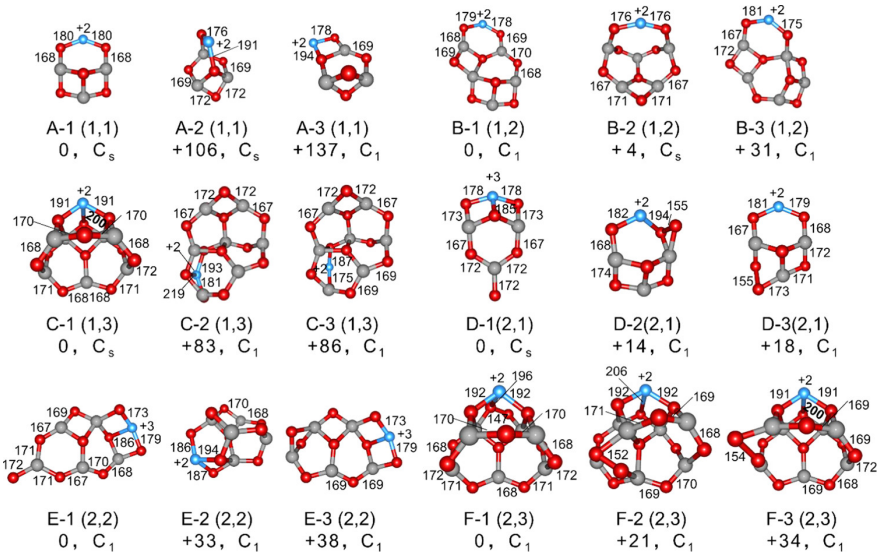

Figure 10.3: B3LYP/def2-tzvp minimum-energy structures of low energy isomers of $(NiO_m)(Al_2O_3)_n(AlO)^+$ cations with m = 1-2 and n = 1-3 (color code: blue, Ni; gray, Al; red, O). Only electronic triplet states are considered. The number of m and n are denoted as (m, n) below each structure along with the zero-point vibration-corrected energies (ΔH_{0K}) with respect to the related ground state clusters (kJ/mol), and symmetry of each cluster. Bond lengths for Ni-O bonds, Al-O$_t$ bonds, peroxide bonds, and bonds involved in the highest frequency vibration are listed in units of pm. The oxidation state of each Ni atom is listed next to the atom in each structure.

In order to assign structures to the experimentally obtained IRPD spectra, we performed electronic structure calculations using DFT. We chose the SC-AFIR approach[558–560] as part of a global reaction route mapping (GRRM) strategy,[564,565] as a similar approach has been successfully used in our previous work.[566–568] The geometries of low-energy structural candidates were then optimized using B3LYP/def2-tzvp. For each cluster size, three low-energy isomers are shown in Figure 10.3. In some cases, we find nearly isoenergetic isomers with similar structures and IR spectra, in which case we chose to display the next lowest isomer that exhibits a different structure. The formal oxidation state of the Ni atom is assigned based on an analysis of the spin densities and coordination numbers (see Fig. S2). Relative coordination numbers and other geometric parameters are listed in Table 10.1.

In general, we find that formation of four- (4m) and six-membered (6m) rings is preferred by the atoms comprising the aluminum oxide framework. We also find that the average O and Al coordination numbers are in the range 2.0-2.5 and 3.0-3.6, respectively, which are substantially smaller than the corresponding values of 4 and 6 in bulk α-alumina. The values

for the gas phase clusters are closer to those reported for amorphous alumina as well as thin films (see Table 10.1), while the Ni atom is either doubly or triply coordinated. Moreover, all oxide clusters ($m = 1$) shown in Fig. 3 exclusively contain Ni^{2+} centers, while the oxide-rich clusters ($m = 2$) either contain a peroxo-unit in combination with a Ni^{2+} center or form a structure with a Ni^{3+} species on one side of the cluster and a terminal oxygen radical anion Al-$O^{\cdot -}$ on the other.

Isomer	**O/Al ratio**	**Average CN**		**Ni CN**	**$O^{\cdot -}$**	**O_2^{2-}**	**Ni OS**
		O^{av}	Al^{av}				
A-1	1.67	2.2	3	2	0	0	+2
B-1	1.6	2.25	3.2	2	0	0	+2
C-1	1.57	2.36	3.29	3	0	0	+2
D-1	2	2.02	3	3	1	0	+3
D-2	2	2.33	3.33	2	0	1	+2
E-1	1.8	2.11	3.2	3	1	0	+3
F-1	1.71	2.33	3.29	3	0	1	+2
F-2	1.71	2.47	3.57	3	0	1	+2
amorphous alumina	1.53	2-3	4-5				
thin film	1.3	3	3.9				
α-alumina	1.5	4	6				

Table 10.1: O/Al ratio, average coordination numbers (CN), number of terminal oxygen radical anions ($O_t^{\cdot -}$) and peroxide (O_2^{2-}) units as well as Ni oxidation state (OS) for all low-energy isomers.

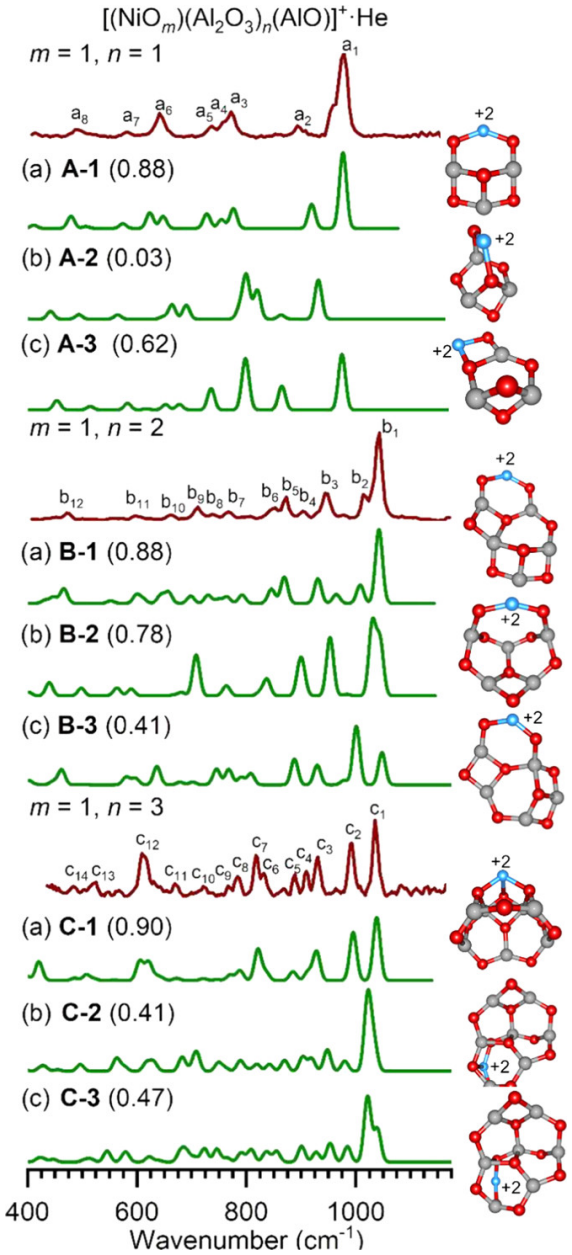

Figure 10.4: Experimental IRPD spectra (dark red) of He-tagged $(NiO)(Al_2O_3)_n(AlO)^+$ cations with n = 1-3 and simulated IR spectra (green) of low-energy isomers (without He). ZPE-corrected energies ΔH_{0K} are given in kJ/mol. The cosine similarity score is shown in parentheses. See Table 10.3 for the band positions and assignments.

The experimental IRPD spectra of He-tagged $(NiO)(Al_2O_3)_n(AlO)^+$ cations with n = 1-3 are compared to the computed spectra of the corresponding low-energy isomers (see Figure 10.3) in Figure 10.4. Table 10.3 in the SI summarizes the experimental band positions,

computed scaled frequencies and band assignments.

For $n = 1$, the lowest energy isomer (**A-1**) has C_s symmetry. It comprises two edge-sharing 4m rings as part of a Al_3O_3 book-like moiety and a 6m ring including the doubly coordinated Ni^{2+} atom, which lies in the symmetry plane (Ni-O bond length: 180 pm). **A-2** is found 106 kJ/mol higher in energy. It comprises two 6m rings and one 4m ring, with the Ni forming a short and a long Ni-O bond (176/191 pm). **A-3** (+137 kJ/mol) is the most disordered structure and has a doubly coordinated Ni^{2+} in a locally asymmetric environment.

The simulated spectrum of the lowest energy isomer **A-1** exhibits the highest cosine similarity score (0.88) and is much higher than that of the spectra of the other two isomers **A-2** (0.03) and **A-3** (0.62). We therefore assign the symmetric structure **A-1** to the $(NiO)(Al_2O_3)(AlO)^+$ cation. The highest energy band at 978 cm^{-1} results from excitation of the symmetric combination of the two symmetry-equivalent antisymmetric O^2-Al^3-O^2 stretching modes (see Figure 10.11). The other IR-active bands are mainly due to the stretching or bending modes involving the two edge-sharing 4m rings (700-900 cm^{-1}) and the stretching or bending modes of the O-Ni-O moiety (450-650 cm^{-1}).

The lowest energy isomer for $n = 2$ is the quasi-planar C_1 structure **B-1**. Its Al-O framework shows similarities with **A-1** in so far as it also contains the Al_3O_3 book-like motif as well as a doubly coordinated Ni^{2+} atom as part of a 6m-ring, but with slightly shorter Ni-O bond lengths (179/178 pm). **B-2** is slightly higher in energy (+4 kJ/mol). It is a cage-like, more symmetric structure (C_s), consisting of one 4m and two 6m AlO rings, as well as an 8m ring with a symmetric O^-Ni-O moiety. The higher energy isomer **B-3** (+31 kJ/mol) is again a sheet like structure with similarities to **B-1**, such as the Al_3O_3 book motif and a 6m ring containing the doubly coordinated Ni^{2+} center.

The simulated spectrum of the lowest energy isomer **B-1** exhibits the highest similarity score (0.88) of the three isomers. It reproduces the experimental spectrum satisfactorily, while the spectra of **B-2** (0.78) and **B-3** (0.41) predict bands with substantial IR activity below 1000 cm^{-1} that are not observed. We therefore assign structure **B-1** to the $(NiO)(Al_2O_3)_2(AlO)^+$ cation. The highest energy band at 1044 cm^{-1} (b1) can be assigned to a mode that is similar to the one described for **A-1** involving a combination of two antisymmetric O^2-Al^3-O^2 stretching modes joined by the Ni^{2+} atom (see Fig. S6).

The lowest energy isomer for $n = 3$ (**C-1**) is a three-dimensional structure of C_1 symmetry and the first to contain two four-fold coordinated Al^{3+} sites together with a triply-coordinated Ni^{2+} atom. It consists of five 6m and three 4m fused rings. These form a cone-like structure with a rim consisting of a characteristic 10m AlO ring, quite similar to that reported for $(Al_2O_3)_3(AlO)^+$.[549] The higher energy isomers **C-2** (+83 kJ/mol) and **C-3** (+86 kJ/mol) only exhibit a single four-fold coordinated Al^{3+} atom and adopt more quasi-planar structures.

The simulated spectrum of the lowest energy isomer (**C-1**) again exhibits a significantly higher cosine similarity score (0.90) than the spectra of the other two isomers **C-2** (0.41) and **C-3** (0.47). We therefore assign the cone-like structure **C-1** to the $(NiO)(Al_2O_3)_3(AlO)^+$ cation. The two highest energy bands c_1 (1035 cm^{-1}) and c_2 (993 cm^{-1}) are assigned to antisymmetric -O-(Al)-O- stretches within the 10m ring (see Fig. S6). Note that these vibrational frequencies are similar to the highest energy rim modes (1029 cm^{-1}) reported

previously for the pure aluminum oxide cation $(Al_2O_3)_3(AlO)^+$ lending further support to this assignment.[549]

Collectively, the structures found for the oxide series $(NiO)(Al_2O_3)_{1-3}(AlO)$ correspond to insertion of a Ni-O moiety into an Al-O bond of the previously reported lowest energy $(Al_2O_3)_{1-3}AlO^+$ isomers for all three sizes.[550] Moreover, nickel is formally always present as Ni^{2+} in a d^8 configuration and either doubly ($n = 1$, 2) or triply coordinated ($n = 3$). Here, we have focused on Ni in its high spin d^8 configuration (triplet state). The corresponding singlet states (low spin d^8 configuration) are found to be nearly isoenergetic and with similar IR spectra (see SI). The most intense IR features are found at the highest wavenumbers, namely at 978 cm^{-1} ($n = 1$), 1044 cm^{-1} ($n = 2$), and 1035 cm^{-1} ($n = 3$). They involve excitation of particularly short Al-O bonds (168-174 pm, see Table 10.4) as part of a combination of O^2-Al^3-O^2 antisymmetric stretching modes. This matches well with results reported previously on aluminum oxide anions, where frequencies in this spectral range 900 - 1050 cm^{-1} were reported for similar modes.[552] The IR intensities of the bands associated with Ni-O modes ($n = 1$: $a_{6,7}$; $n = 2$: $b_{10,11}$; $n = 3$: $c_{10,13,14}$), on the other hand, are rather small.

Experimental IRPD spectra of the oxygen-rich $(NiO_2)(Al_2O_3)_n(AlO)^+$ cations with n = 1-3 are compared to the computed spectra of the corresponding low-energy isomers (see Figure 10.3) in Figure 10.5. Experimental band positions, computed scaled frequencies and band assignments can be found in Table 10.3.

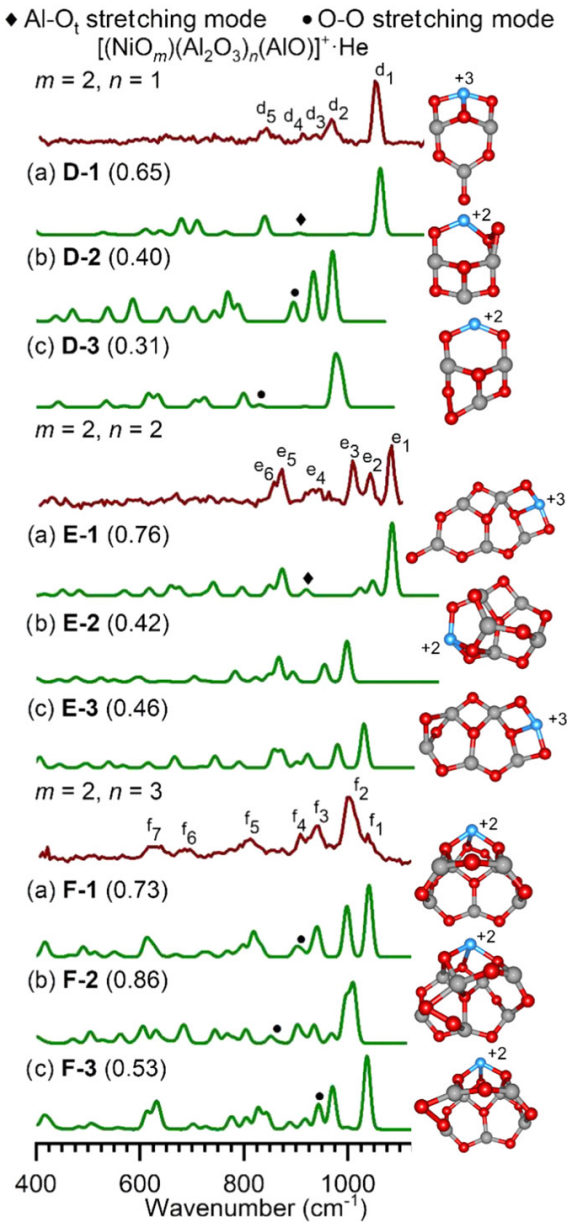

Figure 10.5: Experimental IRPD spectra (dark red) of He-tagged $(NiO_2)(Al_2O_3)_n(AlO)^+$ cations with n = 1-3 and simulated IR spectra (green) of low-energy isomers (without He). ZPE-corrected energies ΔH_{0K} are given in kJ/mol. The cosine similarity score is shown in parentheses. See Table 10.3 for the band positions and assignments.

The lowest energy isomer predicted for $n = 1$ is the quasi-planar C_s structure **D-1**. Its structure is similar to that of **A-1**, but the positions of the Ni- and the Al-atom in the symmetry plane are switched and the extra O-atom is added such that metal centers

are now triply coordinated. In comparison to the $m = 1$ structures, **D-1** includes a triply coordinated Ni-site and a terminal oxygen-centered radical anion (Al-O$^{\cdot-}$) on the opposite side of the cation. Analysis of the spin densities, including spin polarization effects, suggests the presence of a Ni^{3+} species, where the spin is delocalized over the Ni(-O-)$_3$ moiety, either in a high-spin (quartet) or low-spin (doublet) configuration. The additional unpaired electron centered on the terminal oxygen atom can then be coupled in either a parallel or antiparallel fashion yielding states of quintet, triplet or singlet multiplicity. For simplicity, we focus on the triplet states here, but note that the IR spectra of the corresponding quintet state (see Figs. S4) is very similar. Of the two possible triplets, **D-1** corresponds to the one with the low-spin configuration on the Ni(-O-)$_3$ moiety and a parallel spin on the terminal oxygen atom. The higher energy isomers **D-2** (+14 kJ/mol) and **D-3** (+18 kJ/mol) are variants of structure **A-1**, in which the Ni-atom remains in its original position in the form of a doubly-coordinated Ni^{2+} center. The additional O-atom is incorporated in the form of an O_2^{2-} unit, between either Ni/Al or Al/Al sites and with a bond length (155 pm) that is typical for peroxo species.[551]

The simulated spectrum of the lowest energy isomer **D-1** exhibits the highest cosine similarity of these three isomers, but its magnitude (0.65) is considerably smaller than the scores found for the best matches for the $m = 1$ series (≥ 0.88). Three bands (d_{2-4}) observed in the experiment are not reproduced by the simulated spectrum and two bands are predicted around 700 cm^{-1}, which are not observed experimentally. Despite these discrepancies, the spectrum of **D-1** is the best match, and we assign the structure accordingly. The spectrum of the higher energy isomer **D-2** (0.40) reproduces the unassigned bands d2-4 and therefore is probably present in the experiment, but with lower abundance than **D-1**. The assignment of the highest energy band d_1 (1053 cm^{-1}) is similar to that of band a_1 in the spectrum of **A-1** (see Fig. S6). The band corresponding to the Al-O$^{\cdot-}$ stretching mode is predicted at 906 cm^{-1} with low IR-intensity and is tentatively assigned to the feature at 912 cm^{-1} in the experimental IRPD spectrum.

For $n = 2$, the situation is quite similar to that for $n = 1$. The lowest energy isomer **E-1** can be derived from the corresponding $m = 1$ structure **B-1**. Similar to **D-1**, **E-1** includes a triply coordinated Ni^{3+} site in combination with a terminal oxygen radical at the opposite end of the cation. The cage-like structure **E-2**, which contains two 4-fold coordinated Al^{3+} sites, is predicted +33 kJ/mol higher in energy and includes a triply coordinated Ni^{2+} site with three spins located on the NiO_2 moiety forming two Ni-O bonds (186/187 pm). The higher energy isomer **E-3** (+38 kJ/mol) is similar to **E-1** in that it is quasi-planar and contains a triply-coordinated Ni^{3+} site. Interestingly, it does not exhibit a terminal O radical with a localized spin, but rather the spin is now delocalized over the two O atoms of the 4m Al_2O_2 ring. The distance between these two oxygen atoms is 224 pm, much larger than that for a typical superoxo unit (∼132 pm).[551]

The cosine similarity score of the **E-1** spectrum (0.76) is considerably higher than those of **E-2** (0.42) and **E-3** spectrum (0.46) and we assign the structure to the $(NiO_2)(Al_2O_3)_2$ $(AlO)^+$ cation accordingly. However, smaller contributions to the experimental IRPD spectrum from other isomers, specifically **E-2**, are likely. The assignment of the highest energy

band e_1 (1084 cm^{-1}) is the same as for **D-1** and involves the two O^2-Al^3-O^2 moieties adjacent to the terminal Al-$O^{\cdot -}$ unit. Band e_4 (933 cm^{-1}) is then tentatively assigned to the Al-$O^{\cdot -}$ stretching mode (see Table 10.2).

Species	Cluster	Isomer	Exp.	B3LYP	Al-O/O-O Bond Length
Terminal Al–$O_t^{\cdot}$	*n = 1*	**D-1**	912	906	172
	n = 2	**E-1**	933	920	172
Peroxide	*n = 1*	**D-2**	912	895	155
	n = 3	**F-1**	908	911	147
	n = 3	**F-2**	908	864	152

Table 10.2: Experimental and calculated scaled harmonic vibrational frequencies (in cm^{-1}) of different oxygen species in $(NiO_2)(Al_2O_3)$n$(AlO)^+$ with n = 1-3 and the related Al–$O_t^{\cdot}$/O-O Bond length (pm).

For $n = 3$, all three low-energy isomers exhibit three-dimensional structures containing exclusively triply-coordinated Ni^{2+} centers. All three structures represent variations of the corresponding $m = 1$ cone-like structure **C-1**. They only differ in the location of the peroxo-group, which is found adjacent to the Ni atom in **F-1** and further away as part of the rim structure in **F-2** (+21 kJ/mol) and **F-3** (+34 kJ/mol).

This is the only system for which the spectrum of the lowest energy isomer does not yield the highest cosine similarity score. The score for the spectrum of **F-1** (0.73) is smaller than the corresponding value for the spectrum for **F-2** (0.86). Indeed, it seems likely that both isomers contribute to the experimental spectrum with **F-2** being the main contributor. While the spectrum of **F-2** reproduces nearly all features at lower energies, only the spectrum of **F-1** can account for the highest energy peak f_1 (1039 cm^{-1}). The spectrum of **F-3** exhibits the lowest similarity score (0.53) of the three isomers. Bands f_1 and f_2 are attributed to the same mode as already described for **C-1** (see Fig. S6). The peroxo stretching modes are predicted at 911 cm^{-1} (**F-1**) and 864 cm^{-1} (**F-2**) with low IR intensity and in a congested spectral range, making their identification challenging.

Altogether, the structures identified for the $m = 2$ (oxygen-rich) series $(NiO_2)(Al_2O_3)_{1-3}(AlO)^+$ are related to the structures found for the $m = 1$ (oxide) series in that they exhibit a similar framework. In contrast to the $m = 1$ cations, however, multiple isomers probably contribute to the spectra of the $m = 2$ cations, probably due to the lower relative stability of the latter (see also Figure 10.1). Further, we find that the additional O-atom can be incorporated in two ways. For $n = 2$, we find the Ni^{3+}/Al-$O^{\cdot -}$ motif, while the most stable structures for $n = 3$ prefer the Ni^{2+}/O_2^{2-} motif. Both structural motifs are found to contribute to the experimental spectrum for $n = 1$. With increasing cluster size, the number of fourfold- (and higher-fold) coordinated Al-atoms increases and three-dimensional (3D) structures are preferred and these stabilize the Ni^{2+}/O_2^{2-} motif. Note that the chemical

reactivity is expected to be different for the two types of oxygen species (O_2^{2-} vs. Al-$O^{\cdot -}$). Al-$O^{\cdot -}$ groups are typically more reactive and the ability of terminal oxygen radicals to activate methane is well documented.[578]

For the moderate cluster sizes ($n = 3$) characterized here, we find that cone-like 3D structures, originally identified for the corresponding $(Al_2O_3)_{1-4}(AlO)^+$ cations[549] are particularly stable. While the most intense IR bands in these spectra are due to combinations of O^2-Al^3-O^2 antisymmetric stretching modes involving particularly short Al-O bonds ($<$ 173 pm), the modes involving the characteristic oxygen species (either O_2^{2-} or Al-$O^{\cdot -}$) as well as the Ni-O modes are predicted too low in IR intensity to be observed unambiguously experimentally.

DFT does a surprisingly good job for these challenging systems, which really should be treated with multi-reference approaches. Even though the DFT energies are not predictive for transition metal containing systems as studied here,[555] the lowest energy isomer is typically (but not always) found to be the structure that contributes predominantly to the IRPD spectrum. For most systems, we find satisfactory agreement with the spectra of clusters containing the Ni atom in a high spin configuration. However, since the predicted spectra for the corresponding systems with lower multiplicity are typically very similar, we cannot infer reliably on their spin state. This would require the application of other techniques, like x-ray magnetic circular dichroism spectroscopy.[579]

10.6 Conclusion

Vibrational spectra of nickel-doped aluminum oxide cations, $(NiO_m)(Al_2O_3)_n(AlO)^+$ m = 1–2, n = 1–3 have been obtained using IRPD spectroscopy of He-tagged ions. These spectra show a wealth of vibrational structure in the 400-1200 cm^{-1} spectral range and assignments are facilitated through comparison with computed harmonic IR spectra of low energy isomers. For $m = 1$, we find satisfactory agreement with the spectra of clusters that show the insertion of a Ni–O moiety into an Al–O bond of the corresponding $(Al_2O_3)_{1-3}(AlO)^+$ cations, resulting in doubly and triply-coordinated Ni^{2+} centers. The oxigen-rich cations $(NiO_2)(Al_2O_3)_{1-3}(AlO)^+$ contain either a Ni^{3+}/Al-$O^{\cdot -}$ or a Ni^{2+}/O_2^{2-} motif and represent gas phase model systems for undercoordinated alumina-supported Ni-sites in oxygen-rich environments. Further reactivity studies on these model systems have the potential to unravel the mechanism of the industrially-relevant ODH of alkanes by alumina-supported nickel-based catalysts, in particular, the origin of the observed high selectivity.

10.7 Supplemental Materials

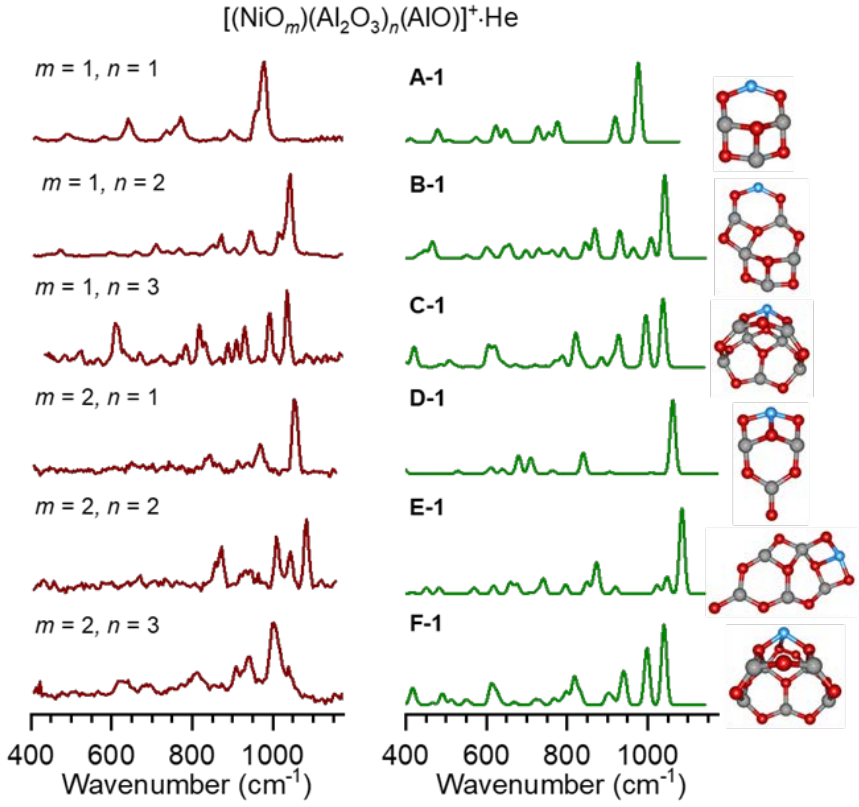

Figure 10.6: Experimental IRPD spectra of $(NiO_m)(Al_2O_3)_n(AlO)^+$·He with m = 1-2 and n = 1-3 (1st column, dark red traces), computed B3LYP/def2-tzvp harmonic IR spectra (2nd column, green), and related structures (3rd column). All the harmonic frequencies are scaled by 1.011.

Species	Mode	Band	Exp.	B3LYP
m = 1, n = 1	ν^{as}(O–Al–O)	a_1	978	977
(A-1)	ν^{as}(O–Al–O)	a_2	893	920
	ν^{as}(Al–O–Al)	a_3	772	776
	δ(Al–O–Al)	a_4	757	755
	ν^{as}(Al–O–Al)	a_5	736	728
	ν^{s}(O–Ni–O) and ν^{as}(O–Ni–O)	a_6	641	648/623
	δ(O–Ni–O)	a_7	584	574
	δ(Al–O–Al)	a_8	486	479

m = 1, n = 2	ν^{as}(O–Al–O)	b_1	1044	1042
(B-1)	ν^{as}(O–Al–O)	b_2	1014	1008
	ν^{as}(O–Al–O)	b_3	943	931
	–	b_4	903	–
	ν^{as}(O–Al–O)	b_5	873	869
	ν^{as}(O–Al–O) and δ(Al–O–Al)	b_6	853	846
	δ(Al–O–Al)	b_7	767	764
	δ(O–Al–O)	b_8	736	730
	δ(O–Al-O), ν^{as}(O–Ni–O)	b_9	711	698
	δ(Al–O-Al), and ν^{as}(O–Ni–O)	b_{10}	661	658/643
	ν^{s}(O–Ni–O), δ(Al/Ni–O–Al)	b_{11}	596	611/599
	δ(O–Al–O)	b_{12}	471	466
m = 1, n = 3	10m ring breathing mode	c_1	1035	1038
(C-1)	10m ring breathing mode	c_2	993	995
	ν^{as} (O-Al-O)	c_3	931	928
	ν^{as}(Al-O-Al) in 6m ring	c_4	910	913
	ν^{as}(Al-O-Al) in 6m ring	c_5	889	885
	ν^{as}(O-Al-O) in 6m ring	c_6	832	836
	δ(O–Al-O) in 4m ring	c_7	817	821
	v (Al^3-O^3)	c_8	784	788
	v (Al^3-O^3)	c_9	766	771
	ν^{as}(O–Ni–O)	c_{10}	721	721
	δ(Al–O-Al)	c_{11}	670	673
	δ(Al–O-Al)/ δ(O-Ni-O)	c_{12}	609	621/606
	δ(O-Ni–O), ν^{as}(O-Ni-O), and rocking of NiO_2	c_{13}	525	525/522/508
	ν(O_2Ni–OAl_2)	c_{14}	483	486
m = 2, n = 1	ν^{as}(O–Al–O)	d_1	1053	1062
(D-1/D-2)	ν^{as}(O–Al–O)	d_2	968	971
	ν^{as}(O–Al–O)	d_3	940	934
	ν(Al–$O_t^{\cdot}$)/ν(O–O)	d_4	912	906/895
	ν^{as}(O–Al–O)	d_5	844	840
m = 2, n = 2	ν^{as}(O–Al–O)	e_1	1084	1085
(E-1)	ν^{as}(O–Al–O)	e_2	1044	1048
	ν^{as}(Al–O–Al)	e_3	1008	1023
	ν(Al–$O_t^{\cdot}$)	e_4	933	920
	ν^{as}(Al–O–Al)	e_5	873	873
	ν(Al^3–O^3)	e_6	858	849
m = 2, n = 3	10m ring breathing mode	f_1	1039	1041
(F-1)	10m ring breathing mode	f_2	1003	998
	ν^{as}(Al–O–Al)/ δ(O–Al–O)	f_3	943	942/933

ν(O-O)/ ν^{as}(Al-O-Al)	f_4	908	911/900
δ(Al–O–Al)	f_5	812	818
δ(O–Al–O)	f_6	686	670
δ(Al–O–Al)/δ(Al^4–O^3)	f_7	626	631/623/612

Table 10.3: Experimental and calculated harmonic vibrational frequencies (in cm^{-1}) of $(NiO_m)(Al_2O_3)_n(AlO)^+$ with m = 1-2 and n = 1-3, including main contributions of local modes.

CN Al, Ni or O / CN O	O^1	O^2	O^3	O^4
Al^3	172	168-174	175-186	-
Al^4	-	169-193	177-193	195-199
Ni^2	-	178-182	194	-
Ni^3	-	176-178	185-219	-
O^3	-	147-155	-	-

Table 10.4: Al-O, Ni-O, O-O bond distances (pm) as a function of the respective Al, Ni, O and O coordination numbers (CN) for $(NiO_m)(Al_2O_3)_n(AlO)^+$ with m = 1-2 and n = 1-3 calculated.

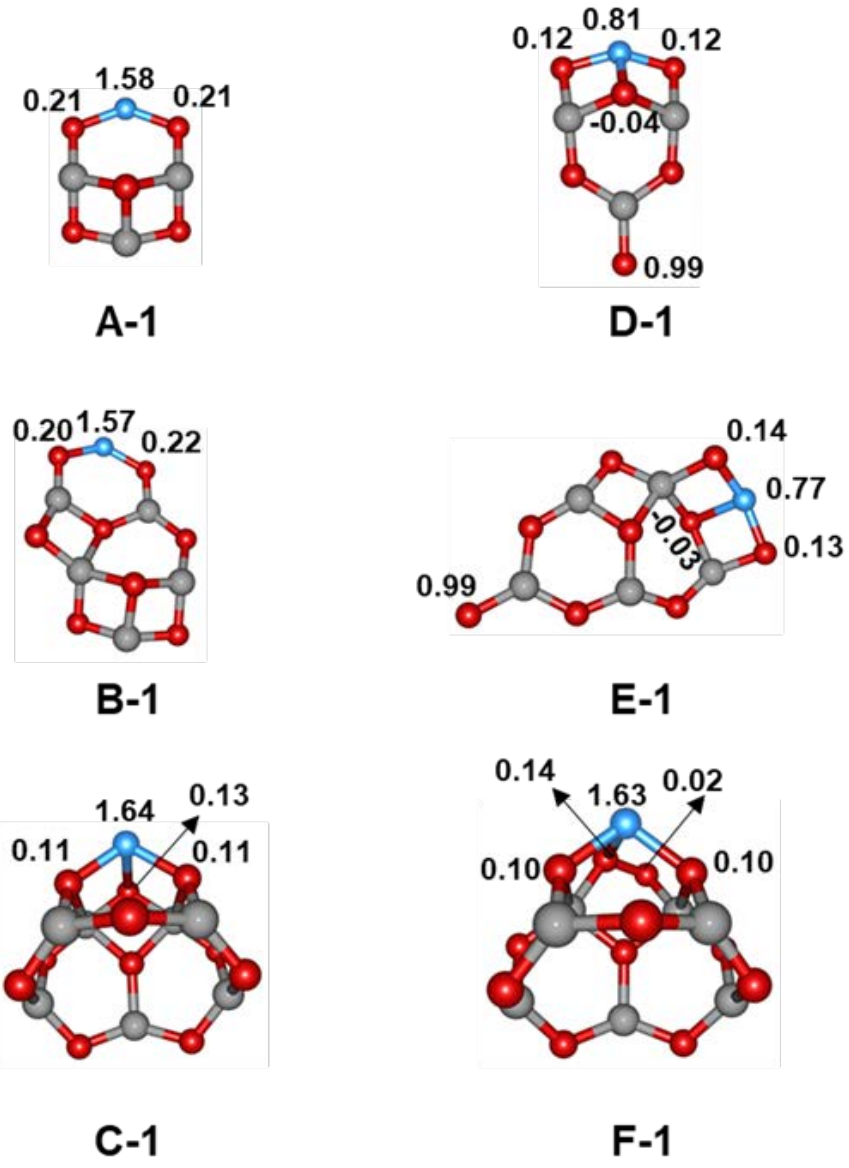

Figure 10.7: Spin density distribution for structures **A-1**, **B-1**, **C-1** (left column) vs. **D-1**, **E-1**, **F-1** (right column) for the triplet states.

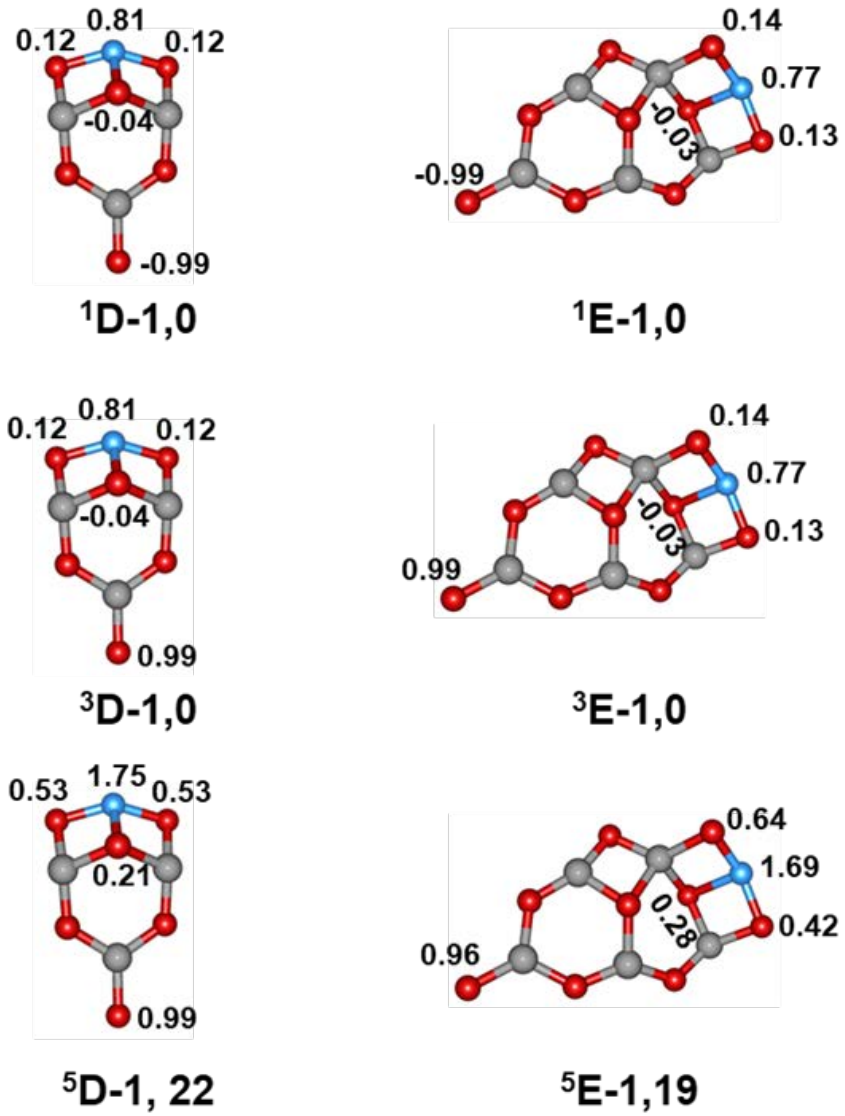

Figure 10.8: Spin density distribution for singlet, triplet and quintet **D-1** (left column) vs. **E-1** (right column). The related energies are also shown in kJ/mol.

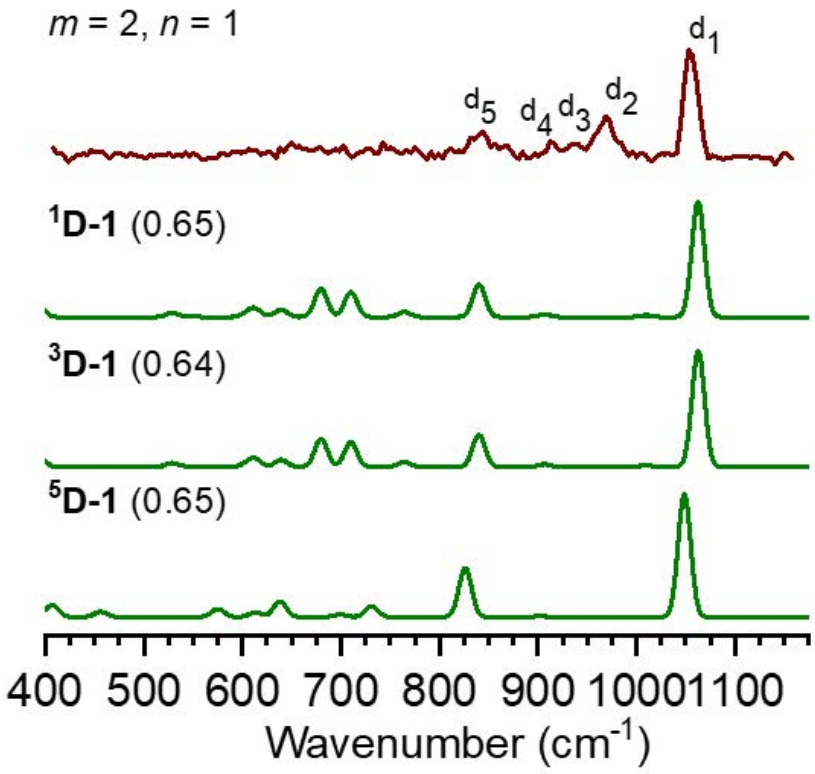

Figure 10.9: Experimental IRPD spectra (dark red) of He-tagged $(NiO_m)(Al_2O_3)_n(AlO)^+$ cation ($m = 2$, $n = 1$) with simulated IR spectra (green) of singlet, triplet, and quintet low-energy isomer **D-1** (without He). The cosine similarity score is shown in parentheses. See Table 10.3 for the band positions and assignments.

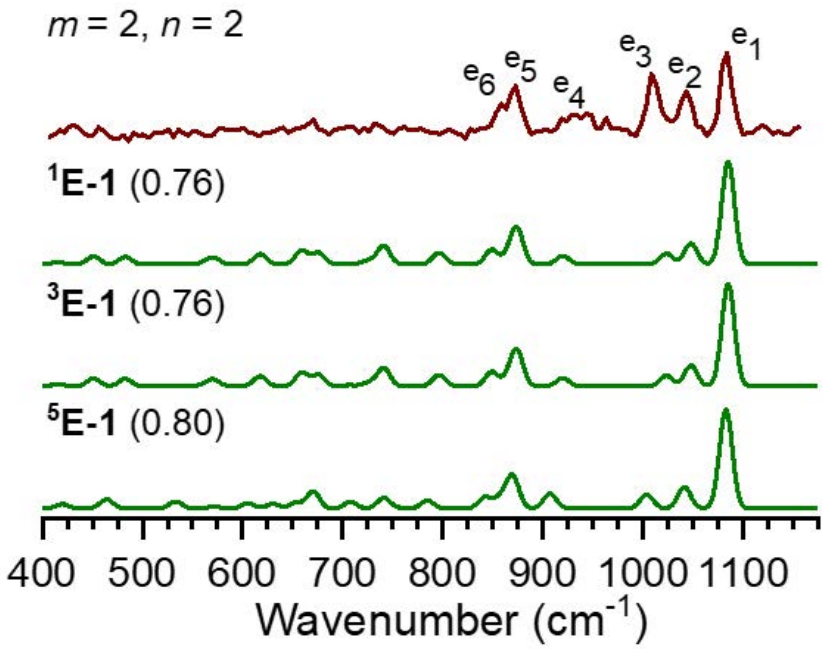

Figure 10.10: Experimental IRPD spectra (dark red) of He-tagged $(NiO_m)(Al_2O_3)_m(AlO)^+$ cation ($m = 2$, $n = 2$) with simulated IR spectra (green) of singlet, triplet, and quintet low-energy isomer(^{1}**E-1**, ^{3}**E-1**, ^{5}**E-1**) (without He). The cosine similarity score is shown in parentheses. See Table 10.3 for the band positions and assignments.

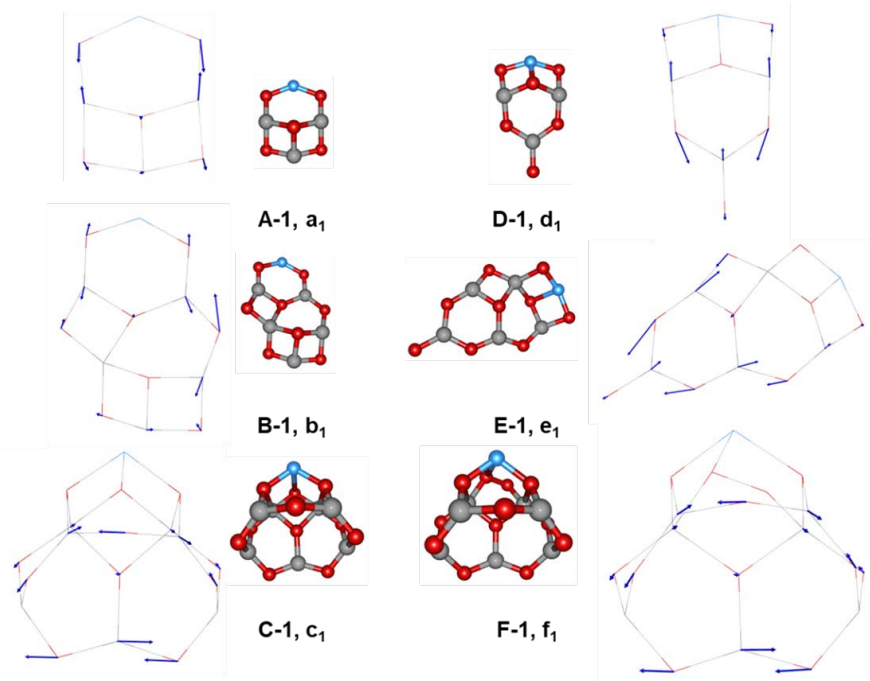

Figure 10.11: The highest energy vibrational mode in each cluster is shown with arrows.

Chapter 11

Probing the hydrolysis of ZrO_2

The content and figures of this chapter are reprinted or adapted with permission from A. A. Taka, M. C. Babin, X. Sheng, J. A. DeVine, D. M. Neumark, H. P. Hratchian, "Unveiling the Coexistence of *Cis* and *Trans* Isomers in the Hydrolysis of ZrO_2: A Coupled DFT and High-Resolution Photoelectron Spectroscopy Study" *J. Chem Phys.* **153**, 244308 (2020).

11.1 Abstract

High-resolution anion photoelectron spectroscopy of the $ZrO_3H_2^-$ and $ZrO_3D_2^-$ anions and complementary electronic structure calculations are used to investigate the reaction between zirconium dioxide and a single water molecule, $ZrO_2^{0/-} + H_2O$. Experimental spectra of $ZrO_3H_2^-$ and $ZrO_3D_2^-$ were obtained using slow photoelectron velocity-map imaging (cryo-SEVI), revealing the presence of two dissociative adduct conformers and yielding insight into the vibronic structure of the corresponding neutral species. Franck-Condon simulations for both the *cis*– and *trans*–dihydroxide structures are required to fully reproduce the experimental spectrum. Additionally, it was found that water-splitting is stabilized more by ZrO_2 than TiO_2, suggesting Zr-based catalysts are more reactive toward hydrolysis.

11.2 Introduction

Zirconium dioxide (ZrO_2) is an extensively studied material with widespread applications in medicine,[580–582] gas-cleaning technology,[583] ceramics,[584–586] corrosion-resistant materials,[587–589] and heterogeneous catalysis.[590] As in the case of titania (TiO_2), photosensitization of water on a ZrO_2 electrode has inspired the development of ZrO_2 based technologies to exploit its photocatalytic properties for solar–powered hydrogen fuel cells.[591–595] Despite significant effort, these technologies are not yet viable, in part due to the limited mechanistic knowledge needed for further development.[596] Specifically, a more complete understanding of the interaction between ZrO_2 and water is required to develop these devices. Here, we

present high-resolution photoelectron spectra of the $ZrO_3H_2^-$ anion in tandem with electronic structure calculations, providing insight into the simplest reaction of $ZrO_2^{0/-}$ with water.

There is a vast body of work on the surface chemistry of metal oxides aimed at understanding water oxidation,[597–604] with a considerable number of studies specifically probing the ZrO_2 surface.[605–609] From this body of work, it has become clear that defect sites play a critical role in the catalytic process,[610–615] thus investigating the interaction of water molecules at these sites is crucial for gaining insights into the water splitting mechanism. Such studies are challenging, however, owing to the difficulty of synthesizing and probing molecular-scale structures embedded with low density on bulk surfaces.[616–624] Overcoming the hurdles of generating and controlling defect sites can be bypassed by preparing and studying gas–phase metal oxide clusters, as these species show structural motifs that mimic the geometries of common defect sites.[212–214] Further, the relatively small size of these systems makes them computationally tractable, enabling experimentalists and theorists to determine their electronic structure, geometries, and catalytic reaction mechanisms - a task not viable from bulk studies alone.[251,252,506,625,626] There has been substantial progress made in understanding the structure and reactivity of small metal oxide clusters,[627–632] including several studies on the interaction between titanium dioxide clusters and water molecules.[313,633–635]

Of particular relevance is the work of Zheng and co-workers, who performed anion photoelectron spectroscopy (PES) on the anionic $(TiO_2)(H_2O)_{0-7}$ clusters and inferred that dissociative adsorption of water occurs to form a hydroxide species.[633] We recently reinvestigated the $(TiO_2^-)(H_2O)$ system using slow electron velocity-map imaging of cryogenically cooled anions (cryo-SEVI), a high-resolution form of anion PES, coupled with detailed computational simulations.[65] That work shows evidence that the dissociative adduct, *cis*-dihydroxide $TiO(OH)_2^-$, is a planar C_{2v} structure that is energetically favored over a molecularly adsorbed complex and other lower-symmetry dissociative species.

Though still a Group IV metal oxide, ZrO_2 has been studied less extensively than titania.[250,636–641] Within the bulk framework, Sayama et al.[596] initiated significant interest in the field with the discovery of the photocatalytic decomposition of water on pure ZrO_2 powder following UV irradiation. Later, it was shown that adding a carbonate-based salt such as $NaHCO_3$ or Na_2CO_3 to an aqueous ZrO_2 suspension increased the gas evolution rate in the photocatalytic decomposition of water.[642] The interaction of water with bulk zirconia surfaces has been characterized and investigated by X-ray powder diffraction, high-resolution transmission electron microscopy, X-ray photoelectron spectroscopy, calorimetry, and Fourier-transform infrared spectroscopy (FTIR),[643–646] along with periodic density functional theory (DFT) calculations.[647–650] Notably, the FTIR investigation by Holmes and co-workers[646] of water sorption on ZrO_2 found bands corresponding to chemisorbed OH groups, suggesting that water bound to the surface of ZrO_2 forms a $OZr(OH)_2$–like structure.

Bare $(ZrO_2)_n^{0/-}$ clusters have been extensively studied using PES,[59,60,651] matrix-IR spectroscopy,[652] Fourier-transform microwave spectroscopy,[653] laser-induced fluorescence,[654] resonant multi-photon ionization,[654] dispersed fluorescence,[654] and computational methods.[651,652,655–658] Despite this growing body of work, there is no experimental data on the

reactions of these clusters with a water molecule, though computational studies by Dixon et al.[659] on the $(ZrO_2)_n + H_2O$ $(n = 1 - 4)$ reaction find these clusters are capable of splitting water. That work shows the dissociative adduct to be more stable than the molecularly adsorbed species by roughly 200 kJ/mol, at both the DFT and coupled cluster levels of theory, in agreement with experimental observations on bulk zirconia.[650] Further, the optimized geometries of the dissociative adduct were found to adopt only a *cis*-hydroxide geometry in contrast with computational results for the $TiO_2^{0/-} + H_2O$ dissociative adducts, where both *cis* and *trans* isomers were identified.[65,660]

Here, we present a combined computational and experimental investigation of $ZrO_3H_2^-$ and $ZrO_3D_2^-$, thereby probing fundamental aspects of the $ZrO_2^{0/-} + H_2O$ gas-phase reaction. The dense and highly resolved vibrational structure seen in the cryo-SEVI spectra is only reproduced if detachment from both low-lying isomers of the $ZrO(OH)_2^{0/-}$ system, the *cis*-dihydroxide and *trans*-dihydroxide dissociative adducts, are considered. Additionally, the electron affinity of the neutral *cis*-dihydroxide structure and adiabatic electron affinity (ADE) of the anionic *trans*-dihydroxide are reported along with vibrational frequencies of both neutral structures. Further, agreement between experiment and theory facilitates not only the structural determination of these clusters, but also provides insight into the differences between the hydrolysis reactions of TiO_2 and ZrO_2.

11.2.1 Experimental Methods

The cryo-SEVI method has been described in detail previously.[34,35,54] In this work, $ZrO_3H_2^-$ ions were formed using the same modified ablation ion source used to generate TiO_3H_2-.[65] Clusters are produced via a pulse from the frequency-doubled output of a 20 Hz Nd:YAG (2-3 mJ/pulse) that strikes a rotating and translating zirconium target, forming a plasma that is carried through an 80 mm long, 2 mm diameter channel by a pulse of helium gas (150 psi backing pressure, 60 μs pulse width) from an Even-Lavie valve.[245] This expansion allows for the plasma to cool and condense to form charged and neutral molecules and clusters. These then pass through a 1 mm slit into a second channel, 90 mm long, and 2 mm in diameter. In this second channel, a pulsed Series 9 General Valve introduces helium bubbled through room temperature H_2O or D_2O (15 psi backing pressure, pulse width $\sim$160 μs) allowing for the ablation products to cool further, react with H_2O or D_2O, and finally expand into vacuum.

The ions then pass through a radiofrequency (RF) hexapole ion guide and a RF quadrupole mass filter before being directed into a linear RF octupole ion trap held at 5 K and filled with a buffer gas mixture of 20:80 H_2:He. Collisions with the cold buffer gas result in effective vibrational, rotational, and electronic cooling of the ions, leading to internal temperatures of around 10 K.[54,239] After $\sim$40 ms, the clusters are extracted into an orthogonal Wiley-McLaren time of flight mass spectrometer[259] and focused into the interaction region of a velocity-map imaging (VMI) electrostatic lens assembly,[18,36] where they are photodetached by vertically polarized light from a pulsed laser.

The detachment laser configuration is based on the output of a dye laser pumped by the second harmonic of a Nd:YAG laser operating at 20 Hz. For photon energies above ∼1.3 eV (10,500 cm^{-1}, 950 nm), the output of the dye laser is used without modification. For energies below 1.3 eV, the output of the dye laser is focused into a 63-cm long Raman cell containing described previously,[65] resulting in tunable photon energies ranging from ∼1.0 to 1.3 eV (8,000-10,500 cm^{-1}).

The resulting photoelectrons are projected onto a 2D detector comprising two chevron-stacked microchannel plates coupled to a phosphor screen, which is photographed by a CCD camera after each laser shot.[17] Each image is analyzed for individual electron events for which the centroids are calculated and binned in a 2200 × 2200 grid.[271] Slight deviations from circularity in the accumulated images are corrected using the circulization algorithm described by Gascooke et al.[289] The three-dimensional electron velocity distribution is then reconstructed from the circularized images using the Maximum Entropy Velocity Legendre Reconstruction (MEVELER) algorithm.[275] The radial position of features in the reconstructed image is related to electron kinetic energy (eKE) by acquiring VMI images for detachment from atomic Ni^- and O^- at several photon energies.[279,288]

The VMI spectrometer has an approximately constant resolving power, ΔeKE/eKE,[18] yielding the best eKE resolution for slow electrons. As such, a SEVI spectrum is acquired by first taking an overview spectrum at a relatively high photon energy before tuning the detachment laser to energies slightly above features of interest. This procedure results in a collection of high-resolution spectra over narrow energy windows that are concatenated and scaled to match intensities in the overview spectrum, which is less sensitive to variation of the photodetachment cross section with photon energy. Spectra are plotted as a function of electron binding energy (eBE), given by eBE = hv - eKE.

In addition to the eKE distributions, VMI allows for the determination of photoelectron angular distributions (PADs) associated with each detachment transition, given by[91]

$$\frac{d\sigma}{d\Omega} = \frac{\sigma_{tot}}{4\pi}\left[1 + \beta P_2(\cos\theta)\right] \tag{11.1}$$

where σ_{tot} is the total detachment cross section, $P_2(x)$ is the second-order Legendre polynomial, θ is the angle of the outgoing photoelectron velocity vector with respect to the laser polarization axis, and β is the anisotropy parameter. The anisotropy parameter, which ranges from -1 (perpendicular detachment) to +2 (parallel detachment), reflects the angular momentum of the detached electron and is thus tied to the electronic character of each photodetachment transition.[361]

11.2.2 Computational Methods

A variety of DFT-based model chemistries were used to identify possible minimum energy structures along the anionic and neutral ZrO_2 + H_2O surface. Initial benchmark work was carried out by comparing six different functionals (B3LYP, B3PW91, M06, M06L, PBE1PBE and ωB97XD) and two basis sets (def2tzvp and the Stuttgart/Cologne ECP28MHF (SC))

resulting in 12 different model chemistries.[132–135,141,158,164,168,169,661–664] Tables S1-S6 summarize the results obtained from these benchmark calculations. Preliminary results suggested meaningful differences in normal mode frequencies and vertical excitation energies. After a detailed inspection of these results and comparison with the experimental data presented here, we determined that the ωB97XD/SC model chemistry best reproduces the observed relative experimental energies and vibrational frequencies.

A number of electronic states for the anion and neutral species were investigated. For the anion, doublet and quartet spin states were considered, while singlet and triplet states were included for the neutral. All model chemistries predicted lowest spin states (neutral singlet and anion doublet) to be energetically most stable. Excited-state calculations were carried out using the same model chemistry within the (linear response) time–dependent DFT (TDDFT) formalism.[151,152,154]

All calculations were carried out using a local development version of the GAUSSIAN suite of electronic structure programs.[665] Stability was tested on all converged Kohn–Sham determinants.[666,667] Standard methods were used for optimizing molecular geometries,[668] and the nature of located stationary points were verified using analytical second–derivative calculations.[669,670] Franck–Condon (FC) spectra were generated using the implementation by Bloino, Barone, and co–workers.[671,672] Simulated PES spectra, including FC progressions, were adjusted to align with the experimental spectra after shifting DFT force constants of the neutral state. Full details, including scaling factors and shifting parameters, are provided in the SI. Characterization of electron detachment was facilitated by the Natural Ionization Orbital (NIO) model.[673] The NIO model provides the Dyson orbital for a ΔSCF treatment of electron detachment and, within the sudden approximation, provides insight to electron relaxation accompanying electron detachment. The NIO model has been successfully employed in a number of recent studies involving similar systems.[65,673,674]

11.3 Results and Discussion

11.3.1 Experiment

Cryo-SEVI spectra of $ZrO_3H_2^-$ and $ZrO_3D_2^-$ are shown in Figs. 11.1 and 11.2, respectively. In both figures, overview spectra, taken with relatively high photon energies, are displayed in blue atop composite high-resolution scans in black taken with various photon energies. While the overview spectrum displays structure for eBEs up to ~10,750 cm^{-1}, high resolution scans were collected only out to ~10,000 cm^{-1}; see Fig. S1 in the SI for the full overview spectrum. These high-resolution traces highlight structure covering eBEs from 9,300 to 10,000 cm^{-1}, revealing a number of transitions (A-V and A-T in ZrO_3H_2 and ZrO_3D_2, respectively) that correspond to detachment to different vibrational levels of the neutral ZrO_3H_2 and ZrO_3D_2 species. Peaks as narrow as 4 cm^{-1} fwhm are reported, owing to strong photoelectron signal at low eKEs where resolution is highest. It should be noted that ions with $m/z = 140$ were chosen despite the possible contribution from $^{92}ZrO_3^-$ as well as the target $^{90}ZrO_3H_2^-$ species;

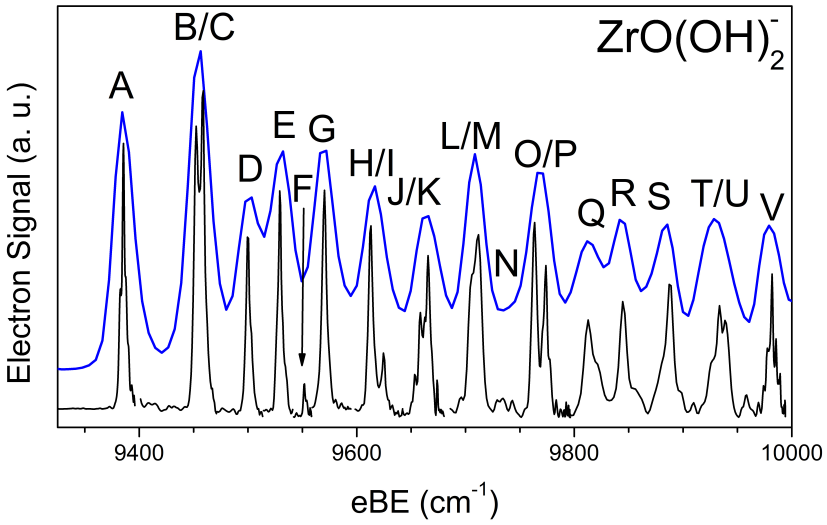

Figure 11.1: Cryo-SEVI spectra of ZrO_3H_2. The overview spectrum (blue, $h\nu$ = 10,747 cm^{-1}) is vertically offset from the high-resolution traces (black, variable photon energies).

the electron affinity of ZrO_3 has not been experimentally determined, but is calculated to be 3.06 eV, substantially higher than the photon energies employed in this work (<1.35 eV), and thus should not contribute to the reported spectra.

The sharp onset of structure at peak A, the vibrational origin, allows for determination of the EAs for ZrO_3H_2 and ZrO_3D_2 as 1.1636(5) and 1.1616(7) eV, respectively. Beyond peak A, we observe a prominent doublet of peaks (B/C) residing just above 9,400 cm^{-1} in both spectra, split by ∼5 cm^{-1}. A similar doublet is observed near 9,800 cm^{-1} in both spectra (peaks O/P in the spectrum of ZrO_3H_2 and S/T in ZrO_3D_2). Owing to the doublet structure, assignment by inspection is not straightforward, as discussed below.

Experimentally determined parameters are reported in Tables 1 and 2 for ZrO_3H_2 and ZrO_3D_2, respectively, while peak positions, widths, and assignments are listed in Tables S13 and S14. Measured PADs of peaks A, B, C, and D are shown in Fig. S10 of the SI. All PADs reported display a similar trend - features have an anisotropy parameter, β, near zero at low eKE that becomes increasingly positive as the eKE rises.

11.3.2 Calculations

The structures found in our previous work[65] on the $TiO_2^{0/-}$+H_2O reaction were used as starting points for minimum energy structure searches. Figure 11.3 shows the minimum

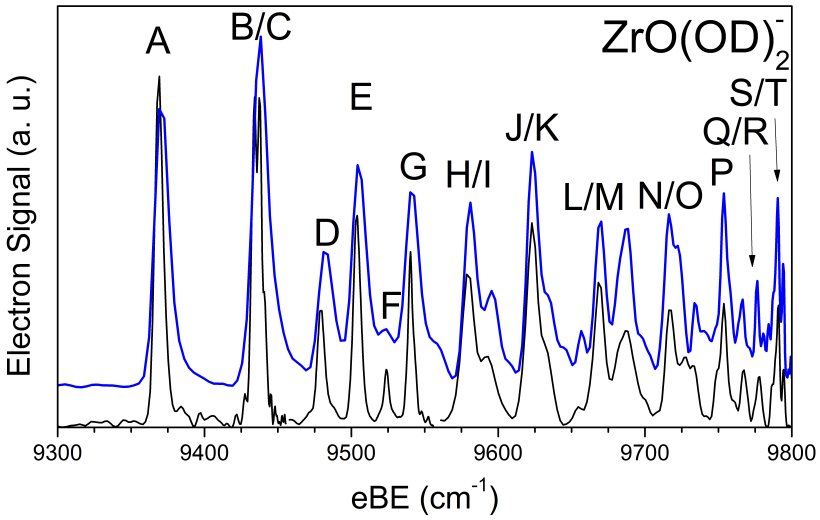

Figure 11.2: Cryo-SEVI spectra of ZrO_3D_2. The overview spectrum (blue, $h\nu$ = 9,802 cm^{-1}) is vertically offset from the high-resolution traces (black, variable photon energies).

energy structures found on the anionic and neutral ZrO_3H_2 potential energy surfaces, along with corresponding zero–point corrected energies relative to **1-1a**. Cartesian coordinates for these optimized structures are provided in the SI. In agreement with previously reported work by Dixon and co-workers[659] and similar to our previous report on $TiO(OH)_2$,[65] a dissociative adduct (**1-1a′**) with a *cis*-OH geometry was found to be the lowest energy neutral structure. Similarly, the **1-1a** geometry was found to be the lowest energy anion structure. Two other structures were identified for both neutral and anion states, labeled **1-1b** (*trans*–OH) and **1-1c** (molecularly adsorbed). Structure **1-1b** differs from **1-1a** by rotation of one hydroxide ligand and lies only 0.07 eV above the global minimum. Thus the two structures, **1-1a** and **1-1b**, are conformers related by OH bond rotation with a barrier in the anion of 0.016 eV. The neutral *trans*-hydroxide **1-1b′** lies at 0.07 eV above neutral **1-1a′**, while the lowest energy neutral molecularly adsorbed species is 3.11 eV above the anion minimum while it's anion is 2.14 eV above the minimum of the anionic *cis* structure. Interestingly, unlike $TiO_3H_2^{0/-}$, the $ZrO_3H_2^{0/-}$ dissociative adducts are found to have non-planar optimized structures.

Given its high relative energy with respect to the dissociative adducts, the molecularly adsorbed adduct **1-1c** was excluded from further consideration. The calculated adiabatic detachment energies (ADEs) for **1-1a** and **1-1b**, 1.04 eV and 1.11 eV respectively, are both in good agreement with the experimental value of 1.1636(5) eV, determined by the position of peak A. NIO analysis for both **1-1a** and **1-1b** shows the detached electron originates

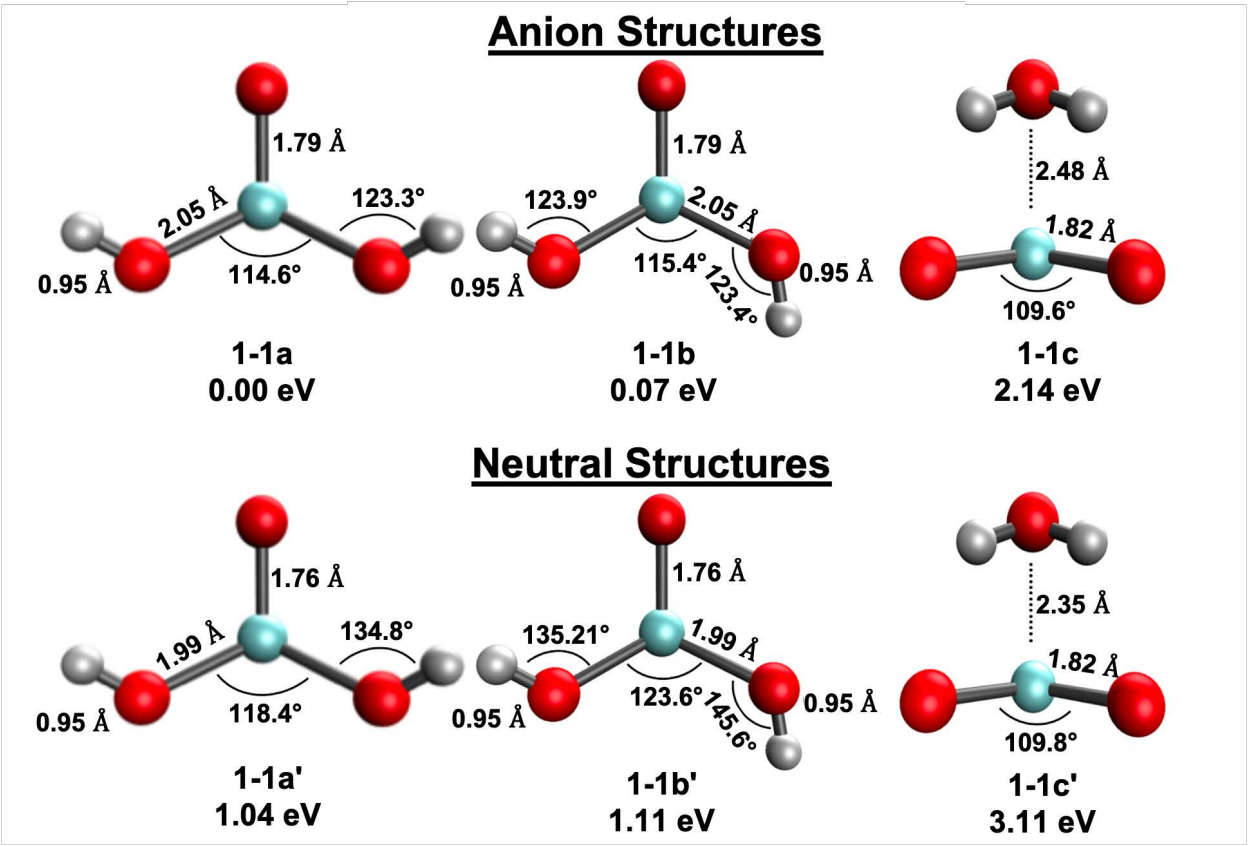

Figure 11.3: Optimized geometries of anionic and neutral ZrO_3H_2 found with ωB97XD/SC. Energies are provided relative to the **1-1a** geometry of the anion and include zero-point corrections. Geometric parameters are also provided.

in the anion HOMO, which is localized on Zr and strongly resembles a metal d_{z^2} orbital (Fig. 11.4). The similarity of the NIO results suggests that both structures should have similar photodetachment cross-sections and angular distributions.

11.4 Analysis

11.4.1 Assignment of spectra

To examine the possible contributions of the two candidate structures and whether one or both of them are responsible for the observed experimental detachment transitions, we considered FC simulations for electron detachment from both isomers, shown as red sticks for **1-1a** and blue sticks for **1-1b** in Fig. 11.5 and 11.6, using experimental frequencies when available. Simulated spectra using unscaled frequencies are shown in Figs. S2-5 in

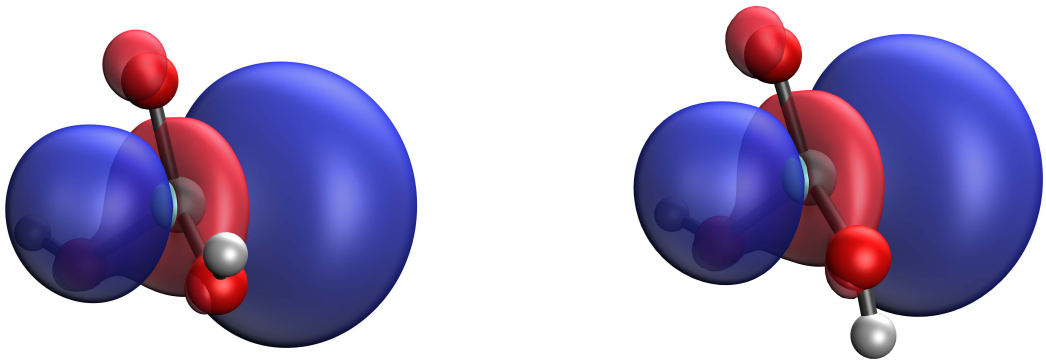

(a) (b)

Figure 11.4: NIO describing the electron detachment from the anion of **1-1a** (a) and **1-1b** (b) to corresponding ground electronic state of the neutral species.

the SI. Each isomer has distinct FC progressions; that corresponding to **1-1a** shows a short progression in the out-of-plane bending mode, ν_{12} (ω_{12a} = 73 cm^{-1}), while that of **1-1b** shows an extended progression for the same mode (ω_{12b} = 67 cm^{-1}), owing to a greater change in the dihedral angle between **1-1b** and **1-1b′** than in the **1-1a** manifold as outlined in Tables S7 and S8. Further, FC-simulations for the **1-1b** manifold show considerably more structure due to activity along the ν_{10} and ν_{11} O-H wagging modes (ω_{10b} = 167 cm^{-1}, ω_{11b} = 115 cm^{-1}) that serve as the isomerization coordinate to the **1-1a′** structure.

As shown in Fig. 11.5, simulation of detachment from **1-1a** only replicates features A, B, P, Q, and V of the cryo-SEVI spectrum of ZrO_3H_2, failing to capture the majority of the observed structure. Conversely, simulations for the **1-1b** isomer capture the majority of the spectral structure, but fail to replicate the doublets B/C and O/P observed in the high-resolution traces. A composite of both simulations replicates the observed experimental spectrum well, including the doublet structure of peaks B/C and O/P, suggesting the presence of both isomers in the experiment.

In addition to enabling identification of the anion isomers, the well-resolved vibrational structure in the spectra allows us to determine vibrational frequencies of the neutral **1-1a′** and **1-1b′** isomers of $ZrO(OH)_2$ and $ZrO(OD)_2$, as reported in Tables 1 and 2, respectively. Remarkably, we are able to distinguish features arising from transitions along the ν_{12} modes of the **1-1a′** and **1-1b′** isomers, despite their frequencies differing by only 6 cm^{-1}. One dominant pattern in the spectrum (peaks C, E, and H in both $ZrO(OH)_2$ and $ZrO(OD)_2$) corresponds to a progression of the ν_{12} out-of-plane bend of the **1-1b′** isomer with a vibrational frequency of 73(3) cm^{-1} (69(3) cm^{-1} in $ZrO(OD)_2$). Further, agreement between experimental and computational results allows for assignment of peaks D, F, and N to the vibrational fundamentals of the ν_{11}, ν_{10}, and ν_8 modes of the **1-1b′** isomer, allowing for the determination of their vibrational frequencies as 115(3), 167(2), and 358(3) cm^{-1} (110(4), 155(3), and 347(5) cm^{-1} in $ZrO(OD)_2$).

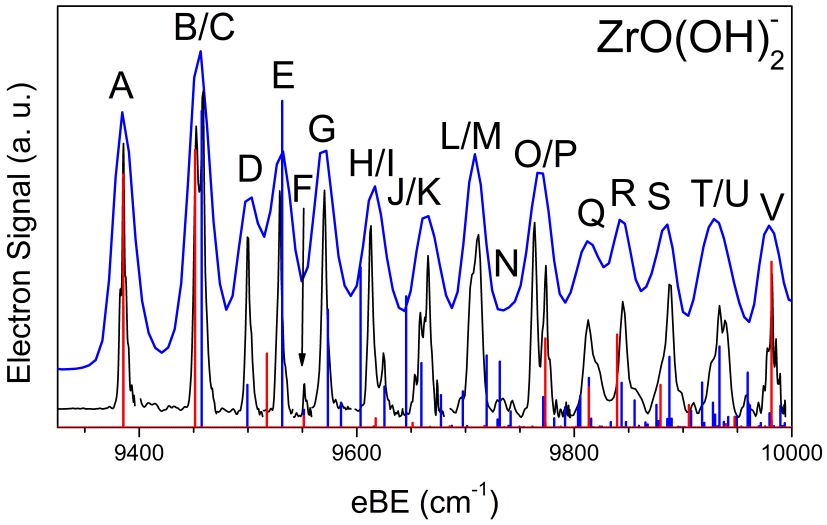

Figure 11.5: Cryo-SEVI spectra of $ZrO_3H_2^-$ overlaid with Franck-Condon stick spectra for the **1-1a** (red) and **1-1b** (blue) isomers.

A similar treatment can be applied for the detachment transition to **1-1a′**. Features B, F, P, Q, and V correspond to transitions involving one quanta along the ν_{12}, ν_{11}, ν_9, ν_6, and ν_5 normal coordinates, allowing for determination of their vibrational frequencies as 67(3), 167(2), 388(4), 429(6), and 597(2) cm^{-1} in $ZrO(OH)_2$. The same vibrational modes are observed in the deuterated spectra, with the exception of the ν_5 mode owing to the truncation of this spectra before its appearance, appearing as features B, F, P, and T with vibrational frequencies of 65(3), 155(3), 384(5), and 425(3) cm^{-1}. The remaining structure in both spectra corresponds to transitions with excitation along multiple vibrational modes; details of these assignments can be found in Tables S13 and S14 of the SI for $ZrO(OH)_2$ and $ZrO(OD)_2$, respectively.

Given that the **1-1b** simulations reproduce most of the spectral features observed, one needs to consider if it is possible to interpret the spectrum with this isomer alone. Previous cryo-SEVI studies have uncovered myriad non-Born Oppenheimer behavior in small molecules that fail to be reproduced by FC simulations, most notably vibronic coupling.[41,100,104,675] The signatures of this phenomenon in cryo-SEVI are well established, arising due to borrowed electronic character from an excited state.[14,65,100,104,478,481,676] Among these signatures are differing photoelectron angular distributions between transitions that are allowed only through vibronic coupling and those that are FC-allowed.

In the present work, doublet splittings of peaks B and P are notably absent from the **1-1b**

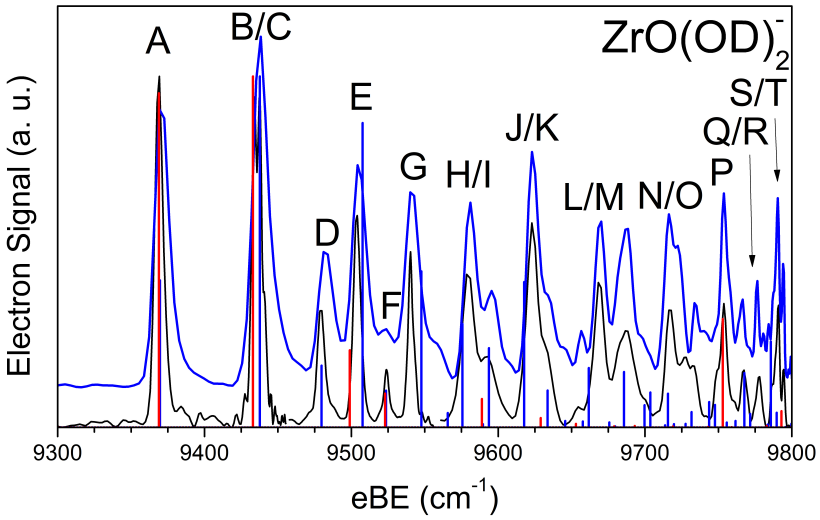

Figure 11.6: Cryo-SEVI spectra of $ZrO_3D_2^-$ overlaid with Franck-Condon stick spectra for the **1-1a** (red) and **1-1b** (blue) isomers.

simulations. For peak B to correspond to a vibronic coupling induced transition, as opposed to a Franck-Condon allowed transition within the **1-1a** band of transitions as listed in Table 1, would require a non-totally-symmetric vibrational frequency on the order of 70 cm^{-1} in the **1-1b′** isomer. No calculated frequency is within a factor of 2 of this value; indeed, the best candidate is the ν_{11} mode (ω_{11} = 141 cm^{-1}) corresponding with the transition that produces peak D. Further, the PADs of features B/C do not differ from one another, as shown in Fig. S10. The similar PADs for detachment from both isomers are in agreement with our NIO analyses that suggest the detached electron resides in a similar orbital for **1-1a** and **1-1b**, resulting in outgoing electrons with similar partial wave composition. As the measured PADs reflect the angular momentum of the detached electron, they are tied to the electronic character of each photodetachment transition and are thus expected not to differ between detachment from **1-1a** or **1-1b**.

An alternative option is that peaks B and P could report on transitions from or to excited anionic or neutral states. The calculated values of the lowest anion and neutral excited electronic states, 1.5 and 4.5 eV above their respective ground states, render them inaccessible as the cryogenic nature of the cryo-SEVI experiment produces ions with electronic temperatures on the order of 10K (0.86 meV)[41,54,239] and the photon energies employed in this experiment are < 1.35 eV.

As much of the structure in the **1-1b** FC simulation originates from the ν_{12} umbrella-

Table 11.1: Summary of electronic and vibrational energies for neutral $ZrO(OH)_2$ extracted from the cryo-SEVI experiment compared to the (unscaled) results from ωB97XD/SC calculations.

	1-1a′		**1-1b′**	
	Exp	Theor	Exp	Theor
ADE (eV)	1.1636(5)	1.04	1.1636(5)	1.04
ν_5 (cm^{-1})	597(2)	622.8		
ν_6 (cm^{-1})	429(6)	513.7		
ν_8 (cm^{-1})			358(3)	416.8
ν_9 (cm^{-1})	388(4)	428.8		
ν_{10} (cm^{-1})			167(2)	191.0
ν_{11} (cm^{-1})	167(2)	170.3	115(3)	141.0
ν_{12} (cm^{-1})	67(3)	87.6	73(3)	75.0

mode, an alternative possibility for the origin of the doublet structure of peaks B/C and O/P is inversion doubling. Such a process occurs when a vibrational mode distorts a molecule such that it breaks planar symmetry, leading to a double-well potential surface splitting the vibrational levels supported by such a surface, most famously occurring in the umbrella mode of ammonia.[109] If such a double-well surface is capable of supporting both a left and right wavefunction on the anionic potential and both sides of the well are populated, this will give rise to a doublet of transitions following photodetachment.[42,110] Our calculations indicate that the inversion barrier for the **1-1b** isomer is 1.64 eV, owing to the large dihedral angle of this structure. Considering the high barrier, we expect for contributions from tunneling splitting to be too small to observe. The structure observed in the cryo-SEVI spectra presented is thus most reasonably assigned to photodetchment from two different anion isomers, each resulting in a neutral isomer of similar molecular symmetry and overall structure.

The observation of multiple structural isomers in a cryo-SEVI experiment has been observed previously in the cryo-SEVI spectra of $Ti_2O_4^-$ and $Zr_2O_4^-$.[60] In that work, the spectra were assigned to detachment from anionic structural isomers with relative energetics (6.7 kJ/mol and 10.5 kJ/mol, respectively) that are comparable to those reported in the present study (7.5 kJ/mol).[60] The assignment to two different isomers of $Ti_2O_4^-$ and $Zr_2O_4^-$ was suggested and supported by FC progressions with dichotomous PADs and notably different onsets resulting from unique adiabatic detachment energies for each isomer. As the structures observed here are conformers related by a bond rotation, it is unsurprising that neither the PADs or ADEs differ substantially in the present work, suggesting the **1-1a** and **1-1b** isomers have ADEs lying within our experimental resolution (2 cm^{-1}). This result is con-

Table 11.2: Summary of electronic and vibrational energies for neutral $ZrO(OD)_2$ extracted from the cryo-SEVI experiment compared to the (unscaled) results from ωB97XD/SC calculations.

	1-1a′		**1-1b′**	
	Exp	Theor	Exp	Theor
ADE (eV)	1.1616(7)	1.04	1.1616(7)	1.04
ν_6 (cm^{-1})	425(3)	395.2		
ν_8 (cm^{-1})			347(5)	316.4
ν_9 (cm^{-1})	384(5)	323.8		
ν_{10} (cm^{-1})			155(3)	181.1
ν_{11} (cm^{-1})	155(3)	159.9	110(4)	117.3
ν_{12} (cm^{-1})	65(3)	82.4	69(3)	70.9

sistent with the calculated energetics that show the energy difference between the *cis* and *trans* conformers are virtually identical in the anion and neutral.

11.4.2 Comparison to $TiO(OH)_2$

The presence of two low-lying anion isomers of the ZrO_2 + H_2O dissociative adduct is in contrast with our previous findings for the Ti-containing analogue of this system, in which we observe detachment solely from the **1-1a** isomer.[65] In that work, the cryo-SEVI spectrum is relatively sparse, displaying less structure in the first 2,000 cm^{-1} than is observed in the 800 cm^{-1} of spectral structure presented here and shows no signs of contribution from the **1-1b** isomer. Given that the experimental conditions to generate both species differ only by the identity of the metal target used to generate clusters of interest, the observation of two isomers in the present study is particularly interesting.

Our calculations show that the energetics of both Ti- and Zr- containing **1-1a** and **1-1b** anions are nearly identical with the **1-1a** structure more stable than **1-1b** by 0.08 and 0.07 eV in the Ti- and Zr- systems, respectively. Further, the calculated barriers to interconversion between the *cis*-**1-1a** and *trans*-**1-1b** structures are similar for these two systems. Here, we calculate the *cis*-to-*trans* barrier for $TiO(OH)_2^-$ to be 803 cm^{-1} (0.100 eV) while the *trans*-to-*cis* barrier is 159 cm^{-1} (0.020 eV). For $ZrO(OH)_2^-$, these barriers are calculated as 737 cm^{-1} (0.091 eV) and 130 cm^{-1} (0.016 eV), respectively, suggesting one might expect similar populations of conformers in each experiment.

Given the similarity in the geometries, energetics, and barriers of these clusters, it is likely that the observation of both the **1-1a** and **1-1b** species in $ZrO(OH)_2^-$ but not $TiO(OH)_2^-$

results from disparate ion temperatures in these two systems. Such a disparity could result from the method by which these clusters are generated – laser ablation of a metal target generates a hot plasma that condenses to form the clusters of interest. It is well established that the cluster condensation process results in significant heating,[43] as the binding energy of each additional atom is deposited into the cluster. Given that such growth events can occur late in the clustering channel and the bond enthalpy of Zr-O exceeds that of Ti-O by nearly 100 kJ/mol,[677] it is likely these two systems will have differing thermal populations prior to entering the cryogenic trap, with $ZrO(OH)_2^-$ hotter than $TiO(OH)_2^-$. The increased temperature will enhance the population of higher lying isomers relative to the global minimum structure and such a distribution is likely to be mirrored in the trap, as buffer gas cooling is known to favor kinetic trapping.[47,48] Such a result would agree with previous cryo-SEVI studies of clusters, where we find trapping of ions in low-lying local minima.[60,101,103]

It should also be noted that in the case of TiO_3H_2, the appearance of the umbrella mode (ν_{12} here, ν_8 in TiO_3H_2) was ascribed to vibronic coupling,[65] while no such non-Born-Oppenheimer process is observed here, despite similar energetics for the states involved. In that work, the Ti-containing analogue was determined to be a planar C_{2v} structure in both its neutral and anionic forms, resulting in an FC-forbidden umbrella mode, as the out-of-plane motion of this vibrational mode breaks the C_{2v} symmetry of the molecule. Conversely, the Zr-containing systems presently observed are non-planar C_s structures with dihedral angles ranging from 20°-30° whose molecular symmetry is not perturbed by the umbrella mode. While this motion can only be observed through vibronic coupling in the Ti-system, such a mode is readily accessible for ZrO_3H_2 without violating the Born-Oppenheimer approximation.

11.4.3 Reactivity of MO_2 with H_2O

The cryo-SEVI spectrum of unreacted ZrO_2^- has been previously reported, giving an electron affinity of 1.6397(5) eV for the singlet ground state of ZrO_2.[59] The electron affinity of the $ZrO(OH)_2$ dissociative adducts reported here are lower by nearly 0.5 eV, suggesting the neutral $ZrO_2 + H_2O \rightarrow ZrO(OH)_2$ reaction is more exothermic than its anionic counterpart. The reaction with water to form the dissociative $ZrO(OH)_2$ adduct stabilizes neutral ZrO_2 more than it does the anion, implying that the neutral, which has a zirconium center with a +4 oxidation state, is more reactive toward water than anionic ZrO_2 where Zr has an oxidation state of +3. A similar trend in electron affinities was seen for TiO_2 and $TiO(OH)_2$. Taken together, these results suggest that this charge effect likely derives from donation of electron density from the incoming water molecule to the metal center, favoring a higher oxidation state.[65]

Notably, the measured difference in EA for the Ti–containing system was roughly 0.3 eV, suggesting that the addition of water to the Zr-based system stabilizes ZrO_2 relative to its anion a full 0.2 eV (19.2 kJ/mol) more than the Ti–based system. In turn, this implies an increased reactivity of the ZrO_2 moiety compared to TiO_2. As single site catalyst studies have found high photocatalytic activity attributed to the increased reactivity of single TiO_2

structures anchored onto porous surfaces,[678,679] the results presented here show promise for the development of Zr-based analogues with increased efficiency. While it is difficult to make a direct comparison between the chemistry occurring at the bulk surface and the gas-phase $ZrO_2^{0/-}$ reaction, the trends reported here do reflect the electrochemical behavior of the bulk,[679] especially with respect to a higher oxidation state resulting in a more energetically favorable interaction with water.

11.5 Conclusion

A joint DFT and high–resolution photoelectron study has been used to investigate the hydrolysis of $ZrO_2^{0/-}$. Experimental spectra of $ZrO_3H_2^-$ are reported using slow electron velocity map imaging of cryogenically cooled anions, revealing the presence of two dissociative adduct conformers and yielding insights into the vibronic structure and energetics of the corresponding neutral species. The high resolution afforded by this technique reveals a dense vibrational manifold dissimilar to the well–separated peaks obtained in the cryo-SEVI study of the titanium analogue.[65] Franck-Condon simulations for both the cis– (**1-1a**) and *trans*–dihydroxide (**1-1b**) structures are required to fully reproduce the complicated cryo-SEVI spectra, representing the first report of the *trans*–hydroxide (**1-1b**) structure of the ZrO_3H_2 system. The appearance of these two isomers is attributed to differing cluster temperatures prior to reaction with H_2O or D_2O, resulting in an enhancement of the population of structure **1-1b** in $ZrO_3H_2^-$. Further, the greater stabilization of water-splitting by ZrO_2 than TiO_2 suggests higher reactivity for Zr-based catalysts, offering new insights into the development of single-site catalysts for H_2 production.

11.6 Supplemental Materials

11.6.1 Geometries

11.6.1.1 Optimized Anion Geometries

The Cartesian coordinates for the optimized geometries of the doublet anion $ZrO_3H_2^-$ species identified by ωB97XD/SC are provided below. The total converged SCF energy is also given for each structure.

Zr	-0.17653491	0.14741320	0.00000000
O	-0.17653491	-0.96122535	1.72894132
O	-0.17653491	-0.96122535	-1.72894132
O	1.13307209	1.38221915	0.00000000
H	0.41068900	-0.78733776	-2.46539459
H	0.41068900	-0.78733776	2.46539459

Table 11.3: **1-1a**, SCF= -273.680703012 E_h

Zr	0.00224031	0.07100173	-0.21275434
O	-1.60014474	-1.12838066	0.23540247
O	1.84515558	-0.67677432	0.33093769
O	-0.21961565	1.75174680	0.38631180
H	2.09942250	-1.59299417	0.21211062
H	-2.39219647	-0.381980958	0.67684718

Table 11.4: **1-1b**, SCF= -273.677687402 E_h

Zr	-0.45547340	-0.00001041	0.25604928
O	-0.10951737	1.49537562	-0.74043818
O	-0.10943080	-1.49537720	-0.74044033
O	2.03218352	0.00004343	0.27622859
H	1.85653478	-0.76618443	-0.30238602
H	1.85651829	0.76626591	-0.30238572

Table 11.5: **1-1c**, SCF= -273.604888118 E_h

11.6.1.2 Optimized Neutral Geometries

The Cartesian coordinates for the optimized geometries of the singlet neutral ZrO_3H_2 species identified by ωB97XD/SC are provided below. The total converged SCF energy is also given for each structure.

Zr	-0.139370	0.102224	0.000000
O	-0.139370	-0.916493	1.716582
O	-0.139370	-0.916493	-1.716582
O	0.899747	1.526420	0.000000
H	0.303360	-0.818216	-2.560212
H	0.303360	-0.818216	2.560212

Table 11.6: **1-1a**, SCF= -273.643424650 E_h

Zr	-0.000033	0.042830	-0.138065
O	-1.677871	-0.994163	0.157195
O	1.827503	-0.697161	0.180508
O	-0.121664	1.760309	0.244604
H	2.336248	-1.477916	0.392220

Table 11.7: **1-1b**, SCF= -273.638688778 E_h

Zr	-0.363473	0.200499	0.000000
O	0.514401	0.741324	1.467455
O	0.514401	0.741324	-1.467455
O	0.514401	-1.980668	0.000000
H	1.096654	-2.017909	-0.770067
H	1.096654	-2.017909	0.770067

Table 11.8: **1-1c**, SCF= -273.568886517 E_h

11.6.2 Tables

Table 11.9: Absolute energies without including ZPE for optimized **1-1a** anion and **1-1a'** neutral geometries and the calculated ADEs using initial candidate model chemistries. Energies are presented in Hartree unless otherwise noted.

Model Chemistry	**Anion**	**Neutral**	**ADE(eV)**
B3LYP/Def2TZVP	274.2558806	274.2143184	1.13
B3LYP/SC	273.7720854	273.7262703	1.25
ωB97XD/Def2TZVP	274.1629665	274.1299711	0.90
ωB97XD/SC	273.68070	273.6434247	1.01
B3PW91/Def2TZVP	274.1829258	274.1435448	1.07
B3PW91/SC	273.7006408	273.6580344	1.16
M06L/Def2TZVP	274.1939821	274.1669927.	0.73
M06L/SC	273.7239104	273.6964000	0.75
DSDPBEP86/Def2TZVP	273.2305063	273.1963100	0.93
DSDPBEP86/SC	272.7459145	272.7065000	1.07
PBE1PBE/Def2TZVP	273.9775000	273.9394262	1.04
PBE1PBE/SC	273.4962528	273.4544886	1.14

Table 11.10: Absolute energies including ZPE for optimized **1-1a** anion and **1-1a'** neutral geometries and the calculated ADEs using initial candidate model chemistries. Energies are presented in Hartree unless otherwise noted.

Model Chemistry	**Anion**	**Neu**	**ADE(eV)**
B3LYP/Def2TZVP	-274.228913	-274.186326	1.16
B3LYP/SC	-273.745086	-273.698169	1.28
ωB97XD/Def2TZVP	-274.135416	-274.101485	0.92
ωB97XD/SC	-273.653117	-273.614931	1.04
B3PW91/Def2TZVP	-274.155631	-274.115309	1.10
B3PW91/SC	-273.673349	-273.62971	1.19
M06L/Def2TZVP	-274.167045	-274.138852	0.77
M06L/SC	-273.696712	-273.668007	0.78
DSDPBEP86/Def2TZVP	-273.631667	-273.596151	0.97
DSDPBEP86/SC	-273.096346	-273.056491	1.08
PBE1PBE/Def2TZVP	-273.95000	-273.911023	1.06
PBE1PBE/SC	-273.468754	-273.425994	1.16

Table 11.11: Absolute energies without including ZPE for optimized **1-1b** anion and **1-1b'** neutral geometries and the calculated ADEs using initial candidate model chemistries. Energies are presented in Hartree unless otherwise noted.

Model Chemistry	**Anion**	**Neutral**	**ADE(Ev)**
B3LYP/Def2TZVP	-274.2526755	-	-
B3LYP/SC	-273.7692272	-273.722743	1.26
ωB97XD/Def2TZVP	-274.159672	-	-
ωB97XD/SC	-273.6776874	-273.6386888	1.03
B3PW91/Def2TZVP	-274.1796354	-	-
B3PW91/SC	-273.69770	-273.6543431	1.18
M06L/Def2TZVP	-274.1916209	-	-
M06L/SC	-273.7209521	-273.6926436	0.77
DSDPBEP86/Def2TZVP	-273.2272116	-	-
DSDPBEP86/SC	-272.7427958	-272.7036951	1.06
PBE1PBE/Def2TZVP	-273.9742372	-	-
PBE1PBE/SC	-273.4933016	-273.450847	1.16

Table 11.12: Absolute energies including ZPE for optimized **1-1b** anion and **1-1b'** neutral geometries and the calculated ADEs using initial candidate model chemistries. Energies are presented in Hartree unless otherwise noted.

Model Chemistry	**Anion**	**Neu**	**ADE(Ev)**
B3LYP/Def2TZVP	-274.22599	-	-
B3LYP/SC	-273.742466	-273.695245	1.28
ωB97XD/Def2TZVP	-274.135416	-	-
ωB97XD/SC	-273.6503	-273.610722	1.04
B3PW91/Def2TZVP	-274.15262	-	-
B3PW91/SC	-273.670616	-273.626476	1.20
M06L/Def2TZVP	-274.164979	-	-
M06L/SC	-273.693786	-273.664728	0.79
DSDPBEP86/Def2TZVP	-273.628824	-	-
DSDPBEP86/SC	-273.093789	-273.05401	1.08
PBE1PBE/Def2TZVP	-273.947001	-	-
PBE1PBE/SC	-273.466038	-273.422846	1.18

Table 11.13: Absolute energies without including ZPE for optimized **1-1c** anion and **1-1c'** neutral geometries and the calculated ADEs using initial candidate model chemistries. Energies are presented in Hartree unless otherwise noted.

Model Chemistry	**Anion**	**Neutral**	**ADE(eV)**
B3LYP/Def2TZVP	-274.18030207	-274.13788055	1.15
B3LYP/SC	-273.69705894	-273.65431302	1.16
ωB97XD/Def2TZVP	-274.08812593	-274.05096200	1.01
ωB97XD/SC	-273.60488812	-273.56888652	0.98
B3PW91/Def2TZVP	-274.10959592	-274.06841387	1.12
B3PW91/SC	-273.62851630	-273.58746213	1.12
M06L/Def2TZVP	-274.1238743	-274.09444318	0.80
M06L/SC	-273.65201195	-273.62745912	0.67
DSDPBEP86/Def2TZVP	-273.14408280	-273.10332587	1.11
DSDPBEP86/SC	-272.65968617	-272.61817811	1.13
PBE1PBE/Def2TZVP	-273.90436899	-273.86364332	1.11
PBE1PBE/SC	-273.42415240	-273.38340727	1.11

Table 11.14: Absolute energies including ZPE for optimized **1-1c** anion and **1-1c'** neutral geometries and the calculated ADEs using initial candidate model chemistries. Energies are presented in Hartree unless otherwise noted.

Model Chemistry	**Anion**	**Neu**	**ADE(Ev)**
B3LYP/Def2TZVP	-274.150733	-274.108175	1.16
B3LYP/SC	-273.668736	-273.624781	1.20
ωB97XD/Def2TZVP	-274.057899	-274.020648	1.01
ωB97XD/SC	-273.57454	-273.538753	0.97
B3PW91/Def2TZVP	-274.079871	-274.038453	1.13
B3PW91/SC	-273.600535	-273.557588	1.17
M06L/Def2TZVP	-274.094029	-274.064567	0.80
M06L/SC	-273.622262	-273.59754	0.67
DSDPBEP86/Def2TZVP	-273.5593	-273.521209	1.04
DSDPBEP86/SC	-273.025923	-272.98685	1.06
PBE1PBE/Def2TZVP	-273.874383	-273.833515	1.11
PBE1PBE/SC	-273.395825	-273.353275	1.16

Table 11.15: Structural parameters for the **1-1a** anion and **1-1a'** neutral geometries obtained at the ωB97XD/SC level, as well as the percent changes in these parameters that occur upon detachment.

Vibrational Modes	**Anion**	**Neutral**	**change**	**%**
ν_{12} dihedral angle	29.2°	23.00°	6.2°	21%
ν_{11} OZrOH angle	118.6°	114.7°	3.9°	3 %
ν_{10} ZrOH in-plane	123.3°	134.8°	11.5°	9%
ν_9 ZrOH out-of-plane	123.3°	134.8°	11.5°	9%
ν_8 sym. ZrO(H) str.	2.05Å	1.99Å	0.06Å	3

Table 11.16: Structural parameters for the **1-1b** anion and **1-1b'** neutral geometries obtained at the ωB97XD/SC level, as well as the percent changes in these parameters that occur upon detachment.

Vibrational Modes	**Anion**	**Neutral**	**Change**	**%**
ν_{12} dihedral	29.5°	18.8°	10.7°	36%
ν_{11} OZrOH angle (trans)	123.4°	145.6°	22.2°	18%
ν_{10} (H)OMO(H)	115.4°	123.6°	8.2°	7%
ν_9 Trans OMOH	112.2°	114.6°	2.4°	2%
ν_8 OZrOH angle (trans)	123.4°	145.6°	22.2°	18%
ν_7 OZrOH angle (cis)	123.9°	135.2°	11.3°	9%
ν_5 sym. ZrO(H) str.	2.05Å	1.99Å	0.06Å	3

Table 11.17: Vibrational frequencies in cm^{-1} for the lowest energy neutral state of **1-1a** ZrO_3H_2 obtained at the ωB97XD/SC level. The scaling factors used to adjust neutral **1-1a'** frequencies are also provided.

Vibrational Modes	**Computed Frequency**	**Scaled frequency**	**Scaling factor**
ν_{12}	87.6	66.9	0.76
ν_{11}	170.2	166.0	0.97
ν_{10}	213.1	175.0	0.82
ν_9	428.7	380.3	0.89
ν_8	439.5	393.9	0.90
ν_7	492.7	419.3	0.85
ν_6	513.7	428.3	0.83
ν_5	622.8	597.0	0.96

Table 11.18: Vibrational frequencies in cm^{-1} for the lowest energy neutral state of **1-1a** ZrO_3D_2 obtained at the ωB97XD/SC level. The scaling factors used to adjust neutral **1-1a'** frequencies are also provided.

Vibrational Modes	**Computed Frequency**	**Scaled frequency**	**Scaling factor**
ν_{12}	82.4	65.0	0.79
ν_{11}	159.9	155.0	0.97
ν_{10}	196.9	175.0	0.89
ν_9	323.8	384.0	1.18
ν_8	339.5	393.0	1.16
ν_7	385.7	419.0	1.08
ν_6	395.2	425.0	1.07
ν_5	606.9	597.0	0.98

Table 11.19: Vibrational frequencies in cm^{-1} for the lowest energy neutral state of **1-1b** ZrO_3H_2 obtained at the ωB97XD/SC level. The scaling factors used to adjust neutral **1-1b'** frequencies are also provided.

Vibrational Modes	**Computed Frequency**	**Scaled frequency**	**Scaling factor**
ν_{12}	75.0	72.4	0.96
ν_{11}	141.0	113.9	0.81
ν_{10}	191.0	169.0	0.88
ν_9	234.6	204.0	0.87
ν_8	416.8	350.0	0.84
ν_7	468.5	405.0	0.86
ν_6	506.2	430.3	0.85
ν_5	643.6	547.1	0.85

Table 11.20: Vibrational frequencies in cm^{-1} for the lowestenergy neutral state of **1-1b** ZrO_3D_2 obtained at the ωB97XD/SC level. The scaling factors used to adjust neutral **1-1b'** frequencies are also provided.

Vibrational Modes	**Computed Frequency**	**Scaled frequency**	**Scaling factor**
ν_{12}	70.9	69.0	0.97
ν_{11}	117.3	110.0	0.94
ν_{10}	181.1	155.0	0.86
ν_9	218.6	196.0	0.90
ν_8	316.4	347.0	1.10
ν_7	361.1	379.0	1.05
ν_6	390.0	430.3	1.10
ν_5	626.7	548.0	0.88

Table 11.21: Electronic and vibrational energies for neutral **1-1a'** extracted from the $ZrO(OH)_2^-$ cryo-SEVI spectrum, and compared to the (unscaled) results obtained from ωB97XD/SC calculations.

1-1a	**CryoSEVI**	**ωB97XD/SC**
EA (eV)	1.1636(5)	1.04
ν_{12} (cm^{-1})	67(3)	87.6
ν_{11} (cm^{-1})	167(2)	170.3
ν_9 (cm^{-1})	388(4)	428.8
ν_6 (cm^{-1})	429(6)	513.7
ν_5 (cm^{-1})	597(2)	622.8

Table 11.22: Electronic and vibrational energies for neutral **1-1b'** extracted from the $ZrO(OH)_2^-$ cryo-SEVI spectrum, and compared to the (unscaled) results obtained from ωB97XD/SC calculations.

1-1b	**CryoSEVI**	**ωB97XD/SC**
EA (eV)	1.1636(5)	1.04
ν_{12} (cm^{-1})	73(3)	75.0
ν_{11} (cm^{-1})	115(3)	141.0
ν_{10} (cm^{-1})	167(2)	191.0
ν_9 (cm^{-1})	201(4)	234.6
ν_8 (cm^{-1})	356(6)	416.9

Table 11.23: Peak positions, shifts from peak A, and assignments for the detachment transitions in the cryo-SEVI spectrum of $ZrO(OH)_2^-$. Uncertainties in peak positions correspond to one standard deviation obtained from a Gaussian fit to the corresponding feature in the high-resolution scan.

Peak	**eBE**	**Shift**	**Assignment**	
			1-1a'	**1-1b'**
A	9385(4)	0	0_0^0	0_0^0
B	9452(4)	67	12_0^1	
C	9458(4)	73		12_0^1
D	9500(4)	115		11_0^1
E	9529(4)	144		12_0^2
F	9552(2)	167	11_0^1	10_0^1
G	9570(4)	185		$11_0^1 12_0^1$
H	9613(4)	228		12_0^3
I	9624(2)	239		$10_0^1 12_0^1$
J	9659(6)	274		$9_0^1 12_0^1$
K	9666(4)	281		12_0^4
L	9705(6)	320		$10_0^1 12_0^2$
M	9712(6)	327		$11_0^1 12_0^3$
N	9743(4)	358		8_0^1
O	9763(4)	378		
P	9773(4)	388	9_0^1	$10_0^1 12_0^3$
Q	9814(12)	429	6_0^1	$8_0^1 12_0^1$
R	9844(6)	459	$9_0^1 12_0^1$	$10_0^1 11_0^1 12_0^1$
S	9887(8)	502	$6_0^1 12_0^1$	$11_0^3 12_0^2$
T	9933(3)	548		$10_0^1 11_0^2 12_0^2$
U	9939(4)	554		
V	9982(1)	597	5_0^1	$7_0^1 11_0^1 12_0^1$

Table 11.24: Peak positions, shifts from peak A, and assignments for the detachment transitions in the cryo-SEVI spectrum of $ZrO(OD)_2^-$. Uncertainties in peak positions correspond to one standard deviation obtained from a Gaussian fit to the corresponding feature in the high-resolution scan.

Peak	**eBE**	**Shift**	**Assignment**	
			1-1a'	**1-1b'**
A	9369(6)	0	0_0^0	0_0^0
B	9434(3)	65	12_1^0	
C	9438(3)	69		12_1^0
D	9479(5)	110		11_1^0
E	9504(5)	135		12_2^0
F	9524(3)	155	11_1^0	10_1^0
G	9540(4)	171		$11_0^1 12_0^1$
H	9579(8)	210		12_3^0
I	9593(11)	224	$11_0^1 12_0^1$	$10_0^1 12_0^1$
J	9623(8)	254		$11_0^1 12_0^2$
K	9634(7)	265		$9_0^1 12_0^1$
L	9669(7)	300		$10_0^1 12_0^2$
M	9686(12)	317		$11_0^1 12_0^3$
N	9716(7)	347		8_1^0
O	9729(16)	360		$10_0^1 12_0^3$
P	9753(7)	384	9_1^0	
Q	9767(4)	398		$11_0^3 12_1^0$
R	9778(3)	409		
S	9790(3)	421		$8_0^1 12_1^0$
T	9794(1)	425	6_1^0	

11.7 Figures

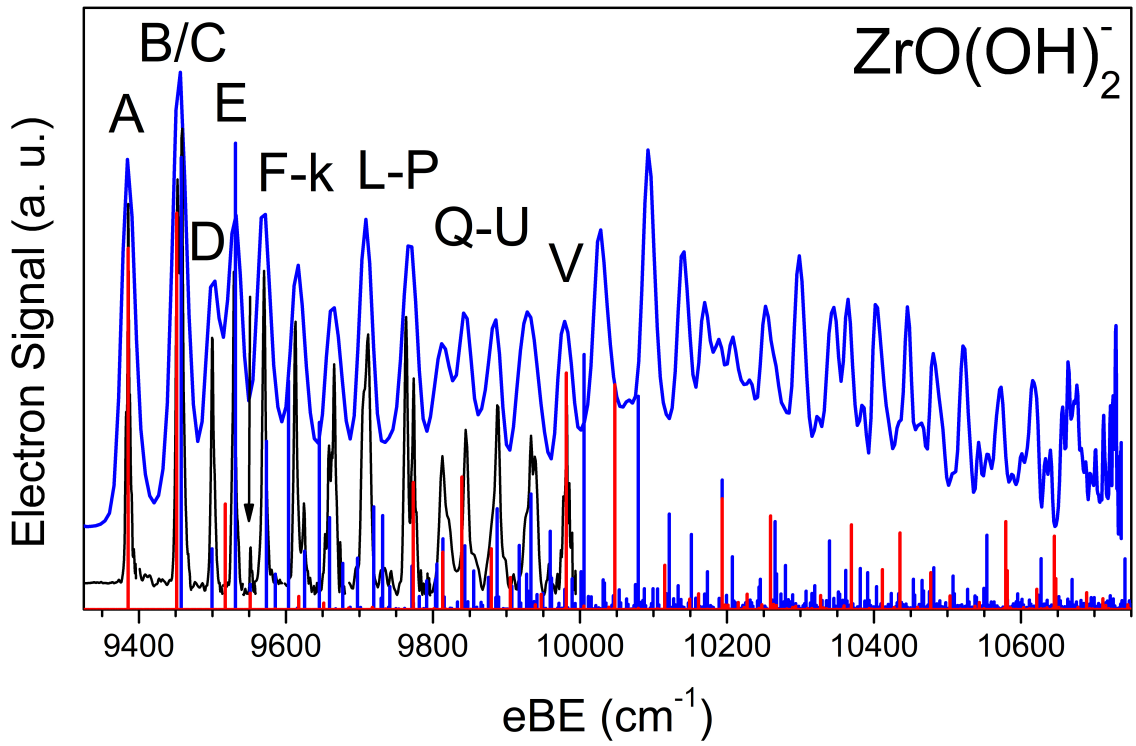

Figure 11.7: Cryo-SEVI spectrum of ZrO_3H_2 displaying the full range of the overview spectrum ($h\nu$ = 10,747 cm^{-1}). High resolution spectra were collected only up to ~10,000 cm^{-1}. Red and blue sticks correspond to FC-simulations for detachment from the **1-1a** and **1-1b** isomers of ZrO_3H_2, respectively.

11.7.1 Spectra with FC-simulations (theor. values)

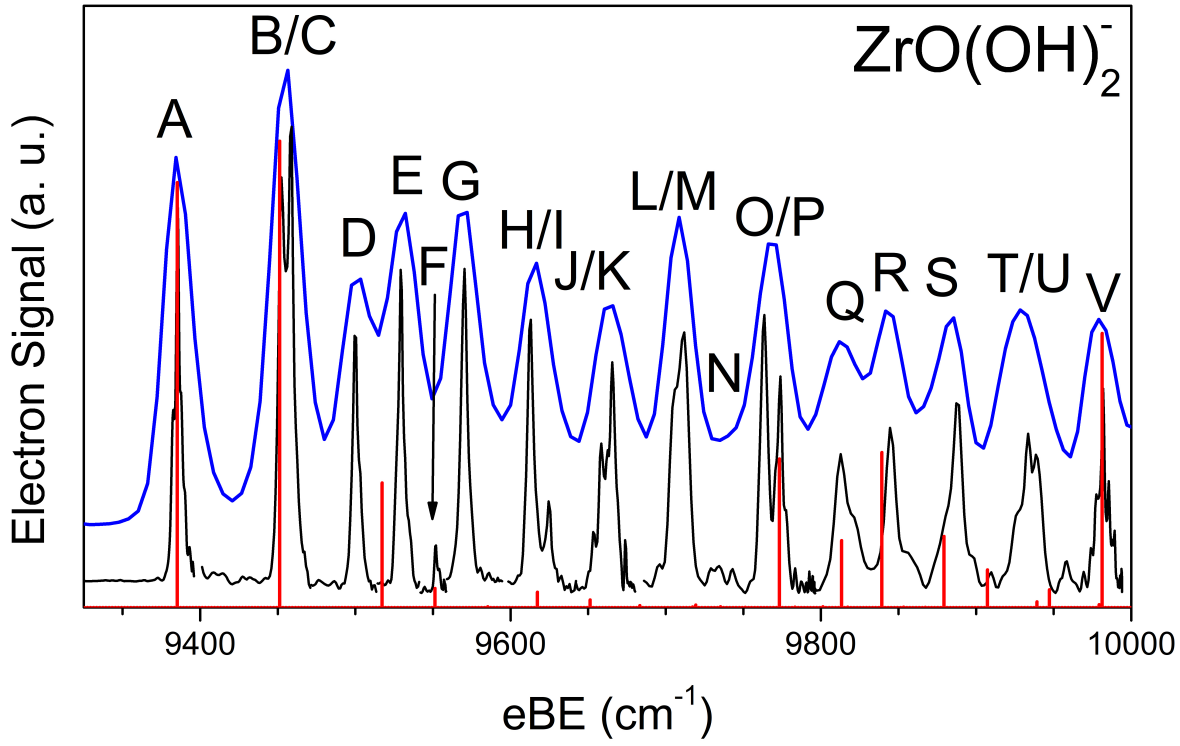

Figure 11.8: Cryo-SEVI spectrum of ZrO_3H_2 with Franck-Condon simulations for detachment from the **1-1a** structure of $ZrO(OH)_2^-$ using neutral frequencies that have not been scaled.

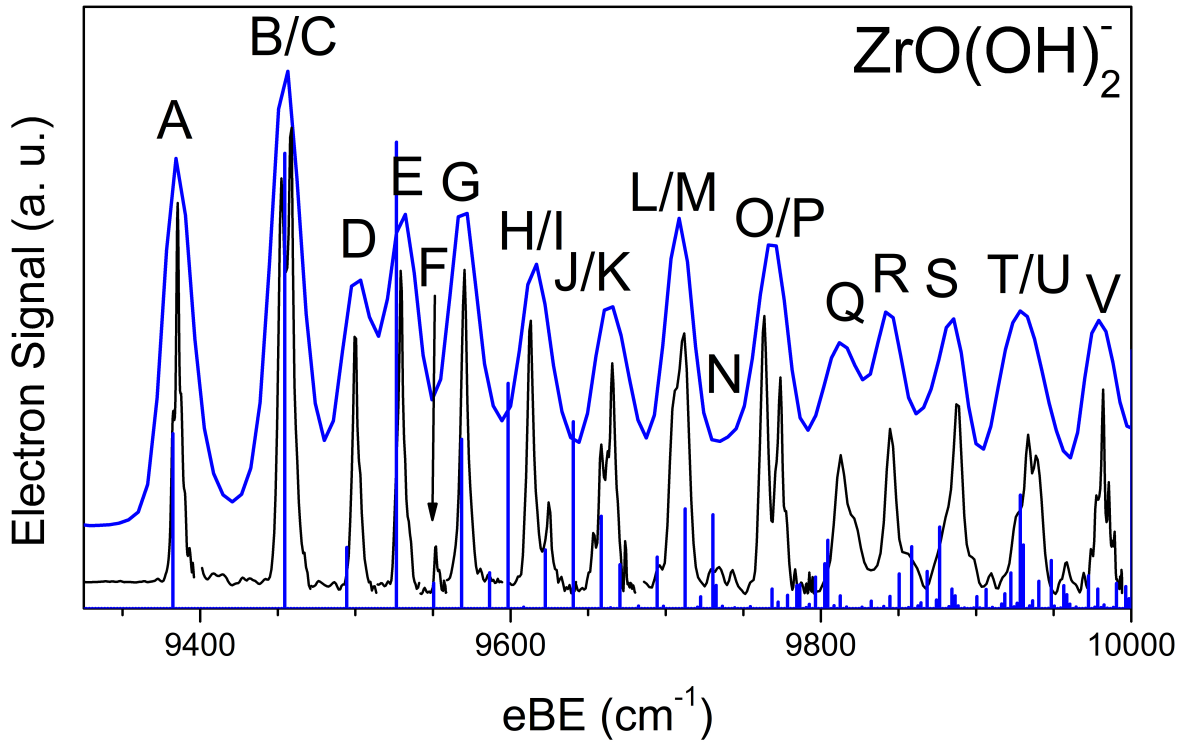

Figure 11.9: Cryo-SEVI spectrum of ZrO_3H_2 with Franck-Condon simulations for detachment from the **1-1b** structure of $ZrO(OH)_2^-$ using neutral frequencies that have not been scaled.

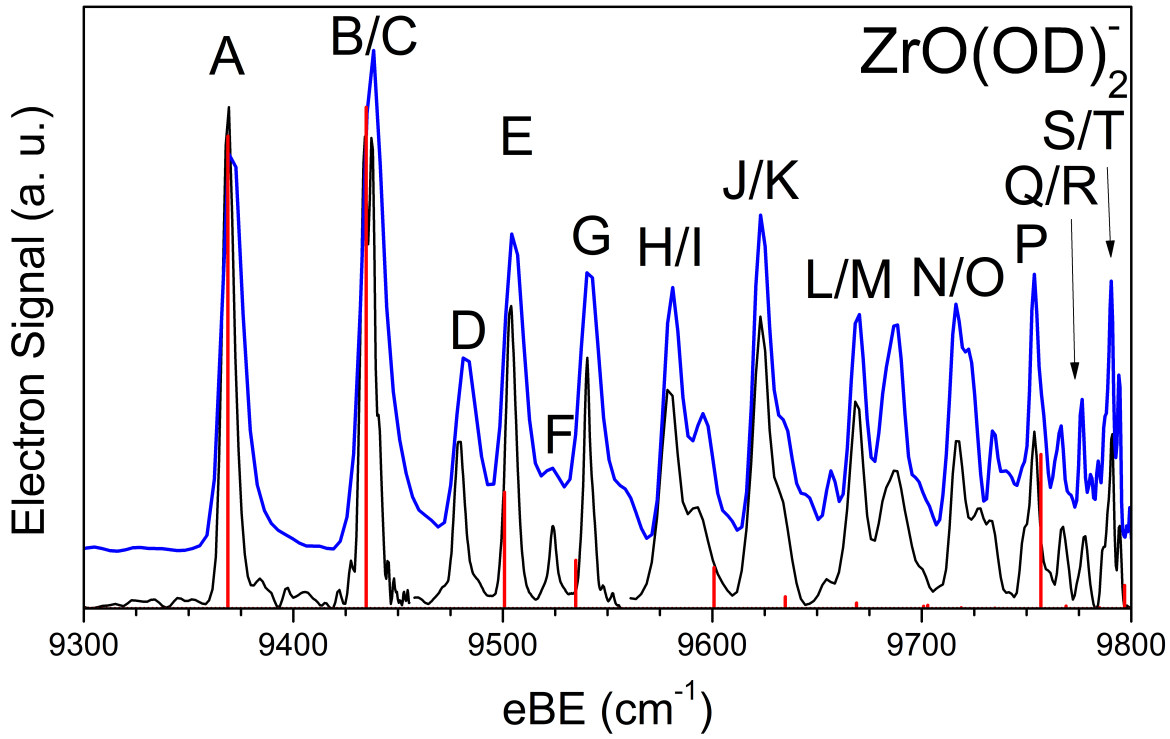

Figure 11.10: Cryo-SEVI spectrum of ZrO_3D_2 with Franck-Condon simulations for detachment from the **1-1a** structure of $ZrO(OD)_2^-$ using neutral frequencies that have not been scaled.

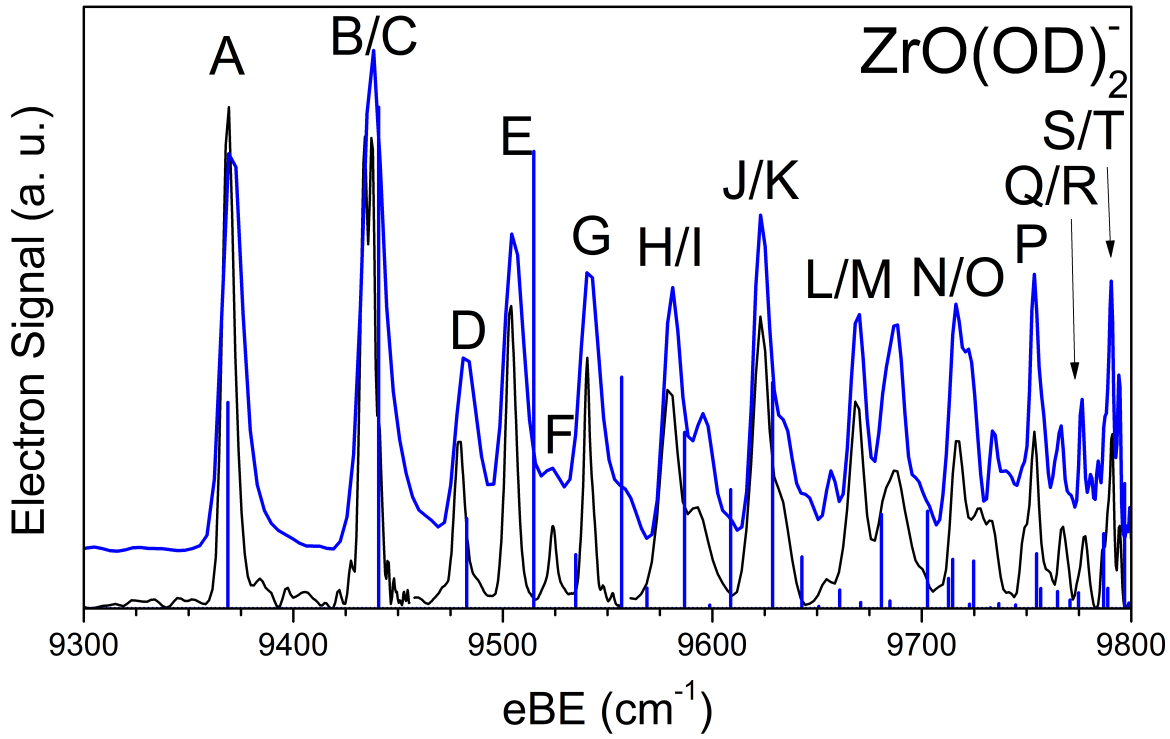

Figure 11.11: Cryo-SEVI spectrum of ZrO_2D_2 with Franck-Condon simulations for detachment from the **1-1b** structure of $ZrO(OD)_2^-$ using neutral frequencies that have not been scaled.

11.7.2 Spectra with FC-simulations (scaled values)

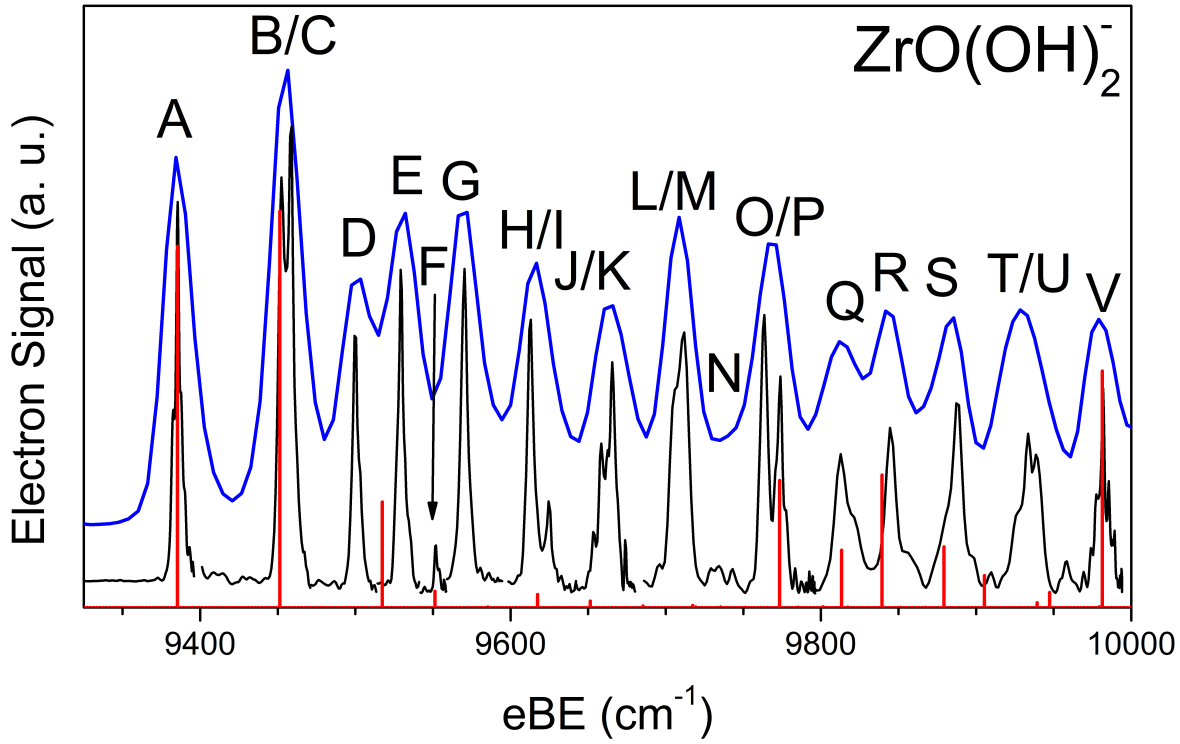

Figure 11.12: Cryo-SEVI spectrum of ZrO_3H_2 with Franck-Condon simulations for detachment from the **1-1a** structure of $ZrO(OH)_2^-$ using experimental values where possible.

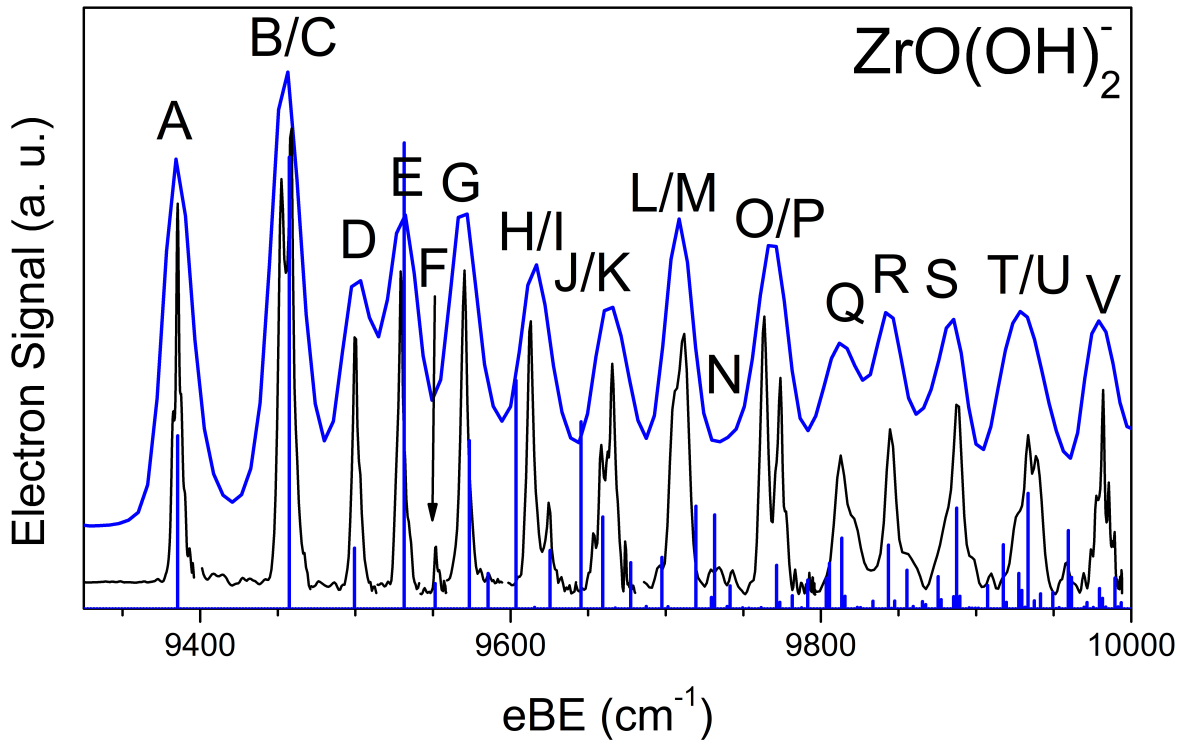

Figure 11.13: Cryo-SEVI spectrum of ZrO_3H_2 with Franck-Condon simulations for detachment from the **1-1b** structure of $ZrO(OH)_2^-$ using experimental values where possible.

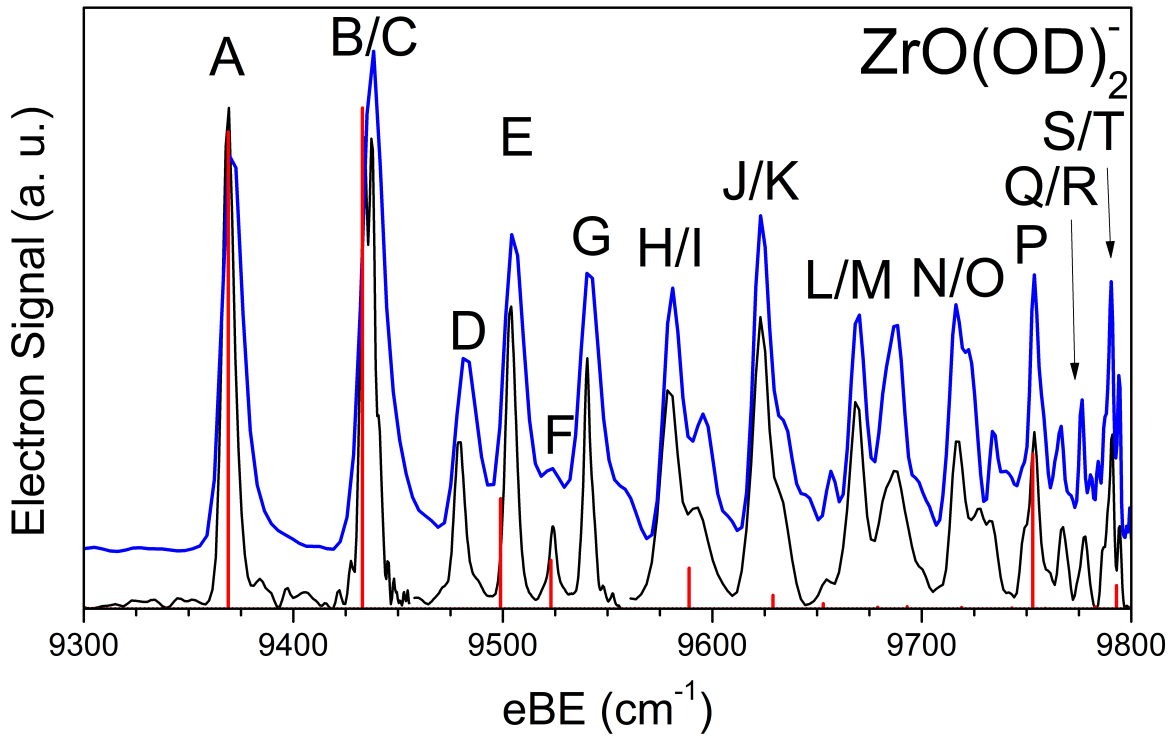

Figure 11.14: Cryo-SEVI spectrum of ZrO_3D_2 with Franck-Condon simulations for detachment from the **1-1a** structure of $ZrO(OD)_2^-$ using experimental values where possible.

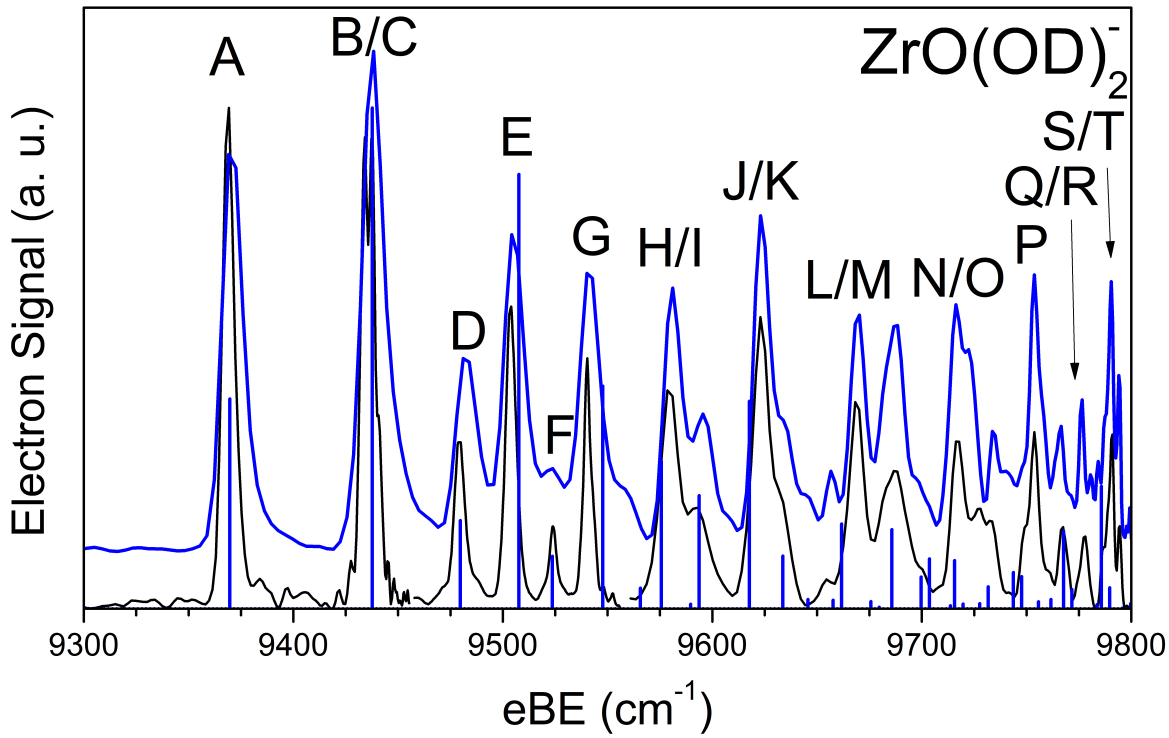

Figure 11.15: Cryo-SEVI spectrum of ZrO_3D_2 with Franck-Condon simulations for detachment from the **1-1b** structure of $ZrO(OD)_2^-$ using experimental values where possible.

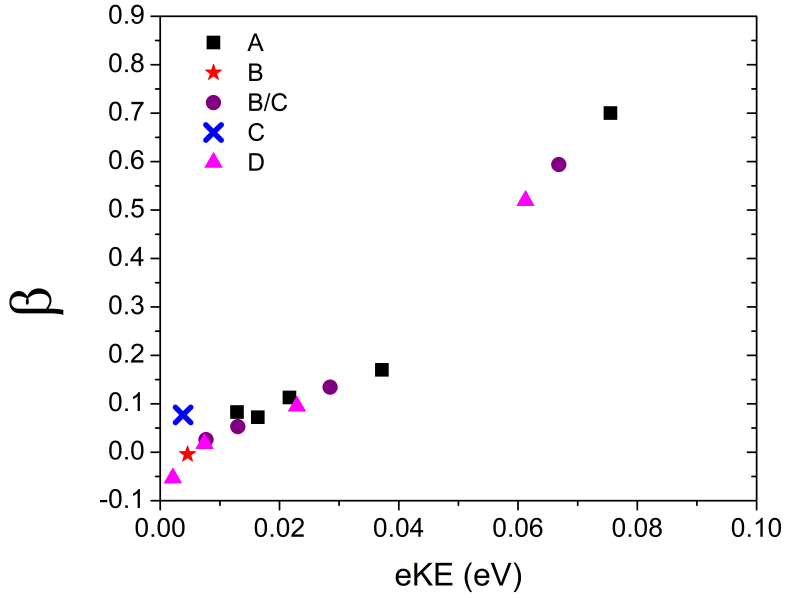

Figure 11.16: Photoelectron angular distributions for peaks A, B, C, and D of ZrO_3H_2

Part IV

Appendix

Bibliography

(1) Turner, D. W. Molecular photoelectron spectroscopy. *Phil. Trans. Roy. Soc. Long. A* **1970**, 7–31.

(2) Pertot, Y.; Schmidt, C.; Matthews, M.; Chauvet, A.; Huppert, M.; Svoboda, V.; von Conta, A.; Tehlar, A.; Baykusheva, D.; Wolf, J.-P.; Wörner, H. J. Time-resolved x-ray absorption spectroscopy with a water window high-harmonic source. *Science* **2017**, *355*, 264–267.

(3) Kraus, P. M.; Zürch, M.; Cushing, S. K.; Neumark, D. M.; Leone, S. R. The ultrafast X-ray spectroscopic revolution in chemical dynamics. *Nature Reviews Chemistry* **2018**, *2*, 82–94.

(4) Brehm, B.; Gusinow, M. A.; Hall, J. L. Electron Affinity of Helium Via Laser Photodetachment of its Negative Ion. *Phys. Rev. Lett.* **1967**, *19*, 737–741.

(5) Weichman, M. L.; Neumark, D. M. Slow Photoelectron Velocity-Map Imaging of Cryogenically Cooled Anions. *Annual Review of Physical Chemistry* **2018**, *69*, PMID: 29401036, 101–124.

(6) Posey, L. A.; Deluca, M. J.; Johnson, M. A. Demonstration of a pulsed photoelectron spectrometer on mass-selected negative ions: O^-, O_2^-, and O_4^-. *Chemical Physics Letters* **1986**, *131*, 170–174.

(7) Cheshnovsky, O.; Yang, S.; Pettiette, C.; Craycraft, M.; Liu, Y.; Smalley, R. Ultraviolet photoelectron spectroscopy of semiconductor clusters: Silicon and germanium. *Chemical Physics Letters* **1987**, *138*, 119–124.

(8) Weaver, A.; Metz, R.; Bradforth, S.; Neumark, D. Observation of the $\tilde{A}(^2B_2)$ and $\tilde{C}(^2A_2)$ states of NO_2 by negative ion photoelectron spectroscopy of NO_2^-. *The Journal of chemical physics* **1989**, *90*, 2070–2071.

(9) Kitsopoulos, T.; Metz, R.; Weaver, A.; Neumark, D. In *AIP Conference Proceedings*, 1988; Vol. 172, pp 573–576.

(10) Weaver, A.; Metz, R.; Bradforth, S. E.; Neumark, D. Spectroscopy of the I+ HI transition-state region by photodetachment of IHI^-. *The Journal of Physical Chemistry* **1988**, *92*, 5558–5560.

(11) Metz, R.; Kitsopoulos, T.; Weaver, A.; Neumark, D. Study of the transition state region in the Cl + HCl reaction by photoelectron spectroscopy of $ClHCl^-$. *The Journal of chemical physics* **1988**, *88*, 1463–1465.

(12) Kruit, P.; Read, F. H. Magnetic field paralleliser for 2π electron-spectrometer and electron-image magnifier. *Journal of Physics E: Scientific Instruments* **1983**, *16*, 313–324.

(13) Rienstra-Kiracofe, J. C.; Tschumper, G. S.; Schaefer, H. F.; Nandi, S.; Ellison, G. B. Atomic and Molecular Electron Affinities: Photoelectron Experiments and Theoretical Computations. *Chemical Reviews* **2002**, *102*, PMID: 11782134, 231–282.

(14) Ervin, K. M.; Lineberger, W. C. Photoelectron spectra of C_2^- and C_2H^-. *The Journal of Physical Chemistry* **1991**, *95*, 1167–1177.

(15) Metz, R. B.; Weaver, A.; Bradforth, S. E.; Kitsopoulos, T. N.; Neumark, D. M. Probing the transition state with negative ion photodetachment: the chlorine atom + hydrogen chloride and bromine atom + hydrogen bromide reactions. *The Journal of Physical Chemistry* **1990**, *94*, 1377–1388.

(16) Wang, L.-S.; Cheng, H.-S.; Fan, J. Photoelectron spectroscopy of size-selected transition metal clusters: Fe_n, n=3–24. *The Journal of Chemical Physics* **1995**, *102*, 9480–9493.

(17) Chandler, D. W.; Houston, P. L. Two-dimensional imaging of state-selected photodissociation products detected by multiphoton ionization. *The Journal of Chemical Physics* **1987**, *87*, 1445–1447.

(18) Eppink, A. T. J. B.; Parker, D. H. Velocity map imaging of ions and electrons using electrostatic lenses: Application in photoelectron and photofragment ion imaging of molecular oxygen. *Review of Scientific Instruments* **1997**, *68*, 3477–3484.

(19) Baguenard, B.; Pinaré, J. C.; Bordas, C.; Broyer, M. Photoelectron imaging spectroscopy of small tungsten clusters: Direct observation of thermionic emission. *Phys. Rev. A* **2001**, *63*, 023204.

(20) Surber, E.; Mabbs, R.; Sanov, A. Probing the Electronic Structure of Small Molecular Anions by Photoelectron Imaging. *The Journal of Physical Chemistry A* **2003**, *107*, 8215–8224.

(21) Müller-Dethlefs, K.; Sander, M.; Schlag, E. W. Two-colour photoionization resonance spectroscopy of NO: Complete separation of rotational levels of NO^+ at the ionization threshold. *Chemical Physics Letters* **1984**, *112*, 291–294.

(22) Muller-Dethlefs, K.; Schlag, E. W. High-Resolution Zero Kinetic Energy (ZEKE) Photoelectron Spectroscopy of Molecular Systems. *Annual Review of Physical Chemistry* **1991**, *42*, 109–136.

(23) Kitsopoulos, T.; Waller, I.; Loeser, J.; Neumark, D. High resolution threshold photodetachment spectroscopy of negative ions. *Chemical Physics Letters* **1989**, *159*, 300–306.

(24) Lenzer, T.; Yourshaw, I.; Furlanetto, M. R.; Reiser, G.; Neumark, D. M. Zero electron kinetic energy spectroscopy of the $ArCl^-$ anion. *The Journal of Chemical Physics* **1999**, *110*, 9578–9586.

(25) Reiser, G.; Mueller-Dethlefs, K. Rotationally resolved (zero kinetic energy) photoelectron spectroscopy of nitric oxide. *The Journal of Physical Chemistry* **1992**, *96*, 9–12.

(26) Arnold, C. C.; Neumark, D. M. Study of Si_4 and Si_4^- using threshold photodetachment (ZEKE) spectroscopy. *The Journal of Chemical Physics* **1993**, *99*, 3353–3362.

(27) Waller, I. M.; Kitsopoulos, T. N.; Neumark, D. M. Threshold photodetachment spectroscopy of the iodine atom + hydrogen iodide transition-state region. *The Journal of Physical Chemistry* **1990**, *94*, 2240–2242.

(28) Arnold, C. C.; Neumark, D. M.; Cyr, D. M.; Johnson, M. A. Negative Ion Zero Electron Kinetic Energy Spectroscopy of $I^- \cdot CH_3I$. *The Journal of Physical Chemistry* **1995**, *99*, 1633–1636.

(29) Burton, G. R.; Xu, C.; Arnold, C. C.; Neumark, D. M. Photoelectron spectroscopy and zero electron kinetic energy spectroscopy of germanium cluster anions. *The Journal of Chemical Physics* **1996**, *104*, 2757–2764.

(30) Lenzer, T.; Furlanetto, M. R.; Pivonka, N. L.; Neumark, D. M. Zero electron kinetic energy and threshold photodetachment spectroscopy of Xe_nI^- clusters (n=2–14): Binding, many-body effects, and structures. *The Journal of Chemical Physics* **1999**, *110*, 6714–6731.

(31) Blondel, C.; Delsart, C.; Dulieu, F. The Photodetachment Microscope. *Phys. Rev. Lett.* **1996**, *77*, 3755–3758.

(32) Valli, C.; Blondel, C.; Delsart, C. Measuring electron affinities with the photodetachment microscope. *Phys. Rev. A* **1999**, *59*, 3809–3815.

(33) Delsart, C.; Goldfarb, F.; Blondel, C. Molecular Photodetachment Microscopy. *Phys. Rev. Lett.* **2002**, *89*, 183002.

(34) Neumark, D. M. Slow Electron Velocity-Map Imaging of Negative Ions: Applications to Spectroscopy and Dynamics. *J. Phys. Chem. A* **2008**, *112*, 13287–13301.

(35) Osterwalder, A.; Nee, M. J.; Zhou, J.; Neumark, D. M. High resolution photodetachment spectroscopy of negative ions via slow photoelectron imaging. *The Journal of Chemical Physics* **2004**, *121*, 6317–6322.

(36) Weichman, M. L.; DeVine, J. A.; Levine, D. S.; Kim, J. B.; Neumark, D. M. Isomer-specific vibronic structure of the 9-, 1-, and 2-anthracenyl radicals via slow photoelectron velocity-map imaging. *Proceedings of the National Academy of Sciences* **2016**, *113*, 1698–1705.

(37) DeWitt, M.; Babin, M. C.; Neumark, D. M. High-Resolution Photoelectron Spectroscopy of Vibrationally Excited OH^-. *The Journal of Physical Chemistry A* **2021**, *125*, PMID: 34433266, 7260–7265.

(38) Lojko, M. S.; Beers, Y. A Table of Rotational Constants of Symmetric Top Molecules Giving Rise to Microwave Spectra. *Journal of research of the National Bureau of Standards. Section A, Physics and chemistry* **1969**, *73*, 233.

(39) Kim, J. B. Slow Photoelectron Imaging Spectroscopy of Cryogenically-Cooled Anions, English, Ph.D. Thesis, 2014, p 247.

(40) DeVine, J. A.; Weichman, M. L.; Zhou, X.; Ma, J.; Jiang, B.; Guo, H.; Neumark, D. M. Non-Adiabatic Effects on Excited States of Vinylidene Observed with Slow Photoelectron Velocity-Map Imaging. *Journal of the American Chemical Society* **2016**, *138*, PMID: 27936652, 16417–16425.

(41) DeVine, J. A.; Weichman, M. L.; Laws, B.; Chang, J.; Babin, M. C.; Balerdi, G.; Xie, C.; Malbon, C. L.; Lineberger, W. C.; Yarkony, D. R.; Field, R. W.; Gibson, S. T.; Ma, J.; Guo, H.; Neumark, D. M. Encoding of vinylidene isomerization in its anion photoelectron spectrum. *Science* **2017**, *358*, 336–339.

(42) Weichman, M. L.; Kim, J. B.; Neumark, D. M. Rovibronic structure in slow photoelectron velocity-map imaging spectroscopy of CH_2CN^- and CD_2CN^-. *The Journal of Chemical Physics* **2014**, *140*, 104305.

(43) Duncan, M. A. Invited review article: laser vaporization cluster sources. *Review of Scientific Instruments* **2012**, *83*, 041101.

(44) Gerlich, D. In *Advances in Chemical Physics*; John Wiley & Sons, Ltd: 1992, pp 1–176.

(45) Wester, R. Radiofrequency multipole traps: tools for spectroscopy and dynamics of cold molecular ions. *Journal of Physics B: Atomic, Molecular and Optical Physics* **2009**, *42*, 154001.

(46) Krems, R.; Friedrich, B.; Stwalley, W. C., *Cold molecules: theory, experiment, applications*; CRC press: 2009; Chapter 13.

(47) Harrilal, C. P.; DeBlase, A. F.; Fischer, J. L.; Lawler, J. T.; McLuckey, S. A.; Zwier, T. S. Infrared Population Transfer Spectroscopy of Cryo-Cooled Ions: Quantitative Tests of the Effects of Collisional Cooling on the Room Temperature Conformer Populations. *J. Phys. Chem. A* **2018**, *122*, 2096–2107.

(48) Voronina, L.; Rizzo, T. R. Spectroscopic studies of kinetically trapped conformations in the gas phase: the case of triply protonated bradykinin. *Phys. Chem. Chem. Phys.* **2015**, *17*, 25828–25836.

(49) Wang, X.-B.; Woo, H.-K.; Kiran, B.; Wang, L.-S. Observation of Weak C-H···O Hydrogen Bonding to Unactivated Alkanes. *Angewandte Chemie International Edition* **2005**, *44*, 4968–4972.

(50) Wang, X.-B.; Wang, L.-S. Development of a low-temperature photoelectron spectroscopy instrument using an electrospray ion source and a cryogenically controlled ion trap. *Review of Scientific Instruments* **2008**, *79*, 073108.

(51) Ma, L.; Majer, K.; Chirot, F.; von Issendorff, B. Low temperature photoelectron spectra of water cluster anions. *The Journal of Chemical Physics* **2009**, *131*, 144303.

(52) Ma, L.; v. Issendorff, B.; Aguado, A. Photoelectron spectroscopy of cold aluminum cluster anions: Comparison with density functional theory results. *The Journal of Chemical Physics* **2010**, *132*, 104303.

(53) Hock, C. Nanocalorimetry and angle-resolved photoelectron spectroscopy on sodium, aluminum, and water clusters, Ph.D. Thesis, 2010.

(54) Hock, C.; Kim, J. B.; Weichman, M. L.; Yacovitch, T. I.; Neumark, D. M. Slow photoelectron velocity-map imaging spectroscopy of cold negative ions. *The Journal of Chemical Physics* **2012**, *137*, 244201.

(55) Kim, J. B.; Weichman, M. L.; Neumark, D. M. Low-lying states of FeO and FeO^- by slow photoelectron spectroscopy. *Molecular Physics* **2015**, *113*, 2105–2114.

(56) Endres, E. S.; Ndengué, S.; Lakhmanskaya, O.; Lee, S.; Gianturco, F. A.; Dawes, R.; Wester, R. Temperature-dependent rotationally inelastic collisions of OH^- and He. *Phys. Rev. A* **2021**, *103*, 052807.

(57) Weichman, M. L.; Kim, J. B.; DeVine, J. A.; Levine, D. S.; Neumark, D. M. Vibrational and Electronic Structure of the α- and β-Naphthyl Radicals via Slow Photoelectron Velocity-Map Imaging. *Journal of the American Chemical Society* **2015**, *137*, PMID: 25602742, 1420–1423.

(58) Kim, J. B.; Weichman, M. L.; Yacovitch, T. I.; Shih, C.; Neumark, D. M. Slow photoelectron velocity-map imaging spectroscopy of the C_9H_7 (indenyl) and $C_{13}H_9$ (fluorenyl) anions. *The Journal of Chemical Physics* **2013**, *139*, 104301.

(59) Kim, J. B.; Weichman, M. L.; Neumark, D. M. High-resolution anion photoelectron spectra of TiO_2^-, ZrO_2^-, and HfO_2^- obtained by slow electron velocity-map imaging. *Phys. Chem. Chem. Phys.* **2013**, *15*, 20973–20981.

(60) Kim, J. B.; Weichman, M. L.; Neumark, D. M. Structural isomers of Ti_2O_4 and Zr_2O_4 anions identified by slow photoelectron velocity-map imaging spectroscopy. *J. Am. Chem. Soc.* **2014**, *136*, 7159–7168.

(61) Weichman, M. L.; DeVine, J. A.; Neumark, D. M. High-resolution photoelectron imaging spectroscopy of cryogenically cooled Fe_4O^- and Fe_5O^-. *The Journal of Chemical Physics* **2016**, *145*, 054302.

(62) Weichman, M. L.; Vlaisavljevich, B.; DeVine, J. A.; Shuman, N. S.; Ard, S. G.; Shiozaki, T.; Neumark, D. M.; Viggiano, A. A. Electronic structure of SmO and SmO^- via slow photoelectron velocity-map imaging spectroscopy and spin-orbit CASPT2 calculations. *The Journal of Chemical Physics* **2017**, *147*, 234311.

(63) Babin, M. C.; DeWitt, M.; DeVine, J. A.; McDonald, D. C.; Ard, S. G.; Shuman, N. S.; Viggiano, A. A.; Cheng, L.; Neumark, D. M. Electronic structure of NdO via slow photoelectron velocity-map imaging spectroscopy of NdO^-. *The Journal of Chemical Physics* **2021**, *155*, 114305.

(64) Kim, J. B.; Weichman, M. L.; Neumark, D. M. Vibronic structure of VO2 probed by slow photoelectron velocity-map imaging spectroscopy. *The Journal of Chemical Physics* **2014**, *140*, 034307.

(65) DeVine, J. A.; Abou Taka, A.; Babin, M. C.; Weichman, M. L.; Hratchian, H. P.; Neumark, D. M. High-resolution photoelectron spectroscopy of $TiO_3H_2^-$: Probing the TiO_2^- + H_2O dissociative adduct. *J. Chem. Phys.* **2018**, *148*, 222810.

(66) Abou Taka, A.; Babin, M. C.; Sheng, X.; DeVine, J. A.; Neumark, D. M.; Hratchian, H. P. Unveiling the coexistence of cis- and trans-isomers in the hydrolysis of ZrO_2: A coupled DFT and high-resolution photoelectron spectroscopy study. *The Journal of Chemical Physics* **2020**, *153*, 244308.

(67) Griffiths, D. J.; Schroeter, D. F., *Introduction to Quantum Mechanics*, 3rd ed.; Cambridge University Press: 2018.

(68) Einstein, A. Über einen die Erzeugung und Verwandlung des Lichtes betreffenden heuristischen Gesichtspunkt. *Annalen der Physik* **1905**, *322*, 132–148.

(69) Millikan, R. A. A Direct Photoelectric Determination of Planck's "h". *Phys. Rev.* **1916**, *7*, 355–388.

(70) Szabo, A.; Ostlund, N. S., *Modern quantum chemistry: introduction to advanced electronic structure theory*; Courier Corporation: 2012.

(71) Herzberg, G., *Electronic spectra and electronic structure of polyatomic molecules*; Van Nostrand: New York, 1966.

(72) Balasubramanian, K.; McLean, A. D. The singlet–triplet energy separation in silylene. *The Journal of Chemical Physics* **1986**, *85*, 5117–5119.

(73) Zhai, H.-J.; Wang, L.-S. Probing the Electronic Structure and Band Gap Evolution of Titanium Oxide Clusters $(TiO_2)_n^-$ (n = 1-10) Using Photoelectron Spectroscopy. *Journal of the American Chemical Society* **2007**, *129*, PMID: 17300196, 3022–3026.

(74) Wenthold, P. G.; Squires, R. R.; Lineberger, W. C. Ultraviolet Photoelectron Spectroscopy of the *o*-, *m*-, and *p*-Benzyne Negative Ions. Electron Affinities and Singlet-Triplet Splittings for *o*-, *m*-, and *p*-Benzyne. *Journal of the American Chemical Society* **1998**, *120*, 5279–5290.

(75) Goldfarb, F.; Drag, C.; Chaibi, W.; Kröger, S.; Blondel, C.; Delsart, C. Photodetachment microscopy of the P, Q, and R branches of the $OH^-(\nu = 0)$ to $OH(\nu = 0)$ detachment threshold. *The Journal of Chemical Physics* **2005**, *122*, 014308.

(76) Engelking, P. C.; Lineberger, W. C. Laser photoelectron spectrometry of NH^-: Electron affinity and intercombination energy difference in NH. *The Journal of Chemical Physics* **1976**, *65*, 4323–4324.

(77) Kasdan, A.; Herbst, E.; Lineberger, W. Laser photoelectron spectrometry of CH^-. *Chemical Physics Letters* **1975**, *31*, 78–82.

(78) Rau, A. R. P.; Fano, U. Theory of Photodetachment near Fine-Structure Thresholds. *Phys. Rev. A* **1971**, *4*, 1751–1759.

(79) Hotop, H.; Patterson, T. A.; Lineberger, W. C. High resolution photodetachment study of OH^- and OD^- in the threshold region 7000–6450 Å. *The Journal of Chemical Physics* **1974**, *60*, 1806–1812.

(80) McCarthy, M. C.; Mohamed, S.; Brown, J. M.; Thaddeus, P. Detection of low-frequency lambda-doublet transitions of the free ^{12}CH and ^{13}CH radicals. *Proceedings of the National Academy of Sciences* **2006**, *103*, 12263–12268.

(81) Wigner, E. P. On the Behavior of Cross Sections Near Thresholds. *Phys. Rev.* **1948**, *73*, 1002–1009.

(82) Rau, A. R. P. Threshold laws. *Comments on Atomic and Molecular Physics* **1984**, *14*, 285–306.

(83) Reed, K. J.; Zimmerman, A. H.; Andersen, H. C.; Brauman, J. I. Cross sections for photodetachment of electrons from negative ions near threshold. *The Journal of Chemical Physics* **1976**, *64*, 1368–1375.

(84) Surber, E.; Mabbs, R.; Sanov, A. Probing the Electronic Structure of Small Molecular Anions by Photoelectron Imaging. *The Journal of Physical Chemistry A* **2003**, *107*, 8215–8224.

(85) Mabbs, R.; Grumbling, E. R.; Pichugin, K.; Sanov, A. Photoelectron imaging: an experimental window into electronic structure. *Chem. Soc. Rev.* **2009**, *38*, 2169–2177.

(86) DeVine, J. A.; Babin, M. C.; Blackford, K.; Neumark, D. M. High-resolution photoelectron spectroscopy of the pyridinide isomers. *The Journal of Chemical Physics* **2019**, *151*, 064302.

(87) Laws, B.; Cavanagh, S.; Lewis, B.; Gibson, S. Wigner Near-Threshold Effects in the Photoelectron Angular Distribution of NO_2^-. *The Journal of Physical Chemistry A* **2019**, *123*, 10418–10425.

(88) Simpson, M.; Nötzold, M.; Schmidt-May, A.; Michaelsen, T.; Bastian, B.; Meyer, J.; Wild, R.; Gianturco, F. A.; Milovanović, M.; Kokoouline, V.; Wester, R. Threshold photodetachment spectroscopy of the astrochemical anion CN^-. *The Journal of Chemical Physics* **2020**, *153*, 184309.

(89) Simpson, M.; Nötzold, M.; Michaelsen, T.; Wild, R.; Gianturco, F. A.; Wester, R. Influence of a Supercritical Electric Dipole Moment on the Photodetachment of C_3N^-. *Phys. Rev. Lett.* **2021**, *127*, 043001.

(90) O'Malley, T. F. Effect of Long-Range Final-State Forces on the Negative-Ion Photodetachment Cross Section near Threshold. *Phys. Rev.* **1965**, *137*, A1668–A1672.

(91) Cooper, J.; Zare, R. N. Angular Distribution of Photoelectrons. *The Journal of Chemical Physics* **1968**, *48*, 942–943.

(92) Zare, R.; Herschbach, D. Doppler line shape of atomic fluorescence excited by molecular photodissociation. *Proceedings of the IEEE* **1963**, *51*, 173–182.

(93) Hanstorp, D.; Bengtsson, C.; Larson, D. J. Angular distributions in photodetachment from O^-. *Phys. Rev. A* **1989**, *40*, 670–675.

(94) DeVine, J. A.; Weichman, M. L.; Lyle, S. J.; Neumark, D. M. High-resolution photoelectron imaging of cryogenically cooled α- and β-furanyl anions. *Journal of Molecular Spectroscopy* **2017**, *332*, Molecular Spectroscopy in Traps, 16–21.

(95) Grumbling, E. R.; Sanov, A. Photoelectron angular distributions in negative-ion photodetachment from mixed sp states. *The Journal of Chemical Physics* **2011**, *135*, 164302.

(96) Sanov, A.; Grumbling, E. R.; Goebbert, D. J.; Culberson, L. M. Photodetachment anisotropy for mixed *s-p* states: 8/3 and other fractions. *The Journal of Chemical Physics* **2013**, *138*, 054311.

(97) Khuseynov, D.; Blackstone, C. C.; Culberson, L. M.; Sanov, A. Photoelectron angular distributions for states of any mixed character: An experiment-friendly model for atomic, molecular, and cluster anions. *The Journal of Chemical Physics* **2014**, *141*, 124312.

(98) Oana, C.; Krylov, A. Cross sections and photoelectron angular distributions in photodetachment from negative ions using equation-of-motion coupled-cluster Dyson orbitals. *The Journal of Chemical Physics* **2009**, *131*, 124114.

(99) Gozem, S.; Krylov, A. I. ezDyzon 3.0.

(100) Babin, M. C.; DeVine, J. A.; DeWitt, M.; Stanton, J. F.; Neumark, D. M. High-Resolution Photoelectron Spectroscopy of Cryogenically Cooled NO_3^-. *The Journal of Physical Chemistry Letters* **2020**, *11*, PMID: 31765169, 395–400.

(101) Babin, M. C.; DeWitt, M.; Weichman, M. L.; DeVine, J. A.; Neumark, D. M. High-resolution anion photoelectron spectroscopy of cryogenically cooled 4-atom silicon carbides. *Molecular Physics* **2021**, *119*, e1817596.

(102) Babin, M. C.; DeVine, J. A.; Weichman, M. L.; Neumark, D. M. Slow photoelectron velocity-map imaging of cold C_7^- and C_9^-. *The Journal of chemical physics* **2018**, *149*, 174306.

(103) DeVine, J. A.; Babin, M. C.; Neumark, D. M. Photoelectron spectra of $Al_2O_2^-$ and $Al_3O_3^-$ via slow electron velocity-map imaging. *Faraday Discuss.* **2019**, *217*, 235–255.

(104) Weichman, M. L.; Cheng, L.; Kim, J. B.; Stanton, J. F.; Neumark, D. M. Low-lying vibronic level structure of the ground state of the methoxy radical: Slow electron velocity-map imaging (SEVI) spectra and Köppel-Domcke-Cederbaum (KDC) vibronic Hamiltonian calculations. *The Journal of Chemical Physics* **2017**, *146*, 224309.

(105) Weaver, A.; Arnold, D. W.; Bradforth, S. E.; Neumark, D. M. Examination of the $^2A_2'$ and $^2E'$ states of NO_3 by ultraviolet photoelectron spectroscopy of NO_3^-. *The Journal of Chemical Physics* **1991**, *94*, 1740–1751.

(106) Hirota, E. Assignment of the photoelectron spectrum of the nitrate anion NO_3^- and vibronic interactions in the nitrate free radical. *Journal of Molecular Spectroscopy* **2018**, *343*, Spectroscopy of Large Amplitude Vibrational Motion, on the Occasion of Jon Hougen's 80th Birthday – Part II, 81–84.

(107) Nee, M. J.; Osterwalder, A.; Zhou, J.; Neumark, D. M. Slow electron velocity-map imaging photoelectron spectra of the methoxide anion. *The Journal of Chemical Physics* **2006**, *125*, 014306.

(108) Weichman, M. L.; Kim, J. B.; Neumark, D. M. Vibrational fine structure of C_5 via anion slow photoelectron velocity-map imaging. *The Journal of Chemical Physics* **2013**, *139*, 144314.

(109) Cleeton, C. E.; Williams, N. H. Electromagnetic Waves of 1.1 cm Wave-Length and the Absorption Spectrum of Ammonia. *Phys. Rev.* **1934**, *45*, 234–237.

(110) Oliveira, A. M.; Lu, Y.-J.; Lehman, J. H.; Changala, P. B.; Baraban, J. H.; Stanton, J. F.; Lineberger, W. C. Photoelectron Spectroscopy of the Methide Anion: Electron Affinities of $\cdot CH_3$ and $\cdot CD_3$ and Inversion Splittings of CH_3^- and CD_3^-. *Journal of the American Chemical Society* **2015**, *137*, PMID: 26389796, 12939–12945.

(111) Berry, R. S. Ionization of Molecules at Low Energies. *The Journal of Chemical Physics* **1966**, *45*, 1228–1245.

(112) Simons, J. Propensity rules for vibration-induced electron detachment of anions. *Journal of the American Chemical Society* **1981**, *103*, 3971–3976.

(113) DeVine, J. A.; Weichman, M. L.; Xie, C.; Babin, M. C.; Johnson, M. A.; Ma, J.; Guo, H.; Neumark, D. M. Autodetachment from Vibrationally Excited Vinylidene Anions. *The Journal of Physical Chemistry Letters* **2018**, *9*, PMID: 29438618, 1058–1063.

(114) Heath, J. R.; Cooksy, A. L.; Gruebele, M. H.; Schmuttenmaer, C. A.; Saykally, R. J. Diode-Laser Absorption Spectroscopy of Supersonic Carbon Cluster Beams: the ν_3 Spectrum of C_5. *Science* **1989**, *244*, 564–566.

(115) Hilpert, G.; Linnartz, H.; Havenith, M.; ter Meulen, J.; Meerts, W. Tunable infrared and far-infrared direct absorption spectroscopy of molecular ions in a supersonic jet expansion. *Chemical Physics Letters* **1994**, *219*, 384–388.

(116) Wolk, A. B.; Leavitt, C. M.; Garand, E.; Johnson, M. A. Cryogenic Ion Chemistry and Spectroscopy. *Accounts of Chemical Research* **2014**, *47*, PMID: 23972279, 202–210.

(117) Okumura, M.; Yeh, L. I.; Myers, J. D.; Lee, Y. T. Infrared spectra of the cluster ions $H_7O_3^+ \cdot H_2$ and $H_9O_4^+ \cdot H_2$. *The Journal of Chemical Physics* **1986**, *85*, 2328–2329.

(118) Schöllkopf, W.; Gewinner, S.; Junkes, H.; Paarmann, A.; von Helden, G.; Bluem, H. P.; Todd, A. M. M. In *Advances in X-ray Free-Electron Lasers Instrumentation III*, ed. by Biedron, S. G., SPIE: 2015; Vol. 9512, pp 238–250.

(119) Cohen-Tannoudji, C.; Diu, B.; Laloë, F., *Quantum Mechanics. Vol. 1.* Wiley: New York, NY, 1977.

(120) Born, M.; Oppenheimer, R. Zur Quantentheorie der Molekeln. *Annalen der Physik* **1927**, *389*, 457–484.

(121) Slater, J. C. Cohesion in Monovalent Metals. *Phys. Rev.* **1930**, *35*, 509–529.

(122) Pople, J. A.; Nesbet, R. K. Self-Consistent Orbitals for Radicals. *The Journal of Chemical Physics* **1954**, *22*, 571–572.

(123) Hall, G. G.; Lennard-Jones, J. E. The molecular orbital theory of chemical valency VIII. A method of calculating ionization potentials. *Proceedings of the Royal Society of London. Series A. Mathematical and Physical Sciences* **1951**, *205*, 541–552.

(124) Roothaan, C. C. J. New Developments in Molecular Orbital Theory. *Rev. Mod. Phys.* **1951**, *23*, 69–89.

(125) Ziegler, T. Approximate density functional theory as a practical tool in molecular energetics and dynamics. *Chemical Reviews* **1991**, *91*, 651–667.

(126) Kohn, W.; Becke, A. D.; Parr, R. G. Density Functional Theory of Electronic Structure. *The Journal of Physical Chemistry* **1996**, *100*, 12974–12980.

(127) Mardirossian, N.; Head-Gordon, M. Thirty years of density functional theory in computational chemistry: an overview and extensive assessment of 200 density functionals. *Molecular Physics* **2017**, *115*, 2315–2372.

(128) Hohenberg, P.; Kohn, W. Inhomogeneous Electron Gas. *Phys. Rev.* **1964**, *136*, B864–B871.

(129) Kohn, W.; Sham, L. J. Self-Consistent Equations Including Exchange and Correlation Effects. *Phys. Rev.* **1965**, *140*, A1133–A1138.

(130) Dirac, P. A. M. Note on Exchange Phenomena in the Thomas Atom. *Mathematical Proceedings of the Cambridge Philosophical Society* **1930**, *26*, 376–385.

(131) Perdew, J. P.; Ruzsinszky, A.; Tao, J.; Staroverov, V. N.; Scuseria, G. E.; Csonka, G. I. Prescription for the design and selection of density functional approximations: More constraint satisfaction with fewer fits. *The Journal of Chemical Physics* **2005**, *123*, 062201.

(132) Becke, A. D. Density-functional thermochemistry. III. The role of exact exchange. *The Journal of Chemical Physics* **1993**, *98*, 5648–5652.

(133) Stephens, P. J.; Devlin, F. J.; Chabalowski, C. F.; Frisch, M. J. Ab Initio Calculation of Vibrational Absorption and Circular Dichroism Spectra Using Density Functional Force Fields. *The Journal of Physical Chemistry* **1994**, *98*, 11623–11627.

(134) Becke, A. D. Density-functional exchange-energy approximation with correct asymptotic behavior. *Phys. Rev. A* **1988**, *38*, 3098–3100.

(135) Lee, C.; Yang, W.; Parr, R. G. Development of the Colle-Salvetti correlation-energy formula into a functional of the electron density. *Phys. Rev. B* **1988**, *37*, 785–789.

(136) Tirado-Rives, J.; Jorgensen, W. L. Performance of B3LYP Density Functional Methods for a Large Set of Organic Molecules. *Journal of Chemical Theory and Computation* **2008**, *4*, PMID: 26620661, 297–306.

(137) Grimmel, S.; Schoendorff, G.; Wilson, A. K. Gauging the Performance of Density Functionals for Lanthanide-Containing Molecules. *Journal of Chemical Theory and Computation* **2016**, *12*, PMID: 26848891, 1259–1266.

(138) Hait, D.; Head-Gordon, M. How Accurate Is Density Functional Theory at Predicting Dipole Moments? An Assessment Using a New Database of 200 Benchmark Values. *Journal of Chemical Theory and Computation* **2018**, *14*, PMID: 29562129, 1969–1981.

(139) Hait, D.; Head-Gordon, M. How accurate are static polarizability predictions from density functional theory? An assessment over 132 species at equilibrium geometry. *Phys. Chem. Chem. Phys.* **2018**, *20*, 19800–19810.

(140) Ferbinteanu, M.; Stroppa, A.; Scarrozza, M.; Humelnicu, I.; Maftei, D.; Frecus, B.; Cimpoesu, F. On The Density Functional Theory Treatment of Lanthanide Coordination Compounds: A Comparative Study in a Series of Cu–Ln (Ln = Gd, Tb, Lu) Binuclear Complexes. *Inorganic Chemistry* **2017**, *56*, PMID: 28782949, 9474–9485.

(141) Chai, J.-D.; Head-Gordon, M. Long-range corrected hybrid density functionals with damped atom–atom dispersion corrections. *Phys. Chem. Chem. Phys.* **2008**, *10*, 6615–6620.

(142) Møller, C.; Plesset, M. S. Note on an Approximation Treatment for Many-Electron Systems. *Phys. Rev.* **1934**, *46*, 618–622.

(143) Helgaker, T.; Gauss, J.; Jørgensen, P.; Olsen, J. The prediction of molecular equilibrium structures by the standard electronic wave functions. *The Journal of Chemical Physics* **1997**, *106*, 6430–6440.

(144) Purvis, G. D.; Bartlett, R. J. A full coupled-cluster singles and doubles model: The inclusion of disconnected triples. *The Journal of Chemical Physics* **1982**, *76*, 1910–1918.

(145) Raghavachari, K.; Trucks, G. W.; Pople, J. A.; Head-Gordon, M. A fifth-order perturbation comparison of electron correlation theories. *Chemical Physics Letters* **1989**, *157*, 479–483.

(146) Hait, D.; Tubman, N. M.; Levine, D. S.; Whaley, K. B.; Head-Gordon, M. What Levels of Coupled Cluster Theory Are Appropriate for Transition Metal Systems? A Study Using Near-Exact Quantum Chemical Values for 3d Transition Metal Binary Compounds. *Journal of Chemical Theory and Computation* **2019**, *15*, PMID: 31465217, 5370–5385.

(147) Roos, B. O. In *Advances in Chemical Physics*; John Wiley & Sons, Ltd: 1987, pp 399–445.

(148) Szalay, P. G.; Müller, T.; Gidofalvi, G.; Lischka, H.; Shepard, R. Multiconfiguration Self-Consistent Field and Multireference Configuration Interaction Methods and Applications. *Chemical Reviews* **2012**, *112*, PMID: 22204633, 108–181.

(149) Weichman, M. L.; DeVine, J. A.; Babin, M. C.; Li, J.; Guo, L.; Ma, J.; Guo, H.; Neumark, D. M. Feshbach resonances in the exit channel of the F + $CH_3OH \rightarrow$ HF + CH_3O reaction observed using transition-state spectroscopy. *Nature Chemistry* **2017**, *9*, 950–955.

(150) Dreuw, A.; Head-Gordon, M. Single-Reference ab Initio Methods for the Calculation of Excited States of Large Molecules. *Chemical Reviews* **2005**, *105*, PMID: 16277369, 4009–4037.

(151) Bauernschmitt, R.; Ahlrichs, R. Treatment of electronic excitations within the adiabatic approximation of time dependent density functional theory. *Chem. Phys. Lett.* **1996**, *256*, 454–464.

(152) Stratmann, R. E.; Scuseria, G. E.; Frisch, M. J. An efficient implementation of time-dependent density-functional theory for the calculation of excitation energies of large molecules. *J. Chem. Phys.* **1998**, *109*, 8218–8224.

(153) Chong, D. P., *Recent Advances in Density Functional Methods*; WORLD SCIENTIFIC: 1995.

(154) Casida, M. E.; Jamorski, C.; Casida, K. C.; Salahub, D. R. Molecular excitation energies to high-lying bound states from time-dependent density-functional response theory: Characterization and correction of the time-dependent local density approximation ionization threshold. *The Journal of Chemical Physics* **1998**, *108*, 4439–4449.

(155) Laurent, A. D.; Jacquemin, D. TD-DFT benchmarks: A review. *International Journal of Quantum Chemistry* **2013**, *113*, 2019–2039.

(156) Stanton, J. F.; Bartlett, R. J. The equation of motion coupled-cluster method. A systematic biorthogonal approach to molecular excitation energies, transition probabilities, and excited state properties. *The Journal of Chemical Physics* **1993**, *98*, 7029–7039.

(157) Nagy, B.; Jensen, F. In *Reviews in Computational Chemistry*; John Wiley & Sons, Ltd: 2017; Chapter 3, pp 93–149.

(158) Pritchard, B. P.; Altarawy, D.; Didier, B.; Gibson, T. D.; Windus, T. L. New Basis Set Exchange: An Open, Up-to-Date Resource for the Molecular Sciences Community. *Journal of Chemical Information and Modeling* **2019**, *59*, PMID: 31600445, 4814–4820.

(159) Xu, X.; Truhlar, D. G. Accuracy of Effective Core Potentials and Basis Sets for Density Functional Calculations, Including Relativistic Effects, As Illustrated by Calculations on Arsenic Compounds. *Journal of Chemical Theory and Computation* **2011**, *7*, PMID: 26605468, 2766–2779.

(160) Jensen, F. Atomic orbital basis sets. *WIREs Computational Molecular Science* **2013**, *3*, 273–295.

(161) Ditchfield, R.; Hehre, W. J.; Pople, J. A. Self-Consistent Molecular-Orbital Methods. IX. An Extended Gaussian-Type Basis for Molecular-Orbital Studies of Organic Molecules. *The Journal of Chemical Physics* **1971**, *54*, 724–728.

(162) Dunning, T. H. Gaussian basis sets for use in correlated molecular calculations. I. The atoms boron through neon and hydrogen. *The Journal of Chemical Physics* **1989**, *90*, 1007–1023.

(163) Woon, D. E.; Dunning, T. H. Gaussian basis sets for use in correlated molecular calculations. V. Core-valence basis sets for boron through neon. *The Journal of Chemical Physics* **1995**, *103*, 4572–4585.

(164) Weigend, F.; Ahlrichs, R. Balanced basis sets of split valence, triple zeta valence and quadruple zeta valence quality for H to Rn: Design and assessment of accuracy. *Phys. Chem. Chem. Phys.* **2005**, *7*, 3297–3305.

(165) Zobel, J. P.; Widmark, P.-O.; Veryazov, V. The ANO-R Basis Set. *Journal of Chemical Theory and Computation* **2020**, *16*, PMID: 31738554, 278–294.

(166) Wadt, W. R.; Hay, P. J. Ab initio effective core potentials for molecular calculations. Potentials for main group elements Na to Bi. *The Journal of Chemical Physics* **1985**, *82*, 284–298.

(167) Küchle, W.; Dolg, M.; Stoll, H.; Preuss, H. Ab initio pseudopotentials for Hg through Rn. *Molecular Physics* **1991**, *74*, 1245–1263.

(168) Martin, J. M.; Sundermann, A. Correlation consistent valence basis sets for use with the Stuttgart–Dresden–Bonn relativistic effective core potentials: The atoms Ga–Kr and In–Xe. *J. Chem. Phys.* **2001**, *114*, 3408–3420.

(169) Andrae, D.; Haeussermann, U.; Dolg, M.; Stoll, H.; Preuss, H. Energy-adjusted ab initio pseudopotentials for the second and third row transition elements. *Theor. Chim. Acta* **1990**, *77*, 123–141.

(170) Ross, R. B.; Powers, J. M.; Atashroo, T.; Ermler, W. C.; LaJohn, L. A.; Christiansen, P. A. Ab initio relativistic effective potentials with spin–orbit operators. IV. Cs through Rn. *The Journal of Chemical Physics* **1990**, *93*, 6654–6670.

(171) Metz, B.; Schweizer, M.; Stoll, H.; Dolg, M.; Liu, W. A small-core multiconfiguration Dirac-Hartree-Fock-adjusted pseudopotential for Tl - application to TlX (X = F, Cl, Br, I). *Theoretical Chemistry Accounts* **2000**, *104*, 22–28.

(172) Stevens, W. J.; Krauss, M.; Basch, H.; Jasien, P. G. Relativistic compact effective potentials and efficient, shared-exponent basis sets for the third-, fourth-, and fifth-row atoms. *Canadian Journal of Chemistry* **1992**, *70*, 612–630.

(173) Marques, J. M. C.; Martínez-Núñez, E.; Hase, W. L. Editorial: Application of Optimization Algorithms in Chemistry. *Frontiers in Chemistry* **2020**, *8*, 198.

(174) Matthews, D. A.; Cheng, L.; Harding, M. E.; Lipparini, F.; Stopkowicz, S.; Jagau, T.-C.; Szalay, P. G.; Gauss, J.; Stanton, J. F. Coupled-cluster techniques for computational chemistry: The CFOUR program package. *The Journal of Chemical Physics* **2020**, *152*, 214108.

(175) Mozhayskiy, V. A.; Krylov, A. I. ezSpectrum 3.0.

(176) Duschinsky, F. The importance of the electron spectrum in multi atomic molecules. Concerning the Franck-Condon principle. *Acta Physicochim. URSS* **1937**, *7*, 551–566.

(177) Melania Oana, C.; Krylov, A. I. Dyson orbitals for ionization from the ground and electronically excited states within equation-of-motion coupled-cluster formalism: Theory, implementation, and examples. *The Journal of Chemical Physics* **2007**, *127*, 234106.

(178) Liu, Y.; Ning, C. Calculation of photodetachment cross sections and photoelectron angular distributions of negative ions using density functional theory. *The Journal of Chemical Physics* **2015**, *143*, 144310.

(179) Epifanovsky, E. et al. Software for the frontiers of quantum chemistry: An overview of developments in the Q-Chem 5 package. *The Journal of Chemical Physics* **2021**, *155*, 084801.

(180) Frisch, M. J. et al. Gaussian 16 Rev. C.01, Computer Program, 2016.

(181) Neese, F.; Wennmohs, F.; Becker, U.; Riplinger, C. The ORCA quantum chemistry program package. *The Journal of Chemical Physics* **2020**, *152*, 224108.

(182) Gomberg, M. Organic Radicals. *Chemical Reviews* **1924**, *1*, 91–141.

(183) Wentrup, C. From Reactive Intermediates to Stable Compounds. *Science* **2002**, *295*, 1846–1847.

(184) Yan, M.; Lo, J. C.; Edwards, J. T.; Baran, P. S. Radicals: Reactive Intermediates with Translational Potential. *Journal of the American Chemical Society* **2016**, *138*, PMID: 27631602, 12692–12714.

(185) Scheer, A. M.; Mukarakate, C.; Robichaud, D. J.; Ellison, G. B.; Nimlos, M. R. Radical Chemistry in the Thermal Decomposition of Anisole and Deuterated Anisoles: An Investigation of Aromatic Growth. *The Journal of Physical Chemistry A* **2010**, *114*, PMID: 20695633, 9043–9056.

(186) Johansson, K. O.; Head-Gordon, M. P.; Schrader, P. E.; Wilson, K. R.; Michelsen, H. A. Resonance-stabilized hydrocarbon-radical chain reactions may explain soot inception and growth. *Science* **2018**, *361*, 997–1000.

(187) Aloisio, S.; Francisco, J. S. Radical-Water Complexes in Earth's Atmosphere. *Accounts of Chemical Research* **2000**, *33*, PMID: 11123881, 825–830.

(188) Orlando, J. J.; Tyndall, G. S.; Wallington, T. J. The Atmospheric Chemistry of Alkoxy Radicals. *Chemical Reviews* **2003**, *103*, PMID: 14664628, 4657–4690.

(189) Hart, D. J. Free-Radical Carbon-Carbon Bond Formation in Organic Synthesis. *Science* **1984**, *223*, 883–887.

(190) Imlay, J. A.; Linn, S. DNA Damage and Oxygen Radical Toxicity. *Science* **1988**, *240*, 1302–1309.

(191) Macintyre, H. L.; Evans, M. J. Sensitivity of a global model to the uptake of N_2O_5 by tropospheric aerosol. *Atmospheric Chemistry and Physics* **2010**, *10*, 7409–7414.

(192) Brown, S. S.; Stutz, J. Nighttime radical observations and chemistry. *Chem. Soc. Rev.* **2012**, *41*, 6405–6447.

(193) Ferrière, K. M. The interstellar environment of our galaxy. *Rev. Mod. Phys.* **2001**, *73*, 1031–1066.

(194) McGuire, B. A. 2018 census of interstellar, circumstellar, extragalactic, protoplanetary disk, and exoplanetary molecules. *The Astrophysical Journal Supplement Series* **2018**, *239*, 17.

(195) Van Orden, A.; Saykally, R. J. Small Carbon Clusters: Spectroscopy, Structure, and Energetics. *Chemical Reviews* **1998**, *98*, PMID: 11543299, 2313–2358.

(196) Tielens, A. G. G. M. The molecular universe. *Rev. Mod. Phys.* **2013**, *85*, 1021–1081.

(197) Jochnowitz, E. B.; Maier, J. P. Electronic Spectroscopy of Carbon Chains. *Annual Review of Physical Chemistry* **2008**, *59*, PMID: 18393678, 519–544.

(198) Bettens, R. P. A.; Herbst, E. The Formation of Large Hydrocarbons and Carbon Clusters in Dense Interstellar Clouds. *The Astrophysical Journal* **1997**, *478*, 585–593.

(199) Douglas, A. Laboratory Studies of the lambda 4050 Group of Cometary Spectra. *The Astrophysical Journal* **1951**, *114*, 466.

(200) Hinkle, K. W.; Keady, J. J.; Bernath, P. F. Detection of C_3 in the Circumstellar Shell of IRC+10216. *Science* **1988**, *241*, 1319–1322.

(201) Bernath, P. F.; Hinkle, K. H.; Keady, J. J. Detection of C_5 in the Circumstellar Shell of IRC+10216. *Science* **1989**, *244*, 562–564.

(202) Herbst, E. Chemistry in the Interstellar Medium. *Annual Review of Physical Chemistry* **1995**, *46*, 27–54.

(203) Thaddeus, P.; Cummins, S.; Linke, R. Identification of the SiCC radical toward IC+ 10216-The first molecular ring in an astronomical source. *The Astrophysical Journal* **1984**, *283*, L45–L48.

(204) Cernicharo, J.; Gottlieb, C.; Guelin, M.; Thaddeus, P.; Vrtilek, J. Astonomical and laboratory detection of the SiC radical. *The Astrophysical Journal* **1989**, *341*, L25–L28.

(205) Ohishi, M.; Kaifu, N.; Kawaguchi, K.; Murakami, A.; Saito, S.; Yamamoto, S.; Ishikawa, S.-I.; Fujita, Y.; Shiratori, Y.; Irvine, W. M. Detection of a new circumstellar carbon chain molecule, C4Si. *The Astrophysical Journal* **1989**, *345*, L83–L86.

(206) Apponi, A.; McCarthy, M.; Gottlieb, C.; Thaddeus, P. The rotational spectrum of rhomboidal SiC_3. *The Journal of chemical physics* **1999**, *111*, 3911–3918.

(207) Apponi, A.; McCarthy, M.; Gottlieb, C.; Thaddeus, P. Astronomical detection of rhomboidal SiC_3. *The Astrophysical Journal Letters* **1999**, *516*, L103.

(208) Cernicharo, J.; McCarthy, M.; Gottlieb, C.; Agúndez, M.; Prieto, L. V.; Baraban, J.; Changala, P.; Guélin, M.; Kahane, C.; Martin-Drumel, M., et al. Discovery of SiCSi in IRC+ 10216: A missing link between gas and dust carriers of Si–C bonds. *The Astrophysical Journal Letters* **2015**, *806*, L3.

(209) Xu, Y.-J.; Zhang, Y.-F.; Li, J.-Q. Investigating the role of cationic vacancy on the MgO (001) defect surface: Embedded cluster models study. *Chemical physics* **2005**, *315*, 267–276.

(210) Konig, T.; Simon, G. H.; Rust, H.-P.; Pacchioni, G.; Heyde, M.; Freund, H.-J. Measuring the charge state of point defects on MgO/Ag (001). *Journal of the American Chemical Society* **2009**, *131*, 17544–17545.

(211) Benedetti, S.; Nilius, N.; Myrach, P.; Valenti, I.; Freund, H.-J.; Valeri, S. Spontaneous oxidation of Mg atoms at defect sites in an MgO surface. *The Journal of Physical Chemistry C* **2011**, *115*, 3684–3687.

(212) Lang, S. M.; Bernhardt, T. M. Gas phase metal cluster model systems for heterogeneous catalysis. *Phys. Chem. Chem. Phys.* **2012**, *14*, 9255–9269.

(213) Castleman, A. W. Cluster structure and reactions: gaining insights into catalytic processes. *Catalysis letters* **2011**, *141*, 1243–1253.

(214) Zhai, H.-J.; Wang, L.-S. Probing the electronic structure of early transition metal oxide clusters: Molecular models towards mechanistic insights into oxide surfaces and catalysis. *Chem. Phys. Lett.* **2010**, *500*, 185–195.

(215) Johnson, G. E.; Mitrić, R.; Bonačić-Koutecký, V.; Castleman Jr, A. Clusters as model systems for investigating nanoscale oxidation catalysis. *Chemical Physics Letters* **2009**, *475*, 1–9.

(216) Böhme, D. K.; Schwarz, H. Gas-phase catalysis by atomic and cluster metal ions: The ultimate single-site catalysts. *Angew. Chem. Int. Ed.* **2005**, *44*, 2336–2354.

(217) Zemski, K.; Justes, D.; Castleman, A. Studies of metal oxide clusters: Elucidating reactive sites responsible for the activity of transition metal oxide catalysts, 2002.

(218) Anpo, M.; Sima, T.; Kodama, S.; Kubokawa, Y. Potocatalytic hydrogenation of CH_3CCH with H_2O on small-particle TiO_2-size quantization effects and reaction intermediates. *Journal of physical chemistry* **1987**, *94*, 4305–4301.

(219) Bürgel, C.; Reilly, N. M.; Johnson, G. E.; Mitrić, R.; Kimble, M. L.; Castleman Jr, A.; Bonačć-Koutecký, V. Influence of charge state on the mechanism of CO oxidation on gold clusters. *Journal of the American Chemical Society* **2008**, *130*, 1694–1698.

(220) Johnson, G. E.; Reveles, J. U.; Reilly, N. M.; Tyo, E. C.; Khanna, S. N.; Castleman Jr, A. Influence of stoichiometry and charge state on the structure and reactivity of cobalt oxide clusters with CO. *The Journal of Physical Chemistry A* **2008**, *112*, 11330–11340.

(221) Johnson, G. E.; Reilly, N. M.; Castleman Jr, A. Effect of charge state and stoichiometry on the structure and reactivity of nickel oxide clusters with CO. *International Journal of Mass Spectrometry* **2009**, *280*, 93–100.

(222) Reveles, J. U.; Johnson, G. E.; Khanna, S. N.; Castleman Jr, A. Reactivity trends in the oxidation of CO by anionic transition metal oxide clusters. *The Journal of Physical Chemistry C* **2010**, *114*, 5438–5446.

(223) Aramouni, N. A. K.; Touma, J. G.; Tarboush, B. A.; Zeaiter, J.; Ahmad, M. N. Catalyst design for dry reforming of methane: Analysis review. *Renewable and Sustainable Energy Reviews* **2018**, *82*, 2570–2585.

(224) Alvarez-Galvan, C.; Melian, M.; Ruiz-Matas, L.; Eslava, J. L.; Navarro, R. M.; Ahmadi, M.; Roldan Cuenya, B.; Fierro, J. L. G. Partial oxidation of methane to syngas over nickel-based catalysts: influence of support type, addition of rhodium, and preparation method. *Frontiers in chemistry* **2019**, *7*, 104.

(225) Heracleous, E.; Lee, A.; Wilson, K.; Lemonidou, A. Investigation of Ni-based alumina-supported catalysts for the oxidative dehydrogenation of ethane to ethylene: structural characterization and reactivity studies. *Journal of Catalysis* **2005**, *231*, 159–171.

(226) Zhou, Y.; Wei, F.; Lin, J.; Li, L.; Li, X.; Qi, H.; Pan, X.; Liu, X.; Huang, C.; Lin, S., et al. Sulfate-Modified NiAl Mixed Oxides as Effective C–H Bond-Breaking Agents for the Sole Production of Ethylene from Ethane. *ACS Catalysis* **2020**, *10*, 7619–7629.

(227) Li, Y.-K.; Zhao, Y.-X.; He, S.-G. Selective Conversion of Methane by Rh1-Doped Aluminum Oxide Cluster Anions $RhAl_2O_4^-$: A Comparison with the Reactivity of $PtAl_2O_4^-$. *The Journal of Physical Chemistry A* **2018**, *122*, PMID: 29578712, 3950–3955.

(228) Zhao, Y.-X.; Li, Z.-Y.; Yuan, Z.; Li, X.-N.; He, S.-G. Thermal methane conversion to formaldehyde promoted by single platinum atoms in $PtAl_2O_4^-$ cluster anions. *Angewandte Chemie* **2014**, *126*, 9636–9640.

(229) Zhao, Y.-X.; Li, Z.-Y.; Yang, Y.; He, S.-G. Methane activation by gas phase atomic clusters. *Accounts of chemical research* **2018**, *51*, 2603–2610.

(230) Schwarz, H.; Asmis, K. R. Identification of active sites and structural characterization of reactive ionic intermediates by cryogenic ion trap vibrational spectroscopy. *Chemistry–A European Journal* **2019**, *25*, 2112–2126.

(231) Zhao, Y.-X.; Yang, B.; Li, H.-F.; Zhang, Y.; Yang, Y.; Liu, Q.-Y.; Xu, H.-G.; Zheng, W.-J.; He, S.-G. Photoassisted Selective Steam and Dry Reforming of Methane to Syngas Catalyzed by Rhodium–Vanadium Bimetallic Oxide Cluster Anions at Room Temperature. *Angewandte Chemie International Edition* **2020**, *59*, 21216–21223.

(232) DeVine, J. A. High-resolution Photoelectron Imaging and Infrared Photodissociation Spectroscopy of Cold Negative Ions, English, Ph.D. Thesis, 2019, p 333.

(233) Polanyi, J. C.; Zewail, A. H. Direct Observation of the Transition State. *Accounts of Chemical Research* **1995**, *28*, 119–132.

(234) Wenthold, P. G.; Hrovat, D. A.; Borden, W. T.; Lineberger, W. C. Transition-State Spectroscopy of Cyclooctatetraene. *Science* **1996**, *272*, 1456–1459.

(235) Neumark, D. M. Probing the transition state with negative ion photodetachment: experiment and theory. *Phys. Chem. Chem. Phys.* **2005**, *7*, 433–442.

(236) Ervin, K. M.; Ho, J.; Lineberger, W. C. A study of the singlet and triplet states of vinylidene by photoelectron spectroscopy of H2C=C$^-$, D2C=C$^-$, and HDC=C$^-$. Vinylidene–acetylene isomerization. *The Journal of Chemical Physics* **1989**, *91*, 5974–5992.

(237) Burnett, S. M.; Stevens, A. E.; Feigerle, C.; Lineberger, W. Observation of X^1A_1 vinylidene by photoelectron spectroscopy of the $C_2H_2^-$ ion. *Chemical Physics Letters* **1983**, *100*, 124–128.

(238) Metz, R. B.; Bradforth, S. E.; Neumark, D. M. In *Advances in Chemical Physics*; John Wiley & Sons, Ltd: 1992, pp 1–61.

(239) Kim, J. B.; Hock, C.; Yacovitch, T. I.; Neumark, D. M. Slow photoelectron velocity-map imaging spectroscopy of cold thiozonide (S_3^-). *The Journal of Physical Chemistry A* **2013**, *117*, 8126–8131.

(240) Nee, M. J. Chemical dynamics and structure studied with slow electron velocity map imaging spectroscopy and infrared dissociation, English, Ph.D. Thesis, 2005, p 133.

(241) Zhou, J. Slow electron velocity-map imaging spectroscopy of small radicals and infrared multiphoton dissociation study of solvated systems, English, Ph.D. Thesis, 2007, p 221.

(242) Garand, E. Slow photoelectron imaging and infrared dissociation spectroscopy of ionic clusters, English, Ph.D. Thesis, 2010, p 264.

(243) Yacovitch, T. I. Slow Photoelectron Velocity-Map Imaging of Transient Species and Infrared Multiple Photon Dissociation of Atmospherically Relevant Anion Clusters, English, Ph.D. Thesis, 2012, p 292.

(244) Weichman, M. L. Slow Photoelectron Velocity-Map Imaging and Infrared Photodissociation Spectroscopy of Cryo-Cooled Molecular and Cluster Anions, English, Ph.D. Thesis, 2017, p 391.

(245) Even, U.; Jortner, J.; Noy, D.; Lavie, N.; Cossart-Magos, C. Cooling of large molecules below 1 K and He clusters formation. *The Journal of Chemical Physics* **2000**, *112*, 8068–8071.

(246) Simons, J. Molecular anions. *The Journal of Physical Chemistry A* **2008**, *112*, 6401–6511.

(247) DePuy, C.; Bierbaum, V. M.; Flippin, L.; Grabowski, J. J.; King, G. K.; Schmitt, R. J.; Sullivan, S. Gas-phase reactions of anions with substituted silanes. *Journal of the American Chemical Society* **1980**, *102*, 5012–5015.

(248) Dietz, T. G.; Duncan, M. A.; Powers, D. E.; Smalley, R. E. Laser production of supersonic metal cluster beams. *The Journal of Chemical Physics* **1981**, *74*, 6511–6512.

(249) Powers, D. E.; Hansen, S. G.; Geusic, M.; Puiu, A.; Hopkins, J.; Dietz, T.; Duncan, M.; Langridge-Smith, P.; Smalley, R. Supersonic metal cluster beams: laser photoionization studies of copper cluster (Cu_2). *The Journal of Physical Chemistry* **1982**, *86*, 2556–2560.

(250) Geusic, M.; Morse, M.; O'brien, S.; Smalley, R. Surface reactions of metal clusters I: The fast flow cluster reactor. *Review of Scientific Instruments* **1985**, *56*, 2123–2130.

(251) Ramabhadran, R. O.; Mann, J. E.; Waller, S. E.; Rothgeb, D. W.; Jarrold, C. C.; Raghavachari, K. New insights on photocatalytic H_2 liberation from water using transition-metal oxides: lessons from cluster models of molybdenum and tungsten oxides. *Journal of the American Chemical Society* **2013**, *135*, 17039–17051.

(252) Fagiani, M. R.; Song, X.; Debnath, S.; Gewinner, S.; Schöllkopf, W.; Asmis, K. R.; Bischoff, F. A.; Müller, F.; Sauer, J. Dissociative water adsorption by $Al_3O_4^+$ in the gas phase. *The journal of physical chemistry letters* **2017**, *8*, 1272–1277.

(253) Grimm, R.; Weidemüller, M.; Ovchinnikov, Y. B. Optical dipole traps for neutral atoms. *Advances in atomic, molecular, and optical physics* **2000**, *42*, 95–170.

(254) Gerlich, D. Ion-neutral collisions in a 22-pole trap at very low energies. *Physica Scripta* **1995**, *1995*, 256.

(255) Teloy, E.; Gerlich, D. Integral cross sections for ion—molecule reactions. I. The guided beam technique. *Chemical Physics* **1974**, *4*, 417–427.

(256) Mikosch, J.; Frühling, U.; Trippel, S.; Otto, R.; Hlavenka, P.; Schwalm, D.; Weidemüller, M.; Wester, R. Evaporation of trapped anions studied with a 22-pole ion trap in tandem time-of-flight configuration. *Physical Review A* **2008**, *78*, 023402.

(257) Majima, T.; Santambrogio, G.; Bartels, C.; Terasaki, A.; Kondow, T.; Meinen, J.; Leisner, T. Spatial distribution of ions in a linear octopole radio-frequency ion trap in the space-charge limit. *Physical Review A* **2012**, *85*, 053414.

(258) Levine, R. D., *Molecular Reaction Dynamics*; Cambridge University Press: 2005.

(259) Wiley, W. C.; McLaren, I. Time-of-Flight Mass Spectrometer with Improved Resolution. *Rev. Sci. Instrum.* **1955**, *26*, 1150–1157.

(260) Boesl, U. Time-of-flight mass spectrometry: introduction to the basics. *Mass spectrometry reviews* **2017**, *36*, 86–109.

(261) Bakker, J. A beam-modulated time-of-flight mass spectrometer. II. Experimental work. *Journal of Physics E: Scientific Instruments* **1974**, *7*, 364.

(262) Bakker, J. A beam-modulated time-of-flight mass spectrometer. I. Theoretical considerations. *Journal of Physics E: Scientific Instruments* **1973**, *6*, 785.

(263) Carrascosa, E.; Meyer, J.; Wester, R. Imaging the dynamics of ion–molecule reactions. *Chemical Society Reviews* **2017**, *46*, 7498–7516.

(264) Bartels, C. Angular distributions of photoelectrons from cold, size-selected sodium cluster anions. **2008**.

(265) León, I.; Yang, Z.; Liu, H.-T.; Wang, L.-S. The design and construction of a high-resolution velocity-map imaging apparatus for photoelectron spectroscopy studies of size-selected clusters. *Review of Scientific Instruments* **2014**, *85*, 083106.

(266) Townsend, D.; Minitti, M. P.; Suits, A. G. Direct current slice imaging. *Review of scientific instruments* **2003**, *74*, 2530–2539.

(267) Cavanagh, S.; Gibson, S.; Gale, M.; Dedman, C. J.; Roberts, E.; Lewis, B. High-resolution velocity-map-imaging photoelectron spectroscopy of the O^- photodetachment fine-structure transitions. *Physical Review A* **2007**, *76*, 052708.

(268) Ogi, Y.; Kohguchi, H.; Niu, D.; Ohshimo, K.; Suzuki, T. Super-resolution photoelectron imaging with real-time subpixelation by field programmable gate array and its application to NO and benzene photoionization. *The Journal of Physical Chemistry A* **2009**, *113*, 14536–14544.

(269) Harrison, A. W.; Ryazanov, M.; Sullivan, E. N.; Neumark, D. M. Photodissociation dynamics of the methyl perthiyl radical at 248 and 193 nm using fast-beam photofragment translational spectroscopy. *The Journal of chemical physics* **2016**, *145*, 024305.

(270) Li, W.; Chambreau, S. D.; Lahankar, S. A.; Suits, A. G. Megapixel ion imaging with standard video. *Review of scientific instruments* **2005**, *76*, 063106.

(271) M. B. Doyle, C. A.; Suits, A. G. NuACQ, 2012.

(272) Carter, M.; Patchett, B.; Read, P.; Waltham, N.; Van Breda, I. New techniques in photon counting detectors. *Nuclear Instruments and Methods in Physics Research Section A: Accelerators, Spectrometers, Detectors and Associated Equipment* **1991**, *310*, 305–310.

(273) Betzig, E.; Patterson, G. H.; Sougrat, R.; Lindwasser, O. W.; Olenych, S.; Bonifacino, J. S.; Davidson, M. W.; Lippincott-Schwartz, J.; Hess, H. F. Imaging intracellular fluorescent proteins at nanometer resolution. *Science* **2006**, *313*, 1642–1645.

(274) Hansen, E. W.; Law, P.-L. Recursive methods for computing the Abel transform and its inverse. *JOSA A* **1985**, *2*, 510–520.

(275) Dick, B. Inverting ion images without Abel inversion: maximum entropy reconstruction of velocity maps. *Physical Chemistry Chemical Physics* **2014**, *16*, 570–580.

(276) Dribinski, V.; Ossadtchi, A.; Mandelshtam, V. A.; Reisler, H. Reconstruction of Abel-transformable images: The Gaussian basis-set expansion Abel transform method. *Review of Scientific Instruments* **2002**, *73*, 2634–2642.

(277) Garcia, G. A.; Nahon, L.; Powis, I. Two-dimensional charged particle image inversion using a polar basis function expansion. *Review of Scientific Instruments* **2004**, *75*, 4989–4996.

(278) Dick, B. MELEXIR: maximum entropy Legendre expanded image reconstruction. A fast and efficient method for the analysis of velocity map imaging or photoelectron imaging data. *Physical Chemistry Chemical Physics* **2019**, *21*, 19499–19512.

(279) Blondel, C.; Chaibi, W.; Delsart, C.; Drag, C.; Goldfarb, F.; Kröger, S. The electron affinities of O, Si, and S revisited with the photodetachment microscope. *The European Physical Journal D-Atomic, Molecular, Optical and Plasma Physics* **2005**, *33*, 335–342.

(280) Blondel, C.; Delsart, C.; Goldfarb, F. Electron spectrometry at the μeV level and the electron affinities of Si and F. *Journal of Physics B: Atomic, Molecular and Optical Physics* **2001**, *34*, L281.

(281) Berzinsh, U.; Gustafsson, M.; Hanstorp, D.; Klinkmüller, A.; Ljungblad, U.; Mårten sson-Pendrill, A.-M. Isotope shift in the electron affinity of chlorine. *Phys. Rev. A* **1995**, *51*, 231–238.

(282) Neumark, D.; Lykke, K.; Andersen, T.; Lineberger, W. Laser photodetachment measurement of the electron affinity of atomic oxygen. *Physical Review A* **1985**, *32*, 1890.

(283) Blondel, C.; Chaibi, W.; Delsart, C.; Drag, C. The fine structure of S and S^- measured with the photodetachment microscope. *Journal of Physics B: Atomic, Molecular and Optical Physics* **2006**, *39*, 1409.

(284) Moore, C. E., *Tables of spectra of hydrogen, carbon, nitrogen, and oxygen atoms and ions*, 1993.

(285) Martin, W. C.; Zalubas, R.; Musgrove, A. Energy Levels of Sulfur, S i through S xvi. *Journal of physical and chemical reference data* **1990**, *19*, 821–880.

(286) Moore, C. E. Atomic Energy Levels as Derived from the Analyses of Optical Spectra. **1971**, *I*.

(287) Radziemski, L. J.; Kaufman, V. Wavelengths, energy levels, and analysis of neutral atomic chlorine (Cl I). *JOSA* **1969**, *59*, 424–443.

(288) Scheer, M.; Brodie, C. A.; Bilodeau, R. C.; Haugen, H. K. Laser spectroscopic measurements of binding energies and fine-structure splittings of Co^-, Ni^-, Rh^-, and Pd^-. *Physical Review A* **1998**, *58*, 2051.

(289) Gascooke, J. R.; Gibson, S. T.; Lawrance, W. D. A "circularisation" method to repair deformations and determine the centre of velocity map images. *The Journal of chemical physics* **2017**, *147*, 013924.

(290) Bethune, D. Dye cell design for high-power low-divergence excimer-pumped dye lasers. *Applied optics* **1981**, *20*, 1897–1899.

(291) Stoicheff, B. High resolution Raman spectroscopy of gases: IX. Spectra of H_2, HD, and D_2. *Canadian Journal of Physics* **1957**, *35*, 730–741.

(292) James, T.; Schlösser, M.; Fischer, S.; Sturm, M.; Bornschein, B.; Lewis, R. J.; Telle, H. Accurate depolarization ratio measurements for all diatomic hydrogen isotopologues. *Journal of Raman Spectroscopy* **2013**, *44*, 857–865.

(293) Grossmann, B.; Singh, U.; Higdon, N.; Cotnoir, L.; Wilkerson, T.; Browell, E. Raman-shifted dye laser for water vapor DIAL measurements. *Applied optics* **1987**, *26*, 1617–1621.

(294) Yamamoto, Y.; Murahashi, S.-I.; Moritani, I. Direct and sensitized photodecompositions of 1-phenyldiazoethane: The spin state in the 1, 2-hydrogen migration to the carbene center. *Tetrahedron* **1975**, *31*, 2663–2667.

(295) Stanton, J. F.; Gauss, J. Vibrational structure in the vinylidene anion photoelectron spectrum: Closing the gap between theory and experiment. *The Journal of chemical physics* **1999**, *110*, 6079–6080.

(296) Gerardi, H. K.; Breen, K. J.; Guasco, T. L.; Weddle, G. H.; Gardenier, G. H.; Laaser, J. E.; Johnson, M. A. Survey of Ar-tagged predissociation and vibrationally mediated photodetachment spectroscopies of the vinylidene anion, $C_2H_2^-$. *The Journal of Physical Chemistry A* **2010**, *114*, 1592–1601.

(297) Boyd, R. W., *Nonlinear optics*; Academic press: 2020.

(298) Franken, e. P.; Hill, A. E.; Peters, C.; Weinreich, G. Generation of optical harmonics. *Physical Review Letters* **1961**, *7*, 118.

(299) Maiman, T. H. et al. Stimulated optical radiation in ruby. **1960**.

(300) Michaelsen, T.; Bastian, B.; Strübin, P.; Meyer, J.; Wester, R. Proton transfer dynamics modified by CH-stretching excitation. *Physical Chemistry Chemical Physics* **2020**, *22*, 12382–12388.

(301) Leavitt, C. M.; Wolk, A. B.; Fournier, J. A.; Kamrath, M. Z.; Garand, E.; Van Stipdonk, M. J.; Johnson, M. A. Isomer-specific IR–IR double resonance spectroscopy of D_2-tagged protonated dipeptides prepared in a cryogenic ion trap. *The journal of physical chemistry letters* **2012**, *3*, 1099–1105.

(302) Knorke, H.; Li, H.; Warneke, J.; Liu, Z.-F.; Asmis, K. R. Cryogenic ion trap vibrational spectroscopy of the microhydrated sulfate dianions $SO_4^{2-}(H_2O)_{3-8}$. *Physical Chemistry Chemical Physics* **2020**, *22*, 27732–27745.

(303) Paschotta, R., *Encyclopedia of laser physics and technology*; Wiley-vch: 2008; Vol. 1.

(304) Rosenbaum, N. H.; Owrutsky, J. C.; Tack, L. M.; Saykally, R. J. Velocity modulation laser spectroscopy of negative ions: the infrared spectrum of hydroxide (OH^-). *The Journal of chemical physics* **1986**, *84*, 5308–5313.

(305) Kaiser, W.; Spitzer, W.; Kaiser, R.; Howarth, L. Infrared Properties of CaF_2, SrF_2, and BaF_2. *Physical Review* **1962**, *127*, 1950.

(306) Li, H. Refractive index of alkaline earth halides and its wavelength and temperature derivatives. *Journal of Physical and Chemical Reference Data* **1980**, *9*, 161–290.

(307) Daimon, M.; Masumura, A. High-accuracy measurements of the refractive index and its temperature coefficient of calcium fluoride in a wide wavelength range from 138 to 2326 nm. *Applied optics* **2002**, *41*, 5275–5281.

(308) Malitson, I. H. A redetermination of some optical properties of calcium fluoride. *Applied Optics* **1963**, *2*, 1103–1107.

(309) Arnold, D. W.; Xu, C.; Neumark, D. M. Spectroscopy of the transition state: Elementary reactions of the hydroxyl radical studied by photoelectron spectroscopy of $O^-(H_2O)$ and $H_3O_2^-$. *The Journal of chemical physics* **1995**, *102*, 6088–6099.

(310) De Beer, E.; Kim, E.; Neumark, D.; Gunion, R.; Lineberger, W. Transition state spectroscopy of the OH + H_2 → H_2O + H reaction via photodetachment of H_3O^- and D_3O^-. *The Journal of Physical Chemistry* **1995**, *99*, 13627–13636.

(311) Sugiura, Y.; Takayanagi, T. Franck–Condon simulations of transition-state spectra for the OH + H_2O and OD + D_2O reactions. *Physical Chemistry Chemical Physics* **2020**, *22*, 20685–20692.

(312) Flygare, W. H. Molecular relaxation. *Accounts of Chemical Research* **1968**, *1*, 121–127.

(313) Wang, T.-H.; Fang, Z.; Gist, N. W.; Li, S.; Dixon, D. A.; Gole, J. L. Computational study of the hydrolysis reactions of the ground and first excited triplet states of small TiO_2 nanoclusters. *J. Phys. Chem. C* **2011**, *115*, 9344–9360.

(314) Marsh, B. M.; Voss, J. M.; Garand, E. A dual cryogenic ion trap spectrometer for the formation and characterization of solvated ionic clusters. *The Journal of chemical physics* **2015**, *143*, 204201.

(315) Moore, J. H.; Davis, C. C.; Coplan, M. A.; Greer, S. C., *Building scientific apparatus*; Cambridge University Press: 2009.

(316) Huber, M.; Harvey, A., *Viscosity of Gases*; 92nd Ed. CRC-Press, Boca Raton, FL: 2011.

(317) Wadhwa, C., *High voltage engineering*; New Age International: 2006.

(318) Lieberman, M. A.; Lichtenberg, A. J., *Principles of plasma discharges and materials processing*; John Wiley & Sons: 2005.

(319) Malović, G.; Strinić, A.; Zivanov, S.; Marić, D.; Petrović, Z. L. Measurements and analysis of excitation coefficients and secondary electron yields in Townsend dark discharges. *Plasma Sources Science and Technology* **2003**, *12*, S1.

(320) Marić, D.; Savić, M.; Sivoš, J.; Škoro, N.; Radmilović-Radjenović, M.; Malović, G.; Petrović, Z. L. Gas breakdown and secondary electron yields. *The European Physical Journal D* **2014**, *68*, 1–7.

(321) Carazzetti, P.; Shea, H. R. Electrical breakdown at low pressure for planar microelectromechanical systems with 10- to 500-μm gaps. *Journal of Micro/Nanolithography, MEMS, and MOEMS* **2009**, *8*, 031305.

(322) Torres, C.; Reyes, P.; Castillo, F.; Martínez, H. In *Journal of Physics: Conference Series*, 2012; Vol. 370, p 012067.

(323) Chappuis, J. Étude spectroscopique sur l'ozone. *Ann. L'Ecole Norm. Sup.* **1882**, *11*, 137–186.

(324) Monks, P. S. Gas-phase radical chemistry in the troposphere. *Chemical Society Reviews* **2005**, *34*, 376–395.

(325) Kawaguchi, K.; Ishiwata, T.; Tanaka, I.; Hirota, E. Fourier-transform infrared-spectroscopy of the NO_3 radical. *Chemical Physics Letters* **1991**, *180*, 436–440.

(326) Ishiwata, T.; Tanaka, I.; Kawaguchi, K.; Hirota, E. High-resolution infrared spectroscopy of NO_3 in the 2500 cm^{-1} region. *Journal of Molecular Spectroscopy* **1992**, *153*, 167–180.

(327) Kawaguchi, K.; Ishiwata, T.; Hirota, E.; Tanaka, I. Infrared spectroscopy of the NO_3 radical. *Chemical Physics* **1998**, *231*, 193–198.

(328) Kawaguchi, K.; Shimizu, N.; Fujimori, R.; Tang, J.; Ishiwata, T.; Tanaka, I. Fourier transform infrared spectroscopy of the ν_4 hot band of NO_3. *Journal of Molecular Spectroscopy* **2011**, *268*, 85–92.

(329) Kawaguchi, K.; Fujimori, R.; Tang, J.; Ishiwata, T. FTIR spectroscopy of NO_3: perturbation analysis of the $\nu_3 + \nu_4$ state. *Journal of Physical Chemistry A* **2013**, *117*, 13732–13742.

(330) Fujimori, R.; Shimizu, N.; Tang, J.; Ishiwata, T.; Kawaguchi, K. Fourier transform infrared spectroscopy of the ν_2 and ν_4 bands of NO_3. *Journal of Molecular Spectroscopy* **2013**, *283*, 10–17.

(331) Kawaguchi, K.; Fujimori, R.; Tang, J.; Ishiwata, T. On the vibrational assignment in the ground electronic state of NO_3. *Journal of Molecular Spectroscopy* **2015**, *314*, 73–78.

(332) Kawaguchi, K.; Narahara, T.; Fujimori, R.; Tang, J.; Ishiwata, T. Infrared spectroscopy of $2\nu_4$ and $\nu_3 + 2\nu_4$ bands of the NO_3 radical. *Journal of Molecular Spectroscopy* **2017**, *334*, 10–21.

(333) Kawaguchi, K.; Fujimori, R.; Ishiwata, T. Infrared spectroscopy of the $\nu_1 + \nu_4$ and $3\nu_4$ bands of the nitrate radical. *Journal of Molecular Spectroscopy* **2018**, *347*, 56–62.

(334) Kawaguchi, K.; Fujimori, R.; Tang, J.; Ishiwata, T. Infrared spectroscopy of the NO_3 radical from 2000 to 3000 cm^{-1}. *Journal of Molecular Spectroscopy* **2018**, *344*, 6–16.

(335) Nelson, H. H.; Pasternack, L.; Mcdonald, J. R. Laser-induced excitation and emission spectra of nitrate radical (NO_3). *Journal of Physical Chemistry* **1983**, *87*, 876.

(336) Ishiwata, T.; Fujiwara, I.; Naruge, Y.; Obi, K.; Tanaka, I. Study of NO_3 by Laser-Induced Fluorescence. *Journal of Physical Chemistry* **1983**, *87*, 1349–1352.

(337) Kim, B. S.; Hunter, P. L.; Johnston, H. S. NO_3 Radical Studied by Laser-Induced Fluorescence. *Journal of Chemical Physics* **1992**, *96*, 4057–4067.

(338) Ishiwata, T.; Tanaka, I.; Kawaguchi, K.; Hirota, E. Infrared diode laser spectroscopy of the NO_3 ν_3 band. *Journal of Chemical Physics* **1985**, *82*, 2196–2205.

(339) Hirota, E.; Ishiwata, T.; Kawaguchi, K.; Fujitake, M.; Ohashi, N.; Tanaka, I. Near-infrared band of the nitrate radical NO_3 observed by diode laser spectroscopy. *Journal of Chemical Physics* **1997**, *107*, 2829–2838.

(340) Jacox, M. E.; Thompson, W. E. The infrared spectroscopy and photochemistry of NO_3 trapped in solid neon. *Journal of Chemical Physics* **2008**, *129*, 204306.

(341) Jacox, M. E.; Thompson, W. E. $\tilde{A}^2E" - \tilde{X}^2A_2'$ transition of NO_3 trapped in solid neon. *Journal of Physical Chemistry A* **2010**, *114*, 4712–4718.

(342) Okumura, M.; Stanton, J. F.; Deev, A.; Sommar, J. New insights into the Jahn-Teller effect in NO_3 via the dark $A^2E"$ state. *Physica Scripta* **2006**, *73*, C64–C70.

(343) Codd, T.; Chen, M. W.; Roudjane, M.; Stanton, J. F.; Miller, T. A. Jet cooled cavity ringdown spectroscopy of the $\tilde{A}^2E" \leftarrow \tilde{X}^2A_2'$ transition of the NO_3 radical. *Journal of Chemical Physics* **2015**, *142*, 184305.

(344) Davy, R. D.; Schaefer, H. F. Is there an absence of threefold symmetry at the equilibrium geometry of the ground electronic state for NO_3. *Journal of Chemical Physics* **1989**, *91*, 4410–4411.

(345) Kaldor, U. The ground-state geometry of the NO_3 radical. *Chemical Physics Letters* **1990**, *166*, 599–601.

(346) Mayer, M.; Cederbaum, L. S.; Koppel, H. Ground-state dynamics of NO_3 - multimode vibronic borrowing including thermal effects. *Journal of Chemical Physics* **1994**, *100*, 899–911.

(347) Eisfeld, W.; Morokuma, K. Ab initio investigation of the vertical and adiabatic excitation spectrum of NO_3. *Journal of Chemical Physics* **2001**, *114*, 9430–9440.

(348) Stanton, J. F. On the vibronic level structure in the NO_3 radical. I. The ground electronic state. *Journal of Chemical Physics* **2007**, *126*, 134309.

(349) Faraji, S.; Koppel, H.; Eisfeld, W.; Mahapatra, S. Towards a higher-order description of Jahn-Teller coupling effects in molecular spectroscopy: The $\tilde{A}^2$E" state of NO_3. *Chemical Physics* **2008**, *347*, 110–119.

(350) Simmons, C. S.; Ichino, T.; Stanton, J. F. The ν_3 fundamental in NO_3 has been seen near 1060 cm^{-1}, albeit some time ago. *Journal of Physical Chemistry Letters* **2012**, *3*, 1946–1950.

(351) Mukherjee, B.; Mukherjee, S.; Sardar, S.; Shamasundar, K. R.; Adhikari, S. A beyond Born-Oppenheimer treatment of five state molecular system NO_3 and the photodetachment spectra of its anion. *Chemical Physics* **2018**, *515*, 350–359.

(352) Kim, B.; Hammond, B. L.; Lester, W. A.; Johnston, H. S. Ab initio study of the vibrational-spectra of NO_3. *Chemical Physics Letters* **1990**, *168*, 131–134.

(353) Stanton, J. F.; Gauss, J.; Bartlett, R. J. Potential nonrigidity of the NO_3 radical. *Journal of Chemical Physics* **1991**, *94*, 4084–4087.

(354) Stanton, J. F.; Gauss, J.; Bartlett, R. J. On the choice of orbitals for symmetry-breaking problems with application to NO_3. *Journal of Chemical Physics* **1992**, *97*, 5554–5559.

(355) Beckers, H.; Willner, H.; Jacox, M. E. Conflicting observations resolved by a far IR and UV/Vis study of the NO_3 radical. *Chem. Phys. Chem.* **2009**, *10*, 706–710.

(356) Ishiwata, T.; Nakano, Y.; Kawaguchi, K.; Hirota, E.; Tanaka, I. Analyses of the infrared absorption bands of $^{15}NO_3$ in the 1850-3150 cm^{-1} region. *Journal of Physical Chemistry A* **2010**, *114*, 980–986.

(357) Yamada, K.; Ross, S. Paper 2E6-28, Conference Paper, 2016.

(358) Köppel, H.; Domcke, W.; Cederbaum, L. S. Multimode molecular-dynamics beyond the born-oppenheimer approximation. *Advances in Chemical Physics* **1984**, *57*, 59–246.

(359) Asmis, K. R.; Taylor, T. R.; Neumark, D. M. Anion photoelectron spectroscopy of B_2N^-. *Journal of Chemical Physics* **1999**, *111*, 8838–8851.

(360) Signorell, R.; Merkt, F. General symmetry selection rules for the photoionization of polyatomic molecules. *Molecular Physics* **1997**, *92*, 793–804.

(361) Sanov, A. Laboratory-Frame Photoelectron Angular Distributions in Anion Photodetachment: Insight into Electronic Structure and Intermolecular Interactions. *Annu. Rev. Phys. Chem.* **2014**, *65*, 341–363.

(362) Ellison, G. B.; Engelking, P. C.; Lineberger, W. C. Experimental-Determination of Geometry and Electron-Affinity of CH_3. *Journal of the American Chemical Society* **1978**, *100*, 2556–2558.

(363) Rienstra-Kiracofe, J. C.; Tschumper, G. S.; Schaefer, H. F.; Nandi, S.; Ellison, G. B. Atomic and molecular electron affinities: Photoelectron experiments and theoretical computations. *Chemical Reviews* **2002**, *102*, 231–282.

(364) Ichino, T.; Wren, S. W.; Vogelhuber, K. M.; Gianola, A. J.; Lineberger, W. C.; Stanton, J. F. The vibronic level structure of the cyclopentadienyl radical. *Journal of Chemical Physics* **2008**, *129*, 084310.

(365) Lineberger, W. C. Once upon Anion: A Tale of Photodetachment. *Annual Review of Physical Chemistry* **2013**, *64*, 21–36.

(366) Leopold, D. G.; Ho, J.; Lineberger, W. C. Photoelectron-Spectroscopy of Mass-Selected Metal Cluster Anions. I. Cu_n^- n=1-10. *Journal of Chemical Physics* **1987**, *86*, 1715–1726.

(367) Castleman, A. W.; Bowen, K. H. Clusters: Structure, energetics, and dynamics of intermediate states of matter. *Journal of Physical Chemistry* **1996**, *100*, 12911–12944.

(368) Continetti, R. E.; Guo, H. Dynamics of transient species via anion photodetachment. *Chemical Society Reviews* **2017**, *46*, 7650–7667.

(369) Ray, A. W.; Ma, J. Y.; Otto, R.; Li, J.; Guo, H.; Continetti, R. E. Effects of vibrational excitation on the F + $H_2O \rightarrow$ HF + OH reaction: dissociative photodetachment of overtone-excited [F-H-OH]$^-$. *Chemical Science* **2017**, *8*, 7821–7833.

(370) Dousmanis, G. C.; Sanders, T. M.; Townes, C. H. Microwave Spectra of the Free Radicals OH and OD. *Physical Review* **1955**, *100*, 1735–1755.

(371) Beaudet, R. A.; Poynter, R. L. Microwave-Spectra of Molecules of Astrophysical Interest XII. Hydroxyl Radical. *Journal of Physical and Chemical Reference Data* **1978**, *7*, 311–362.

(372) Coxon, J. A. Optimum Molecular Constants and Term Values for the $X^2\Pi(\nu \leq 5)$ and $A^2\Sigma^+(\nu \leq 3)$ States of OH. *Canadian Journal of Physics* **1980**, *58*, 933–949.

(373) Mélen, F.; Sauval, A. J.; Grevesse, N.; Farmer, C. B.; Servais, C.; Delbouille, L.; Roland, G. A new analysis of the OH radical spectrum from solar infrared observations. *Journal of Molecular Spectroscopy* **1995**, *174*, 490–509.

(374) Maillard, J. P.; Chauville, J.; Mantz, A. W. High-resolution emission spectrum of OH in an oxyacetylene flame from 3.7 to 0.9 μm. *Journal of Molecular Spectroscopy* **1976**, *63*, 120–141.

(375) Breyer, F.; Frey, P.; Hotop, H. High-Resolution Photoelectron Spectrometry of Negative-Ions - Rotational Transitions in Laser-Photodetachment of OH^-, SH^-, SD^-. *Zeitschrift Fur Physik a-Hadrons and Nuclei* **1981**, *300*, 7–24.

(376) Schulz, P. A.; Mead, R. D.; Jones, P. L.; Lineberger, W. C. OH^- and OD^- Threshold Photodetachment. *Journal of Chemical Physics* **1982**, *77*, 1153–1165.

(377) Smith, J. R.; Kim, J. B.; Lineberger, W. C. High-resolution threshold photodetachment spectroscopy of OH^-. *Physical Review A* **1997**, *55*, 2036–2043.

(378) Otto, R.; Von Zastrow, A.; Best, T.; Wester, R. Internal state thermometry of cold trapped molecular anions. *Phys. Chem. Chem. Phys.* **2013**, *15*, 612–618.

(379) Lakhmanskaya, O.; Simpson, M.; Wester, R. Vibrational overtone spectroscopy of cold trapped hydroxyl anions. *Physical Review A* **2020**, *102*, 012809.

(380) Jusko, P.; Asvany, O.; Wallerstein, A. C.; Brunken, S.; Schlemmer, S. Two-Photon Rotational Action Spectroscopy of Cold OH^- at 1 ppb Accuracy. *Physical Review Letters* **2014**, *112*, 253005.

(381) Bosenberg, W. R.; Guyer, D. R. Broadly Tunable, Single-frequency Optical Parametric Frequency-conversion System. *Journal of the Optical Society of America B-Optical Physics* **1993**, *10*, 1716–1722.

(382) Weltner, W.; Vanzee, R. J. Carbon Molecules, Ions, and Clusters. *Chemical Reviews* **1989**, *89*, 1713–1747.

(383) Pitzer, K. S.; Clementi, E. Large Molecules in Carbon Vapor. *Journal of the American Chemical Society* **1959**, *81*, 4477–4485.

(384) Raghavachari, K.; Binkley, J. S. Structure, Stability, and Fragmentation of Small Carbon Clusters. *Journal of Chemical Physics* **1987**, *87*, 2191–2197.

(385) Martin, J. M. L.; Taylor, P. R. Structure and vibrations of small carbon clusters from coupled-cluster calculations. *Journal of Physical Chemistry* **1996**, *100*, 6047–6056.

(386) Smalley, R. E. Self-Assembly of the Fullerenes. *Accounts of Chemical Research* **1992**, *25*, 98–105.

(387) Von Helden, G.; Hsu, M. T.; Gotts, N.; Bowers, M. T. Carbon Cluster Cations with up to 84 Atoms - Structures, Formation Mechanism, and Reactivity. *Journal of Physical Chemistry* **1993**, *97*, 8182–8192.

(388) Von Helden, G.; Kemper, P. R.; Gotts, N. G.; Bowers, M. T. Isomers of Small Carbon Cluster Anions - Linear-Chains with up to 20 Atoms. *Science* **1993**, *259*, 1300–1302.

(389) Szczepanski, J.; Vala, M. Correlation of Infrared and Uv Visible Bands of Matrix-Isolated Carbon Clusters. *Journal of Physical Chemistry* **1991**, *95*, 2792–2798.

(390) Szczepanski, J.; Ekern, S.; Chapo, C.; Vala, M. Infrared spectroscopy of matrix-isolated carbon clusters, with emphasis on C_8 and C_9. *Chemical Physics* **1996**, *211*, 359–366.

(391) Forney, D.; Freivogel, P.; Grutter, M.; Maier, J. P. Electronic absorption spectra of linear carbon chains in neon matrices . IV. C_{2n+1} n=2-7. *Journal of Chemical Physics* **1996**, *104*, 4954–4960.

(392) Miki, M.; Wakabayashi, T.; Momose, T.; Shida, T. Infrared spectroscopic studies of carbon clusters trapped in solid parahydrogen. *Journal of Physical Chemistry* **1996**, *100*, 12135–12137.

(393) Kranze, R. H.; Rittby, C. M. L.; Graham, W. R. M. Fourier transform infrared and theoretical isotopic study of the $\nu_4(\sigma_u)$ and $\nu_5(\sigma_u)$ modes of linear C_7. *Journal of Chemical Physics* **1996**, *105*, 5313–5320.

(394) Tam, S.; Macler, M.; Fajardo, M. E. Matrix isolation spectroscopy of laser ablated carbon species in Ne, D_2, and H_2 matrices. *Journal of Chemical Physics* **1997**, *106*, 8955–8963.

(395) Vala, M.; Chandrasekhar, T.; Szczepanski, J.; Pellow, R. *High Temp. Sci.* **1988**, *27*, 19.

(396) Gonzalez, E.; Rittby, C. M. L.; Graham, W. R. M. Isotopic Study of New Fundamentals and Combination Bands of Linear C_5, C_7, and C_9 in Solid Ar. *Journal of Physical Chemistry A* **2011**, *115*, 2533–2539.

(397) Heath, J. R.; Sheeks, R. A.; Cooksy, A. L.; Saykally, R. J. The C_7 Cluster - Structure and Infrared Frequencies. *Science* **1990**, *249*, 895–897.

(398) Heath, J. R.; Saykally, R. J. The C_9 Cluster - Structure and Infrared Frequencies. *Journal of Chemical Physics* **1990**, *93*, 8392–8394.

(399) Heath, J. R.; Saykally, R. J. Infrared-Laser Absorption-Spectroscopy of the ν_4 (σ_u) Fundamental and Associated ν_{11} (π_u) Hot Band of C_7 - Evidence for Alternating Rigidity in Linear Carbon Clusters. *Journal of Chemical Physics* **1991**, *94*, 1724–1729.

(400) Heath, J. R.; Van Orden, A.; Kuo, E.; Saykally, R. J. The ν_5 Band of C_7. *Chemical Physics Letters* **1991**, *182*, 17–20.

(401) Van Orden, A.; Hwang, H. J.; Kuo, E. W.; Saykally, R. J. Infrared-Laser Spectroscopy of Jet-Cooled Carbon Clusters - the Bending Dynamics of Linear C_9. *Journal of Chemical Physics* **1993**, *98*, 6678–6683.

(402) Van Orden, A.; Provencal, R. A.; Keutsch, F. N.; Saykally, R. J. Infrared laser spectroscopy of jet-cooled carbon clusters: The ν_5 band of linear C_9. *Journal of Chemical Physics* **1996**, *105*, 6111–6116.

(403) Casaes, R.; Provencal, R.; Paul, J.; Saykally, R. J. High resolution pulsed infrared cavity ringdown spectroscopy: Application to laser ablated carbon clusters. *Journal of Chemical Physics* **2002**, *116*, 6640–6647.

(404) Krieg, J.; Lutter, V.; Hardy, F. X.; Schlemmer, S.; Giesen, T. F. The ν_5 antisymmetric stretching mode of linear C_7 revisited in high resolution. *Journal of Chemical Physics* **2010**, *132*, DOI: 10.1063/1.3431964.

(405) Boguslavskiy, A. E.; Maier, J. P. Gas phase electronic spectra of the carbon chains C_5, C_6, C_8, and C_9. *Journal of Chemical Physics* **2006**, *125*, DOI: 10.1063/1.2276848.

(406) Kolbuszewski, M. Ab-Initio Study of the Optical-Spectra of C_3, C_5, and C_7 Chains. *Journal of Chemical Physics* **1995**, *102*, 3679–3684.

(407) Botschwina, P. The equilibrium structures of linear carbon clusters of type C_{2n+l} (n=1-4). *Theoretical Chemistry Accounts* **2000**, *104*, 160–162.

(408) Cao, Z. X.; Peyerimhoff, S. D.; Grein, F.; Zhang, Q. Ab initio multireference configuration interaction study of the electronic spectra of carbon chain anions C^-_{2n+1} (n=2-5). *Journal of Chemical Physics* **2001**, *115*, 2062–2068.

(409) Kurtz, J.; Adamowicz, L. Theoretical Vibrations of Carbon Chain C_3, C_4, C_5, C_6, C_7, C_8, C_9. *Astrophysical Journal* **1991**, *370*, 784–790.

(410) Szczepanski, J.; Ekern, S.; Vala, M. Vibrational spectroscopy of small matrix-isolated linear carbon cluster anions. *Journal of Physical Chemistry A* **1997**, *101*, 1841–1847.

(411) Freivogel, P.; Grutter, M.; Forney, D.; Maier, J. P. Infrared bands of mass-selected carbon chains C_n (n=8-12) and C_n^- (n=5-10, 12) in neon matrices. *Chemical Physics* **1997**, *216*, 401–406.

(412) Szczepanski, J.; Fuller, J.; Ekern, S.; Vala, M. Electronic absorption and resonance Raman spectra of large linear carbon clusters isolated in solid argon. *Spectrochimica Acta Part a-Molecular and Biomolecular Spectroscopy* **2001**, *57*, 775–786.

(413) Ohara, M.; Shiromaru, H.; Achiba, Y. Resonance-enhanced multiphoton electron detachment spectra of C_7^-, C_9^-, and C_{11}^-. *Journal of Chemical Physics* **1997**, *106*, 9992–9995.

(414) Tulej, M.; Kirkwood, D. A.; Maccaferri, G.; Dopfer, O.; Maier, J. P. Electronic spectra of linear carbon anions. *Chemical Physics* **1998**, *228*, 293–299.

(415) Lakin, N. M.; Pachkov, M.; Tulej, M.; Maier, J. P.; Chambaud, G.; Rosmus, P. Theoretical and experimental study of the $\tilde{A}^2\Pi_u - \tilde{X}^2\Pi_g$ band system of C_7^-. *Journal of Chemical Physics* **2000**, *113*, 9586–9592.

(416) Watts, J. D.; Bartlett, R. J. A Theoretical-Study of Linear Carbon Cluster Monoanions, C_n^-, and Dianions, C_n^{2-} (n=2-10). *Journal of Chemical Physics* **1992**, *97*, 3445–3457.

(417) Botschwina, P. A coupled cluster study of linear C_7: no evidence of floppiness. *Chemical Physics Letters* **2002**, *354*, 148–155.

(418) Giuffreda, M. G.; Deleuze, M. S.; Francois, J. P. Structural, rotational, vibrational, and electronic properties of carbon cluster anions C_n^- (n=3-13). *Journal of Physical Chemistry A* **2002**, *106*, 8569–8582.

(419) Yang, S.; Taylor, K. J.; Craycraft, M. J.; Conceicao, J.; Pettiette, C. L.; Cheshnovsky, O.; Smalley, R. E. Ups of 2-30-Atom Carbon Clusters - Chains and Rings. *Chemical Physics Letters* **1988**, *144*, 431–436.

(420) Arnold, D. W.; Bradforth, S. E.; Kitsopoulos, T. N.; Neumark, D. M. Vibrationally Resolved Spectra of C_2-C_{11} by Anion Photoelectron-Spectroscopy. *Journal of Chemical Physics* **1991**, *95*, 8753–8764.

(421) Kendall, R. A.; Dunning, T. H.; Harrison, R. J. Electron-Affinities of the 1st-Row Atoms Revisited - Systematic Basis-Sets and Wave-Functions. *Journal of Chemical Physics* **1992**, *96*, 6796–6806.

(422) Knowles, P. J.; Hampel, C.; Werner, H. J. Coupled-Cluster Theory for High-Spin, Open-Shell Reference Wave-Functions. *Journal of Chemical Physics* **1993**, *99*, 5219–5227.

(423) Watts, J. D.; Gauss, J.; Bartlett, R. J. Coupled-Cluster Methods with Noniterative Triple Excitations for Restricted Open-Shell Hartree-Fock and Other General Single Determinant Reference Functions - Energies and Analytical Gradients. *Journal of Chemical Physics* **1993**, *98*, 8718–8733.

(424) Martin, J. M. L.; Francois, J. P.; Gijbels, R. Ab initio Study of the Infrared-Spectra of Linear C_n Clusters (n = 6-9). *Journal of Chemical Physics* **1990**, *93*, 8850–8861.

(425) Martin, J. M. L.; Elyazal, J.; Francois, J. P. Structure and Vibrational-Spectra of Carbon Clusters C_N (N=2-10, 12, 14, 16, 18) Using Density-Functional Theory Including Exact Exchange Contributions. *Chemical Physics Letters* **1995**, *242*, 570–579.

(426) Werner, H. J.; Knowles, P. J.; Knizia, G.; Manby, F. R.; Schutz, M. Molpro: a general-purpose quantum chemistry program package. *Wiley Interdisciplinary Reviews-Computational Molecular Science* **2012**, *2*, 242–253.

(427) Frisch, M. J. et al. Gaussian 09, Revision C.01, Computer Program, 2009.

(428) Dolgounitcheva, O.; Zakrzewski, V. G.; Ortiz, J. V. Electron binding energies of nucleobases and nucleotides. *International Journal of Quantum Chemistry* **2002**, *90*, 1547–1554.

(429) Spanner, M.; Patchkovskii, S.; Zhou, C. Y.; Matsika, S.; Kotur, M.; Weinacht, T. C. Dyson norms in XUV and strong-field ionization of polyatomics: Cytosine and uracil. *Physical Review A* **2012**, *86*, DOI: 10.1103/Physreva.86.053406.

(430) Krylov, A. I.; Gill, P. M. W. Q-Chem: an engine for innovation. *Wiley Interdisciplinary Reviews-Computational Molecular Science* **2013**, *3*, 317–326.

(431) Herbert, J. M.; Zhang, X.; Morrison, A. F.; Liu, J. Beyond Time-Dependent Density Functional Theory Using Only Single Excitations: Methods for Computational Studies of Excited States in Complex Systems. *Accounts of Chemical Research* **2016**, *49*, 931–941.

(432) Brinkley, D.; Dietrich, M.; Engel, T.; Farrall, P.; Gantner, G.; Schafer, A.; Szuchmacher, A. A modulated molecular beam study of the extent of H_2O dissociation on TiO_2 (110). *Surf. Sci.* **1998**, *395*, 292–306.

(433) DeVine, J. A.; Weichman, M. L.; Babin, M. C.; Neumark, D. M. Slow photoelectron velocity-map imaging of cold tert-butyl peroxide. *Journal of Chemical Physics* **2017**, *147*, DOI: Artn01391510.1063/1.4979951.

(434) Weichman, M. L.; Kim, J. B.; Neumark, D. M. Slow Photoelectron Velocity-Map Imaging Spectroscopy of the ortho-Hydroxyphenoxide Anion. *Journal of Physical Chemistry A* **2015**, *119*, 6140–6147.

(435) Ou, Q.; Fatehi, S.; Alguire, E.; Shao, Y.; Subotnik, J. E. Derivative couplings between TDDFT excited states obtained by direct differentiation in the Tamm-Dancoff approximation. *The Journal of Chemical Physics* **2014**, *141*, 024114.

(436) Forney, D.; Grutter, M.; Freivogel, P.; Maier, J. P. Electronic absorption spectra of carbon chain anions C_{2n+1}^- (n=2-5) in neon matrices. *Journal of Physical Chemistry A* **1997**, *101*, 5292–5295.

(437) Shao, Y. H. et al. Advances in molecular quantum chemistry contained in the Q-Chem 4 program package. *Molecular Physics* **2015**, *113*, 184–215.

(438) Melinon, P.; Masenelli, B.; Tournus, F.; Perez, A. Playing with carbon and silicon at the nanoscale. *Nature Materials* **2007**, *6*, 479–490.

(439) Zetterling, C.-M., *Process Technology for Silicon carbide Devices*; EMIS Processsing Series; The Institution of Electrical Engineers: New York, 2002.

(440) Honea, E. C.; Ogura, A.; Murray, C. A.; Raghavachari, K.; Sprenger, W. O.; Jarrold, M. F.; Brown, W. L. Raman-Spectra of Size-Selected Silicon Clusters and Comparison with Calculated Structures. *Nature* **1993**, *366*, 42–44.

(441) Li, S.; Vanzee, R. J.; Weltner, W.; Raghavachari, K. Si_3-Si_7 - Experimental and Theoretical Infrared-Spectra. *Chemical Physics Letters* **1995**, *243*, 275–280.

(442) Xu, C. S.; Taylor, T. R.; Burton, G. R.; Neumark, D. M. Vibrationally reserved photoelectron spectroscopy of silicon cluster anions Si_n^- (n=3-7). *Journal of Chemical Physics* **1998**, *108*, 1395–1406.

(443) Presillamarquez, J. D.; Graham, W. R. M. Vibrational-Spectra of Tetra-Atomic Silicon-Carbon Clusters. I. Rhomboidal Si_3C in Ar at 10K. *Journal of Chemical Physics* **1992**, *96*, 6509–6514.

(444) Presillamarquez, J. D.; Gay, S. C.; Rittby, C. M. L.; Graham, W. R. M. Vibrational-Spectra of Tetra-Atomic Silicon-Carbon Clusters. II. Si_2C_2 in Ar at 10K. *Journal of Chemical Physics* **1995**, *102*, 6354–6361.

(445) McCarthy, M. C.; Apponi, A. J.; Thaddeus, P. A second rhomboidal isomer of SiC_3. *Journal of Chemical Physics* **1999**, *111*, 7175–7178.

(446) McCarthy, M. C.; Apponi, A. J.; Thaddeus, P. Rhomboidal SiC_3. *Journal of Chemical Physics* **1999**, *110*, 10645–10648.

(447) McCarthy, M. C.; Apponi, A. J.; Gottlieb, C. A.; Thaddeus, P. Laboratory detection of five new linear silicon carbides: SiC_3, SiC_5, SiC_6, SiC_7, and SiC_8. *Astrophysical Journal* **2000**, *538*, 766–772.

(448) Stanton, J. F.; Dudek, J.; Theule, P.; Gupta, H.; McCarthy, M. C.; Thaddeus, P. Laser spectroscopy of Si_3C. *Journal of Chemical Physics* **2005**, *122*, DOI: `Artn12431410.1063/1.1869981`.

(449) Reilly, N. J.; Steglich, M.; Kokkin, D. L.; Maier, J. P.; Stanton, J. F.; McCarthy, M. C. Optical spectrum of Si_3C, and a re-analysis of the $\tilde{C}^1B_1 \leftarrow \tilde{X}^1A_1$ transition. *Journal of Molecular Spectroscopy* **2015**, *310*, 135–140.

(450) Steglich, M.; Mater, J. P. Electronic transitions of jet-cooled SiC_2, Si_2C_n (n=1-3), Si_3C_n (n=1,2), and SiC_6H_4 between 250 and 710 nm. *Astrophysical Journal* **2015**, *801*, DOI: `Artn11910.1088/0004-637x/801/2/119`.

(451) Truong, N. X.; Savoca, M.; Harding, D. J.; Fielicke, A.; Dopfer, O. Vibrational spectra and structures of Si_nC clusters (n=3-8). *Physical Chemistry Chemical Physics* **2015**, *17*, 18961–18970.

(452) Nakajima, A.; Taguwa, T.; Nakao, K.; Gomei, M.; Kishi, R.; Iwata, S.; Kaya, K. Photoelectron-Spectroscopy of Silicon-Carbon Cluster Anions ($Si_nC_m^-$). *Journal of Chemical Physics* **1995**, *103*, 2050–2057.

(453) Davico, G. E.; Schwartz, R. L.; Lineberger, W. C. Photoelectron spectroscopy of C_3Si and C_4Si_2 anions. *Journal of Chemical Physics* **2001**, *115*, 1789–1794.

(454) Stanton, J. F.; Gauss, J.; Christiansen, O. Equilibrium geometries of cyclic SiC_3 isomers. *Journal of Chemical Physics* **2001**, *114*, 2993–2995.

(455) Trucks, G. W.; Bartlett, R. J. Isomers of Si_2C_2 - an Mbpt Study. *Journal of Molecular Structure-Theochem* **1986**, *28*, 423–428.

(456) Lammertsma, K.; Guner, O. F. Structures and Energies of Disilicon Dicarbide, C_2Si_2. *Journal of the American Chemical Society* **1988**, *110*, 5239–5245.

(457) Sudhakar, P. V.; Guner, O. F.; Lammertsma, K. Bond Stretch Isomerism in Rhombic C_2Si_2. *Journal of Physical Chemistry* **1989**, *93*, 7289–7292.

(458) Fitzgerald, G. B.; Bartlett, R. J. Optimum Structures and Vibrational Frequencies of $(SiC)_2$ Clusters. *International Journal of Quantum Chemistry* **1990**, *38*, 121–128.

(459) Alberts, I. L.; Grev, R. S.; Schaefer, H. F. Geometrical Structures and Vibrational Frequencies of the Energetically Low-Lying Isomers of SiC_3. *Journal of Chemical Physics* **1990**, *93*, 5046–5052.

(460) Rittby, C. M. L. An Abinitio Study of the Structure and Infrared-Spectrum of Si_3C. *Journal of Chemical Physics* **1992**, *96*, 6768–6772.

(461) Hunsicker, S.; Jones, R. O. Structure and bonding in mixed silicon-carbon clusters and their anions. *Journal of Chemical Physics* **1996**, *105*, 5048–5060.

(462) Gomei, M.; Kishi, R.; Nakajima, A.; Iwata, S.; Kaya, K. Ab initio MO studies of neutral and anionic SiC_n clusters (n=2-5). *Journal of Chemical Physics* **1997**, *107*, 10051–10061.

(463) Bandyopadhyay, P.; Ten-no, S.; Iwata, S. Structures and photoelectron spectroscopies of $Si_2C_2^-$ studied with ab initio multicanonical Monte Carlo simulation. *Journal of Physical Chemistry A* **1999**, *103*, 6442–6447.

(464) Rintelman, J. M.; Gordon, M. S. Structure and energetics of the silicon carbide clusters SiC_3 and Si_2C_2. *Journal of Chemical Physics* **2001**, *115*, 1795–1803.

(465) Sattelmeyer, K. W.; Schaefer, H. F.; Stanton, J. F. The global minimum structure of SiC_3: The controversy continues. *Journal of Chemical Physics* **2002**, *116*, 9151–9153.

(466) Jiang, Z. Y.; Xu, X. H.; Wu, H. S.; Jin, Z. H. Ab initio investigation of structures and stability of Si_nC_m clusters. *Journal of Physical Chemistry A* **2003**, *107*, 10126–10131.

(467) Kurashige, Y.; Nakano, H.; Hirao, K. The most stable structure of SiC_3 studied by multireference perturbation theory with general multiconfiguration self-consistent field reference functions. *Journal of Physical Chemistry A* **2004**, *108*, 3064–3067.

(468) Rintelman, J. M.; Gordon, M. S.; Fletcher, G. D.; Ivanic, J. A systematic multireference perturbation-theory study of the low-lying states of SiC_3. *Journal of Chemical Physics* **2006**, *124*, DOI: `Artn03430310.1063/1.2140687`.

(469) Linguerri, R.; Rosmus, P.; Carter, S. Anharmonic vibrational levels of the two cyclic isomers of SiC_3. *Journal of Chemical Physics* **2006**, *125*, DOI: `Artn03430510.1063/1.2209693`.

(470) Duan, X. F.; Wei, J.; Burggraf, L.; Weeks, D. Mapping ground-state properties of silicon carbide molecular clusters using quantum mechanical calculations: Si_mC_n and $Si_mC_n^-$ (m, $n \leq 4$). *Computational Materials Science* **2010**, *47*, 630–644.

(471) Yang, T.; Bertels, L.; Dangi, B. B.; Li, X. H.; Head-Gordon, M.; Kaiser, R. I. Gas phase formation of c-SiC_3 molecules in the circumstellar envelope of carbon stars. *Proceedings of the National Academy of Sciences of the United States of America* **2019**, *116*, 14471–14478.

(472) Monkhorst, H. J. Calculation of Properties with Coupled-Cluster Method. *International Journal of Quantum Chemistry* **1977**, 421–432.

(473) Emrich, K. An Extension of the Coupled Cluster Formalism to Excited-States: (II). Approximations and Tests. *Nuclear Physics A* **1981**, *351*, 397–438.

(474) Dalgaard, E.; Monkhorst, H. J. Some Aspects of the Time-Dependent Coupled-Cluster Approach to Dynamic-Response Functions. *Physical Review A* **1983**, *28*, 1217–1222.

(475) Ghosh, S.; Mukherjee, D. Use of Cluster-Expansion Techniques in Quantum-Chemistry - a Linear Response Model for Calculating Energy Differences. *Proceedings of the Indian Academy of Sciences-Chemical Sciences* **1984**, *93*, 947–963.

(476) Geertsen, J.; Rittby, M.; Bartlett, R. J. The Equation-of-Motion Coupled-Cluster Method - Excitation-Energies of Be and Co. *Chemical Physics Letters* **1989**, *164*, 57–62.

(477) Koch, H.; Jorgensen, P. Coupled Cluster Response Functions. *Journal of Chemical Physics* **1990**, *93*, 3333–3344.

(478) Bailey, C. G.; Dessent, C. E. H.; Johnson, M. A.; Bowen, K. H. Vibronic effects in the photon energy-dependent photoelectron spectra of the CH_3CN^- dipole-bound anion. *J. Chem. Phys.* **1996**, *104*, 6976–6983.

(479) Zhou, J.; Garand, E.; Neumark, D. M. Slow electron velocity-map imaging spectroscopy of the C_4H^- and C_4D^- anions. *Journal of Chemical Physics* **2007**, *127*, DOI: `Artn15432010.1063/1.2795723`.

(480) Huang, D. L.; Dau, P. D.; Liu, H. T.; Wang, L. S. High-resolution photoelectron imaging of cold C_{60}^- anions and accurate determination of the electron affinity of C_{60}. *Journal of Chemical Physics* **2014**, *140*, DOI: `Artn22431510.1063/1.4881421`.

(481) Kregel, S. J.; Thurston, G. K.; Garand, E. Photoelectron spectroscopy of anthracene and fluoranthene radical anions. *J. Chem. Phys.* **2018**, *148*, 234306.

(482) Liu, H. T.; Ning, C. G.; Huang, D. L.; Dau, P. D.; Wang, L. S. Observation of Mode-Specific Vibrational Autodetachment from Dipole-Bound States of Cold Anions. *Angewandte Chemie-International Edition* **2013**, *52*, 8976–8979.

(483) Huang, D. L.; Liu, H. T.; Ning, C. G.; Wang, L. S. Vibrational state-selective autodetachment photoelectron spectroscopy from dipole-bound states of cold 2-hydroxyphenoxide: *o*-$HO(C_6H_4)O^-$. *Journal of Chemical Physics* **2015**, *142*, DOI: 10.1063/1.4916122.

(484) Huang, D. L.; Liu, H. T.; Ning, C. G.; Zhu, G. Z.; Wang, L. S. Probing the vibrational spectroscopy of the deprotonated thymine radical by photodetachment and state-selective autodetachment photoelectron spectroscopy via dipole-bound states. *Chemical Science* **2015**, *6*, 3129–3138.

(485) Andersen, T.; Lykke, K. R.; Neumark, D. M.; Lineberger, W. C. Autodetachment Study of the Electronic Spectroscopy of FeO^-. *Journal of Chemical Physics* **1987**, *86*, 1858–1867.

(486) Xu, C. S.; Burton, G. R.; Taylor, T. R.; Neumark, D. M. Photoelectron spectroscopy of C_4^--, C_6^-, and C_8^-. *Journal of Chemical Physics* **1997**, *107*, 3428–3436.

(487) Schunk, R.; Nagy, A., *Ionospheres: Physics, Plasma Physics, and Chemistry*; Cambridge University Press: Cambridge, 2009.

(488) Bilitza, D.; Altadill, D.; Zhang, Y.; Mertens, C.; Truhlik, V.; Richards, P.; McKinnell, L.-A.; Reinisch, B. The International Reference Ionosphere 2012 - a model of international collaboration. *J. Space Weather Space Clim.* **2014**, *4*, A07.

(489) Kil, H.; Paxton, L. J.; Oh, S.-J. Global Bubble Distribution Seen From ROCSAT-1 and its Association with the Evening Prereversal Enhancement. *Journal of Geophysical Research* **2009**, *114*, A06308.

(490) Haldoupis, C. In *Aeronomy of the Earth's Atmosphere and Ionosphere*, M. Abdu, D. P., Ed.; IAGA Special Sopron Book Series; Springer: Dordrecht, 2011.

(491) Shuman, N.; Hunton, D. E.; Viggiano, A. Ambient and modified atmospheric ion chemistry: From top to bottom. *Chem. Rev.* **2015**, *115*, 4542–4570.

(492) Schofield, K. An Overlooked Series of Gas Phase Diatomic Metal Oxide Ions That Are Long-Lived. *Journal of Physical Chemistry A* **2006**, *110*, 6938–6947.

(493) Bernhardt, P. A.; Siefring, C. L.; Briczinski, S. J.; Viggiano, A. A.; Caton, R. G.; Pedersen, T. R.; Holmes, J. M.; Ard, S. G.; Shuman, N. S.; Groves, K. M. A physics-based model for the ionization of samarium by the MOSC chemical releases in the upper atmosphere. *Radio Science* **2017**, *52*, 559–577.

(494) Holmes, J. M.; Dressler, R. A.; Pedersen, T. R.; Caton, R. G.; Miller, D. A combined spectroscopic and plasma chemical kinetic analysis of ionospheric samarium releases. *Radio Science* **2017**, *52*, 521–538.

(495) Caton, R. G. et al. Artificial ionospheric modification: The Metal Oxide Space Cloud experiment. *Radio Science* **2017**, *52*.

(496) Pedersen, T. R.; Caton, R. G.; Miller, D.; Holmes, J. M.; Groves, K. M.; Sutton, E. Empirical modeling of plasma clouds produced by the Metal Oxide Space Clouds experiment. *Radio Science* **2017**, *52*, 578–596.

(497) Retterer, J.; Groves, K. M.; Pedersen, T. R.; Caton, R. G. The electrodynamic effects of MOSC-like plasma clouds. *Radio Science* **2017**, *52*, 604–615.

(498) Larsen, M.; Mikkelsen, I. S.; Meriwether, J. W.; Niciejewski, R.; Vickery, K. Simultaneous Observations of Neutral Winds and Electric Fields at Spaced Locations in the Dawn Auroral Oval. *J. Geo. Phys. Res.* **1989**, *94*, 17235–17243.

(499) Cox, R. M.; Kim, J.; Armentrout, P. B.; Bartlett, J.; VanGundy, R. A.; Heaven, M. C.; G., A. S.; Melko, J. J.; Shuman, N. S.; Viggiano, A. A. Evaluation of the exothermicity of the chemi-ionization reaction Sm + O $\rightarrow$ SmO^+ + e^-. *J. Chem. Phys.* **2015**, *142*, 134307.

(500) Lachowicz, A.; Perez, E. H.; Shuman, N. S.; Ard, S. G.; Viggiano, A. A.; Armentrout, P. B.; Goings, J. J.; Sharma, P.; Li, X.; Johnson, M. A. Determination of the SmO^+ bond energy by threshold photodissociation of the cryogenically cooled ion. *The Journal of Chemical Physics* **2021**, *155*, 174303.

(501) Ard, S. G.; Shuman, N. S.; Martinez Jr., O.; Brumbach, M. T.; Viggiano, A. A. Kinetics of chemi-ionization reactions of lanthanide metals (Nd, Sm) at 150-450 K. *J. Chem. Phys.* **2015**, *143*, 204303.

(502) Ard, S. G.; Shuman, N. S.; Martinez Jr, O.; Armentrout, P.; Viggiano, A. A. Chemi-ionization reactions of La, Pr, Tb, and Ho with atomic O and La with N_2O from 200 to 450 K. *Journal of Chemical Physics* **2016**, *145*, 084302.

(503) Ghiassee, M.; Kim, J.; Armentrout, P. Evaluation of the Exothermicity of the Chemi-Ionization Reaction Nd + O $\rightarrow$ NdO^+ + e^- and Neodymium Oxide, Carbide, Dioxide, and Carbonyl Cation Bond Energies. *Journal of Chemical Physics* **2019**, *150*, 144309.

(504) VanGundy, R. A.; Persinger, T. D.; Heaven, M. C. Low Energy States of NdO^+ Probed by Photoelectron Spectroscopy. *Journal of Chemical Physics* **2019**, *150*, 114302.

(505) Kramida, A.; Ralchenko, Y.; Reader, J., *NIST Atomic Spectra Database (ver 5.8), [Online]. Available: http://physics.nist.gov/asd*; National Institue of Standards and Technology: Gaithersburg, MD, 2021.

(506) Mason, J. L.; Harb, H.; Topolski, J. E.; Hratchian, H. P.; Jarrold, C. C. Exceptionally Complex Electronic Structures of Lanthanide Oxides and Small Molecules. *Acc. Chem. Res.* **2019**, *52*, 3265–3273.

(507) Zhou, Y.; Ng, K. B.; Cheng, L.; Gresh, D. N.; Field, R. W.; Ye, J.; Cornell, E. A. Visible and ultraviolet laser spectroscopy of ThF. *Journal of Molecular Spectroscopy* **2019**, *358*, 1–16.

(508) Chi, C. X.; Xie, H.; Cong, R.; Tang, Z. C.; Zhou, M. F. Electron Affinities of the Early Lanthanide Monoxide Molecules. *Chinese Journal of Chemical Physics* **2011**, *24*, 604–610.

(509) Kaledin, L. A.; Shenyavskaya, E. A. Electron Spectrum of Neodymium Monoxide. *Optika I Spektroskopiya* **1979**, *47*, 1015–1018.

(510) Kaledin, L. A.; Shenyavskaya, E. A.; Kovacs, I. Electronic Spectrum of NdO. *Acta Physica Hungarica* **1983**, *54*, 189–212.

(511) Shenyavskaya, E. A.; Bernard, A.; Verges, J. High Resolution Study of Near-Infrared Emission Spectra of ^{142}NdO. *Journal of Molecular Spectroscopy* **2003**, *222*, 240–247.

(512) Linton, C.; Effantin, C.; Crozet, P.; Ross, A. J.; Shenyavskaya, E. A.; d'Incan, J. Laser induced fluorescence spectroscopy of ^{142}NdO. *Journal of Molecular Spectroscopy* **2004**, *225*, 132–144.

(513) Effantin, C.; Bernard, A.; Crozet, P.; Ross, A. J.; d'Incan, J. Spectroscopy of ^{142}NdO: New Results. *Journal of Molecular Spectroscopy* **2005**, *231*, 154–164.

(514) Allouche, A. R.; Aubert-Frecon, M.; Umanskiy, S. Y. Structure of Low-Lying Electronic States of NdO: Quantum Chemical Calculations. *Journal of Chemical Physics* **2006**, *124*, 184317.

(515) Krauss, M.; Stevens, W. J. Comparitive Electronic Structure of a Lanthanide and Actinide Diatomic Oxide: Nd Versus U. *Molecular Physics* **2003**, *101*, 125–130.

(516) Wu, Z. J.; Guan, W.; Meng, J.; Su, Z. M. Density Functional Studies of Diatomic LaO to LuO. *Journal of Cluster Science* **2007**, *18*, 444–458.

(517) Kaledin, L. A. The Electronic Structure of Neodymium Monoxide: Ligand Field Assignment of States in the range 0 - 3 eV. *Journal of Molecular Spectroscopy* **2019**, *365*, 111207.

(518) Veirs, D. K.; Rosenblatt, G. M. Raman line positions in molecular hydrogen: H_2, HD, HT, D_2, DT, and T_2. *J. Mol. Spectrosc.* **1997**, *121*, 401–419.

(519) Angeli, C.; Cimiraglia, R.; Evangelisti, S.; Leininger, T.; Malrieu, J. P. Introduction of n-electron valence states for multireference perturbation theory. *Journal of Chemical Physics* **2001**, *114*, 10252–10264.

(520) Schapiro, I.; Sivalingam, K.; Neese, F. Assessment of n-Electron Valence State Perturbation Theory for Vertical Excitation Energies. *Journal of Chemical Theory and Computation* **2013**, *9*, 3567–3580.

(521) Yost, S. R.; Head-Gordon, M. Size consistent formulations of the perturb-then-diagonalize Moller-Plesset perturbation theory correction to non-orthogonal configuration interaction. *Journal of Chemical Physics* **2016**, *145*, DOI: `Artn05410510.1063/1.4959794`.

(522) Dolg, M.; Stoll, H.; Preuss, H. Energy-Adjusted Abinitio Pseudopotentials for the Rare-Earth Elements. *Journal of Chemical Physics* **1989**, *90*, 1730–1734.

(523) Weigend, F.; Häser, M.; Patzelt, H.; Ahlrichs, R. RI-MP2: optimized auxiliary basis sets and demonstration of efficiency. *Chemical Physics Letters* **1998**, *294*, 143–152.

(524) Liu, J. Z.; Shen, Y.; Asthana, A.; Cheng, L. Two-component relativistic coupled-cluster methods using mean-field spin-orbit integrals. *Journal of Chemical Physics* **2018**, *148*, DOI: 10.1063/1.5009177.

(525) Dyall, K. G. Interfacing relativistic and nonrelativistic methods I. Normalized elimination of the small component in the modified Dirac equation. *Journal of Chemical Physics* **1997**, *106*, 9618–9626.

(526) Liu, W. J.; Peng, D. L. Exact two-component Hamiltonians revisited. *Journal of Chemical Physics* **2009**, *131*, DOI: Artn03110410.1063/1.3159445.

(527) Lu, Q.; Peterson, K. A. Correlation consistent basis sets for lanthanides: The atoms La-Lu. *Journal of Chemical Physics* **2016**, *145*, DOI: Artn05411110.1063/1.4959280.

(528) Carette, P.; Hocquet, A. Ligand-Field Calculation of the Lower Electronic-Energy Levels of the Lanthanide Monoxides. *Journal of Molecular Spectroscopy* **1988**, *131*, 301–324.

(529) Ackermann, R. J.; Rauh, E. G.; Thorn, R. J. Thermodynamics of Ionization of Gaseous Oxides - 1st Ionization-Potentials of Lanthanide Metals and Monoxides. *Journal of Chemical Physics* **1976**, *65*, 1027–1031.

(530) Field, R. W. Diatomic Molecule Electronic-Structure Beyond Simple Molecular-Constants. *Berichte Der Bunsen-Gesellschaft-Physical Chemistry Chemical Physics* **1982**, *86*, 771–779.

(531) Kafader, J. O.; Topolski, J. E.; Marrero-Colon, V.; Iyengar, S. S.; Jarrold, C. C. The electron shuffle: Cerium influences samarium $4f$ orbital occupancy in heteronuclear Ce-Sm oxide clusters. *Journal of Chemical Physics* **2017**, *146*, DOI: Artn19431010.1063/1.4983335.

(532) Kafader, J. O.; Ray, M.; Jarrold, C. C. Photoelectron spectrum of PrO^-. *Journal of Chemical Physics* **2015**, *143*, DOI: Artn06430510.1063/1.4928371.

(533) Ray, M.; Felton, J. A.; Kafader, J. O.; Topolski, J. E.; Jarrold, C. C. Photoelectron spectra of CeO^- and $Ce(OH)_2^-$. *Journal of Chemical Physics* **2015**, *142*, DOI: Artn06430510.1063/1.4907714.

(534) Mason, J. L.; Harb, H.; Abou Taka, A.; McMahon, A. J.; Huizenga, C. D.; Corzo, H.; Hratchian, H. P.; Jarrold, C. C. Photoelectron Spectra of $Gd_2O_2^-$ and Nonmonotonic Photon- Energy-Dependent Variations in Populations of Close-Lying Neutral States. *Journal of Physical Chemistry A* **2021**, *125*, 857–866.

(535) Willson, S. P.; Andrews, L. Characterization of the reaction products of laser-ablated early lanthanide metal atoms with molecular oxygen. Infrared spectra of LnO, LnO^+, LnO^-, LnO_2, LnO_2^+, LnO_2^-, and LnO_3^-, and $(LnO)_2$ in solid argon. *Journal of Physical Chemistry A* **1999**, *103*, 3171–3183.

(536) Felton, J.; Ray, M.; Jarrold, C. C. Measurement of the electron affinity of atomic Ce. *Physical Review A* **2014**, *89*, DOI: ARTN03340710.1103/PhysRevA.89.033407.

(537) Sauer, J.; Freund, H.-J. Models in Catalysis. *Catalysis Letters* **2015**, *145*, 109–125.

(538) Andris, E.; Navrátil, R.; Jašík, J.; Terencio, T.; Srnec, M.; Costas, M.; Roithová, J. Chasing the Evasive Fe=O Stretch and the Spin State of the Iron(IV)–Oxo Complexes by Photodissociation Spectroscopy. *Journal of the American Chemical Society* **2017**, *139*, 2757–2765.

(539) Desai, S. R.; Wu, H. B.; Wang, L. S. Vibrationally resolved photoelectron spectroscopy of AlO^- and AlO_2^-. *International Journal of Mass Spectrometry and Ion Processes* **1996**, *159*, 75–80.

(540) Desai, S. R.; Wu, H.; Rohlfing, C. M.; Wang, L.-S. A study of the structure and bonding of small aluminum oxide clusters by photoelectron spectroscopy: $Al_xO_y^-$ (x=1–2, y=1–5). *Journal of Chemical Physics* **1997**, *106*, 1309–1317.

(541) Wu, H. B.; Li, X.; Wang, X. B.; Ding, C. F.; Wang, L. S. Al_3O_y (y=0-5) clusters: Sequential oxidation, metal-to-oxide transformation, and photoisomerization. *Journal of Chemical Physics* **1998**, *109*, 449–458.

(542) Archibong, E. F.; St-Amant, A. On the Structure of Al_2O_3 and Photoelectron Spectra of $Al_2O_2^-$ and $Al_2O_3^-$. *Journal of Physical Chemistry A* **1999**, *103*, 1109–1114.

(543) Akin, F. A.; Jarrold, C. C. Addition of water and methanol to $Al_3O_3^-$ studied by mass spectrometry and anion photoelectron spectroscopy. *Journal of Chemical Physics* **2003**, *118*, 5841–5851.

(544) Meloni, G.; Ferguson, M. J.; Neumark, D. M. Negative ion photodetachment spectroscopy of the Al_3O_2, Al_3O_3, Al_4O_x, Al_5O_x (x = 3–5), Al_6O_5, and Al_7O_5 clusters. *Phys. Chem. Chem. Phys.* **2003**, *5*, 4073–4079.

(545) Van Heijnsbergen, D.; Demyk, K.; Duncan, M. A.; Meijer, G.; von Helden, G. Structure determination of gas phase aluminum oxide clusters. *Physical Chemistry Chemical Physics* **2003**, *5*, 2515–2519.

(546) Das, U.; Raghavachari, K.; Jarrold, C. C. Addition of water to $Al_5O_4^-$ determined by anion photoelectron spectroscopy and quantum chemical calculations. *Journal of Chemical Physics* **2004**, *122*, 014313.

(547) Stosser, G.; Schnockel, H. The molecules AlO_2, $Al(O_2)_2$, and $Al(O_2)_3$: experimental and quantum-chemical investigations on the oxidation of aluminum atoms. *Angew Chem Int Ed Engl* **2005**, *44*, 4261–4.

(548) Sierka, M.; Doebler, J.; Sauer, J.; Santambrogio, G.; Bruemmer, M.; Woeste, L.; Janssens, E.; Meijer, G.; Asmis, K. R. Unexpected structures of aluminum oxide clusters in the gas phase. *Angewandte Chemie-International Edition* **2007**, *46*, 3372–3375.

(549) Santambrogio, G.; Janssens, E.; Li, S.; Siebert, T.; Meijer, G.; Asmis, K. R.; Doebler, J.; Sierka, M.; Sauer, J. Identification of Conical Structures in Small Aluminum Oxide Clusters: Infrared Spectroscopy of $(Al_2O_3)_{1-4}(AlO)^+$. *Journal of the American Chemical Society* **2008**, *130*, 15143–15149.

(550) Sierka, M.; Döbler, J.; Sauer, J.; Zhai, H.-J.; Wang, L.-S. The $[(Al_2O_3)_2]^-$ Anion Cluster: Electron Localization–Delocalization Isomerism. *ChemPhysChem* **2009**, *10*, 2410–2413.

(551) Song, X.; Fagiani, M. R.; Gewinner, S.; Schoellkopf, W.; Asmis, K. R.; Bischoff, F. A.; Berger, F.; Sauer, J. Gas phase structures and charge localization in small aluminum oxide anions: Infrared photodissociation spectroscopy and electronic structure calculations. *Journal of Chemical Physics* **2016**, *144*, DOI: 10.1063/1.4954158.

(552) Song, X.; Fagiani, M. R.; Gewinner, S.; Schoellkopf, W.; Asmis, K. R.; Bischoff, F. A.; Berger, F.; Sauer, J. Gas-Phase Vibrational Spectroscopy of the Aluminum Oxide Anions $(Al_2O_3)_{1-6}AlO_2^-$. *ChemPhysChem* **2017**, *18*, 868–872.

(553) Lopez, G. V.; Czekner, J.; Jian, T.; Li, W. L.; Yang, Z.; Wang, L. S. Probing the electronic and vibrational structure of $Au_2Al_2^-$ and Au_2Al_2 using photoelectron spectroscopy and high resolution photoelectron imaging. *Journal of Chemical Physics* **2014**, *141*.

(554) Debnath, S.; Knorke, H.; Schollkopf, W.; Zhou, S. D.; Asmis, K. R.; Schwarz, H. Experimental Identification of the Active Site in the Heteronuclear Redox Couples $[AlVO_x]^+\cdot/CO/N_2O$ (x=3,4) by Gas-Phase IR Spectroscopy. *Angewandte Chemie-International Edition* **2018**, *57*, 7448–7452.

(555) Müller, F.; Stuckrath, J. B.; Bischoff, F. A.; Gagliardi, L.; Sauer, J.; Debnath, S.; Jorewitz, M.; Asmis, K. R. Valence and Structure Isomerism of $Al_2FeO_4^+$: Synergy of Spectroscopy and Quantum Chemistry. *Journal of the American Chemical Society* **2020**, *142*, 18050–18059.

(556) Asmis, K.; Brümmer, M.; Kaposta, C.; Santambrogio, G.; von Helden, G.; Meijer, G.; Rademann, K.; Wöste, L. Mass-Selected Infrared Photodissociation Spectroscopy of $V_4O_{10}^+$. *Physical Chemistry Chemical Physics* **2002**, *4*, 1101–4.

(557) Brümmer, M.; Kaposta, C.; Santambrogio, G.; Asmis, K. R. Formation and photodepletion of cluster ion-messenger atom complexes in a cold ion trap: Infrared spectroscopy of VO^+, VO_2^+, and VO_3^+. *Journal of Chemical Physics* **2003**, *119*, 12700–12703.

(558) Maeda, S.; Ohno, K.; Morokuma, K. Systematic exploration of the mechanism of chemical reactions: the global reaction route mapping (GRRM) strategy using the ADDF and AFIR methods. *Physical Chemistry Chemical Physics* **2013**, *15*, 3683–3701.

(559) Maeda, S.; Taketsugu, T.; Morokuma, K. Exploring transition state structures for intramolecular pathways by the artificial force induced reaction method. *Journal of Computational Chemistry* **2014**, *35*, 166–173.

(560) Maeda, S.; Harabuchi, Y.; Takagi, M.; Taketsugu, T.; Morokuma, K. Artificial Force Induced Reaction (AFIR) Method for Exploring Quantum Chemical Potential Energy Surfaces. *The Chemical Record* **2016**, *16*, 2232–2248.

(561) Goebbert, D. J.; Wende, T.; Bergmann, R.; Meijer, G.; Asmis, K. R. Messenger-Tagging Electrosprayed Ions: Vibrational Spectroscopy of Suberate Dianions. *Journal of Physical Chemistry A* **2009**, *113*, 5874–5880.

(562) Goebbert, D. J.; Meijer, G.; Asmis, K. R. 10K Ring Electrode Trap - Tandem Mass Spectrometer for Infrared Spectroscopy of Mass Selected Ions. *AIP Conf. Proc.* **2009**, *1104*, 22–29.

(563) Heine, N.; Asmis, K. R. Cryogenic Ion Trap Vibrational Spectroscopy of Hydrogen-Bonded Clusters Relevant to Atmospheric Chemistry. *International Reviews in Physical Chemistry* **2016**, *34*, 1–34.

(564) Maeda, S.; Harabuchi, Y.; Takagi, M.; Saita, K.; Suzuki, K.; Ichino, T.; Sumiya, Y.; Sugiyama, K.; Ono, Y. Implementation and performance of the artificial force induced reaction method in the GRRM17 program. *Journal of Computational Chemistry* **2018**, *39*, 233–251.

(565) Maeda, S.; Harabuchi, Y.; Sumiya, Y.; Takagi, M.; Suzuki, K.; Hatanaka, M.; Osada, Y.; Taketsugu, T.; Morokuma, K.; Ohno, K. GRRM17, see http://iqce. jp. *GRRM/index_ e. shtml (accessed date 10 Sep., 2020).*

(566) Gao, M.; Lyalin, A.; Maeda, S.; Taketsugu, T. Application of Automated Reaction Path Search Methods to a Systematic Search of Single-Bond Activation Pathways Catalyzed by Small Metal Clusters: A Case Study on H–H Activation by Gold. *Journal of Chemical Theory and Computation* **2014**, *10*, 1623–1630.

(567) Song, X.; Fagiani, M. R.; Debnath, S.; Gao, M.; Maeda, S.; Taketsugu, T.; Gewinner, S.; Schöllkopf, W.; Asmis, K. R.; Lyalin, A. Excess charge driven dissociative hydrogen adsorption on $Ti_2O_4^-$. *Physical Chemistry Chemical Physics* **2017**, *19*, 23154–23161.

(568) Debnath, S.; Song, X.; Fagiani, M. R.; Weichman, M. L.; Gao, M.; Maeda, S.; Taketsugu, T.; Schöllkopf, W.; Lyalin, A.; Neumark, D. M.; Asmis, K. R. CO_2 Adsorption on $Ti_3O_6^-$: A Novel Carbonate Binding Motif. *Journal of Physical Chemistry C* **2019**, *123*, 8439–8446.

(569) Balasubramani, S. G. et al. TURBOMOLE: Modular program suite for ab initio quantum-chemical and condensed-matter simulations. *Journal of Chemical Physics* **2020**, *152*, 184107.

(570) TURBOMOLE V7.0-7.5 2020, a Development of University of Karlsruhe and Forschungszentrum Karlsruhe GmbH, 1989-2007, TURBOMOLE GmbH, since 2007; Available from https://www.turbomole.org.

(571) Schäfer, A.; Horn, H.; Ahlrichs, R. Fully optimized contracted Gaussian basis sets for atoms Li to Kr. *Journal of Chemical Physics* **1992**, *97*, 2571–2577.

(572) Perdew, J. P. Density-functional approximation for the correlation energy of the inhomogeneous electron gas. *Physical Review B* **1986**, *33*, 8822–8824.

(573) Eichkorn, K.; Weigend, F.; Treutler, O.; Ahlrichs, R. Auxiliary basis sets for main row atoms and transition metals and their use to approximate Coulomb potentials. *Theoretical Chemistry Accounts* **1997**, *97*, 119–124.

(574) Kempkes, L. J. M.; Martens, J.; Berden, G.; Houthuijs, K. J.; Oomens, J. Investigation of the position of the radical in z_3-ions resulting from electron transfer dissociation using infrared ion spectroscopy. *Faraday Discussions* **2019**, *217*, 434–452.

(575) Jiang, W.; DeYonker, N. J.; Wilson, A. K. Multireference Character for 3*d* Transition-Metal-Containing Molecules. *Journal of Chemical Theory and Computation* **2012**, *8*, 460–468.

(576) Andersson, K.; Malmqvist, P. A.; Roos, B. O.; Sadlej, A. J.; Wolinski, K. Second-order perturbation theory with a CASSCF reference function. *Journal of Physical Chemistry* **1990**, *94*, 5483–5488.

(577) Werner, H.-J.; Knowles, P. J. An efficient internally contracted multiconfiguration–reference configuration interaction method. *Journal of Chemical Physics* **1988**, *89*, 5803–5814.

(578) Feyel, S.; Döbler, J.; Hoeckendorf, R.; Beyer, M. K.; Sauer, J.; Schwarz, H. Activation of methane by oligomeric $(Al_2O_3)_x^+$ (x=3,4,5): The role of oxygen-centered radicals in thermal hydrogen-atom abstraction. *Angewandte Chemie-International Edition* **2008**, *47*, 1946–1950.

(579) Lau, J. T.; Rittmann, J.; Zamudio-Bayer, V.; Vogel, M.; Hirsch, K.; Klar, P.; Lofink, F.; Möller, T.; v. Issendorff, B. Size Dependence of $L_{2,3}$ Branching Ratio and 2*p* Core-Hole Screening in X-Ray Absorption of Metal Clusters. *Phys. Rev. Lett.* **2008**, *101*, 153401.

(580) Patil, N. A.; Kandasubramanian, B. Biological and mechanical enhancement of zirconium dioxide for medical applications. *Ceram. Int.* **2019**.

(581) Hingsammer, L.; Grillenberger, M.; Schagerl, M.; Malek, M.; Hunger, S. Biomechanical testing of zirconium dioxide osteosynthesis system for Le Fort I advancement osteotomy fixation. *J. Mech. Behav. Biomed. Mater.* **2018**, *77*, 34–39.

(582) Chen, T.-W.; Vasantha, A. S.; Chen, S.-M.; Al Farraj, D. A.; Elshikh, M. S.; Alkufeidy, R. M.; Al Khulaifi, M. M. Sonochemical synthesis and fabrication of honeycomb like zirconium dioxide with chitosan modified electrode for sensitive electrochemical determination of anti-tuberculosis (TB) drug. *Ultrason. Sonochem.* **2019**, *59*, 104718.

(583) Sjoholm, P.; Ingham, D. b.; Lehtimaki, M.; Perttu-Roiha, L.; Goodfellow, H.; Torvela, H. In *Industrial Ventilation Design Guidebook*; Elsevier: 2001, pp 1197–1316.

(584) Dudczig, S.; Veres, D.; Aneziris, C. G.; Skiera, E.; Steinbrech, R. W. Nano-and micrometre additions of SiO_2, ZrO_2 and TiO_2 in fine grained alumina refractory ceramics for improved thermal shock performance. *Ceram. Int.* **2012**, *38*, 2011–2019.

(585) Aneziris, C. G.; Dudczig, S.; Gerlach, N.; Berek, H.; Veres, D. Thermal shock performance of fine grained Al_2O_3 ceramics with TiO_2 and ZrO_2 additions for refractory applications. *Adv. Eng. Mater.* **2010**, *12*, 478–485.

(586) Chen, M.; Lu, C.; Yu, J. Improvement in performance of MgO–CaO refractories by addition of nano-sized ZrO_2. *J. Eur. Ceram. Soc.* **2007**, *27*, 4633–4638.

(587) Henrich, V. E.; Cox, P. A., *The surface science of metal oxides*; Cambridge university press: 1996.

(588) Shishkovsky, I.; Yadroitsev, I.; Bertrand, P.; Smurov, I. Alumina–zirconium ceramics synthesis by selective laser sintering/melting. *Appl. Surf. Sci.* **2007**, *254*, 966–970.

(589) Fehrenbacher, L. L. Stabilized zirconium dioxide and hafnium dioxide compositions, US Patent 3,634,113, 1972.

(590) Gogotsi, G. A. Deformational behaviour of ceramics. *J. Eur. Ceram. Soc.* **1991**, *7*, 87–92.

(591) Lintz, H.-G.; Vayenas, C. G. Solid ion conductors in heterogeneous catalysis. *Angew. Chem. Int. Ed. Engl.* **1989**, *28*, 708–715.

(592) Sverdrup, E. F.; Glasser, A. D.; Archer, D. H. Fuel cell comprising a stabilized zirconium oxide electrolyte and a doped indium or tin oxide cathode, US Patent 3,558,360, 1971.

(593) Nozik, A. J. Photoelectrolysis of water by solar radiation, US Patent 4,011,149, 1977.

(594) Stambouli, A. B.; Traversa, E. Solid oxide fuel cells (SOFCs): a review of an environmentally clean and efficient source of energy. *Renewable Sustainable Energy Rev.* **2002**, *6*, 433–455.

(595) Iannaci, A.; Sciarria, T. P.; Mecheri, B.; Adani, F.; Licoccia, S.; D'Epifanio, A. Power generation using a low-cost sulfated zirconium oxide based cathode in single chamber microbial fuel cells. *J. Alloys Compd.* **2017**, *693*, 170–176.

(596) Sayama, K.; Arakawa, H. Photocatalytic decomposition of water and photocatalytic reduction of carbon dioxide over zirconia catalyst. *J. Phys. Chem.* **1993**, *97*, 531–533.

(597) Yang, L.; Zhou, H.; Fan, T.; Zhang, D., *Semiconductor photocatalysts for water oxidation: current status and challenges*; 15; Royal Society of Chemistry: 2014; Vol. 16, pp 6810–6826.

(598) Muhler, M.; Schlögl, R.; Ertl, G. The nature of the iron oxide-based catalyst for dehydrogenation of ethylbenzene to styrene 2. Surface chemistry of the active phase. *J. Catal.* **1992**, *138*, 413–444.

(599) Perry, N. H.; Ishihara, T. Roles of bulk and surface chemistry in the oxygen exchange kinetics and related properties of mixed conducting perovskite oxide electrodes. *Materials* **2016**, *9*, 858.

(600) Seker, F.; Meeker, K.; Kuech, T. F.; Ellis, A. B. Surface chemistry of prototypical bulk II- VI and III- V semiconductors and implications for chemical sensing. *Chem. Rev.* **2000**, *100*, 2505–2536.

(601) Darmstadt, H.; Sümmchen, L.; Ting, J.-M.; Roland, U.; Kaliaguine, S.; Roy, C. Effects of surface treatment on the bulk chemistry and structure of vapor grown carbon fibers. *Carbon* **1997**, *35*, 1581–1585.

(602) Al-Abadleh, H. A. Review of the bulk and surface chemistry of iron in atmospherically relevant systems containing humic-like substances. *RSC Adv.* **2015**, *5*, 45785–45811.

(603) Marcos, J.; Buitrago, R.; Lombardo, E. Surface chemistry and catalytic activity of $La_{1-y}M_yCoO_3$ perovskite (M= Sr or Th): 1. Bulk and surface reduction studies. *J. Catal.* **1987**, *105*, 95–106.

(604) Prellier, W.; Singh, M.; Murugavel, P. The single-phase multiferroic oxides: from bulk to thin film. *J. Phys.: Condens. Matter* **2005**, *17*, R803.

(605) Xu, Z.; Kitchin, J. R. Relationships between the surface electronic and chemical properties of doped 4d and 5d late transition metal dioxides. *J. Chem. Phys.* **2015**, *142*, 104703.

(606) Horkans, J.; Shafer, M. An investigation of the electrochemistry of a series of metal dioxides with rutile-type structure: MoO_2, WO_2, ReO_2, RuO_2, OsO_2, and IrO_2. *J. Electrochem. Soc.* **1977**, *124*, 1202–1207.

(607) Tang, Y.; Zhao, S.; Long, B.; Liu, J.-C.; Li, J. On the nature of support effects of metal dioxides MO_2 (M= Ti, Zr, Hf, Ce, Th) in single-atom gold catalysts: Importance of quantum primogenic effect. *J. Phys. Chem. C* **2016**, *120*, 17514–17526.

(608) Kung, H. H., *Transition metal oxides: surface chemistry and catalysis*; Elsevier: 1989; Vol. 45.

(609) Busca, G.; Lorenzelli, V. Infrared spectroscopic identification of species arising from reactive adsorption of carbon oxides on metal oxide surfaces. *Mater. Chem.* **1982**, *7*, 89–126.

(610) Kristoffersen, H. H.; Hansen, J. Ø.; Martinez, U.; Wei, Y.; Matthiesen, J.; Streber, R.; Bechstein, R.; Lægsgaard, E.; Besenbacher, F.; Hammer, B., et al. Role of steps in the dissociative adsorption of water on rutile TiO_2 (110). *Phys. Rev. Lett.* **2013**, *110*, 146101.

(611) Henrich, V. E.; Cox, P. Fundamentals of gas-surface interactions on metal oxides. *Appl. Surf. Sci.* **1993**, *72*, 277–284.

(612) Calatayud, M.; Markovits, A.; Menetrey, M.; Mguig, B.; Minot, C. Adsorption on perfect and reduced surfaces of metal oxides. *Catal. Today* **2003**, *85*, 125–143.

(613) Daturi, M.; Binet, C.; Bernal, S.; Omil, J. A. P.; Lavalley, J. C. FTIR study of defects produced in ZrO_2 samples by thermal treatment Residual species into cavities and surface defects. *J. Chem. Soc., Faraday Trans.* **1998**, *94*, 1143–1147.

(614) Chuah, G.; Jaenicke, S. The preparation of high surface area zirconia—influence of precipitating agent and digestion. *Appl. Catal., A* **1997**, *163*, 261–273.

(615) Xia, X.; Oldman, R.; Catlow, R. Computational modeling study of bulk and surface of yttria-stabilized cubic zirconia. *Chem. Mater.* **2009**, *21*, 3576–3585.

(616) Haas, G.; Menck, A.; Brune, H.; Barth, J.; Venables, J.; Kern, K. Nucleation and growth of supported clusters at defect sites: Pd/MgO (001). *Phys. Rev. B* **2000**, *61*, 11105.

(617) Heim, K.; Coyle, S.; Hembree, G.; Venables, J.; Scheinfein, M. Growth of nanometer-size metallic particles on CaF_2 (111). *J. Appl. Phys.* **1996**, *80*, 1161–1170.

(618) Venables, J. A. Nucleation growth and pattern formation in heteroepitaxy. *Phys. A (Amsterdam, Neth.)* **1997**, *239*, 35–46.

(619) Fahsold, G.; Pucci, A.; Rieder, K.-H. Growth of Fe on MgO (001) studied by He-atom scattering. *Phys. Rev. B* **2000**, *61*, 8475.

(620) Solomon, E. I.; Jones, P. M.; May, J. A. Electronic structures of active sites on metal oxide surfaces: definition of the copper-zinc oxide methanol synthesis catalyst by photoelectron spectroscopy. *Chem. Rev.* **1993**, *93*, 2623–2644.

(621) Yamamoto, H.; Watanabe, N.; Wada, A.; Domen, K.; Hirose, C. Adsorption and decomposition of formic acid on MgO (001) surface as investigated by temperature programmed desorption and sum-frequency generation spectroscopy: Recurrence induced defect sites. *J. Chem. Phys.* **1997**, *106*, 4734–4744.

(622) Wu, Z.; Li, M.; Howe, J.; Meyer III, H. M.; Overbury, S. H. Probing defect sites on CeO_2 nanocrystals with well-defined surface planes by Raman spectroscopy and O_2 adsorption. *Langmuir* **2010**, *26*, 16595–16606.

(623) Borda, M. J.; Elsetinow, A. R.; Strongin, D. R.; Schoonen, M. A. A mechanism for the production of hydroxyl radical at surface defect sites on pyrite. *Geochim. Cosmochim. Acta* **2003**, *67*, 935–939.

(624) Joubert, J.; Salameh, A.; Krakoviack, V.; Delbecq, F.; Sautet, P.; Copéret, C.; Basset, J. M. Heterolytic Splitting of H_2 and CH_4 on γ-Alumina as a Structural Probe for Defect Sites. *J. Phys. Chem. B* **2006**, *110*, 23944–23950.

(625) Raghavachari, K.; Halls, M. D. Quantum chemical studies of semiconductor surface chemistry using cluster models. *Mol. Phys.* **2004**, *102*, 381–393.

(626) Mann, J. E.; Mayhall, N. J.; Jarrold, C. C. Properties of metal oxide clusters in non-traditional oxidation states. *Chem. Phys. Lett.* **2012**, *525*, 1–12.

(627) Zhang, G.; Hattori, H.; Tanabe, K. Aldol addition of acetone, catalyzed by solid base catalysts: magnesium oxide, calcium oxide, strontium oxide, barium oxide, lanthanum (III) oxide and zirconium oxide. *Appl. Catal.* **1988**, *36*, 189–197.

(628) Atsu, S. S.; Kilicarslan, M. A.; Kucukesmen, H. C.; Aka, P. S. Effect of zirconium-oxide ceramic surface treatments on the bond strength to adhesive resin. *J. Prosthet. Dent.* **2006**, *95*, 430–436.

(629) Nakano, Y.; Iizuka, T.; Hattori, H.; Tanabe, K. Surface properties of zirconium oxide and its catalytic activity for isomerization of 1-butene. *J. Catal.* **1979**, *57*, 1–10.

(630) Hausmann, D. M.; Gordon, R. G. Surface morphology and crystallinity control in the atomic layer deposition (ALD) of hafnium and zirconium oxide thin films. *J. Cryst. Growth* **2003**, *249*, 251–261.

(631) Bachiller-Baeza, B.; Rodriguez-Ramos, I.; Guerrero-Ruiz, A. Interaction of carbon dioxide with the surface of zirconia polymorphs. *Langmuir* **1998**, *14*, 3556–3564.

(632) Hess, A.; Kemnitz, E. Surface acidity and catalytic behavior of modified zirconium and titanium dioxides. *Appl. Catal., A* **1997**, *149*, 373–389.

(633) Li, R.-Z.; Xu, H.-G.; Cao, G.-J.; Xu, X.-L.; Zheng, W.-J. Interaction of TiO_2^- with water: Photoelectron spectroscopy and density functional calculations. *J. Chem. Phys.* **2013**, *139*, 184303.

(634) Xu, H.-G.; Li, X.-N.; Kong, X.-Y.; He, S.-G.; Zheng, W.-J. Interaction of TiO^+ with water: infrared photodissociation spectroscopy and density functional calculations. *Phys. Chem. Chem. Phys.* **2013**, *15*, 17126–17133.

(635) Weichman, M. L.; Debnath, S.; Kelly, J. T.; Gewinner, S.; Schöllkopf, W.; Neumark, D. M.; Asmis, K. R. Dissociative water adsorption on gas-phase titanium dioxide cluster anions probed with infrared photodissociation spectroscopy. *Top. Catal.* **2018**, *61*, 92–105.

(636) Wu, X.-N.; Ma, J.-B.; Xu, B.; Zhao, Y.-X.; Ding, X.-L.; He, S.-G. Collision-induced dissociation and density functional theory studies of CO adsorption over zirconium oxide cluster ions: Oxidative and nonoxidative adsorption. *J. Phys. Chem. A* **2011**, *115*, 5238–5246.

(637) Zhao, Y.-X.; Ding, X.-L.; Ma, Y.-P.; Wang, Z.-C.; He, S.-G. Transition metal oxide clusters with character of oxygen-centered radical: a DFT study. *Theor. Chem. Acc.* **2010**, *127*, 449–465.

(638) Ma, J.-b.; Wu, X.-n.; Zhao, Y.-x.; Ding, X.-l.; He, S.-g. Experimental and theoretical study of hydrogen atom abstraction from C_2H_6 and C_4H_{10} by zirconium oxide clusters anions. *Chin. J. Chem. Phys.* **2013**, *23*, 133.

(639) Ma, J.-B.; Xu, B.; Meng, J.-H.; Wu, X.-N.; Ding, X.-L.; Li, X.-N.; He, S.-G. Reactivity of atomic oxygen radical anions bound to titania and zirconia nanoparticles in the gas phase: low-temperature oxidation of carbon monoxide. *J. Am. Chem. Soc.* **2013**, *135*, 2991–2998.

(640) Wu, X.-n.; Zhao, Y.-x.; He, S.-g.; Ding, X.-l. Experimental and theoretical study of hydrogen atom abstraction from ethylene by stoichiometric zirconium oxide clusters. *Chin. J. Chem. Phys.* **2013**, *22*, 635.

(641) Kreutzer, J.; Blaha, P.; Schubert, U. Assessment of different basis sets and DFT functionals for the calculation of structural parameters, vibrational modes and ligand binding energies of $Zr_4O_2(\text{carboxylate})_{12}$ clusters. *Comput. Theor. Chem.* **2016**, *1084*, 162–168.

(642) Sayama, K.; Arakawa, H. Effect of carbonate addition on the photocatalytic decomposition of liquid water over a ZrO_2 catalyst. *J. Photochem. Photobiol., A* **1996**, *94*, 67–76.

(643) Li, J.; Chen, J.; Song, W.; Liu, J.; Shen, W. Influence of zirconia crystal phase on the catalytic performance of Au/ZrO_2 catalysts for low-temperature water gas shift reaction. *Appl. Catal., A* **2008**, *334*, 321–329.

(644) Zinatloo-Ajabshir, S.; Salavati-Niasari, M. Facile route to synthesize zirconium dioxide (ZrO_2) nanostructures: structural, optical and photocatalytic studies. *J. Mol. Liq.* **2016**, *216*, 545–551.

(645) Moafi, H. F.; Shojaie, A. F.; Zanjanchi, M. A. The comparison of photocatalytic activity of synthesized TiO_2 and ZrO_2 nanosize onto wool fibers. *Appl. Surf. Sci.* **2010**, *256*, 4310–4316.

(646) Agron, P.; Fuller Jr, E.; Holmes, H. IR studies of water sorption on ZrO_2 polymorphs. I. *J. Colloid Interface Sci.* **1975**, *52*, 553–561.

(647) Piskorz, W.; Gryboś, J.; Zasada, F.; Zapała, P.; Cristol, S.; Paul, J.-F.; Sojka, Z. Periodic DFT study of the tetragonal ZrO_2 nanocrystals: equilibrium morphology modeling and atomistic surface hydration thermodynamics. *J. Phys. Chem. C* **2012**, *116*, 19307–19320.

(648) Subhoni, M.; Kholmurodov, K.; Doroshkevich, A.; Asgerov, E.; Yamamoto, T.; Lyubchyk, A.; Almasan, V.; Madadzada, A. In *Journal of Physics: Conference Series*, 2018; Vol. 994, p 012013.

(649) Lousada, C. M.; Johansson, A. J.; Brinck, T.; Jonsson, M. Reactivity of metal oxide clusters with hydrogen peroxide and water–a DFT study evaluating the performance of different exchange–correlation functionals. *Phys. Chem. Chem. Phys.* **2013**, *15*, 5539–5552.

(650) Ushakov, S. V.; Navrotsky, A. Direct measurements of water adsorption enthalpy on hafnia and zirconia. *Appl. Phys. Lett.* **2005**, *87*, 164103.

(651) Zheng, W.; Bowen, K. H.; Li, J.; Dabkowska, I.; Gutowski, M. Electronic structure differences in ZrO_2 vs HfO_2. *J. Phys. Chem. A* **2005**, *109*, 11521–11525.

(652) Chertihin, G. V.; Andrews, L. Reactions of Laser Ablated Titanium, Zirconium, and Hafnium Atoms with Oxygen Molecules in Condensing Argon. *J. Phys. Chem.* **1995**, *99*, 6356–6366.

(653) Brugh, D. J.; Suenram, R. D.; Stevens, W. J. Fourier transform microwave spectroscopy of jet-cooled ZrO_2 produced by laser vaporization. *J. Chem. Phys.* **1999**, *111*, 3526–3535.

(654) Le, A.; Steimle, T. C.; Gupta, V.; Rice, C. A.; Maier, J. P.; Lin, S. H.; Lin, C.-K. The visible spectrum of zirconium dioxide, ZrO_2. *J. Chem. Phys.* **2011**, *135*, 104303.

(655) Li, S.; Dixon, D. A. Molecular Structures and Energetics of the $(ZrO_2)_n$ and $(HfO_2)_n$ (n= 1- 4) Clusters and Their Anions. *J. Phys. Chem. A* **2010**, *114*, 2665–2683.

(656) Woodley, S. M.; Hamad, S.; Mejías, J. A.; Catlow, C. R. A. Properties of small TiO_2, ZrO_2 and HfO_2 nanoparticles. *J. Mater. Chem.* **2006**, *16*, 1927–1933.

(657) Kaupp, M. On the Relation between π Bonding, Electronegativity, and Bond Angles in High-Valent Transition Metal Complexes. *Chem. Eur. J.* **1999**, *5*, 3631–3643.

(658) Mok, D. K. W.; Chau, F.-t.; Dyke, J. M.; Lee, E. P. F. A combined ab initio and Franck–Condon simulation study of the photodetachment spectrum of ZrO_2^-. *Chem. Phys. Lett.* **2008**, *458*, 11–14.

(659) Fang, Z.; Outlaw, M. D.; Smith, K. K.; Gist, N. W.; Li, S.; Dixon, D. A.; Gole, J. L. Computational Study of the Hydrolysis Reactions of Small MO_2 (M= Zr and Hf) Nanoclusters with Water. *J. Phys. Chem. C* **2012**, *116*, 8475–8492.

(660) Chen, M.; Straatsma, T. P.; Dixon, D. A. Molecular and Dissociative Adsorption of Water on $(TiO_2)_n$ Clusters, n = 1–4. *J. Phys. Chem. A* **2015**, *119*, 11406–11421.

(661) Adamo, C.; Barone, V. Toward reliable density functional methods without adjustable parameters: The PBE0 model. *J. Chem. Phys.* **1999**, *110*, 6158–6170.

(662) Zhao, Y.; Truhlar, D. G. The M06 suite of density functionals for main group thermochemistry, thermochemical kinetics, noncovalent interactions, excited states, and transition elements: two new functionals and systematic testing of four M06-class functionals and 12 other functionals. *Theor. Chem. Acc.* **2008**, *120*, 215–241.

(663) Zhao, Y.; Truhlar, D. G. A new local density functional for main-group thermochemistry, transition metal bonding, thermochemical kinetics, and noncovalent interactions. *J. Chem. Phys.* **2006**, *125*, 194101.

(664) Perdew, J. P.; Burke, K.; Ernzerhof, M. Generalized gradient approximation made simple. *Phys. Rev. Lett.* **1996**, *77*, 3865.

(665) Frisch, M.; Trucks, G.; Schlegel, H.; Scuseria, G.; Robb, M.; Cheeseman, J.; Scalmani, G.; Barone, V.; Mennucci, B.; Petersson, G., et al. Gaussian Development Version Revision H. j04+. *Gaussian Inc., Wallingford CT* **2011**.

(666) Bauernschmitt, R.; Ahlrichs, R. Stability analysis for solutions of the closed shell Kohn–Sham equation. *J. Chem. Phys.* **1996**, *104*, 9047–9052.

(667) Seeger, R.; Pople, J. A. Self-consistent molecular orbital methods. XVIII. Constraints and stability in Hartree–Fock theory. *J. Chem. Phys.* **1977**, *66*, 3045–3050.

(668) Hratchian, H.; Schlegel, H. Theory and Applications of Computational Chemistry: The First 40 Years. *Dykstra, CE* **2005**, 195–249.

(669) Schaefer III, H. F.; Yamaguchi, Y. A New dimension to quantum chemistry: Theoretical methods for the analytic evaluation of first, second, and third derivatives of the molecular electronic energy with respect to nuclear coordinates. *J. Mol. Struct.: THEOCHEM* **1986**, *135*, 369–390.

(670) Stratmann, R. E.; Burant, J. C.; Scuseria, G. E.; Frisch, M. J. Improving harmonic vibrational frequencies calculations in density functional theory. *J. Chem. Phys.* **1997**, *106*, 10175–10183.

(671) Santoro, F.; Improta, R.; Lami, A.; Bloino, J.; Barone, V. Effective method to compute Franck-Condon integrals for optical spectra of large molecules in solution. *J. Chem. Phys.* **2007**, *126*, 084509.

(672) Santoro, F.; Lami, A.; Improta, R.; Barone, V. Effective method to compute vibrationally resolved optical spectra of large molecules at finite temperature in the gas phase and in solution. *J. Chem. Phys.* **2007**, *126*, 184102.

(673) Thompson, L. M.; Harb, H.; Hratchian, H. P. Natural ionization orbitals for interpreting electron detachment processes. *J. Chem. Phys.* **2016**, *144*, 204117.

(674) Thompson, L. M.; Jarrold, C. C.; Hratchian, H. P. Explaining the $MoVO_4^-$ photoelectron spectrum: Rationalization of geometric and electronic structure. *J. Chem. Phys.* **2017**, *146*, 104301.

(675) Zhou, J.; Garand, E.; Neumark, D. M. Slow electron velocity-map imaging spectroscopy of the C_4H^- and C_4D^- anions. *J. Chem. Phys.* **2007**, *127*, 154320.

(676) Ko, Y. J.; Wang, H.; Cao, R.; Radisic, D.; Eustis, S. N.; Stokes, S. T.; Lyapustina, S.; Tian, S. X.; Bowen, K. H. Photoelectron spectroscopy of homogeneous nucleic acid base dimer anions. *Phys. Chem. Chem. Phys.* **2010**, *12*, 3535–3541.

(677) *CRC Handbook of Chemistry and Physics*, 81st; Lide, D. R., Ed.; CRC Press: 2000.

(678) Anpo, M.; Aikawa, N.; Kubokawa, Y.; Che, M.; Louis, C.; Giamello, E. Photoformation and structure of oxygen anion radicals (O_2^-) and nitrogen-containing anion radicals adsorbed on highly dispersed titanium oxide anchored onto porous Vycor glass. *J. Phys. Chem.* **1985**, *89*, 5689–5694.

(679) Schneider, J.; Matsuoka, M.; Takeuchi, M.; Zhang, J.; Horiuchi, Y.; Anpo, M.; Bahnemann, D. W. Understanding TiO_2 Photocatalysis: Mechanisms and Materials. *Chem. Rev.* **2014**, *114*, 9919–9986.

Index of Abbreviations Used

ADE	Adiabatic Detachment Energy
AFIR	Artificial Force Induced Reaction Method
ASE	Amplified Stimulated Emission
B88	Becke's 1988 functional
BBO	β-barium borate
BO	Born-Oppenheimer
CAS	Complete Active Space methods
CASPTn	Complete Active Space perturbative methods
CASSCF	Complete Active Space self-consistent field methods
CC	Coupled-Cluster
CCD	Charge-Coupled Device
CCSD	Coupled-Cluster Singles and Doubles
CCSD(T)	Coupled-Cluster Singles and Doubles with perturbative Triples
CCSDT	Coupled-Cluster Singles, Doubles, and Triples
CCSDTQ	Coupled-Cluster Singles, Doubles, Triples, and Quadruples
CF	Conflat
COM	Center of Mass
cryo-cryo-SEVI	Slow Photoelectron Velocity-Map Imaging of cryogenically cooled (dual trap configuration)
cryo-SEVI	Slow Photoelectron Velocity-Map Imaging of cryogenically cooled anions
cw	Continuous-Wave
DF	Dispersed Fluorescence
DFG	Difference Frequency Generation
DFT	Density Functional Theory
DH	Double Hybrid functional
DIB	Diffuse Interstellar Band
EA	Electron Affinity
eBE	Electron Binding Energy
ECP	Effective Core Potential
eKE	Electron Kinetic Energy
EL	Even-Lavie

EOM	Equation of Motion
FC	Franck-Condon
FEL	Free Electron Laser
FHI	Fritz Haber Institute
fIR	Far-IR
FPN	Fixed Pattern Noise
FTIR	Fourier-Transform Infrared Spectroscopy
fwhm	Full Width at Half Maxmimum
GGA	Generalized Gradient Approximation
GH	Global Hybrid functional
HF	Hartree-Fock
HR	High Reflector
HT	Herzberg-Teller
iIR	Intermediate-IR
IMS	Ion-Mobility Spectrometer
IR	Infrared
IR-cryo-SEVI	Slow Photoelectron Velocity-Map Imaging of cryogenically cooled and vibrationally pre-excited anions
IR-DFG	Infrared Difference Frequency Generation
IRMPD	Infrared Multiple Photon Dissociation
IRPD	Infrared Photodissociation
IR-UV2CI	Infrared-Ultraviolet Two-Color Ionization
IVR	Intramolecular Vibrational Energy Relaxation
JT	Jahn-Teller
KDC	Köppel-Domcke-Cederbaum
KTA	Potassium Titanyl Arsenate
KTP	Potassium Titanyl Phosphate
LBNL	Lawrence Berkeley National Laboratory
LIF	Laser Induced Fluorescence
LIR	Laser-Induced Reactivity
LN2	Liquid Nitrogen (N2)
LSDA	Local Spin-Density Approximation
MCP	Microchannel Plate
MCSCF	Multi-Configurational Self-Consistent Field Method
MEVELER	Maximum Entropy Velocity Legendre Reconstruction
MEVELER	Maximum Entropy Velocity Legendre Reconstruction
MGCF	Molecular Graphics and Computation Facility at Berkeley
mIR	Mid-IR
MO	Molecular Orbital
MOSC	Metal Oxide Space Cloud
MP	Møller-Plesset
MP2	Møller-Plesset Perturbation Theory (2nd order)

MPn	Møller-Plesset Perturbation Theory (nth order)
MRCI	Multi-Reference Configuration Interaction
Nd:YAG	Neodymium-doped Yttrium-Aluminum-Garnet
NEVPT2	N-Electron Valence Second-Order Perturbation Theory
NIO	Natural Ionization Orbital
nIR	Near-IR
ODH	Oxidative Dehydrogenation
OPA	Optical Parametric Amplication
OPO	Optical Parametric Oscillator
OR	Optical Rectification
PAD	Photoelectron Angular Distribution
PAH	Polycyclic Aromatic Hydrocarbon
PES	Photoelectron Spectroscopy
PFI-ZEKE	Pulsed-Field Ionization Zero Electron Kinetic Energy
pJT	pseudo-Jahn-Teller
QMF	Quadrupole Mass Filter
R2C2PI	Resonant Two-Color Two-Photon Ionization
RF	Radiofrequency
RPA	Random Phase Approximation
RT	Renner-Teller
SCF	Self-consistent Field
SEVI	Slow Photoelectron Velocity-Map Imaging
SFG	Sum-Frequency Generation
SHG	Second-Harmonic Generation
TD-DFT	Time-dependent Density Functional Theory
TFP	Thin Film Polarizer
TMP	Turbomolecular Pump
TOF	Time of Flight
TS	Transition State
TTL	Transistor-Transistor Logic
VDE	Vertical Detachment Energy
VMI	Velocity-Map Imaging
WKB	Wentzel-Kramers-Brillouin Theory
WMC	Wiley-McLaren
ZEKE	Zero Electron Kinetic Energy
ZGP	Zinc Germanium Phosphide
ZPE	Zero-Point Energy

Part Numbers

cryo-SEVI Components

This appendix attempts to catalogue most of the components that make up cryo-SEVI, though it is certainly abbreviated from the full list. As of this writing, a complete list of all orders made by Jongjin and Christian reside in the SEVI office, and maybe be a good source of hunting down part numbers if needed.

Pumps

Table 11.26: Pumps used for cryo-SEVI.

Region	Turbo Pump	Pumping Speed for N_2 (L/s)	Backing pump
1	Seiko Seiki STP-A2203C	2200	Welch DuoSeal 1397
2	Boc Edwards STP-H2001K	2200	Edwards E2M40
3	Shimadzu TMP-803M	800	Edwards E2M18
4	Shimadzu TMP-303M	320	Edwards E2M18
5	Seiko Seiki STP-400	420	Varian SD-300
Manifold	–	–	Welch DuoSeal 1400

The turbomolecular pumps used for cryo-SEVI are all connected *via* ConFlat seals to the chambers, while they are backed by mechanical pumps connected *via* Kwik Flange (KF) of various sizes (usually KF40 or KF25). There are also a number of other components involved, including thermocouple sensors for detecting the foreline pressure, solenoid valves to close the forelines, metal sieve traps, miscellaneous vacuum components, and a lead acid battery used for the detector turbo controller. Broadly, components for the pumps and associated plumbing are purchased from Duniway Stockroom, Kurt J Lesker, and Nor-Cal Vacuum, depending on availability and pricing. Below are common replacement parts and maintenance components purchased to keep the machine running.

Table 11.27: Various components associated with pumps.

Item	Vendor	Part Number
Oil Filter, Edwards E2M40	Duniway Stockroom	OF-22304041
V-Belt, Welch Model 1400	Duniway Stockroom	4L-340
V-Belt, Welch Model 1397	Duniway Stockroom	4L-490
Thermocouple Sensor Tube	Duniway Stockroom	DV-6R
KF40 Flange, Flex Coupling	Duniway Stockroom	KF40-FX20
KF40 Centering Ring	Duniway Stockroom	KF40-CR
KF40 Clamp	Duniway Stockroom	KF40-CP
KF40 Flange, Tee	Duniway Stockroom	KF40-TE
Mechanical Pump Oil	Duniway Stockroom	MPO-190-5
Flushing Fluid	Duniway Stockroom	DSFF-5
Humphrey solenoid valve	Kurt J Lesker Co	SE120A3SC310
Sorbent for Oil	McMaster Carr	7516T51
Pneumatic Angle Valve	MDC Vacuum	311074
NW-40 Angle Metal Sieve Trap	Nor-Cal Vacuum	FTA-6-1502-NWB
12-Volt, 8 Ah Lead Acid Battery	Home Depot	UB1280

Source

The ion source can be readily changed between using the ionizer and laser ablation sources, though some components are constants in both setups. Below are relevant components used to keep the EL valve running, backing gas, and bolts used on the flange. Importantly, the distance from the nozzle (i.e. start of expansion) and the skimmer are to remain constant, requiring two different spacers to be placed on the source flange to maintain this for the ionizer and the laser ablation setups. These use different length bolts, but both are M8 threads.

Table 11.28: Various components used in the ion source

Item	Vendor	Part Number
EL Gaskets	Potomec Photonics	Custom
Button Head Hex Drive Screw, M8, 55 mm Long	McMaster Carr	91239A450
Button Head Hex Drive Screw, M8, 35 mm Long	McMaster Carr	91239A438
Button Head Hex Drive Screw, M8, 40 mm Long	McMaster Carr	91239A442
Helium, 99.999% K Style Cylinder	Praxair	He 5.0UH-K

Additionally, any number of source gases may be required to produce the ions of in-

terest. Common vendors to procure these are Praxair and Sigma-Aldrich, both who sell a considerable variety of gaseous species, though Praxair tends to sell fewer hydrocarbons.

Ionizer

Many of the ionizer components are no longer sold by the original vendor, so we have had to procure a number of replacement parts from other vendors. Importantly, the wires purchased from GoodFellow can be complicated, as they no longer do business with UC Berkeley. This can be circumvented by directly purchasing these materials and getting reimbursed, however.

Table 11.29: Various components for the ionizer

Item	Vendor	Part Number
18-8 Stainless Steel Hex Nut 2-56 Thread	McMaster Carr	96537A110
99.95% Tungsten, 0.25mm	GoodFellow	W-00-WR-000150
99.0% Nickel, 0.75mm	GoodFellow	NI00-WR-000158
Thorated Tungsten	GoodFellow	W-14-WR-000170
Ionizer Voltage Supply	Kepco	APH 1000M
Ionizer Current Supply	Kepco	ATE 75-8M

Laser Ablation

Our laser ablation source is home-built, with many of the machine drawings readily accessible in the SEVI backup. Some components of this, however, are commercial and are outlined below. These include the laser and associated optics with telescoping the beam and directing it onto the target, as well as some components within the ablation setup itself. Importantly, sputtering targets from Kurt Lesker can be purchased that fit our target holder nicely. Thinner targets (such as the 1/8" graphite target below) can be purchased, though these require a washer be glued to the back so that the set-screws that hold the targets in place can grip the target while it is flush with the channel walls.

Table 11.30: Various components for the laser ablation set-up

Item	Vendor	Part Number
Nd:YAG laser	Litron	Nano S 120-20
Flashlamp for Nano S	Litron	FX25
532 nm Mirrors	NB1-K12	Thorlabs
532 nm coated UVFS lens (±500 mm)	LA4184-532	Thorlabs
DC motor	Faulhaber	1000001780
PTFE O-Ring 1/16 Fractional Width	McMaster Carr	9559K117
Water Chiller	Coherent	T255P
9 pin KF Adapter	MDC Vacuum	9153005
Switch Snap Action	Digikey	SW986-ND
Nd target, 1" diameter, 0.250" thick	Kurt J Lesker Co	EJTNDXX301A4
Graphite Target, 1" diameter, 0.125"	Kurt J Lesker Co	EJTCXXX501A2

Trap

The trap is by and large custom-built, though there are a considerable amount of commercial components integrated into this. Many of these are detailed below in the dual-trap build section, including the valve, driver, vacuum regulator, and many of the materials used in constructing the trap. The main difference with the current trap, however, is that it is cooled using a closed-cycle helium refrigerator, and the temperature is controlled by an external heater/controller. These components are detailed below:

Table 11.31: Various components associated with heating/cooling the trap.

Item	Vendor	Part Number
He cold head	Sumitomo	RDK-408D2
He refrigerator	Sumitomo	F-70L
Silicon Diode	Lakeshore (now Janis)	DT-670C-ET
Temp controller	Stanford Research Systems	CTC100
Cartridge Heater	Lakeshore (now Janis)	HTR-25-100

Additionally, the helium compressor itself sometimes requires service (see Section IV). The components required for such service are listed below

Table 11.32: Various components associated servicing the helium compressor.

Item	Vendor	Part Number
Gas clean-up adapter	Sumitomo	255919B2
Gas recharge adapter	Sumitomo	267191A
Dust Plug (size 8)	Sumitomo	44643

Detector

The detector comprises a home-built VMI apparatus coupled to a commercial MCP/phosphor screen assembly. The VMI is powered by a home-built power supply, while the MCPs and phosphor screen are powered by commercial high-voltage boxes and connected *via* SHV-5 and SHV-B connections, respectively. Further, the retractable MCP detector used for measuring ion time-of-flight is built from a linear translation stage coupled to two chevron-stacked MCPs, 1" in diameter and powered by another commercial power supply, connected once more *via* SHV-5.

Table 11.33: Various components associated with the detector.

Item	Vendor	Part Number
SHV-B Coax Connector	MDC Vacuum	9922005
High Voltage Power Supply (10 kV)	Spellman High Voltage	230-10R
6 kV Power Supply	Spellman High Voltage	SL6PN30/115Vac
Phosphor Screen	PHOTONIS	39082
CCD Camera	IDS	UI-2230SE-M
Linear Feedthrough	MDC Vacuum	663016

Laser

Aside from the laser itself, there are a number of items that are useful when aligning and characterizing the beam, a short list of these are detailed below.

Table 11.34: Various components for use with the lasers of SEVI.

Item	Vendor	Part Number
pyroelectric detector (IR detection)	Thorlabs	ES111C
Power Meter	Ophir	Nova II
High power head (for YAG)	Ophir	7Z02738
Low power head (for dye laser)	Ophir	7Z02622
WaveMaster	Coherent	33-2650
UV-Vis Spectrometer	Ocean Optics	USB4000
far-IR card	Thorlabs	VRC6
near-IR card	Thorlabs	VCR2
Flip Mount for 1" optics	Thorlabs	TRF90
Flip Mount for 1/2" optics	Thorlabs	TR05F90
CaF_2 Prism	Thorlabs	PS704

SHG

SHG is relatively simple, only requiring the use of the BBO crystals from Radiant Dyes and a harmonic separator (Inrad Optics, 752-104)

IR-DFG

Infrared Difference Frequency Generation (IR-DFG) is perhaps the most complicated laser configuration in SEVI. All of the required components are listed below.

Table 11.35: Various components for IR-DFG.

Item	Vendor	Part Number
$LiNbO_3$ crystal (48° cut)	Sirah Lasertechnik	DFM-3800-T
$LiNbO_3$ crystal (56° cut)	Sirah Lasertechnik	DFM-2400-T
400-800 nm achromatic half-wave plate	Thorlabs	AQWP05M-600
fast-responding pyroelectric detector	Thorlabs	ES111C
1064 TFP	CVI	TFP-1064-PW
1064 HRs	CVI	Y1-1025-45
long-pass filter, 900 nm cutoff	Thorlabs	FEL900
long-pass filter, 1100 nm cutoff	Thorlabs	FEL1100
CaF_2 mirror with 1064 coating	Eksma	Custom
CaF_2 mirror with 600-900 coating	Eksma	Custom

Raman Shifter

Raman-shifted light requires a number of optics, all of which are listed below.

Table 11.36: Various components for generated Raman-shifted light.

Item	Vendor	Part Number
+500 mm focus BK7 plano-convex lens	Thorlabs	LA1908-AB
900 nm cut-on long-pass mirror	Thorlabs	DMLP900
long-pass filter, 900 nm cutoff	Thorlabs	FEL900
long-pass filter, 1100 nm cutoff	Thorlabs	FEL1100
600-1100 nm Linear Polzarizer	Thorlabs	LPNIRE100-B

Electronics

While the majority of the voltage supplies used in SEVI are home-built, a few are commercial. Importantly, Bertan (now Spellman) produces the high-voltage power supplies that we use for any DC voltage greater than ~ 100 V.

Table 11.37: Various commercial electronics boxes

Item	Vendor	Part Number
WMP high voltage pulse boxes	DEI	PVX-4140
Quad power supply	Ardara	694301
Hex/Oct power supply	Ardara	695501
Power supply for WMC/MCPs	Spellman High Voltage	SL6PN30/115Vac

Miscellaneous

There are countless other components in cryo-SEVI that are not listed above or easily categorized, so a few selected components are listed below.

Table 11.38: Other components useful for SEVI

Item	Vendor	Part Number
Fuses for Variacs (12A, 250VAC)	Grainger	1BX44
Ion Gauge Controller	Granville-Phillips	307
Ion Gauge Controller	Terranova	934
pulse boxes	Quantum Composers	9528
Mixed Domain Oscilloscope	Tektronix	MDO3024

IR-cryo-SEVI Build

Item	Vendor	Part Number
Laser Components		
SureLite EX Nd:YAG	Amplitude	RVF # 161150
FL611-06 FLASHLAMP	Amplitude	203-001900
Optical Table, 0.9 x 1.8 m, M6 Threads	Newport	M-RPR-36-8
OPO/OPA system with far-IR extension	LaserVision	Custom
Optics		
1" mIR Enhanced Gold Mirror	Thorlabs	PF10-03-M02
1" CaF_2 lens	Thorlabs	La5370
VIS/IR Detector Card, 400 - 640 nm, 800 - 1700 nm	Thorlabs	VRC2
1" IR Bandpass Filter, 1.75 µm, FWHM = 500 nm	Thorlabs	FB1750-500
1" IR Bandpass Filter, 2.50 µm, FWHM = 500 nm	Thorlabs	FB2500-500
1" IR Bandpass Filter, 2.00 µm, FWHM = 500 nm	Thorlabs	FB2000-500
Aluminum Breadboard 8" x 8" x 1/2", 1/4"-20 Taps	Thorlabs	mb8
Aluminum Breadboard 4" x 6" x 1/2", 1/4"-20 Taps	Thorlabs	MB4
Magnetic Laser Safety Screen, 300 mm x 75 mm	Thorlabs	TPSM2/M
Lens Mount for 18 mm Optics, 8-32 Tap	Thorlabs	LMR18
2.40μm, 25mm, Infrared Longpass Filter	Edmund Optics	68-653
Periscope		
Rotating Beam Steering Assembly, Imperial	Thorlabs	Rs99B
Tip/Tilt Rotation Beam Steering Assembly, Metric	Thorlabs	RS99T
1.25" Studded Pedestal Base Adapter, 1/4"-20 Thread	Thorlabs	BE1
1" Pillar Post, 1/4"-20 Taps, L = 12"	Thorlabs	RS12
1" Pillar Post, 1/4"-20 Taps, L = 3", 8-32 Adapter Included	Thorlabs	RS3
Laser Enclosure		
Blackcore Foam Board	Blick Art	13202-2006
Table-Guard Connector	Kentek	PT-TGC1
Table-Guard Panels 36"x12"	Kentek	PT-TG36
Table-Guard Panels 6"x12"	Kentek	PT-TG6
Table-Guard Panels 12"x12"	Kentek	PT-TG12
Lens Tube Cover, 24" Long	Thorlabs	SC2L24
2 in. PVC Coupling	Home Depot	232750
Brewster Tubes		
304ss Tube, 0.12" Wall, 3/4" OD	McMaster-Carr	89495K195
DN25CF Mini ConFlat Flange, Non-Rotatable, 304ss	MDC Vacuum	110006
50mm x 5mm, 8-12μm Coated, ZnSe Window	Edmund Optics	39-438
Temperature and Humidity Probe		
Temperature and Humidity Data Recorder	McMaster-Carr	3272K57
Software/USB Cord for Temperature and Humidity Probe	McMaster-Carr	3053K91
Active USB 2.0 Extension Cable	Digikey	TL1877-ND

dual-trap SEVI Build

Below are all the components purchased to facilitate the dual-trap SEVI build.

Item	Vendor	Part Number
Octupole Rods	McMaster-Carr	1263K54
Hexapole Rods	McMaster-Carr	1263K48
Indium Foil	McMaster-Carr	8898N12
Vespel	McMaster-Carr	87405K48
Sapphire Windows	Edmund Optics	43-637
General Valve	Parker	009-1643-900
General Valve Driver - Iota One	Parker	060-0010-900
Vacuum Regulator	Matheson	SEQ3494
6-way Cross	Nor-Cal Vacuum	6C-800
Turbo	Pfeiffer	CKF00052
Edwards M28	Ideal Vaccum	P101034
Dual RF Power Supply Controller	Ardara	E-53-201
RF High-Q Head	Ardara	E-54-101
LN2 Cryostat	Lake Shore Cryotronics	A0/VPF-100
Trap Temp Controller	Lake Shore Cryotronics	335
HV Power Supply	Spellman	SL6PN30/115Vac
9528 Pulse Generator	Quantum Composers	9528-AT20-AT20-AT20 -AT20-IA15-S-S-US

Tips, Tricks, and other Lab-Lore

The SEVI lab has been built by generations of graduate students from the early days of anion PES, ZEKE, SEVI, cryo-SEVI, and now XX-cryo-SEVI. As the constructors of this lab are transient, and many of the components in the experiment are custom or home-built, the experiment requires a considerable amount of institutional knowledge (lab-lore) to upkeep.

While much of the history of the experiment is detailed in Chapter 2, some finer details are outlined below.

Source Components

Notes on the EL valve

The Even-Lavie vale works great, until it doesn't. During my time in the group, we've encountered a few issues with the valve that deserve note.

Backing Line Adapter

The gas line that backs the EL valve requires an adapter to connect the tubing to the quick-connect piece that mates with the valve. This adapter is built from a 1/2" to 1/16" Swagelok adapter coupled to the 7/16" fitting on the quick connect unit. To connect both female Swagelok components, a short stainless steel tube ($\sim$ 3/4" long, 1/16" OD, 1/32" ID) is used. This tube is easily cracked or broken if the gas line is dropped after being disconnected from the valve, or if the line is struck or bent through normal operation. For this reason, a hook/handle was installed on the mount that holds the chambers to hold the gas line when the chamber is vented.

Importantly, this component should be leak-tested frequently and rebuilt as needed. If the backing gas cylinder (source cylinder) is left closed, but the gas line is not vented/pumped out, a decrease in the pressure of the line over $\sim$30 minutes indicates that this is likely leaking. Spare parts have been purchased/machined and are in the grey tackle-box that contains parts of the EL valve. If more steel tubing is required, it should be cut by the machine shop - most methods we have available in the lab will crimp such a small tube, rendering it useless.

Rebuilding the Valve

In the event the valve starts leaking, it needs to be rebuilt. The procedure for this is outlined in the manual (both the physical copy and the scanned digital version on the lab computer), though a few point should be considered. First, when re-tightening the large nut that holds the body together, it is imperative that tightening is stopped as soon as resistance is encountered. Over-tightening this nut can cause the threading to be stripped, as occurred in 2017-2018, and required assistance from the machine shop to both remove the nut and re-thread this component. We were warned that given the tolerances involved, this procedure can only occur once more.

Additionally, the gaskets now used are not from the vendors of the EL valve, but custom-cut for us by Potomac laser-cutting, who cuts them out of Kapton. The machine drawing for this is on file with them, in the event more need to be ordered.

Rebuilding the Ionizer

The ionizer itself needs to be rebuilt with some regularity, and the procedure for this is not in the manual. If the ion signal is non-existent or very weak, the power supplies on the ionizer are shorting, or the ionizer itself is not glowing when powered, the machine should be vented and the ionizer inspected. Most commonly, the filament inside the ionizer will have worn out and shattered, requiring a rebuild. Most of the components required to rebuild this component reside in D6 (the FPES lab), including small forceps, a hex socket-head, the raw materials, and the spot-welder.

To rebuild the ionizer, it must be deconstructed first, by removing the three 2-56 threaded nuts on the back that hold everything together. From here, the back plate, white insulating spacers, and grounding plate/mesh should be removed to reveal the filament. Take note of the insulating spacers - these are easily cracked and so are rarely still circular, resulting in certain configurations not insulating the top plate from the grounding plate. Inspect the filament, which is likely damaged and/or disintegrated. If this is the case, the filament must be re-built.

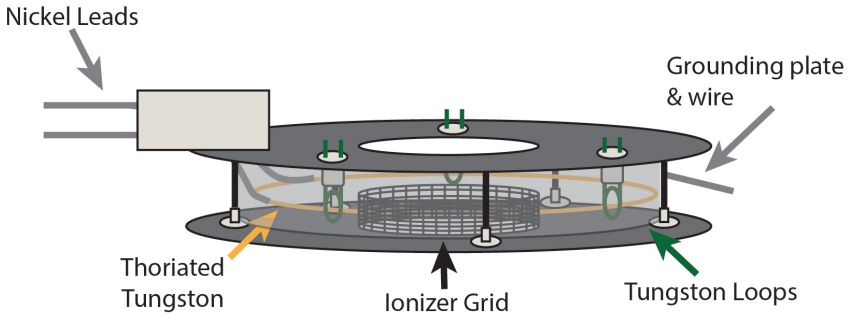

Figure 11.17: Schematic of the ionizer.

Often, this can be done without re-installing the small tungsten rings that hold the ionizer in place or the nickel leads that connect to the power supply (housed in the white plastic box). If this is the case, a piece of thoriated tungsten (0.2 mm diameter) should be cut ~ 3" long. This metal should be threaded through the existing tungsten loops and spot welded to both nickel leads. The spot welder resides in the FPES lab (Latimer D6) and should be set to 28 Watt-Seconds before use. Care should be taken to ensure the tips of the spot welder are not in contact with the mesh inside the ionizer, as this will burn a hole in the mesh. After welding, check that the wires are properly connected by lightly tugging on the tungsten and nickel leads.

These loops are held in isolating spacers that themselves are held in place by small set screws on the bottom of the ionizer - check that these set screws are tight. Leaving these loose may result in the filament shifting and breaking. From here, connection should be checked in the usual manner (between the leads and with the base plate). From here, the ionizer can be re-built by placing the grounding plate/mesh back (and ensuring that the lead on this is not in contact with the threaded rods that hold the entire apparatus together), followed by the base plate and nuts. Electrical connections should once again be checked.

In the event that the tungsten rings are damaged, these must also be reconstructed. Remove the insulating spacers that hold each of the the three rings by losing the set screws that hold these in place. Create new rings by cutting three pieces of tungsten (0.25 mm diameter) ~ 1" in length and bending into the appropriate shape by wrapping them around a 1/8" hex key. Feed the two excess pieces of metal through two holes diagonally separated and replace the spacers into the ionizer body, ensuring that the center of the rings are roughly level.

All metals involved are purchased from GoodFellow, though they currently have an issue with UC Berkeley and will not do business with them. This has required us to purchase the components on personal credit cards and file for reimbursement. Additionally, care should be taken when dealing with the mesh, as we do not own replacements and they are no longer manufactured commercially.

Notes on the Ablation Source

Much like the EL valve, the ablation source has worked remarkably well over the years, until it breaks.

Maintenance

There are a number of things that can be done to avoid damage to the laser ablation setup. First, when removing the ablation stage after use, there is often a fine powder of metal oxide coating the components. This coating can blown off of many components with compressed air, but care should be taken to clean the threads of the rod that holds the actual target. A cloth with methanol should be run thoroughly over these threads to avoid the stage locking, causing the translation motor to seize.

Additionally, the ablation and laser channels should be inspected and cleaned with some regularity. This can be done with the tool we keep near the ablation stage that has a small sharp tipped metal piece, allowing for the channels to be scraped clean. Following this, compressed air should be passed through these channels to ensure nothing remains. Inspection by eye should tell if the channels are clogged.

The ablation target and holder should also be inspected - the target should be flush with the spacer on the front of the target holder and have an even spiral pattern (unless already damaged) - deviations from this indicate motor issues. The target holder itself should be checked - the hexagonal hole cut in the back that mates with the motor drive shaft can be stripped and requires a new holder to be machined.

Repairs

The most common issues with the laser ablation setup are mechanical - a seizing of the motors or poor alignment. In the event that the Teflon spacer on the target holder needs replacement, spares are located in the yellow tackle box.

Deconstructing the ablation stage is non-trivial, as the torsion on the threaded rod can be significant (if the motors are seized) and can cause damage to components if not relieved. The simplest way to do this is to loosen the motor itself from the threaded rod.

To replace the motor itself, a new motor should be installed (spares should be available, if not, order more from Faulhaber). This should be physically connected first, then the electrical connections need to be soldered onto the leads on the back of the motor. Orientation of these leads need not be conserved (as this will only flip the direction in which the motor rotates).

Trap

The ion trap has been remarkably steady over the first near-decade of its life, but the effects of age are starting to show. Notably, in 2021, we had a few issues with electrical connections in the trap. These stemmed from the indium foil used for thermal and electrical contact, which is a semi-liquid and eventually "leaked" out of the seals, putting components in contact that should not be (namely, grounding the octupole rods by contacting them with the copper box surrounding them).

Additionally, the helium compressor and cold head have served us well, but are aging systems themselves with some quirks.

Below these considerations, and others, are outlined.

Daily Operation

The helium compressor needs to operate at pressures > 160 psi before an interlock triggers, requiring it to be serviced (see below). When operational, the compressor take 1 hour and 45

minutes to cool the ion trap from room temperature to 4 K, though this can be automated using the timer on the control panel that turns on the compressor at 6am ("prog").

If using the "prog" setting, the compressor will shut itself off at ∼5:30 pm, which can cause issues if the experiment is being run during this time, and especially if H_2 is used in the trap. For this reason, the compressor should always be taken off of "prog" once experiments have begun for the day.

The reason that H_2 in the trap is particularly problematic for the trap shutting off is that we operate below the freezing point of H_2 (14 K at 1 atm), meaning that a layer of H_2 freezes onto the trap walls while operating. Care must be taken to heat the trap slowly after use of H_2 to avoid a sudden evaporation of the frozen H_2, leading to pressure spikes that can be dangerous. For this reason, we usually ramp the trap temperatures up very slowly between 5-7 K, where we see large pressure spikes (from chamber pressures of 5×10^{-6} Torr to $\sim 5 \times 10^{-5}$). Once the pressure of this chamber has dropped to 1×10^{-7}, the trap temperature can be increased to 10 K slowly to ensure the complete expulsion of H_2. At this point the compressor can be turned off and the trap warmed for either venting or idle time.

Warming the trap after this point to a temperature of 280 K (i.e. above the freezing point of H_2O) currently takes nearly 4 hours, as the cartridge heater on the trap itself heats the inner stage of the trap rapidly, but can only heat the shield stage through radiative heating. As such, it might be advisable to install a second heater onto the shield at some point to expedite this process, as we often have to vent the source (and thus trap) region to service the valve.

Helium Compressor

Sometime in the mid 2010's, the helium compressor was mistakenly filled with low-quality helium (i.e. 99.0% instead of the required 99.9999% purity). The contaminants in the gas line introduced from the impurities in the helium resulted in freezing of the gases at near-cryogenic temperatures, requiring the unit to be serviced.

While everything is now operational, the compressor itself has a small leak, requiring that the helium be refilled every $\sim$ 6 months. This can be done by taking the 6.0 purity helium (i.e. 99.9999% pure) and wheeling it near the compressor, chaining it in this location, and attaching a CGA 580 regulator with a stainless steel SwageLok adapter. The regulator should be connected using plastic tubing to the adapter to the helium compressor, a brass piece with a needle valve. The adapter should be attached to the "He fill" port on the compressor, which requires that a brass plug be removed and this component screwed into place using a 3/4" wrench. At this point, the line needs to be flushed for 5 minutes with the helium - open the cylinder and regulator, passing $\sim$ 100 psi He through the line, leaving the SwageLok connector to the He compressor adapter loose.

After the allotted time, the SwageLok connection can be tightened and the needle valve on the adapter can be opened, allowing for He to enter into the compressor reservoir. The pressure in the compressor can be monitored using the gauge on the side of the unit. The

final goal is to fill this to 220 psi, so keep a hand on the needle valve and close this quickly so as to not overshoot.

At this point, disassemble in reverse; remove the adapter and cap the plug on the He compressor, close the cylinder, let the gas out of the line, close the compressor, disconnect all SwageLok and the regulator, return the cylinder to its storage location.

Altogether, this process will take $\sim$ 15 minutes.

All components required for this process should be resting atop the compressor unit, though the helium nanodroplet project at LBNL sometimes needs to borrow these.

It is **imperative** that the right helium is used to avoid further damaging the compressor or gas lines, so take care to check that 6.0 helium is used.

Flushing the Compressor

In the event that the compressor is filled with 5.0 helium (the source mix gas) or another gas, the entire system must be flushed. A protocol for doing so is printed and resides in the front pocket of the manual binder. This process requires the same tools, plus two special adapter fittings.

In brief, the gas-lines should be removed and plugged using a 5/4" wrench. From here, the two adapter fittings (P/N 255919B2) should be located, ensuring that their needle valves are closed. Attach them to the supply and return coupling on the compressor. Connect a 6.0 helium supply to the charge line and purge as described above. Fill to 220 psi, close the valves and run the compressor for at least 30 minutes to heat the oil inside this unit to operational temperature.

Open the vent valve on the supply coupling of the compressor and vent to 5-10 psi. Recharge to 220 psi, close all valves, and run the compressor for 30-45 seconds. Vent to 5-10 psi, recharge to 220 psi, and turn on for 30-45 seconds. Repeat this process 10 times.

Charge the compressor to 220 psi, then wait for the compressor to cool ($\sim$ 2 hours), top off once cooled to 220 psi. Close the cylinder, vent the line, remove the adapters, and re-attach the gas lines, checking for leaks.

Altogether, this process will take 3-4 hours.

Trap Repairs

In mid- and late- 2021, the trap required service as the electrical components began shorting (namely the DC voltage on the trap). This issue stems from the indium foil used to ensure electrical and thermal contact between components of the trap, which is semi-fluid. Over the years, it appears that some of this foil leaked out between mating parts, leading to errant electrical connections.

The trap was serviced by disconnecting the source chamber from the trap chamber, sliding it along the ion flight path to allow access to the entrance side of the trap. From here, the shield was able to be removed and the front plate was removed, allowing for servicing of the entrance electrode and aperture. Checking of electrical connection was performed both

inside the chamber and by checking the connections on the vacuum connectors, allowing for the pinpointing of the short location.

Later repairs were required as this plate was put back in slightly angled, leading to a connection between the octupole rods and the ring electrodes that surround it. Further, in late 2021, a similar issue came about with the exit electrode plate, requiring similar service, though accessing the exit plate is more challenging and required removal of the WMC plates and the entire trap assembly from the vacuum chamber by detaching it from the cold head of the helium compressor.

Lasers & Optics

While the optics involved in SEVI are not terribly complicated, there is a good bit of work that has been performed on the lasers that we use for (IR) cryo-SEVI, much of which is detailed below.

SureLite EX Divergence

At the end of 2020, the SureLite EX beam profile was found to be convergent in the horizontal direction, but not in the vertical direction, resulting in an ovular beam shape after a few meters, and resulting in focusing of the beam within the LaserVision OPO/OPA system.

In February of 2021 (when Amplitude's technicians finally decided to reply to our many emails), this was corrected by both tweaking the rear HR mirror in the oscillator cavity and adjusting the cylindrical lens at the output of the laser. The inclusion of this lens is to compensate for divergence in the oscillator beam profile, which is expected to occur along the vertical direction in Continuum/Amplitude Nd:YAG lasers. Rotating this optic then changes the correction of vertical divergence and thus the beam shape in the far-field.

The mount holding this optic is marked, along with the base it is mounted within, to denote the factory set position, which was rotated $\sim 5^o$ to correct the beam profile into something that was appropriate for our needs.

QuantaRay Pro

The SpectraPhysics QuantaRay Pro 290-30 that pumps our dye laser has been a thorn in the side of SEVI since its installation in 2017. Modifications by technicians were required to run the laser at the 20 Hz repetition rate needed for SEVI, instead of the 30 Hz the laser was engineered to operate at. It has no internal shutter, making warm-up tedious. And we've had quite a few issues with the stability of this laser's power output and beam profile. Outlined below are two sections - the first details repairs we have performed in-house and without the need for a technician, while the second outlines issues that have required a service visit from SpectraPhysics (now owned by Newport).

Repairs (for you)

The most common issue with this laser for quite some time was poor power output and bad power stability. The root cause of this is the rear mirror in the oscillator cavity (a 1064 nm HR mirror closest to the dye laser). This mirror tends to drift over time, disrupting the mode in the laser and decreasing the power output and beam profile. We've found that tweaking this mirror tends to be the most common trick to address the power.

Importantly, there are two set-screws that hold the mount in place in the vertical and horizontal direction, respectively. These for a long time were not tightened, worsening the drift of this mirror. Further, servicing of the laser in late 2021 revealed that a piezo-electric stage connected to this stage for injection seeded (which we do not use as the piezo is broken) was causing the mirror to move within the mount at random, worsening the power instability and pointing issues out of the laser. This piece has since been removed, and the stability appears to have improved following.

Concurrently with this issue is the collimation of the 1064 nm (and thus the 532 or 355 nm output), which again stems from poor alignment of this rear mirror. This was again addressed by a technician when visiting in 2021, who ended up replacing a few burnt optics in the amplifier cavity (burned due to bad alignment of the 1064 nm light through the amplifier cavity). The beam profile can additionally be corrected using this mirror, but steering through the rest of the laser cavity needs to be touched up on the two fold mirrors connecting the oscillator and amplifier cavities.

All tweaking of optics in the laser MUST be performed on long-pulse mode to reduce the potential for damage to the laser and optics contained therein, and often does not require use of the amplifier, which can be bypassed using a button on the control unit.

Repairs (for a technician)

Some repairs are beyond the scope of what we are capable of handling ourselves. Most electrical issues with the laser should be handled by trained technicians, especially those involving the flashlamps, which are pulsed at high enough voltages that they can cause serious harm to the user and/or the laser.

Additionally, if there are larger issues (such as a shattered YAG rod in the amplifier, leading to cooling water pouring out of the laser cavity - as happened in late 2017), these should immediately be handled by trained professionals.

Maintenance / General Advice

Maintenance of this laser is rather minimal, but should be performed with regularity. The cooling water level should be checked / topped up weekly, and totally flushed every ~ 6 months. Further, the air and water filters in the control unit should be checked on a similar time scale and replaced once their indicators show the need for this.

Changing flashlamps in this laser is relatively straight forward, though the system should be completely shut off, unplugged from the wall, and the existing flashlamps should be

grounded before being serviced. The flashlamps we use typically last for $\sim$ 1 year, depending on the amount of up-time for the other components of the experiment. Once these become cloudy or burned, they should be replaced, which should increase the output power modestly without impacting the beam steering significantly.

Again, using the appropriate flashlamps is imperative, as the system we have is old and the electronics are degrading slightly, leading to lower voltages applied to the lamps than operates the original ones were designed for. For this reason, we use special flashlamps that operate at lower simmer voltages (see Section 2.10).

Importantly, the power output of the QuantaRay, when fully functional, is substantially higher than what is needed for SEVI. To decrease the power output, we modulate the Q-switch timing relative to the flashlamp timing, with a delay different than 180 μs leading to a decrease in power. Importantly, we tend to operate $\sim 70\mu$s off of this value to give an output power of $\sim$ 1.5 W of 532 nm light. Here, is is important that this shift be positive (i.e. to 250 μs delay, not 110 μs), as this does not lead to a significant increase in the jitter of the laser.

Warming up the laser is typically performed at high powers for $\sim$ 30 minutes before decreasing the Q-switch delay time. Following this, the 532 or 355 nm power tends to decrease as the crystals used in the generation of these beams cool slightly and may require fine-tuning of the crystal angle periodically to regain sufficient green or UV light.

Detector Region

Baking the Chamber

It is often helpful to bake the detector chamber after venting it to service other components in this region, or if high photon energies (>4 eV) are to be employed.

Below is a protocol for baking the detector region (the only region to be baked, owing to the fact that all other regions use elastomer O-ring seals that can melt at baking temperatures.

1. Turn off all electronics and close the gate valve
2. Remove all electrical connections (other than VacCon)
    a) Three BNC connections on retractable detector
    b) Two BNC and one SHV-B on phosphor screen
3. Collect 4 VaryAcs (as of 7/2/20, SEVI has 2 working ones) and the clip ammeter
4. Plug the 4 power strips with heating tape connected to them into the VaryAcs and plug them into the wall - this usually requires them to be set on a chair near the sink

5. Turn on the VaryAcs to 25% of the listed amperage on each power strip (check this with clip ammeter
    a) Listed amperages are 1.2, 1.2, 1.4, and 2.4 A (going along the direction of travel for the ToF)
    b) Clip ammeter goes around just one wire of heating tape to read out DC current (first setting)
        i. Xbeam usually has the clip ammeter
6. Note pressure, date, time, and VaryAc settings in table in lab notebook
7. After several hours (6+), check the pressure and note it in the lab notebook. If the pressure is not high enough to be dangerous to increase, increase the amperage on the VaryAcs to 50% of the listed value. Let sit overnight
8. The next day, check the temperature of the chamber by hand - they should be warm to the touch. Repeat Step 7, moving the amperage to 100% of listed value (if needed for a full bake)
9. Let sit at 100%. The pressure will peak and begin to drop. The bake is complete when the pressure stabilizes on a value. You may need to degas the ion gauge at this point to confirm that the pressure has stabilized (depending on the pressure differential of start to finish).
    a) Note that the pressure read on the gauge will increase over the course of the day if running. We have noticed the room temperature increases throughout the day as we use the YAG, so this may be the cause.
10. Turn off all VaryAcs, unplug the powerstrips and VaryAcs, let the chambers cool overnight before replacing electrical connections.
11. The pressure should be lower than the initial value before baking
    a) If not, check that all Conflat is still tight - in 2018, I found heating tape sitting on a flange and that flange was no longer even hand tight; tightening the bolts here dropped pressures quickly and resolved this issue (did require another bake).
        i. Do this by waiting for cool chambers, then spray a little methanol on flange, if the pressure spikes, tighten this
        ii. Alternatively, there is a helium leak detector in the machine shop that can be used (as a more selective/better method than methanol). To date, SEVI has not used this, but LPES has.

Repairing VaryAcs

In the event that a VaryAc is giving you trouble, check the fuse on the front, as this likely has blown. Replacement fuses (12A 250V AC) are in the lab or can be readily ordered to replace this. Test that the fuse does not blow when powering the lamp in the lab to see if the VaryAc itself blew the fuse or if a bad connection with the heating tape is the cause.

In the event of bad heating tape, replace the heating tape with new tape, as the old tape can crack, leading to shorts and breaking the VaryAc fuses.

Retractable Detector

Care should be taken when moving the retractable detector, as the wires within the vacuum chamber are easily broken by too fast motion. Servicing the detector requires breaking vacuum in the detector region, which is not ideal. The signature of these broken wires are the sudden disappearance of ion signal without any other clear reason (check that ions are still being trapped, etc). An easy check can also be performed by sending high photon energy light into the detector and looking for electron signal from scattered light. Notably, the WMC-TOF plates still may show up on the readout from this detector, but they may look strange.

To service this component, the electronics in the detector region should be turned off, the gate valve closed, and the turbo spun down. Following this, close the foreline to the detector pump and loosen the Conflat flange holding the retractable detector in place, before opening the vent N_2 cylinder and opening the line into the detector chamber. Importantly, there is not a blow-off valve here, meaning that if the flange with the retractable detector is not loosened, the chamber can pressurize and rupture. As soon as the N_2 flow is begun into the chamber, pressure should be applied to the flange holding the retractable MCPs to try and remove them from the chamber. Within a few minutes (~ 3), the chamber should be vented sufficiently to remove this component. Cover the open flange with foil to prevent anything from getting into the machine, and examine the retractable detector.

Most commonly, the wires that connect to the MCPs are broken and need to be re-attached. These wires coil around the rod to which the MCPs are mounted and can be loosened slightly to reduce the tension on them, though a balance should be struck such that the wires cannot get into the ion path.

Ions

Producing ions is perhaps the most specialized skill of SEVI - doing so often feels more like an art than a science. Below are a few notes on this process.

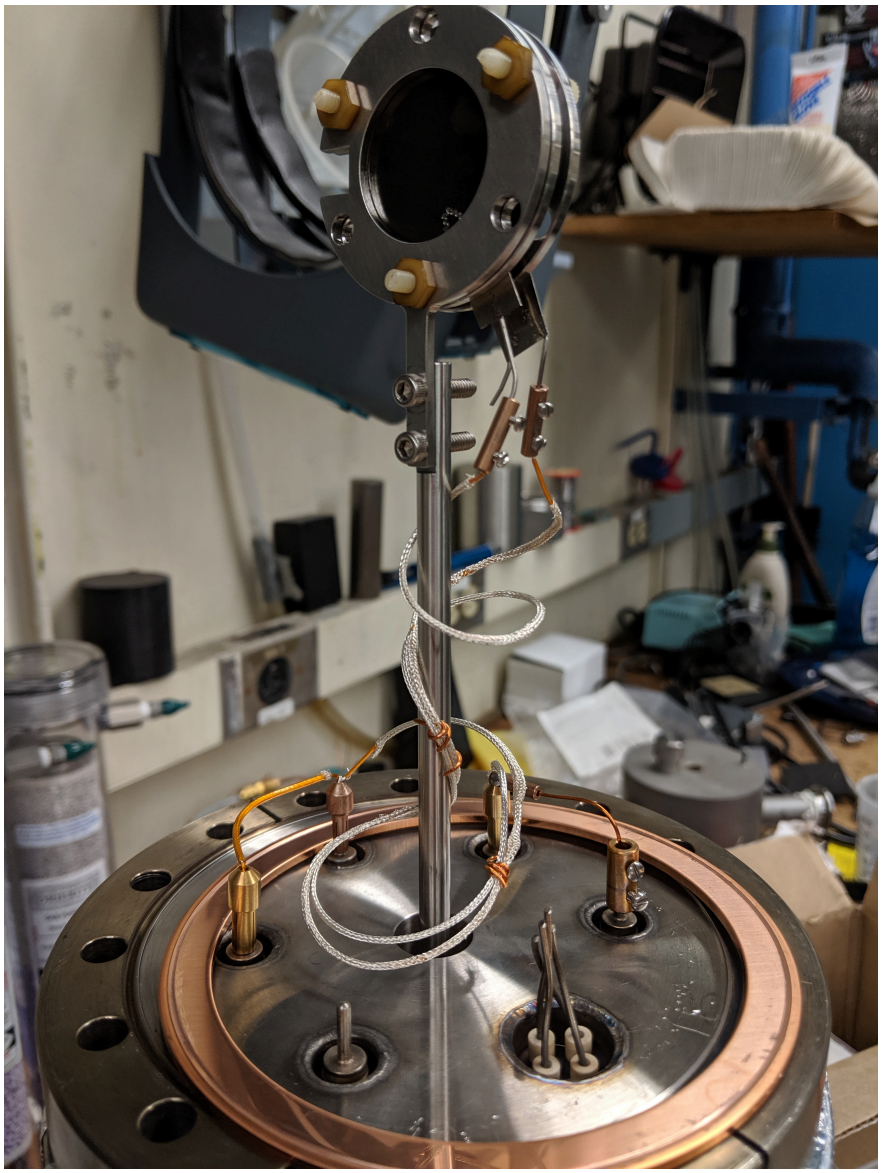

Figure 11.18: Photo of the retractable detector when being serviced.

Trapping Ions

In early 2020, we had an exceptionally hard time trapping NdO^- ions produced *via* laser ablation. It was possible that this was related to the degrading conditions of the ion trap, though those took another year to materialize.

To alleviate this, we produced carbon clusters with laser ablation - this method generates clusters ranging from 2-15 atoms readily, spanning a wide mass range. Optimizing the settings in the machine such that we trapped C_{13}^-, which has a similar mass to $^{144}NdO^-$ (156

vs. 160 amu, respectively), was found to give settings that also trapped appreciable NdO^- ions, allowing for a further optimization and successful study of these species.

As such, it should be viable to generate a simple species of similar mass to that of the desired species to be studied, optimize for this simple species, and change to the more complex species. This has yet to be seen for the ionizer, though it should likely behave similarly, barring impacts from chemistry occurring through collisions in the ion path or in the trap. Further, it may be possible to use carbon clusters for this trick irrespective of the source chemistry of the desired species - we have not yet tried doing so.

TOF issues

The distribution of ions entering the VMI region of the machine can also often cause issues. The most common issue is an ion packet striking the retractable detector that is not Gaussian in shape. This often stems from poor focusing of the ion packet out of the trap and into the WMC-TOF plates, as the donut-shaped distribution in the trap will lead to a double-Gaussian distribution on the retractable detector if not corrected. As such, the four knobs that control the einzel lens/deflector between the trap and WMC-TOF plates are key to regaining a Gaussian distribution of ions.

At times, there will be noise in SEVI images that is clearly not random. This often stems from poor steering of the ions into the interaction region, resulting in part of the ion packet clipping on an aperture, ejecting electrons with a high velocity vector along a direction. For instance, if the ion packet strikes the top left of the aperture, the ejected electrons will contain an appreciable velocity vector along the top and left directions, owing to the large velocity imparted to the ions from the WMC-TOF plates. These electrons are then collected with near unit-efficiency by the VMI plates.

Corrections for this often require use of both sets of deflector plates to correct for the ion path while retaining maximum intensity. In practice, this is done by tuning one plate (i.e. up/down for noise that is not perfectly horizontal, left/right for the opposite situation) to reduce the noise and with it the ion signal, then using the other plate that controls this direction to regain ion signal. This process is then iterated until the noise is sufficiently low, and for both the up/down and left/right directions.

Importantly, this noise can cause issues with image reconstruction as the centroid of the image is first calculated before MEVELER begins its procedure. If there is significant noise in an image, this center can be calculated incorrectly by a few pixels, introducing an artificial blur to the images.

General Lab Notes

Safety - design considerations

Lab can be a dangerous place, so there are many precautions that we take to avoid injury. First and foremost among these are design considerations to reduce risk of injury.

Campus dictates that a 3' walkway must be accessible throughout the lab for fire escape reasons. This is why the laser table is exactly 3 feet from the walls, and must be considered if adding new components to the lab.

Further, each lab requires 2 exits. Ours are the main entrance/exit and the exit in the LPES lab, which itself has an exit through a back hallway to the stairs. We currently use the hallway for group storage, meaning that this exit can be blocked at times. This should be checked/corrected with some regularity.

While we have a considerable number of 120V, 12A outlets (standard US outlets), there are far fewer of the specialized outlets we often need for high-power systems (lasers, turbo pumps, etc). It would be wise to confirm that something can be powered and still perform its desired function in the lab prior to purchase. For this reason, the power supply unit of the SureLite EX resides awkwardly under the dye laser - the power cord is short enough that it cannot be placed conveniently under the laser head.

Along these lines, extension cords can be used in some cases, but come in different gauges. It is imperative that the extension cord used is rated for the current drawn by the equipment it is to supply. This is particularly important for large mechanical pumps, as these cables can overheat, short, and crash the mechanical pump (and the rest of the experiment with it).

To further prevent fires, it is important to ground all flammable gas cylinders to avoid the build-up of static charge, which could lead to a spark. Fortunately, the atmosphere in each lab is fully cycled in 6 minutes, meaning that there should not be much build-up of gas in the lab from small leaks, but for a larger leak or while running a cylinder, this spark could be disastrous.

Maintenance

Of course, many of the issues detailed here can be avoided or delayed with proper maintenance, much of which can be done on a semi-annual maintenance day. This includes changing the oil in all of the mechanical pumps, checking the water level in the QuntaRay (along with the water and air filters), checking the molecular sieves in the mechanical pumps, and changing out the water in the cooling unit for the ablation motor setup.

This maintenance requires spinning down of the turbos, and thus, part of a day vented - a good opportunity to service anything in the chamber that might be a little off.

More regularly, the foreline N_2 should be checked to ensure the pressure delivered is above 85 psi and the cylinder itself contains more than 500 psi, as well as the venting N_2 cylinder and the backing He cylinder.

As mentioned above, flashlamps should be changed with some regularity, but this is likely closer to an annual update, depending on how long the lasers have been run.

Times

A list of the times certain things take.

- The turbos take 8.5 minutes to spin down with backing forelines open.
- The trap takes 1 hour, 45 minutes to cool from room temp to 4K and takes just under 4 hours to warm to 280 K from 4 K.
- Importantly, the manual outlines that the WMC pulse box (DEI boxes) should be left on ∼5 minutes after the power supplies for these are turned off to let current dissipate from the capacitors.
- When venting the main chambers (not the detector), filling with N_2 takes $\sim$ 5 minutes, depending on how much the needle valve is opened.
- The Nd:YAG that pumps the dye laser should be run at max power for 30-60 min before use to allow for complete warm-up. The SureLite EX has an internal timer that prevents the internal shutter from opening within 25 minutes of it being opened.

Computations

While I am not a professional theorist in the slightest, I have had the good fortune of working with many who have taught me a touch about their world. Below is much of what I have learned from them and from toying around with theory myself, but in no way should be considered a complete guide to theory.

I am most familiar with Q-Chem (4.0 - 5.4) and Gaussian (09 and 16), as these were the packages originally available on the Neumark group computational cluster in 2016 when I joined the group. Since, we have moved to the Molecular Graphics Computational Facility at UC Berkeley, which has much more computational power and many more resources.

Regardless, every package I have used first requires a guess geometry for the molecular structure before optimization. There are a number of graphical interfaces that simplify this considerably - namely GaussView and IQmol. I strongly recommend these for generating guess structures for calculations. Importantly, pay attention to bond lengths, angles, and generally the molecular symmetry. Geometry optimization calculations often exploit molecular symmetry to expedite the computations, so you can accelerate your calculations if you create a symmetric guess structure that shares a point group with the final structure you believe should be determined. This, however, can be limiting, as these codes will rarely

break symmetry, meaning that you may need to generate multiple guess structures to determine the true ground state. For example, NiO_2 is either linear or bent, so I created guess geometries of both linear and bent structures to optimize.

Often, there will be some theoretical work done on a system of interest for SEVI, so using the optimized geometries previously determined is a good starting point - though the literature rarely focuses on the structures of anions. In this case, a guess geometry that matches the neutral is likely a good starting point.

In all cases, however, both the singlet and triplet manifolds, as well as the doublet and quartet manifolds of states should be explored to determine the true ground state of the anion and neutral, respectively. Importantly, if the singlet/triplet (or doublet/quartet) splitting in the neutral is relatively small, we may access both manifolds of states *via* photodetachment, so this can come in handy. Further, it is not uncommon that we observe multiple isomers of molecules (especially those formed from laser ablation), so a thorough geometry search can be helpful in identifying contributions from other species. I should note, however, that we rarely find quartets to reside below doublets, and the same is true of triplets and singlets, though metal oxides tend to be the exception.

Upon finishing a geometry optimization, it is imperative to first check the vibrational frequencies - if they are negative (Guassian) or imaginary (Q-Chem), the structure you have optimized is effectively a transition state (saddle point) between two more stable geometries. Distorting the molecule slightly along the normal coordinate(s) that have these imaginary frequencies and re-optimizing should resolve the issue and give you an optimized structure with real, positive frequencies. Note, however, that this can at times indicate the level of theory is insufficient - in the case of NiO_2, I attempted many calculations at the ωB97X-D level of theory for linear species, all of which gave negative frequencies. This is a result of DFT not accurately capturing the multireference character of these molecules, resulting in a breaking of the molecular symmetry. This was corrected by performing multireference calculations - though these proved to be beyond the scope of my abilities and so we contacted a professional theorist.

From a successful calculation, you should be able to retrieve the molecular geometry, normal modes, vibrational frequencies, SCF energy of the structure, as well as the zero-point energy (ZPE) correction. The first three of these are required by ezSpectrum to simulate a PES spectrum, while the latter two can be used to calculate the ZPE-corrected electron affinity or adiabatic detachment energy of the structure, which can be matched with experiment. It is important to include ZPE corrections, as these often alter the ordering of low-lying states (i.e. linear and bent structures).

A comparison of values for different structures should always be done at the same level of theory and basis set, as changing either will introduce differences in these properties that cannot be easily disentangled. Further, running excited-state calculations should be done at the same level of theory for similar reasons. Because of these concerns, we have found that using large basis sets augmented with diffuse orbitals is best - as these are required to treat excited states and often are helpful for treating atomic orbitals.

Miscellaneous

To anyone about to write their thesis, or who is just joining SEVI - I strongly recommend reading the acknowledgements of the SEVI theses that predate you. I've found them to be a source of immense joy and scope - you're part of something much bigger than any one of us, and in the trenches, that's so easy to overlook. Take a moment and soak it in.

General Notes & Graduate School Advice

Befriend and be kind to the administrators you have to deal with - their goodwill is worth more than gold in graduate school. In particular, anyone who can help you with purchasing should be someone you frequently thank, as you will almost certainly need their help more often than any other admin.

Similarly, the folks in the machine shop, wood shop, and electrical shop are wildly helpful and kind - make a point to seek out their help, especially on projects that are out of your depth. Many of our electronics are home-built by students who had formal training in electronics, or at least a strong background in them - the avenues to learn this formally seem to have diminished, so don't kick yourself for not knowing this as well as they did.

Along these lines, I have found it always better to admit that I don't know something and ask questions than to feign knowledge. There's so much in grad school to learn about - the minutia of the experiment, science, relationships, and yourself - that it is always better to take the time and explore.

This is especially important in the first ~ 6 months of being a senior student. This time can be described as some mixture of overwhelming and terrifying - everything is now your responsibility, and Dan will ask a lot of you. I have found that he is very understanding of this challenge, so have faith that you will figure it out - we all have struggled through and so you will you.

Finally, during your time as a senior student, it is easy to lose scope of things as you get bogged down with everything. First, it is important to recognize that your to-do list will always be longer than you can realistically accomplish, so you must pick your battles. Second, don't get so swept up with this work as to ignore your coworkers - we're all in this together, and a sense of group camaraderie is beneficial to everyone. Third, at times you may feel pressured to finish things faster than they can be accomplished while also teaching your younger student / new postdoc - do not succumb to this temptation as it will bite you later. Training the next generation is a huge part of the job and will, in the long-run, be immensely worthwhile and satisfying.

Best of luck on your journey - it can be arduous, stressful, soul-crushing at times, but you'll make it through. And when you're done, or at least writing the final words in your thesis, you can look back at all you have accomplished, survived, and learned - and with this scope, I hope you can truly appreciate what you've done - its remarkable.

Code

Gaussian 16 Output Condenser

This code was built in Python 2.X to take the output file from Gaussian 16 (opt, opt+freq jobs) and determine

- if the calculation ran to completion / if there were errors
- what the final energy of the system is
- the zero point energy
- the final molecular geometry
- the frequencies and accompanying normal modes of the system

These are all output into a .txt file that should be easy to read and also includes these outputs reformatted for use with ezSpectrum.

Notes

This code will not work on other versions of Gaussian, which give slightly differently formatted output files, for which this code fails to work. Additionally, the most recent version of this code, as well as the code for Gaussian 09 can be found at my github (click here).

Code

```
#=============================================
#                   NOTES
#=============================================
#
# This was built to analyze and condense the output of Gaussian
    16 using DFT or wavefunction methods
# for opt OR opt+freq calculations.
#
```

```
# Input: python G16_OCv5.py input_name output_name
# (or whatever version this is on in case I forget to update the
   vX)
#
# Output: a text file (or .whatever you specify) formatted as
   follows:
#=================================
#=================================
#       Using G16 Version 5.0
#This section is for [input filename]
#   Success                TRUE/FALSE
#=================================
#=================================
#
#  Either: error code & last optimization step number
#  OR:      energy, method, zpe, frequency, normal modes calculated
#           input for ezSpectrum 3.0
#           input for re-orientation Wolfram code (in the same
   GitHub as this code)
#           There are options to create input information for
   MOBCAL (see section below)
#                this has not been tested on G16 outputs
#
#  Note: This code currenlty has support for B3LYP and wB97XD DFT
   methods
#        To add others, see line ~100 and add the method of
   interest
#
#  For updates to this code, check posts to the associated GitHub
   repo:
#  https://github.com/MarkCBabin/Calculation-Condenser
#  If issues arise, or for questions/request, contact
   markcbabin@gmail.com
#
#=================================
#              START
#              SCRIPT
#=================================

import sys

#=================================
```

```
#                    DEFINE
#                   VARIABLES
#============================================
titlebox = '='*100+'\n'
# annoying titlebox line I didn't want to rewrite a bunch

i = j = 0
# here i and j are counters for the number of times "Normal
    Termination"
# and "Error Termination" appear in the file. A succssful
    opt+freq calc
# will have i > 1, while a successful opt calc will have i = 1.
    Any
# failure in the Gaussian calculation will lead to j > 0.

inFile = sys.argv[1]
outFile = sys.argv[2]
f = open(inFile,'r')
# takes input from the user to select file from terminal and
    opens file
f1 = open(outFile,'a')
# takes input from user to select file from terminal and writes
    to it

freq = []
errorlines = []
symmetry = '␣The␣symmetry␣of␣this␣system␣has␣not␣been␣
    determined\n'
method = 'undetermined␣(i.e.␣not␣a␣supported␣format␣-␣contact␣
    markcbabin@gmail.com␣for␣fixes)\n'
energy = []
zpe = []
# zpe is the zero point energy
wavefunction = 0
# wavefunction is a variable to track whether or not a
    wavefunction-based method (i.e. MP2, MP4, coupled cluster)
# is employed. If so, the reporting of the final energy is
    different than DFT methods. This impacts the energy
# determination 'if' statments below.
```

```
#=====================================
#          TRANSLATIONS
#=====================================

numbertosymbol = {'␣1':'H␣', '␣2':'He', '␣3':'Li', '␣4':'Be', '␣
    5':'B␣', '␣6':'C␣', '␣7':'N␣', '␣8':'O␣', '␣9':'F␣',
    '10':'Ne', '11':'Na', '12':'Mg', '13':'Al', '14':'Si','15':'P␣
    ', '16':'S␣', '17':'Cl', '18':'Ar', '19':'K␣', '20':'Ca',
    '21':'Sc', '22':'Ti', '23':'V␣', '24':'Cr', '25':'Mn',
    '26':'Fe', '27':'Co', '28':'Ni', '29':'Cu', '30':'Zn',
    '31':'Ga', '32':'Ge', '33':'As', '34':'Se', '35':'Br',
    '36':'Kr', '37':'Rb', '38':'Sr', '39':'Y␣', '40':'Zr',
    '41':'Nb', '42':'Mo', '43':'Tc', '44':'Ru', '45':'Rh',
    '46':'Pd', '47':'Ag', '48':'Cd', '49':'In', '50':'Sn',
    '51':'Sb', '52':'Te', '53':'I␣', '54':'Xe', '55':'Cs',
    '72':'Hf', '73':'Ta', '74':'W␣', '75':'Re', '76':'Os',
    '77':'Os', '78':'Pt', '79':'Au', '80':'Hg', '81':'Tl',
    '82':'Pb', '83':'Bi', '84':'Po', '85':'At', '86':'Rn'}
# dictionary for atomic # -> atomic symbol
# this has been updated, needs to be tested that I didn't somehow
    mess up the syntax on this... Does not include the lanthanides
    or actinides

numbertomass = {'␣1':'␣1', '␣6':'12', '␣7':'14', '␣8':'16',
    '11':'23', '14':'28', '22':'48', '26':'56', '40':'91'}
# dictionary for atomic # -> atomic mass (for MOBCAL)
# this is limited to elements MOBCAL can handle


#=====================================
#              DO STUFF
#=====================================

for line in f:
        if 'Step␣number' in line:
                steps = line
        if 'The␣electronic␣state' in line:
                symmetry = line
        if '␣Frequencies␣--␣' in line:
                freq.append(line)
        if 'Error␣termination' in line:
                j = j+1
```

```
                errorlines.append(line)
        if 'Zero-point correction=' in line:
                zpe.append(line)
        if 'Normal termination' in line:
                i = i+1
# opens/searches the file for a number of useful things and
    writes to
# the desired output accordingly, except normal modes (see
    section below)
        if 'mp2' in line:
                method = 'MP2'
                wavefunction = 1
        if 'ccsd' in line:
                method = 'CCSD'
                wavefunction = 2
        if 'b3lyp' in line:
                method = 'B3LYP'
        if 'wb97x' in line: #this has not been tested; i am not
           sure if it is "x" or "xd"
                method = 'wB97X-D'
# determining the method (imporant later for determining
    energy)
        if wavefunction == 0:
        #if DFT: easy way to report final energy
                if 'SCF Done:' in line:
                        energy = line
# determining the final energy of a geometry changes depending on
    whether a wavefunction method
# or a DFT method is employed.
if wavefunction > 0:
# if wavefunction method; harder to report energy
        energy_index =[]
        f = open(inFile,'r')
        lines = f.readlines()
        #reset some variable
        with open(inFile) as myFile:
                for num, line in enumerate(myFile, 1):
                        if wavefunction == 1:
                                if 'MP2=' in line:
                                        energy_index.append(num)
                        if wavefunction == 2:
                                if 'CCSD=' in line:
```

```
                                                energy_index.append(num)
        energy.append(lines[energy_index[0]-1])
        energy.append(lines[energy_index[0]])
        energy1 = str(energy[0]) + str(energy[1])
        #make a string out of "energy" so we can clean this up
        energy2 = energy1.translate(None, '[]\n/ ')
        #cleans up this string
        energy3 = energy2.split('\\')
        final_energy1 = [energy3[k] for k in range(len(energy3))
            if method in energy3[k]]
        # this is called a list comprehension!!
        # performs the following for and if statements, without
            giving list index error
        #       for k in range(len(energy3)):
        #               if method in energy3[k]:
        #                       final_energy = energy[k]
        # which basically selects just the string containing the
            energy for the method employed
        final_energy2 = str(final_energy1)
        final_energy = final_energy2.translate(None,'[\']')
        # cleans up the output of the list comprehension so that
            the output is readable!

zpe1 = str(zpe)
zpe2 = zpe1.translate(None, "[]\\Hartree/Particle()zo-pnZ=' ")
# zero point energy cleanup


#=================================
#           WRITE
#            TO
#            FILE
#=================================

f1.write(titlebox+titlebox+'\t\t\t\t\tUsing G16OC Version
    4.0\n\t\t\t\tThis section is for ')
f1.write(str(inFile))
# writes header to file

#determining if the output terminated correctly or not
if i > 0:
        f1.write('\n\t\t\t\t\tSuccess:\tTRUE\n')
```

```
        f1.write(titlebox+titlebox+'\n')
        f1.write('␣The␣method␣is␣')
        f1.write(str(method) + '\n')
        if wavefunction == 0:
                f1.write(str(energy))
        if wavefunction > 0:
                f1.write('␣The␣final␣energy␣is␣' +
                   str(final_energy) +'\n')
        f1.write('␣The␣Zero-point␣energy␣=␣' + str(zpe2)+ '\n')
        f1.write(str(symmetry))
        f1.writelines(['%s' % item for item in freq])
# writes to file all the important info determined thus far!

if i == 0:
        f1.write('\n\t\t\t\tSuccess:\tFALSE\n')
        f1.write(titlebox+titlebox+'\nThis␣file␣did␣not␣terminate␣
           normally\n\n')

if j == 1:
        f1.write('\n\t\t\t\tSuccess:\tFALSE\n')
        f1.write(titlebox+titlebox+'\n')
        f1.write(str(errorlines[0]))
        f1.write(str(steps))

if j > 1:
        f1.write('\n\t\t\t\tSuccess:\tFALSE\n')
        f1.write(titlebox+titlebox+'\n')
        f1.write(str(errorlines[1]))
        f1.write(str(steps))
# completes the header for all cases I've encountered from
   Gaussian16
# this header should look a lot like what is described at the top.



#=============================================
#               NORMAL
#               MODES
#=============================================

f = open(inFile,'r')
lines = f.readlines()
```

```
norm_modes = []
# empty array, will populate with normal modes
mol_size = []
# used to calculate molecule size (see loop below)
motions = []
# ultimately the normal modes written into the file
input_orientations = []
# used to get geometry information from the file
geom = []
# ultimately the geometry written into the file
mulliken = []
# mulliken charges for each atom in molecule - used for MOBCAL
    input (see next section)
dummy = []
# used in determining molecular size - working on it.
with open(inFile) as myFile:
        for num, line in enumerate(myFile, 1):
                if '  Atom  AN  ' in line:
                        norm_modes.append(num)
                if '                    Distance matrix
                   (angstroms):' in line:
                        dummy.append(num)
                if '                          Input orientation:'
                   in line:
                        input_orientations.append(num)
                if ' Mulliken charges and spin densities:' in
                   line:
                        mullikenindex = num
                if ' Mulliken charges:' in line:
                        mullikenindex = num
        mol_size = dummy[0] - input_orientations[0] - 6
# this calculates, correctly, the molecule size by taking some of
    the keywords used
# in the Gaussin input and subtracting their difference the -7 is
    used to account for
# blank spaces, etc. in the file

if i > 0:
        for l in range(len(norm_modes)):
                for j in range(mol_size):
                        index = norm_modes[l]+j
                        motions.append(lines[index])
```

```
                motions.append('\n')
        for l in range(mol_size):
                index = input_orientations[-1]+l+4
                geom.append(lines[index])
        for l in range(mol_size):
                index = mullikenindex + l + 1
                mulliken.append(lines[index])
        f1 = open(outFile,'a')
        f1.write('\nNormal Modes:\n')
        f1.writelines(['%s' % item for item in motions])
        f1.write('Geometry:\n')
        f1.writelines(['%s' % item for item in geom])
        f1.write('\n\n\n')

# using the molecule size calculated above, this correctly
    populates
# the arrays 'geom' 'motions' and 'mulliken' which will be written
# to the file in this section (except 'mulliken' which is used
    below)

#=================================
#               MOBCAL
#               INPUT
#=================================
#
#       NOTE: THIS HAS NOT BEEN TESTED ON G16 OUTPUTS (built in
    G09 OUTPUT CONDENSER)
#
if i > 0:
        geom1 = []
        geom2 = []
        mulliken1 = []

## arrays of modified strings to correct for the MOBCAL input
####### NOTE: UN-COMMENT THE FOLLOWING 6 ROWS TO WRITE MOBCAL OUT
#       f1.write('MOBCAL INPUT:\n\n')
#       shortfilename = inFile.replace(".log","")
#       f1.write(str(shortfilename))
#       f1.write('.mfj\numbertosymboln1\n')
#       f1.write(str(mol_size))
#       f1.write('\nang\ncalc\n1.0000\n')
        for l in range(len(geom)):
```

```
                test = geom[l]
                Test = mulliken[l]
                j = l+1
                if j <= 9:
                        string1 = '      %d          ' % j
                        String1 = '     %d  ' % j
                if j >= 10:
                        string1 = '     %d          ' % j
                        String1 = '     %d  ' % j
                test1 = test.replace(str(string1),"")
                Test1 = Test.replace(str(String1),"")
                geom1.append(test1)
                mulliken1.append(Test1)
# clipping out the first part of each line
        for l in range(len(geom)):
                test = geom1[l]
                test1 = test[:2]
                geom2.append(test1)
# making a copy that is only the first 2 values of the shortened
    geom
# array. Used below to get the desired formatting
        geom3 = geom1[:]
# makes a copy of geom1 here for usage in the ezSpectrum section
    below
        for l in range(len(geom2)):
                test = geom1[l]
                Test = mulliken1[l]
                if geom2[l] in numbertosymbol:
                        test1 = test.replace('%s          0      
                            '%geom2[l], "\t")
                        length = len(test1)-2
                        string = numbertosymbol.get(geom2[l]) + '
                            '
                        Test1 = Test.replace(string,"")
                        string1 = numbertomass.get(geom2[l])

                        geom1[l] = test1[:length] + ' ' +
                            str(string1) + '\t' + Test1
# uses all parts created to finalize the format as MOBCAL
    reequires

#f1.writelines(['%s' % item for item in geom1])
```

```
#f1.write('\n\n')

#=================================
#              ezSpectrum
#                INPUT
#=================================

if i > 1:
        f1.write('*****************************')
        f1.write('ezSpectrum input')
        f1.write('*****************************\n\n')
        f1.write('  Geometry:\n')
        for l in range(len(geom)):
                test = geom3[l]
                if geom2[l] in numbertosymbol:
                        test1 = test.replace('%s           0       '
                           ' '%geom2[l], "       %s       "
                           "%numbertosymbol.get(geom2[l]))
                        length = len(test1)-2
                        geom3[l] = test1[:length] +  str('\n')
        f1.writelines(['%s' % item for item in geom3])
        f1.write('\n\n')

# this sections generates the normal modes input
# as of 4/28/2020, this works with molecules with up to 99 atoms
if i > 1:
        f1.write('  Normal Modes:\n')
        motions1 = []
        garbage = []
        Garbage = []
        Geom2 = []
        GEOM2 = []
        index = (len(motions) + 1) / (len(geom) + 1)
                # indexes number of sets of lines of normal modes
        for l in range(len(geom)+1):
                j = l+1
                if j <= 9:
                        string1 = '     %d  ' % j
                if j >= 10:
                        string1 = '    %d  ' % j
                garbage.append(string1)
        Garbage = garbage * index
```

```
        geom2.append("␣")
        Geom2 = geom2 * index
                # creates the appropriate string to be replaced
                   (for loop)
                # populates an array the correct number of times
        for l in range(len(motions)):
                test = motions[l]
                test1 =
                   test.replace(str(Garbage[l])+str(Geom2[l]),"␣␣␣
                   ␣␣")
                motions1.append(test1)
                # correctly formats the first part of each line
        f1.writelines(['%s' % item for item in motions1])
        f1.write('\n\n')

# this section generates the atom list used
if i >1 :
        f1.write('␣␣Atom␣list:\n')
        atomlist =  '"␣␣␣'
        spacing = '␣␣␣␣␣'
        for l in range(len(geom)):
                atomlist += numbertosymbol.get(geom2[l]) + spacing
                atomlist = atomlist.replace('␣␣␣␣␣␣', "␣␣␣␣␣")
        atomlist = atomlist + "␣␣"
        atomlist = atomlist.replace('␣␣␣␣␣␣␣', "␣␣")
        atomlist = atomlist + '"'
        f1.write(str(atomlist))
        f1.write('\n\n')

# this section generates the frequency input
if i > 1:
        f1.write('␣␣Frequency:\n')
        freq1 = []
        for l in range(len(freq)):
                test = freq[l]
                test1 = test.replace('␣Frequencies␣--␣␣', "␣␣␣␣␣␣␣
                   ")
                freq1.append(test1)
        f1.writelines(['%s' % item for item in freq1])
        f1.write('\n\n')

#=============================
```

```
#          REORIENTATION
#              INPUT
#=====================================

# this section generates the geometry re-orientation input
if i > 1:
        f1.write('*****************************')
        f1.write('reorientation input')
        f1.write('*****************************\n\n')
        test4 = "{"
        for l in range(len(geom)):
                test = geom3[l]
                test1 = "{"+test[14:]
                test2 = test1.replace("   ",",")
                test3 = test2.replace("\n","") +"}"
                test4 += test3 + ","
        test5 = test4 + ",};"
        test6 = test5.replace(",,","")
        f1.write(str(test6))
        f1.write('\n\n')



#=====================================
#                 END
#=====================================
```

LaserVision IR calculator

This code was written in HTML to determine the output wavelength of the LaserVision OPO/OPA, based on measurement of the OPO output wavelength. This can also be found at my github (click here).

Code

```
<html>
<head>
        <title> Unit Converter </title>
        <style>
        input::-webkit-outer-spin-button,
        input::-webkit-inner-spin-button {
                /* display: none; <- Crashes Chrome on hover */
                -webkit-appearance: none;
                margin: 0; /* <-- Apparently some margin are
                   still there even though it's hidden */
                }
        input[type=number] {
                -moz-appearance:textfield; /* Firefox */
                }
        /* These commands hide the arrows that normally show on a
           "number" type input field in html for all broswers
           (commented out to say which) */
        *{box-sizing: border-box;}
        .column {float: left; padding: 10px;}
                .left {width: 25%;}
                .left_right {width: 25%;}
                .right_left {width: 25%;}
                .right {width: 25%;}
        .row:after {content: ""; display: table; clear: both;}
        </style>
</head>
<!-- This creates a footer at the bottom of the page, used to
   hold the "Last Updated" section -->
 <style>
.footer {
  position: fixed;
  left: 0;
  bottom: 0;
  width: 100%;
```

```
  color: black;
  text-align: left;
}
</style>

<div class="footer">
  <p>  <center>YAG fundamental: 1064.216nm, as measured on
     3/29/21 <br> This page last updated: 4/1/21</center></p>
</div>



<body>
<font size ="5"><center>LaserVision
   Calculator</center></font><br><br>
<div class="row"><div class="column left">
        What is the OPO nIR wavelength? Measured in air (nm)
           <br><br>
        What is the YAG wavelength? Measured in air (nm) <br>
  </div>

<div class="column left_right" >
        <input type="number" id="userInput1"=></input><br><br>
        <input type="number" id="userInput2"=></input><br>
 </div>
<div class="column right_left" >
What is your desired frequency? (vac, cm<sup>-1</sup>)
</div>
<div class="column right" >
<input type="number" id="cm_desired"=></input><br><br>
</div>

</div>
<!-- gives an input box, defines it as a numeric input, and gives
   it an ID for the later functions -->
<hr width=100% align=center>
<style>
        *{box-sizing: border-box;}
        .column {float: left; padding: 10px;}
                .left {width: 25%;}
                .right {width: 25%;}
        .row:after {content: ""; display: table; clear: both;}
```

```
</style>
</head>
<body>
<!-- these got flipped in my head, so the function labels below
   are messed up. It was easier to change this than all
   variables! -->
<div class="row"><div class="column left">
iIR wavelength in vac (nm) is: <br><br>
iIR frequency in vac (cm<sup>-1</sup>) is: <br><br>
mIR wavelength in vac (nm) is: <br><br>
mIR frequency in vac (cm<sup>-1</sup>) is: <br><br>
</div>

<div class="column right" >
        </label>
        <input type="textbox" name="display"/>
        <br><br>
        <label for="displayValue"></label>
        <input type="textbox" name="display_cm"/>
        <br><br>
        <label for="displayValue"></label>
        <input type="textbox" name="display2"/>
        <br><br>
        <label for="displayValue"></label>
        <input type="textbox" name="display2_cm"/>
        <br>
</div>
<div class="column left_right" >
Should measure this nIR to use iIR: (air)<br><br>
Should measure this nIR to use mIR: (air)<br>
</div>
<div class="column right" >
</label>
        <input type="textbox" name="mIR_req"/>
        <br><br>
</label>
        <input type="textbox" name="iIR_req"/>
        <br><br><br><br>
<button onclick="ReadMe()">Confused? Read me!</button>
</div>
</div>
```

```
<!-- These create the output boxes for our calculated values! -->
    <script>
        document.getElementById("userInput1").onkeyup =
           function() {mIR();iIR();mIR_cm();iIR_cm()};
        document.getElementById("userInput2").onkeyup =
           function() {mIR();iIR();mIR_cm();iIR_cm()};
<!-- using "onkeyup" tells the javascript to run upon a keystroke
   being completed -->
<!-- this syntax says "once a key is released on either of these
   two boxes, run both functions" -->
        function mIR()
        {
        var OPO = document.getElementById("userInput1").value;
        var YAG_harmonic =
           document.getElementById("userInput2").value/2;
        var mIR_out = OPO*YAG_harmonic/(OPO-YAG_harmonic)
        var mIR_out_vac = mIR_out / 1.000273050027
        document.getElementsByName('display')[0].value=
           mIR_out_vac;
        }
<!-- function to calc mIR wavelength; takes two wavelengths and
   converts to the third -->
<!-- prints output to the 'display' tag on this page -->
        function iIR()
        {
        var OPO = document.getElementById("userInput1").value;
        var YAG = document.getElementById("userInput2").value;
        var mIR = OPO*(YAG/2)/(OPO-(YAG/2))
        var iIR_out = YAG*mIR/(mIR-YAG)
        var iIR_out_vac = iIR_out / 1.000273050027
        document.getElementsByName('display2')[0].value=
           iIR_out_vac;
        }
        function mIR_cm()
        {
        var OPO = document.getElementById("userInput1").value;
        var YAG_harmonic =
           document.getElementById("userInput2").value/2;
        var mIR_out = OPO*YAG_harmonic/(OPO-YAG_harmonic)
        var mIR_out_vac = mIR_out / 1.000273050027
        var mIR_cm = 10000000/mIR_out_vac
```

```
        document.getElementsByName('display_cm')[0].value= mIR_cm;
        }
        function iIR_cm()
        {
        var OPO = document.getElementById("userInput1").value;
        var YAG = document.getElementById("userInput2").value;
        var mIR = OPO*(YAG/2)/(OPO-(YAG/2))
        var iIR_out = YAG*mIR/(mIR-YAG)
        var iIR_out_vac = iIR_out / 1.000273050027
        var iIR_cm = 10000000/iIR_out_vac
        document.getElementsByName('display2_cm')[0].value=
           iIR_cm;
        }
document.getElementById("cm_desired").onkeyup = function()
   {mIR_required();iIR_required()};
        function mIR_required()
        {
        var mIR_cm = document.getElementById("cm_desired").value;
        var mIR_req_vac = 10000000/mIR_cm
        var mIR_req = mIR_req_vac * 1.000273050027
        var nIR_req = 532*mIR_req/(mIR_req-532)
        if (nIR_req < 710) {
                document.getElementsByName('mIR_req')[0].value=
                   "out of range";
                }
        else if (nIR_req > 880) {
                document.getElementsByName('mIR_req')[0].value=
                   "out of range";
                }
        else {
        document.getElementsByName('mIR_req')[0].value= nIR_req;
                }
        }
        function iIR_required()
        {
        var iIR_cm = document.getElementById("cm_desired").value;
        var iIR_req_vac = 10000000/iIR_cm
        var iIR_req = iIR_req_vac * 1.000273050027
        var nIR_req = 1064.216*iIR_req/(1064.216+iIR_req)
        if (nIR_req < 710) {
                document.getElementsByName('iIR_req')[0].value=
                   "out of range";
```

```
        }
else if (nIR_req > 880) {
        document.getElementsByName('iIR_req')[0].value=
           "out of range";
        }
else {
document.getElementsByName('iIR_req')[0].value= nIR_req;
        }
}
function ReadMe()
{document.write("To use the <q>LaserVision Calculator</q>
   enter values into the boxes above the horizontal line.
   Each column is a standalone calculator and requires
   all boxes above the line to be filled in to work.
   <br><br> The language in this calculator mirrors that
   of the LaserVision manual (specifically from the
   <q>Optical Theory of the System</q> page). Notably,
   the three abbreviations pulled are <br><br> nIR = near
   IR (710-880nm output of OPO) <br> iIR = intermediate
   IR (1.35-2.128 &mu;m output of OPO) <br> mIR = mid IR
   (4.7 &mu;m and beyond output of OPA) <br><br> Values
   to be entered must be in the units specified (nm on
   the left, wavenumber on the right) and must be numeric
   - they can be integers or contain decimals. Using the
   arrow keys will adjust the value by a full integer and
   trigger the calculator. <b>All values on the left
   column must be measured in air</b> (not using the vac
   setting on the WaveMaster), as the output is converted
   to vacuum. Similarly, the out of the right column are
   wavelenth values in air, not vacuum! The refractive
   index used here is the average refractive index over
   1.35 and 14 &mu;m - calculated as 1.000273050027 from
   this <a href='https://refractiveindex.info/?
shelf=other&book=air&page=Mathar-7.5'>reference</a>.
   Numerical testing (using <a href =
   'https://emtoolbox.nist.gov/Wavelength/Ciddor.asp'>
   this source</a>) has indicated that variance of the
   refractive index due to wavelenth, temperature,
   humidity, [CO<sub>2</sub>], and pressure cause
   differences less than 0.1 cm<sup>-1</sup> and so an
   average is sufficient for our needs, given the
   bandwidth of the LaserVision. <br><br> The calculator
```

```
            on the right currently assumes that the YAG
            fundamental is 1064.216, as measured by Mark on
            3/29/21 using the WaveMeter probe - this can be
            adjusted in the .html file if that has changed (only
            should if cavity is adjusted). <br><br> The output of
            the calculator should be clearly labeled, and the
            functions that do this calculation are triggered upon
            a keystroke. The rightmost calculator will report
            <q>out of range</q> if the desired frequency is not
            capable of being produced by the mIR or iIR output on
            the system (based on the nIR OPO output limitations
            stated in the manual). <br><br> To get out of this
            instructional page and back to the calculator, reload
            the page!")
        }
    </script>
</body>
</html>
```

Publications from Graduate Work

* indicates equal contribution.

1. **M. C. Babin**, M. DeWitt, J. Lau, H. Guo, D. M. Neumark "Spectroscopic Observation of Resonances in the F+NH_3 Reaction" (in preparation)

2. M. DeWitt, **M. C. Babin**, J. Lau, D. M. Neumark "High-Resolution Photoelectron Spectra of the Acetyl Anion" (in preparation)

3. **M. C. Babin**, M. DeWitt, J. Lau, D. M. Neumark "Photoelectron Spectra of NiO_2^- via Slow Electron Velocity-map Imaging" (in preparation)

4. Y. Li,* **M. C. Babin**,* S. Debnath, S. Gewinner, W. Schöllkopf, A. Lyalin, D. M. Neumark, K. Asmis "Structural Identification of Nickel Doped Aluminum Oxide Clusters $[NiAlO_{1-3}(Al_2O_3)_{1-3}]^+$ by Gas-Phase Vibrational Spectroscopy" *J. Phys. Chem. A* **125**, 9527 (2021).

5. **M. C. Babin**,* M. DeWitt,* J. A. DeVine, D. C. McDonald, S. G. Ard, N. S. Shuman, A. A. Viggiano, L. Cheng, D. M. Neumark "Electronic Structure of NdO via slow photoelectron velocity-map imaging spectroscopy of NdO^-" *J. Chem. Phys.* **155**, 114301 (2021).

6. M. DeWitt,* **M. C. Babin**,* D. M. Neumark "High Resolution Photoelectron Spectroscopy of Vibrationally Excited OH^-" *J. Phys Chem. A* **125**, 7260 (2021).

7. A. A. Taka,* **M. C. Babin**,* X. Sheng, J. A. DeVine, D. M. Neumark, H. P. Hratchian "Unveiling the Coexistence of Structural Isomers in the Hydrolysis of ZrO2: A Combined Computational and Photoelectron Spectroscopy Study" *J. Chem. Phys.* **153**, 244308 (2020).

8. **M. C. Babin**, M. DeWitt, M. L. Weichman, J. A. Devine, D. M. Neumark "High-resolution anion photoelectron spectroscopy of cryogenically cooled 4-atom silicon carbides" *Molecular Physics* **119** e1817596 (2020).

9. **M. C. Babin**, J. A. DeVine, M. DeWitt, J. F. Stanton, D. M. Neumark "High-Resolution Photoelectron Spectroscopy of Cryogenically Cooled NO_3^-" *J. Phys. Chem. Lett.* **11**, 395 (2020).

10. J. A. DeVine, **M. C. Babin**, K. Blackford, D. M. Neumark "High-Resolution Photoelectron Spectroscopy of the Pyridinide Isomers" *J. Chem. Phys.* **151**, 064302 (2019).

11. J. A. DeVine, **M. C. Babin**, D. M. Neumark "Photoelectron spectra of $Al_2O_2^-$ and $Al_3O_3^-$ via slow electron velocity-map imaging" *Faraday Discuss.* **217**, 235 (2019).

12. **M. C. Babin**, J. A. DeVine, M. L. Weichman, D. M. Neumark "Slow photoelectron velocity-map imaging of cold C_7^- and C_9^-" *J. Chem. Phys.* **149**, 174306 (2018)

13. J. A. DeVine, A. A. Taka, **M. C. Babin**, M. L. Weichman, H. P. Hratchian, D. M. Neumark "Slow Electron Velocity-Map Imaging of $TiO_3H_2^-$: Probing the TiO_2^- Dissociative Adduct" *J. Chem. Phys.* **148**, 222810 (2018)

14. J. A. DeVine, M. L. Weichman, C. Xie, **M. C. Babin**, M. A. Johnson, J. Ma, H. Guo, D. M. Neumark "Autodetachment from Vibrationally Excited Vinylidene Anions" *J. Phys. Chem. Lett.* **9**, 1058-1063 (2018).

15. J. A. DeVine, M. L. Weichman, B. Laws, J. Chang, **M. C. Babin**, G. Balerdi, C. Xie, C. L. Malbon, W. C. Lineberger, D. R. Yarkony, R. W. Field, S. T. Gibson, J. Ma, H. Guo, D. M. Neumark "Encoding of vinylidene isomerization in its anion photoelectron spectrum" *Science* **358**, 336-339 (2017).

16. M. L. Weichman, J. A. DeVine, **M. C. Babin**, J. Li, L. Guo, J. Ma, H. Guo, D. M. Neumark "Feshbach resonances in the exit channel of the F + $CH_3OH \rightarrow HF + CH_3O$ reaction observed using transition-state spectroscopy" *Nat. Chem.* **9**, 950-955 (2017).

17. J. A. DeVine, M. L. Weichman, **M. C. Babin**, D. M. Neumark "Slow photoelectron velocity-map imaging of cold tert-butyl peroxide" *J. Chem. Phys.* **147**, 013915 (2017).